



AGARD-R-754

# AGARD

ADVISORY GROUP FOR AEROSPACE RESEARCH & DEVELOPMENT

7 RUE ANCELLE 92200 NEUILLY SUR SEINE FRANCE

AGARD-Report No.754

## Special Course on Missile Aerodynamics

DTIC  
ELECTE  
JUL 18 1988  
S D  
E

NORTH ATLANTIC TREATY ORGANIZATION



DISTRIBUTION AND AVAILABILITY  
ON BACK COVER

88 7 15 022

NORTH ATLANTIC TREATY ORGANIZATION  
ADVISORY GROUP FOR AEROSPACE RESEARCH AND DEVELOPMENT  
(ORGANISATION DU TRAITE DE L'ATLANTIQUE NORD)

AGARD Report No.754  
SPECIAL COURSE  
ON  
MISSILE AERODYNAMICS



|                    |                                     |
|--------------------|-------------------------------------|
| Accession For      |                                     |
| NTIS GRA&I         | <input checked="" type="checkbox"/> |
| DTIC TAB           | <input type="checkbox"/>            |
| Unannounced        | <input type="checkbox"/>            |
| Justification      |                                     |
| By                 |                                     |
| Distribution/      |                                     |
| Availability Codes |                                     |
| Avail and/or       |                                     |
| Dist               | Special                             |
| A-1                |                                     |

The material assembled in this book was prepared under the combined sponsorship of the Fluid Dynamics Panel, the von Kármán Institute and the Consultant and Exchange Program of AGARD and was presented as an AGARD Special Course at the von Kármán Institute, Rhode-Saint-Genèse, Belgium on 30 March-3 April 1987, and as Short Courses at Athens, Greece on 18-19 May 1987 and at Ankara, Turkey on 21-22 May 1987.

## THE MISSION OF AGARD

According to its Charter, the mission of AGARD is to bring together the leading personalities of the NATO nations in the fields of science and technology relating to aerospace for the following purposes:

- Recommending effective ways for the member nations to use their research and development capabilities for the common benefit of the NATO community;
- Providing scientific and technical advice and assistance to the Military Committee in the field of aerospace research and development (with particular regard to its military application);
- Continuously stimulating advances in the aerospace sciences relevant to strengthening the common defence posture;
- Improving the co-operation among member nations in aerospace research and development;
- Exchange of scientific and technical information;
- Providing assistance to member nations for the purpose of increasing their scientific and technical potential;
- Rendering scientific and technical assistance, as requested, to other NATO bodies and to member nations in connection with research and development problems in the aerospace field.

The highest authority within AGARD is the National Delegates Board consisting of officially appointed senior representatives from each member nation. The mission of AGARD is carried out through the Panels which are composed of experts appointed by the National Delegates, the Consultant and Exchange Programme and the Aerospace Applications Studies Programme. The results of AGARD work are reported to the member nations and the NATO Authorities through the AGARD series of publications of which this is one.

Participation in AGARD activities is by invitation only and is normally limited to citizens of the NATO nations.

The content of this publication has been reproduced directly from material supplied by AGARD or the authors.

Published April 1988  
Copyright © AGARD 1988  
All Rights Reserved

ISBN 92-835-0452-6



Printed by Specialised Printing Services Limited  
40 Chigwell Lane, Loughton, Essex IG10 3TZ

## PREFACE

This volume is a compilation of the edited proceedings of the "Missile Aerodynamics" course, held at the Von Kármán Institute (VKI) in Rhode-Saint-Genèse, Belgium, from March 30 to April 3, 1987. A condensed version of this course has been presented at the Air Academy in Athens, Greece, 18–19 May 1987 and at the Development and Research Department in Ankara, Turkey, 21–22 May, 1987.

This series of lectures supported by the AGARD Fluid Dynamics Panel and the Von Kármán Institute followed previous courses organized at VKI: 1974 (VKI LS67), 1976 (VKI LS88) and 1979 (AGARD LS98). This course was intended for practical engineers and researchers, beginners or experienced professionals, for military and engineering teaching institutions. The speakers, from industry and research establishments, paid particular attention to illustrate their presentation with numerous practical applications.

In recent years remarkable progress has been made in the field of tactical missile aerodynamics by theoretical and by experimental means and the objective of this course was to present the current state of the art in fundamental knowledge and in practical predictive methods (semi-empirical and numerical), with future trends. Special attention was focussed on nonlinear aerodynamics and unconventional configurations such as airbreathing missiles. For the first time numerical methods based on the resolution of the Euler equations with flow separation vortices were included in a course specific to missiles. In addition to the general aspects of missile aerodynamics, the course also dealt with particular problems such as the aerodynamics of air intakes, kinetic heating and base flows. The design of the next generation supersonic and hypersonic missiles was discussed in the last lecture.

We want to thank all the speakers for their outstanding work and AGARD and VKI for the organization of this course. Our thanks also go to the local coordinators in Athens and Ankara for their hospitality.

\*\*\*

Ce volume regroupe les notes concernant le cours "Aérodynamique des Missiles" présenté à l'Institut Von Kármán (VKI) de Rhode-Saint-Genèse, Belgique, du 30 Mars au 3 Avril 1987 et dont une version condensée a été présentée à l'Académie de l'Air d'Athènes, Grèce, les 18–19 Mai 1987 et au Département Recherche et Développement d'Ankara, Turquie, les 21–22 Mai 1987.

Ce cycle de conférences conçu et réalisé sous l'égide du Panel de Dynamique des Fluides de l'AGARD et du VKI faisait suite à des cours similaires organisés au VKI en 1974 (VKI LS67), 1976 (VKI LS88) et 1979 (AGARD LS98). Ce cours était destiné aux ingénieurs de l'industrie et aux chercheurs, débutants ou confirmés, ainsi qu'aux militaires et écoles d'ingénieurs. Les conférenciers appartenant au secteur industriel et à des organismes de recherche s'attachèrent à illustrer leur présentation avec de nombreuses applications pratiques.

Des progrès considérables ayant été réalisés ces dernières années dans le domaine de l'aérodynamique des missiles tactiques aussi bien par voie théorique que par voie expérimentale, ce cours avait pour but de présenter l'état actuel des connaissances fondamentales et des méthodes de calcul utilisées (semi-empiriques et numériques) avec leur évolution future. Une attention toute particulière a été apportée aux effets non-linéaires et aux configurations non conventionnelles telles que les missiles aérobies. Pour la première fois les méthodes numériques basées sur la résolution des équations d'Euler avec prise en compte de structures tourbillonnaires ont été développées dans un cours spécifique aux missiles. Outre les aspects généraux de l'aérodynamique des missiles, les sujets traités au cours des conférences englobaient certains problèmes particuliers tels que l'aérodynamique des prises d'air, l'aérothermique et les écoulements de culot. La conception des missiles supersoniques et hypersoniques futurs a été présentée en conclusion de ce cours.

Nous tenons à remercier tous les conférenciers pour l'excellent travail qu'ils ont accompli ainsi que les organisateurs de l'AGARD et du VKI sans qui ce cours n'aurait pu avoir lieu, sans oublier les coordinateurs locaux de la Grèce et de la Turquie pour leur hospitalité.

R.G.Lacau  
Directeur du cycle de conférences

#### SPECIAL COURSE STAFF

Special Course Director: Mr R.G.Lacau  
Aérospatiale — Annexe des Gatines  
Service ECS/AT  
91370 Verrière le Buisson  
France

#### LECTURERS

|  |  |
|--|--|
| Mr R.G.Lacau<br>(See Course Director)  | Mr A.B.Wardlaw, Jr<br>Naval Surface Weapons Center<br>New Hampshire Avenue<br>Silver Spring, MD 20910<br>USA               |
| M.J.Chattot<br>MATRA<br>37 Avenue Louis Breguet<br>92140 Velizy<br>France                              | Dr J.E.Williams<br>McDonnell Douglas Astronautics Co.<br>St. Louis Division — Box 516<br>St. Louis — Missouri 63166<br>USA |
| M.J.Delery<br>ONERA<br>4 rue des Vertugadins<br>92190 Meudon<br>France                                 | Dr M.F.E.Dillenius<br>Nielsen Engineering & Research Inc.<br>510 Clyde Avenue<br>Mountain View<br>CA 94043-2287<br>USA     |
| Dr H.Fuchs<br>Dornier GmbH<br>Postfach 1420<br>7990 Friedrichshafen 1<br>Federal Republic of Germany   | Dr M.J.Hemsh<br>PRC Kentron<br>303 Butler Farm Road<br>Suite 100<br>Hampton<br>VA 23666<br>USA                             |
| Dr R.Kapp<br>Dornier GmbH<br>Postfach 1420<br>7990 Friedrichshafen 1<br>Federal Republic of Germany    |  |
| Mr C.S.Jell<br>Naval Weapons Division<br>FFC 67<br>POB 5<br>Filton — Bristol BS12 QW<br>United Kingdom |  |

#### LOCAL COORDINATOR

Professor J.Wendt  
Von Kármán Institute for Fluid Dynamics  
Chaussée de Waterloo 72  
B-1640 Rhode St. Genèse  
Belgium

#### AGARD REPRESENTATIVE

M.C.Fischer  
Fluid Dynamics Panel Executive  
AGARD  
7 rue Ancelle  
92200 Neuilly sur Seine  
France

## CONTENTS

|   | Page      |
|---|-----------|
| PREFACE   | iii       |
| SPECIAL COURSE STAFF  | iv        |
|   | Reference |
| AN INTRODUCTION TO TACTICAL MISSILE AERODYNAMICS<br>by R.G.Lacau  | 1         |
| ACCURACY CRITERIA FOR EVALUATING SUPERSONIC AERODYNAMIC COEFFICIENT<br>PREDICTIONS<br>by J.E.Williams and R.J.Krieger | 2         |
| SURVEY ON NONLINEAR EFFECTS<br>by M.F.E.Dillenius and S.C.Perkins, Jr   | 3         |
| SEMI-EMPIRICAL METHODS FOR CONVENTIONAL AND UNCONVENTIONAL MISSILES<br>by M.J.Hensch                                  | 4         |
| SPACE MARCHING EULER SOLVERS<br>by A.B.Wardlaw, Jr  | 5         |
| NUMERICAL METHODS: EULER TIME DEPENDENT SOLVER<br>by J.J.Chattot  | 6         |
| PREDICTION OF DYNAMIC DERIVATIVES<br>by H.Fuchs and R.Kapp  | 7         |
| AIR INTAKE AERODYNAMICS<br>by C.S.Jell  | 8         |
| SEMI-EMPIRICAL METHODS FOR AIRBREATHING MISSILES<br>by J.E.Williams and R.J.Krieger                                   | 9         |
| AERODYNAMIC HEATING OF MISSILES<br>by R.Kapp, H.Mathauer and H.Rieger   | 10        |
| PREDICTION OF BASE-FLOWS<br>by J.Delery and R.G.Lacau   | 11        |
| NEXT GENERATION MISSILE DESIGN<br>by J.E.Williams and R.J.Krieger   | 12        |

**AN INTRODUCTION  
TO TACTICAL MISSILE  
AERODYNAMICS**

*R.G. LACAU*

**aérospatiale - DIVISION ENIGNS TACTIQUES  
92320 CHATILLON - France**

**SUMMARY**

The present lecture provides a general review of tactical missile aerodynamics considerations. The different aspects considered are : the general aerodynamics design with some problems encountered on existing and future missiles, the specificities of tactical missile aerodynamics and a survey of the most important semi-empirical and numerical methods. The semi-empirical methods has led to the development of a large variety of practical tools, not expensive in computer time they are routinely used by the project engineers, but they are restricted to conventional missile and global aerodynamics. The numerical methods, much more recent, which consist of solving the Navier-Stokes equations, the Euler equations, the full potential equation and the linearized equation are essential to treat complicated configurations, to determine load distributions and local flow field properties. In each case, a list of various codes is provided with their actual capabilities.

**TABLE OF CONTENTS**

**SUMMARY**

**1. INTRODUCTION**

**2. GENERAL AERODYNAMIC DESIGN CONSIDERATIONS**

- 2.1. INTRODUCTION TO TACTICAL MISSILES
- 2.2. TACTICAL MISSILE DESIGN
- 2.3. TYPES OF CONFIGURATIONS
- 2.4. TYPES OF PROPULSION
- 2.5. TYPES OF CONTROL
  - 2.5.1. AERODYNAMIC CONTROLS
  - 2.5.2. JET CONTROLS
- 2.6. CONTROL CONFIGURATIONS
- 2.7. TRENDS IN TACTICAL MISSILE DEVELOPMENT
- 2.8. IMPROVEMENT AREAS AND CONTRIBUTING FACTORS

**3. MISSILE AERODYNAMICS**

- 3.1. SPECIFICITIES OF TACTICAL MISSILE AERODYNAMICS
  - 3.1.1. DIFFERENCES BETWEEN AIRCRAFT AND MISSILES
  - 3.1.2. MAIN CHARACTERISTICS OF MISSILE AERODYNAMICS
- 3.2. AERODYNAMIC ANALYSIS
  - 3.2.1. GLOBAL AERODYNAMIC STUDIES
  - 3.2.2. LOCAL AERODYNAMIC STUDIES
  - 3.2.3. PARTICULAR AERODYNAMIC STUDIES
- 3.3. STUDIES OF FUTURE INTEREST

**4. COMPUTATIONAL METHODS**

- 4.1. SEMI-EMPIRICAL METHODS
  - 4.1.1. PRINCIPLES
  - 4.1.2. NORMAL FORCE AND CENTER OF PRESSURE OF BODIES
  - 4.1.3. NORMAL FORCE AND CENTER OF PRESSURE OF WINGS
  - 4.1.4. INTERACTIONS
  - 4.1.5. GLOBAL FORCES AND MOMENTS
  - 4.1.6. SURVEY OF SEMI-EMPIRICAL PROGRAMS
  - 4.1.7. CONCLUDING STATEMENT
- 4.2. NUMERICAL METHODS
  - 4.2.1. NAVIER-STOKES EQUATIONS
  - 4.2.2. EULER EQUATIONS
  - 4.2.3. FULL-POTENTIAL EQUATION
  - 4.2.4. LINEARIZED POTENTIAL EQUATION
  - 4.2.5. GRID GENERATION
  - 4.2.6. GEOMETRY DEFINITION

**5. CONCLUSION**

**REFERENCES**

- LIST A : TEXT REFERENCES
- LIST B : TABLE REFERENCES

**FIGURES**

**TABLES**

## 1. Introduction

During the last few years remarkable progress has been made in the field of tactical missile aerodynamics by theoretical and experimental means.

The aim of this special course is to present the current state of the art in fundamental knowledge and in predictive methods. Special attention will be focussed on non-linear aerodynamics and on airbreathing configurations.

In this first lecture we shall give a general survey of tactical missile aerodynamics with aerodynamic problems encountered on existing and future missiles and of the most important computer codes. The lecture is divided into three parts.

The first part is concerned with general aerodynamic design considerations. It presents the tactical missiles with the various types of geometrical configurations, propulsive systems and control systems. Because of the high level of maneuverability needed by actual and future missiles, the control system is more than ever the heart of the aerodynamic design of a guided missile. So, each type of control systems will be presented with its advantages and disadvantages. Trends in tactical missiles will be given for each missile family and we shall attempt to determine for future missiles the associated new aerodynamic problems. A brief look on improvement areas and contributing factors for improved performance ends this first part.

The second part presents the specificities of tactical missile aerodynamics and the different aerodynamic tasks and problems involved in tactical missile aerodynamic studies which are classified in global, local and particular aerodynamic studies.

The third part is dedicated to computational methods used for estimating the aerodynamic characteristics of different configurations. These predictive methods fall into two categories. Category 1 includes semi-empirical methods based on a component buildup approach which couples simple theories and data correlations together to take advantage of the strength and minimize the weakness of each one. These codes which need only a minimal amount of computer time are the main engineering tools for the project engineers. Nevertheless they are mainly restricted to conventional missile and global aerodynamics. Twenty-five programs used by different industries and research laboratories with their actual capabilities and limitations are listed. Category 2 includes numerical methods, more and more important with the increasing speed and the size of computers and the increasing development of new algorithms. In comparison to semi-empirical methods they can be used to treat complicated configurations and provide a better modelling of the physics of the flow field. This paper summarizes the actual capabilities and limitation of several full Navier-Stokes codes, parabolized Navier-Stokes codes, Euler codes, full potential codes and linear potential codes used by industry and research laboratories.

## 2. General aerodynamic design considerations

### 2.1. Introduction to tactical missiles

A tactical missile is a moving body flying in the atmosphere, self-propelled, expendable, pilotless, guided and controlled either remotely or by an autopilot; its purpose is to destroy a static or moving target by a direct hit or explosion of a warhead, normally of conventional design, sometimes with low nuclear power.

A tactical missile is a short, medium or long range weapon (respectively a few kilometers, tens of kilometers and a few hundred kilometers), of small size and aimed against a military target. It may be launched from the ground, from aircraft, including helicopters, from ships, from submarines...

Tactical missiles can be classified according to the various following criteria :

- the shape : cruciform or not
- the propulsion system : solid-propellant rocket motor or air-breathing engine
- the control system : deflected aerodynamic surfaces (canard,...), jet controls
- the firing and interception conditions
- the target.

The following classification is generally adopted :

- Surface-to-Air (HAWK, RAPIER, ROLAND, CROTALE,...)
- Air-to-Air (MAGIC, SUPER 530, SIDEWINDER,...)
- Air-to-Surface (AS-30, ASMP, MAVERICK,...)
- Anti-tank (MILAN, HOT, TOW,...)
- Anti-ship (EXOCET family, OTOMAT, HARPOON,...)
- Surface-to-Surface (LANCE, PLUTON,...)

Let us quote other missiles the aerodynamic design of which is similar : target drones (C22, FIREBEE,...) and remote-piloted-vehicles RPV (AQUILA, CL289,...), also some rockets, guided bombs and submarine vehicles (SM39,...).

A missile generally consists of (fig. 1, Ref. 1, and 2) :

- a body which contains the warhead, the guidance and control system, the propulsion unit, and various equipment (batteries, control actuators,...)
- wings for the lift and control surfaces for guidance, which provide also the missile stability.

Propulsion is provided

- in the acceleration phase by a jettisonable (wrap around or in tandem) or integrated solid-propellant booster system (fig. 2)
- in the cruise phase by a solid-propellant rocket motor or an air-breathing engine (turbojet, ramjet).

The control system may be of the following types (fig. 3) :

- aerodynamic controls, hence linked with dynamic pressure
- jet controls.

### 2.2. Tactical missile design

The process of designing a missile begins first of all by the analysis of parameters concerning the target and the firing and interception conditions.



**The target is characterized by :**

- its size : this may be large (airport, bridge, ship,...) or small (tank, missile, ...)
- its signature : infrared, electromagnetic radiation,
- its hardness : tank, helicopter, radar station,...
- its kinematics : range of speed, altitude and maneuverability.

**The firing and interception conditions are characterized by :**

- the nature of the launcher :
  - . aircraft, helicopter
  - . ground vehicle, man
  - . ship
  - . submarine
- the dynamic pressures to be encountered by the flying missile and which depend on its speed and its altitude.

The study then goes on in a close collaboration with the teams concerned by the various functions of missile definition (see the interactive design cycle, fig. 4, Ref. 3) :

- aerodynamics
- propulsion
- structures
- guidance and control
- warhead
- other technologies (power supply,...).

**2.3. Types of configurations**

As the application field of missiles is very large (anti-tank, anti-ship,...), it does not exist a unique optimum configuration even if tendency is to develop multi-purpose missiles (ex. : air-to-air missile for long range and close range interception). The distinction is, therefore, made between the following (fig. 5) :

**- Body alone**

It does not contain any lifting surface and therefore must be controlled by deflecting the jet from the propulsion unit by means of rotating nozzles; this implies that propulsion continues all over the flight. This configuration of tactical missiles is not used very often, except for strategic missiles.

**- Finned body**

At the rear part of the body lifting surfaces are mounted which may be used for several tasks :

- stabilizing surfaces (e.g. : HOT, MILAN)
- control surfaces (e.g. : LANCE, PLUTON).

If they are only stabilizing surfaces the missile must be controlled by jet controls.  
This configuration is usually cruciform.

**- Conventional missile**

The wings are mounted close to the center of gravity of the missile and increase the body lift. The control surfaces with a span and an area smaller than those of the wings, are mounted on the rear part of the body, they increase the missile stability and provide its setting in incidence. The configuration is cruciform and is the one the most often used.  
e.g. : EXOCET.

**- Long wing missile (or very small aspect ratio wings)**

This is a conventional missile, except that the wing chord is very large compared to the span. The control surfaces, mounted near the base, generally have a span larger than that of the wings. The use of long wings proceeds from research into missiles of reduced bulk, in order to increase the number of missiles on the launcher, and to facilitate handling, storage and setting into battery. Moreover a long wing missile behaves well at high angles of attack.

**- Canard missile**

The canard fins are mounted near the nose and are used for control. The wings, with a large span and area, are mounted on the rear part of the body. All these surfaces are located far from the center of gravity. This configuration, cruciform, is mostly used for small missiles.  
e.g. : SIDEWINDER, CROTALE,...

**- Moving wing missile**

The wings which are used for control are placed close to the center of gravity and the others at the rear part of the body.  
e.g. : SPARROW.

**- Air breathing missile**

The body is fitted with air-intakes for the feeding of a ramjet or a turbojet. The air-intakes may be :

- lateral, two in number (ASMP), or three or four (ANS)
- ventral (HARPOON)
- frontal (SEA DART)
- dorsal (ALCM)

They lead to an external arrangement peculiar to the missile.

In all the above different types of configurations the body is generally of revolution with a constant or variable diameter (boat-tailed afterbody, tandem booster configuration,...) and a sharp or blunt nose. The length-to-diameter ratio of the whole body is on an average :

1-4

- 8 for anti-tank
- 12 for surface-to-surface, anti-ship and air-to-surface
- 16 for surface-to-surface
- 18 for air-to-air.

The lifting surfaces generally have a low aspect ratio ( $AR < 4$ ) and even sometimes very low as for the long wing missiles ( $AR < 0.3$  - SUPER 530, MAVERICK, PHOENIX). Their planform is simple : delta truncated or not, trapezoidal or rectangular, just like their airfoil section, the thickness chord ratio of which does not exceed 8 % : double-wedge or modified double-wedge and symmetrical sharp-nosed airfoil. In a few particular cases, as for cruise missiles, more sophisticated airfoils are used (ex. : NACA airfoil).

#### 2.4. Types of propulsion

The main propulsion modes used are :

- solid-propellant rocket motors
- liquid-propellant rocket motors
- liquid or much more recently solid fuel ramjets
- turbojets.

The most used is the solid-propellant rocket motor the main features of which are :

- reliability and safety
- ease of operation, maintenance-free storage, noteworthy durability (solid-propellant motors stored for 14 years have run without any problem)
- suitable performance for medium range.

The liquid fuel motor, more sophisticated, is no longer used in practice for the tactical missiles because it is more complicated, and deployment safety conditions are not very consistent with the severe environmental conditions of these missiles.

The ramjet provides a good specific impulse (4 to 5 times more energy than solid-propellant) but it is necessary to boost the missile to a supersonic speed before it can operate. Up to now, it is the only propulsor able to sustain a long range supersonic flight at low altitude. Its thrust may be easily modulated in order either to accelerate the missile or to maintain its speed during flight maneuvers and this in a wide altitude range.

The turbojet which has a relative discretion against the infrared detectors is of great interest only for long ranges. Its low thrust does not allow sufficient initial speed, so it is necessary to use auxiliary boosters. Furthermore it needs careful maintenance for the turning parts (for pumps,...).

#### 2.5. Types of control

The main control modes used are :

- aerodynamic controls : deflected aerodynamic monobloc surfaces, trailing edge flaps (HAWK), spoilers (anti-tank COBRA, MAMBA), these last two now seldom used
- jet controls :
  - . thrust vector control of the main motor
  - . lateral jet controls.

##### 2.5.1. Aerodynamic controls (fig. 6) (Ref. 1, 4, 5)

These have to insure good efficiency with correct hinge moments. Their aerodynamic behaviour depends on the configuration : tail controls, canard controls, wing controls.

Missiles with canard and tail surfaces are controlled by moment : deflection of a control surface produces moment around the center of gravity which changes the angle of attack of the missile involving a lift force and a load factor.

Missiles with moving wings are controlled by force : the deflection of the wing produces a direct force applied to the center of gravity.

##### a) Tail controls (e.g. : EXOCET)

Advantages :

- the local angle of attack remains moderate
- saturation of the control surfaces is not reached, even for deflections up to  $20^\circ$  or  $30^\circ$
- the aerodynamic behaviour is linear
- the hinge moments are relatively small
- the pitch-yaw coupling is small.

Disadvantages :

- the tail surfaces produce a loss in lift, therefore an opposite force to the desired direction of missile flight
- the response of the missile is slow
- because of the control actuators are at the rear an extension tube must be used for the propulsion unit (see fig. 1), which is not suitable for small missiles.

##### b) Canard controls (e.g. : MAGIC)

Advantages :

- the canard controls produce a lift in the desired direction of missile flight
- maneuverability is high : the lift of the canard controls involves a loss in lift on the tail surfaces and the moment thus obtained is large
- response is fast
- integration is easy.

**Disadvantages :**

- the local angle of attack is high
- saturation of the canard controls is quickly reached
- aerodynamics is non-linear
- the hinge moments are high
- the pitch-yaw coupling is high
- the interference of the canard on the tail surfaces is complex : so the roll efficiency may be reduced or even inverted because of a roll moment having an opposite direction on the tail.

In order to avoid some of these problems, a fixed surface is added in front of the canard (reduction of the local angle of attack) and the tail is free-to-rotate (no roll interference).

**c) Wing controls**

This type of control develops a wing force close to the center of gravity.

**Advantages :**

- the angle of attack of the missile body is small, which for electromagnetic seeker missiles reduces the radome boresight error slope (e.g. : SPARROW)
- the response is very fast.

**Disadvantages :**

- loss in tail effectiveness due to a strong downwash is relatively large
- body lift is not used
- wing location is critical because the position of the center of gravity is not constant
- integration is difficult.

Figures 7 and 8 (Ref. 5) give respectively a comparison of the missile responses and lift distribution for these three kinds of controls.

The main disadvantage of the aerodynamic controls is their inefficiency when dynamic pressure is very weak. That is the case, for instance, for anti-tank missiles launched with a very low velocity so that the weapon can be fired within a confined space, for the surface-to-air and anti-ship missiles vertically launched and needing a quick turn over, for the air-to-air missiles launched with a low speed or at very high altitude. In these cases it is necessary to use jet controls.

**2.5.2. Jet controls**

Jet controls may be divided into two types of operation :

- by deflection of the thrust vector which produces a moment generating an incidence and so an aerodynamic force
- by lateral jet streams located either forward or backwards (moment control), or at the center of gravity (force control).

**a) Thrust vector controls (fig. 9a) (Ref. 1, 4, 6)**

There are three main methods :

- **Thrust oriented by a shock wave in the nozzle**

A fluid must be injected into the nozzle or an obstruction must be located at the exit section in order to have a flow separation and then a shock wave inside the nozzle producing a region of high pressure.

The main devices are :

- the jet deflectors or semaphores : there is one (e.g. : HOT, MILAN), or there are two (e.g. : ROLAND) or four (e.g. : AS 30 LASER, SM39)
- the dome deflector, the jetavator (e.g. : SWINGFIRE), the axial deflector
- fluid injection into the nozzle (freon or gas bled from the combustion chamber).

**Advantages :**

- simple devices needing no high power
- erosion which can be relatively small.

**Disadvantages :**

- limited efficiency
- impossible roll control with a single nozzle, so an auxiliary roll control device is necessary or a missile design adapted to autorotation.

- **Thrust oriented by rotating nozzle**

That can be done with one, two, or four nozzles.

**Advantages :**

- no loss if the jet is not deflected
- very important deflection may be possible (up to about 25°).

**Disadvantages :**

- technology problem for the pivot mechanism of the nozzle
- roll control impossible with a single nozzle.

The latter device applies mainly to missile having a relatively large diameter, having overall dimension problems and/or needing a large maneuverability (e.g. : SRAAM, AGILE).

- **Deflectors located in the nozzle** (e.g. : roll control of the OTTOMAT)

The control is the same as tail control

**Advantages :**

- relatively simple device
- roll control possible

**Disadvantages :**

- difficult erosion and temperature behaviour problems
- limited deflection

The main advantage of all these thrust vector controls is their efficiency which does not depend on the dynamic pressure and the lack of interference with external flow, that is to say with missile aerodynamics.

Their main disadvantage is the impossibility of using them after the propulsion phase.

**b) Lateral jet controls (fig. 9b) (Ref. 4)****• Lateral jets close to the center of gravity (force control)**

As in the case of wing controls the principle consists in creating a direct force at the center of gravity

**Systems used :**

- a first possibility is to fit the missile with a set of multiple small side-thrusters arranged peripherally along the body length close to the center of gravity. The axis of each side-thruster must be inclined so the elementary force crosses the center of gravity. The transversal component of this side force is used for control and the axial component force is used to maintain the speed. As it is difficult, in practice, to increase the number of side-thrusters, this control mode is used when the flight time and the maneuverability needs are low (e.g. : anti-tank DRAGON).
- another possibility which allows a higher maneuverability is to use a continuous gas generator linked with jet interceptors (e.g. : anti-tank ERYX) or with a steam distributor towards the nozzles. There are 2 nozzles for an autorotating missile (anti-tank ERYX), 3 or 4 for a stabilized missile in rotation. On the other hand, as in the side-thruster control, the nozzle can be inclined backwards to maintain the speed.

If these systems are disconnected for the cruise velocity, they can be used even after the propulsive phase.

**This control force :**

- does not depend on flight conditions (speed, altitude)
- is directly obtained without trying to get an aerodynamic lift
- is located at the center of gravity, therefore there is no induced moment and the missile can maneuver at a zero angle of attack.

**The constraints of these systems are :**

- the need for a very slight variation of the center of gravity
- the interference of the jet wake with the external flow and in particular with the lifting surfaces, if the latter are located downstream the nozzle
- the need to have short using times so as to keep propellant weight low.

**• Lateral jets located at the rear part or at the forward part of the body (moment control)**

As in the case of tail or canard controls the principle consists in creating a moment generating an incidence and so an aerodynamic force.

The systems used are the same as those for lateral jets close to the center of gravity. The control force does not depend on flight conditions (velocity, altitude) and the constraints are the interference of the jet wake with the external flow and the need to have short using times...

For some advanced missiles a combined aerodynamic and jet controls is considered in order to obtain very steep attitude changes of the missile in the launch phase (vertically launched surface-to-air, low speed launched air-to-air missiles) or in the terminal flight a short time response in order to increase the accuracy.

**2.6. Control configurations**

Just considering the main configurations we can see two categories of missiles : the conventional axisymmetrical cruciform missiles and the aircraft type missiles with one symmetrical plane.

**a) Conventional axisymmetrical cruciform missiles**

They may be - or not - stabilized in roll.

**• Roll stabilized missiles**

In this case the transverse maneuvers result from two separate sets of control surfaces which create independently the incidence and the sideslip.

The geometrical roll or sometimes simply the rate of roll is kept approximately to zero either by the action of a separate control surface or by differential deflection of the yaw and/or pitch control surfaces.

**Examples :**

EXOCET anti-ship missile : the roll, yaw and pitch control orders are executed by 4 independent aerodynamic control surfaces at the rear part of the missile.

R 530 air-to-air missile : the yaw and pitch control orders are executed by two sets of aerodynamic control fins at the rear part of the missile and roll control is achieved by an independent trailing edge flap control surface.

**• Non roll-stabilized missiles (autorotating missiles)**

In this case the lifting surfaces are set at an angle such that it imparts a rolling motion to the missile : this averages the effects of structural, propulsive, and aerodynamic dissymmetries. The motions in yaw-pitch may then result, as above, from the action of two axis control or more simply from the action of one axis control initiated when passing along the desired direction.

Such a configuration is particularly well suited for the smaller missiles.

**Examples :**

SA7, RED EYE : one set of aerodynamic control surfaces  
HOT, MILAN : one jet deflector.

**b) Aircraft type missile**

Such missiles have a monoplane layout. Through an action on roll this monoplane is located perpendicularly to the direction of the desired maneuver, then, through an action on the pitch control surfaces, the angle-of-attack builds up. The sideslip is kept near zero either through the aerodynamic effect in yaw or through an action by the control surfaces.

**Example :**

ASMP (airbreathing missile) : 4 aerodynamic control surfaces in yaw-pitch-roll.

**2.7. Trends in tactical missile development**

The development of tactical missiles and, generally speaking, armament, is always the result of a continuing exchange between the military who explain their needs or define the guidelines, and the technician, who proposes solutions or submits new ideas which appear to be promising. It is within the framework of this exchange that, for many years, the general staff has asked questions, and defined the requirements to which the industrial concerns have tried to find the answers.

**The beginning...**

The first real stimulus that occurred in the field of missiles and associated technologies, was given at PEENEMÜNDE in Germany, in 1937. In this centre, over a period of seven years, theoretical and experimental activities were undertaken which gave Germany the first operational missiles in 1944.

The following missiles can be mentioned :

- the V1 with a 400 km range. It was launched mainly from ramps but could also be launched from aircraft. Its form was that of a present-day flying target : high aspect ratio wings and a ramjet engine over the top of the fuselage.
- the V2, first operational ballistic missile to be developed. Its form was that of a present-day surface-to-surface missile. It had a symmetrical fuselage with four tail fins.
- the WASSERFALL, first surface-to-air guided missile. It had a symmetrical fuselage and was provided with low aspect ratio wings and tail fins with control surfaces on the trailing edges.
- the remote-controlled gliding bomb X1, first air-to-surface missile.

Many other projects were not completely developed, like the ROTKAPCHEN wire-guided anti-tank missile, supersonic missiles or submarine-launched missiles.

This brief review shows that all, or almost all the fields of possible future developments had already been foreseen in the 1939/45 period ; only the technological shortcomings prevented certain developments from being completed

**The missiles of yesterday, to-day and to-morrow**

After the second World War, an enormous surge in the development of missiles took place, taking advantage of all the innovations of modern technology (electronics, automation, etc.). The instigators of this development have been, and still are :

- the increasing improvements in the enemy's forces (the everlasting fight between the sword and the shield)
- the lessons drawn from the following wars :
  - the battle of Berlin in May 1945, which highlighted the importance of anti-tank defences in an urban environment,
  - the attack of the EILATH, hit by a STYX missile during the 6 day war which showed the importance of anti-ship weapons,
  - the KIPPOUR war, which showed the extreme efficiency of anti-tank missiles,
  - the FALKLANDS conflict, which showed the efficiency of anti-ship missiles and the dissuasive effect of anti-aircraft defence missile systems,
  - the IRAN-IRAK war, which emphasized the lessons learned in the Falklands and, moreover, has shown the efficiency of air-to-air weapon systems.

We are now going to review the main groups of tactical missiles, only considering those of which the characteristics have had a direct effect on aerodynamics, and only the most striking cases will be mentioned.

**a) The anti-tank missiles**

Immediately after the war, a first generation of light anti-tank missiles was developed, mainly in Europe, using solid propellants and manual wire-guided remote-control guidance systems. Among these missiles, we can mention :

SS10 and ENTAC in France  
VIGILANT in Great Britain  
COBRA in Germany  
SNAPPER in the USSR

All these missiles, with ranges of 1000 m to 1500 m, are of symmetrical cruciform cross-section with two pairs of fairly large wings, and controlled by either solid spoilers in the lifting surfaces or by thrust deflectors (SS10 and ENTAC).

The 2nd generation, currently operational, has paved the way for faster missiles :

MILAN (2 km), HOT (4 km), a joint France-Germany project  
DRAGON (1 km), TOW (3 km) in the USA  
SWINGFIRE in Great Britain  
SAGGER in the USSR

These missiles are characterized by smaller stabilizing surfaces, which can be folded to allow the missile to be placed in a tube which fulfils the triple function of storage container, transportation container and launching container. Flight control is made by thrust deflection (MILAN, HOT), jetavator (SWINGFIRE), by aerodynamic control surfaces at the rear (TOW), or by lateral thrusters (DRAGON).

As the armour plate of the tanks has been improved to keep abreast with anti-tank missiles progress, it has become necessary to improve this second generation of missiles by increasing the size of the warhead. This has resulted in an increased missile

diameter and a modification of the nose which includes a fixed probe for stand-off warhead initiation, that is to say, an unconventional nose shape from an aerodynamic point of view.

For the 3rd generation of anti-tank missiles, fulfilling the needs from the year 2000 onwards, development work is taking place in two directions :

- the renewal of the actual series of medium range (2 km) and long range (4 km) missiles,
- the perfecting of short range (25 m to 600 m) missiles.

There will probably never be any great changes made to the shapes which will remain conventional, that is to say, cylindrical cruciform with folding stabilizers at the rear. Nevertheless, for certain of these future anti-tank missiles (AC3G, ERYX) an original construction method will be adopted :

- motor at the front and hollow-charge warhead at the rear, thus enhancing warhead efficiency,
- force-type flight control system, enabling launching at reduced speed (enhanced launching possibilities within restricted areas, fig. 10), and a possibility of guidance at low speed (efficiency at very short ranges).

This new flight control system will lead to lateral jets for the missile, causing complex three-dimensional flow patterns (fig. 11).

#### b) The anti-ship missiles

The destruction of the Israeli frigate EILAT in 1967, by a small Egyptian patrol boat armed with STYX anti-ship missiles, triggered or accelerated the development of several programmes of anti-ship missiles in the western world :

KORMORAN, as a joint Germany-France project  
 MM38, first version of the EXOCET, in France  
 OTOMAT, as a joint France-Italy venture  
 HARPOON in the USA  
 PENGUIN in Norway  
 GABRIEL in Israel

All these missiles possess a high subsonic speed.

They are propelled either by a solid propellant motor (KORMORAN, MM38, PENGUIN, GABRIEL), or by a turbojet (OTOMAT, HARPOON). The latter mode of propulsion has had the effect of giving the missile an unconventional shape, due to the presence of air intakes (one for the HARPOON, four for the OTOMAT). They are all controlled by rear control surfaces, with the exception of the PENGUIN which is controlled by canard forward control surfaces.

From certain of these missiles, derivative versions have been produced (fig. 12) :

EXOCET-MM40, OTOMAT, PENGUIN... in coastal batteries  
 EXOCET-AM39, OTOMAT, PENGUIN, GABRIEL... carried by an aircraft or a helicopter  
 EXOCET-SM39 carried by a submarine.

In the future, due to the foreseen developments of anti-missile systems, missiles with a greater range and a greater target penetration capability must be developed. These results will be obtained by increasing the missile speeds to speeds that are well beyond the speed of sound (Mach 2) and by bringing them over the targets at very low heights with terminal stage maneuvering at high load factors. In the range of speeds and altitudes to be covered, the most satisfactory means of propulsion is the ramjet engine. This is the type of propulsion selected for the ANS, successor to the EXOCET, which is being developed as a joint France-Germany venture. The choice of this type of propulsion has had the effect of giving the missile an unconventional shape, due to the existence of air intakes (fig. 13).

#### c) The surface-to-air missiles

Anti-aircraft defences are a vital necessity for ground forces. After the war, this necessity led to the creation of sophisticated missiles efficient at high and medium altitudes :

NIKE, 150 km range, interception altitude 45 km  
 HAWK, 40 km range, interception altitude 18 km.

Since then, the ground forces have expressed the need for lighter weapons capable of short range to very short range missions.

Examples of short range missiles :

ROLAND, CROTALE in France  
 RAPIER in Great Britain  
 CHAPARRAL in the USA

Examples of very short range missiles :

MISTRAL in France  
 BLOWPIPE in Great Britain  
 REDEYE in the USA  
 SAM7 in the USSR

All these missiles are controlled by canard control surfaces, except for the ROLAND missile which is controlled by jet-deflection.

They are cylindrical, cruciform.

As the surface-to-air missiles have demonstrated their efficiency against attacking aircraft (i.e. the FALKLANDS campaign and the IRAN-IRAK war), the attacking aircraft must now be equipped with jamming counter-measures to confuse surface-to-air missiles, and air-to-surface missiles that can be launched while the aircraft is beyond the range of the anti-aircraft defences. For these reasons, future surface-to-air missiles must be capable of dealing not only with high performance aircraft, but also with supersonic missiles possessing diving or surface-skimming flight paths, a high degree of maneuverability (fig. 14) and that were launched out of defensive range.

The response to these threats necessitates :

- vertical launching and turning over in all directions (reduction of launching sequence time)
- a very high degree of maneuverability (50 g). In order to obtain such maneuverability, but above all a very short response time

so as to render the evasive actions of the enemy aircraft ineffective, a very advanced technical solution has been selected for the ASTER missile, which is being designed in France. This consists in a force-type flight control by lateral jets, which provides very short response time, operating in conjunction with a conventional aerodynamic form of flight control that makes the most important contribution to the maneuverability. For the missile, these new characteristics will lead to very high angles of incidence and lateral jets causing complex three-dimensional flow pattern (fig. 15).

#### d) The air-to-air missiles

In the field of air-to-air missiles, the weapon systems must be capable of engaging very maneuverable targets whose speed and difference of height relative to the launcher can be very great. The need covers combat at close quarters, during which the launcher endeavours to adopt a target intercepting position (dogfights), and also combat at long range.

In the first case, maneuverability and acceleration are needed, in the second case, the necessity is for horizontal and climbing speeds, range and maneuverability.

The most stringent limitations in both cases are the weight and the size of the missile.

Examples of short range missiles :

MAGIC in France  
SIDEWINDER in the USA

These two missiles are controlled by canard control surfaces.

Examples of long range missiles :

SUPER 530 in France  
SPARROW in the USA

The Super 530 is controlled by rear control surfaces and it has a wing with a very long chord which makes it very compact. The SPARROW is controlled by wings located about the centre of gravity.

The development of the threat that can be anticipated at the end of this century necessitates the definition of new missiles that are capable of hitting very maneuverable targets that may be dispersed throughout a very large range of altitudes (fig. 16)

In order to fulfil this requirement, work is actually being undertaken in two directions :

- renewal of the present-day missiles

Examples :

AMRAAM for long ranges  
ASRAAM for short ranges  
both types being developed within an international framework

- development of a light missile capable of fulfilling requirements for long range interception missions and dogfights.

Example :

The MICA missile which is being developed in France. This missile is small, of low weight, very compact (long chord wings), and provided with a mixed flight control system, incorporating both aerodynamic control surfaces and jet control surfaces, which allows very great variations of attitude. The choice of long chord wings and rear control surfaces enables high angles of incidence while allowing the missile to be slung directly against the underside of the aircraft (fig. 17).

#### e) The air-to-surface missiles

With regard to air-to-surface missiles, the object is to launch a missile from an aircraft while it is beyond the range of the enemy defences. Moreover, this missile must be capable of destroying or significantly damaging the target by just one hit. This requirement covers not only the launching of conventional missiles (battle-field objectives, short range single-target interception objectives,...) but also the launching of nuclear weapons at a much greater distance to hit targets of relatively widespread dimensions.

In the first case, the main requirement is accuracy, in the second case, it is the range considered in conjunction with the minimum degree of accuracy required for the efficiency of the weapon. In both cases, weight and size are limitations of prime importance.

##### • Conventional missiles

As a bridge pier should not be attacked in the same way that a tank should be attacked, it has been necessary to create as many types of missiles as there are types of targets, each missile being dedicated to a certain type of target and provided with a suitable warhead and guidance system.

To illustrate this subject, the following missiles can be taken as examples :

MARTEL designed to destroy radar antennae  
MAVERICK designed to destroy single hardened targets (tanks,...)  
AS30 Laser designed to destroy single and very-strongly hardened targets (command posts, bridges, etc.).

These missiles have all a conventional shape but they have various types of controls.

##### • Long range, highly accurate missiles

Due to the difficulty of perfecting such missiles, they are in limited numbers.

Among the most noteworthy missiles, the following can be mentioned :

TOMAHAWK in the USA  
ASMP in France

Both are air-breathing missiles, the TOMAHAWK being propelled by a jet engine (one ventral air intake), and the ASMP propelled by a ramjet engine with an integral booster (a pair of two-dimensional lateral air intakes). Their shapes are therefore unconventional (fig. 19). Flight control is aerodynamic, by means of rear control surfaces.

A new generation of cluster-type air-to-surface weapons is being prepared for future requirements (for instance, MOBIDIC,

APACHE, MSQW developed as an international venture). These modular subsonic missiles are designed to carry loads of sub-projectiles suited to designated fixed or moving targets at a range of several tens of kilometers, while allowing the launching aircraft to remain out of range of the ground-to-air defence systems of these targets. These missiles will no longer have a symmetrical shape, they will have long folding wings (fig. 18). Their shape will be designed by taking geometrical constraints into consideration in association with the reduction of the radar cross-section (RCS).

## 2.8. Improvement areas and contributing factors

Fire fast and far, without being detected, with a maximum rate of success, that is the technical challenge for the 2000's.

This requirement necessitates the following performance areas to be improved :

- range
- maneuverability
- penetrativity

Penetrativity is closely related to detectability, performance in range comprises both range and time-to-target capability, and maneuverability is predominant on terminal accuracy.

Note that for strategic missions, penetrativity is the most important of the priorities, and for tactical, defensive, air-to-air or surface-to-air missions, maneuverability and range will constitute the primary aim.

The contributing factors for improved performance are given in figure 20 (Ref. 3). The three technology areas : aerodynamics, propulsion and structures are assembled in the way that they are thought to contribute towards improvement.

In figure 21 (Ref. 3) the three main performance areas are related to improvement areas. It can be seen that :

- higher-speed missiles would improve range, maneuverability and penetrativity
- an optimization of lift to drag ratio (L/D) would improve range
- high-lift devices would improve maneuverability
- low radar signature would improve penetrativity

Since reduced detectability is becoming more and more important the missile designer might be faced with a compromise between a highly efficient missile airframe and propulsion system with undesirable radar cross-section, or a very low radar cross-section for a somewhat less efficient missile. This dilemma indicates the need for RCS consideration from the outset of the aerodynamic shape design.

## 3. Missile aerodynamics

### 3.1. Specificities of tactical missile aerodynamics

#### 3.1.1. Differences between aircraft and missiles (fig. 22 and 23)

The **civil aircraft** is built for an economical cruise. The main part of the aircraft is the wing with a large aspect ratio (AR-10), working at the largest possible fineness ratio, and itself responsible for approximately 80 % of the total lift.

Its flight envelope is :

- in cruise :  $0 < \text{Mach} < 2$  (Concorde)  
 $\alpha < 2^\circ$
- when taking off and landing :  $\text{Mach} < 0.2$   
 $\alpha < 12^\circ$

Civil aircraft aerodynamics is essentially linear. Wing tip vortices induce only little vortex lift.

The **fighter aircraft** is built for a high maneuverability. The load factor is limited by the low human resistance to acceleration. Its flight envelope is much larger than the one of civil aircraft but it remains much lower than the one of missiles.

During dog-fight the flow separates on wings which induces non linear aerodynamics similar to that of missiles.

The **missile** is built to bear up against high load factors in a wide speed range. Some missiles bear ten times the gravity acceleration, lengthwise (acceleration due to propulsion) as well as transversally ( $< 50 g$ ). This acceleration changes the flight path.

Its flight envelope is very wide :

- 0 < altitude < 30 000 m.
- 0 < Mach < 6
- $0^\circ < \alpha < 90^\circ$
- $0^\circ < \phi < 360^\circ$

At high incidences aerodynamics is strongly non linear : separations happen from the leading edge inducing vortices over the upper surface, which influences all the downstream flow. Flow separates also on the body inducing typical vortex sheets.

All these vortical structures depend, in a complicated way, on the geometry, the Mach number, the Reynolds number,... Moreover the flow is highly three-dimensional.

#### 3.1.2. Main characteristics of missile aerodynamics

##### a) Non linearities (fig. 23)

Missile aerodynamics is characterised by important non linearities due to the fact that :

- in inviscid flows the compressibility effects induce shocks
- in viscous flows viscosity effects induce separation and vortices.

At low incidences non linearities due to vortices are usually small. The conventional cylindrical cruciform missile shape leads to aerodynamics independent from the rolling, which makes it interesting.



At high incidences vortical non linearities become large (Ref. 7). Aerodynamics becomes non linear and is no longer independent from the roll angle  $\phi$ . Particularly the  $\times$  shape ( $\phi = 45^\circ$ ) has a smaller lift than the  $+$  shape ( $\phi = 0^\circ$ ) but on the other hand it is more efficient at a given deflection.

A detailed description of these non linear phenomena will be given during this special course.

#### b) Interactions

The flow, which is highly tridimensional, is characterised by numerous interactions (Ref. 8). There are roughly two large categories :

- non vortical interactions
  - . wing-fuselage interactions in incidence  $\alpha$
  - . wing-fuselage interactions in deflection  $\delta$
  - . wing-fuselage in rolling  $\phi$
  - . adjacent wings
- vortical interactions
  - . body vortices
  - . front wing vortices (wing-tail interaction)

A detailed description of these interactions and the corresponding calculation methods will be given during this special course.

### 3.2. Aerodynamics analysis

The desired aerodynamic qualities are essentially a function of the mission required from the missile.

They result from studies of :

- maneuverability
- stability, in relation to the control surfaces efficiency
- drag

There are also dimensional constraints due to the carriage, the implementation (same storage and launching tube). Consequently wings and control surfaces spans are smaller or foldable or retractable.

Thus it is necessary for the design :

- to define the mathematical models for the performance analysis, the guidance and control analysis, the hardware in the loop simulation, the store separation analysis,...
- to compute the airloads for structure analysis, the hinge moment for control actuator, the kinetic heating for the choice of insulation materials,...

All these tasks are supported by calculation as well as wind tunnel tests.

Figures 24 and 25 give a survey of aerodynamic tasks.

Figure 24 taken from Ref. 3 shows precisely the many and varied tasks from the pre-feasibility study phase through the various project stages along to the decision on production concessions.

Figure 25 shows the connections between aerodynamics and the other fields of study.

The problems encountered during these tasks can be classified according to three categories :

- global aerodynamic studies
- local aerodynamic studies
- particular studies

#### 3.2.1. Global aerodynamics studies

##### a) Aerodynamic maneuverability (lift), stability, control surfaces efficiency

Achievement of maneuverability-stability and stability-efficiency trade-offs should lead to an aerodynamics as linear as possible, which is not always the case taking into account the non-linearities and the interactions.

##### b) Drag

The drag directly influences the missile range. This parameter perhaps is not essential for short flight time missiles, but it is however significant for long range missiles and drag should be then reduced in most cases.

The drag is made of three terms :

- pressure drag
- friction drag
- base drag

Consequently :

- the shapes must be thinned : slender and sharp nose, thin and sharp leading edges, wing sweep,...
- surfaces conditions should be carefully refined
- trailing edges must be thin and the base must be provided with a boattail.

##### c) Induced roll

When there is incidence and side-slip the flow is asymmetrical. It induces lateral forces  $C_Y$ ,  $C_n$  and especially roll which depends on the configuration, the total incidence and the Mach number ; roll should remain controllable throughout the maneuvering envelope.

##### d) Dynamic stability derivatives

With more and more maneuvering missiles the influence of certain dynamics derivatives on the performance can no longer be considered as small.

This has been demonstrated by T.F. LANGHAM (Ref. 10) who studied the effects of various dynamic derivatives on bank-to-turn and yaw-to-turn missile stability in both level and turning flight for several Mach numbers and altitude conditions. He showed that the longitudinal and lateral-directional dynamic moment derivatives  $Cm_q$ ,  $Cm_{\dot{\alpha}}$ ,  $Cn_r$ ,  $Cl_p$  and  $Cn_p$  may significantly alter the respective longitudinal and lateral-directional stability modes. Also he showed the significant coupling effect between the longitudinal and lateral-directional motions resulting from variations in the cross-coupling derivatives  $Cl_q$ ,  $Cn_q$  and  $Cm_p$ . The force and moment derivatives  $CL_q$ ,  $CL_{\dot{\alpha}}$ ,  $CY_r$ ,  $CY_p$  and  $Cm_r$  are shown to have little or no effect on the missile stability modes and, therefore, are not considered important to motion simulation studies.

**e) Cross-coupling**

We can mention, as an example, the influence of sideslip on the longitudinal stability.

Except friction drag all these subjects will be covered during this symposium. A detailed description of friction drag and its calculation is given in Ref. 9.

**3.2.2. Local aerodynamics studies**

**a) Aerodynamic loads**

The studies of aerodynamic loads of a missile make possible to improve its structure and to reduce its weight.

Loads are obtained by wind tunnel tests (pressure and experimental forces measurements) or very often given by numerical calculation (EULER,...) with an experimental resetting.

**b) Deformations**

They must be precisely known in order to assess the consequences :  $CN_0$ ,  $Cm_0$ , CA, decrease in stability and efficiency,...

Their study, made in relation with the experts in structure, is often done theoretically.

**c) Control surfaces, hinge moments (Ref. 11 and 12)**

The study of these moments is very complicated and essentially experimental. They depend on the shape and the thickness of the control surfaces and the flight conditions : Mach number, altitude, incidence, side-slip and deflection.

The location of the hinge line that reduces these moments to the minimum inside the flight envelope is selected in order to make them acceptable for the available control actuator dimension and power. Note that at subsonic speed the center of pressure is close to 25 % of the chord and at supersonic speed it tends to 50 %. It is possible to reduce this variation which is considerable by using composite control surfaces with two trapezoidal parts.

**d) Kinetic heating (Ref. 13, 14, 15)**

The choice of materials and heat shield depends on this heating.

Three phenomena are taken into account :

- convection
- radiation
- conductivity

A detailed description of the calculation methods of convection fluxes will be given during this special course.

**e) Flutter**

The aeroelastic phenomena on missile concern essentially control surfaces. They result from the interaction between spring forces, inertial forces and aerodynamic forces induced by oscillatory deformation of the structure resulting from external disturbances, maneuvers, atmospheric turbulences and blast of wind.

The problem occurs when these deformations induce additional aerodynamic forces which produce additional deformations.

Aeroelastic phenomena can lead to rupture of the control surfaces and consequently to the destruction of the missile. Thus, it is highly important to know the speed at which the control surfaces become structurally unstable. This speed called "critical speed" or "flutter" must imperatively be out of the flight envelope.

The calculation of the critical speed of control surfaces is very difficult because of the numerous non linearities that they may have (set of attachments, variable stiffnesses). Numerous wind tunnel tests and the use of theoretical methods are currently required to solve this difficult problem.

To increase the critical speed it is enough to know the vibration mode for which there is a flutter risk and to stiffen the structure according to this mode.

This problem is not described in this special course but a detailed description of the phenomena and of the calculation methods is given in the reference 16.

**3.2.3. Particular aerodynamic studies**

**a) Problems in connection with the base**

The phenomena which occur in the base area may have an important impact on missile performance.

They concern :

- the base drag which can reach 20 % to 30 % of the total drag (Ref. 17, 18)
- the possible separation on the afterbody induced by the interaction between the propulsive jet and the external flow which can lead to a loss of stability and a loss of rear control surfaces efficiency.

A detailed description of the base flow and their calculation methods will be given during this special course.

**b) Aerodynamics at high incidences**

High incidences are encountered essentially when a missile is :

- fired vertically in a turnover phase. During this stage at low speed, incidence can reach 70° and sometimes even 90° with blasts of wind
- submitted to high load factors for instance during interceptions. In that case the incidence can reach 50° in transsonic and 30° in supersonic.

At these high incidences the flow separates all over the missile inducing very complicated vortical structures (Ref. 7).

A detailed description of these separated flows and their calculations will be given during this special course.

#### c) Store separation from aircraft

Launch flow field interactions are complicated and depend on the following conditions :

- aircraft : Mach number, incidence (load factor)
- missile : missile launcher geometry, position of missile under body or wing.

The setting of store separation conditions (attitude speed, relative velocity) and the choice of the firing sequence (motor ignition, control system starting up) are done according to the following studies results :

- safety studies : in the case of a breakdown of the control system, aircraft-missile miss-distance must remain superior to a given distance
- minimal firing altitude study : the loss of altitude during the store separation must remain small.

The store separation study is done :

- in wind tunnel by means of a six-degree-of-freedom - device which makes possible to achieve tests using grid system and captive trajectory system
- by calculation tridimensional mathematical model based on linearized potential flow.

This problem is not described in this special course but a detailed description of the phenomena and of the calculation methods is given in the references 19, 20 and 21.

#### d) Submunition launches from a missile

The problem concerns :

- the aerodynamics of unusual projectile configuration
- the launch flow field interference.

The setting of the submunition launch is done experimentally (model propelled at a high speed on a rail) because of the complexity of phenomena.

This problem is not described in this special course but some informations are given in the references 22 and 23.

#### e) Lateral jet interaction with external flow

The lateral control jet(s) are an obstacle to the main flow, which induces an interaction field with the external aerodynamics. The trend of the phenomena is shown at figure 26.

Schematically, there are two different interaction areas :

- a close-in area in the vicinity of the jet exit section, with overpressures and negative pressures upstream and downstream of the nozzle, respectively
- a distant region resulting from the jet trail ; it is arranged in two contra-rotative vortices likely to affect the missile tail lifting surfaces.

All these complex phenomena put together result in the fact that, instead of the thrust force  $F_0$  that can be measured on the static test bench, a force wrench  $T$  is obtained, characterized by :

- a force  $F = K(\text{Mach}, \alpha, \dots)$
- a torque  $C(\text{Mach}, \alpha, \dots) \neq 0$

Efficiency  $K$  over the force depends on a high number of parameters (geometry, Mach number, incidence, pressure, ...). It can be lower or higher than the unit.

Considering the complexity of the problems encountered, the study of the aerodynamic definition of the missile with lateral jets is essentially, for the moment, supported by wind tunnel testing. This interaction problem is not dealt with in this special course but it is covered by references 24 and 25.

#### f) Aerodynamic problems connected with airbreathing missiles

The choice of the air breathing propulsion by means of turbojets or ramjets implies a particular shape because of the air intake which alters missile aerodynamics (Ref. 26).

##### - Lift, stability

Because of the air intakes, lift generally increases and stability is altered.

##### - Control surfaces efficiency, hinge moments

Generally control surfaces are located on the fairings of air intakes and no more on a circular fuselage. The flow is very complex, and the analysis of efficiency and hinge moments has to be improved.

##### - Drag

The important impact of air intakes may reach 40 % of the total drag with 10 % of it due to the additive drag (cowl, bleed, ...).

In addition to the friction drag, there are the following pressure drags :

- drag from cowl, boattail fairing, base fairing
- additive drag
- drag from external and internal bleeds

The improvement of an air breathing missile must be done regarding the thrust-drag as a function of the angle of attack.

- The analysis of an air breathing missile must be done taking into account the two following aspects :
- external : missile aerodynamics, consequence of air intakes and ejection
  - internal : air intakes performance

A detailed study of air intakes and of their effects on the overall aerodynamic characteristics will be given during this special course.

### 3.3. Studies of future interest

The need of missiles which neutralize quickly stand-off targets has led to the studies of the hypersonic air breathing missiles.

A number of feasibility studies have been made to determine aerodynamically efficient missile configurations of this type :

- KRIEGER (Ref. 28) has proposed a non circular body concept and a lifting body concept. These concepts will be presented in detail during this symposium.

- SCHINDEL (Ref. 29) and RASMUSSEN (Ref. 30, 31) have proposed to adapt the waverider airplane concept to hypersonic missiles. Waveriders are configurations designed inversely to fit a known flow field, riding on a plane or a conical shock wave. This property tends to make the pressure relatively high in the windward side. In addition the leeward side can be formed by streamline planes. The resulting configuration is a non circular lifting body with blended wing-body which has lower drag, higher lift or higher lift/drag ratio than a conventional shape, particularly at hypersonic speeds.

A large number of waverider configurations are available. Figure 27 presents some examples.

In order to check waverider design and performances principles, SCHINDEL tested a conical waverider like configuration at Mach 6. The model is basically a caret wing with its central region partially filled by a section of circular cone (fig. 27) for suitable volume storage. At incidence  $\alpha = 0^\circ$  he obtained L/D = 4.

For the future there is a number of problems that need much more attention and developments. They are :

- aerodynamic design implications : inlets, integration, controls integration, seeker constraints,...
- influence of viscous effects : flow separation, heat transfer,...
- base drag, etc....

Note that most of EULER codes can be applied fruitfully to calculate waverider configurations characteristics at on and off design conditions.

## 4. Computation

In missile aerodynamics, two main types of methods are used :

- semi-empirical methods
- numerical methods

### 4.1. Semi-empirical methods

#### 4.1.1. Principles

These methods are based upon :

- approximate theoretical methods : slender body, linearized potential
- compilation of a great number of experimental and theoretical results

This way, the missile calculation consists in determining :

- each elementary element in itself : body, wing, tail
- interaction between these elements.

These principles being the basis of usual calculation programs, we are now going to briefly discuss the main methods of calculation of the coefficients  $C_N$ ,  $C_m$  and  $C_l$  of conventional missiles (axisymmetrical and cruciform shaped).

Some semi-empirical methods for conventional and unconventional missiles will be described during this special course.

We shall then come to the main programs used among industry and research laboratories in various countries (U.S.A., FRANCE, GERMANY, ...)

#### 4.1.2. Normal force and center of pressure of bodies

Many theoretical studies have dealt with the determination of  $C_N$  and  $X_{cp}$ , and their evolution depending upon the angle of attack. But, elaborating a computational model available for any case of Mach number, Reynolds number and geometry configuration is quite difficult because of the aerodynamic real phenomena complexity.

Methods based upon ALLEN's (Ref. 32) and JORGENSEN's (Ref. 33) works are the most widespread : the potential and the viscous part of flow are computed separately ; thus for approximately  $\alpha < 20^\circ$

$$C_N = C_{N\alpha} \cdot \alpha + C_{NT}$$

$C_{N\alpha}$  : normal force slope at  $\alpha = 0^\circ$

$C_{NT}$  : viscous normal force.

#### a) Potential flow

$C_{N\alpha}$  and  $X_{cp}$  are calculated from data-bases or approximate theories.

The main data-bases are :

- R.A.E. Data Sheets (Ref. 34)
- DATCOM - USA Air Force (Ref. 35)

- MICOM - USA Army Missile Command (Ref. 36)
- DFVLR - RFA - MBB (Ref. 37)

The theories most generally used are :

- subsonic : slender body theory (Ref. 8)
- supersonic :
  - linear theory (Ref. 38)
  - hybrid theory (axial solution 2° order & solution 1° order) (Ref. 39)
  - shock-expansion theory (2° order) (Ref. 40).

Note that EULER computational methods are left out : complexity of use and computation time are too high.

#### b) Viscous flow

The simplest formula were proposed by ALLEN (Ref. 32) as early as 1949, and improved by JØRGENSEN (Ref. 33). They assume that the viscous component  $C_{Df}$  looks like the drag of a cylinder in a permanent flow normal to its axis, whose speed would be  $V_{\infty} \sin \alpha$  and Reynolds  $Re_D \sin \alpha$ .

#### 4.1.3. Normal force and center of pressure of wings

Two ways are usually considered :

- semi-empirical methods (potential and viscous flow are computed separately)
- data-bases

##### Semi-empirical methods :

- potential flow :
  - subsonic : lifting surface theory (Ref. 41)
  - supersonic :
    - ACKERET bidimensional linear theory (Ref. 42)
    - BUSEMANN bidimensional 2° order theory (Ref. 42)
    - tridimensional linear theory (Ref. 43)
- viscous flow : cross flow theory (Ref. 32).

##### Data-bases :

The most famous are the STALLING - LAMB's data-bases from NASA (Ref. 44) and BRIGGS-REED-NIELSEN's ones (Ref. 45). These permit dealing with non-linear effects such as saturation or vortex-breakdown difficult to calculate for missiles sharp-edged wings.

#### 4.1.4. Interactions

##### 4.1.4.1. Linear angle of attack range (Ref. 8 and 46)

This deals with interactions such as :

- body-wing at angle of attack  $\alpha$
- body-fin with fin deflection  $\delta$
- body-wing in roll position  $\phi$
- adjacent fins' influence
- wing-tail

Each of them has an interaction coefficient :  $K_w, k_w, K_B, k_B, \dots$

Thus, the normal force on one wing panel (the other panels are undeflected) is :

$$C_{N_1} = (K_w \cdot \alpha + k_w \cdot \delta) C_{N\alpha} \cos \phi + K_{\phi} \cdot C_{N\alpha} \cdot \sin \phi \cos \phi \alpha^2$$

and the normal force due to the wing on the body is :

$$dC_{NB} = (K_B \cdot \alpha + k_B \cdot \delta) C_{N\alpha}$$

Notice that the linear normal force of a cruciform missile does not depend on the roll position  $\phi$  (coupling term does not exist).

##### - Interaction coefficients : $K_w, k_w, \dots$ (fig. 28)

The only simple theory to compute all these coefficients is the slender body theory (independent of Mach number).

For axisymmetrical configurations with 2, 4, 6 or even 8 fins arranged in an uniform way, this theory has been analytically developed.

For special cross-section missiles, such as wrapped around fins or arbitrary cross-section (e.g. : missiles with air intakes), a numerical approach of the slender body theory has been developed :

##### - Circular cross section with arbitrary wings (e.g. : folding wings) :

Each wing panel is represented by  $n$  vortices, and the body by a doublet. By assuming that the velocity is tangent to the body, one can find out the vortices' strength. Thus, lift and interaction factor  $K_w$  can be determined.

##### - Any cross-section :

A conformal mapping transforms the body section to a circle. Then, it is the same case as above.

Note that in the supersonic Mach number range, J.N. NIELSEN developed an approximate linear method to improve the computation of  $K_B$  and  $k_B$ .

##### - Interaction wing-tail factor "I"

It is evaluated by a combination of strip theory and slender body theory. The wing-tail interaction slope is proportional to "I" and the normal force slope on the wing. When the angle of attack increases, this approach is replaced by a vortical model, which is described in the next paragraph.

#### 4.1.4.2. Non-linear angle of attack range

##### a) Equivalent angle of attack (fig. 29)

This was introduced in the 80's by M.J. HEMSCH and J.N. NIELSEN (Ref. 47) to improve the interaction prediction. They assume that each interaction on a panel wing can be computed at an angle of attack. By summing up all the interactions, one can get the equivalent angle of attack on the wing as if it was isolated. Thus, using the normal force evolution  $CN(\alpha)$  of the wing alone, one finds out the normal force on the wing panel.

Note that, by using this concept, one must know quite well the behaviour of isolated wings according to the angle of attack.

This concept will be described during this special course.

##### b) Vortices interaction

There are two kinds :

- on the wing due to the body
- on the tail due to the wing

The vortical models most used are :

- body vortices : two or n vortices (fig. 30)
- wing vortices : one vortex by wing panel (fig. 31)

To obtain these interactions, there are many possibilities. Among them, the one based upon the following hypotheses :

- infinite line vortex

- free vortex

and the BIOT & SAVART's law (Ref. 42), which allows to compute the normal velocities and thus, the induced angles of attack (fig. 32).

#### 4.1.5. Global forces and moments

When the forces and the center of pressure have been calculated on each element (body, wing and tail panels), one can sum up to obtain the entire missile characteristics : CN, Cm, and Cl. Taking into account the fins roll position and deflection, one can write :

$$CN = CNB + \sum_i \cos \delta_i \cdot \cos \phi_i CN_i \left( 1 + \frac{K_B}{K_{wi}} \frac{S_{wi}}{S_{ref}} \right)$$

$$Cm = CmB + \sum_i \cos \delta_i \cdot \cos \phi_i CN_i \frac{X_m - X_{cpwi}}{D} \left( 1 + \frac{K_B}{K_{wi}} \frac{X_m - X'_{cpwi}}{X_m - X_{cpwi}} \frac{S_{wi}}{S_{ref}} \right)$$

$$Cl = - \sum_i \cos \delta_i \cdot CN_i \frac{Y_{cpwi}}{D} \frac{S_{wi}}{S_{ref}}$$

with  $i = 1, \dots, n$  (number of panels).

#### 4.1.6. Survey of semi-empirical programs

A great number of engineering prediction codes exists for estimating the forces and moments acting on wing-body and wing-body-tail combinations from subsonic to hypersonic speeds.

During an inquiry with industries and research laboratories we have collected 25 programs which at least can handle a wing-body configuration.

The possibilities of all these programs are summarized in two tables :

- table 1 shows the configurations capabilities
- table 2 shows the range of calculations : Mach number, incidence, aerodynamic coefficients,....

##### a) Configuration capabilities (Table 1)

The various classes of configuration considered are :

- conventional cruciform configurations :
  - wing-body
  - wing-body-tail
  - boosted configuration with 3 sets of lifting surfaces
- unconventional configurations :
  - lifting shapes with non circular cross section
  - airbreathing with intakes open or closed.

Most of the programs can compute conventional missiles with one or two series of cruciforms fins but only half of them can handle boosted configurations.

In the unconventional type (elliptic cross section, square cross section, airbreathing,...) just a few can be used.

| Configurations | CONVENTIONAL |     |                     | UNCONVENTIONAL          |              |        |
|----------------|--------------|-----|---------------------|-------------------------|--------------|--------|
|                | Classical    |     | Boosted<br>DD + 3CF | Lifting<br>elliptic,... | Airbreathing |        |
|                | 1CF          | 2CF |                     |                         | Open         | Closed |
| Nb of codes    | 25           | 22  | 12                  | 5                       | 5            | 5      |

##### b) Range of calculations (Table 2, and fig. 33)

We can notice about all these programs :

- Mach number range is generally less than 5

- one can separate the programs into 2 families according to the angle of attack :
  - . low angle of attack  $\alpha < 30^\circ$
  - . high angle of attack  $\alpha < 90^\circ$  or  $180^\circ$
- only 7 programs can be used for high angles of attack and only half of them apply to unconventional shapes.
- only half of the programs compute the effects of a roll variation and it is the same for interdigitated fins
- more than half of the programs have all movable control capabilities
- most programs compute static stability coefficients but only half of them compute axial force and one third dynamic derivatives.

To summarize :

| Configurations | FINS    |         | All movable control capabilities | AERODYNAMIC COEFFICIENTS |            |          |
|----------------|---------|---------|----------------------------------|--------------------------|------------|----------|
|                | In-line | Interd. |                                  | CA                       | CN, Cm, Cl | Cmq, Clp |
| Nb of codes    | 22      | 12      | 15                               | 14                       | 22         | 9        |

#### 4.1.7. Concluding statement

Semi-empirical programs constitute the main tool preferred by missiles designers : they need only a minimal amount of computer time and memory and as they have been made interactive (fig. 35-Ref.48) they are especially well suited for systematic calculations of configurations.

They allow to compute the main aerodynamic characteristics of conventional and unconventional missiles in a wide range of Mach number and angle of attack :

$$0 < M_\infty < 8.0$$

$$0^\circ < \alpha < 180^\circ$$

In general, they provide reasonably accurate estimates of aerodynamic characteristics (fig. 34) consistent with preliminary design studies. Note that all aerodynamic coefficients are not predicted with the same reliability in the whole range of applicability and more details will be given during this special course.

Because of their concept, each program has its own limits which explains their large number and their specificities.

Nevertheless, it is important to develop more programs to compute unconventional missiles, such as airbreathing ones mainly for determining the effects of airframe-inlet interference on drag, stability and control.

It is also necessary to improve methods for determining axial force, control effectiveness, hinge moments, control cross-coupling, dynamic derivatives, for conventional cruciform missiles at low and large angles of attack.

#### 4.2. Numerical methods

This approach is essential to treat complicated configurations, to determine load distributions, local flow field properties (e.g. velocity profiles at an inlet face), temperature distributions, and to provide important insights into understanding complex flow mechanisms.

We can distinguish four levels of equations which are from the most complex ones to the less complex :

- Navier-Stokes equations
- Euler equations
- Full potential equation
- Linearized potential equation

The simplification of these models permits more applications to complex geometries but with a loss of information, some results becoming unavailable like nonlinearities due to vortical effects and nonlinear compressibility associated with shocks.

During the last ten years remarkable progress has been made in numerical methods for solving the equations that govern aerodynamic flow regimes. At the beginning these methods were mainly applied to civil aircraft aerodynamics less complex than military aircraft and missile aerodynamics which is highly three-dimensional. Then with the speed and storage increasing of new computers and the improvement of algorithms, CFD methods have so much progressed that now three-dimensional inviscid nonlinear flow fields computations around complete military aircraft and missile configurations can be carried out.

In 1982, KLOPPFER and NIELSEN were the first to make a detailed survey on CFD applications to missile aerodynamics (Ref. 49).

We will now briefly discuss the different types of equations and present for each a list of the most important computer codes used in missile aerodynamics (Table 1 to 12).

##### 4.2.1. Navier-Stokes equations

###### 4.2.1.1. Full and thin-layer Navier-Stokes equations

The Navier-Stokes equations describe any type of flow over a missile at any speed and angle of attack. They can predict shock waves, vortex sheets, large scale separation,.... They also apply to turbulence, three-dimensional phenomena that involve many characteristic scales ranging over several orders of magnitude. Unfortunately, present computer capabilities do not permit the resolution of all scales and some approximation has to be done.

The first step of approximation is to resort to time averaging of rapidly fluctuating components. So are obtained the full Reynolds averaged equations, which require a turbulent model for closure. These equations should be used for the most complex flows including large scale separation, but so far their use is limited by the turbulent modeling (universally satisfactory turbulent model has not yet been found, especially for separated flows) and by the lack of adequate mesh resolution due to computer constraints (speed and storage).

The second step of approximation is to neglect the viscous terms in the streamwise and or spanwise direction. This yields to the thin-layer equations which can be used when mild streamwise separations occurs.

Both systems of equations are hyperbolic-parabolic and they are solved by a time-marching method. For steady flows the flow variables are advanced until an asymptotic solution is reached. This is a very costly procedure.

From our codes inquiry we have counted four Navier-Stokes programs (Table 4). Three are from NASA AMES and one from DORNIER. Only NASA has done some applications limited to wing-body configurations and airbreathing configurations with closed intakes but at the present time we do not have information about these calculations.

#### 4.2.2.2. Parabolized Navier-Stokes equations (PNS)

These equations are a simplification of the full Reynolds-averaged Navier-Stokes equations where the unsteady terms and the streamwise viscous diffusion terms are neglected and the streamwise convective flux vector modified to obtain stable calculations. This makes the PNS equations parabolic in the streamwise direction, enabling a space-marching technique procedure over the body which permits substantial savings in both computer time and storage. The PNS equations are valid only for supersonic flows without streamwise separation and flow reversal. However, crossflow separations which are very important for missiles are permitted.

In our codes inquiry we have only counted two programs (table 6) : the laminar and turbulent PNS code from NASA AMES and the laminar PNSFVM code from DORNIER. Note that the NASA code is also used by other research laboratories (BRL and Sandia Lab.). All calculations are done for : classical wing-body (Ref. 50) and elliptic lifting body configurations.

At the present time Navier-Stokes solvers are not yet ready (turbulent model,...) and are too costly to have an impact on the design of complete tactical missile airframe, even for simple configurations like projectiles, so we do not present them during this special course.

#### 4.2.2. Euler equations

The approximation where the viscous and conduction terms are neglected in the Navier-Stokes equations leads to the Euler equations which represent inviscid rotational flows at all Mach numbers. These equations can be used for flows with shock waves and vortex sheets.

To compute steady flows with Euler equations two ways are possible :

- solve the steady equations. In this case the equations are hyperbolic in space and a space-marching technique is used. This procedure is valid only for supersonic flows
- solve the unsteady equations. In this case the full-three-dimensional array of flow variables is advanced in time until an asymptotic limit is reached. This procedure is valid for any speed range.

Details about Euler methods will be given during this special course.

#### • Survey of Euler codes

In our codes inquiry we have counted 11 programs. The possibilities of all these programs and some details on their models are summarized in two tables :

- table 8 presents the configuration capabilities
- table 9 presents details on the models and the capability about flow separation.

#### Configuration capabilities

From table 8 we notice :

- all programs could calculate all configurations. Most programs have computed a wing-body, nearly half of the programs have computed a complete conventional missile and only three programs have computed an airbreathing missile.
- there is only one program which has computed all configurations. This program, called SWINT and developed by WARDLAW at NSWCC, is the most widely used (see table 10).

#### Details on the models

From table 9 we notice :

- the numbers of steady and unsteady solvers are quite the same. Nearly half of the programs are able to calculate flows at all speed.
- all models are conservative. So Euler equations admit solutions with shocks and contact surfaces
- most numerical schemes are centered
- accuracy is second order
- most meshes are structured
- nearly half of the programs can compute separation on smooth surfaces with Kutta condition.

#### • Remarks about flow separation calculation

Flow can separate from sharp edges (leading and tip edges of wings) or smooth surfaces. It is now well known that Euler codes can calculate sharp edge separation without any modification. The common explanation is that numerical dissipation which locally generates entropy in such distorted regions is responsible for the phenomenon. For smooth surface separation, the problem is more complicated. Some authors (RIZZI, NEWSOME) showed separated flows without any modification of the codes. But the results are strongly dependant on the mesh used. With a very fine grid separation can even disappear. Another approach consists in applying a local treatment (Kutta like condition) that rotates the body surface velocity vectors near separation points to make them parallel to a given separation line. The results obtained with both sharp edge and smooth surface separation are very similar to experimental measurements except near the center of the vortices. Much theoretical work has to be done to explain why we get such nice results with perfect gaz models. From an engineer point of view we can say that «it works» and can give useful qualitative and quantitative results in aircraft, missile and even car aerodynamics. One way to determine the separation line used for smooth surface separation calculation is to use boundary-layer codes coupled with Euler codes.

#### • Applications of Euler codes

To demonstrate the capability of Euler codes to calculate separated flows around missiles we present some typical examples.

The Euler codes used are (Ref. 25 liste B) :

- SUP which is a space-marching code limited to fuselages
- FLU3C which is a time-dependent code able to calculate complete missile configurations (see table 7).

**Fuselages at incidence - Flows computed with SUP**



– **2D ogive + 11D cylinder fuselage at Mach number 3 and incidence 15°**

The comparison between the results of SUP and SWINT (WARDLAW - Ref. 28 list B) with the same separation line is good for surface pressure coefficients (fig. 36) and excellent for local normal force coefficient and position of the center of pressure (fig. 37). The slight differences obtained in the separated region could come from the different grids used.

– **3D ogive + 7D cylinder fuselage at Mach number 1.98 and incidence 15°**

The comparison between the results of SUP and experimental values (Ref. 51) is good for surface pressure coefficients in the last section (fig. 38a). For the coefficient of normal force (fig. 38b), a difference appears in the cylinder region which perhaps comes from a bad estimation of the separation line. Nevertheless the error on the global normal force coefficient is only 10 % and the center of pressure is well predicted (4.0D instead of 4.1D).

– **3D ogive + 12D cylinder fuselage at Mach number 2 and incidence 15°**

Figure 39 gives the comparison between the results of SUP and experimental measurements by ONERA for transversal velocity vectors in the last section. We can note that the position of the vortex is relatively well predicted.

– **3D ogive + 10D cylinder fuselage at Mach number 2.8**

Figure 40 presents comparisons between the results of SUP and experimental values (Ref. 52). The agreement is excellent even at incidence 20 degrees. The linear extrapolation of the normal force coefficient from its value at incidence 4 degrees shows the non linearity of the flow at high incidence.

All these results emphasize what Euler codes can bring to industrial studies. One limitation for the separation on smooth surfaces stays in the determination of the separation line.

**Missile at incidence - ASTER missile computed with FLU3C**

At high incidence the aerodynamics of the Aerospatiale ASTER missile is non-linear due to the vortex sheets generated at the tip edges of its long wings. To illustrate the vortex structure we present isopressure lines in a transversal plane at Mach 2 and incidence 10 degrees on figure 41. Figure 42 presents a comparison of the surface pressure on the wing calculated with FLU3C and measured at ONERA at incidence 0, 4 and 10 degrees. The results are very good as well as for the wind side as for the lee side. The small differences between computed and experimental values at incidence 10 degrees can be attributed at least for some part, to the lack of separation on the fuselage with FLU3C. This very practical case (300.000 points) shows the capabilities of Euler codes to determine aerodynamic loading of missiles.

**Calculation of flows with transversal jets**

The interaction of a supersonic jet coming from the surface of a missile with the external supersonic flow gives a very complicated flow the theoretical knowledge on which is rather limited. The vorticity requires at least the Euler equations and though they do not enable to find all the real effects (separation upstream of the jet,...) they provide us with interesting information on the structure of the flow. Figure 43 presents iso pressure lines ; we can see :

- the detached shock with the subsonic region in front of the jet
- a very strong expansion on the fuselage after the jet
- the bypassing round the jet by the external flow.

This case illustrates the interest of Euler codes to study very complicated 3D flows.

**4.2.3. Full-potential equation (FPE)**

If we assume the flow to be steady and irrotational we can introduce a velocity potential and the Euler equations reduce to the single potential equation. This equation is only valid for flows without strong shocks and without flow separations.

Prediction methods based on the full potential equation are used regularly for treating transonic (Ref. 53) and supersonic (Ref. 54) flow over realistic aircraft configurations, but as we can notice from our inquiry (see table 11) there is practically no interest for this formulation in missile aerodynamics. The main reason is that FPE methods cannot calculate separated flows and so is limited for predicting missile aerodynamics characteristics at zero or very low angles of attack. As this FPE formulation is not used in missile aerodynamics we do not present it during this symposium but a detailed description of a full-potential code called NCOREL (not listed table 11) and used for missile body aerodynamics in supersonic is given in Ref. 55.

**4.2.4. Linearized potential equation**

For flows over obstacles in which the velocity departs slightly from free stream values, the potential equation for the perturbation velocity can be linearized and reduces to a simple second-order linear equation called Prandtl-Glauert equation. This equation is the least complex and describes both subsonic and supersonic flows. The main methods used to solve this equation are the surface singularity techniques.

For analysis of subcritical flows, these methods, often referred to as «panel methods», have been demonstrated to be very effective engineering tools and a variety of different numerical codes have been developed all of them capable of calculating arbitrarily complex and detailed 3D configurations. The extension of the surface singularity techniques to supersonic flows has been more limited for some numerical reasons explained further on. As a result, only a limited number of supersonic panel methods have been developed.

Panel methods have been in existence for a long time and most of them, if not all, have been developed for aircraft studies. It is only recently that aerodynamicists try to apply them to complete missile configurations, mainly to unconventional airframe shapes which cannot be calculated by classical methods. Notice that the singularity technique is not unknown by missile aerodynamicists, they use line singularity method for economically modeling axisymmetric pointed bodies for a long time.

Subsonic panel codes which are perfect are well known also we will only give a brief outline for supersonic codes.

– **Low-order codes**

This category includes for instance :

- USSAERO (Ref. 56) which employs constant sources on the body and linearly varying sources and doublets on lifting surfaces
- NLRAERO (Ref. 38 list B) which employs also constant sources on the body but uses linearly varying sources and quadratically varying doublets on lifting surfaces.

Compared to USSAERO, NLRAERO has been greatly improved in computational possibilities. The NLRAERO code can handle any configuration built up out of a fuselage and additional body-like components as tip-tanks, pods, stores,.... and a wing and other wing-like components. For conventional missiles it gives good results for global characteristics  $CN_\alpha$  and  $X_{cp}$  and pressure distributions. For airbreathing missiles it gives acceptable results for the global characteristics but we observe (see fig. 45) strong fluctuations on pressure resulting from the reflexion of virtual Mach waves in the interior of the body and the discontinuities of source distributions across panels. To prevent the propagation and reflection of virtual Mach waves, WOODWARD developed a new singularity called a triplet (superposition of a vortex distribution and a constant source). Use of this triplet has been demonstrated to be successful in the analysis of isolated bodies with regular panelling but its extension to wing-body combinations has shown some problems mainly related to the modeling of geometrical complex configurations where regular panelling is not possible.

#### -- High-order codes

To cancel or, at least, to minimize the oscillations, a higher order panel methods has been developed. In this method, strict continuity of higher order source (linear) and doublet (quadratic) distributions across panel edges eliminates any singular term in the velocity function. Mixed internal/external boundary conditions are then used to cancel or minimize flow perturbation inside any closed surface.

This category includes :

- PAN-AIR developed by EHLERS and al. at BOEING (Ref. 41 list B)
- HISSS developed by FORNASIER at MBB (Ref. 34 list B).

These codes give better results than the low order codes but are much more costly in computing time.

Figure 46 shows the pressure distribution on the classical test configuration cone-cylinder-cone.

Figure 45 shows the pressure distribution along an airbreathing missile.

As we can notice the pressure fluctuation is quite eliminated on the cone-cylinder-cone and practically eliminated on the airbreathing missile.

Panel methods can be applied to very complex configurations (see figure 44) and can predict with a good level of accuracy global and local aerodynamics. However, they are linear and therefore limited to very low angles of attack. As this limitation is very restrictive for missile, some panel methods have been extended to nonlinearities due to vortical effects and nonlinear compressibility associated with shock waves. The most important studies on nonlinear extensions based on panel methods have been done by NIELSEN Eng. Reference 57 presents techniques for calculating the effects of leading and trailing edge vortical wakes and nonlinear compressibility on missile forces and moments.

Because of time limitation, this subject will not be covered in this special course, but we hope that the numerous references given table 12 will be useful to the reader.

#### -- Survey of linearized potential codes

Table 12 presents the configuration capabilities of 17 programs.

We can notice :

- most are low order programs. Only HISSS, PAN-AIR and PHOBOS are high order programs
- only 7 programs can compute all configurations
- 4 programs are restricted to supersonic flows, 5 to subsonic flows and 8 can compute both flow regimes
- 7 programs include models for the formation and the tracking of vortices.

#### 4.2.5. Grid generation (Ref. 58 and 59)

To numerically solve the Navier-Stokes, Euler and full potential equations, the entire space around the object must be discretized. One of the main difficulties is applying exact boundary conditions on an irregular shape. In finite difference techniques, one practical way of overcoming this difficulty is to map the physical flow region (physical domain) into a more regular one (computational domain) for which a uniform rectangular grid is appropriate. With such a transformation all computations can be performed on a fixed rectangular grid regardless of the shape of the physical region.

Boundary conditions may be expressed by finite differences involving only grid points (at the intersections of coordinate lines) without the need for interpolations. The inverse transformation maps the regular grid into a curvilinear boundary conforming grid.

The grid employed can have a profound influence on the quality and the convergence rate of the solution.

The grid should be :

- smooth so that to limit the diffusion like truncation error
- orthogonal (or nearly) at the boundaries to allow accurate implementation of boundary conditions.

Several methods are used to generate grids : they may be classified into two groups :

- the algebraic methods, in which the coordinates are determined by interpolation
- the partial differential equation methods, in which the coordinates are the solution of the equations.

#### • Algebraic methods

They consist basically in interpolating functions among boundaries and/or intermediate curves or surfaces in the field. The functions specify the values (and perhaps some derivatives) of the coordinates on the boundaries. Values in the interior are determined by transfinite interpolation using specified interpolation functions called blending functions.

Advantages :

- fast generation
- explicit control of the grid point distribution

Disadvantages :

- propagation into the field of slope discontinuities
- difficulties (overlap) with severely distorted regions

• **PDE's methods**

The most widely used method is based on the system of Poisson equations which are of elliptic type :

$$\nabla^2 \xi^i = p^i ; i = 1, \dots, n \quad (n = 2 \text{ or } 3)$$

where  $\xi^i$  are the curvilinear coordinate system and  $p^i$  are functions which serve to control the coordinate line distributions and orientations.

**Advantages :**

- the extremum principles (exhibited by some elliptic systems) guarantee a one to one mapping
- the generated grid is smooth.

**Disadvantage :**

- the system of PDE's must be solved by an interactive procedure (convergence - computer time).

Hyperbolic and parabolic equations are also used

Hyperbolic systems will propagate boundary slope discontinuities into the field. Neither of these systems allow the entire boundary to be specified. The grid is generated by marching outward from the inner boundary, the outer boundary being free. Nevertheless they have the advantage of being generally faster than elliptic generation system

All the preceding methods are applicable to general three-dimensional configurations. However, with complicated three-dimensional regions, it may be difficult to generate a single grid that is smooth and has adequate point distributions everywhere. An approach to this problem is to divide the flow into sub-regions. Each zone can be topologically simple so that generating grid is relatively easy.

In a supersonic flow calculation by a marching technique the situation is easier. The grid needs to be generated in every marching plane as the calculation proceeds. We have to use just a two-dimensional solver. An example of such a grid is shown in figure 47.

**4.2.6 Geometry definition**

Before generating the grid points, the grid boundaries conform to the body surfaces must be determined. Thus, the body surface must be defined and a set of surface points maintaining an accurate representation of the body surface supplied as input to the grid generator. For performing the geometry definition which includes the modeling of surfaces along with the process of redistributing points on these surfaces, a computer-aided-design (CAD) system can be used.

Fig. 48 presents the flow chart of an entire geometry definition and verification procedure. The first step is to subdivide the missile into simple components and to fit each of them with BEZIER-surfaces. Then the grid topology must be determined in order to define the type of surface grid needed on the body. For the current applications, axis-normal body cross sections are desired. So intersections of a plane of constant x with all of the surfaces on the body are computed and two-dimensional splines are constructed. These splines are ordered end to end and geometry points are fitted with them. When this is done the points are redistributed according to the requirements of the grid generator. Before passing the surface grid to the grid generator and flow solution code, it should be checked for errors to verify that the geometry is being represented accurately and in a manner consistent with the data base. For most applications it is sufficient to verify visually the surface definition by displaying the surface graphically. Toward this end, shaded-surface and wire-frame displays have proved useful.

**5 Conclusion**

This paper was intended to present a review of tactical missile aerodynamics with some problems encountered on existing and future missiles and a state of the art for the industrial aerodynamic prediction codes.

Among the problems involved in missile designs are :

- high angle of attack aerodynamics for highly maneuverable missiles and/or vertically launched missiles with quick turn-over
- airframe-inlet interference in airbreathing missiles
- aerodynamics of unconventional shape missiles
- kinetic heating
- lateral jet control
- drag problem for missiles operating at long ranges

All these problems received much attention during the last years but some of them are only partially solved.

With regard to the overview of aerodynamic prediction codes we note a great number of programs each of them having its own capabilities and limits : there is no a universal code. Semi-empirical methods permit external preliminary missile design without expensive wind tunnel tests, reducing design time and cost, but a number of specific advancements are needed. These include in particular methods for better determining :

- nonlinear aerodynamics
- control effectiveness, hinge moments
- effects of airframe-inlet interference on drag, stability and control
- drag.

The continuing development and improvement of numerical methods is the result of advances in algorithms and computers. The panel methods and the Euler equations permit detailed study and complex configuration design. The Euler methods will be in the near future among the principal tools for missile designers but they need before a great deal of work in all areas from mesh generation to finding better ways of treating separation, and an increasing of computer speed and memory size. The Navier-Stokes applications stay limited and there will be a long time before using them routinely in conceptual design. The foreseeable trends in the use of computational methods are given fig. 49.

## REFERENCES

## List A : text references

1. CHIN S.S., «Missile Configuration Design», Mc. Graw-Hill, 1961
2. BREBNER G.G., «A brief review of flight weapons», Missile Aerodynamics, AGARD Lecture series n°98, 1979
3. KNOCHE H.G., «Trends in missile development and their corresponding requirements with respect to aerodynamics», AGARD - CP - 336, 1982
4. BREBNER G.G., «The control of guided weapons», Missile Aerodynamics, AGARD Lecture series n°98, 1979
5. BARTH H., «Aerodynamics characteristics of complete configurations», Missile Aerodynamics, VKI, Lecture series n°98, 1976
6. ANDERSON J. Mc., «Thrust vector control - Spoiler controls», Missile Aerodynamics, VKI, Lecture series n° 67, 1974
7. WARDLAW A.B., «High-angle-of-attack missile aerodynamics», Missile Aerodynamics, AGARD Lecture series n°98, 1979
8. NIELSEN J.N., «Missile Aerodynamics», Mc. Graw-Hill, 1960
9. KRIEGER R.J. and VUKELICH S.R., «Tactical Missile Drag», Tactical Missile Aerodynamics, volume 104, Progress in Astronautics and Aeronautics Published by AIAA, 1986
10. LANGHAM T.F., «Missile Motion Sensitivity to Dynamic Stability Derivatives», Arnold Engineering Development Center, AEDC - TR - 80 - 11, 1979
11. NIELSEN J.N. and GOODWIN F.K., «Preliminary method for estimating hinge moments of all-movable controls», Nielsen Engineering & Research, NEAR - TR - 268, 1982
12. GOODWIN F.K. and NIELSEN J.N., «Determination of optimum fin planform and airfoil section for minimizing fin hinge moment», Nielsen Engineering & Research, NEAR - TR - 286
13. RICHARDS B.E., «Kinetic heating of high speed missiles», Missiles Aerodynamics, AGARD Lecture series n° 92, 1979
14. MATHAUER H., «Aerodynamic heating of missiles», Missile Aerodynamics, AGARD - CP - 336 - 1982
15. NEUMANN R.D. and HAYES R.J., «Introduction to Aerodynamic heating analysis of supersonic missiles», Tactical Missile Aerodynamics, volume 104, Progress in Astronautics and Aeronautics Published by AIAA, 1986
16. BISPLINGHOFF R.L. and ASHLEY H., «Principles of Aeroelasticity», Wiley, 1962
17. DELERY J. and SIRIEX M., «Ecoulements de Culot», AGARD LS-98, 1979 or ONERA TP n°1979-14F
18. BERRUE P., LACAU R.G. and DELERY J., «Modélisation de l'écoulement au culot des missiles», XXIème Colloque d'Aérodynamique Appliquée, 1984
19. BREBNER G.G., «Weapon/aircraft interactions», Missile Aerodynamics, VKI, Lecture series n°67, 1974
20. MATHEWS C.B., «Store Separation», Missile Aerodynamics, AGARD Lecture series n°98, 1979
21. Store Airframe Aerodynamics, AGARD - CP - 389, 1985
22. PURVIS J.W., «A rigid body collision model for submunition dispersion simulation», AIAA paper n°82-363
23. STALLINGS R.L., «Store separation from cavities at supersonic speeds», AIAA paper n°82-372
24. CASSEL L.A., DURANDO N.A., BULLARD C.W., KELSO J.M., «Jet interaction control effectiveness for subsonic and supersonic flight», AD - 862483, Sept. 1968
25. SPAID F.W. and CASSEL L.A., «Aerodynamic interference induced by reaction controls», AGARD - AG - 173, 1973
26. CHAMPIGNY P., «Problèmes liés à l'aérodynamique externe des missiles aérobies», Missile Aerodynamics, AGARD - CP - 336, 1982
27. LARUELLE G., «Prises d'air pour missile probatoire de statofusée», L'Aérodynamique et l'Astronautique n°98, 1983
28. KRIEGER R.J., «Summary of design and performance characteristics of aerodynamic configured missiles», AIAA paper 81-286
29. RASMUSSEN M.L. and DANIEL D.C., «Aerodynamics of cone-derived waverider missile configurations», AGARD - CP - 336
30. SCHINDEL L.H., «High lift/drag ratio hypersonic missiles» AGARD - CP - 336
31. SCHINDEL L.H., «Waveriders», Tactical Missile Aerodynamics, volume 104, Progress in Astronautics and Aeronautics Published by AIAA, 1986
32. ALLEN H.J., «Estimation of the forces and moments acting on inclined bodies of revolution of high fineness ratio», NACA RM A9126, 1949
33. JORGENSEN L.H., «Prediction of aerodynamic characteristics for slender bodies alone and with lifting surfaces to high angles of attack», AGARD C.P. 247 - 1978
34. Engineering Sciences Data Unit, Royal Aeronautical Society
35. USAF Stability and Control Handbook - DATCOM, Wright - Patterson Air Force Base, Ohio 1969
36. Design of Aerodynamically Stabilized Free Rockets, U.S. Army Material Command AMCP 706-280
37. BARTH H., «Die Normalkraft, Druckpunkt, und Tangentialkraft charakteristiken schlanker Bug-Zylinder Konfigurationen im Machzahlbereich 0.8 bis 4.0», BMVg-FBWT 73-32

38. TSIEN H-S., «Supersonic flow over an inclined body of revolution», *Journal of the Aeronautical Sciences*, volume 5, n° 12, pp-480-483, 1938
39. VAN DYKE M.D., «First and second-order theory of supersonic flow past bodies of revolution», *Journal of Aeronautical Sciences*, volume 18, n° 3, March 1951
40. SYVERTSON C.A., DENNIS D.H., «A second order shock-expansion method applicable to bodies of revolution near zero lift» NACA Report 1328, 1957
41. MULTHOFF H., «Methods for calculating the lift distribution of wings (subsonic lifting-surface theory)», ARC R & M n° 2884, 1950
42. BERTIN J.J. and SMITH N.L., «Aerodynamics for Engineers», Prentice Hall, 1979
43. FENAIN M. and GUIRAUD-VALLEE D., «Calcul numérique des ailes en régime supersonique stationnaire et instationnaire», *Recherche Aerospatiale* n° 115, 1966
44. STALLINGS R.L. and LAMB M., «Wing alone aerodynamic characteristics for high angles of attack at supersonic speeds», NASA - TP - 1889, 1981
45. BRIGGS M.M., REED R.E. and NIELSEN J.N., «Wing alone aerodynamic characteristics to high angles of attack at subsonic and transonic speeds», NEAR - TR - 269, 1982
46. NIELSEN J.N., PITTS W.C., KAATTARI G.E., «Lift and center of Wing-Body-Tail combinations at subsonic, transonic and supersonic speeds», NACA R 1307, 1957
47. HEMSCH M.J. and NIELSEN J.N., «The equivalent angle-of-attack concept for engineering analysis», in *Tactical Missile Aerodynamics*, AIAA Progress in Astronautics and Aeronautics, volume 104, 1986
48. ARTERBURY R.L., BAKER W.B., «Critical evaluation of eight semi-empirical aerodynamic coefficient prediction programs for missiles and stores», AIAA paper n° 83-0185
49. KLOPFER G.H., NIELSEN J.N., «Computational fluid dynamic applications to missile aerodynamics», AGARD - CP - 336, 1982
50. CHAUSSEE D.S., «High speed viscous flow calculations about complex configurations», AGARD - CP - 412 - 1986
51. PERKINS E.W., JORGENSEN L.H., «Comparison of experimental and theoretical normal force distribution on an ogive-cylinder body at Mach number 1.98», NACA TN-3716, 1966
52. OSBORNE W.K., «Guided weapons aerodynamic study. Tests on a body alone, and in combination with delta wings», RAE TR - 65109, 1965
53. JAMESON A., «Transonic Potential flow calculations using conservative form», AIAA 2nd. Computational Fluid Dynamic Conference, 1975
54. SHANKAR V., SZEMA K.Y., OSHER S., «Treatment of supersonic flows with embedded subsonic regions», AIAA Journal, volume 23, 1985
55. PITTMANN J.L., MILLER D.S., SICLARI M.J., «Supersonic full-potential method applied to missile bodies», *Tactical Missile Aerodynamics*, volume 104, Progress in Astronautics and Aeronautics, Published by AIAA, 1986
56. WOODWARD F.A., «An improved method for the aerodynamic analysis of wing-body-tail configuration in subsonic and supersonic flows, NASA-CR-2228, 1973
57. DILLENIUS M.F.E., ALLEN J.M., «Paneling methods with vorticity effects and corrections for nonlinear compressibility», *Tactical Missile Aerodynamics*, volume 104, Progress in Astronautics and Aeronautics, Published by AIAA, 1986
58. THOMPSON J.F., «A survey of grid generation techniques in computational fluid dynamics», AIAA paper 83-0447
59. THOMPSON J.F., WARSJI Z.U.A., MASTIN C.W., «Numerical grid generation», North-Holland Elsevier Science Publishing Co, Inc, 1985

## REFERENCES

List B : table references

1. HERRING P.G.C., «A computer program which evaluates the longitudinal aerodynamic characteristics of typical weapon configurations», AGARD - CP - 336, 1982
2. HASSELOT A., «Beräkning aerodynamiska koefficienter för rammotorroboter», FFA AU-166, 1980
3. GUSTAFSSON A., «A computer program for the prediction of aerodynamic characteristics of wing-body-tail combinations at subsonic and supersonic speeds», FFA AU-635, 1972
4. BAKER W.B., «An aerodynamic coefficient prediction technique for slender bodies with low aspect ratio fins at transonic Mach numbers and angles of attack to 180 degrees», AEDC - TR - 77.97, 1978
5. EATON P.T., «A method for predicting the static aerodynamic characteristics of low-aspect-ratio configurations», DTMB-2216, 1966
6. SUN J., HANSEN S.G., CUMMING R.M., AUGUST H., «Missile aerodynamics prediction (MAP) code», AIAA paper n° 84-0389, 1984
7. VUKELICH S.R., JENKINS J.E., «Missile DATCOM : aerodynamic prediction on conventional missiles using component build-up techniques», AIAA paper n° 84-0388, 1984
8. BOIZARD B., «Missile ONERA» in *Activities ONERA 1985 - Aerodynamique (II-10)*

9. SMITH C.A., NIELSEN J.N., «Prediction of aerodynamic characteristics of cruciform missiles to high angles of attack utilizing a distributed vortex wake», NEAR - TR - 208, 1979
10. HEMSCH M.J., MULLEN J., «Analytical extension of the MISSILE 1 and MISSILE 2 computer programs», NEAR - TR - 272, 1982
11. DILLENIUS M.F., HEMSCH M.J., SAWYER W.C., ALLEN J.M., BLAIR A.B., «Comprehensive Missile aerodynamics programs for preliminary design», J. Spacecraft, volume 20, n°4, 1983
12. LESIEUTRE D.J., MENDENHALL M.R., NAZARIO S.M., «Prediction of the aerodynamic characteristics of cruciform missiles including effects of roll angle and control deflection», NEAR - TR - 360, 1986
13. LESIEUTRE D.J., MENDENHALL M.R., NAZARIO S.M., «Aerodynamic characteristics of cruciform missiles at high angles of attack», AIAA paper n°87-0212
14. MOORE F.G., «Aerodynamics of guided and unguided weapons», NWL - TR - 3018, Jan. 1975
15. DEVAN L., MASON L.A., «Aerodynamics of tactical weapons to Mach number 8 and angle of attack 180°», AIAA paper n°82 - 0250
16. DEVAN L., MOORE F.G., «Aerodynamic prediction for tactical weapons», AIAA paper n°79 - 0361
17. WILLIAMS J.E., VUKELICH S.R., «USAF stability and control DATCOM», AFFDL - TR - 75 - 45
18. GENTRY A.E., SMYTH D.N., OLIVIER W.R., «The MARK IV supersonic - hypersonic arbitrary body program», AFFDL TR - 73 - 159, 1973
19. BARROWMAN, «An improved theoretical aerodynamic derivatives computer program for sounding rockets», AIAA paper n°79 - 0504
20. SCHIFF L.B. and STEGER J.L., «Numerical simulation of steady supersonic viscous flow», AIAA paper n°79 - 0130, 1979
21. KAUL U.K. and CHAUSEE, «AFWAL parabolized Navier-Stokes code : 1983», AFWAL/NASA Merged baseline version, AFWAL - TR - 83 - 3118, 1984
22. EBERLE A., «Euler solution for a complete fighter aircraft at sub and supersonic speed», AGARD - CP - 412, 1986
23. CHATTOT J.J., KOCK C. and ELSAESSER E., «Solution of the EULER equations for missiles configurations», Proceedings of the six GAMM - Conference on Numerical Methodes in Fluid Mechanics, volume 13, 1986, Vieweg
24. BORREL M., MONTAGNE J.L., «Numerical study of a non-centered scheme with applications to aerodynamics», AIAA paper n°85 - 1497, 1985
25. LORDON J., GUILLEN P., MORTEL P., LACAU R.G., «Calcul d'écoulements supersoniques autour de missiles tactiques», 23ème Colloque d'Aérodynamique Appliquée, 1986
26. WARDLAW A.B., PRIOLO F.G. and SOLOMON J.M., «An inviscid multiple zone method for supersonic tactical missiles», NSWC - TR - 85 - 484, 1985
27. DAYWITT J.E., BRANT D. and BOSWORTH F., «Computational technique for three-dimensional inviscid flow fields about reentry vehicles», SAMSO TR - 79 - 5, 1978
28. WARDLAW A.B., BALTAKIS F.P., SOLOMON J.M. and HACKERMAN L.B., «An inviscid computational method for tactical missile configuration» NSWC - TR - 81 - 457, 1981
29. WARDLAW A.B., NSWC TR-86-506, 1986
30. WOLFE W.P. and OBERKAMPF W.L., «Drag predictions for projectiles and finned bodies in incompressible flow», AIAA paper n°85 - 0104
31. WOLFE W.P. and OBERKAMPF W.L., «SANDRAG - A computer code for predicting drag of bodies of revolution at zero angle of attack in incompressible flow», SAND 85-0515, 1985
32. DILLENIUS M.F.E. and ALLEN J.M., «Paneling methods with vorticity effects and corrections for nonlinear compressibility», in Tactical Missile Aerodynamics, AIAA Progress in Astronautics and Aeronautics, volume 104, 1986
33. DILLENIUS M.F.E. and KEIRSTEAD, «Panel methods applied to supersonic inlets alone and to complete supersonic air breathing configurations», NASA CR-3979, 1986
34. FORNASSIER L., «Linearized potential flow analysis of complex aircraft configurations by HISSS, a higher-order panel method», AIAA paper n° 85-0281
35. FFA Report 138, 1983
36. DEVAN L., «Nonaxisymmetric body, supersonic, aerodynamic prediction», NSWC TR - 86 - 253, 1986
37. NIKOLITSCH D., «Calculation of pressure distributions, forces and moments of cruciform wing-body combination up to high angles of attack», AIAA paper n°81 - 0397
38. HOEIJMAKERS H.W.M., «A panel method for the prediction of aerodynamic characteristics of complex configurations in linearized subsonic and supersonic flow», in Missile Aerodynamics, AGARD CP - 336, 1982
39. SHANKAR V.J., SZEMA K.Y. and BONNER E., «Full-potential methods for analysis-design of complex aerospace configurations», NASA CR-3982, 1986
40. DILLENIUS M.F.E., PERKINS S.C., LESIEUTRE D.J., «Modified NWCDM-NSTRN and supersonic store separation programs for calculating NASTRAN forces acting on Missiles attached to supersonic aircraft», NEAR TR-369, 1986

41. SIDWELL K.W., BARUAH P.K., BUSSOLETTI J.E., «A computer program for predicting subsonic or supersonic linear potential flows about arbitrary configurations using a higher order panel method», volume II NASA CR 3252, 1980
42. LOTSTEDT P., «A three-dimensional higher order panel method for subsonic flow problems description and applications», SAAB L-O-1R 100, 1984
43. HENNIG P., HARTNER E., «Instationäre beiwerte von flugkörpern, Teil V ; Derivative der längsstabilität von flügel-rumpf leitwerks - anordnungen in unter und überschallströmung», MBB - Bericht UA-830-84, 1985
44. DILLENIUS M.F., NIELSEN J.N., «Computer programs for calculating pressure distributions including vortex effects on supersonic monoplane or cruciform using-body-tail combinations with round or elliptical bodies», NASA CR-3122, 1979
45. NIKOLITSCH D., «Flügel-rumpfkombinationen im nichtlinearen ausstellwinkel-bereich, Teil III», MBB-Bericht UA-676/82, 1982

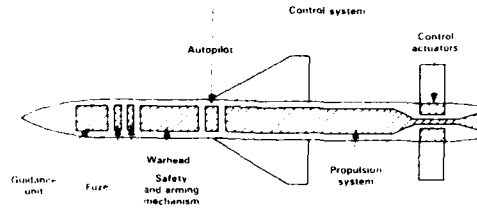


Fig 1 - LAYOUT OF A TYPICAL GUIDED WEAPON

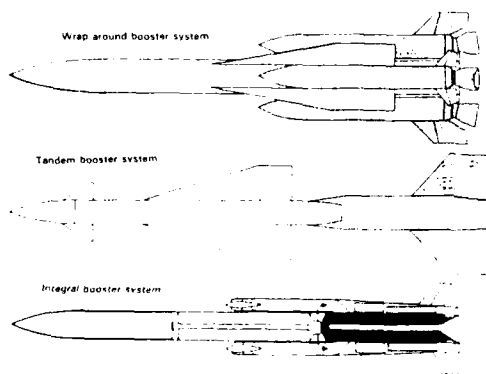


Fig 2 - TYPES OF POWERPLANT INSTALLATIONS IN THE ACCELERATION PHASE

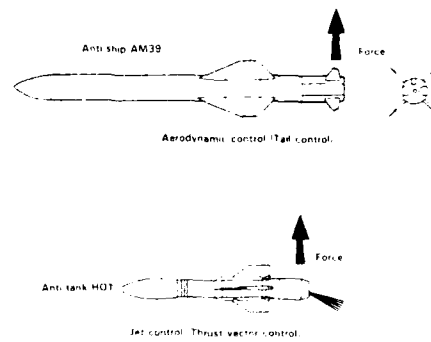


Fig 3 - TYPES OF CONTROL SYSTEMS

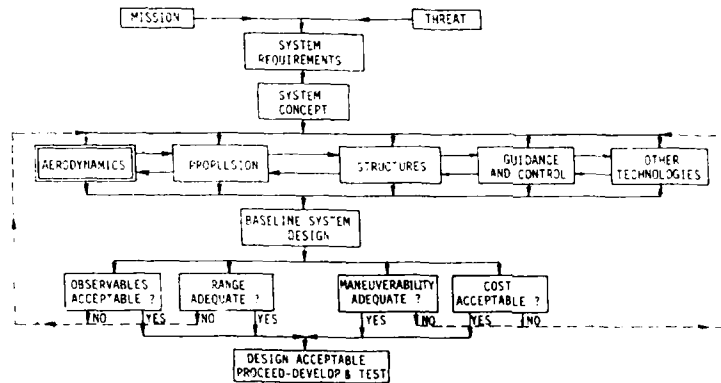


Fig. 4 - ITERATIVE DESIGN CYCLE [3]

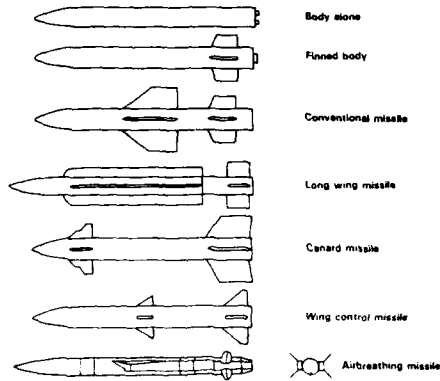


Fig. 5 - TYPES OF CONFIGURATIONS

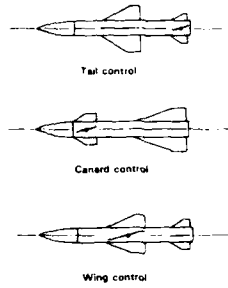


Fig. 6 - AERODYNAMIC CONTROLS

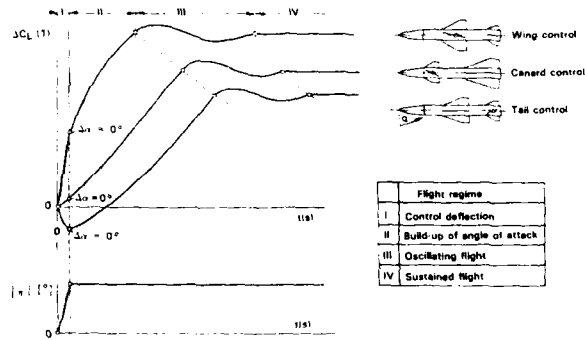


Fig. 7 - LIFT BUILD-UP WITH CONTROL DEFLECTION  $\eta$  VERSUS TIME

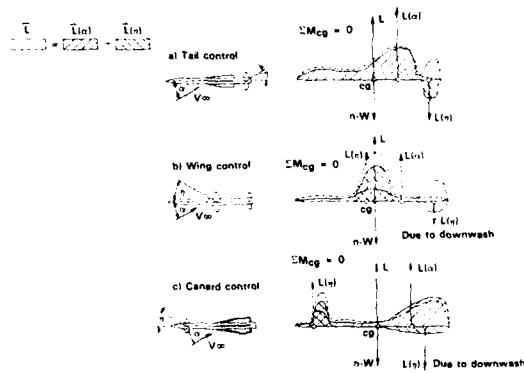


Fig. 8 - TAIL, WING, AND CANARD CONTROL MISSILE AND THEIR RESPECTIVE LIFT MECHANISMS



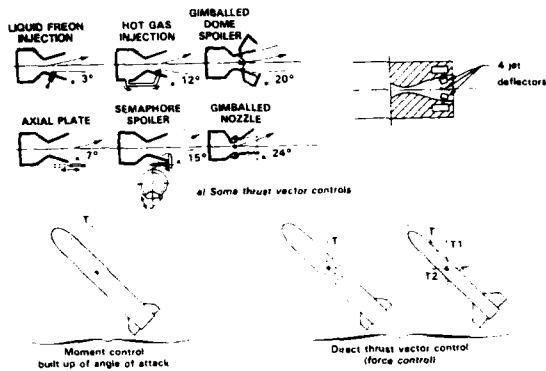


Fig. 9 - JET CONTROLS



Fig. 10 - FUTURE ANTI-TANK MISSILE ERYX LOW-POWER PROPULSION UNIT PERMITS LAUNCHES FROM CONFINED SPACES

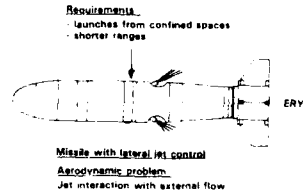


Fig. 11 - SOME TRENDS IN FUTURE ANTI-TANK MISSILES AND RESULTING NEW AERODYNAMIC PROBLEM

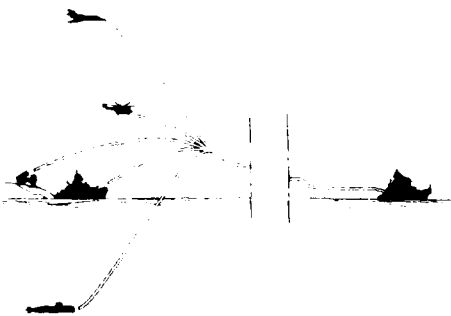


Fig. 12 - TYPICAL TRAJECTORIES FOR ANTI-SHIP MISSILES

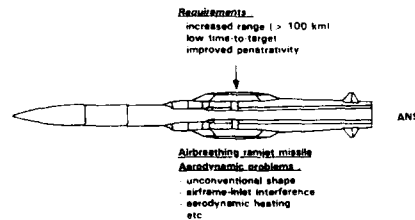


Fig. 13 - SOME TRENDS IN FUTURE ANTI-SHIP MISSILES AND RESULTING NEW AERODYNAMIC PROBLEMS

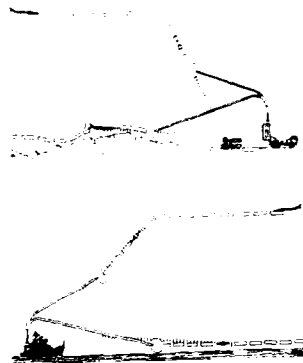
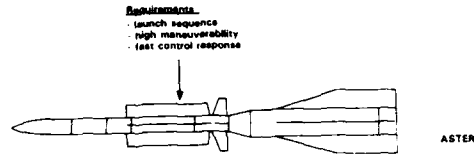


Fig. 14 - ANTI-MISSILE GROUND/SURFACE-TO-AIR SYSTEMS FOR THE NINETIES (ex. ASTER 15)



- Vertically launched missiles with quick turn-over
- Combined control systems (aerodynamic control and jet control)

- Aerodynamic problems:
  - high angle-of attack aerodynamics
  - lateral jet interaction with external flow

Fig. 15 - SOME TRENDS IN FUTURE GROUND/SURFACE-TO-AIR MISSILES AND RESULTING NEW AERODYNAMIC PROBLEMS

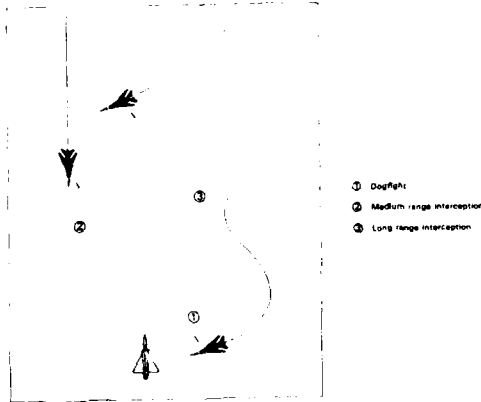
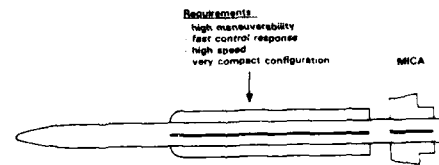


Fig. 16 - AIR-TO-AIR MISSILES FOR THE NINETIES (ex. MICA)



- Missiles with long noses
- Combined control systems (aerodynamic control and jet deflector control)

- Aerodynamic problem:
  - High angle of attack aerodynamics ( $> 20^\circ$ )

Fig. 17 - SOME TRENDS IN FUTURE AIR-TO-AIR MISSILES AND RESULTING NEW AERODYNAMIC PROBLEMS

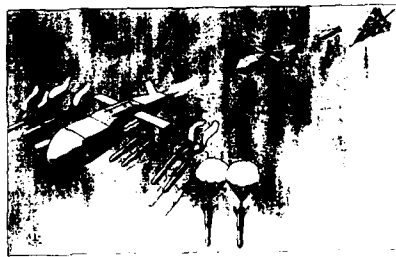


Fig. 18 - MODULAR STAND-OFF WEAPON CONCEPT (ex. MOBIDIC)

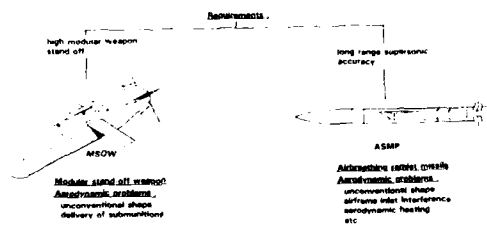


Fig. 19 - SOME TRENDS IN AIR-GROUND/SURFACE MISSILES AND RESULTING NEW AERODYNAMIC PROBLEMS

| Performance Improvement Areas |                   | Contributing Factors |          |                |                  |        |        |                      |
|-------------------------------|-------------------|----------------------|----------|----------------|------------------|--------|--------|----------------------|
|                               |                   | Cruise Speed         | Altitude | Axial Maneuver | Lateral Maneuver | Weight | Volume | Launcher Constraints |
| Penetrativity                 | Detectability     | A P S                | A P S    | A P            | A P S            | -      | A P S  | A P S                |
| Range                         | Range             | A P                  | A P      | -              | -                | A P S  | A P S  | -                    |
|                               | Time-to-Target    | A P S                | A P S    | A P            | -                | A P S  | -      | -                    |
| Maneuverability               | Terminal Accuracy | A P S                | -        | A P            | A P S            | A P S  | -      | P S                  |

A = Aerodynamics  
P = Propulsion  
S = Structures

Fig. 20 - PERFORMANCE IMPROVEMENT AREAS RELATED TO CONTRIBUTING FACTORS [3]

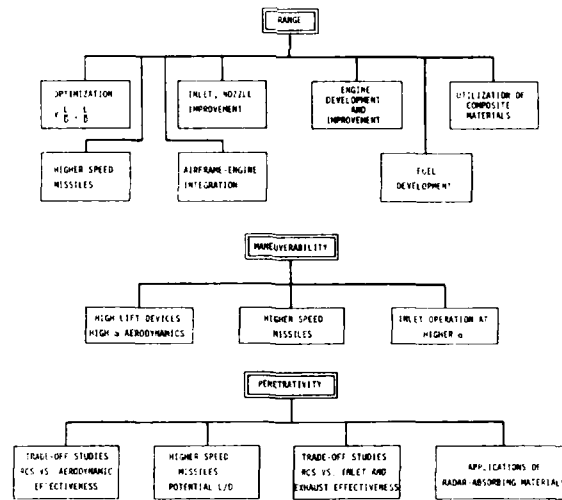


Fig. 21 - TECHNOLOGY IMPROVEMENT AREAS RELATED TO RANGE, MANEUVERABILITY AND PENETRATIVITY [3]

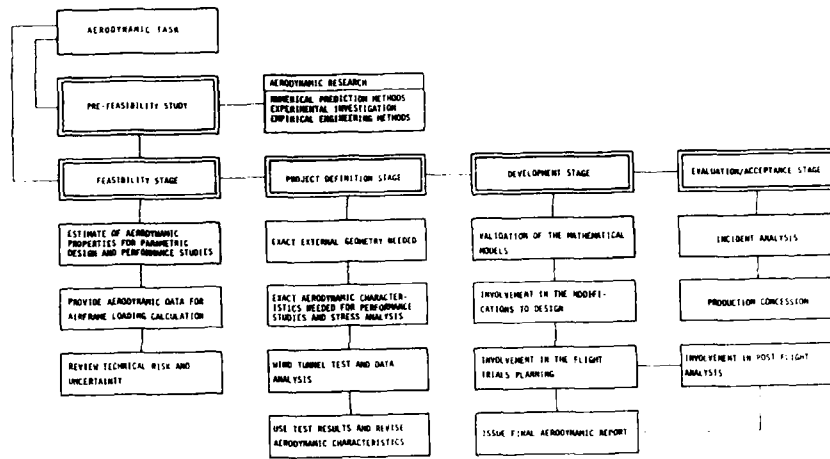
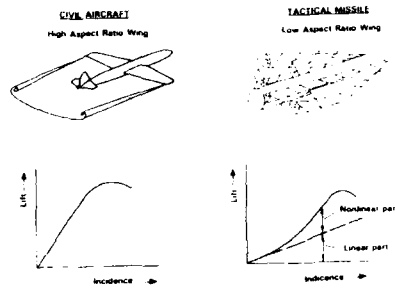
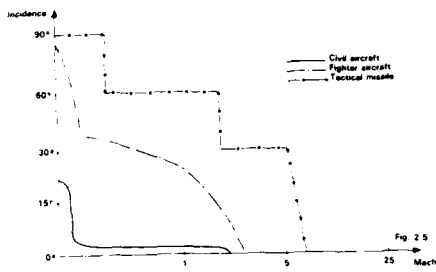


Fig. 24 - AERODYNAMIC DESIGN TASKS AT DIFFERENT PROJECT STAGES [3]

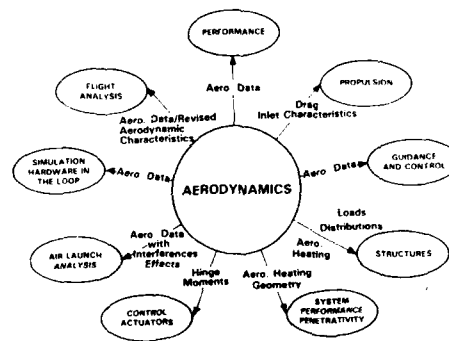
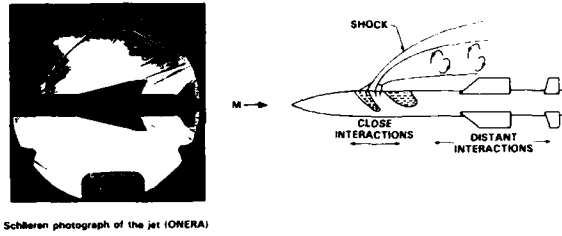


Fig. 25 - CONNECTIONS BETWEEN AERODYNAMICS AND THE OTHER TECHNOLOGY AREAS



Schlieren photograph of the jet (ONERA)

Fig. 26 - LATERAL JET INTERACTIONS

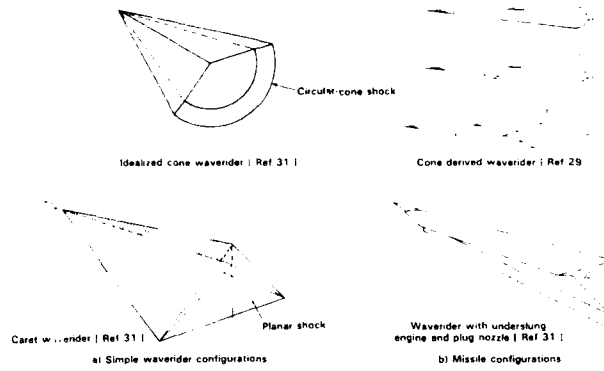


Fig. 27 - WAVERIDER-TYPE CONFIGURATIONS IN HYPERSONIC FLOW

| Body/wing at angle of attack     | Body-fin with fin deflection     | Body/wing at roll position  | Adjacent fins influence                        |
|----------------------------------|----------------------------------|---|--|
|                                  |                                  |   |  |
| $tg \alpha_{eq} = K_w tg \alpha$ | $tg \alpha_{eq} = k_w tg \delta$ | $\begin{cases} \cos \alpha_{eq} = \cos \alpha \\ \sin \alpha_{eq} = \sin \alpha \end{cases}$<br>$tg \alpha_{eq} = (1 + K_w \sin^2 \alpha) \times (K_w / \cos \alpha)$ | $tg \alpha_{eq} = \sum \Delta f_j tg \delta_j$ |

Fig. 28 - INTERACTION COEFFICIENTS

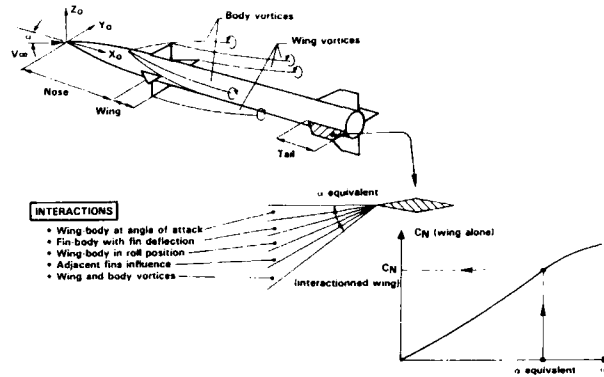


Fig. 29 - EQUIVALENT ANGLE OF ATTACK

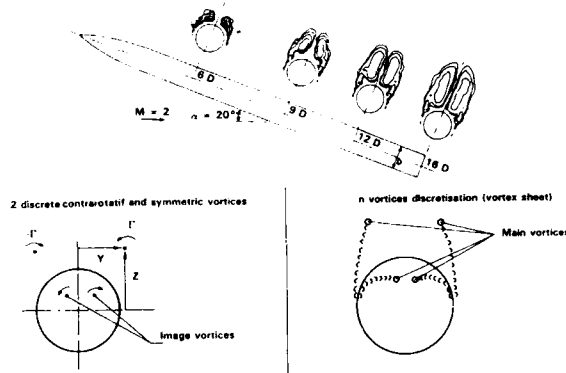


Fig. 30 - BODY VORTICES MODELS

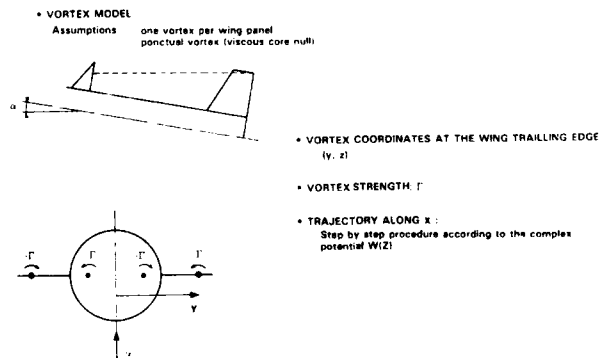


Fig. 31 - WING-TAIL INTERACTION

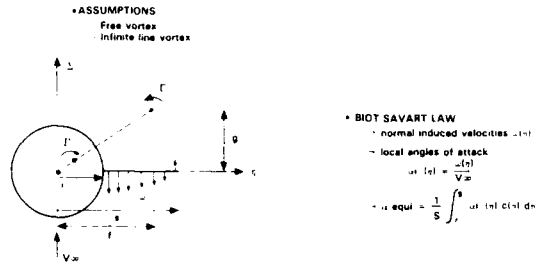


Fig. 32 - VORTEX INDUCED ANGLE OF ATTACK

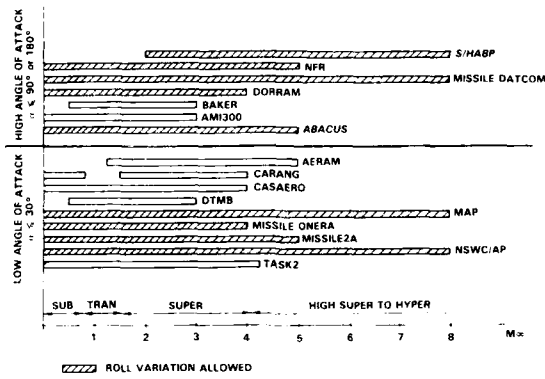


Fig. 33 - SEMI-EMPIRICAL METHODS : FLIGHT REGIME CAPABILITY

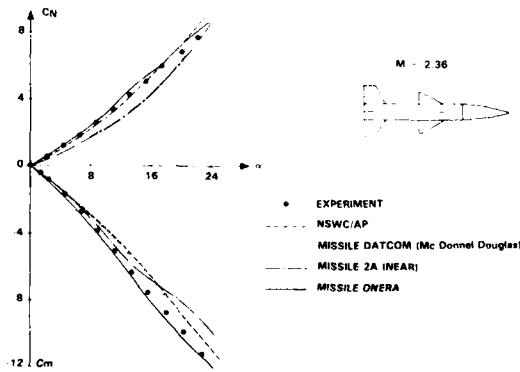


Fig. 34 - BODY-WING-TAIL SAMPLE CASE CALCULATED BY DIFFERENT CODES

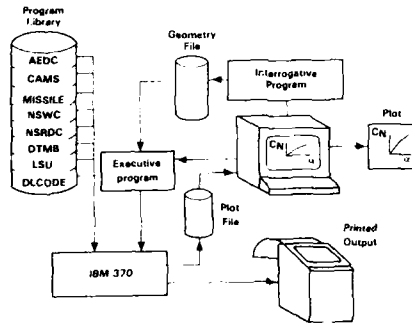


Fig. 35 - INTERACTIVE GRAPHICS ACCESS SYSTEM ( 48 )

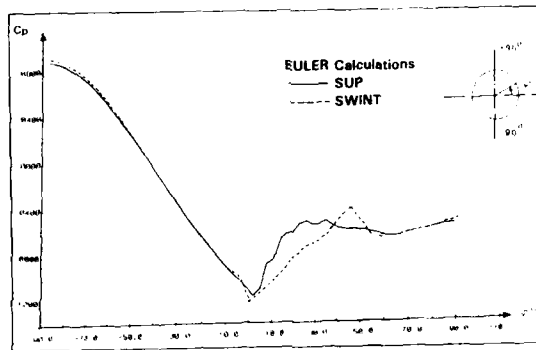


Fig. 36 - CIRCUMFERENTIAL PRESSURE PROFILE FOR AN OGIVE CYLINDER AT MACH 3, 15 - deg INCIDENCE, X/D = 13

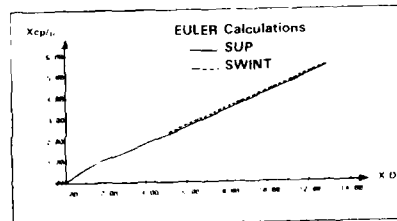
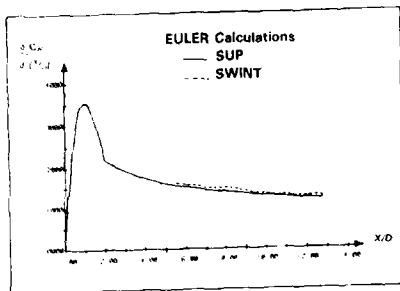


Fig. 37 - LOCAL NORMAL FORCE AND CENTER-OF-PRESSURE COEFFICIENTS FOR AN OGIVE CYLINDER AT MACH 3, 15 - deg INCIDENCE



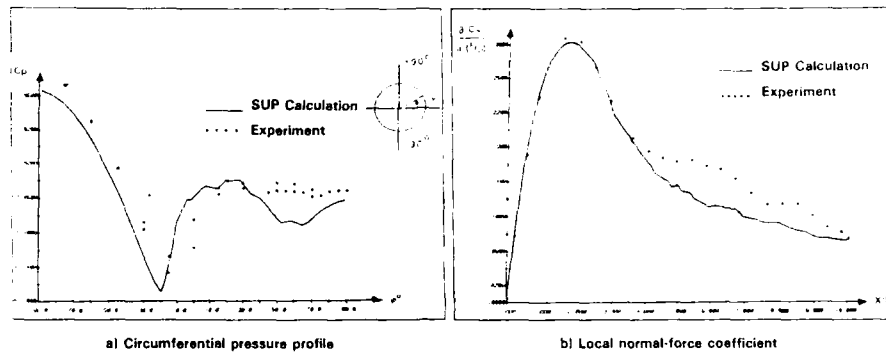


Fig. 38 - COMPARISON OF EXPERIMENT AND THEORY FOR AN OGIVE-CYLINDER AT MACH 1.98, 15 - deg INCIDENCE

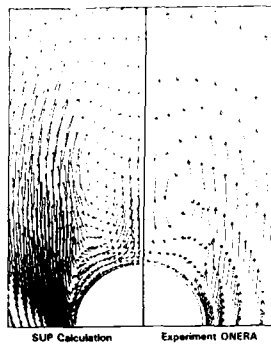


Fig. 39 - CALCULATED AND MEASURED CROSS-FLOW VELOCITY FIELD ON THE LEE SIDE OF AN OGIVE-CYLINDER AT MACH 2.0 15 deg INCIDENCE. X/D = 15

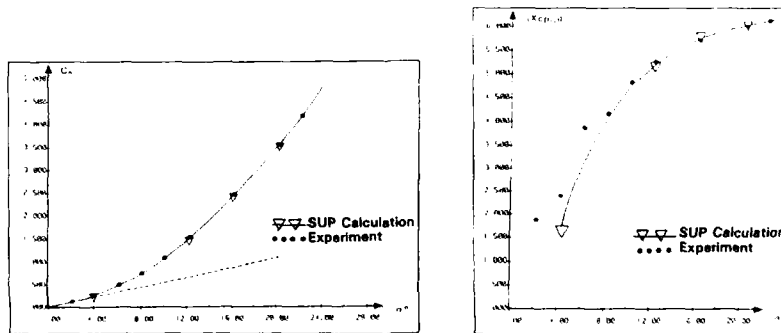


Fig. 40 - NORMAL-FORCE AND CENTER-OF-PRESSURE COEFFICIENTS FOR AN OGIVE-CYLINDER AT MACH 2.8

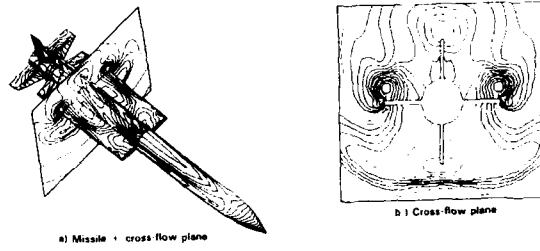


Fig. 41 - ISOBAR PATTERN - ASTER MISSILE AT MACH 2.5, 10 deg INCIDENCE

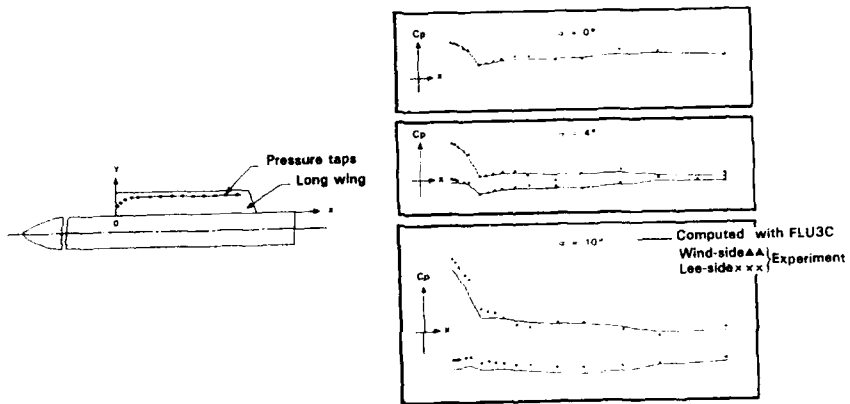


Fig. 42 - CALCULATED AND MEASURED SURFACE PRESSURES ON A LONG WING MISSILE ASTER (Mach 2.5)

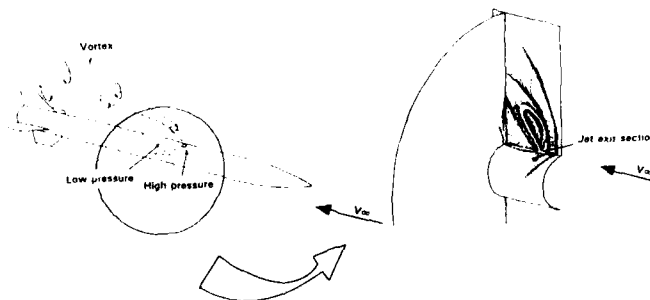


Fig. 43 - ISOBAR PATTERN - LATERAL JET INTERACTIONS WITH AN EXTERNAL FLOW - FLU3C CALCULATION

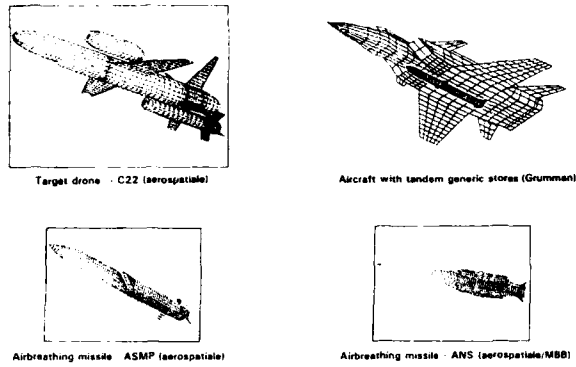


Fig. 44 - COMPLEX CONFIGURATIONS PANELING

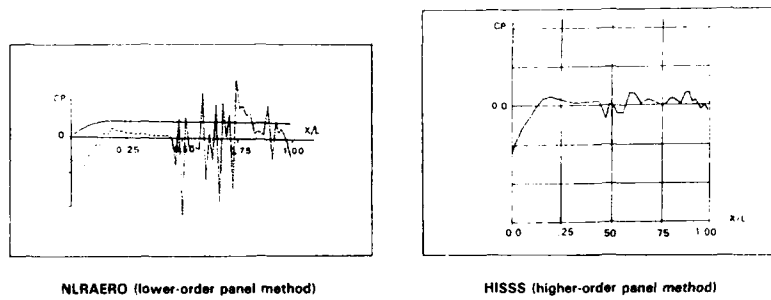


Fig. 45 - AIRBREATHING MISSILE (ANS) AT MACH 2.  
2 - DEGREE INCIDENCE, LONGITUDINAL SURFACE  
PRESSURE DISTRIBUTION

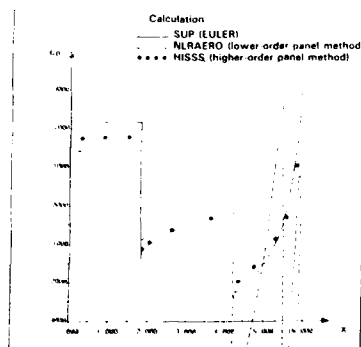


Fig. 46 - CONE-CYLINDER-CONE CONFIGURATION  
AT MACH 2.0, 0 - DEGREE INCIDENCE  
LONGITUDINAL SURFACE PRESSURE  
DISTRIBUTION

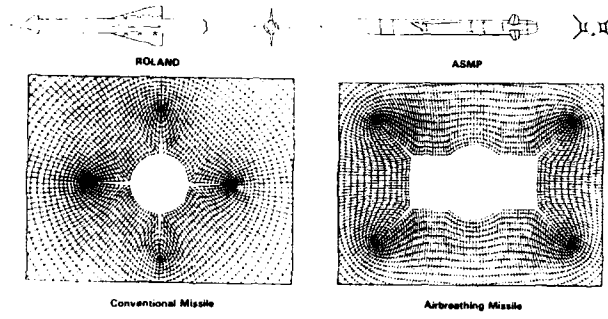


Fig. 47 - TYPICAL COMPUTATIONAL MESHES

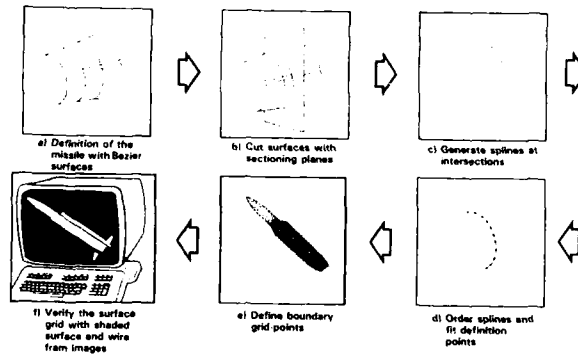


Fig. 48 - GEOMETRY DEFINITION/VERIFICATION PROCEDURE WITH CAD/CAM SYSTEM

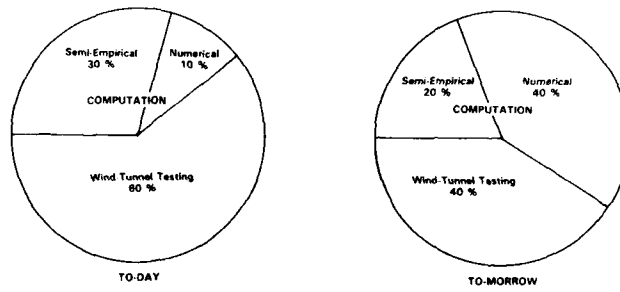


Fig. 49 - REPARTITION OF AERODYNAMIC PREDICTIVE MEANS

### CAPABILITIES OF EMPIRICAL AND SEMI-EMPIRICAL CODES FOR MISSILES

| CODE NAME       | MACH RANGE | INCIDENCE ANGLE | ROLL RANGE   | PWS | CONTROL   | AERODYNAMIC COEFFICIENTS |         |
|-----------------|------------|-----------------|--------------|-----|-----------|--------------------------|---------|
|                 |            |                 |              |     |           | STATIC                   | DYNAMIC |
|                 |            |                 |              |     |           | Roll                     | Yaw     |
| ABACUS          | M=1.50     | 90° x 1.50°     | 180° x 1.50° | /   | PITCH/YAW | /                        | /       |
| ABRAM           | 1.74 M=0.3 | 0°-20°          | 0°-20°       | /   | PITCH/YAW | /                        | /       |
| AM300           | M=1.50     | 0°-60°          | 0°-60°       | /   | PITCH/YAW | /                        | /       |
| BAKER           | 0.5 M=0.3  | 0°-180°         | 0°-180°      | /   | PITCH/YAW | /                        | /       |
| BOVINCY         | 0.5 M=0.3  | 0°-180°         | 0°-180°      | /   | PITCH/YAW | /                        | /       |
| CABANG          | 0.4 M=0.3  | 0°-20°          | 0°-20°       | /   | PITCH/YAW | /                        | /       |
| CASABRO         | M=1.40     | 0°-20°          | 0°-20°       | /   | PITCH/YAW | /                        | /       |
| DORRAM          | M=1.40     | 0°-20°          | 0°-20°       | /   | PITCH/YAW | /                        | /       |
| DRAG            | M=1.70     | 0°-20°          | 0°-20°       | /   | PITCH/YAW | /                        | /       |
| DTMB            | 0.5 M=0.3  | 0°-20°          | 0°-20°       | /   | PITCH/YAW | /                        | /       |
| NAP             | M=1.80     | 0°-60°          | 0°-60°       | /   | PITCH/YAW | /                        | /       |
| MISSILE DATCOM  | M=1.60     | 0°-60°          | 0°-60°       | /   | PITCH/YAW | /                        | /       |
| MISSILE NEAR    | M=1.4      | 0°-25°          | 0°-25°       | /   | PITCH/YAW | /                        | /       |
| MISSILE 1 NEAR  | M=1.4      | 0°-25°          | 0°-25°       | /   | PITCH/YAW | /                        | /       |
| MISSILE 2A NEAR | M=1.5      | 0°-60°          | 0°-60°       | /   | PITCH/YAW | /                        | /       |
| MISSILE 3 NEAR  | M=1.5      | 0°-60°          | 0°-60°       | /   | PITCH/YAW | /                        | /       |
| MRT             | M=1.5      | 0°-20°          | 0°-20°       | /   | PITCH/YAW | /                        | /       |
| NIR             | M=1.5      | 90° x 1.50°     | 180° x 1.50° | /   | PITCH/YAW | /                        | /       |
| NSWC AP         | M=1.80     | 0°-60°          | 0°-60°       | /   | PITCH/YAW | /                        | /       |
| PORTANCE        | M=1.60     | 0°-20°          | 0°-20°       | /   | PITCH/YAW | /                        | /       |
| SFA DATCOM      | M=1.60     | 0°-60°          | 0°-60°       | /   | PITCH/YAW | /                        | /       |
| SMBRP           | M=1.70     | 90° x 1.50°     | 180° x 1.50° | /   | PITCH/YAW | /                        | /       |
| PAD             | M=1.60     | 0°-20°          | 0°-20°       | /   | PITCH/YAW | /                        | /       |
| TASK2           | M=1.42     | 0°-20°          | 0°-20°       | /   | PITCH/YAW | /                        | /       |
| TRAFRO          | M=1.40     | 0°-20°          | 0°-20°       | /   | PITCH/YAW | /                        | /       |

Configuration type has been compared

TABLE 2

### CAPABILITIES OF EMPIRICAL AND SEMI-EMPIRICAL CODES FOR MISSILES

| CODE NAME       | ORIGINE | REF # | DATE | CONVENTIONAL |     |    | UNCONVENTIONAL |     |    |
|-----------------|---------|-------|------|--------------|-----|----|----------------|-----|----|
|                 |         |       |      | 1CF          | 2CF | DD | 1CF            | 2CF | DD |
|                 |         |       |      |              |     |    |                |     |    |
| ABACUS          | BAA     | 1     | 1977 | /            | /   | /  | /              | /   | /  |
| ABRAM           | DA      | 7     | 1980 | /            | /   | /  | /              | /   | /  |
| AM300           | DA      | 7     | 1980 | /            | /   | /  | /              | /   | /  |
| BAKER           | DA      | 4     | 1980 | /            | /   | /  | /              | /   | /  |
| BOVINCY         | DA      | 4     | 1980 | /            | /   | /  | /              | /   | /  |
| CABANG          | DA      | 4     | 1980 | /            | /   | /  | /              | /   | /  |
| CASABRO         | DA      | 4     | 1980 | /            | /   | /  | /              | /   | /  |
| DORRAM          | DA      | 4     | 1980 | /            | /   | /  | /              | /   | /  |
| DRAG            | DA      | 4     | 1980 | /            | /   | /  | /              | /   | /  |
| DTMB            | DA      | 4     | 1980 | /            | /   | /  | /              | /   | /  |
| NAP             | DA      | 4     | 1980 | /            | /   | /  | /              | /   | /  |
| MISSILE DATCOM  | DA      | 4     | 1980 | /            | /   | /  | /              | /   | /  |
| MISSILE NEAR    | DA      | 4     | 1980 | /            | /   | /  | /              | /   | /  |
| MISSILE 1 NEAR  | DA      | 4     | 1980 | /            | /   | /  | /              | /   | /  |
| MISSILE 2A NEAR | DA      | 4     | 1980 | /            | /   | /  | /              | /   | /  |
| MISSILE 3 NEAR  | DA      | 4     | 1980 | /            | /   | /  | /              | /   | /  |
| MRT             | DA      | 4     | 1980 | /            | /   | /  | /              | /   | /  |
| NIR             | DA      | 4     | 1980 | /            | /   | /  | /              | /   | /  |
| NSWC AP         | DA      | 4     | 1980 | /            | /   | /  | /              | /   | /  |
| PORTANCE        | DA      | 4     | 1980 | /            | /   | /  | /              | /   | /  |
| SFA DATCOM      | DA      | 4     | 1980 | /            | /   | /  | /              | /   | /  |
| SMBRP           | DA      | 4     | 1980 | /            | /   | /  | /              | /   | /  |
| PAD             | DA      | 4     | 1980 | /            | /   | /  | /              | /   | /  |
| TASK2           | DA      | 4     | 1980 | /            | /   | /  | /              | /   | /  |
| TRAFRO          | DA      | 4     | 1980 | /            | /   | /  | /              | /   | /  |

Configuration type has been compared

TABLE 1

**SEMI-EMPIRICAL CODES**

| ORGANISATIONS | CODES   |
|---------------|---|
| aerospaciale  | AMIS00, BAKER, CABANG, PORTANCE, MISSILE ONERA, MISSILE 2A, TAD |
| Blae          | ABACUS, IFR, S/HARP, DRAG                                       |
| BRL           | NSWC-AP, MISSILE DATCOM   |
| CITEFA        | SEA DATCOM, MRRT  |
| DORNIER       | DORRAM, MISSILE 1   |
| FFA           | MISSILE DATCOM, MISSILE 2A                                      |
| HUQUES        | MAP   |
| MATRA         | CASAERO, TRAIPRO  |
| MBB           | BOVINCY, MISSILE 2A, TABR2                                      |
| NASA Langley  | MISSILE 2A, MISSILE 3, NSWC-AP S/HARP                           |
| NEAR          | MISSILE 2A, MISSILE 3, NSWC-AP S/HARP                           |
| NSWC          | NSWC-AP, S/HARP   |
| SAAB          | AERAM, MISSILE DATCOM   |
| SANDIA Lab.   | NSWC-AP, DTMB   |

TABLE 3

**CAPABILITIES OF FULL NAVIER-STOKES CODES FOR MISSILES**

| CODE NAME | ORIGINE        | REF N° | DATE | LAMINAR TURBULENT | MACH | CONVENTIONAL (one-half conventional cross section, wings) |          | UNCONVENTIONAL (arbitrary cross section, wings) |              |
|-----------|----------------|--------|------|-------------------|------|---|----------|---|--------------|
|           |                |        |      |                   |      | CLASSICAL   | BOOSTED  | LIFTING   | UNWEATHERING |
| ARC3D     | NASA ARC (USA) |        |      | L, B, T           | < 1  | 1CF   | DO + 3CF | ELUPTIC   | OPEN CLOSED  |
| F3D       | NASA (USA)     |        | 1986 | L, B, T           | > 1  | 2CF   |          |   |              |
| MASBMG    | DORNIER (FRG)  |        | 1987 |                   | > 1  |   |          |   |              |
| UWNN      | NASA ARC (USA) |        | 1987 |                   | > 1  |   |          |   |              |

1CF : ONE CRUCIFORM-FINNED SECTION  
 2CF : TWO  
 3CF : THREE  
 DD : DOUBLE DIAMETER

Configuration type has been computed  
 C Configuration type could be computed

**FULL NAVIER STOKES CODES**

| ORGANIZATIONS | CODES            |
|---------------|------------------|
| DORNIER       | MASBMG           |
| NASA Ames     | ARC3D, F3D, UWNN |

TABLES 4 and 5

### CAPABILITIES OF PARABOLIZED NAVIER-STOKES CODES FOR MISSILES

ICF : ONE CRUCIFORM-FINNED SECTION  
 1CF : TWO CRUCIFORM-FINNED SECTION  
 3CF : THREE CRUCIFORM-FINNED SECTION  
 DD : DOUBLE DIAMETER

| CODE NAME | ORG/IN          | REF # | DATE | MACH | LAMINAR FLOW | CONVENTIONAL |         | UNCONVENTIONAL |               |
|-----------|-----------------|-------|------|------|--------------|--------------|---------|----------------|---------------|
|           |                 |       |      |      |              | CLASSICAL    | BOOSTED | LIFTING        | WINGBREATHING |
| PNS       | NASA ARDC (USA) | 20    | 1979 | 1.5  | 1            | 1            | 1       | 1              | 1             |
| PNS/AM    | DORNIER (FR)    | 21    | 1984 | 1.5  | 1            | 1            | 1       | 1              | 1             |
|           |                 |       | 1986 | 1.5  | 1            | 1            | 1       | 1              | 1             |

Configuration type has been computed

### PARABOLIZED NAVIER STOKES CODES

| ORGANIZATIONS | CODES  |
|---------------|--------|
| BRL           | PNS    |
| DORNIER       | PNS/AM |
| NASA Ames     | PNS    |
| SANDIA Lab    | PNS    |

TABLES 6 and 7

### CAPABILITIES OF EULER CODES FOR MISSILES

ICF : ONE CRUCIFORM-FINNED SECTION  
 1CF : TWO CRUCIFORM-FINNED SECTION  
 3CF : THREE CRUCIFORM-FINNED SECTION  
 DD : DOUBLE DIAMETER

| CODE NAME | ORG/IN                        | REF # | DATE | MACH | CONVENTIONAL |         | UNCONVENTIONAL |               |
|-----------|-------------------------------|-------|------|------|--------------|---------|----------------|---------------|
|           |                               |       |      |      | CLASSICAL    | BOOSTED | LIFTING        | WINGBREATHING |
| EUFLEX    | MBB (FR)                      | 22    | 1984 | 2.1  | 1            | 1       | 1              | 1             |
| EUBMG     | DORNIER (FR)                  |       | 1983 | 2.1  | 1            | 1       | 1              | 1             |
| EULEN3D   | MATRA (FR)                    | 23    | 1985 | 2.1  | 1            | 1       | 1              | 1             |
| EULESSM   | DORNIER (FR)                  |       | 1986 | 2.1  | 1            | 1       | 1              | 1             |
| EMERA     | ONERA (FR)                    | 24    | 1980 | 2.1  | 1            | 1       | 1              | 1             |
| FLUXC     | perceptics (FR)               | 25    | 1980 | 2.1  | 1            | 1       | 1              | 1             |
| MISSILE   | NASA ARDC (USA)               |       | 1972 | 2.1  | 1            | 1       | 1              | 1             |
| MUSE      | NSWC (USA)                    | 26    | 1985 | 2.1  | 1            | 1       | 1              | 1             |
| SANDAC    | SANDIA General Electric (USA) | 27    | 1986 | 2.1  | 1            | 1       | 1              | 1             |
| SWINT     | NSWC (USA)                    | 28    | 1982 | 2.1  | 1            | 1       | 1              | 1             |
| WING42    | FFA (SW)                      | 46    | 1983 | 2.1  | 1            | 1       | 1              | 1             |
| ZIUS      | NSWC (USA)                    | 29    | 1980 | 2.1  | 1            | 1       | 1              | 1             |

Configuration type has been computed

TABLE 8

**EULER CODES**

| CODE NAME | EQUATIONS              |                                      | METHOD | NUMERICAL SCHEME         |                              |                       |                                | MESH |     | MACH | NOTES ABOUT SEPARATION (1), (2), (3), (4), (5) |
|-----------|------------------------|--------------------------------------|--------|--------------------------|------------------------------|-----------------------|--------------------------------|------|-----|------|--|
|           | STEADY OR UNSTEADY (1) | CONSERVATIVE OR NON-CONSERVATIVE (2) |        | IMPLICIT OR EXPLICIT (3) | CENTERED OR NON-CENTERED (4) | ORDER OF ACCURACY (5) | STRUCTURED OR UNSTRUCTURED (6) | (1)  | (2) |      |  |
| EUFLEX    | U                      | C                                    | FV     | E + I                    | NC                           | 1, 2                  | 1, 4                           | NS   | *   | *    |  |
| EULBMC    | U                      | C                                    | FV     | E                        | C                            | 2                     | 2                              | S    | *   | *    | SSS  |
| EULERID   | U                      | C                                    | FV     | E                        | C                            | /                     | 2                              | S    | *   | *    | SSS  |
| EULSSM    | S                      | C                                    | FV     | I                        | C                            | /                     | 2                              | NS   | *   | *    |  |
| FLUSC     | U                      | C                                    | FV     | E                        | NC                           | 2                     | 2                              | S    | *   | *    |  |
| MISSILE   | S                      | C                                    | FD     | E                        | C                            | /                     | 2                              | S    | /   | *    |  |
| MOUSE     | S                      | C                                    | FD     | E                        | C                            | /                     | 2                              | S    | /   | *    | SSS  |
| SANDIAC   | S                      | C + NC                               | FD     | E                        | NC                           | /                     | 2                              | S    | /   | *    |  |
| SWIRT     | S                      | C                                    | FD     | E                        | L                            | /                     | 2                              | S    | /   | *    | SSS  |
| WINGAZ    | U                      | C                                    | FV     | E                        | C                            | /                     | 2                              | S    | *   | *    |  |
| ZEUS      | S                      | C                                    | FV     | E                        | NC                           | /                     | 2                              | S    | /   | *    | SSS  |

(1) Put only the first letter of the answer

(2) \* for YES

for NO

SSS Separation on Smooth Surface with Kutta Condition

**TABLE 9**

| ORGANIZATIONS | CODES              |
|---------------|--------------------|
| agropatelle   | FLUSC              |
| BAA           | SWIRT              |
| BRL           | SWIRT              |
| DORNIER       | EULBMC, EULSSM     |
| FFA           | WINGAZ             |
| MATRA         | EULERID            |
| MBB           | EUFLEX             |
| NASA Ames     | MISSILE            |
| NASA Langley  | SWIRT              |
| NIELSEN Lab.  | SWIRT              |
| RSMC          | SWIRT, MOUSE, ZEUS |
| SANDIA        | SANDIAC            |

**TABLE 10**

**EULER CODES FOR MISSILES**



# CAPABILITIES OF LINEARIZED POTENTIAL CODES FOR MISSILES

| CODE NAME | ORIGINE | REF # | DATE | MACH | CONVENTIONAL |         | UNCONVENTIONAL |              |
|-----------|---------|-------|------|------|--------------|---------|----------------|--------------|
|           |         |       |      |      | CLASSICAL    | BOOSTED | LIFTING        | AIRBREATHING |
| NEAR      | USA     | 17    | 1986 | 15   | Y            | Y       | Y              | Y            |
| NEAR      | USA     | 13    | 1986 | 15   | Y            | Y       | Y              | Y            |
| DM3DL     | USA     | 14    | 1985 | 11   | Y            | Y       | Y              | Y            |
| HSSS      | FRG     | 34    | 1985 | 11   | Y            | Y       | Y              | Y            |
| PLP       | SWI     | 35    | 1983 | 11   | Y            | Y       | Y              | Y            |
| MELING    | FRG     | 36    | 1987 | 11   | Y            | Y       | Y              | Y            |
| MANC      | USA     | 36    | 1987 | 11   | Y            | Y       | Y              | Y            |
| MARUBSUP  | FRG     | 37    | 1982 | 11   | Y            | Y       | Y              | Y            |
| NERARU    | NLD     | 38    | 1982 | 11   | Y            | Y       | Y              | Y            |
| NEWCAP    | USA     | 15    | 1981 | 11   | Y            | Y       | Y              | Y            |
| NEAR      | USA     | 40    | 1986 | 15   | Y            | Y       | Y              | Y            |
| RODRING   | USA     | 41    | 1984 | 11   | Y            | Y       | Y              | Y            |
| DORNER    | FRG     | 42    | 1984 | 11   | Y            | Y       | Y              | Y            |
| PHOBOS    | SWI     | 42    | 1984 | 11   | Y            | Y       | Y              | Y            |
| MBWHEISEN | FRG     | 43    | 1984 | 11   | Y            | Y       | Y              | Y            |
| RAY       | USA     | 44    | 1980 | 11   | Y            | Y       | Y              | Y            |
| WBC       | FRG     | 45    | 1985 | 15   | Y            | Y       | Y              | Y            |
| MASA/FA   | USA     | 35    | 1982 | 11   | Y            | Y       | Y              | Y            |

TABLE 12

# CAPABILITIES OF FULL POTENTIAL CODES FOR MISSILES

| CODE NAME | ORIGINE | REF # | DATE | MACH | CONVENTIONAL |         | UNCONVENTIONAL |              |
|-----------|---------|-------|------|------|--------------|---------|----------------|--------------|
|           |         |       |      |      | CLASSICAL    | BOOSTED | LIFTING        | AIRBREATHING |
| SANDIA    | USA     | 30    | 1985 | 11   | Y            | Y       | Y              | Y            |
| SMP       | USA     | 39    | 1982 | 11   | Y            | Y       | Y              | Y            |

TABLE 11

ACCURACY CRITERIA FOR EVALUATING SUPERSONIC AERODYNAMIC  
COEFFICIENT PREDICTIONS

J. E. Williams  
Unit Chief - Technology  
and  
R. J. Krieger  
Chief - Technology  
McDonnell Douglas Astronautics Company  
P.O. Box 516, St. Louis, MO 63166  
USA

ABSTRACT

Aerodynamic prediction methods are traditionally compared with wind tunnel test data. However, the assessment of accuracy is left to an arbitrary interpretation. An accuracy criteria has been developed that defines the required prediction accuracy in terms of allowable errors in missile performance and design parameters. Equations have been selected that relate these parameters to the aerodynamic drag, stability and control coefficients. These equations are differentiated with respect to the aerodynamic coefficients and simplified when possible. Allowable errors in the performance or design parameters are estimated, based on preliminary design requirements, and the required aerodynamic coefficient accuracy calculated. The results allow a quantitative evaluation of prediction accuracy.

NOMENCLATURE

|                  |   |
|------------------|---|
| A                | wing or fin area  |
| b                | reference length  |
| C <sub>A</sub>   | axial force coefficient   |
| C <sub>D</sub>   | drag coefficient  |
| C <sub>L</sub>   | lift coefficient  |
| C                | rolling moment coefficient  |
| C <sub>m</sub>   | pitching moment coefficient   |
| C <sub>N</sub>   | normal force coefficient  |
| C <sub>n</sub>   | yawing moment coefficient   |
| C <sub>t</sub>   | thrust coefficient  |
| C <sub>Y</sub>   | side force coefficient  |
| g                | gravitational constant  |
| h                | altitude  |
| I                | moment of inertia   |
| K                | stability parameter   |
| K <sub>S</sub>   | longitudinal static stability parameter                                       |
| K <sub>S1</sub>  | bank/roll static stability parameter  |
| K <sub>S3</sub>  | yaw static stability parameter  |
| K <sub>X</sub>   | roll yaw cross-coupling parameter   |
| k                | induced drag factor   |
| k <sub>QV</sub>  | slope of C <sub>D0</sub> V <sup>2</sup> versus V curve                        |
| N/A              | not applicable  |
| n                | aerodynamic load factor   |
| P <sub>S</sub>   | specific excess power   |
| q                | dynamic pressure  |
| R                | range   |
| r                | turn radius   |
| S                | reference area  |
| T                | thrust  |
| V                | velocity  |
| V <sub>0</sub>   | velocity at which linear C <sub>D0</sub> V <sup>2</sup> curve intercepts axis |
| V                | acceleration  |
| W                | weight  |
| X <sub>CG</sub>  | axial center of gravity   |
| X <sub>CP</sub>  | axial center of pressure  |
| Y <sub>CP</sub>  | wing lateral moment arm about centerline                                      |
| α                | angle of attack   |
| β                | yaw angle   |
| β <sub>a</sub>   | atmosphere density exponent   |
| δ                | control deflection  |
| δ <sub>A</sub>   | aileron deflection  |
| δ <sub>R</sub>   | rudder deflection   |
| Δ                | parameter increment   |
| Γ                | dihedral angle  |
| ρ                | atmospheric density   |
| ρ <sub>ref</sub> | reference density   |
| φ                | bank angle  |
| ψ                | angular turn rate   |
| τ                | response time   |

Superscripts:

'           referenced to panel area

## Subscripts:

|            |   |
|------------|---|
| B          | body-alone                                    |
| CONTROL    | control value                                 |
| F          | final value                                   |
| T          | tail value                                    |
| TRIM       | trim value                                    |
| W          | wing value                                    |
| V          | vertical tail value $\alpha$                  |
| $\alpha$   | derivative with                               |
| $\beta$    | derivative with $\beta$                       |
| $\delta$   | derivative with $\delta$                      |
| $\delta_A$ | derivative with $\delta_A$                    |
| $\delta_R$ | derivative with $\delta_R$                    |
| o          | initial value for V,W                         |
|            | value at $\alpha=0^\circ$ for $C_A$ and $C_D$ |

## INTRODUCTION

Results from aerodynamic prediction methods are constantly being compared with wind tunnel data. However, in the majority of cases, the assessment of accuracy is left to the viewer's interpretation of what is a good or poor comparison. Figure 1 is a typical example of a pitching moment comparison. Is it a good or poor prediction of  $C_m$ ? The purpose of this paper is to provide an accuracy criteria for supersonic missiles which answers this question for six static aerodynamic force and moment coefficients,  $C_A, C_N, C_m, C_y, C_n, C_z$ . The paper presents the selection of governing equations, development of accuracy equations, selection of allowable performance/design errors and example allowable coefficient accuracies.

Two primary reasons aerodynamic coefficients are calculated are for 1) predicting missile performance, and 2) establishing the missile design. Therefore, aerodynamic prediction techniques which satisfy the accuracy requirements associated with these processes are desired. Historically, prediction accuracies have been related directly to the coefficients. For example, a normal force coefficient prediction within 10% of data might be judged as good agreement. But what does this mean in terms of missile range, maneuverability, or wing size? This paper presents the equations which relate performance parameters (such as range) and design parameters (such as wing area) to aerodynamic coefficients (such as  $C_A$  and  $C_N$ ). When these equations are differentiated with respect to the aerodynamic coefficients and simplified, the resulting equations related aerodynamic coefficient accuracy directly to errors in performance or design parameters. As a consequence, instead of specifying accuracy by an arbitrary assignment of a coefficient percentage or increment, an allowable error on a performance/design parameter is determined, and the accuracy criteria equation used to compute the allowable coefficient accuracy. For example, a range error of 10% results in an allowable  $C_N$  accuracy of 20%.

The magnitude of the allowable performance/design errors can be selected to represent any level of design detail: conceptual, preliminary or point design. However, because of the approximations used in deriving the governing equations the criteria are best suited for conceptual and preliminary design. In this paper, allowable accuracies are examined for the configurations displayed in Fig. 2. These provide the extremes of aerodynamic characteristics from a conventional to high-lift, aero-configured missile concept. The development and application of the accuracy criteria are described in the following text.

## SELECTION OF GOVERNING EQUATIONS

Governing equations were selected which related performance, configuration design, and autopilot design parameters to aerodynamic coefficients. Closed-form equations<sup>1,2</sup>, differential equations of motion<sup>2</sup> and specific energy expressions<sup>3</sup> were selected for the performance relations. These are often derived with assumptions such as constant velocity or level flight. For the purpose of deriving accuracy criteria, these are not considered restrictive assumptions. These simplified forms emphasize the first order effect of the aerodynamic coefficients on the performance or design. Figure 3 summarizes the performance/design relationships selected to develop the accuracy criteria. The right-hand column indicates the resulting coefficients in each equation. The performance relations relate parameters such as range to aerodynamic coefficients such as normal and axial force. Configuration design relations relate, for example, fin area to body moment coefficients and are typically force and moment balances for configuration components. Autopilot design parameters are related to moment and control levels. Normal and axial force coefficients were substituted for lift and drag coefficients to provide body axis sensitivities.

Figure 4 presents the selected performance relations, Eqs. (1) through (15), and their references. This list is not intended to be complete and contains representative equations which can be used to develop accuracy criteria. The response time, Eq. (1), has no reference and was developed by determining the time required to pitch a missile through an angle of attack, using a control deflection. Also, Eq. (13) was derived from the force and moment balances, Eqs. (1) through (12).

Figure 5 contains selected configuration design relations, Eqs. (16) through (27), derived from force and moment balances commonly used in the design of missiles. The equations include fin and wing sizing, dihedral and trim deflection angle definition and center of gravity location.

The autopilot design relations, Eqs. (28) through (31), of Fig. 6 define the stability parameters  $K_S, K_{S1}, K_{S3}$ , and  $K_X$  which are used in autopilot design. For example, the static stability parameter,  $K_S$ , is the ratio of  $C_{m\alpha}/C_{m\delta}$  at any angle of attack. It is a measure of the amount of control deflection required to achieve a given change in angle of attack. For a very stable vehicle  $C_{m\alpha}$  is a large and high control deflections are required. Large control deflections are also required if  $C_{m\delta}$  is small. In either case, the vehicle is difficult to control. This is indicated by a large value of  $K_S$ . Similar magnitudes arise for  $K_{S1}$  and  $K_{S3}$ . A feasible autopilot design is possible for these parameters between the values of approximately -0.50 and +1.0. The negative limit is for unstable

airframes. The cross-coupling parameter,  $K_X$ , is the ratio of the roll-yaw cross coupling derivatives to the roll-yaw control derivatives. Values of this ratio less than 0.50 are desirable in autopilot designs.<sup>4</sup>

#### DEVELOPMENT OF ACCURACY EQUATIONS

The equations of Fig 4, 5, and 6 were differentiated with respect to aerodynamic coefficients to obtain the accuracy equations. An example of this derivation process, beginning with Eq. (8) for instantaneous load factor, follows.  $C_L$  is assumed approximately equal to  $C_N$  and Eq. (8) differentiated with respect to  $C_N$  to give

$$\frac{\partial n}{\partial C_N} = \frac{qS}{W} \quad (32)$$

The right hand side,  $qS/W$ , is then replaced using Eq. (8) and the normalized equation obtained,

$$\frac{\partial n}{n} = \frac{\partial C_N}{C_N} \quad (33)$$

Eq. (33) is referred to as the accuracy criteria equation. An allowable error on the performance parameter,  $n$ , is estimated based upon design requirements, e.g.,

$$\frac{\Delta n}{n} \leq 0.20 \quad (34)$$

Substitution into Eq. (33), provides the allowable accuracy on  $C_N$  in the form

$$\frac{\Delta C_N}{C_N} \leq 0.20 \quad (35)$$

Eq. (35) gives the allowable prediction accuracy on  $C_N$  which results in a 20% error in load factor.

Figure 7 provides the  $C_N$  accuracy relations, Eqs. (36) through (41), derived from the various performance/design equations of Figure 4 and 5. (All minus signs are dropped because the equations represent absolute values of the errors). Note that two equation forms result. The simplest form such as Eqs. (36) through (39) are independent of configuration characteristics or flight conditions. Only the aerodynamic coefficient and performance/design parameter enter the equation. The allowable accuracy is only a function of the allowable error in the performance/design parameter. The second equation form is configuration dependent such as Eqs. (40) and (41). The accuracy is a function of the performance/design parameters such as weight, reference area or dynamic pressure and aerodynamic characteristics such as the ratio of wing to body normal force,  $C_{NW}/C_{NB}$ . Therefore, each configuration class has a different allowable accuracy.

Figure 8 presents the  $C_A$  accuracy criteria, Eqs. (42) through (45), derived from Fig. 4 and 5. Equations (42) and (43) are the simple form and Eqs. (44) and (45) have configuration and flight condition-dependent coefficients. Figure 9 summarizes the pitching moment criteria in Eqs. (46) through (52). Care must be taken in applying criteria such as Eqs. (46) and (48) when the moment or its derivative is near zero. For example, if  $C_m$  is zero, response time is infinite. Equations (49) and (50) can be applied by setting a minimum acceptable  $\Delta \delta_{TRIM}$  or  $\Delta X_{CG}$  such as 2 degrees and 0.2 calibers, respectively. This results in the definition of a minimum value for  $C_m$ . Figures 10 and 11 present similar criteria for  $C_Y, C_N$ , and  $C_Z$  coefficients in Eqs. (53) through (66). The derivation of all the accuracy relations on Figures 7 through 11 is given in the Appendix.

#### SELECTION OF ALLOWABLE PERFORMANCE/DESIGN ERRORS

Many of the accuracy equations of Fig. 7 through 11 have performance parameter allowable errors (e.g.,  $R$ ) divided by the performance parameters (e.g.,  $\Delta R$ ). Therefore, only the fractional error  $\Delta R/R$  must be selected. For these cases, Fig. 12 provides typical allowable errors based upon preliminary design requirements. The user of the accuracy criteria may select other allowable errors based upon his particular design problem. Range is desired within 10%, maneuvering and design parameters within 20%.  $C_A$  has the most severe requirement of 10% based upon allowable range accuracies.  $C_m$  prediction for response time is least severe at 40%.

Allowable errors for autopilot design parameters are more complex because  $K_S, K_{S1}, K_{S3}$  and  $K_X$  can have values between 0 and  $\infty$ . Figures 13 and 14 describe a recommended approach for determining  $K$ . When the parameter,  $K$ , is within acceptable levels for autopilot design, relatively large errors in its magnitude can still result in an acceptable design. Therefore,  $\Delta K=0.25$  is recommended. At slightly unacceptable levels of  $K$  between 1 and 5 larger errors are tolerable as long as  $K$  is predicted within these levels. This results in an error definition of  $\Delta K=0.25K$ . Once  $K$  becomes greater than 5, the autopilot design becomes impractical, independent of the level of  $K$ . This condition usually occurs when the control derivatives,  $C_{m\delta}, C_{\delta A}$  or  $C_{n\delta R}$  are close to zero. This often occurs at high angle of attack when controls are in separated flow regions. For these cases, the expressions shown provide an increment for the control power which is a function of the numerators of the appropriate equations. The plot at the bottom of Fig. 13 shows a typical variation of  $\Delta K/K$  using this model. Figure 14 provides a similar approach for definition of the cross-coupling parameter,  $K_X$ .

Equations (40), (44), and (47) of Figs. 7, 8, and 9 require flight characteristics such as  $q/V$ ,  $1/qV$  and  $Ba/q$ . Typical values of these parameters are shown in Fig. 15 as a function of altitude. A  $\Delta P_S$  of 100 ft per second is approximately 10% of a typical  $P_S$  for ramjet missiles. A  $\Delta h$  of 1000 feet represents an acceptable error in estimating cruise altitude. Equation (45) of Fig. 8 requires the ratio of  $C_p/C_A \cos \alpha$ . Typical values for configurations shown in Fig. 2 are given in Fig. 16. Wind tunnel

data<sup>5-8</sup> were used to obtain these curves. As angle of attack increases, the ratio increases indicating that  $C_A$  is a small contribution to  $C_p$ . Also, at a fixed angle of attack, the aero-configured and elliptic shapes have higher ratios and therefore,  $C_A$  contributions are less important.

Equation (41) of Fig. 7 requires the ratio of  $C_{NW}$  to  $C_{NB}$ . Figure 17 provides typical variation of this ratio with angle of attack. Since wing size can vary greatly this ratio is very sensitive to particular configuration type. Ratios as low as 0.1 and greater than 1.2 are possible. The ratio does decrease as angle of attack increases and body lift becomes more important. Figure 18 summarizes typical values of design/performance dependent coefficients for the four configuration classes and the equations indicated. Note that design characteristics such as  $W/S$  and  $W/S_b$  appear in the coefficients. Because  $S$  and  $b$  are reference area and length which vary depending on user preference they are left to the user to define. Not applicable appears for conventional and elliptic classes because these concepts are assumed to be rocket-powered, boost-glide concepts. Equations (40), (44), and (47) are only applicable to missile with airbreathing propulsion where  $P_g$  and cruise altitude are important design parameters.

#### EXAMPLE COEFFICIENT ACCURACY

The parameter allowable errors established by Fig. 12 through 18 were applied to the Mach 4.02 wind tunnel data of the aero-configured non-circular body Phase II configuration<sup>8</sup> shown in the lower right of Figure 2. The predictions were obtained using the Supersonic/Hypersonic Arbitrary Body Program<sup>9</sup> and the ACM Rationale<sup>10</sup> which defines the pressure methods to be applied to various regions of the configurations. Figure 19 compares data predictions and accuracy bands for pitching moment variation with angle of attack. The triangular and circular symbols are data for zero and 10 degree pitch deflection, respectively. The two solid lines are predictions for each case. The response time, accuracy band is computed by substituting  $\Delta\tau/r=0.20$  from Fig. 12 into Eq. (46) of Fig. 9 and solving for  $\Delta C_{m_0} \pm 0.40 C_{m_0}$ . The value of  $C_{m_0}$  used is that given by the test data at each angle of attack. Eqs. (49), (51) and (52) were used in a similar manner to develop the accuracy bands identified in "trim" and "static stability". The minimum allowable trim deflection error was limited to 2 degrees.

The zero deflection prediction is outside the resulting "trim" error band from 4.5 to 16.5 degrees angle of attack and would be a poor prediction for establishing trim deflection within 2 degrees. The shaded wedge-shaped regions identified as "static stability" are the slope from Eq. (52) required to accurately predict static stability. At almost all conditions the predicted slope is outside this error band. The prediction with pitch deflection is within the error band established by Eq. (46) for response time and Eq. (51) for static stability. Therefore, the prediction of the effect of deflection on  $C_m$  is good for preliminary design purposes.

Figure 20 shows a good prediction for axial force. The accuracy bands are from Eq. (42) for powered range and Eq. (45) for maneuver deceleration. The large increase in the band at high angle of attack represents the small contribution of  $C_A$  to  $C_D$  at this condition.

Figure 21 shows a  $C_n$  prediction which is within the accuracy band at angles of attack up to 12 degrees. Above 14 degrees the predictions are poor. The accuracy criteria are based on Eq. (56) and (57).

#### CONCLUSIONS

Accuracy criteria are presented which can be applied at any point in the design process by selecting the appropriate allowable error in performance/design parameters. Criteria are established for the six static force and moment coefficients,  $C_A, C_N, C_m, C_y, C_n, C_L$ . Allowable errors for performance and design parameters are estimated by the user and the accuracy criteria equations used to relate these to allowable coefficient accuracies. Although example allowable errors are given in this paper, the user can select his own to reflect his level of design detail. The criteria developed are best suited for comparing predictions with existing wind tunnel data during the development and evaluation of prediction techniques.

#### ACKNOWLEDGEMENTS

Part of this work was performed for the Air Force under the contract, "Aerodynamic Analysis for Missiles"<sup>11</sup>.

#### REFERENCES

1. Krieger, R. J., et al, Aerodynamic Configured Missile Development Final Report, Volume II - Appendix B - Relations Between Aerodynamic Characteristics and Performance, AFWAL-TR-80-3071, July 1980.
2. Miller, L. E., and Koch, P. G., Aircraft Flight Performance Methods, AFFDL-TR-75-89, July 1975.
3. Rutowski, E. S., "Energy Approach to the General Aircraft Performance Problem", Journal of Aeronautical Sciences, Vol. 21, No. 3, March 1954, pp. 187-195.
4. Froning, H. D., Jr., "Aerodynamic Design of Slender Missiles for Bank-to-Turn Flight at High Angles of Attack", AIAA Paper 81-0289, January 1981.
5. Gomillion, G. R., "A Compilation of Static Stability and Fin Loads Data for Slender Body Missile Models with and without Tail Fins and Wings", AEDC-Tr-75-125, AFATL Tr-76-23, March 1976.
6. Graves, E. G., "Aerodynamic Characteristics of a Monoplanar Missile Concept with Bodies of Circular and Elliptical Cross Sections", NASA TM-74079, December 1977.

7. Hayes, C., "Aerodynamic Characteristics of a Series of Airbreathing Missile Configurations", Paper No. 24, 12th Navy Symposium on Aeroballistics, DTNSRDC, May 1981.
8. Lanham, D. L., "Static Force and Oil Flow Visualization Tests of Aerodynamic Configured Missiles at Mach Numbers 2.5 to 5.0", AEDC-TSR-79-V54, September 1979.
9. Gentry, A. E., Smyth, D. N., and Oliver, W. R., The Mach IV Supersonic Hypersonic Arbitrary-Body program, Vol. I Users Manual, Vol. II Program Formulation, Vol. III Program Listings, AFFDL-TR 79-59, November 1972.
10. Gregoire, J. E., and Krieger, R. J., "Aerodynamic Prediction Rationale for Advanced Arbitrarily Shaped Missile Concepts", AIAA paper 80-0256, January 1980.
11. Aerodynamic Analysis for Missiles, Air Force Wright Aeronautical Laboratory Contract F33615-80-C-3026 (AFWAL/FIMG), September 1980.

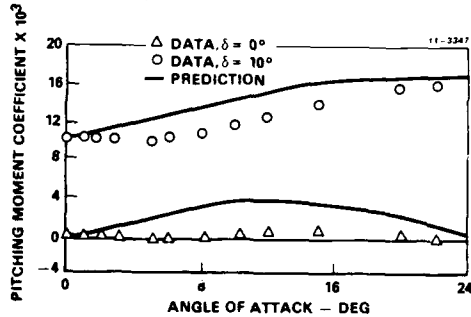


FIGURE 1. IS THIS A GOOD DATA/THEORY COMPARISON?

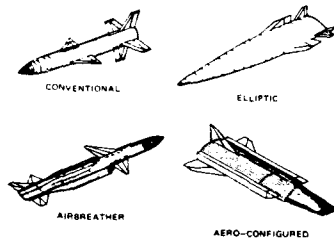


FIGURE 2. CRITERIA DEVELOPED FOR VARIETY OF CONFIGURATIONS

| PERFORMANCE   | DOMINANT AERO COEFFICIENTS   |
|---|--|
| <ul style="list-style-type: none"> <li>• POWERED RANGE IN TERMS OF WEIGHT</li> <li>• COAST RANGE TO A GIVEN VELOCITY</li> <li>• INSTANTANEOUS TURN RADIUS</li> <li>• INSTANTANEOUS TURN RATE</li> <li>• INSTANTANEOUS LOAD FACTOR</li> <li>• RESPONSE TIME</li> <li>• CRUISE ALTITUDE AFFECTED BY TRIM</li> <li>• SPECIFIC EXCESS POWER</li> <li>• MANEUVER DECELERATION</li> </ul> | $C_n, C_A$<br>$C_A$<br>$C_n$ OR $C_v$<br>$C_n$ OR $C_v$<br>$C_n$<br>$C_m \delta$<br>$C_m$<br>$C_n \delta, C_A$   |
| <b>CONFIGURATION DESIGN</b> <ul style="list-style-type: none"> <li>• HORIZONTAL FIN AREA</li> <li>• VERTICAL FIN AREA</li> <li>• DHEORAL ANGLE</li> <li>• WING AREA</li> <li>• TRIM CONTROL DEFLECTION</li> <li>• CENTER OF GRAVITY LOCATION</li> </ul>   | $C_m \delta$<br>$C_n \delta$<br>$C_l$<br>$C_n \delta$<br>$C_m$<br>$C_m$  |
| <b>AUTOPILOT DESIGN</b> <ul style="list-style-type: none"> <li>• LONGITUDINAL STATIC STABILITY</li> <li>• BANK/ROLL STATIC STABILITY</li> <li>• YAW STATIC STABILITY</li> <li>• ROLL-YAW COUPLING</li> </ul>  | $C_{m \delta}, C_{m \delta}$<br>$C_{l \delta}, C_{n \delta}, C_{l \delta A}$<br>$C_{n \delta}, C_{l \delta}, C_{n \delta R}$<br>$C_{n \delta A}, C_{l \delta R}, C_{n \delta R}, C_{l \delta A}$ |

FIGURE 3. VARIETY OF CLOSED FORM PERFORMANCE/ DESIGN RELATIONS USED

|  |      |
|--|------|
| <b>POWERED RANGE IN TERMS OF WEIGHT (REF 2, EQ B5-1)</b><br>$R = \frac{2.828}{C_D} \frac{C_L}{C_D} (W_0^2 - W_1^2)$  | (1)  |
| <b>COAST RANGE TO A GIVEN VELOCITY (REF 2, EQS B4.8, B1-1)</b><br>$R = \frac{2W}{\rho S C_D V_{OV}} \left[ V_A - V_1 \cdot V_B \cdot \ln \left( \frac{V_A - V_B}{V_1 - V_B} \right) \right]$ | (2)  |
| $k_{OV} = C_{D_0} V^2 (V - V_B) = \text{CONSTANT}$   | (3)  |
| <b>INSTANTANEOUS TURN RADIUS (REF 3, EQS 6-16)</b><br>$r = V^2 / g (n^2 - 1)^{1/2}$  | (4)  |
| <b>FOR BANK-TO-TURN</b><br>$(n^2 - 1)^{1/2} = C_L q S / W \sin \delta$   | (5)  |
| <b>FOR SKID-TO-TURN</b><br>$(n^2 - 1)^{1/2} = C_Y q S / W$   | (6)  |
| <b>INSTANTANEOUS TURN RATE (REF 3, EQS 6-20)</b><br>$\dot{\psi} = \frac{g (n^2 - 1)^{1/2}}{V}$   | (7)  |
| <b>INSTANTANEOUS LOAD FACTOR (REF 3, EQS 6-23)</b><br>$n = g \frac{C_L}{W}$  | (8)  |
| <b>RESPONSE TIME</b><br>$T = \sqrt{\frac{2I \alpha}{C_m \delta q S b}}$  | (9)  |
| <b>CRUISE ALTITUDE AFFECTED BY TRIM</b><br>$W/q S C_{L_{TRIM}} = 1$  | (10) |
| $C_{L_{TRIM}} = C_L + \Delta C_{L_{CONTROL}}$  | (11) |
| $C_{m_{TRIM}} = 0 = C_m + \left( \frac{x_{CG} - x_{CP_T}}{D} \right) \Delta C_{L_{CONTROL}}$   | (12) |
| <b>SOLVING FOR h:</b><br>$h = \frac{1}{\beta} \ln \left\{ \frac{2W}{P_{REF} V^2 S} \left[ \frac{C_L}{(x_{CG} - x_{CP_T})} \right] \right\}$  | (13) |
| <b>SPECIFIC EXCESS POWER (REF 4, EQS 5)</b><br>$P_s = \frac{V}{W} \left\{ T - [C_{D_0} + k \left( \frac{W}{q S} \right)^2] q S \right\}$   | (14) |
| <b>MANEUVER DECELERATION (REF 3, EQS 5-31)</b><br>$\dot{V} = -C_D q S / M$   | (15) |

FIGURE 4. SELECTED PERFORMANCE EQUATIONS

11-3314

|  |  |
|--|--|
| <p>HORIZONTAL FIN AREA SIZING BASED ON PITCHING MOMENT</p> $C_m \cdot 0 + C_{mB} + \frac{1}{bS} (X_{CG} - X_{CP}) C_{N_T} A_T \quad (16)$ <p>SOLVING FOR <math>A_T</math>:</p> $A_T = \frac{C_{mB} \cdot bS}{1X_{CG} - X_{CP}) C_{N_T}} \quad (17)$    |  |
| <p>VERTICAL FIN AREA SIZING BASED ON YAWING MOMENT</p> $C_n \cdot 0 + C_{nB} + \frac{1}{bS} (X_{CG} - X_{CP}) C_{N_V} A_V \quad (18)$ <p>SOLVING FOR <math>A_V</math></p> $A_V = \frac{-C_{nB} \cdot bS}{1X_{CG} - X_{CP}) C_{N_V}} \quad (19)$        |  |
| <p>DIHEDRAL ANGLE BASED ON ROLLING MOMENT</p> $C_l = 0 + C_{lB} - \frac{Y_{CP} C_{N_{dW}}}{D} \delta \sin \Gamma \quad (20)$ <p>SOLVING FOR <math>\sin \Gamma</math>:</p> $\sin \Gamma = \frac{-C_{lB} \cdot b}{Y_{CP} C_{N_{dW}} \cdot D} \quad (21)$ |  |
| <p>WING AREA SIZING BASED ON NORMAL FORCE</p> $C_N = C_{NB} + C_{NW} A_W^2 \quad (22)$ <p>SOLVING FOR <math>A_W</math>:</p> $A_W = \frac{(C_N - C_{NB}) S}{C_{NW}} \quad (23)$   |  |
| <p>TRIM CONTROL DEFLECTION</p> $C_{m_{TRIM}} = 0 + C_m + C_{m\delta} \delta_{TRIM} \quad (24)$ <p>SOLVING FOR <math>\delta_{TRIM}</math>:</p> $\delta_{TRIM} = \frac{-C_m}{C_{m\delta}} \quad (25)$  |  |
| <p>CENTER OF GRAVITY LOCATION</p> $C_m = (X_{CG} - X_{CP}) C_N \quad (26)$ <p>SOLVING FOR <math>X_{CG}</math></p> $X_{CG} = \frac{C_m}{C_N} + X_{CP} \quad (27)$   |  |

FIGURE 5. SELECTED DESIGN EQUATIONS

11-3315

|  |  |
|--|--|
| <p>STATIC STABILITY</p> $K_S = \delta/a + C_{m\alpha} / C_{m\delta} \quad (28)$  |  |
| <p>BANK/ROLL STATIC STABILITY</p> $K_{S1} = \frac{a}{1+a\beta} \frac{C_{l\beta} \cos \alpha + C_{l\beta} \sin \alpha}{C_{l\delta A}} \quad (29)$ |  |
| <p>YAW STABILITY</p> $K_{S2} = \delta_R / \beta = - \frac{C_{n\beta} \cos \alpha - C_{n\beta} \sin \alpha}{C_{n\delta R}} \quad (30)$            |  |
| <p>ROLL YAW CONTROL CROSS COUPLING<br/>(REF 5, FIG 10)</p> $K_X = \frac{C_{n\delta A} - C_{l\delta R}}{C_{n\delta R} C_{l\delta A}} \quad (31)$  |  |

FIGURE 6. AUTOPILOT DESIGN EQUATIONS

11-3316

| PARAMETER               | PERFORMANCE DESIGN EQUATION | RELATIONSHIP   |
|-------------------------|-----------------------------|--|
| POWERED RANGE           | (11)                        | $\frac{\Delta C_N}{C_N} = \frac{2 \Delta R}{R}$ (36)                               |
| TURN RADIUS             | (14, 5)                     | $\frac{\Delta C_N}{C_N} = \frac{\Delta r}{r}$ (37)                                 |
| TURN RATE               | (17)                        | $\frac{\Delta C_N}{C_N} = \frac{\Delta \dot{v}}{\dot{v}}$ (38)                     |
| LOAD FACTOR             | (18)                        | $\frac{\Delta C_N}{C_N} = \frac{\Delta n}{n}$ (39)                                 |
| SPECIFIC EXCESS POWER   | (14)                        | $\frac{\Delta C_{N_d}}{C_{N_d}} = \frac{(q \cdot V) \Delta P_S}{(W \cdot S)}$ (40) |
| WING SIZE (LOAD FACTOR) | (23)                        | $\frac{\Delta C_{NB}}{C_{NB}} = \frac{C'_{NW} \Delta A_W}{C_{NB} A_W}$ (41)        |

FIGURE 7.  $C_N$  ACCURACY CRITERIA

11-3317

| PARAMETER             | PERFORMANCE DESIGN EQUATION | RELATIONSHIP   |
|-----------------------|-----------------------------|--|
| POWERED RANGE         | (11)                        | $\frac{\Delta C_A}{C_A} = \frac{\Delta R}{R}$ (42)                                 |
| COAST RANGE           | (2, 3)                      | $\frac{\Delta C_A}{C_A} = \frac{\Delta R}{R}$ (43)                                 |
| SPECIFIC EXCESS POWER | (14)                        | $\frac{\Delta C_{A_0}}{C_A} = \frac{W \cdot S}{q \cdot V} \Delta P_S$ (44)         |
| MANEUVER DECELERATION | (15)                        | $\frac{\Delta C_A}{C_A} = \frac{C_D \Delta \dot{v}}{C_A \cos \alpha \dot{v}}$ (45) |

FIGURE 8.  $C_A$  ACCURACY CRITERIA

11-3318

| PARAMETER                  | PERFORMANCE DESIGN EQUATION | RELATIONSHIP  |
|----------------------------|-----------------------------|---|
| RESPONSE TIME              | (19)                        | $\frac{\Delta C_{m\delta}}{C_{m\delta}} = \frac{2 \Delta \tau}{\tau}$ (46)  |
| CRUISE ALTITUDE            | (10, 13)                    | $\frac{\Delta C_m}{C_m} = \frac{\Delta \beta}{\beta} \left[ \frac{W (X_{CG} - X_{CP})}{S b} \right] \Delta \tau$ (47) |
| HORIZONTAL FIN AREA        | (16, 17)                    | $\frac{\Delta C_{m\delta}}{C_{m\delta}} = \frac{\Delta A_T}{A_T}$ (48)  |
| TRIM CONTROL DEFLECTION    | (24, 25)                    | $\frac{\Delta C_m}{C_m} = \frac{\Delta \delta_{TRIM}}{\delta_{TRIM}}$ (49)  |
| CENTER OF GRAVITY LOCATION | (26, 27)                    | $\frac{\Delta C_m}{C_m} = \frac{\Delta X_{CG}}{X_{CG} - X_{CP}}$ (50)   |
| STATIC STABILITY           | (28)                        | $\frac{\Delta C_{m\delta}}{C_{m\delta}} = \frac{\Delta K_S}{K_S}$ (51)  |
| STATIC STABILITY           | (28)                        | $\frac{\Delta C_{m\alpha}}{C_{m\alpha}} = \frac{\Delta K_S}{K_S}$ (52)  |

FIGURE 9.  $C_m$  ACCURACY CRITERIA

11-3319

| PARAMETER             | PERFORMANCE/DESIGN EQUATION | RELATIONSHIP  |
|-----------------------|-----------------------------|---|
| • TURN RADIUS         | (4, 6)                      | $\frac{\Delta C_Y}{C_Y} = \frac{\Delta r}{r}$ (53)                                    |
| • TURN RATE           | (6, 7)                      | $\frac{\Delta C_Y}{C_Y} = \frac{\Delta \dot{\psi}}{\dot{\psi}}$ (54)                  |
| • VERTICAL FIN AREA   | (18)                        | $\frac{\Delta C_{nB}}{C_{nB}} = \frac{\Delta A_V}{A_V}$ (55)                          |
| • BANK/ROLL STABILITY | (29)                        | $\Delta C_{n\beta} = \frac{ \alpha  C_{l\delta A} \Delta K_{S1}}{a \sin \alpha}$ (56) |
| • YAW STABILITY       | (30)                        | $\Delta C_{n\beta} = \frac{C_{n\delta R} \Delta K_{S3}}{\cos \alpha}$ (57)            |
| • YAW STABILITY       | (30)                        | $\frac{\Delta C_{n\delta R}}{C_{n\delta R}} = \frac{\Delta K_{S3}}{K_{S3}}$ (58)      |
| • CROSS COUPLING      | (31)                        | $\frac{\Delta C_{n\delta R}}{C_{n\delta R}} = \frac{\Delta K_X}{K_X}$ (59)            |
| • CROSS COUPLING      | (31)                        | $\frac{\Delta C_{n\delta A}}{C_{n\delta A}} = \frac{\Delta K_X}{K_X}$ (60)            |

FIGURE 10.  $C_Y$  AND  $C_n$  ACCURACY CRITERIA

11-3320

| PARAMETER                    | PERFORMANCE/DESIGN EQUATION | RELATIONSHIP  |
|------------------------------|-----------------------------|---|
| • DIHEDRAL ANGLE             | (20, 21)                    | $\frac{\Delta C_l}{C_l} = \frac{\Delta \Gamma}{\Gamma}$ (61)                          |
| • BANK/ROLL STATIC STABILITY | (29)                        | $\Delta C_{l\beta} = \frac{ \alpha  C_{l\delta A} \Delta K_{S1}}{a \cos \alpha}$ (62) |
| • BANK/ROLL STATIC STABILITY | (29)                        | $\frac{\Delta C_{l\delta A}}{C_{l\delta A}} = \frac{\Delta K_{S1}}{K_{S1}}$ (63)      |
| • YAW STABILITY              | (30)                        | $\Delta C_{l\beta} = \frac{C_{l\delta R} \Delta K_{S3}}{\sin \alpha}$ (64)            |
| • CROSS COUPLING             | (31)                        | $\frac{\Delta C_{l\delta A}}{C_{l\delta A}} = \frac{\Delta K_X}{K_X}$ (65)            |
| • CROSS COUPLING             | (31)                        | $\frac{\Delta C_{l\delta R}}{C_{l\delta R}} = \frac{\Delta K_X}{K_X}$ (66)            |

FIGURE 11.  $C_l$  ACCURACY CRITERIA

11-3321

| PARAMETER                            | ACCURACY CRITERIA EQUATION | ALLOWABLE ERROR | AERODYNAMIC COEFFICIENT        | ALLOWABLE ACCURACY             |
|--------------------------------------|----------------------------|-----------------|--------------------------------|--------------------------------|
| $\Delta R/R$ (POWERED)               | 36                         | 0.10            | $\Delta C_N/C_N$               | 0.20                           |
| $\Delta r/r$                         | 37                         | 0.20            |                                | 0.20                           |
| $\Delta \dot{\psi}/\dot{\psi}$       | 38                         | 0.20            |                                | 0.20                           |
| $\Delta n/n$                         | 39                         | 0.20            |                                | 0.20                           |
| $\Delta R/R$ (POWERED)               | 42                         | 0.10            | $\Delta C_A/C_A$               | 0.10                           |
| $\Delta R/R$ (COAST)                 | 43                         | 0.10            |                                | 0.10                           |
| $\Delta r/r$                         | 46                         | 0.20            | $\Delta C_{m\beta}/C_{m\beta}$ | 0.40                           |
| $\Delta A_T/A_T$                     | 48                         | 0.20            |                                | $\Delta C_{m\beta}/C_{m\beta}$ |
| $\Delta \delta_{TRIM}/\delta_{TRIM}$ | 49                         | 0.20            | $\Delta C_m/C_m$               | 0.20                           |
| $\Delta X_{CG}/(X_{CG} - X_{CP})$    | 50                         | 0.20            |                                | $\Delta C_m/C_m$               |
| $\Delta r/r$                         | 53                         | 0.20            | $\Delta C_Y/C_Y$               | 0.20                           |
| $\Delta \dot{\psi}/\dot{\psi}$       | 54                         | 0.20            |                                | 0.20                           |
| $\Delta A_V/A_V$                     | 55                         | 0.20            | $\Delta C_{nB}/C_{nB}$         | 0.20                           |
| $\Delta \Gamma/\Gamma$               | 61                         | 0.20            |                                | $\Delta C_l/C_l$               |

FIGURE 12. ALLOWABLE ACCURACIES THAT RELATE DIRECTLY TO ALLOWABLE ERROR



| MAGNITUDE OF K  |  | 11-3322                                   |  |  |
|---|--|---|--|--|
|   |  | STATIC STABILITY                          | BANK/ROLL STABILITY  | YAW STABILITY  |
| $\Delta K$ VALUE FOR EQS.   |  | (51, 52)                                  | (56, 62, 63)   | (57, 58, 64)   |
| $ K  \leq 1$  |  | 0.25                                      | 0.25   | 0.25   |
| $1 <  K  \leq 5$  |  | 0.25 K                                    | 0.25 K   | 0.25 K   |
| $ K  > 5$   |  | $\Delta C_{m\delta} = 0.05  C_{m\alpha} $ | $\Delta C_{l\delta A} = 0.05 \times  C_{l\beta} \cos \alpha + C_{n\beta} \sin \alpha $ | $\Delta C_{l\delta R} = 0.05 \times  C_{n\beta} \cos \alpha - C_{l\beta} \sin \alpha $ |
| IF $\frac{\Delta C_{m\delta}}{C_{m\alpha}} \cdot \frac{\Delta C_{l\delta A}}{C_{l\beta}} \cdot \frac{\Delta C_{l\delta R}}{C_{n\beta}} > 0.5$ SET EQUAL TO 0.50 |  |   |  |  |

TYPICAL PLOT

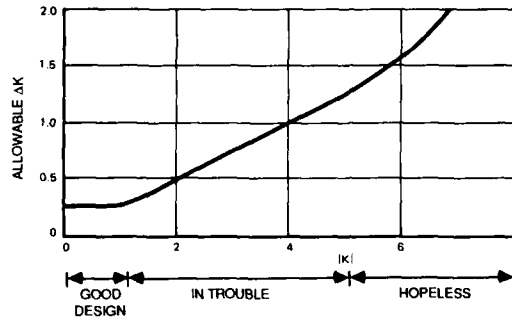


FIGURE 13. ALLOWABLE ERRORS FOR AUTOPILOT DESIGN PARAMETERS

| MAGNITUDE OF K  |  | CROSS COUPLING   |
|---|--|--|
|   |  | (59, 60, 65, 66)   |
| $\Delta K$ VALUE FOR EQS.   |  |  |
| $ K  \leq 0.5$  |  | 0.125  |
| $0.5 <  K  \leq 2.5$  |  | 0.125 K  |
| $ K  > 2.5$   |  | $\Delta C_{n\delta R} = 0.05 \frac{C_{n\delta A} C_{l\delta R}}{C_{l\delta A}}$<br>$\Delta C_{l\delta A} = 0.05 \frac{C_{n\delta A} C_{l\delta R}}{C_{n\delta H}}$ |
| IF $\frac{\Delta C_{n\delta A}}{C_{n\delta A}} \cdot \frac{\Delta C_{l\delta R}}{C_{l\delta R}} > 0.50$ SET EQUAL TO 0.50 |  |  |

FIGURE 14. ALLOWABLE ERRORS FOR CROSS-COUPLING DERIVATIVES

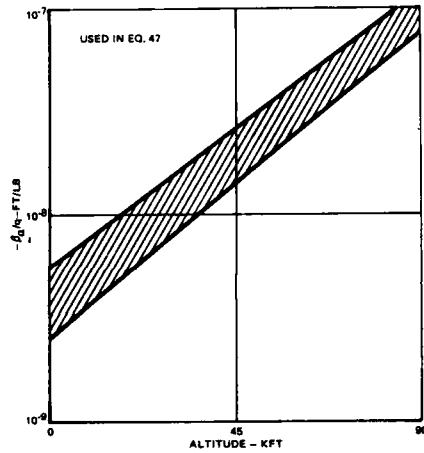
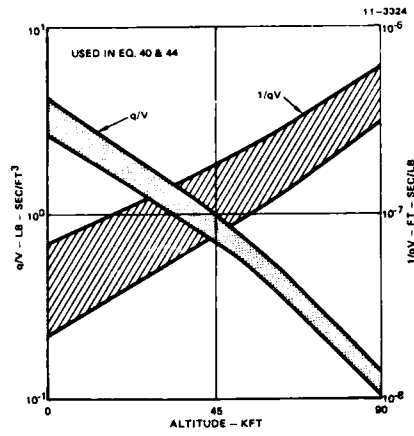


FIGURE 15. TYPICAL VARIATION OF TRAJECTORY RELATED PARAMETERS FOR AIRBREATHERS

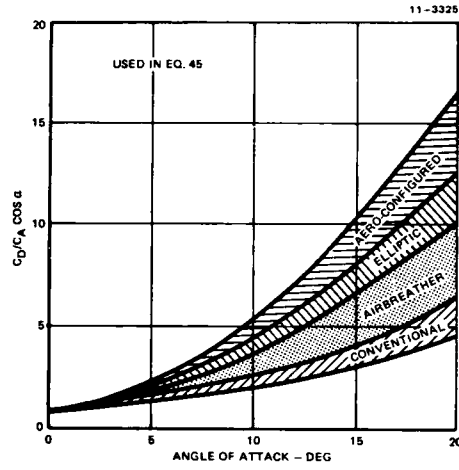


FIGURE 16. TYPICAL VALUES OF  $C_D/C_A \cos \alpha$  FOR FOUR MISSILE CLASSES

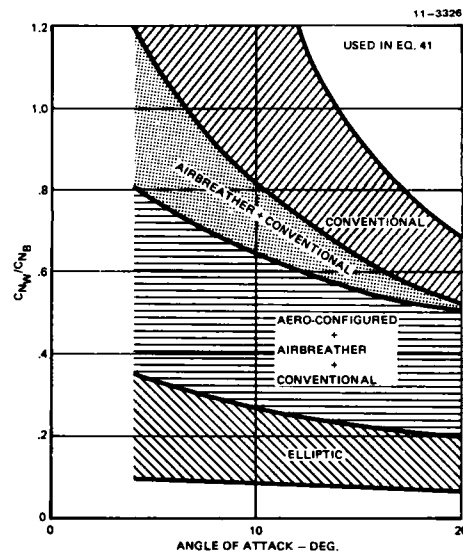


FIGURE 17. TYPICAL VALUES OF  $C_{NW}/C_{NB}$  FOR FOUR MISSILE CLASSES

| CONFIGURATION CLASS | COEFFICIENTS FOR ACCURACY CRITERIA EQUATIONS |                             |                          |                                   |                               |
|---------------------|--|-----------------------------|--------------------------|-----------------------------------|-------------------------------|
|                     | (EQ. 40)<br>(q/V)/(W/S)                      | (EQ. 41)<br>$C_{NW}/C_{NB}$ | (EQ. 44)<br>(W/S)/(qV)   | (EQ. 45)<br>$C_D/C_A \cos \alpha$ | (EQ. 47)<br>$(\beta_a)(W/Sb)$ |
| CONVENTIONAL        | (N/A)  | 0.8                         | (N/A)                    | 2.5                               | (N/A)                         |
| AIRBREATHER         | 0.7/(W/S)                                    | 0.5                         | $1.8 \times 10^{-7} W/S$ | 3.0                               | $-2.5 \times 10^{-6} W/Sb$    |
| ELLIPTIC            | (N/A)  | 0.2                         | (N/A)                    | 4.0                               | (N/A)                         |
| AERO-CONFIGURED     | 0.1/(W/S)                                    | 0.5                         | $6.3 \times 10^{-7} W/S$ | 5.0                               | $-1.2 \times 10^{-7} W/Sb$    |

FIGURE 18. TYPICAL VALUES OF CONFIGURATION/PERFORMANCE DEPENDENT PARAMETERS

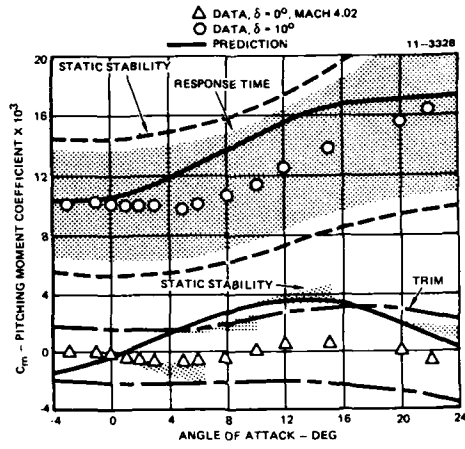


FIGURE 19.  $C_m$  ACCURACY ASSESSMENT

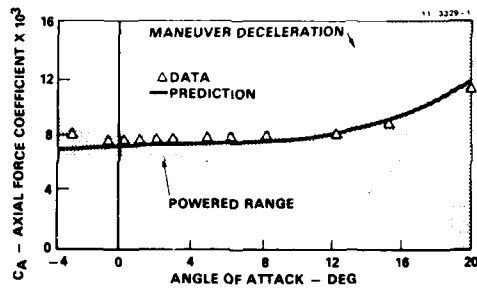


FIGURE 20. A GOOD  $C_A$  COMPARISON WITH DATA

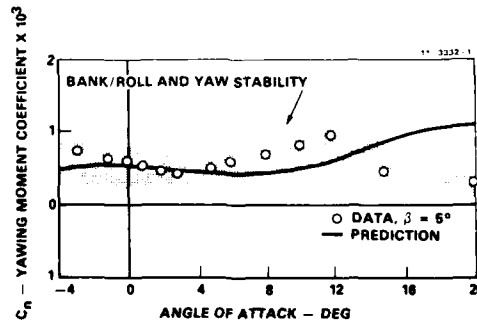


FIGURE 21. A GOOD  $C_n$  PREDICTION AT LOW ANGLE OF ATTACK

## APPENDIX A

## DERIVATION OF ACCURACY RELATIONS

A total of 31 accuracy criteria relations were given on Figures 7 through 11. A summary derivation of equal equation is given in Figures A1 through A30. There are six accuracy relations for  $C_N$ , the relation derived from the load factor equation is given in the text of the paper and the remaining derivations are given in Figures A1 through A5. The four accuracy relations for  $C_A$  are derived in Figures A6 through A9, the seven  $C_m$  relations are derived in Figures A10 through A16, the eight  $C_y$  and  $C_n$  relations are derived in Figures A17 through A24, and the six  $C$  relations are derived in Figures A25 through A30.

DERIVATION OF  $C_N$  POWERED RANGE ACCURACY RELATION

M11-0760

$$R = \frac{2.828}{C_1(P/S)^{1/2}} \frac{C_L^{1/2}}{C_D} (W_0^{1/2} - W_1^{1/2})$$

LOW - :  $C_L = C_N$   
 $C_D = C_A$

$$R = \frac{2.828}{C_1(P/S)^{1/2}} \frac{C_N^{1/2}}{C_A} (W_0^{1/2} - W_1^{1/2})$$

$$\frac{R}{C_N^{1/2}} = \frac{2.828}{C_1(P/S)^{1/2}} \frac{(W_0^{1/2} - W_1^{1/2})}{C_A}$$

$$\frac{\partial R}{\partial C_N} = \frac{1}{2} \frac{2.828}{C_1(P/S)^{1/2}} \frac{(W_0^{1/2} - W_1^{1/2})}{C_A} \frac{1}{C_N^{1/2}}$$

$$\frac{\partial R}{\partial C_N} = \frac{1}{2} \frac{R}{C_N}$$

$$\frac{\Delta C_N}{C_N} = \frac{2 \Delta R}{R}$$

FIGURE A-1

DERIVATION OF  $C_N$  TURN RADIUS ACCURACY RELATION

M11-0761

$$r = \frac{V^2}{g(n^2 - 1)^{1/2}} (n^2 - 1)^{1/2} = (C_L q S W) \sin \phi$$

LEVEL TURN:  $C_N = C_L \cos \phi$

$$r = \frac{V^2 W}{g C_N \cos \phi q S \sin \phi}$$

$$\frac{\partial r}{\partial C_N} = \frac{-V^2 W}{g C_N^2 \cos \phi q S \sin \phi} \cdot \frac{1}{C_N}$$

$$\frac{\partial r}{\partial C_N} = \frac{-r}{C_N}$$

ABSOLUTE VALUE ERROR

$$\frac{\Delta C_N}{C_N} = \frac{\Delta r}{r}$$

FIGURE A-2

DERIVATION OF  $C_N$  TURN RATE ACCURACY RELATION

M11-0762

$$\dot{\psi} = \frac{g(n^2 - 1)^{1/2}}{V} (n^2 - 1)^{1/2} (C_L q S W) \sin \phi$$

LEVEL TURN:  $C_L = C_N \cos \phi$

$$\dot{\psi} = \frac{g q S \sin \phi \cos \phi}{V W} C_N$$

$$\frac{\dot{\psi}}{C_N} = \frac{g q S \sin \phi \cos \phi}{V W}$$

$$\frac{\partial \dot{\psi}}{\partial C_N} = \frac{g q S \sin \phi \cos \phi}{V W} = \frac{\dot{\psi}}{C_N}$$

$$\frac{\Delta C_N}{C_N} = \frac{\Delta \dot{\psi}}{\dot{\psi}}$$

FIGURE A-3

DERIVATION OF  $C_N$  SPECIFIC EXCESS POWER ACCURACY RELATION

M11-0763

$$P_s = \frac{V}{W} \left\{ T - \left[ C_D + K \frac{(Wn)^2}{qS} \right] qS \right\}$$

LEVEL FLIGHT: LOW -

$n = 1$   
 $K = 1/C_N^2$   
 $C_L = C_N = C_N$   
 $C_D = C_A$   
 $Wn q S = C_L = C_N$   
 $C_L^2 = C_N^2$

$$P_s = \frac{V}{W} \left\{ T - \left[ C_A + C_N^2 \right] qS \right\}$$

$$\frac{\partial P_s}{\partial C_N} = - \frac{V q S}{W} \frac{\partial P_s}{\partial C_N}$$

$$\frac{\partial C_N}{\partial C_N} = - \frac{W}{V q S} \frac{\partial P_s}{\partial C_N}$$

$$\frac{\partial C_N}{\partial C_N} = \frac{-W}{V q S} \frac{\partial P_s}{\partial C_N}$$

$$\frac{\partial C_N}{\partial C_N} = \frac{-(qV)}{(WB)} \frac{\partial P_s}{\partial P_s}$$

ABSOLUTE VALUE ERROR

$$\frac{\Delta C_N}{C_N} = \frac{(qV)}{(WB)} \frac{\Delta P_s}{\Delta P_s}$$

FIGURE A-4

**DERIVATION OF  $C_N$  WING SIZE (LOAD FACTOR)  
ACCURACY RELATION**

M11-07944

$$A_W = \frac{(C_N - C_{NB})}{C_{NW}} S$$

$$\frac{\partial A_W}{\partial C_{NB}} = - \frac{S}{C'_{NW}}$$

$$\frac{\partial C_{NB}}{C_{NB}} = - \frac{C'_{NW}}{C_{NB}} \frac{\partial A_W}{S}$$

REFERENCE AREA = WING AREA

$$S = A_W$$

$$\frac{\partial C_{NB}}{C_{NB}} = - \frac{C'_{NW}}{C_{NB}} \frac{\partial A_W}{A_W}$$

ABSOLUTE VALUE ERROR

$$\frac{\Delta C_{NB}}{C_{NB}} = \frac{C'_{NW}}{C_{NB}} \frac{\Delta A_W}{A_W}$$

FIGURE A-5

**DERIVATION OF  $C_A$  POWERED RANGE  
ACCURACY RELATION**

M11-07945

$$R = \frac{2.828}{C_L (\rho S)^{1/2}} \frac{C_L^{1/2}}{C_D} (W_0^{1/2} - W_1^{1/2})$$

CPUNDE:    - - 0  
               $C_L = C_H$   
               $C_D = C_A$

$$R = \frac{2.828}{C_L (\rho S)^{1/2}} \frac{C_L^{1/2}}{C_A} (W_0^{1/2} - W_1^{1/2})$$

$$\frac{\partial R}{\partial C_A} = - \frac{2.828}{C_L (\rho S)^{1/2}} \frac{C_L^{1/2}}{C_A} (W_0^{1/2} - W_1^{1/2}) \cdot \frac{1}{C_A}$$

$$\frac{\partial R}{\partial C_A} = - \frac{R}{C_A}$$

$$\frac{\Delta C_A}{C_A} = - \frac{\Delta R}{R}$$

ABSOLUTE VALUE ERROR

$$\frac{\Delta C_A}{C_A} = \frac{\Delta R}{R}$$

FIGURE A-6

**DERIVATION OF  $C_A$  COAST RANGE  
ACCURACY RELATION**

M11-07946

$$R = \frac{2W}{g \rho S K_{DV}} \left[ V_0 - V_1 + V_B \ln \left( \frac{V_0 - V_B}{V_1 - V_B} \right) \right]$$

$K_{DV} = C_D \frac{V^2}{(V - V_B)}$   
- - 0  
 $C_D = C_A$

$$R = \frac{2W(V - V_B)}{g \rho S C_A V^2} \left[ V_0 - V_1 + V_B \ln \left( \frac{V_0 - V_B}{V_1 - V_B} \right) \right]$$

$$\frac{\partial R}{\partial C_A} = - \frac{2W(V - V_B)}{g \rho S C_A V^2} \left[ V_0 - V_1 + V_B \ln \left( \frac{V_0 - V_B}{V_1 - V_B} \right) \right] \cdot \frac{1}{C_A}$$

$$\frac{\partial R}{\partial C_A} = - \frac{R}{C_A}$$

$$\frac{\Delta C_A}{C_A} = - \frac{\Delta R}{R}$$

ABSOLUTE VALUE ERROR

$$\frac{\Delta C_A}{C_A} = \frac{\Delta R}{R}$$

FIGURE A-7

**DERIVATION OF  $C_A$  SPECIFIC EXCESS POWER  
ACCURACY RELATION**

M11-07947

$$P_S = \frac{V}{W} \left\{ T - \left[ C_{D_0} + K \left( \frac{Wn^2}{qS} \right) \right] qS \right\}$$

$$C_{D_0} = C_{A_0}$$

$$P_S = \frac{V}{W} \left\{ T - \left[ C_{A_0} + K \left( \frac{Wn^2}{qS} \right) \right] qS \right\}$$

$$\frac{\partial P_S}{\partial C_{A_0}} = - \frac{V}{W} qS$$

$$\Delta C_{A_0} = - \frac{W/S}{qV} \Delta P_S$$

ABSOLUTE VALUE ERROR

$$\Delta C_{A_0} = \frac{W/S}{qV} \Delta P_S$$

FIGURE A-8

**DERIVATION OF  $C_A$  MANEUVER DECELERATION  
ACCURACY RELATION**

M11-07044

$$\begin{aligned} \dot{V} &= -C_D q S M \\ \frac{\dot{V}}{C_D} &= -q S M \\ C_D &= C_H \sin \alpha + C_A \cos \alpha \\ \dot{V} &= \frac{(C_H \sin \alpha + C_A \cos \alpha)}{M} q S \\ \frac{\partial \dot{V}}{\partial C_A} &= \frac{-q S}{M} \cos \alpha \\ \frac{\partial \dot{V}}{\partial C_A} &= \frac{\dot{V}}{C_D} \cos \alpha \\ \frac{\partial C_A}{\partial \dot{V}} &= \frac{C_D}{\dot{V} \cos \alpha} \\ \frac{\Delta C_A}{C_A} &= \frac{C_D}{C_A} \frac{\Delta \dot{V}}{\dot{V} \cos \alpha} \end{aligned}$$

FIGURE A-9

**DERIVATION OF  $C_m$  RESPONSE TIME  
ACCURACY RELATION**

M11-07045

$$\begin{aligned} \tau &= \sqrt{\frac{2I_{yy}}{C_{m\delta} \delta q S b}} \\ \frac{\partial \tau}{\partial C_{m\delta}} &= -\frac{1}{2} \sqrt{\frac{2I_{yy}}{\delta q S b C_{m\delta}}} \cdot \frac{1}{C_{m\delta}} \\ \frac{\partial \tau}{\partial C_{m\delta}} &= -\frac{1}{2} \frac{\tau}{C_{m\delta}} \\ \frac{\partial C_{m\delta}}{\partial \tau} &= -\frac{2 \partial \tau}{\tau} \\ \text{ABSOLUTE VALUE ERROR} \\ \frac{\Delta C_{m\delta}}{C_{m\delta}} &= \frac{2 \Delta \tau}{\tau} \end{aligned}$$

FIGURE A-10

**DERIVATION OF  $C_m$  CRUISE ALTITUDE  
ACCURACY RELATION**

M11-07050

$$\begin{aligned} \frac{W}{q S C_L} &= 1 \\ C_{L_{TRIM}} &= C_L + \Delta C_{L_{CONTROL}} \\ C_{m_{TRIM}} &= C_m + \frac{(X_{CG} - X_{CPT})}{b} \Delta C_{L_{CONTROL}} \\ h &= \frac{1}{\beta_a} \ln \left[ \frac{2W}{\rho_{REF} V^2 S \left[ C_L - \frac{C_{m\delta}}{(X_{CG} - X_{CPT})} \right]} \right] \\ \frac{\partial h}{\partial C_m} &= \frac{1}{\beta_a} \frac{b}{\left[ C_L - \frac{C_{m\delta}}{(X_{CG} - X_{CPT})} \right] (X_{CG} - X_{CPT})} \\ \text{CRUISE: } C_L &= C_{L_{TRIM}} \\ \Delta C_{L_{CONTROL}} &= 0 \\ C_{m_{TRIM}} &= 0 \\ \frac{\partial h}{\partial C_m} &= \frac{1}{\beta_a} \frac{b}{C_L (X_{CG} - X_{CPT})} \\ C_L &= \frac{W}{q S} \\ \frac{\partial h}{\partial C_m} &= \frac{1}{\beta_a} \frac{W b q S}{W (X_{CG} - X_{CPT})} \\ \frac{\partial C_m}{\partial h} &= \frac{\beta_a}{q} \frac{W (X_{CG} - X_{CPT})}{b S} \partial h \\ \Delta C_m &= \frac{\beta_a}{q} \frac{W (X_{CG} - X_{CPT})}{S b} \Delta h \end{aligned}$$

FIGURE A-11

DERIVATION OF  $C_m$  HORIZONTAL FIN AREA  
ACCURACY RELATION

SM 11-07801

$$C_m = 0 = C_{m_B} + \frac{(\alpha_{CG} - \alpha_{CP_T}) C'_{N_T} A_T}{b S}$$

$$A_T = \frac{C_{m_B} b S}{(\alpha_{CG} - \alpha_{CP_T}) C'_{N_T}}$$

$$\frac{A_T}{C_{m_B}} = \frac{b S}{(\alpha_{CG} - \alpha_{CP_T}) C'_{N_T}}$$

$$\frac{\partial A_T}{\partial C_{m_B}} = \frac{b S}{(\alpha_{CG} - \alpha_{CP_T}) C'_{N_T}}$$

$$\frac{\partial A_T}{\partial C_{m_B}} = \frac{A_T}{C_{m_B}}$$

$$\frac{\Delta C_{m_B}}{C_{m_B}} = \frac{\Delta A_T}{A_T}$$

FIGURE A-12

DERIVATION OF  $C_m$  TRIM CONTROL DEFLECTION  
ACCURACY RELATION

SM 11-07802

$$C_{m_{TRIM}} = 0 = C_m + C_{m_0} \delta_{TRIM}$$

$$\delta_{TRIM} = -\frac{C_m}{C_{m_0}}$$

$$\frac{\delta_{TRIM}}{C_m} = -\frac{1}{C_{m_0}}$$

$$\frac{\partial \delta_{TRIM}}{\partial C_m} = -\frac{1}{C_{m_0}}$$

$$\frac{\partial \delta_{TRIM}}{\partial C_m} = \frac{\delta_{TRIM}}{C_m}$$

$$\frac{\Delta C_m}{C_m} = \frac{\Delta \delta_{TRIM}}{\delta_{TRIM}}$$

FIGURE A-13

DERIVATION OF  $C_m$  CENTER OF GRAVITY  
LOCATION ACCURACY RELATION

SM 11-07803

$$C_m = (\alpha_{CG} - \alpha_{CP}) C_N$$

$$X_{CG} \frac{C_m}{C_N} + X_{CP}$$

$$\frac{1}{C_N} = \frac{X_{CG} - X_{CP}}{C_m}$$

$$\frac{\partial X_{CG}}{\partial C_m} = \frac{1}{C_N}$$

$$\frac{\partial X_{CG}}{\partial C_m} = \frac{X_{CG} - X_{CP}}{C_m}$$

$$\frac{\partial C_m}{C_m} = \frac{\partial X_{CG}}{X_{CG} - X_{CP}}$$

$$\frac{\Delta C_m}{C_m} = \frac{\Delta X_{CG}}{X_{CG} - X_{CP}}$$

FIGURE A-14

DERIVATION OF  $C_m$  STATIC STABILITY  
ACCURACY RELATION

M11-07654

$$K_S = \frac{\delta}{\epsilon} = \frac{C_{m_{\epsilon}}}{C_{m_{\delta}}}$$

$$\frac{\partial K_S}{\partial C_{m_{\delta}}} = -\frac{C_{m_{\epsilon}}}{C_{m_{\delta}}^2} \cdot \frac{1}{C_{m_{\delta}}}$$

$$\frac{\partial K_S}{\partial C_{m_{\delta}}} = -\frac{K_S}{C_{m_{\delta}}}$$

$$\frac{\Delta C_{m_{\delta}}}{C_{m_{\delta}}} = -\frac{\Delta K_S}{K_S}$$

ABSOLUTE VALUE ERROR

$$\frac{\Delta C_{m_{\delta}}}{C_{m_{\delta}}} = \frac{\Delta K_S}{K_S}$$

FIGURE A-15

DERIVATION OF  $C_m$  STATIC STABILITY  
ACCURACY RELATION

M11-07655

$$K_S = \frac{\delta}{\epsilon} = \frac{C_{m_{\epsilon}}}{C_{m_{\delta}}}$$

$$\frac{K_S}{C_{m_{\epsilon}}} = \frac{1}{C_{m_{\delta}}}$$

$$\frac{\partial K_S}{\partial C_{m_{\epsilon}}} = \frac{1}{C_{m_{\delta}}}$$

$$\frac{\partial K_S}{\partial C_{m_{\epsilon}}} = \frac{K_S}{C_{m_{\epsilon}}}$$

$$\frac{\Delta C_{m_{\epsilon}}}{C_{m_{\epsilon}}} = \frac{\Delta K_S}{K_S}$$

FIGURE A-16

DERIVATION OF  $C_Y$  TURN RADIUS  
ACCURACY RELATION

M11-07664

$$r = \frac{v^2}{g(n^2-1)^{1/2}}$$

$$(n^2-1)^{1/2} = C_Y q S / W$$

$$r = \frac{v^2 W}{g C_Y q S}$$

$$\frac{\partial r}{\partial C_Y} = -\frac{v^2 W}{g C_Y^2 q S} \cdot \frac{1}{C_Y}$$

$$\frac{\partial r}{\partial C_Y} = -\frac{r}{C_Y}$$

$$\frac{\Delta C_Y}{C_Y} = -\frac{\Delta r}{r}$$

ABSOLUTE VALUE ERROR

$$\frac{\Delta C_Y}{C_Y} = \frac{\Delta r}{r}$$

FIGURE A-17

DERIVATION OF  $C_Y$  TURN RATE  
ACCURACY RELATION

M11-07667

$$(n^2-1)^{1/2} = C_Y q S / W$$

$$\dot{\psi} = \frac{g(n^2-1)^{1/2}}{v}$$

$$\dot{\psi} = \frac{g C_Y q S}{v W}$$

$$\frac{\dot{\psi}}{C_Y} = \frac{g q S}{v W}$$

$$\frac{\partial \dot{\psi}}{\partial C_Y} = \frac{g q S}{v W}$$

$$\frac{\partial \dot{\psi}}{\partial C_Y} = \frac{\dot{\psi}}{C_Y}$$

$$\frac{\Delta C_Y}{C_Y} = \frac{\Delta \dot{\psi}}{\dot{\psi}}$$

FIGURE A-18

DERIVATION OF  $C_{n_B}$  VERTICAL FIN AREA  
ACCURACY RELATION

M11-07668

$$C_n = 0 = C_{n_B} + \frac{(X_{CG} - X_{CP_V}) C_Y \dot{\psi} A_V}{b S}$$

$$C_{n_B} = -\frac{(X_{CG} - X_{CP_V}) C_Y \dot{\psi} A_V}{b S}$$

$$\frac{C_{n_B}}{A_V} = -\frac{(X_{CG} - X_{CP_V}) C_Y \dot{\psi}}{b S}$$

$$\frac{\partial C_{n_B}}{\partial A_V} = -\frac{(X_{CG} - X_{CP_V}) C_Y \dot{\psi}}{b S} = \frac{C_{n_B}}{A_V}$$

$$\frac{\Delta C_{n_B}}{C_{n_B}} = \frac{\Delta A_V}{A_V}$$

FIGURE A-19



### DERIVATION OF $C_{n\beta}$ BANK/ROLL STABILITY

#### ACCURACY RELATION

L11-0766

$$K_{S1} = \frac{\delta_A}{\beta} \frac{\alpha}{l \alpha} \frac{C_{L\beta} \cos \alpha + C_{n\beta} \sin \alpha}{C_{L\delta_A}}$$

$$\frac{\partial K_{S1}}{\partial C_{n\beta}} = \frac{\alpha}{l \alpha} \frac{\sin \alpha}{C_{L\delta_A}}$$

$$\partial C_{n\beta} = \frac{l \alpha}{\alpha} \frac{C_{L\delta_A}}{\sin \alpha} \partial K_{S1}$$

$$\Delta C_{n\beta} = \frac{l \alpha}{\alpha} \frac{C_{L\delta_A}}{\sin \alpha} \Delta K_{S1}$$

FIGURE A-20

### DERIVATION OF $C_{n\beta}$ YAW STABILITY

#### ACCURACY RELATION

M11-0760

$$K_{S3} = \frac{\delta_R}{\beta} = - \frac{C_{n\beta} \cos \alpha - C_{L\beta} \sin \alpha}{C_{n\delta_R}}$$

$$\frac{\partial K_{S3}}{\partial C_{n\beta}} = \frac{-\cos \alpha}{C_{n\delta_R}}$$

$$\partial C_{n\beta} = C_{n\delta_R} \frac{\partial K_{S3}}{\cos \alpha}$$

$$\Delta C_{n\beta} = -C_{n\delta_R} \frac{\Delta K_{S3}}{\cos \alpha}$$

#### ABSOLUTE VALUE ERROR

$$\Delta C_{n\beta} = C_{n\delta_R} \frac{\Delta K_{S3}}{\cos \alpha}$$

FIGURE A-21

### DERIVATION OF $C_{n\delta_R}$ YAW STABILITY

M11-0761

#### ACCURACY RELATION

$$K_{S3} = \frac{\delta_R}{\beta} = - \frac{C_{n\beta} \cos \alpha - C_{L\beta} \sin \alpha}{C_{n\delta_R}}$$

$$\frac{\partial K_{S3}}{\partial C_{n\delta_R}} = \frac{C_{n\beta} \cos \alpha - C_{L\beta} \sin \alpha}{C_{n\delta_R}^2} \cdot \frac{1}{C_{n\delta_R}}$$

$$\frac{\partial K_{S3}}{\partial C_{n\delta_R}} = \frac{-K_{S3}}{C_{n\delta_R}}$$

$$\frac{\Delta C_{n\delta_R}}{C_{n\delta_R}} = \frac{-\Delta K_{S3}}{K_{S3}}$$

#### ABSOLUTE VALUE ERROR

$$\frac{\Delta C_{n\delta_R}}{C_{n\delta_R}} = \frac{\Delta K_{S3}}{K_{S3}}$$

FIGURE A-22

DERIVATION OF  $C_{n\delta R}$  CROSS COUPLING

## ACCURACY RELATION

$$K_X = \frac{C_{n\delta A} C_{l\delta R}}{C_{n\delta R} C_{l\delta A}}$$

$$\frac{\partial K_X}{\partial C_{n\delta R}} = -\frac{C_{n\delta A} C_{l\delta R}}{C_{n\delta R}^2 C_{l\delta A}} \cdot \frac{1}{C_{n\delta R}}$$

$$\frac{\partial K_X}{\partial C_{n\delta R}} = -\frac{K_X}{C_{n\delta R}}$$

$$\frac{\Delta C_{n\delta R}}{C_{n\delta R}} = -\frac{\Delta K_X}{K_X}$$

## ABSOLUTE VALUE ERROR

$$\frac{\Delta C_{n\delta R}}{C_{n\delta R}} = \frac{\Delta K_X}{K_X}$$

FIGURE A-23

DERIVATION OF  $C_{n\delta A}$  CROSS COUPLING

## ACCURACY RELATION

$$K_X = \frac{C_{n\delta A} C_{l\delta R}}{C_{n\delta R} C_{l\delta A}}$$

$$\frac{K_X}{C_{n\delta A}} = \frac{C_{l\delta R}}{C_{n\delta R} C_{l\delta A}}$$

$$\frac{\partial K_X}{\partial C_{n\delta A}} = \frac{C_{l\delta R}}{C_{n\delta R} C_{l\delta A}} = \frac{K_X}{C_{n\delta A}}$$

$$\frac{\Delta C_{n\delta A}}{C_{n\delta A}} = \frac{\Delta K_X}{K_X}$$

FIGURE A-24

DERIVATION OF  $C_{l\beta}$  DIHEDRAL ANGLE

## ACCURACY RELATION

$$C_{l\beta} = 0 = C_{l\beta} - \frac{Y_{CP}}{b} C_{N-W} \beta \sin \Gamma$$

$$\sin \Gamma = \frac{C_{l\beta} b}{Y_{CP} C_{N-W} \beta}$$

$$C_{l\beta} = C_{l\beta} / \beta$$

SMALL  $\Gamma$ :  $\sin \Gamma = \Gamma$  (RADIAN)

$$\Gamma = \frac{C_{l\beta} b}{Y_{CP} C_{N-W} \beta^2}$$

$$\frac{\Gamma}{C_{l\beta}} = \frac{b}{Y_{CP} C_{N-W} \beta^2}$$

$$\frac{\partial \Gamma}{\partial C_{l\beta}} = \frac{b}{Y_{CP} C_{N-W} \beta^2} = \frac{\Gamma}{C_{l\beta}}$$

$$\frac{\Delta C_{l\beta}}{C_{l\beta}} = \frac{\Delta \Gamma}{\Gamma}$$

FIGURE A-25

DERIVATION OF  $C_{l\beta}$  BANK/ROLL STATIC STABILITY

## ACCURACY RELATION

$$K_{S1} = \frac{-\omega}{I \omega} \frac{C_{l\beta} \cos \omega + C_{n\beta} \sin \omega}{C_{l\delta A}}$$

$$\frac{\partial K_{S1}}{\partial C_{l\beta}} = \frac{-\omega \cos \omega}{I \omega C_{l\delta A}}$$

$$\frac{\partial K_{S1}}{\partial C_{l\beta}} = \frac{I \omega / C_{l\delta A}}{-\omega \cos \omega} \frac{\partial K_{S1}}{\partial K_{S1}}$$

$$\frac{\Delta C_{l\beta}}{C_{l\beta}} = \frac{I \omega / C_{l\delta A}}{-\omega \cos \omega} \Delta K_{S1}$$

FIGURE A-26

DERIVATION OF  $C_{\lambda\delta A}$  BANK/ROLL STABILITY

M11-07666

$$K_{S1} = \frac{\delta A}{\beta} = \frac{\alpha}{|\alpha|} \frac{C_{\lambda\beta} \cos \alpha + C_{n\beta} \sin \alpha}{C_{\lambda\delta A}}$$

$$\frac{\partial K_{S1}}{\partial C_{\lambda\delta A}} = -\frac{\alpha}{|\alpha|} \frac{C_{\lambda\beta} \cos \alpha + C_{n\beta} \sin \alpha}{C_{\lambda\delta A}^2} \cdot \frac{1}{C_{\lambda\delta A}}$$

$$\frac{\partial K_{S1}}{\partial C_{\lambda\delta A}} = -\frac{K_{S1}}{C_{\lambda\delta A}}$$

ABSOLUTE VALUE ERROR

$$\frac{\Delta C_{\lambda\delta A}}{C_{\lambda\delta A}} = \frac{\Delta K_{S1}}{K_{S1}}$$

FIGURE A-27

DERIVATION OF  $C_{\lambda\beta}$  YAW STABILITY

M11-07667

## ACCURACY RELATION

$$K_{S3} = \frac{\delta R}{\beta} = -\frac{C_{n\beta} \cos \alpha - C_{\lambda\beta} \sin \alpha}{C_{n\delta R}}$$

$$\frac{\partial K_{S3}}{\partial C_{\lambda\beta}} = \frac{\sin \alpha}{C_{n\delta R}}$$

$$\partial C_{\lambda\beta} = \frac{C_{n\delta R}}{\sin \alpha} \partial K_{S3}$$

$$\Delta C_{\lambda\beta} = C_{n\delta R} \frac{\Delta K_{S3}}{\sin \alpha}$$

FIGURE A-28

DERIVATION OF  $C_{\lambda\delta A}$  CROSS COUPLING

## ACCURACY RELATION

M11-07668

$$K_X = \frac{C_{n\delta A} C_{\lambda\delta R}}{C_{n\delta R} C_{\lambda\delta A}}$$

$$\frac{\partial K_X}{\partial C_{\lambda\delta A}} = -\frac{C_{n\delta A} C_{\lambda\delta R}}{C_{n\delta R} C_{\lambda\delta A}^2} \cdot \frac{1}{C_{\lambda\delta A}}$$

$$\frac{\partial K_X}{\partial C_{\lambda\delta A}} = -\frac{K_X}{C_{\lambda\delta A}}$$

$$\frac{\Delta C_{\lambda\delta A}}{C_{\lambda\delta A}} = -\frac{\Delta K_X}{K_X}$$

ABSOLUTE VALUE ERROR

$$\frac{\Delta C_{\lambda\delta A}}{C_{\lambda\delta A}} = \frac{\Delta K_X}{K_X}$$

FIGURE A-29

DERIVATION OF  $C_{\lambda\delta R}$  CROSS COUPLING

M11-07669

## ACCURACY RELATION

$$K_X = \frac{C_{n\delta A} C_{\lambda\delta R}}{C_{n\delta R} C_{\lambda\delta A}}$$

$$\frac{K_X}{C_{\lambda\delta A}} = -\frac{C_{n\delta A}}{C_{n\delta R} C_{\lambda\delta A}^2}$$

$$\frac{\partial K_X}{\partial C_{\lambda\delta R}} = \frac{C_{n\delta A}}{C_{n\delta R} C_{\lambda\delta A}} = \frac{K_X}{C_{\lambda\delta R}}$$

$$\frac{\Delta C_{\lambda\delta R}}{C_{\lambda\delta R}} = \frac{\Delta K_X}{K_X}$$

FIGURE A-30

**SURVEY ON NONLINEAR EFFECTS**

Marnix F. E. Dillenius  
Director of Missile and Store  
Separation Aerodynamics

and

Stanley C. Perkins, Jr.  
Research Engineer

Nielsen Engineering & Research, Inc.  
510 Clyde Avenue  
Mountain View, CA 94043-2287  
USA

**SUMMARY**

This lecture describes a survey of experimental observations and intermediate level prediction methods aimed at nonlinear aerodynamic characteristics of tactical missiles. A description is given of the major differences between missile and aircraft flight and configuration characteristics. The importance of vortical interference and nonlinear compressibility due to shocks is stressed. Nonlinearities associated with deformable fin design, supersonic fin on body interference, wraparound fins, and unsteady flight are discussed. Summarized accounts are provided of the effects of asymmetric body vortex shedding and vortex bursting on overall missile aerodynamic characteristics. Physical examples are given that show vortex structures and shock formations in vapor screen and schlieren pictures. In many instances, the nonlinear aerodynamic effects are illustrated by theoretical results obtained with and without the relevant nonlinearity. Short descriptions are given of intermediate level panel-based missile aerodynamics prediction methods with special attention to the models incorporated to account for vortical and nonlinear compressibility effects. The descriptions include applications to additive force analysis for supersonic inlets and to deformable fins. Additional comparisons with experimental data are provided and the nonlinear effects pointed out. Presently available methods and future needs are summarized in the concluding remarks.

## INTRODUCTION

This lecture is concerned with nonlinear effects of missile aerodynamics. In this context, the nonlinear effects are taken to be those effects which are nonlinear with angle of attack and/or cannot be adequately treated with linear theory. Examples of nonlinear effects associated with tactical missile aerodynamics include formation of flow separation vortices, vortex wakes and vortical interference, nonlinear compressibility due to presence of shocks, and aeroelastic deformation. In addition, the performance of airbreathing missiles can be influenced by off design operation of the inlet, especially at supersonic speeds. All of the nonlinear effects can be complicated further by unsteady flow.

The methods for analysis of missile aerodynamics are fairly new and range from simplest handbook techniques to numerical aerodynamic simulations. The simplest include slender body and linear theory and coded versions thereof (Refs. 1 and 2), semi-empirical based codes (Refs. 3-6), and impact theory codes using two dimensional nonlinear theory neglecting vortical effects (Ref. 7). The intermediate level missile codes are based on singularity distributions using low order panel methods (derived from supersonic linear theory) enhanced with vortical effects (Refs. 8-11). The highest level methods employ numerical simulations based on potential, Euler, and Navier-Stokes solvers (Refs. 12-15).

Generally, the simplest engineering level methods are limited to simple configurations, approximate or neglect completely canard or tail vortical interference, and calculate longitudinal characteristics usually valid in the low range of angle of attack only. Some of the semi-empirical methods incorporate missile body and fin aerodynamic loads that are nonlinear; for example, the data-based missile programs of References 4 and 5. In addition, the handbook methods and the semi-empirical method included in the latest version of Missile Datcom (Ref. 6) provide approximations for the longitudinal stability derivatives.

The intermediate panel-based supersonic missile codes require more user supplied information for input, but they can economically provide detailed aerodynamic loadings for fairly complex missile configurations. The panel-based codes of References 8, 9, and 10 include simplified accounts of vortical formation and interference, and can also combine two dimensional nonlinear theory with three dimensional linear theory for calculation of surface pressures including aerodynamic interference. Code NWCDM-NSTRN (Ref. 9) also allows for roll, pitch, and yaw angular rates.

The highest level missile aerodynamics analysis methods employ numerical simulations or CFD (Computational Fluid Dynamics) codes which can simulate flows about simple geometries with more complex physics including some of the nonlinearities mentioned earlier. Transport aircraft with attached flows are handled very well at the present time by CFD methods but more complex flow phenomena associated with high performance military aircraft are not yet fully amenable to CFD analysis (Ref. 16). CFD methods for unsteady aerodynamic flows have received far less attention than those for steady flows. The viscous unsteady CFD technology is in its infancy. In the application to missile unsteady motions, perhaps simple geometries can be analyzed with inviscid codes, and possibly approaches based on coupled unsteady inviscid codes with steady boundary layer or unsteady two dimensional Navier-Stokes codes will be available in the near future.

The summarized account of the missile aerodynamics analyses given above serves as a basis for methods required now and in the future to handle the special aerodynamic characteristics of missiles in general. It is the objective of this lecture to provide some insight into the nonlinear characteristics of missile aerodynamics.

The lecture starts with descriptions of flight and configuration characteristics that make tactical missile

aerodynamic analysis different from airplane aerodynamic analysis. Physical examples of vortical and shock related phenomena are illustrated. Some comparisons with existing predictions are included. Intermediate level methods of analysis based on singularity distributions and designed to include nonlinear vortical and nonlinear compressibility effects are described. References are made to existing computer programs including a program for estimating additive drag of supersonic inlets based on paneling methods (Refs. 11). Additional comparisons with experimental data and a calculative example for an aeroelastically deformed fin are discussed. The lecture is summarized and some conclusions are offered in the concluding remarks.

#### FLIGHT AND CONFIGURATION CHARACTERISTICS

The following descriptions are primarily aimed at pointing out nonlinear aerodynamic effects of tactical or short range types of missiles as opposed to strategic or long range missiles. The major differences between missile and aircraft aerodynamics are described first. The effects of the presence of shocks (nonlinear compressibility) are summarized and the need to consider nonlinear aerodynamics in aeroelastic problems is discussed. This is followed by a short description of nonlinear fin body interference for supersonic flow in terms of commonly used interference factors used in engineering prediction methods. Some unusual aerodynamic aspects of missiles with wraparound fins are briefly described, and an example of unsteady flight is given as well as summaries of the effects of asymmetric body vortex shedding and vortex bursting. The flight and configuration characteristics listed below may not be complete and are open to discussion.

## MISSILE VS. AIRCRAFT

Tactical missiles can execute high-g maneuvers and fly from subsonic to high supersonic speeds. Angles of attack can be sufficiently high to form strong flow separation vortices from the missile body and fin edges. Thus, forward fin wakes and the body vorticity influence the distribution of aerodynamic loads on the missile, especially the loads acting on the tail fins. This nonlinear effect may not be so important in the case of an aircraft where the wing vortices are usually not very close to the stabilizer surfaces, as shown in Figure 1. On tactical missiles, the forward or canard fin wakes can actually impact the tail fins. As shown in the upper portion of the figure, the missile configuration can be rolled and the body and fins may operate at angle of sideslip in addition to angle of pitch. A given finned section may include two, three, four, or more fins. Therefore, fin on fin interference becomes important. The overall shapes of missiles tend to be slender, and the fins are usually of small aspect ratio giving rise to formation of vortices from the leading and side edges. Examples are discussed in a later section.

Recent designs of airbreathing missiles include large air intakes which may interfere aerodynamically with the airframe and vice versa. Supersonic inlets operating off design (shock ahead of cowl lip) and at subcritical condition (less than maximum possible flow) create additive drag and lift and may generate vortices which can affect aerodynamic loadings on the airframe aft of the inlet. These nonlinear effects are difficult to analyze. A simple method for approximating inlet additive forces is described later in this lecture.

The missile flight and configuration characteristics listed above are generally different from those for an aircraft. Most importantly, the components of a missile experience strong aerodynamic interactions, most of them nonlinear, which are not usually encountered by aircraft. Some special missile aerodynamic characteristics are discussed next.



### PRESENCE OF SHOCKS

At high supersonic Mach numbers, nonlinear compressibility effects will affect the pressures acting on the forebody and fins of a missile. This type of nonlinearity can also be important at lower supersonic flight Mach numbers when the angle of attack and/or local surface shape causes portions of the missile to be near the bow shock and/or the fin leading edge shock. Such situations can occur on, but are not limited to, the windward side of the missile surfaces. Some examples are discussed later in this lecture.

Aerodynamic loads acting on missiles in the vicinity of a supersonic parent aircraft, or aerodynamic loads on submissiles launched from a supersonic dispenser, are affected by the nonlinear effects of shocks in the flow. In addition, the aerodynamic loads are also influenced by missile nose shocks reflecting off the parent aircraft or the dispenser. These nonlinearities will not be addressed in this lecture. Experimental data and approximate methods for handling such problems can be found in the store separation analysis techniques described in Reference 17.

### AEROELASTIC FIN EFFECTS

Recently, development of a fin design procedure has been initiated that is aimed at optimizing the deformable structure of a fin to satisfy an aerodynamic objective; for example, hinge moments minimization for control fins (Ref. 18). In this and other examples of static aeroelastic problems, the aerodynamic and the structural effects interact with one another. In the application to missile control fins, the angle of pitch seen by the fin tends to be relatively high and nonlinearities associated with fin leading and side edge flow separation enter into the picture. The problem is made more difficult by the nonlinear

effects of airgaps between the deflected fin and the missile body. A calculative example of a fin deformed under the influence of aerodynamic forces is discussed later in this lecture.

#### SUPERSONIC FIN BODY INTERFERENCE

The following short description of the nonlinear interference between fins and body is taken from Reference 19 and applies to engineering level prediction methods employing wing ( $K_W$ ) and body ( $K_B$ ) interference factors. For a planar fin body combination, the fin interference factor represents the ratio of aerodynamic normal-force coefficient of the right and left fins combined in the presence of the body to the normal-force coefficient of a wing alone formed by joining the left and right fins at their root chords. The body interference factor represents the aerodynamic normal-force coefficient on the body in the presence of the fins normalized by the wing alone value.

For moderate angles of attack ( $\alpha < 10$  deg) and moderate supersonic Mach numbers ( $M < 2$ ), linear theory based methods for predicting the interference between midwings and the body give adequate results. However, at higher Mach numbers and higher angles of attack, large nonlinearities primarily due to nonlinear body effects occur in wing body interference. Reference 19 provides  $K_W$  factors and the ratios  $K_W/K_B$  obtained from a massive experimental data base for Mach numbers between 2.5 and 4.5 and for angles of attack up to 40 deg. Examples showing the fin interference factor for AR (aspect ratio) = 2 and AR = 0.5 fins with taper ratios of 0.0, 0.5, and 1.0 are shown in Figures 2 and 3. The ratio of body radius to wing semispan (one half of tip to tip span including body) is 0.5.

The concluding remarks in Reference 19 state the following. The interference factor generally indicates that, at small angles of attack (2.5 deg and less), the values of  $K_W$  do not deviate much from slender-body theory. Near zero angle of attack, the

values of  $K_B/K_W$  sometimes exceed the slender-body value and sometimes are less. At high angles of attack, the interference tends to be small so that  $K_W$  tends to unity and  $K_B$  tends to zero. However, in a number of instances, there are significant deviations from these general rules. Therefore, in the application to missile aerodynamics, it is clear that fin body interference at high angles of attack and Mach numbers is influenced by nonlinear effects.

#### WRAPAROUND FINS

Designers of tube and dispenser launched missiles have incorporated wraparound fins. Upon launch, the fins are deployed to provide aerodynamic stability during the flight. However, many instances of unusual quasisteady flight dynamics including angular (coning) motion have been observed.

In Reference 20, recent free flight aerodynamic tests are described for a missile configuration with four wraparound fins at the base. The test results show that an out of plane side (yawing) moment at zero sideslip is generated at subsonic and transonic Mach numbers (up to  $M_\infty = 1.4$ ). In the supersonic range, the side moment causes dynamic instability in that the amplitude of the coning motion continues to increase. The cited reference concludes that the side moment is related to aerodynamics of wraparound fin configurations.

Provided the angle of attack during the flight remains less than 10 deg, the side moment must be generated by the antisymmetric wraparound configuration shown in Figure 4. The prediction of this aerodynamic characteristic is difficult and may require nonlinear aerodynamic theory. However, this lecturer believes that it is possible to estimate supersonic wraparound fin aerodynamics with linear theory at least for low supersonic Mach numbers. It is necessary to include fin thickness and to interact the thickness solution with the lifting solution. Comparisons with experimental data for a wraparound wing concept,

including nonzero rolling moment at zero angle of attack, are shown in Reference 10. The problem definitely becomes nonlinear when the body angle of attack becomes sufficiently large to cause formation of body vortices which also influence the fin loading in a nonlinear manner.

#### UNSTEADY FLIGHT

Unsteady aerodynamic effects associated with missile flight can be important. Because of the missile flight characteristics mentioned earlier, missiles can undergo motions with high rotational rates. A typical vertical launch trajectory is shown in Figure 5. Within approximately the first second, the missile pitches at about 300 deg/sec and the angle of attack can be as high as 50-60 deg during the initial (subsonic) portion of the flight. Under these conditions, the missile forebody at zero sideslip angle can be subjected to out of plane side forces and attendant side or yawing moments which are highly nonlinear and can exceed the available control capability of the missile. This yawing moment contributes to the so called phantom yaw. The side force is due to asymmetric flow separation on the forebody. Observations about this type of body flow separation are given below.

#### Body Vortex Shedding

An extensive review of available information on asymmetric vortex shedding from bodies of revolution compiled and interpreted by Ericsson and Reding is available in Reference 21. For the sake of completeness and for the benefit of missile designers, the following is excerpted from the cited reference.

"There are no easy answers for the missile aerodynamicist concerned about the effects of vortex-induced asymmetric loads at zero sideslip. Existing theoretical techniques are inadequate because they do not account for the viscous aspects of the flow

phenomenon, including the dominant effects of nonuniform surface roughness. In addition, they do not consider the observed large effects of nosetip geometry and vehicle motion. However, the aerodynamicist does know that:

- 1) The phenomenon occurs generally at  $30 \text{ deg} \leq \alpha \leq 60 \text{ deg}$  for most practical configurations.
- 2) Significant side loads occur only for subsonic cross flow.
- 3) The magnitude of the side load is Reynolds number sensitive, with both the maximum and minimum [side force to normal-force ratios] occurring in the critical Reynolds number range.
- 4) The phenomenon is nose dependent, with the asymmetric vortices beginning at a pointed, slender nosetip and on the rear of the body when the nose is blunt.
- 5) Body motion affects the asymmetric loads greatly and can lock in the maximum possible vortex asymmetry achievable at a particular Reynolds number range to cause self-sustained coning motion."

"If needed, the following fixes should be considered:

- 1) Yaw plane strakes or analogous body shaping for bank-to-turn missiles.
- 2) Multiple longitudinal strakes or trips for rolling missiles.
- 3) Nose bluntness, for both kinds of vehicles; but make sure that the effects of the body-induced vortices are not worse than the nose-induced effects.
- 4) Nose blowing, windward side blowing being more efficient than leeward side blowing."

### Vortex Bursting

Another aspect of nonlinear aerodynamic behavior in missile aerodynamics is related to vortex breakdown or bursting

phenomena. Breakdown is generally affiliated with the core flow of the vortex. As mentioned by Luckring in Reference 22, this three dimensional unsteady and turbulent fluid mechanical problem has proven to be difficult to predict. This reference describes a theoretical model to represent the features of the basic flow structure of the flow separation-induced leading edge vortex for slender wings. Low speed (incompressible) tests for a delta wing show that at angles of attack in excess of 30 deg the leading edge vortex core flow breaks down ahead of the trailing edge and that the lift losses due to the breakdown are substantial. Therefore, in the application to missile fins on a low speed missile, the lift loss may occur on one fin of an opposite pair of fins and cause a rolling and yawing moment. In addition, the asymmetric vortex field may stream aft along the missile body and induce asymmetric aerodynamic loads on the tail fins.

It is clear that the highly nonlinear and possibly unsteady aerodynamic effects mentioned above for the sake of completeness are important since they can result in uncontrollable missile dynamic behavior.

In the next section, illustrations are given of some of the aerodynamic nonlinearities described earlier in this section. From here on, the discussions are focused on missiles and their components in supersonic flow.

#### EXAMPLES

In this section, vapor screen and schlieren pictures are presented to illustrate the vortical and shock types of nonlinearities. In addition, pressure distributions acting on bodies under the influence of vortices are shown. Effects of the presence of shocks on wing pressure distributions and overall loads are indicated. In many cases, predicted results are included to show the nonlinear aerodynamic effects. The theoretical methods used in the predictions are summarized later in this lecture. Examples of vortex structures for wings and along a cruciform missile are described first.

### HIGHLY SWEPT WING

An example of the vortex structure on a highly swept wing is shown in Figure 6. This delta wing is discussed in Reference 23. The vapor screen near the trailing edge corresponds to Mach number 2.4 and 12 deg angle of attack. Note that in this supersonic case the vortex structure shows no signs of breaking up (bursting) and includes secondary vortices as indicated in the figure.

In the application to missile fins, leading and side edge vorticity can develop as the angle of attack is increased. If the side edges are long, vorticity can be generated along the edge for angles of attack as low as 5 deg. Along the leading edges, vorticity can be generated at supersonic speeds from the root leading edge (for subsonic leading edges). The leading and side edge vortices may combine and form a pattern of strong vorticity located above the trailing edge. The forward fins may generate vortices that stream aft along the afterbody and tail section and influence the pressures on those components. Examples of vortices along a missile are described next.

### CRUCIFORM MISSILE

Vapor screens showing the vortex structure immediately behind a cruciform canard tail missile model are shown in Figures 7 and 8 for various combinations of angle of attack and roll angle at Mach number 2.36. The experimental test setup and additional data for cases with forward fin deflection are described in Reference 24. In the vapor screen photographs in Figure 7, the core of the vortices are indicated by the dark spots. At the lowest angle of attack, the vortices closest to the body originate from the forebody, and the two vortices above the fin tips are generated by the horizontal canard fins. The tail fin vortices are not as visible because they are relatively weak and

have not been rolled up at the vapor screen location. As the angle of attack is increased, vortex sheets appear and the afterbody contributes to the vorticity. For the lowest included angle of attack,  $\alpha_C = 11.4$  deg, effects of angle of roll are shown in Figure 8. For nonzero angle of roll, the vertical canard fins also generate vortices which interact with the body and horizontal canard fin vortices as they stream aft to the tail section.

The aerodynamic loads acting on the tail fins are definitely influenced by the vortex structures illustrated above. For cases with asymmetric forward fin control or for cases with nonzero roll angle, the tail fins generate induced rolling moments which are usually highly nonlinear with angle of attack.

In both figures, the indicated theoretical results are obtained with the vortex formation and tracking methods embodied in computer program LRCDM2 described fully in Reference 8 and summarized later in this lecture.

#### AXISYMMETRIC BODY

The circumferential pressure distributions shown in Figure 9 act at 3 axial stations aft of the nosetip of a model consisting of a three caliber ( $x/D = 3$ ) ogive nose followed by a 3.67 caliber ( $x/D = 3.67$ ) cylindrical afterbody. The experimental data is extracted from Reference 25 which contains circumferential pressure distribution data at a large number of axial stations for a range of angles of attack and supersonic Mach numbers.

The data shown in Figure 9 correspond to a Mach number of 1.6, included angle of attack of 20 deg, and free-stream Reynolds number based on diameter of  $0.5 \times 10^6$ . At this angle of attack, the body shed vortex wake on the lee side of the body is well developed and consists mainly of a symmetrical pair of vortices connected by vortex sheets to the body. This body vortex



structure is in its developmental stages at the first two axial stations ( $x/D = 0.8$  and  $2.8$ ), and the pressure distributions shown in Figures 9(a) and (b) are weakly influenced by the vortex wake. However, at  $x/D = 5.1$  the vortex wake has developed to such an extent that it has a dominant effect on the pressure distribution shown in Figure 9(c) and, therefore, the integrated aerodynamic forces and moments acting on the body.

In Figure 9(c), the solid and dashed lines represent results obtained with the body vortex prediction program NOZVTX described in Reference 26 and summarized later in this lecture. The difference between the solid and dashed lines is an indication of the nonlinear effects of body vorticity on the pressure distributions. The solid curve, representing the pressure distribution in the presence of the vortex wake, departs from the dashed line, representing results excluding the vortex wake, from polar angle  $\beta = 70$  deg onward. The predicted vortex wake, consisting of many discrete vortices, is indicated in the upper portion of Figure 9(c). Similar data for an elliptic cross section body are discussed next.

#### ELLIPTIC BODY

Vapor screen photographs showing vortex development on a sharp nosed 3:1 elliptic body are shown in Figure 10 for five angles of roll. The axial station is near the base of the body. The Mach number is 2.5 and the included angle of attack is 20 deg. This and additional data are available in References 27 and 28.

At zero roll angle, two symmetric vortices develop near the nose of the model and continue to grow along the sides of the body. At 45 deg roll angle, the right or lower vortex is elongated and stays close to the body surface. The left or upper vortex retains the approximate shape of the zero roll angle vortex but appears weaker and is located further above the body surface. At 90 deg roll angle the vortex structure has changed to a narrow wake formation above the body.

The flow visualization pictures were digitized to define the vortical structures indicated by the solid lines in Figure 11(a) for zero roll angle and in Figure 11(b) for 45 deg roll angle. The dashed lines correspond to results predicted by the body vortex modeling computer program NOZVTX described in Reference 26 and summarized later in this lecture. For zero roll angle, the agreement between the predicted results and experimental results is quite good. The calculated total circulation strength  $\Gamma$  increases three fold from  $x/L = 0.32$  to the base of the body. At 45 deg angle of roll the character of the predicted vortex wake is in fair agreement with experiment.

It should be noted that Reference 29 describes results obtained with a Reynolds averaged Navier-Stokes solver for the same elliptical body. These results compare extremely well with experiment and show large regions of secondary separation near the body shoulders and on the lee side. This is an example of a case which is geometrically simple enough to be treated with a numerical simulation based on more complex physics and giving the best results.

Circumferential pressure distributions for the 3:1 elliptical cross section body at axial station  $x/L = 0.6$  are shown in Figure 12(a) for zero roll angle and in Figure 12(b) for 45 deg roll angle. The Mach number is 2.5 and the included angle of attack is 20 deg. Under these conditions, the pressure distributions on the leeward side of the body are very much affected by the body generated vorticity. Predicted results using the computer program NOZVTX described in Reference 26 are shown in Figure 12 with and without separation effects. It is clear that the addition of the nonlinear aerodynamic effect caused by the presence of the body separation wake improves the pressure predictions. The discrepancy in the pressure comparisons on the windward side near the shoulders of the body are most likely caused by the nonlinear compressibility effects due to the close proximity of the bow shock wave. This nonlinearity is not included in the NOZVTX predictions. Indeed, a numerical

simulation based on the nonlinear full potential equation agrees much better with the experimental data in the shoulder region but lacks agreement on the lee side (Ref. 27). The potential code is called NCOREL (Ref. 12) and is applicable to attached flow conditions.

The nonlinear compressibility due to the presence of shocks is described next.

#### NONLINEAR COMPRESSIBILITY

The schlieren photograph shown in Figure 13 shows a model of a missile in the supersonic wind tunnel at NASA Langley Research Center. The model is at 14 deg included angle of attack, the Mach number is 2.5, and the vertical fins of the canard control model are deflected -5 deg (trailing edge to right). The picture shows that the bow shock attached to the body nose is close to the windward side of the forebody and that the shock touches the tip of the lower vertical canard fin. Thus, it can be expected that for these conditions the pressures on the forebody and possibly the lower fin are influenced by the nonlinear compressibility due to the presence of the bow shock. The lower surfaces of the horizontal fins will also be close to the fin leading edge shocks.

Also visible in Figure 13 are what appear to be concentrated fin tip vortex wakes from the vertical and horizontal fins. In addition, a dark cloud lies on top of the afterbody on the portion of the body visible through the right two windows. This cloud may very well be body shed vorticity developed on the afterbody.

Thus, the features in Figure 13 mentioned above relate to nonlinearities that are typical of high speed missiles. Of interest here are the effects of the presence of shocks. Pressure distributions acting on two wing alone cases are described below.

## RECTANGULAR WING

Experimentally measured and calculated pressure distributions for the rectangular wing shown in Figure 14 are compared in Figure 15. The details of the experimental test and additional data are given in Reference 30. The chordwise pressure distributions acting on the upper and lower surfaces of the wing are shown in Figure 15 near the one-half semispan location for angle of attack 10.3 deg and a Mach number of 2.86. The experimental data show the strong effects of the beveled portions of the wing. Attached to the leading edge is a strong oblique shock which affects the pressures most on the lower surface.

The aerodynamic nonlinearity due to the nonlinear compressibility associated with the leading edge shock is best illustrated by contrasting linear theory results with nonlinear theory results. There are many ways to accomplish this. Here results are used as calculated by computer program LRCDM2 (Ref. 8) which is described later in the lecture.

The supersonic linear theory predictions generated by LRCDM2 are based on a ten chordwise by five spanwise layout of constant u-velocity panels for modeling lift as shown in the lower portion of Figure 14. The same layout of planar source panels is used for modeling thickness effects. The two dimensional shock expansion analysis of LRCDM2 makes use of ten spanwise strips with ten segments in each. The predicted results labeled "linear" are based on linear theory and the compressible Bernoulli pressure coefficient. The results labeled "shock expansion, corrected" are based on shock expansion theory with flow angles (or local Mach numbers) corrected for strip on strip interference by linear theory as implemented in LRCDM2.

Due to the presence of a strong oblique shock attached to the leading edge, the linear theory results underestimate the pressure coefficients on both the upper and lower surfaces up to

the flat portion of the wing. The corrected shock expansion pressure results match the experimental data much better in this region. On the flat portion, both methods agree well with the data. Over the length of the beveled position at the trailing edge, both methods predict lower than measured pressure coefficients on the upper or suction surface. This is most likely due to boundary layer separation effects. On the lower or windward side, the corrected shock expansion method matches the data better.

The above example serves to illustrate the strong effects of nonlinear compressibility induced by the oblique shock attached to the wing leading edge. Note that neither the angle of attack nor the Mach number are very high; however, the wedge angle at the leading edge is large giving rise to the strong shock. In the application to a missile, the effects described above can be very important in the hinge moments experienced by an all movable control fin. An additional example of nonlinear compressibility is described next.

#### DELTA WING

Experimental and predicted chordwise pressure distributions are shown in Figure 16 for an aspect ratio 1 delta wing with a 4% circular arc (biconvex) streamwise section. The experimental data shown in the figure are part of a collection of chordwise pressure distribution data available from Reference 31.

The Mach number is 4.6 for all cases shown here, so that the Mach cone lies just aft of the leading edge of the delta wing (i.e., supersonic leading edge). The dashed line just inside the leading edge of the delta wing corresponds to the Mach cone associated with the free-stream Mach number. Pressure distributions are shown in Figure 16 at the 40% spanwise station for an angle of attack of 20.56 deg. At this spanwise location, the measured pressure coefficients almost lie on straight lines. Effects of leading edge vorticity appear to be minimal for this case with a slightly supersonic leading edge.

As in the rectangular wing case discussed above, the linear and nonlinear aerodynamic aspects can be most conveniently demonstrated by results calculated with computer program LRCDM2 (Ref. 8) described later in this report. The results predicted by LRCDM2 are obtained with a layout of ten chordwise by five spanwise constant u-velocity panels to model linear theory lift and ten chordwise by five spanwise planar source panels to account for linear theory thickness. The nonlinear and combined theories are applied to five chordwise strips on the top and bottom surfaces with ten segments on each strip. The calculated results are categorized as follows.

- 1) Shock expansion: pressure coefficients calculated with shock expansion theory, uncorrected for aerodynamic interference effects.
- 2) Bernoulli (linear theory): compressible Bernoulli pressure coefficients with perturbation velocities induced by the linear theory paneling method.
- 3) Newtonian: Newtonian pressure coefficients calculated on the windward side and  $C_p = 0$  on the leeward side.
- 4) Shock expansion, corrected: category 1 pressure coefficients corrected for interference effects with combined nonlinear/linear theory.
- 5) Newtonian, corrected: category 3 pressure coefficients corrected for interference effects with combined nonlinear/linear theory.

The Newtonian and Bernoulli (linear theory) results are indicated in the top portion of Figure 16 and the same Bernoulli results are shown with shock expansion results in the bottom portion. On the lower surface, the predicted Bernoulli pressure coefficients are much higher than the experimental pressure coefficients except near the leading edge where the Bernoulli

prediction approaches the zero level. At the high angle of attack considered here, this behavior is due to unrealistic (high) values of resultant flow velocity calculated with linear theory and used in the Bernoulli pressure expression. The uncorrected Newtonian results shown in Figure 16 match the windward data best. The corrected shock expansion method definitely improves agreement with experiment. On the suction or upper surface, the level of measured pressure coefficients is at the minimum. The Bernoulli and the uncorrected and corrected shock expansion pressure coefficients are also at the minimum level. Note that the Bernoulli pressure coefficients used with linear theory are limited to the minimum value set by the free-stream Mach number. The uncorrected and corrected Newtonian pressure coefficients are set equal to zero on the suction surface.

The chordwise pressure distributions, one of which is discussed above, are integrated over the upper and lower surfaces of the AR = 1 delta wing to give the normal-force coefficient as a function of angle of attack. In Figure 17, the normal-force coefficient and the center-of-pressure location, measured from the wing apex and normalized by the root chord, are shown as a function of angle of attack. The experimental data are taken from Reference 31. For angles of attack up to 12 deg, the Bernoulli method based on linear theory matches the normal-force data well; however, the center of pressure calculated by that method lies aft of the measured location and the error grows larger with  $\alpha_c$ . This is typical of linear theory in its application to wings at high Mach number. The total normal-force often is estimated well, but the distribution of that force is faulty. The uncorrected and corrected Newtonian normal-force predictions are low at the two angles of attack for which results are shown. This is due to the forced zero pressure coefficient value on the upper surface of the wing. This "shadow flow" approximation holds better at Mach numbers greater than 5. The center of pressure predicted by the Newtonian method is far forward of the measured level at the low angle of attack and matches the data fortuitously at the high angle. The uncorrected

and corrected shock expansion methods match the normal-force and center of pressure data well at the low angle of attack. At the high angle, the agreement in normal-force is definitely better with the corrected shock expansion method. Center of pressure is not affected much by the correction.

In summary, the corrected shock expansion pressure coefficient method appears to give the best results for the delta wing under consideration at  $M_\infty = 4.6$  for both low and high angles of attack. The pressure coefficients are predicted well by the Newtonian pressure methods on the windward side only. For the Mach number under consideration, the Bernoulli results agree fairly well with measured pressures and normal-force at low angles of attack only. However, the center of pressure location is definitely predicted best by the nonlinear shock expansion theory.

#### METHODS OF ANALYSIS

This portion of the report is concerned with the intermediate level methods of analysis embodied in the computer programs referenced in this lecture. The computer programs are based on low order supersonic paneling methods derived from linear supersonic theory. The programs incorporate nonlinear aerodynamic effects associated with fin and body shed vorticity and some form of nonlinear correction related to the presence of shocks.

In very general terms, panel methods can be considered as the simplest (linear theory) form of the computational fluid dynamics (CFD) methods, and they can predict pressure distributions on the components of tactical missiles at low cost compared to nonlinear numerical simulations based on the full potential, Euler, or Navier-Stokes flow equations. The numerical simulations can provide the most accurate results for details of the flow. However, as mentioned earlier in this report, the CFD methods can



simulate flows about complex geometries with simple physics (linear theory) or about simple geometries with more complex physics (nonlinear theory).

Panel methods can be classified into low and high order categories. Both employ distributions of singularities derived from linear, potential theory. The low order panel methods usually employ constant or sometimes linearly varying sources and/or doublet strengths on a panel with no continuity across the panel edges, and the flow tangency boundary condition is applied at the control point in each panel. The high order panel methods incorporate quadratically varying strengths which are made continuous across the panel edges. The boundary condition includes setting the potential on the interior of the paneled component equal to zero. The high order panel method can yield better results than the low order panel methods by virtue of the smoothly varying characteristics of its singularities at the expense of longer computer running times. The modeling of surface details is also better with the high order panel methods. Usually, the level of accuracy obtainable with the low order panel methods is adequate for the missile aerodynamicist especially in view of the lower computation costs.

Panel methods are flexible enough and/or can be manipulated to handle the geometrical details of missile bodies with noncircular cross sections, inlets, and multiple finned sections, including mutual body-on-fin and fin-on-fin interference. Panel methods also lend themselves to combined aerostructural analysis by virtue of their capability to compute load distributions. However, in their application to supersonic tactical missiles, nonlinearities due to vortical effects, nonlinear compressibility associated with shock waves, and effects of inlets can be important in the prediction of aerodynamic forces and moments. Consequently, panel methods based on linear theory are not sufficiently adequate in their application to tactical missiles and need to be enhanced with models accounting for vortical effects and nonlinear compressibility.

In this section, attention will be focussed on the application of low order supersonic panel methods (and line singularity methods for modeling axisymmetric bodies) combined with corrections for nonlinear flow phenomena to a complete missile, to supersonic inlets, and to fin deformation analysis. References are made to particular computer programs, LRCDM2, NOZVTX, DM3INL, NWCDM-NSTRN, in the following descriptions.

In the following description, supersonic low and high order panel methods are listed together with line singularity methods. The essential underlying theoretical background is summarized. This is followed by short descriptions of the wing or fin vortex wake and body separation vortex models. A short discussion of the vortex cloud technique is provided. The nonlinear pressure coefficient calculation method is outlined. A preliminary method employing panels to estimate additive drag and lift acting on supersonic, rectangular inlets is described.

Later in this lecture additional comparison examples are given of applications to missiles of paneling and/or line singularity methods with the appropriate nonlinear corrections. These examples include supersonic inlets and a calculative case for an aeroelastically deformed fin on a missile body.

#### SUPERSONIC PANEL AND LINE SINGULARITY METHODS

Panel methods have been in existence a long time, although for supersonic flow the number of choices is fairly limited. The low order category for supersonic flow includes Woodward's constant pressure panels (Ref. 32), Woodward's USSAERO series panel methods (Ref. 33), their improved derivatives developed at NLR (Ref. 34) in the Netherlands, and Woodward's triplet panels (Ref. 35). There may be other applicable methods, including the Mach box scheme described in Reference 36. The supersonic line singularity method for economically modeling axisymmetric, pointed bodies was conceived before World War II (Refs. 37-39).

The high order paneling category includes the sophisticated method designated PAN AIR (Refs. 40-43) and the related paneling method of the HISSS program (Ref. 44). All of these methods involve layouts of panels on the surfaces or the lifting surface mean planes of the missile, except for the line singularity method which involves distributions along the body centerline instead of on the surface.

For supersonic flow, the panel or line singularity velocity potential  $\phi$  satisfies the Prandtl-Glauert equation for supersonic, linearized flow valid for small velocity perturbations.

$$(M^2 - 1)\phi_{xx} = \phi_{yy} + \phi_{zz} \quad (1)$$

All panel methods assume that angle of attack and angle of sideslip are small. This assumption allows Equation (1) to be written in a reference body-oriented coordinate system  $(x,y,z)$  independent of the free-stream direction. The boundary conditions to be satisfied include tangential flow at the body surface (Neumann condition) subject to regions of influence associated with linearized supersonic flow. The velocity components are obtained from the perturbation potential  $\phi$  and must vanish on the Mach cones which demarcate the regions of influence. The flow tangency boundary condition is satisfied at a finite set of control points, normally one for each panel, giving rise to a set of simultaneous linear algebraic equations from which the panel strengths can be obtained. High order panel methods use more complicated conditions involving the potential (Dirichlet condition) and tangential flow conditions. The line singularity strength solutions are also based on satisfying the flow tangency condition at points on the body surface. The solution is simpler in that the line singularity strength characteristics are obtained from a computationally fast marching procedure from the body nose to the body base.

In essence, the panel solutions are of two types: lifting panels and nonlifting, or volume solution, panels. The

individual distributions of the mathematical singularity on the lifting (doublet) and nonlifting (source) panels range from constant or linearly varying for the low order panels to quadratic and continuous across the edges for the high order panels.

The examples to be described in a later section make use of constant pressure (actually, constant u-velocity) panels (Ref. 32), source panels (Ref. 33), and triplet panels (Ref. 35), in addition to the line singularity method (Ref. 37). The triplet panels are nonlifting panels used primarily to represent bodies with noncircular cross sections. The constant u-velocity panels are used to model lift acting on lifting surfaces. This type of panel is also used to model lift carryover onto the body.

Figure 18 shows a typical paneling layout on a complete configuration consisting of a forward finned section (canard or wing) and a tail finned section mounted on an axisymmetric body. For such a conventional missile configuration, the axisymmetric body is represented by linearly varying source and doublet line singularities for modeling effects of body volume and angle of attack, respectively. The forward and tail finned sections are modeled with a sparse layout of constant u-velocity panels. Only four fin mean planes and one-quarter of the two body interference shells are shown covered with panels. In this model, the effects of the body line singularities are included in the fin constant u-velocity panel boundary conditions for body-on-fin interference. The constant u-velocity panels on the interference shell serve to account for fin-on-body interference. The length of the interference shell in the forward finned section shown in Figure 18 is taken equal to the fin root chords. This is only approximately correct in that additional fin-on-body interference occurs aft of the fin trailing edges depending on the regions of influence determined by the Mach cones emanating from the fin edges. The interference shell(s) can be extended accordingly or some other means for calculating fin effects on the body should be incorporated (effects of fin trailing vortices

on afterbody). For a given finned section, the strengths of the panels on the fins and the interference shell are obtained from one matrix solution.

If the configuration of interest involves a body with a noncircular cross section, the body can be modeled with triplet panels. The fin-on-body interference is still accounted for by the addition of a separate interference shell containing lifting constant u-velocity panels. This is the approach followed in the modeling of unconventional missile configurations by computer program DM3INL described in Reference 11. This program also is capable of providing estimates of additive forces associated with supersonic inlets.

The fin vortex wake model used in programs LRCDM2, DM3INL, AMICDM, and NWCDM-NSTRN is described next.

#### FIN VORTEX WAKE

As discussed earlier in this report, fins can generate leading and side edge separation vorticity as the angle of attack is increased. If the side edges are long, vorticity can be generated along the edge for angles of attack as low as 5 deg. At supersonic speeds, vorticity can be generated along the leading edges provided the edge lies aft of the Mach cone emanating from the root leading edge (subsonic leading edge). The leading and side edge vortices may combine and form a strong vortex located above the trailing edge. The leading and/or side edge vortex is elevated above the fin plane as illustrated in Figure 19. One fin of the forward finned section is shown attached to a body. The angle of pitch seen by the fin is high enough to cause formation of strong leading and side edge vorticity. A vortex feeding sheet forms and at the fin trailing edge it is fully developed. At this position, the vortex system, including the trailing edge vortices, can be represented by a set of concentrated discrete vortices which stream aft along the afterbody and tail section and influence the loads on those components.

The nonlinear fin edge vortex characteristics can be approximated as follows. For fins with leading and/or side edge flow separation, program LRCDM2 (Ref. 8) is capable of determining the augmentation to fin normal-force at high angles of attack from the distributions of suction along those edges. This approach is based on the Polhamus analogy (Ref. 45). The suction distributions are obtained from the in-plane aerodynamic forces calculated as an extension to the constant u-velocity panel theory. This involves redefinition of the panel strengths as horseshoe vortex strengths and application of the Kutta-Joukowski law for aerodynamic forces acting on vortex filaments. The portion of suction converted to normal-force is determined by vortex lift factors  $K_{V_{LE}}$  for the leading edge, and by factor  $K_{V_{SE}}$  for the side edge. Estimates for these factors are given in Reference 46. Usually,  $K_{V_{LE}} = 0.5$  and  $K_{V_{SE}} = 1.0$  for small aspect ratio missile fins and low supersonic speeds.

Along the leading and/or side edges, the growing vorticity strength is calculated as a function of spanwise distance by means of lifting line theory and the distribution of suction converted to normal-force. The lateral position,  $y_v$ , shown in Figure 19, is taken as the c.g. of the suction distributions. The position above the fin plane,  $z_1$ , is approximated as if the concentrated vortex emanates from the tip leading edge along a straight line at angle  $\alpha_1/2$  to the fin, where  $\alpha_1$  is the angle of pitch seen by the fin. Further details of this account are available in Reference 8.

In addition to the leading edge and side edge vortex, one trailing edge vortex is shown in Figure 19. This vortex is associated with the attached flow span loading as opposed to the separated flow edge load augmentations. The strength and location of the trailing edge vortex (vortices) at the fin trailing edge are related to the span load distribution associated with attached flow on the fin. It can be shown (Ref. 47) that under the assumptions of no sideslip, and pressure being

linearly related to the potential, the trailing edge vorticity  $\Gamma_{TE}$  can be related to the span loading as follows.

$$\frac{1}{V_\infty} \frac{\partial \Gamma_{TE}}{\partial y_F} = - \frac{1}{2} \frac{\partial}{\partial y_f} (cc_n) \quad (2)$$

As an approximation, this relationship is used in Reference 8 for fins on a missile using the actual span loading calculated with the Bernoulli pressures, including effects of sideslip. After integration, it turns out that the number of concentrated discrete vortices is given by the number of extrema in the span load distribution plus 1. The result is one or more discrete vortices representing the fully rolled up fin wake. This fin wake model will not be very good for missiles with overlapping or closely spaced canard (or wing) and tail sections.

The above simplified treatment of fin vortex flows does not include effects of vortex breakdown, vortex core modeling, secondary separation, etc. Some of these highly nonlinear phenomena and the possible effects on the aerodynamics of a missile are mentioned earlier in this lecture.

With the strengths and positions of the fin leading and/or side edge vortex and the one or more trailing edge vortices known at the fin trailing edge, these vortices and body nose separation vortices, if present, are tracked aft along the afterbody up to the tail fins. In program LRCDM2 (Ref. 8), the body nose separation vortex strengths and positions in the crossflow plane are specified in a data base as a function of axial distance from the nose. This information is given for a pair of symmetric, concentrated vortices and is based on experimental data described in Reference 48. Program AMICDM (Ref. 10) is equipped with updated forebody vortex characteristics obtained with the vortex cloud model described later in this report. The method for calculating pressures on the forebody under the influence of separation vortices includes the effects of vortex filament inclination with respect to the body centerline.

The forebody and canard fin vortices can also be included in an afterbody vortex shedding analysis. In either case the effects of the moving vortices will influence the aerodynamic performance of the complete missile in a manner nonlinear with angle of attack. In the most general case, the vortices will not be symmetrical with respect to the forward fins either due to angle of roll or due to asymmetric forward fin control. Examples of vortex tracking results are shown in Figures 7 and 8. Additional comparisons are described later in this report.

#### Vortex Tracking Procedure

A procedure for determining the vortex paths in the presence of the body is based on slender body theory. Programs LRCDM2 (Ref. 8), NWCDM-NSTRN (Ref. 9), and AMICDM (Ref. 10) track vortices along axisymmetric bodies in this manner. In essence, the crossflow plane flow potentials are solved at many axial stations along the body in a marching procedure. The two dimensional crossflow potential includes linearly superimposed solutions due to crossflow, vortices in the presence of the body and vortices in the presence of one another. From one station to the next, the vortex paths are directed in accordance with local flow angles. For noncircular body cross sections, a numerical conformal mapping procedure is required (Ref. 26).

In the development of program LRCDM2, it was found that the best method for computing the effects of external vortices on the missile fins involves the following approximation. The vortices are tracked along the unfinned or body alone sections with the method described above. When the vortices reach the leading edge of a finned section, their positions are frozen in the crossflow plane. This means that through the length of the finned section, the external vortices are rectilinear and taken parallel to the body centerline. At points on the body surface, vortex-induced velocity components are calculated using slender body theory for inclusion in the pressure coefficient calculations. On the fins, the flowfield generated by the vortices is calculated in the



presence of the body alone (fins off). The effects of the vortices are then included in the fin loading calculations as follows:

1. Compute the flow velocity normal to the fin plane at the panel control points including effects of the body, angle of attack, and vortex-induced components.
2. Generate the strengths of the constant u-velocity panels laid out on the fins and interference shell subject to the impressed velocities of Step 1.
3. With the fin panel strengths calculated from a matrix solution, compute normal and parallel flow velocity components at the panel control points including vortex-induced contributions.
4. With the compressible Bernoulli pressure velocity relationship, compute pressures acting on the fin with the velocity components from Step 3.

#### BODY VORTEX WAKE

The vortex shedding program NOZVTX described in Reference 26 is capable of generating the characteristics of the vortex flowfield above a body at sufficiently high angle of attack to experience flow separation. The theoretical method embodied in NOZVTX is based on a combination of Woodward's source panels (Ref. 33) for nonaxisymmetric bodies, or line singularities for axisymmetric bodies (Ref. 37), and multiple discrete vortices treated with crossflow plane theory. The body is first modeled with either linear theory method, neglecting flow separation, for the flow condition at hand. Starting at an axial station close to the body nose, the attached flow pressure distribution is calculated on the circumference of the body using the compressible Bernoulli pressure equation. The pressure distribution is examined using modified versions of Stratford's separation criteria which are based on two dimensional

incompressible flow. For example, the laminar separation criterion states that the laminar boundary layer separates when the following condition is met (Ref. 26).

$$C_p^{1/2} \left[ \xi \frac{dC_p}{d\xi} \right] \approx 0.087 \sin \alpha_c \quad (3)$$

Here  $\xi$  is the run length of the boundary layer,  $C_p$  the pressure coefficient and  $\alpha_c$  the included or body angle of attack. In a turbulent boundary layer, the separation point on the circumference is Reynolds number dependent.

$$C_p \left[ \xi \frac{dC_p}{d\xi} \right]^{1/2} (\text{Re}_\xi \times 10^{-6})^{-0.1} \approx 0.35 \sin \alpha_c \quad (4)$$

At the predicted separation points, vortices with strengths proportional to the square of the local resultant velocity are shed into the flow field. The trajectories of these free vortices between one crossflow plane and the next one downstream are determined from a path integration scheme which aligns the vortices in accordance with the local flow field. For bodies with noncircular cross sections, analytical or numerical conformal mapping schemes are employed together with the vortex image technique (circle theorem). At the next downstream crossflow plane, the pressure distribution is calculated including effects of the vortices shed upstream. On the basis of the separation criteria, new vortices are shed. This procedure is carried out in a stepwise fashion over the unfinned lengths of the body resulting in the formation of vortex clouds simulating vortex feeding sheets. Examples of the vortex cloud technique are shown in Figures 9, 11, and 12.

In Figure 20, a conventional missile configuration minus the tail section is shown. Angle of attack is high enough to form body vortices and angle of roll is zero. On the forebody, two vortex feeding sheets are depicted. At the beginning of the canard section, the feeding sheets separate from the body and two concentrated vortices pass through the canard section. On the afterbody, two feeding sheets are schematically indicated. The

actual shape and starting location of these feeding sheets are influenced by the flow conditions and external vortices generated by the forebody and canard fins. Only one trailing edge vortex is shown for each horizontal fin but more may exist.

In program LRCDM2 (Ref. 8) and its derivatives, the axisymmetric forebody vorticity characteristics are obtained from a data base as described earlier in this section. The afterbody vortex shedding calculations are based on the NOZVTX approach described above. The purpose is to represent the entire vortex structure at the beginning of the tail section and to calculate the vortex-induced effects on the tail section using the approximate method described above. Examples are shown later in this lecture.

#### NONLINEAR PRESSURE COEFFICIENT

It is shown in Reference 49 that linearized theory fails to provide realistic estimates of pressure distributions acting on delta wings at about 20 deg angle of attack for Mach numbers larger than 1.5. Apart from the nonlinear effects due to leading edge vortex flow (for subsonic edges), there are effects due to nonlinear compressibility that will influence the pressures on both the lower and upper surfaces. Generally, linear theory will underestimate the positive pressures on the lower surface near the wing leading edge and overestimate the suction pressures on the upper surface. As a result, linear theory often predicts good overall normal-force at high Mach numbers but the pressure distributions are usually faulty.

Some fundamental reasons for the failure of linearized theory to predict pressures at large angles of attack may be explored with the help of Figure 21. The differences in pressure coefficients predicted by two dimensional nonlinear shock or expansion theory and by two dimensional linear theory can be illustrated as follows for a planar surface inclined to the free-stream. In Figure 21, the pressure coefficient calculated for the compression case ( $\delta > 0$ ) with two dimensional oblique shock

relationships increases nonlinearly with deflection angle  $\delta$  up to shock detachment. The pressures are appreciably higher than those obtained with two dimensional linear theory which relates the pressures directly to the deflection angle. For negative deflection angles, the pressures calculated with two dimensional expansion relationships are also higher than the two dimensional linear theory pressures. For large expansion angles, the expansion (Prandtl-Meyer) formulation will automatically limit the pressure coefficient to

$$C_{P,\min} = \left( \frac{P-P_{\infty}}{q_{\infty}} \right)_{\min} = - \frac{2}{\gamma M_{\infty}^2} \quad (5)$$

which corresponds to zero static pressure ( $p = 0$ ).

The three dimensional isentropic compressible Bernoulli pressure coefficient has some nonlinear character because it is composed of linear and quadratic terms involving all three flow components. This nonlinearity is not related to nonlinear compressibility. A minimum value is usually set on the basis of Equation (5).

In an effort to investigate practical methods for accounting for nonlinear compressibility, two schemes were developed and implemented as optional fin pressure calculation options in LRCDM2 (Ref. 8) for preliminary testing.

The first scheme, suggested by Carlson (Ref. 49), involves nonlinear shock expansion (tangent wedge) theory and linear theory for calculating pressure coefficients along chordwise strips on the surfaces of a fin or wing. The nonlinear shock expansion theory is valid for all supersonic Mach numbers provided the shock is attached. The flow deflection angles,  $\delta$ , required by this two dimensional nonlinear theory are determined from the geometry of the surface (streamwise slopes) and then modified by correction angles determined from two and three dimensional linear theory. In two dimensional linear theory, the pressure is proportional to the flow deflection angle. In

program LRCDM2, the three dimensional linear theory is made up of the supersonic panels on the fins and the interference shells on the body and includes the supersonic line singularity method used to model the axisymmetric body itself. The correction angles mentioned above can be viewed as a correction to account for mutual interference effects between the individual strips on a given fin, between the fin and other fins, and between the fin and the body. Therefore, the modified flow deflection angles includes a geometric component and an interference or correction component. In this process, the flow correction angle is calculated on the basis of approximating the difference between interference free two dimensional nonlinear theory (shock expansion or Newtonian) and three dimensional nonlinear theory including interference effects by the difference between interference free two dimensional linear theory and three dimensional linear theory including interference effects. In equation form, this statement can be expressed as follows:

$$[2\text{-D nonlinear theory}] + [(3\text{-D linear theory}) - (2\text{-D linear theory})] = [3\text{-D nonlinear theory}] \quad (6)$$

This procedure is described in detail in Reference 8.

The modified angles are then used to recompute pressure coefficients using the two dimensional nonlinear shock expansion formulation.

In the second scheme, the pressure coefficients are calculated with the simplest form of Newtonian or impact theory. This nonlinear theory is valid only for high supersonic Mach numbers ( $M_\infty > 5$ ). The flow angles,  $\delta$ , required by this theory are modified in the same manner as used with the shock expansion method. Corrected pressures are then calculated with the updated angles used in the impact pressure formulations.

Details of these schemes are given in Reference 8. Examples of the above procedure are shown on Figures 15 and 16 and are discussed in an earlier section.

## SUPERSONIC INLETS

The aerodynamic characteristics of an airbreathing missile are influenced by the forces associated with the internal flow. Such forces exist both for the case of a wind tunnel model with flowing inlets and for the case of a missile in flight powered by its airbreathing propulsion system. In the former, the forces sensed by the force balance must be corrected to remove the internal flow contribution. In the latter, the internal forces result in the net propulsive force which is conventionally specified by the change in impulse of the capture airstream from free-stream conditions at some upstream station to the nozzle exit. In both of these cases, complete accounting of all the involved forces results in the appearance of fictitious forces called additive forces which do not act on the missile surfaces but arise from a bookkeeping procedure. A definitive description of this procedure is given in Reference 50.

The external flow around an inlet can influence the aerodynamic loading acting on the airframe, and the airframe can influence the inlet. This mutual aerodynamic interference can be important for large inlets mounted on airbreathing missiles. The aerodynamic effects of an inlet are nonlinear with respect to angle of attack and flight Mach number. However, paneling methods lend themselves to aerodynamic interference problems. A panel-based method for estimating additive forces and flow field effects induced by inlets is summarized below. The method makes use of the local Mach number concept.

As part of the work reported in Reference 11, a study was made of the feasibility of representing a supersonic two dimensional external compression inlet by a paneling method. Since then the method has been extended to handle supersonic axisymmetric external compression inlets. In these applications, the inlet panel modeling scheme is primarily aimed at estimating the additive drag and additive lift forces for specified mass

flow ratio. In addition, the inlet model is capable of generating flow field velocity components external to the inlet and can include interference effects from upstream components.

Consider the supersonic two dimensional inlet shown in the upper portion of Figure 22. This single ramp inlet is shown operating at off design condition and with critical or supercritical flow (normal shock at or downstream of throat). Angle of pitch and angle of sideslip seen by the inlet are zero. Angle  $\theta_s$  is associated with the attached ramp or oblique shock, and it is determined for  $M_\infty$  and ramp or wedge angle  $\delta_r$  using oblique shock theory. A straight line is drawn forward from the cowl lip (point B) in a direction parallel to the compression ramp to the intersection point A with the ramp shock. From this point forward, the line is parallel with the oncoming stream. The line constructed this way is the bottom or capture streamline of the captured streamtube. The mass flow captured by this inlet under these conditions is less than the mass flow contained in the streamtube with height equal to the inlet height  $h_i$ . Let  $\dot{m}_c$  be the inlet mass flow rate measured at some station downstream from the cowl lip. Define an equivalent captured streamtube with the same mass flow rate  $\dot{m}$  but referenced to  $\rho_\infty$  and  $V_\infty$ . The cross sectional area of the equivalent captured streamtube equals height  $h_c$  times the width  $s$  of the two dimensional inlet. The height of the equivalent captured streamtube is related to the measured inlet mass flow rate as follows.

$$(h_c s) \rho_\infty V_\infty = \dot{m}_c \quad (7)$$

Similarly, the mass flow rate contained in the streamtube with inlet height  $h_i$  is given by

$$(h_i s) \rho_\infty V_\infty = \dot{m}_i \quad (8)$$

The mass flow ratio MFR is then defined as

$$\text{MFR} = \frac{\dot{m}_c}{\dot{m}_i} = \frac{h_c}{h_i} \leq 1 \quad (9)$$

In the upper portion of Figure 22, the amount of mass flow in the streamtube with height  $\Delta h = (h_i - h_c)$  is spilled below the cowl lip. In this case, MFR is the theoretical maximum, the associated additive forces are minimum and the mass flow not captured by the inlet is termed supersonic spillage. In three dimensions there can also be side spillage which is not considered in this mass flow account. In accordance with the description in Reference 50, the aerodynamic forces acting on the bottom streamline of the captured streamtube from A to B are the additive forces. In the lower portion of Figure 22, the flow into the inlet is zero. Thus,  $MFR = 0$  for the fully blocked inlet flow case.

The case for an axisymmetric supersonic inlet is shown in Figure 22(b). In the upper portion of the figure, the capture streamline is not a straight line between points A and B for the maximum flow case. In this case, the maximum mass flow ratio is obtained from a mass balance between the cone shock and the inlet face. The shock and the inlet face surfaces are conical. Therefore, linear (conical) supersonic theory is employed to estimate the velocity component (indicated in Figure 22(b)) normal to the shock and normal to the inlet face. With the radius  $r_c$  of the captured streamtube determined this way, the mass flow ratio for an axisymmetric inlet is expressed as follows.

$$MFR = \frac{r_c^2}{r_i^2} \quad (9a)$$

It is the purpose of the inlet panel model to estimate the additive forces as a function of specified mass flow ratio. The method makes use of but is not limited to triplet panels.

The inlet paneling method of Reference 11 is based on the following approximate scheme. This scheme is the result of many comparisons with experimental data. The triplet panel model is employed to estimate the minimum additive drag (and lift) for a supersonic two dimensional inlet. The corresponding mass flow



rate will be the maximum but need not be equal to unity. For zero mass flow ratio (fully blocked conditions in the inlet), the pressure acting on the throat is assumed equal to stagnation pressure, and the pressure on the compression ramp is taken equal to the surface pressure on a wedge with the oblique shock about to detach from the ramp leading edge. Axisymmetric inlets are handled similarly with conical shock data. The additive force is taken as the sum of the forces acting on the ramp and throat areas. A linear relationship is assumed relating the additive forces to mass flow ratios greater than zero and less than the maximum. The procedure for estimating the minimum drag, minimum lift, and maximum mass flow ratio will now be outlined.

The triplet panels are laid out on the inlet face as follows. In an attempt to simulate the deflection of the capture streamline, the triplet panels in the inlet face directly above the cowl lip have their upper most edges positioned at the same level as the capture streamline. This point is indicated by the crosses (+) shown in Figures 22(a) and 22(b). The Mach number used for the panel strength solution corresponds to a Mach wave made to coincide with the ramp shock. This local Mach number approach constitutes the major nonlinear aerodynamic characteristic in the inlet model. The flow tangency boundary condition is applied to the panels on the inlet walls (for a two dimensional inlet only). The panels on the inlet face receive special treatment: the panels above the capture streamline location are made to deflect the incoming flow parallel below to the compression ramp, and the panels below are made to block the incoming flow. Examples are described later in this lecture including two dimensional and axisymmetric supersonic inlets.

As mentioned earlier, the paneling solution (for the local Mach number) can generate flow field velocities which will be representative of the minimum additive drag or maximum mass flow rate condition. For mass flow ratios less than maximum, the inlet face panels can be used to block the incoming flow by progressively engaging the fully blocked boundary condition for the panels on the inlet face from the cowl lip up to the level of

the capture streamline. The loadings acting on the panels on the inlet face will then underestimate the additive forces, however. Instead, the linear variation method mentioned above should be used for additive forces.

#### FIN DEFORMATION

The work recently performed and described in Reference 18 is concerned with controlling the aerodynamic center of pressure location of a missile control fin by aeroelastic tailoring. Specifically, the principal axis directions of various segments of a composite material fin are varied in order to influence the chordwise location of the center of pressure through elastic fin deformation under nonlinear supersonic aerodynamic loading. Consistent fin deformations are obtained by iterating between the aerodynamic load calculation and the fin displacement calculation. The aerodynamic predictions are performed by a specialized version of program NWCDM-NSTRN (Refs. 9 and 51) which is one of the intermediate level panel-based missile aerodynamics analysis programs. A special program module NASCON converts the aerodynamic forces calculated at the aerodynamic control points to aerodynamic forces at the structural analysis grid points. In this process, total aerodynamic forces and moments are conserved on the missile body and the fin components.

The special requirements for the aerodynamic prediction method include the capability of computing multiple sets of aerodynamic force distributions in minimum time. In addition, fin edge nonlinearities must be included because of the high angles of pitch seen by control fin(s).

Future fin aeroelastic tailoring work will include treatment of the airgap effects. This last nonlinear problem is difficult to treat in any event. It is planned to extend the panel-based method to model the deflected fin and the interference shell on the body (Figure 18) with two separate panel layouts. Calculated examples for a composite material fin and for an aluminum fin will be given later.

### ADDITIONAL COMPARISON EXAMPLES

This section contains additional descriptions of predicted and experimentally measured aerodynamic characteristics influenced by nonlinear vortical effects for two conventional cruciform missile configurations. In addition, additive drag results are presented for two dimensional and axisymmetric supersonic inlets. Finally, a calculative example is provided showing the aerodynamic force distribution and deformation characteristics for a composite material fin and for an aluminum fin. The referenced theoretical results are obtained with the methods described in the previous section.

#### TF-4 CANARD CONTROL MODEL

Program LRCDM2 (Ref. 8) was applied to the canard control wind tunnel model TF-4 shown in Figure 23. The tail fins are large and have a pronounced effect on the overall longitudinal and lateral aerodynamic characteristics. The experiment and additional data are described in Reference 52.

The two results described below are aimed at showing the effects of afterbody vortex shedding on the afterbody loads for a case with zero control and the effects of canard fin vortices and afterbody vortex shedding on the longitudinal and lateral characteristics for the case of roll control. The afterbody is the portion of the missile body between the canard section and the tail section. All forces and moments are specified in the body fixed coordinate system.

For zero canard control, included angle of attack of 20 deg, zero roll angle, and Mach number of 1.6, the calculated vortex structure at the end of the afterbody is shown in Figure 24. These results are obtained with the optional nonlinear afterbody vortex shedding companion program of LRCDM2. The companion program is a derivation of body vortex shedding program NOZVTX (Ref. 26) summarized earlier in this lecture. At this angle of

attack, effects of afterbody vortex shedding are included. In the resulting symmetric picture shown in Figure 24, the wake vortices of the horizontal canard fins appear at the top. These vortices originate from the trailing and side edges of the horizontal canard fins in accordance with the method summarized earlier in this lecture. The canard fin vortices have traveled a considerable distance above the body. Two symmetric forebody or nose vortices,  $\Gamma_{nose}$ , have been "captured" by the many afterbody vortices in the two vortex clouds. The forebody vortices originated on the nose, and as described earlier, program LRCDM2 contains a data base representing the vortices shed by the nose as two discrete concentrated vortices. Unlike the canard vortices, the forebody vortices remain in the vicinity of the afterbody principally due to the interaction with the afterbody vortices.

The calculated distributions of normal-force acting on the afterbody with and without vortex shedding are shown in Figure 25. The upper curve represents the normal-force distribution calculated by the afterbody vortex shedding module including effects of canard section vorticity. Most of the added normal-force is generated toward the aft portion of the afterbody. Simple constant crossflow drag coefficient calculations do not include effects of upstream vortices and would result in a constant distribution of normal-force of higher magnitude. The lower curve is generated by LRCDM2 without afterbody vortex shedding and reflects the download effects of the forebody and canard fin vortices as calculated by the vortex tracking module described earlier.

In Figure 26, the vapor screen shows a vortex pattern at the beginning of the tail section for the case of roll control effected by differential deflection of the horizontal canard fins. Angle of attack equals 15 deg,  $M_{\infty} = 2.5$ , angle of roll is zero, and the afterbody vortex sheets are located asymmetrically above the body. The vortex from the right horizontal canard (with 5 deg trailing edge down deflection) is positioned slightly lower than the vortex from the left horizontal canard fin (with 5 deg trailing edge up deflection).

The vortex structure predicted by program LRCDM2 (Ref. 8), using the optional afterbody vortex module, is shown in Figure 27. The calculated afterbody vorticity is represented by two centroids to the left of the upper tail fin. The vortices with strengths  $\Gamma_{TE}/V_\infty = -0.09$  and  $\Gamma_{TE}/V_\infty = -0.16$  originate from the upper and lower undeflected canard fins, respectively. The strengths of the centroids of afterbody vorticity,  $\Gamma/V_\infty = -3.11$  and  $\Gamma/V_\infty = 0.87$ , are of the same order of magnitude as the trailing edge vortices of the deflected horizontal canard fins.

The asymmetric vortex picture shown in Figure 27 can be compared with the vapor screen shown in Figure 26. The relative positions of the major canard vortices are predicted well with the left vortex slightly higher in elevation and weaker than the right vortex. Next to the body, the vorticity indicated in the vapor screen on the left hand side appears to be stronger and positioned higher than the vorticity on the right hand side. The relative strengths are indicated by the theory but the prediction positions the "right hand" afterbody vortex centroid closer to the "left hand" afterbody vortex centroid than shown in the vapor screen.

Overall aerodynamic results for the case of 5 deg roll control are shown in Figure 28. Normal-force,  $C_N$ , and pitching-moment,  $C_m$ , coefficients are shown in Figure 28(a) as a function of included angle of attack,  $\alpha_c$ . Some nonlinear behavior is indicated by the experimental data throughout the range of  $\alpha_c$ . Calculated results are given with and without afterbody vortex shedding. The differences between the two results are small. In this case, the normal-force and pitching moment are mostly due to the lifting surfaces.

Yawing-moment,  $C_N$ , rolling-moment,  $C_l$ , and side-force,  $C_y$ , coefficients are shown in Figure 28(b) with and without roll control as a function of included angle of attack,  $\alpha_c$ . Strong nonlinearities are indicated by the experimental rolling moment data. Experimentally measured tail-off rolling moment is also

indicated. The effect of the large tail fins is to cancel the canard fins roll control up to about  $\alpha_C = 6$  deg. The measured rolling moment exceeds the rolling moment generated by the canard fins for  $\alpha_C$  greater than 11 deg. Some yawing moment and a small side force are measured.

Tail fins off rolling moment is predicted well by program LRCDM2. With the tail fins on, the nonlinear interaction between the canard fins and tail fins is predicted well for  $\alpha_C$  up to about 6 deg. Above  $\alpha_C = 6$  deg, the predictions without afterbody vortex shedding fail to predict the nonlinear behavior. The calculated rolling moment including effects of afterbody vortex shedding definitely follows the nonlinear trend. The relatively small side-force coefficient also appears to benefit from the inclusion of afterbody vorticity. There may be some experimental error in the lateral characteristics for  $\alpha_C$  greater than 10 deg as indicated by the nonzero experimental results for zero roll control.

In conclusion, the overall rolling moment acting on the TF-4 configuration is affected severely by the nonlinear effects of vorticity generated by the upstream canard fins and body portions. A similar example concerned with aerodynamic loads on deflected tail fins is given next.

#### TAIL FIN CONTROL MODEL

A model of a tail control missile model is indicated in Figure 29. Test data and additional information applicable to this model are available in Reference 53.

Tail fin normal-forces and root bending moments are shown as a function of angle of attack in Figures 30(a) and 30(b), respectively, for  $M_\infty = 1.6$ . Data is shown for zero and -20 deg pitch control. The fin loadings are shown in Figures 31(a) and 31(b) for  $M_\infty = 2.2$ . This data was also extracted from Reference 53. The experimental data exhibits some nonlinear behavior with and without pitch control for both Mach numbers.

The predicted results are generated by an early version of NWCDM-NSTRN (Ref. 9) which is a special version of LRCDM2 (Ref. 8). It should be noted that the tail fins are influenced by the vortical wake of the forward fins. The prediction accounts for this effect, and the calculated normal-force coefficients generally match the data well. For the highest angles of attack, the tail fin normal-force coefficient would be about 25% higher if the nonlinear effects of the forward fin vortical effects were neglected. For the lower Mach number ( $M_\infty = 1.6$ ), the tail fin leading edge is subsonic, and the leading edge augmentation is added to give the total fin aerodynamic force.

#### SUPERSONIC INLETS

Experimentally deduced and predicted results for additive-drag coefficient,  $C_{X,add.}$ , are shown as a function of mass flow ratio MFR in Figure 32 for two rectangular (two dimensional) inlets. The test procedure and additional data are described in Reference 54. The data was converted and replotted as shown in Figure 32 by the authors of the inlet handbook described in Reference 55. The two inlets shown in Figure 32 operate off-design (ramp shock lies ahead of cowl lip) for Mach number 1.3. For both the long ramp and the short ramp inlets, the variation of the additive-drag coefficient with mass flow ratio is fairly linear. This behavior seems to be visible in other supersonic inlet data as well.

The theoretical maximum mass flow ratios shown in Figure 32 are determined with the two dimensional streamline tracing approach outlined earlier in this lecture. Minimum additive-drag coefficients are calculated with a panel layout such as the one shown in Figure 33. The upper most edges of the bottom panels on the inlet face are at the same level as the capture streamline for maximum flow, and the location is indicated by the cross on the inlet face shown in Figures 32 and 33. Variation of additive drag with mass flow ratio is approximated as linear; therefore,

the minimum additive drag value and the maximum additive drag value determine  $C_{x,add}$  vs MFR for a given inlet. The latter values correspond to zero mass flow ratio and are calculated on the assumption that the inlet throat is subjected to stagnation pressure (including normal shock effects) and that the external compression ramp pressure corresponds to the pressure on a wedge with the oblique shock just detached. The additive-drag coefficients calculated this way match the experimental data fairly well and show correctly the effects of the different ramp lengths for the two rectangular inlet configurations. The nonlinear aspect of this problem is related to the local Mach number ( $M_{inlet}$ ) approach for the panel strength solution as described earlier in this lecture and shown in the top position of Figure 33.

Figure 34 shows experimentally deduced and predicted results for additive drag as a function of mass flow ratio for three axisymmetric inlets. The inlets differ by the inlet projected area to throat area ratios. These inlets, test procedure, and additional data are described in Reference 54. The additive drag data was converted and replotted as shown in Figure 34 by the authors of Reference 55. For the Mach number under consideration,  $M_\infty = 1.1$ , these inlets operate off design (compression cone shock lies ahead of cowl lip). The additive-drag coefficient is roughly linear with mass flow ratio.

The theoretical maximum mass flow ratios shown in Figure 34 are based on the mass balance calculation mentioned in an earlier section. The corresponding minimum additive-drag coefficients are calculated with a panel layout such as the one shown in Figure 35. The upper edge of the bottom panels on the inlet face cone is at the same level as the capture streamline for maximum flow, and the location is indicated by the cross on the inlet face shown in Figure 35. The minimum additive drag results are connected with a straight line to the maximum additive drag value which corresponds to zero mass flow. The latter values are based on the assumption that the throat area is subjected to stagnation pressure (including normal shock effects) and that the external



compression cone pressure corresponds to the pressure on a cone with the conical shock just detached. The additive-drag coefficients calculated this way match the experimental data reasonably well and show the same trend indicated by experiment for the effects of inlet to throat area ratios. As in the case for the two dimensional (rectangular) inlets, the main nonlinear effect is related to the local Mach number approach used in the panel strength solution.

#### DEFORMED FINS

The fin tailoring capability described in Reference 18 includes a special version of program NWCDM-NSTRN (Ref. 9) which in turn is based on program LRCDM2 (Ref. 8). As described earlier in this lecture, these panel-based missile aerodynamics prediction programs incorporate models to account for body and fin edge vortical effects. In addition, the programs can optionally compute pressure coefficients based on nonlinear shock expansion or Newtonian theories corrected for aerodynamic interference using linear theory.

The aerodynamic prediction program interacts with a specialized structural analysis program (Ref. 18) for the analysis of fin deformation. In this process, a converged solution is obtained after several iterations as follows. The aerodynamic program generates an aerodynamic force distribution at the grid points of the structural program as described earlier in the lecture. The structural analysis program computes the fin surface deflections subject to the aerodynamic force distribution. The aerodynamic program computes streamwise slopes from the fin surface deflections and recalculates the aerodynamic force distributions. The calculations are repeated until a convergence criteria in terms of the change in successive fin surface deflections is satisfied. An example of the above analysis capability is described below.

One fin of a planar fin section is shown in Figure 36. It is mounted on an axisymmetric body by means of a shaft located at one half root chord (hinge line). The airgap is assumed zero in the following calculations. There are 32 lifting constant u-velocity panels distributed on the fin; one panel is indicated nearest the root chord leading edge. A layout of constant u-velocity panels is wrapped around the body next to the fins to account for fin on body lift carryover. The aerodynamic normal-forces are calculated at the panel centroid points. The aerodynamic forces at the panel centroids are converted to aerodynamic forces at the corners of the trapezoidal elements shown in Figure 37. As described in Reference 18, each trapezoidal element contains two triangular bending elements.

In this example, the fin is assumed to be made up of a laminated graphite-fiber composite. Figure 37 shows the six ply, antisymmetric angle layup used in the calculations. Angles  $\theta_1$  and  $\theta_2$  are the material principal axis directions or design variables for the inboard portion of the fin. In the outboard portion, the principal axis direction is held fixed.

The flight conditions for the following example calculations are specified by included angle of attack  $\alpha_c = 15.4$  deg, angle of roll of the planar fin body combination  $\phi = 0$  deg, Mach number  $M_\infty = 1.6$ , and altitude  $h = 30,000$  ft.

Figure 38 shows an outboard view of the composite material fin with the design variables  $\theta_1$  and  $\theta_2$  set at 45 deg. For this setting, the study in Reference 18 disclosed that fin flexibility is near maximum especially in the chordwise direction. Contrary to what might be expected, however, the fin chordwise bending is concave, rather than convex, with respect to the load direction, which reduces the aerodynamic loads near the leading edge and leads to an aft shift in the location of the center of pressure. Note that for this example, there is a nose down rigid body rotation about the hinge line. This rotation is included in the perspective plots of the deformed fins. Figure 39 presents a

perspective plot of the aerodynamic load distribution corresponding to the deformed fin. This plot shows quite clearly the reduction in loads near the leading edge with chordwise bending.

Figures 40 and 41 show the predicted fin deformation and aerodynamic force distribution, respectively, for an aluminum fin. It is of interest to contrast the behavior of the aluminum fin with that of the composite fin. The aluminum fin has much less spanwise bending and virtually no chordwise bending, and the load distribution displays the peak near the leading edge that is typical of rigid lifting surfaces.

The important observation to be made here is that the inclusion of nonlinear aerodynamic effects can be very important in the determination of the center of pressure location. Furthermore, an airgap is created between the fin and the body for deflected fins. The nonlinear effects of the airgap on the detailed fin load are difficult to predict. It appears possible to assess the inviscid effects by using separate paneling layouts on the fin and on the body.

#### CONCLUDING REMARKS

This lecture describes a survey of experimental observations and intermediate level predictive methods aimed at nonlinear aerodynamic characteristics of tactical missiles. The lecture starts with descriptions of the major differences between missile and aircraft flight and configuration characteristics. The importance of vortical interference and nonlinear compressibility due to shocks is stressed. Descriptions are given of the nonlinearities associated with deformable fin design, supersonic fin on body interference, wraparound fins, and unsteady flight including summarized accounts of the effects of asymmetric body vortex shedding and vortex bursting on overall missile aerodynamic characteristics.

The lecture continues with physical examples of vortex structures and shock formations visible in vapor screen and schlieren pictures. In many instances, the nonlinear aerodynamic effects are illustrated by theoretical results obtained with and without the relevant nonlinearity such as vortex wakes or nonlinear compressibility. Short descriptions are given of the intermediate level panel-based missile aerodynamics prediction methods used in some of the physical examples, with special attention to the models incorporated to account for vortical and nonlinear compressibility effects. The descriptions include applications to additive force analysis for supersonic inlets and deformable fins. Additional comparisons with experimental data are provided and the nonlinear effects pointed out for two cruciform canard-tail missile configurations. Additive drag results are shown for rectangular and axisymmetric inlets. Finally, a calculative example is given for a deformed fin.

It is clear that nonlinear effects are important in the aerodynamics of tactical missiles. In the future, numerical simulations based on Navier-Stokes solvers will be best suited to analyze the details of missile aerodynamics most accurately especially at transonic speeds. The pacing item may well be turbulence modeling. For the present, the supersonic missile designer has at his disposal an Euler-based approach and a set of specialized intermediate level prediction methods based on panel and line singularity theories enhanced with nonlinear models for vortical effects and nonlinear compressibility. For basic overall missile loads, including some nonlinear effects, the simplest category of methods based on handbook techniques and the sometimes sophisticated semi-empirical methods will be applicable for years to come.

## REFERENCES

1. Nielsen, J. N.: Missile Aerodynamics. McGraw-Hill Book Co., Inc., New York, 1960.
2. (a) Finck, R. D.: USAF Stability and Control Datcom. AF Flight Dynamics Laboratory, WPAFB, OH. October 1960 (revised April 1976).  
  
(b) Williams, J. E. and Vukelich, S. R.: The USAF Stability and Control Digital Datcom: Vol. I - Users Manual, Vol. II - Implementation of Datcom Methods, Vol. III - Plot Module. AFFDL-TR-79-3032, April 1979.
3. Devan, L. and Mason, L. A.: Aerodynamics of Tactical Weapons to Mach Number 8 and Angle of Attack 180 Degrees, Part III - Computer Program and Users Guide. NSWC TR-81-358, September 1981.
4. Smith, C. A. and Nielsen, J. N.: Prediction of Aerodynamic Characteristics of Cruciform Missiles to High Angles of Attack Utilizing a Distributed Vortex Wake. NEAR TR-208, November 1979.
5. Hensch, M. J. and Mullen, J., Jr.: Analytical Extension of the Missile1 and Missile2 Computer Programs. NEAR TR-272, March 1982.
6. Vukelich, S. R. and Jenkins, J. E.: Missile Datcom: Aerodynamic Prediction on Conventional Missiles Using Component Build-up Techniques. AIAA Paper No. 84-0388, January 1984.
7. Gentry, A. E., et al: The Mark IV Supersonic-Hypersonic Arbitrary-Body Program. AFFDL-TR-73-159, November 1973.

8. Dillenius, M. F. E.: Program LRCDM2, Improved Aerodynamic Prediction Program for Supersonic Canard-Tail Missiles with Axisymmetric Bodies. NASA CR-3883, April 1985.
9. Dillenius, M. F. E.: Program NWCDM-NSTRN for Calculations of Forces at NASTRAN Grid Points on Supersonic Missile Configurations. NEAR TR-330, September 1984.
10. Dillenius, M. F. E. and Perkins, S. C., Jr.: Computer Program AMICDM, Aerodynamic Prediction Program for Supersonic Army Type Missile Configurations with Axisymmetric Bodies. U.S. Army Missile Command Technical Report RD-CR-84-15, June 1984.
11. Dillenius, M. F. E. and Keirstead, M. M.: Panel Methods Applied to Supersonic Inlets Alone and to Complete Supersonic Air Breathing Configurations. NASA CR 3979, May 1986.
12. Siclari, M. J.: The NCOREL Computer Program for 3-D Nonlinear Supersonic Potential Flow Computations. NASA CR-3694, August 1983.
13. (a) Klopfer, G. H. and Nielsen, J. N.: Basic Studies of Wing-Body Interference at High Angles of Attack and Supersonic Speeds. ONR CR-215-262-1 (also NEAR TR-206), October 1979.  
  
(b) Klopfer, G. H. and Nielsen, J. N.: Basic Studies of Body Vortices at High Angles of Attack and Supersonic Speeds. NEAR TR-226, October 1980.
14. (a) Wardlaw, A. B., Baltakis, F. P., Solomon, J. M., and Hackerman, L. B.: An Inviscid Computational Method for Tactical Missile Configuration. NSWC TR-81-457, December 1981.

- (b) Wardlaw, A. B., Hackerman, L. B., and Baltakis, F. P.: An Inviscid Computational Method for Supersonic Missile Type Bodies - Program Description and User's Guide. NSWC TR-81-459, December 1981.
15. Childs, R. E. and Nixon, D.: Simulation of Impinging Turbulent Jets. AIAA Paper No. 85-0047, January 1985.
  16. National Research Council: Current Capabilities and Future Directions in Computational Fluid Dynamics. National Academy Press, Washington, D.C., 1986.
  17. Goodwin, F. K., Dillenius, M. F. E., and Mullen, J., Jr.: Prediction of Supersonic Store Separation Characteristics Including Fuselage and Stores of Noncircular Cross Section. Vol. I - Theoretical Methods and Comparisons with Experiment. AFWAL-TR-80-3032, Vol. I, November 1980.
  18. McIntosh, S. C., Jr. and Dillenius, M. F. E.: Aeroelastic Tailoring Procedure for Reduction of Fin Hinge Moments. NEAR TR-374, February 1987.
  19. Nielsen, J. N.: Supersonic Wing-Body Interference at High Angles of Attack with Emphasis on Low Aspect Ratios. AIAA Paper No. 86-0568, January 1986.
  20. Winchenbach, G. L., Buff, R. S., Whyte, R. H., and Hathaway, W. H.: Subsonic and Transonic Aerodynamics of a Wraparound Fin Configuration. Journal of Guidance, Control and Dynamics, Vol. 9, No. 6, November-December 1986, pp. 627-632.
  21. Hensch, M. J. and Nielsen J. N., Editors: Tactical Missile Aerodynamics, Vol. 104 Progress in Astronautics and Aeronautics, AIAA, New York, 1986, pp. 243-296.
  22. Luckring, J. M.: A Theory for the Core of a Three-Dimensional Leading-Edge Vortex. AIAA Paper 85-0108, January 1985.

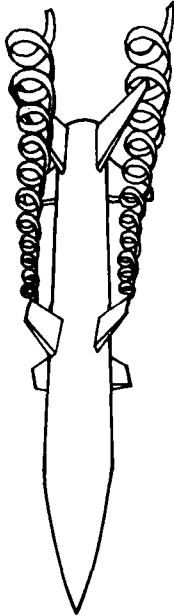
23. Miller, D. S. and Wood, R. M.: Lee-Side Flow Over Delta Wings at Supersonic Speeds, NASA TP-2430, June 1985.
24. Allen, J. M. and Dillenius, M. F. E.: Vortex Development on Slender Missiles at Supersonic Speeds. Journal of Spacecraft and Rockets, Vol. 17, No. 4, July-August 1980, pp. 377-378.
25. Landrum, E. J.: Wind Tunnel Pressure Data at Mach Numbers from 1.6 to 4.63 for a Series of Bodies of Revolution at Angles of Attack from -4 deg to 60 deg. NASA TM X-3558, October 1977.
26. Mendenhall, M. R. and Perkins, S. C. Jr.: Prediction of Vortex Shedding From Circular and Noncircular Bodies in Supersonic Flow. NASA CR-3754, January 1984.
27. Allen, J. M. and Pittman, J. L.: Analysis of Surface Pressure Distributions on Two Elliptic Missile Configurations. AIAA Paper 83-1841, July 1983.
28. Allen, J. M., Hernandez, G., and Lamb, M.: Body Surface Pressure Data on Two Monoplane-Wing Missile Configurations with Elliptical Cross Sections at Mach 2.50. NASA TM-85645, September 1983.
29. Newsome, R. W. and Adams, M. S.: Numerical Simulation of Vortical Flow Over an Elliptical Body Missile at High Angles of Attack. AIAA Paper 86-0559, January 1986.
30. Stallings, R. L., Jr. and Lamb, M.: Wing-Alone Aerodynamic Characteristics for High Angles of Attack at Supersonic Speeds. NASA TP-1889, July 1981.
31. Sorrels, R. B., III and Landrum, E. J.: Theoretical and Experimental Study of Twisted and Cambered Delta Wings Designed for a Mach Number of 3.5. NASA TN D-8247, August 1976.



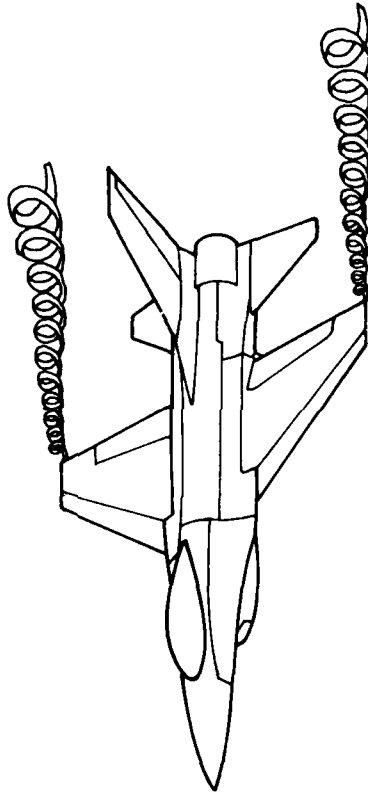
32. Carmichael, R. L. and Woodward, F. A.: An Integrated Approach to the Analysis and Design of Wings and Wing-Body Combinations in Supersonic Flow. NASA TN D-3685, October 1966.
33. Woodward, F. A.: USSAERO Computer Program Development, Versions B and C. NASA CR-3227, April 1980.
34. Hoeljmakers, W. H. M.: A Panel Method for the Determination of the Aerodynamic Characteristics of Complex Configurations in Linearized Subsonic or Supersonic Flow. Part 1: Description and Application. NLR TR-80124 U, Pt. 1, December 1980.
35. Woodward, F. A.: Development of the Triplet Singularity for the Analysis of Wings and Bodies in Supersonic Flow. NASA CR-3466, September 1981.
36. Ashley, H. and Landahl, M.: Aerodynamics of Wings and Bodies. Addison-Wesley Publishing Co., Reading, MA, 1965.
37. Liepmann, H. W. and Roshko, A.: Elements of Gas Dynamics. John Wiley and Sons, New York, 1957.
38. Tsien, H. S.: Supersonic Flow Over an Inclined Body of Revolution. Journal of Aerospace Sciences, Vol. 5, No. 12, 1938, pp. 480-483.
39. Von Karman, T. and Moore, M. B.: Resistance of Slender Bodies Moving with Supersonic Velocities, with Special Reference to Projectiles. ASME Transactions, Vol. 54, December 1932, pp. 303-310.
40. Magnus, A. E. and Epton, M. A.: PAN AIR - A Computer Program for Predicting Subsonic or Supersonic Linear Potential Flows About Arbitrary Configurations Using a Higher Order Panel Method. Volume I - Theory Document (Version 1.0). NASA CR-3252, May 1980.

41. Sidwell, K. W., Baraugh, P. K., and Bussoletti, J. E.: PAN AIR - A Computer Program for Predicting Subsonic or Supersonic Linear Potential Flows About Arbitrary Configurations Using a Higher Order Panel Method. Volume II - User's Manual (Version 1.0). NASA CR-3252, April 1982.
42. Sidwell, K. W. and Derbyshire, T.: PAN AIR - A Computer Program for Predicting Subsonic or Supersonic Linear Potential Flows About Arbitrary Configurations Using a Higher Order Panel Method. Summary Document (Version 1.0). NASA CR-3250, April 1982.
43. Baraugh, P. K., Bussoletti, J. E., Massena, W. A., Nelson, F. D., Purdon, D. J., and Tsurusaki, K.: PAN AIR - A Computer Program for Predicting Subsonic or Supersonic Linear Potential Flows About Arbitrary Configurations Using a Higher Order Panel Method. Volume IV - Maintenance Document (Version 1.0). NASA CR-3254, November 1981.
44. Fornasier, L.: Linearized Potential Flow Analysis of Complex Aircraft Configurations by HISSS, A Higher-Order Panel Method. AIAA Paper 85-0281, January 1985.
45. Polhamus, E. C.: Prediction of Vortex-Lift Characteristics Based on a Leading-Edge Suction Analogy. Journal of Aircraft, Vol. 8, April 1971, pp. 193-199.
46. Mendenhall, M. R. and Nielsen, J. N.: Effect of Symmetrical Vortex Shedding on the Longitudinal Aerodynamic Characteristics of Wing-Body-Tail Combinations. NASA CR-2473, January 1975.
47. Nielsen, J. N., Spangler, S. B., and Hensch, M. J.: A Study of Induced Rolling Moments for Cruciform-Winged Missiles, NEAR TR-61, December 1973, p. 36.

48. Dillenius, M. F. E. and Nielsen, J. N.: Computer Programs for Calculating Pressure Distributions Including Vortex Effects on Supersonic Monoplane or Cruciform Wing-Body-Tail Combinations With Round or Elliptical Bodies. NASA CR-3122, April 1979.
49. Carlson, H. W.: A Modification to Linearized Theory for Prediction of Pressure Loadings on Lifting Surfaces at High Supersonic Mach Numbers and Large Angles of Attack. NASA TP-1406, February 1979.
50. McMillan, O. J. and Nazario, S. M.: Program ININC - A Method to Account for Inlet Spillage in the Supersonic/Hypersonic Arbitrary Body Program. NEAR TR-315, November 1983.
51. Dillenius, M. F. E., Perkins, S. C., Jr., and Lesieutre, D. J.: Modified NWCDM - NSTRN and Supersonic Store Separation Programs for Calculating NASTRAN Forces Acting on Missiles Attached to Supersonic Aircraft. NEAR TR-369, February 1987.
52. Blair, A. B., Jr., Allen, J. M., and Hernandez, G.: Effect of Tail-Fin Span on Stability and Control Characteristics of a Canard-Controlled Missile at Supersonic Mach Numbers. NASA TP-2157, June 1983.
53. Raytheon Company Report: Final Report - Tail Control Sparrow Wind Tunnel Test at NASA/Ames Research Center - January 1976, April 1976.
54. Muller, G. L. and Gasko, W. F.: Subsonic-Transonic Drag [B Supersonic Inlets. J. Aircraft, Vol. 4, No. 3, May-June 1967, pp. 231-237.
55. Perkins, S. C., Jr. and McMillan, O. J.: A Handbook of Experimental Data on the Effects of Inlet Systems on Airbreathing Missile External Aerodynamics. NWC TP-6147, Vol. 3, Part 3. July 1982.

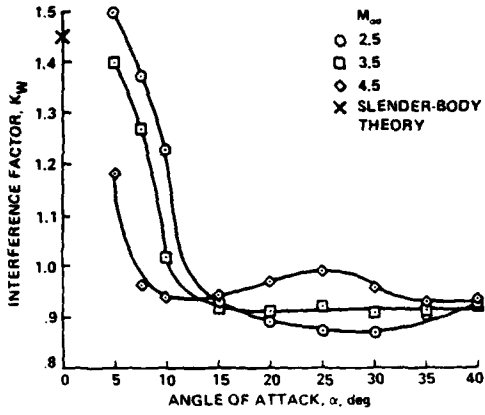


Large wing-vortex interference effects on tails

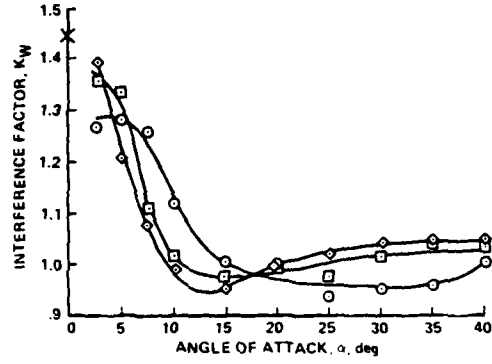


Small wing-vortex interference effects on tails

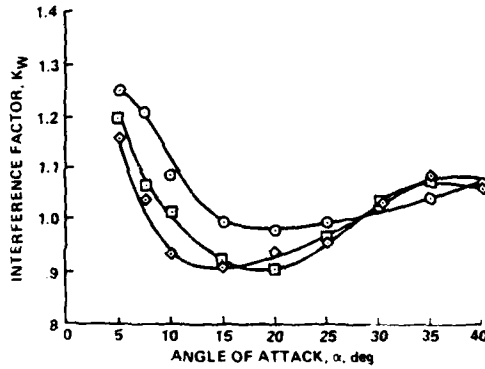
Figure 1.- Typical missile and aircraft wing vortices.



(a)  $\lambda = 0.0$



(b)  $\lambda = 0.5$



(c)  $\lambda = 1.0$

Figure 2.- Effect of angle of attack and Mach number on  $K_w$  for AR = 2 fins. (Additional data available in Ref. 19).

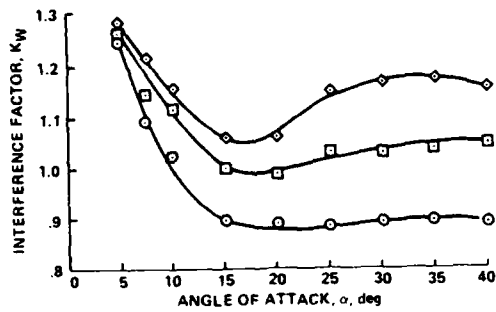
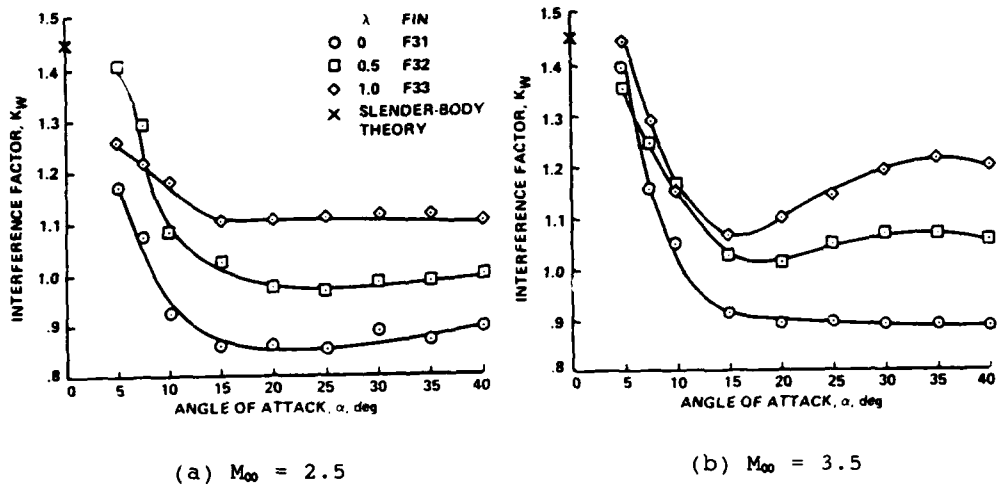


Figure 3.- Effect of taper ratio on  $K_W$  for AR = 0.5 fins.  
(Additional data available in Ref. 19).



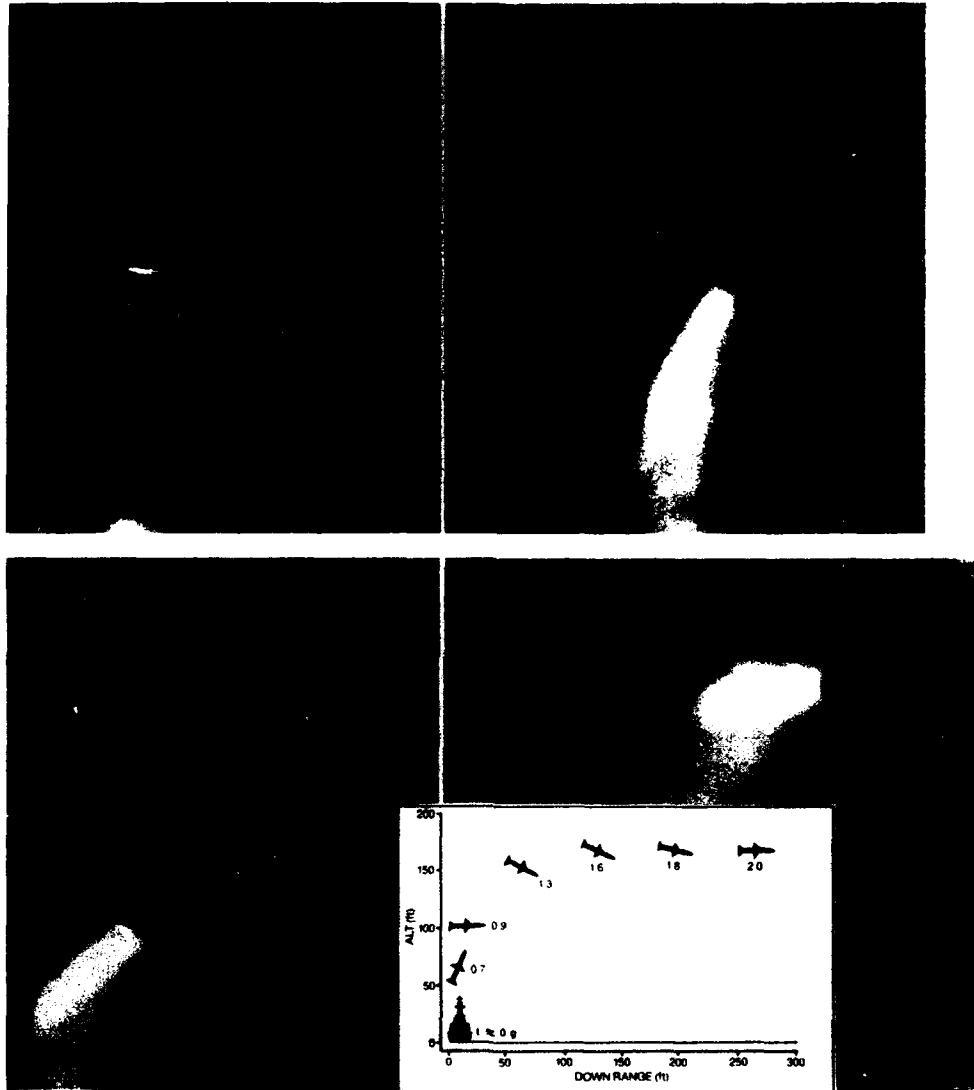


Figure 5.- Typical vertical launch missile trajectory during initial turn.



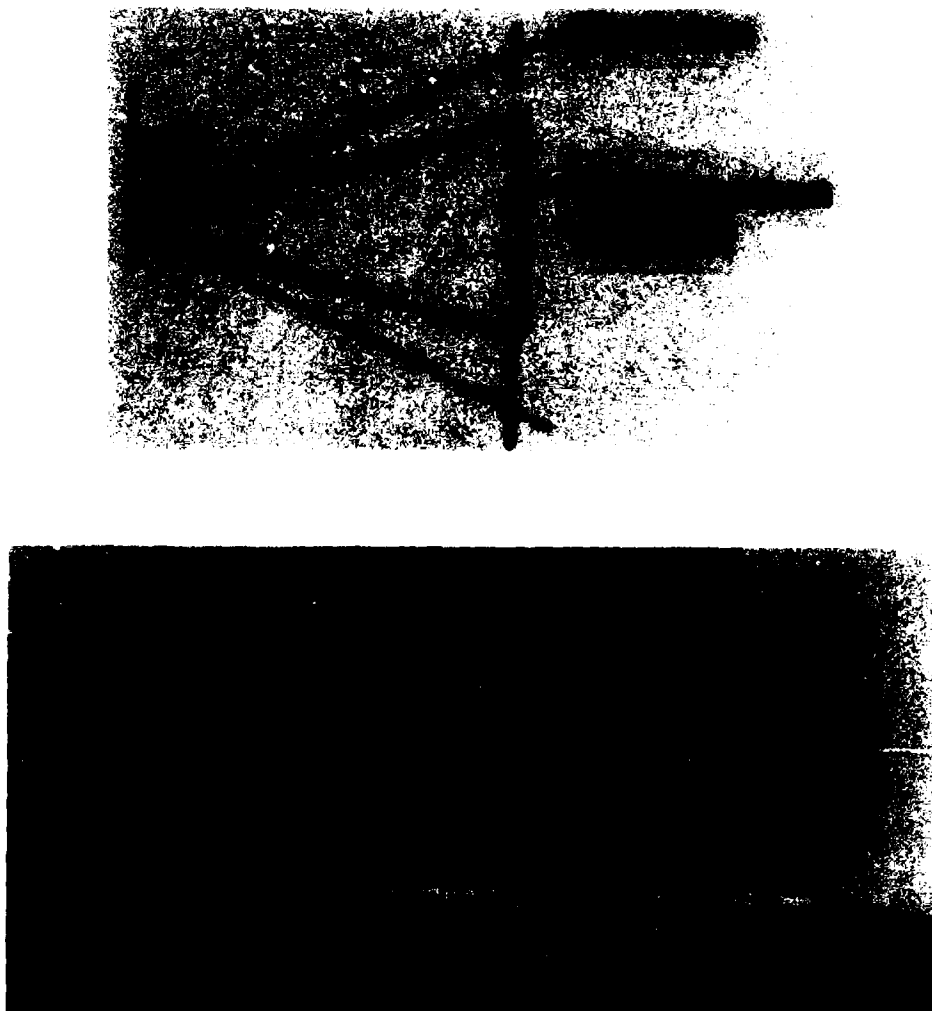
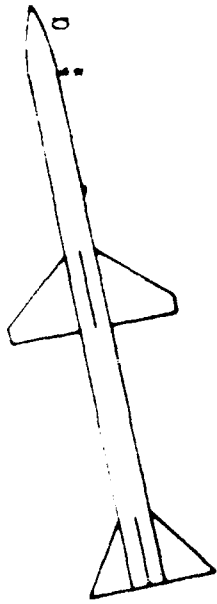


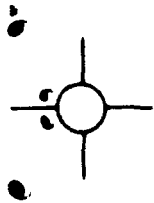
Figure 6.- Experimental leading-edge vortex structure on a highly swept wing;  $M_{\infty} = 2.4$ ,  $\alpha = 12$  deg.

Data (Ref. 24)

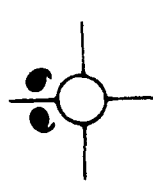
Theory (LRCDM2, Ref. 8)



$\alpha = 11.4^\circ$



$\alpha = 23.1^\circ$



$\alpha = 35.1^\circ$

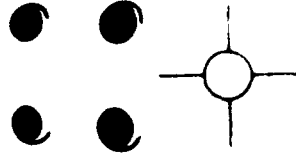


Figure 7.- Effect of angle of attack on vortex patterns on a cruciform, axisymmetric missile;  $\delta_{fins} = 0$  deg,  $M_\infty = 2.36$ ,  $\phi = 0$  deg.

Data (Ref. 24) Theory (LRCDM2, Ref. 8)

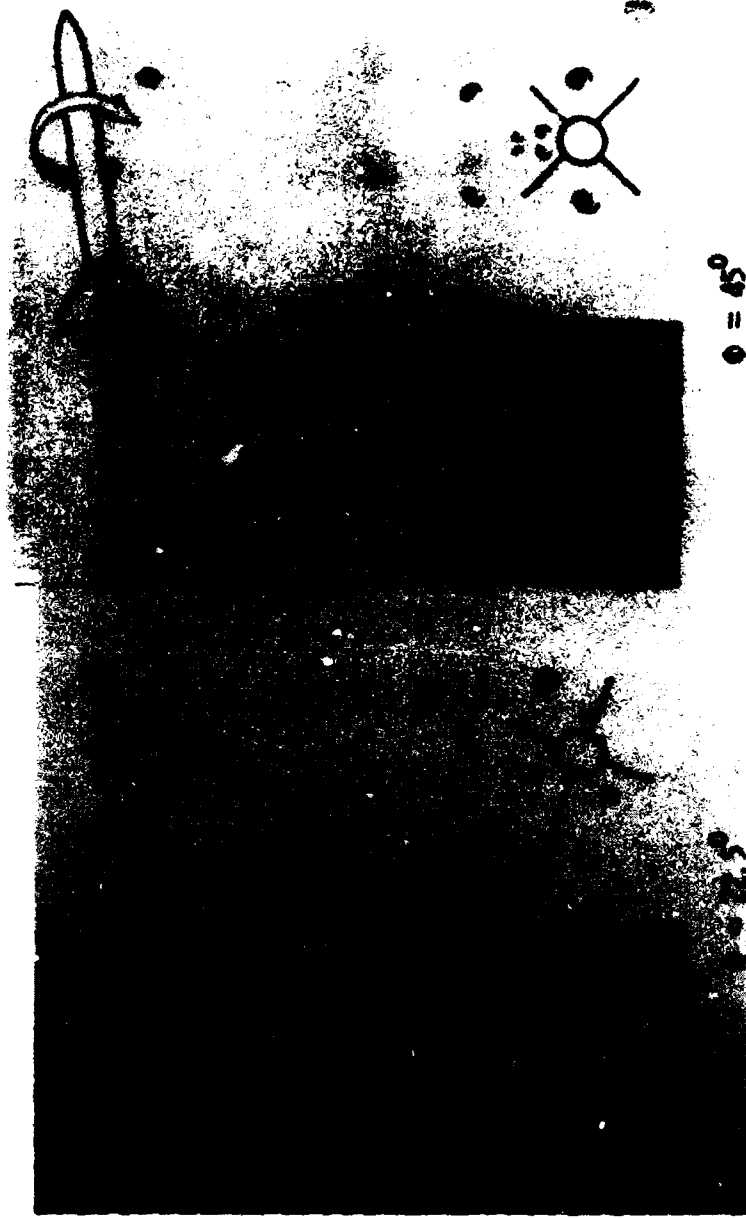


Figure 8.- Effect of roll angle on vortex patterns on a cruciform axisymmetric missile;  $\delta_{fins} = 0$  deg,  $M_{\infty} = 2.36$ ,  $\alpha_C = 11.4$  deg.

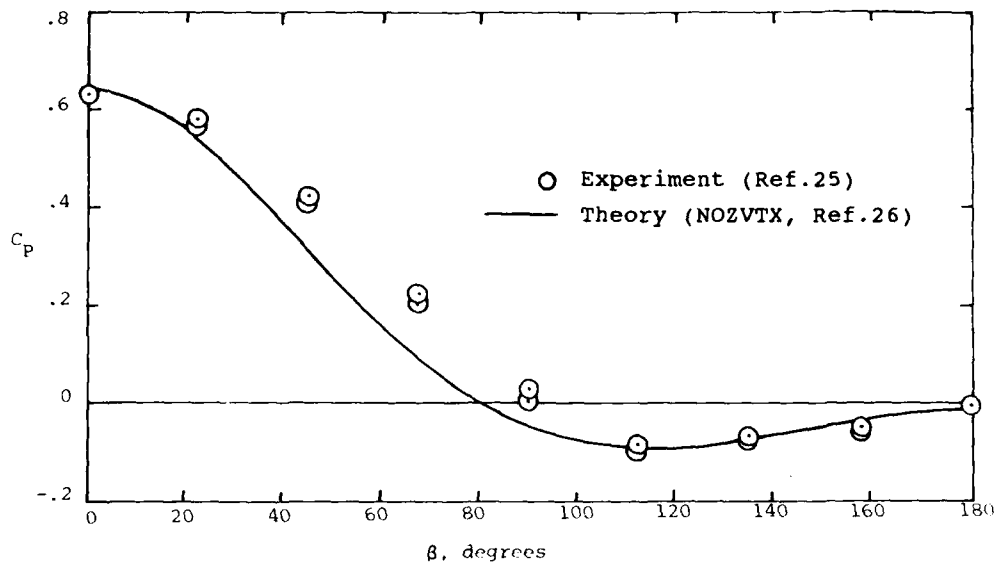
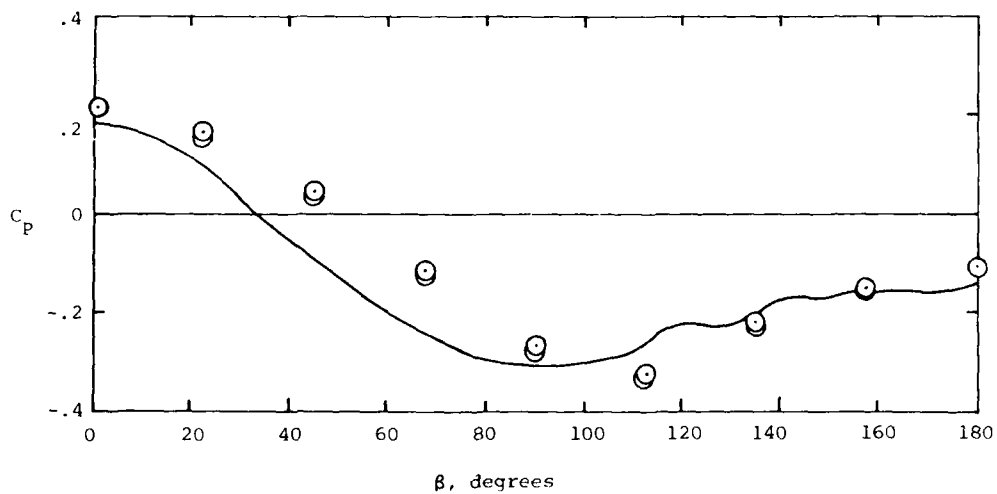
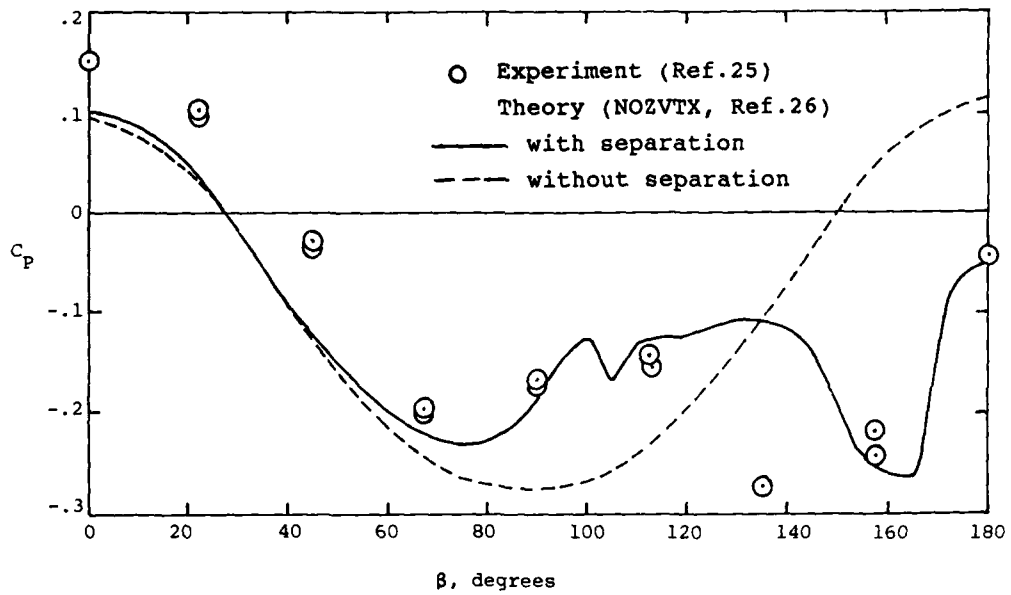
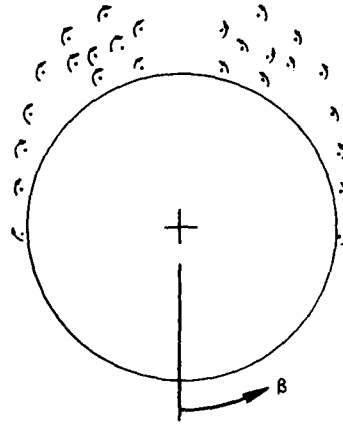
(a)  $x/D = 0.8$ (b)  $x/D = 2.8$ 

Figure 9.- Measured and predicted circumferential pressure distribution on an ogive-cylinder body;  
 $M_\infty = 1.6$ ,  $\alpha_C = 20$  deg.



(c)  $x/D = 5.1$

Figure 9.- Concluded.

$\phi = 0 \text{ deg}$



$\phi = 22.5 \text{ deg}$



$\phi = 45 \text{ deg}$



$\phi = 67.5 \text{ deg}$



$\phi = 90 \text{ deg}$



$x/L \approx 1.0$

Figure 10.- Vapor screen showing vortex development on a 3:1 elliptic cross section body;  $M_{\infty} = 2.5$ ,  $\alpha_C = 20 \text{ deg}$ .

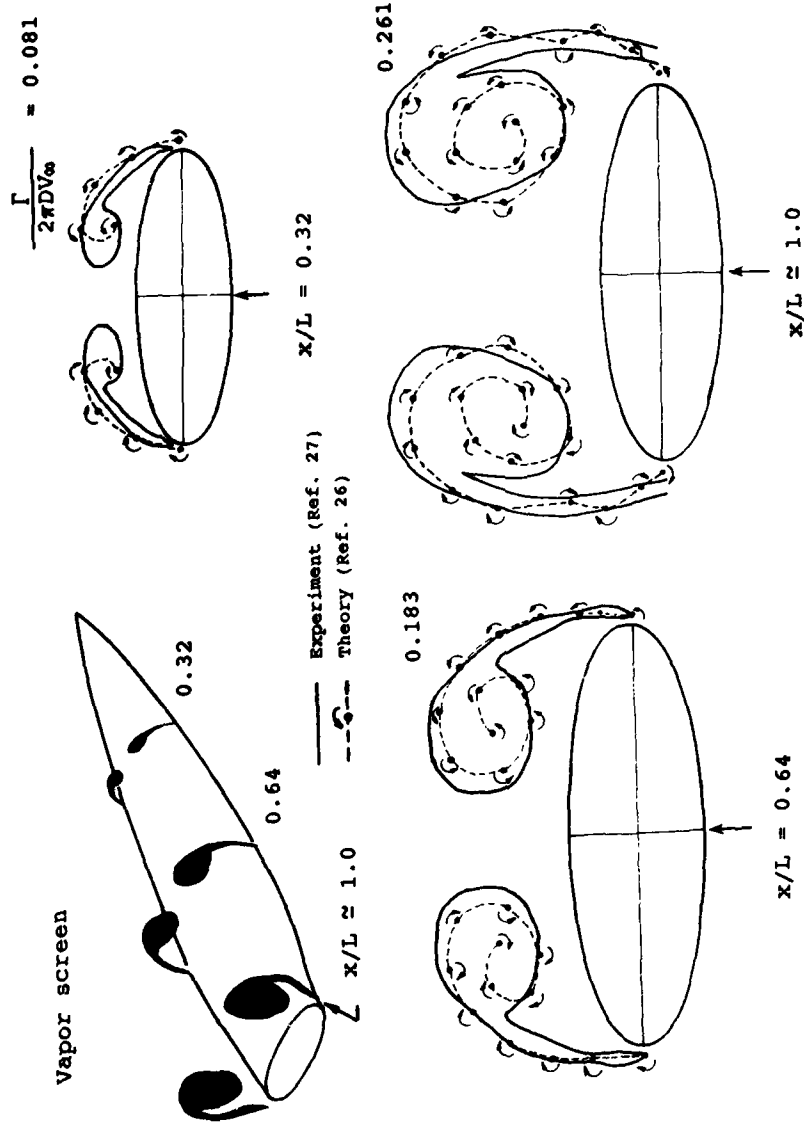
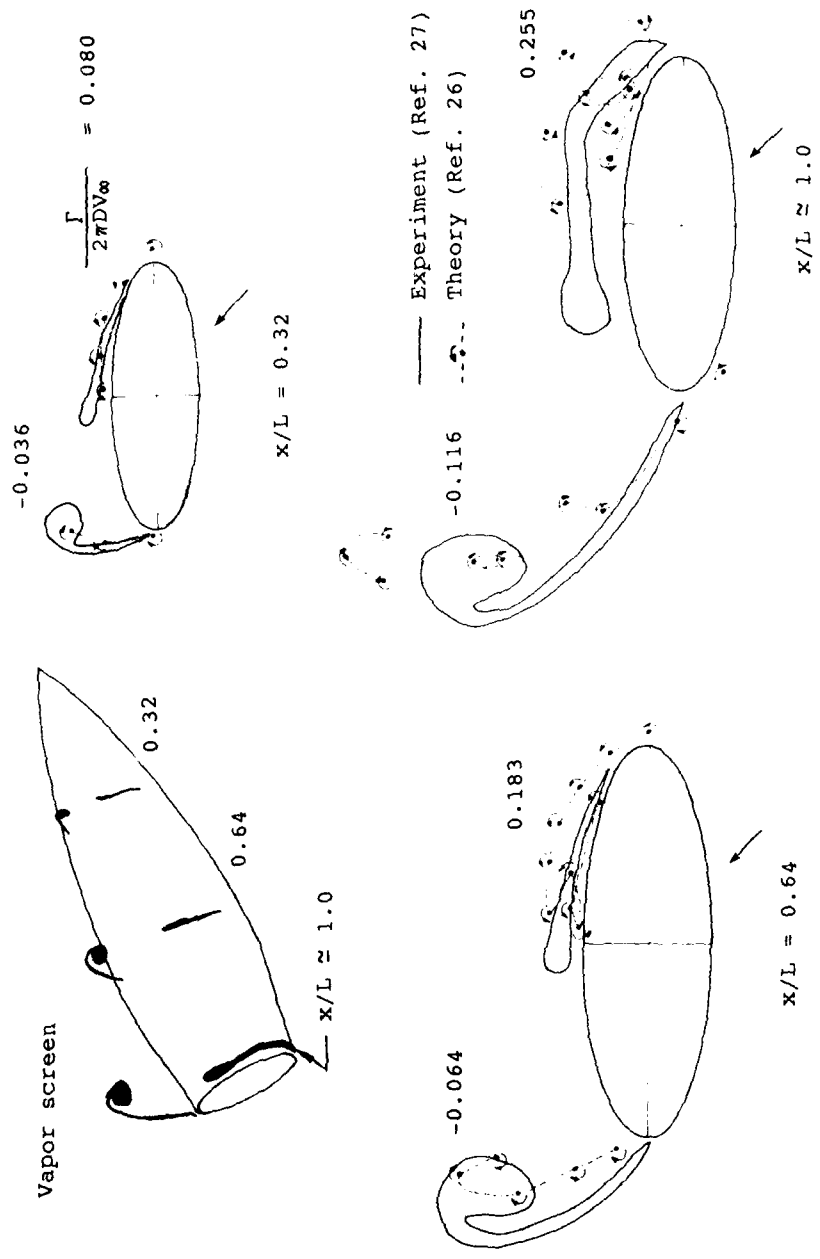


Figure 11.- Measured and predicted vortex patterns on a 3:1 elliptic cross section body;  $M_\infty = 2.5$ ,  $\alpha_c = 20$  deg.



(b)  $\phi = 45^\circ$

Figure 11.- Concluded.



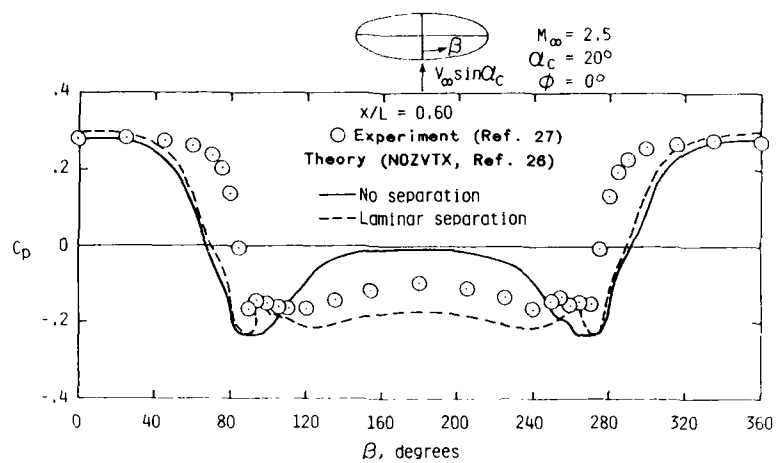
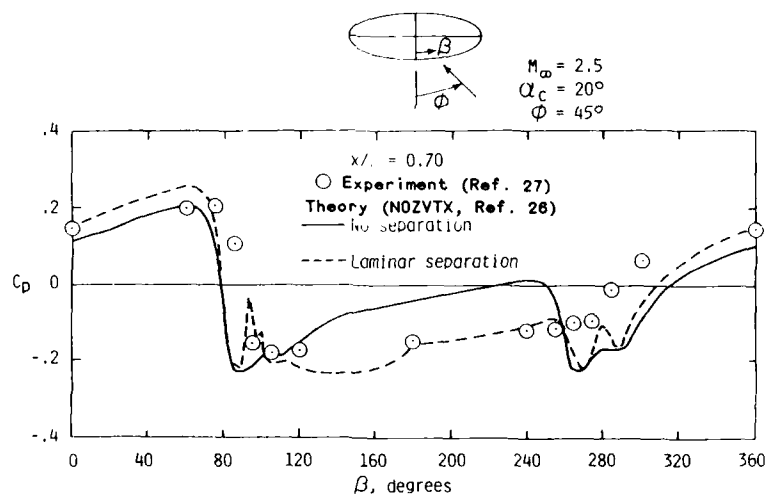
(a)  $\phi = 0^\circ$ (b)  $\phi = 45^\circ$ 

Figure 12.- Measured and predicted circumferential pressure distribution on a 3:1 elliptic cross section missile at  $x/L = 0.60$ ;  $M_\infty = 2.5$ ,  $\alpha_c = 20$  deg.

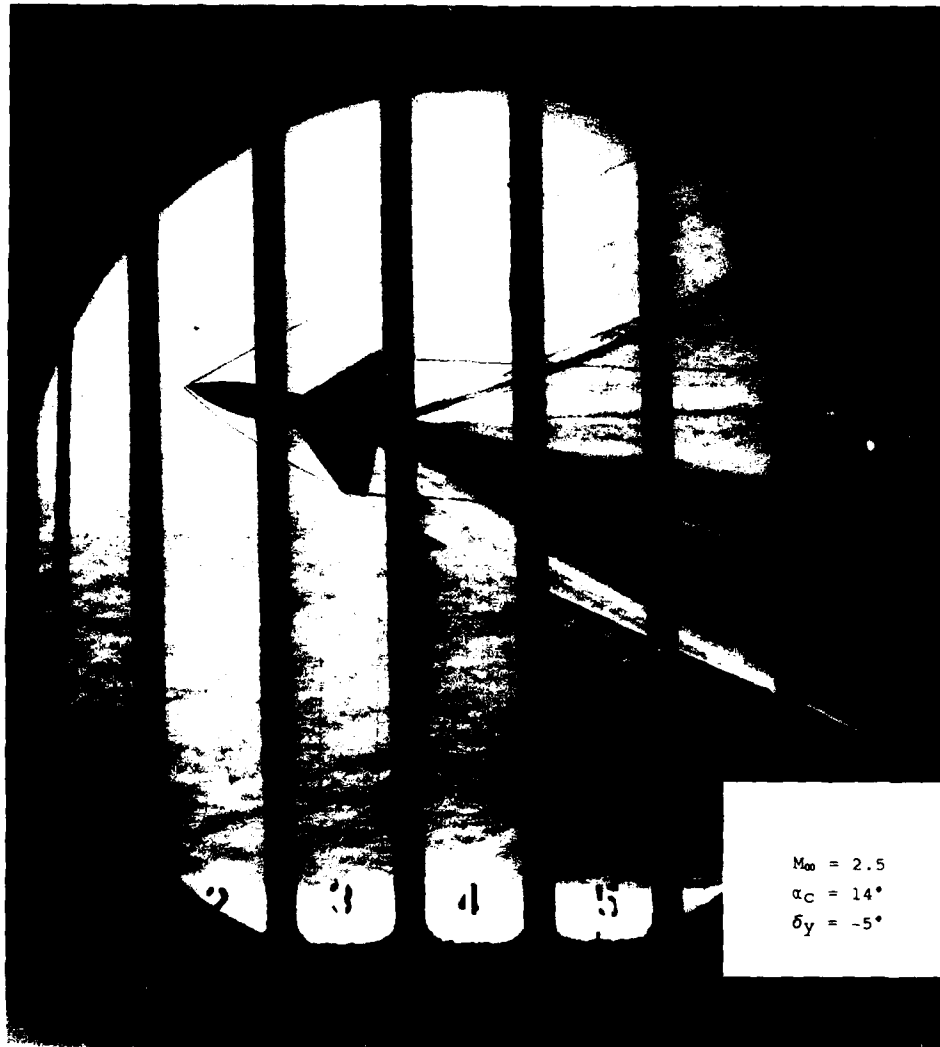
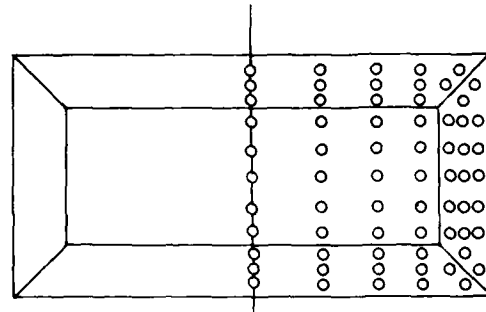
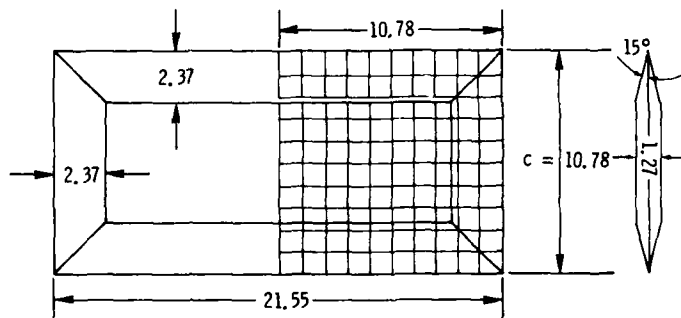


Figure 13.- Schlieren photograph of missile model in wind tunnel (NASA Langley Research Center).

Linear dimensions in centimeters



Pressure tap layout (Ref. 30)



Paneling layout

Figure 14.- Panel and pressure tap layout on a rectangular wing.

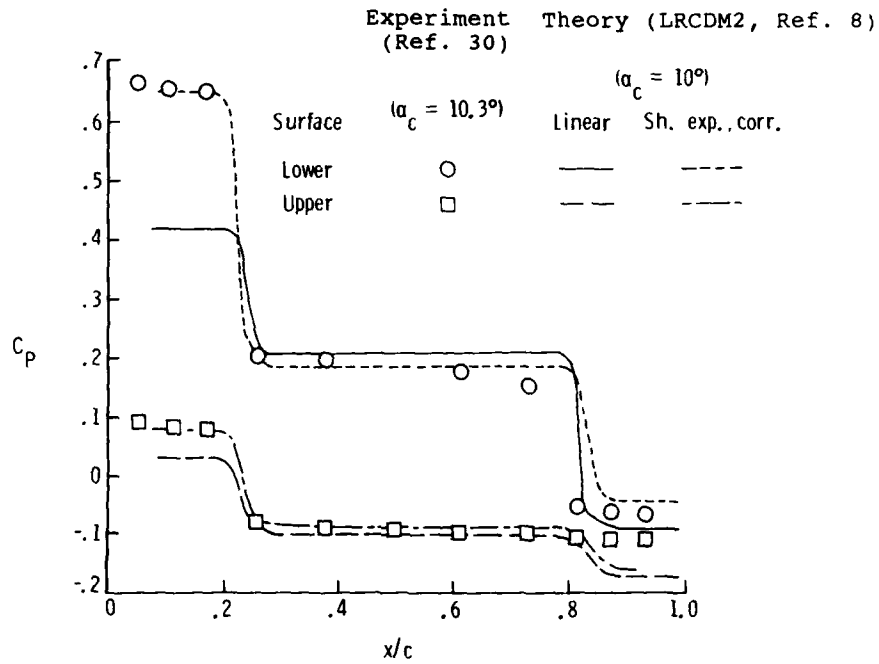
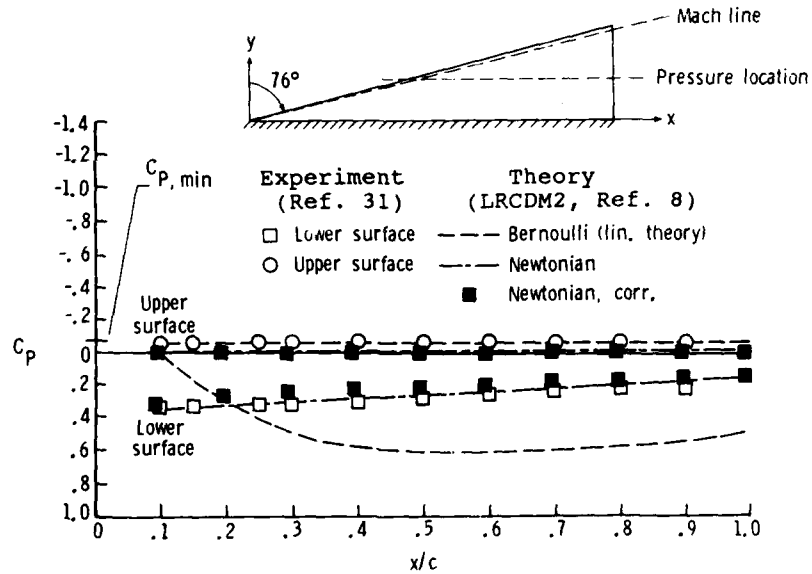
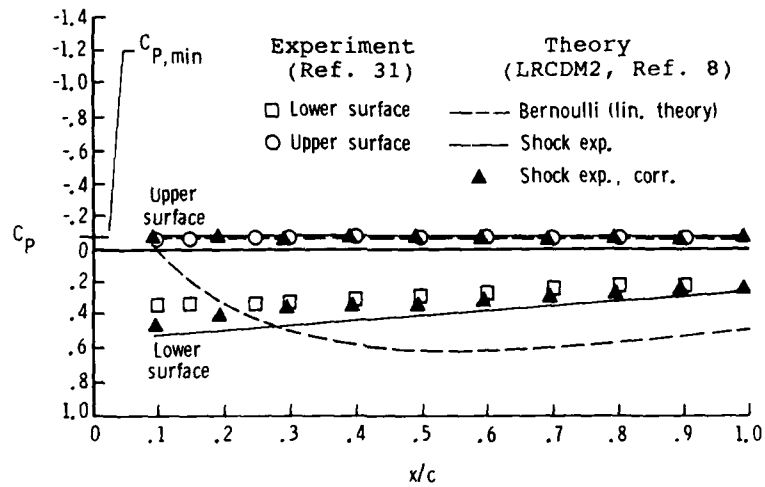


Figure 15.- Theoretical and experimental chordwise pressure distributions on a rectangular wing;  
 $M_\infty = 2.86$ ,  $\alpha_c \approx 10$  deg.

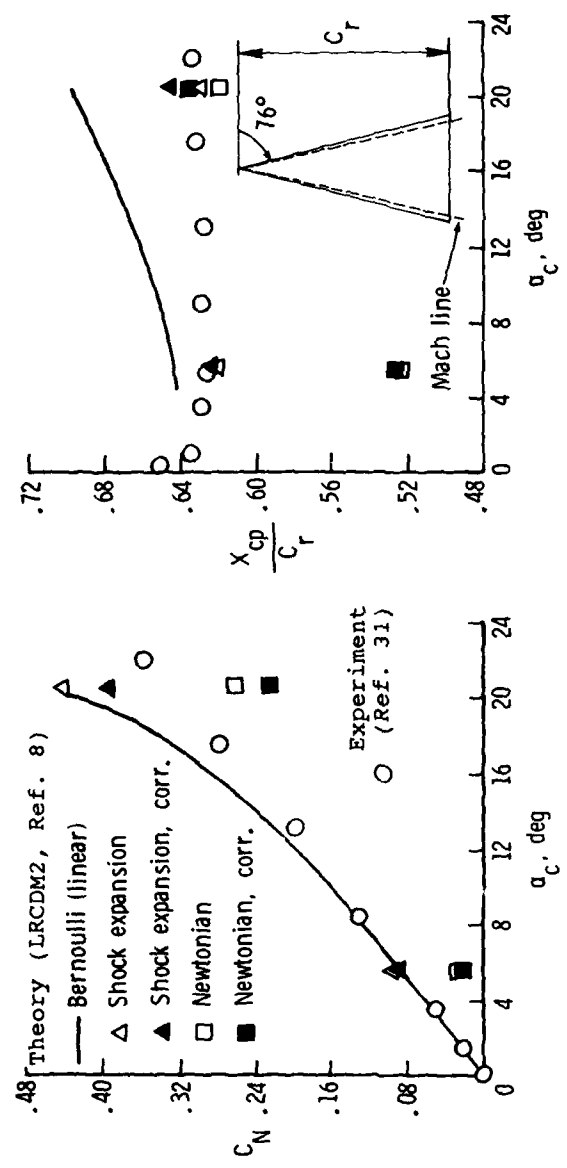


(a) Linear and Newtonian predictions.



(b) Linear and shock expansion predictions.

Figure 16.- Theoretical and experimental pressure distributions on a delta wing at  $y/(b/2) = 0.4$ ;  $M_\infty = 4.6$ ,  $\alpha_c = 20.56$  deg.



(a) Normal-force coefficient (b) Center of pressure

Figure 17.- Theoretical and experimental normal-force and center-of-pressure results on a delta wing,  $M_\infty = 4.6$ .

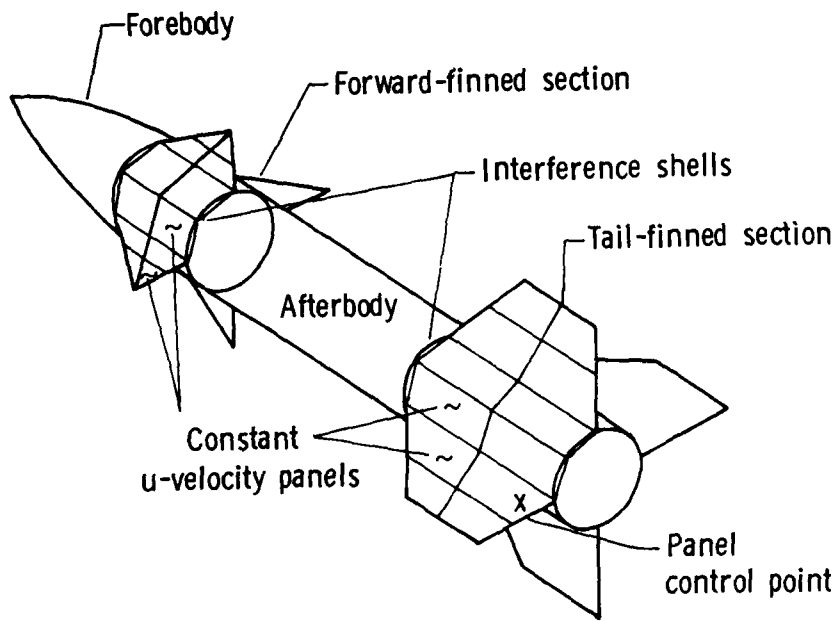


Figure 18.- Typical panel layout on an axisymmetric missile.

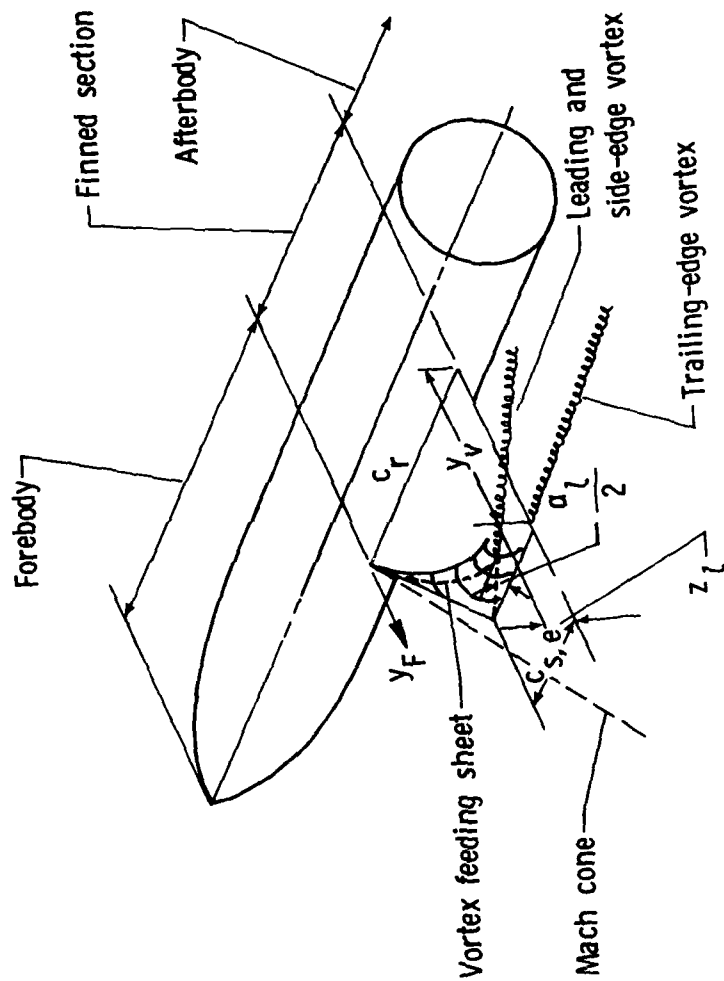


Figure 19.- Typical leading and side edge vortex development.



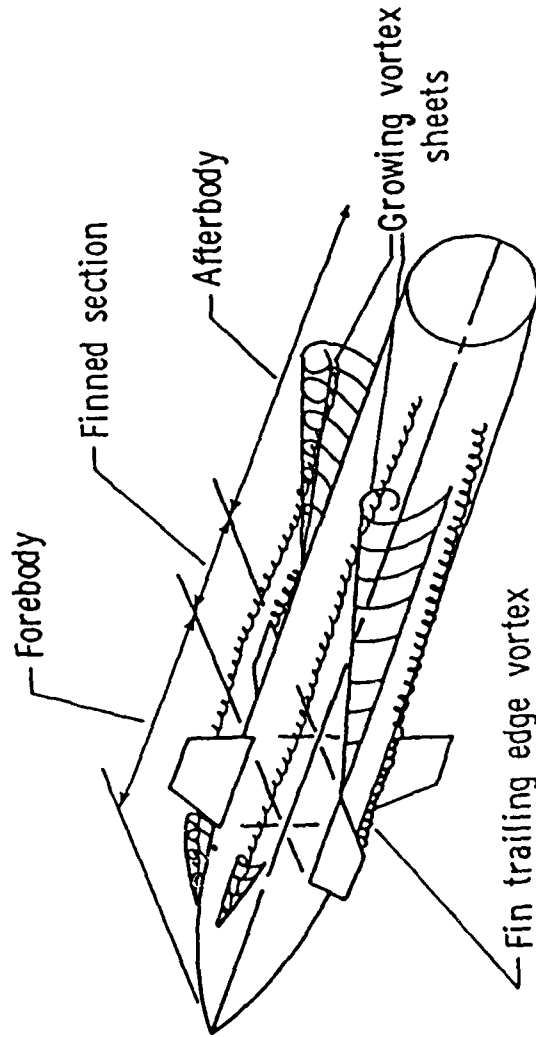


Figure 20.- Schematic representation of body vortex shedding on an axisymmetric missile.

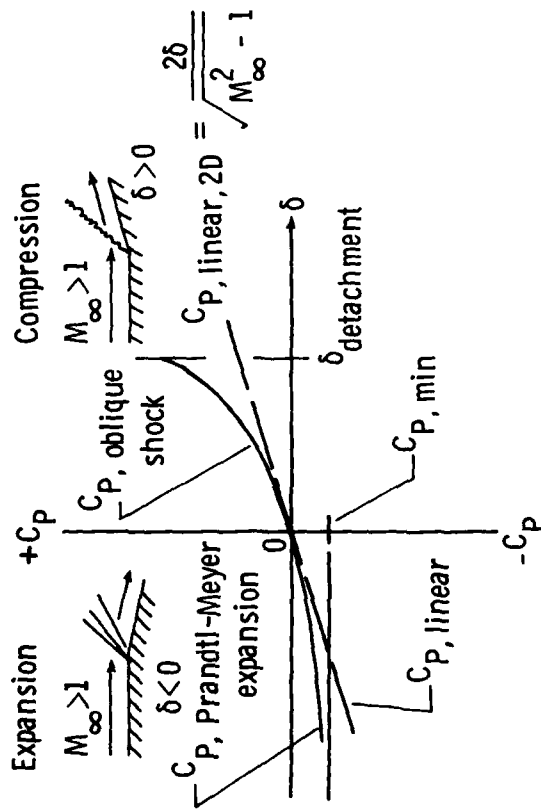
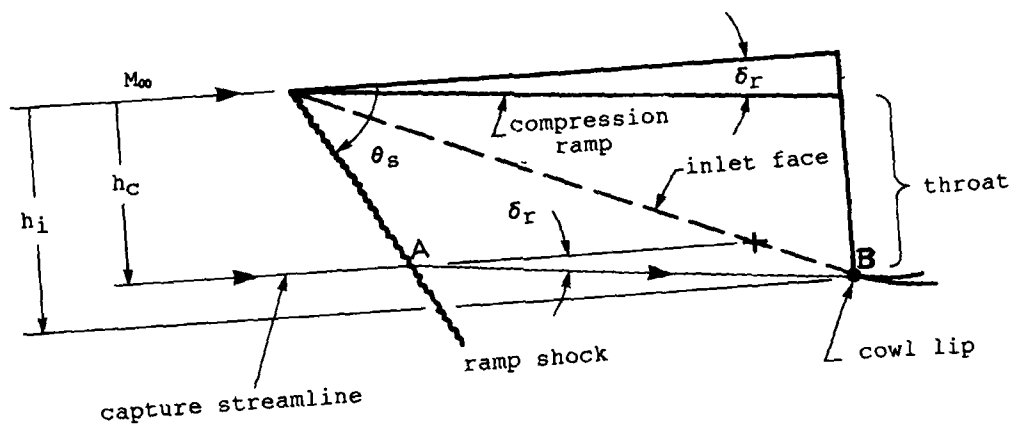
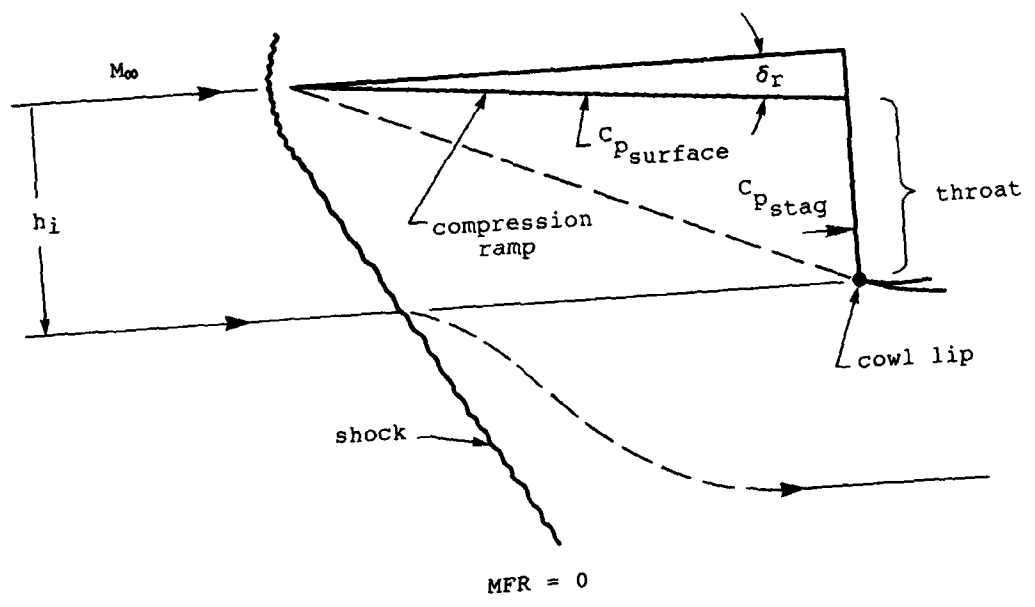


Figure 21.- Nonlinear expansion and compression effects for supersonic Mach numbers.



$MFR = MFR_{max}$



(a) Two-dimensional inlets

Figure 22.- Maximum and minimum flow capture.



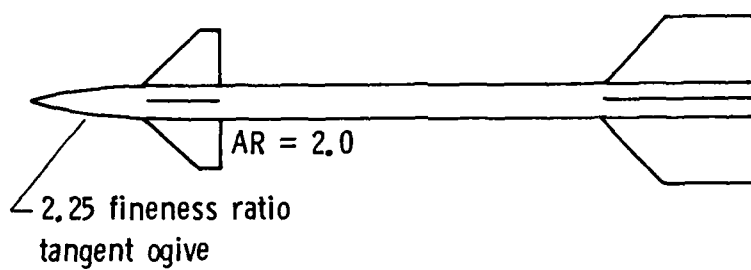


Figure 23.- NASA/Langley Research Center TF-4 canard control model.

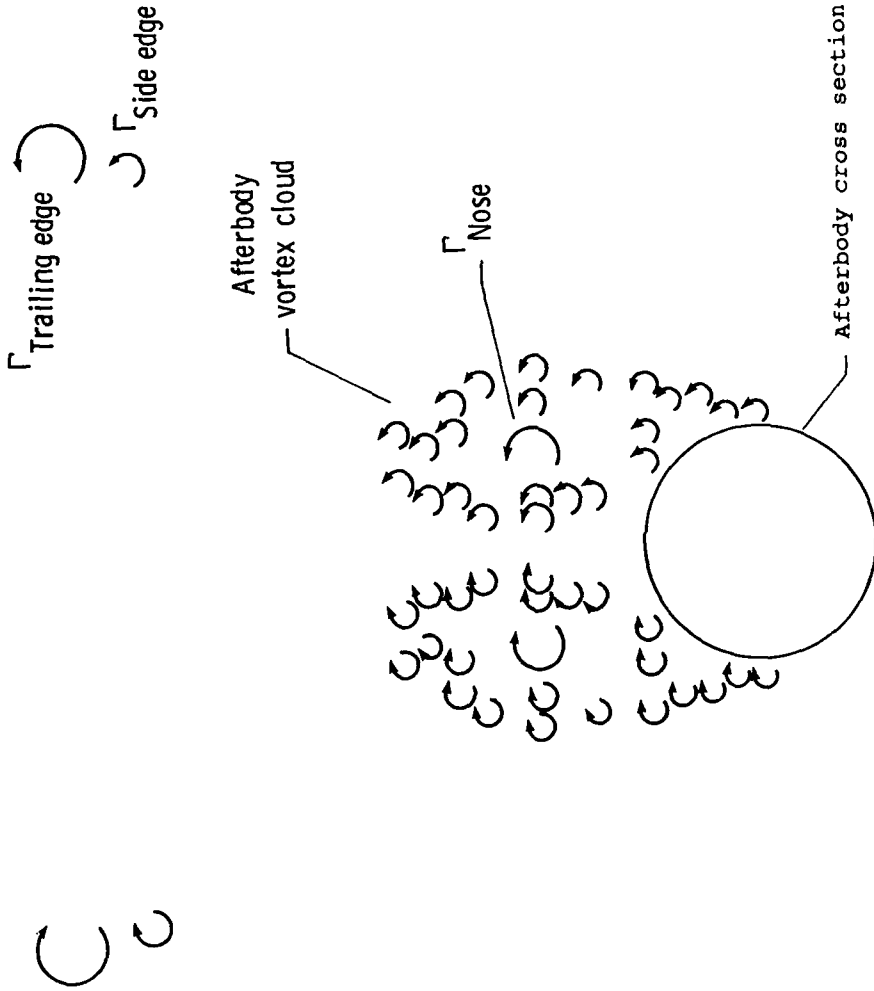


Figure 24.- Calculated vorticity on TF-4 afterbody;  
 $M_\infty = 1.6$ ,  $\alpha_c = 20$  deg,  $\phi = 0$  deg,  $\delta = 0$  deg.

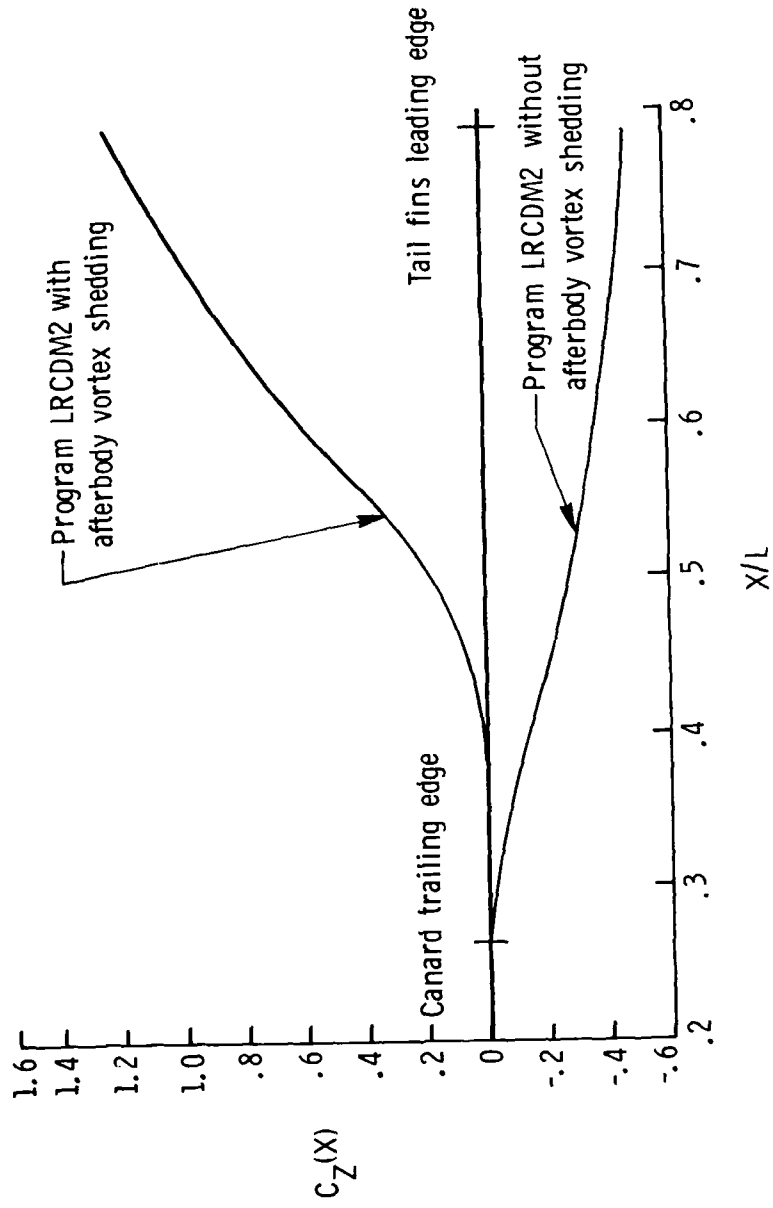


Figure 25.- Calculated normal force accumulation on TF-4 missile afterbody;  $M_\infty = 1.6$ ,  $\alpha_c = 20$  deg,  $\phi = 0$  deg,  $\delta = 0$  deg.

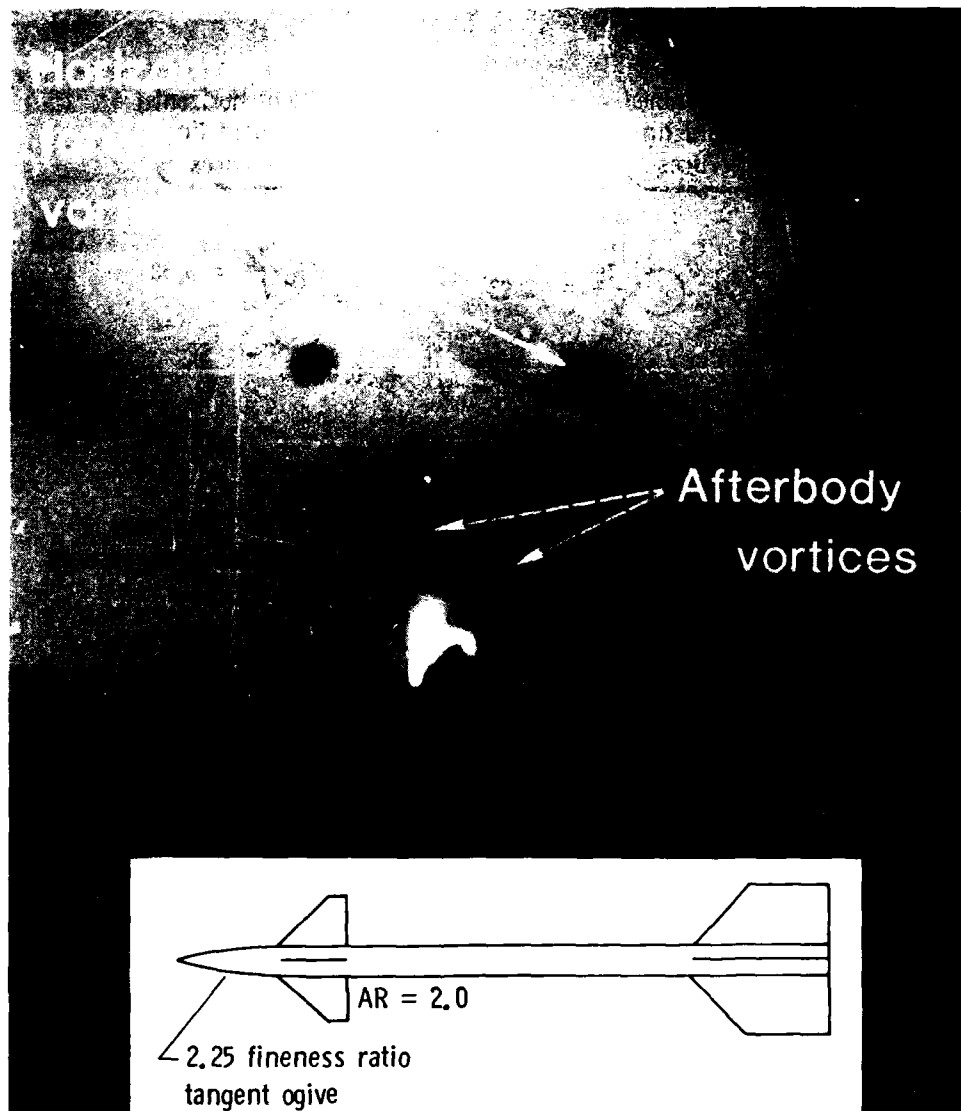


Figure 26.- Experimental vortex pattern on TF-4 model;  
 $M_{\infty} = 2.5$ ,  $\alpha_c = 15$  deg,  $\phi = 0$  deg,  $\delta_{roll} = 5$  deg.



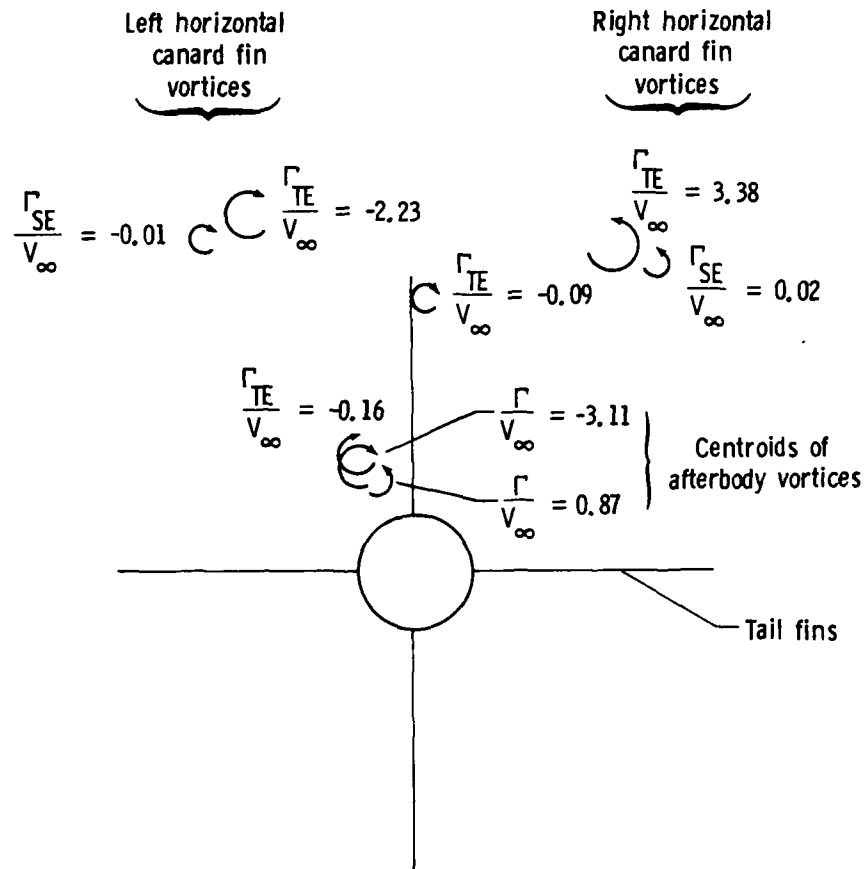
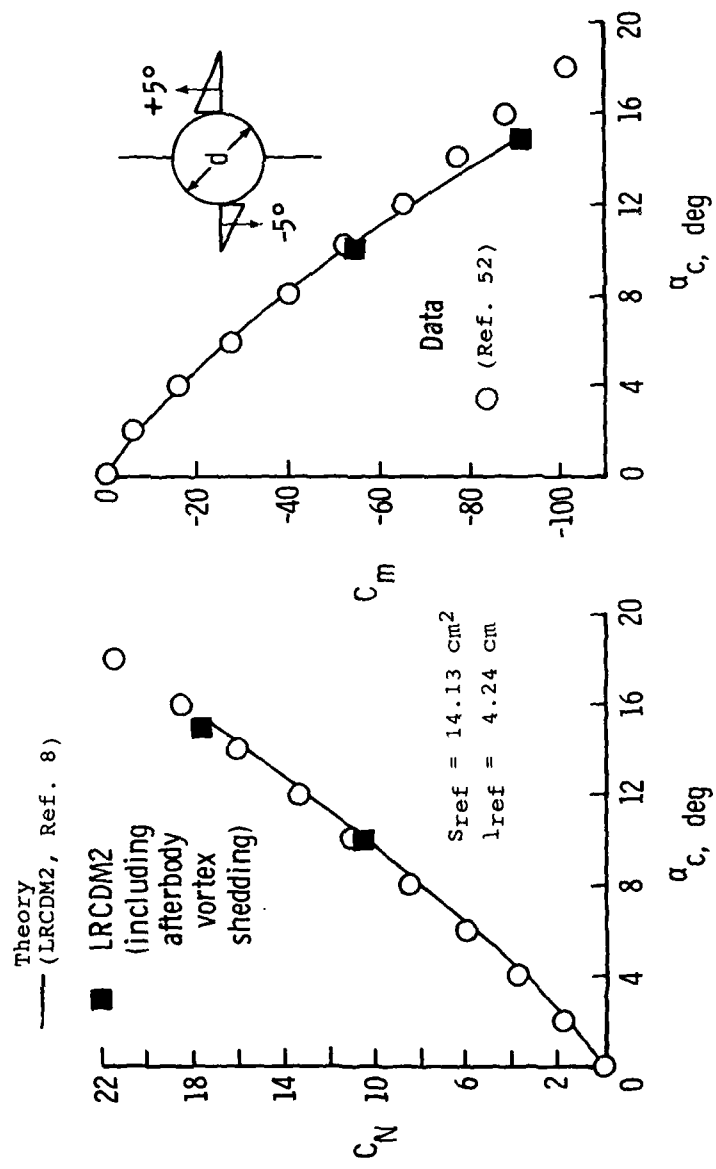
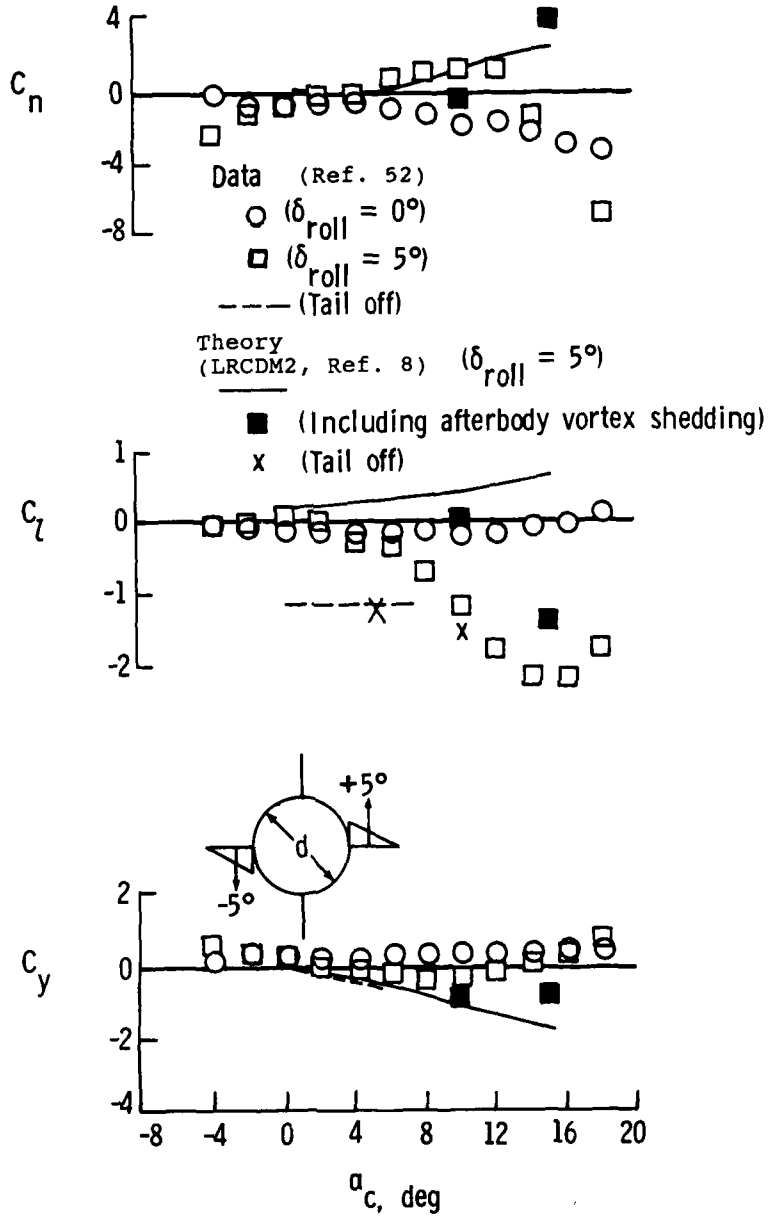


Figure 27.- Calculated vortices on TF-4 at tail section leading edge;  $M_{\infty} = 2.5$ ,  $\alpha_c = 15$  deg,  $\phi = 0$  deg,  $\delta_{roll} = 5$  deg.

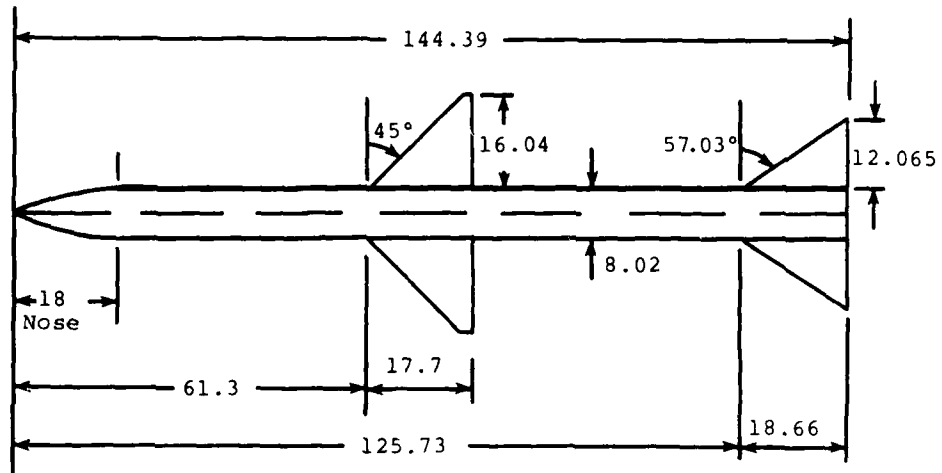


(a) Longitudinal characteristics  
 Figure 28.- Theoretical and experimental aerodynamic results for TF-4 model;  $M_\infty = 2.5$ ,  $\phi = 0$  deg,  $\delta_{roll} = 5$  deg.



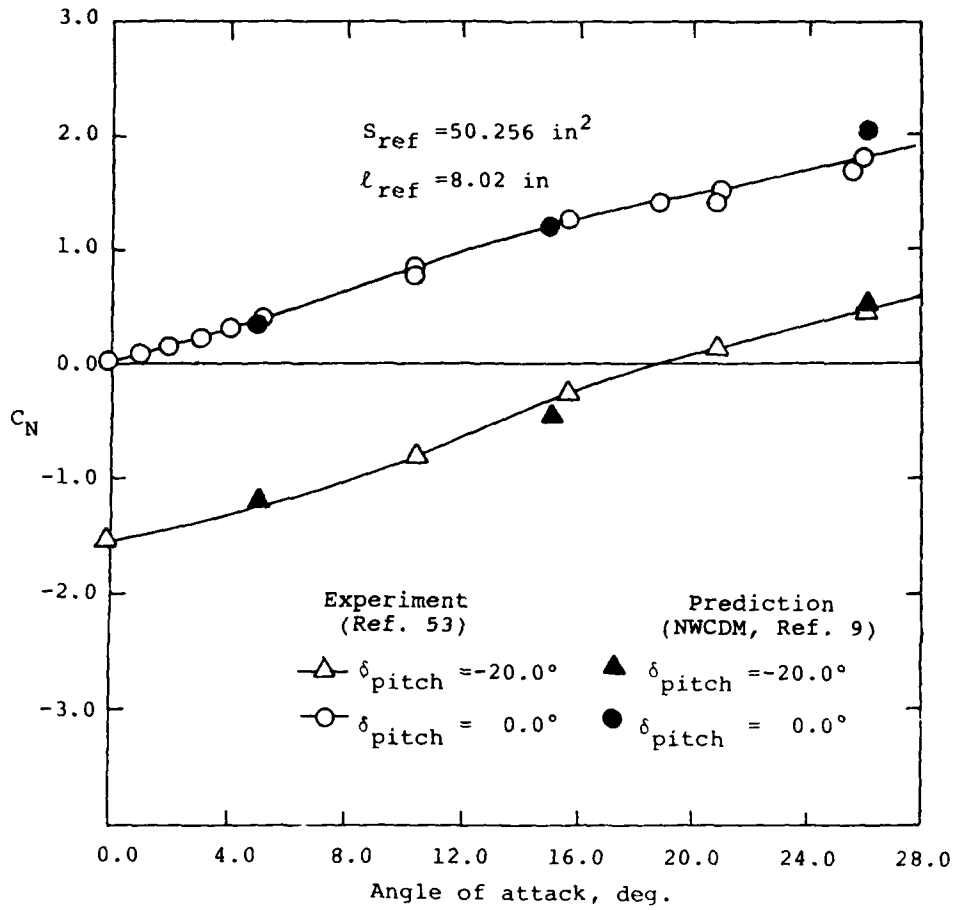
(b) Lateral-directional characteristics

Figure 28.- Concluded.



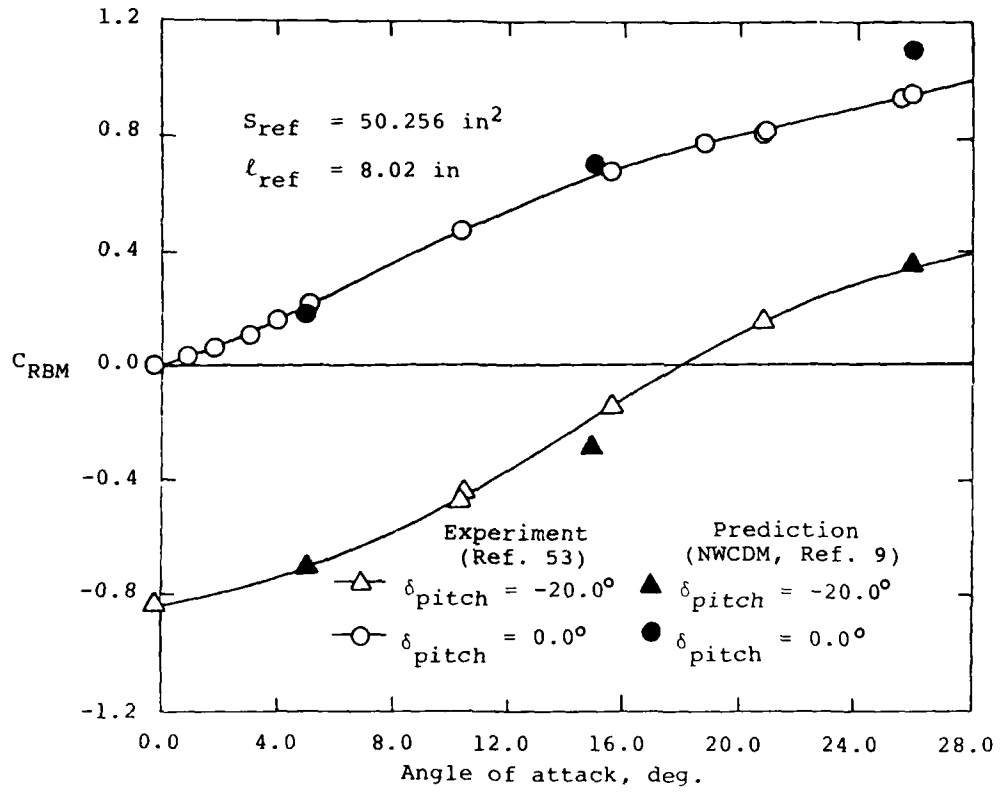
All dimensions in inches

Figure 29.- Tail control wind tunnel model.



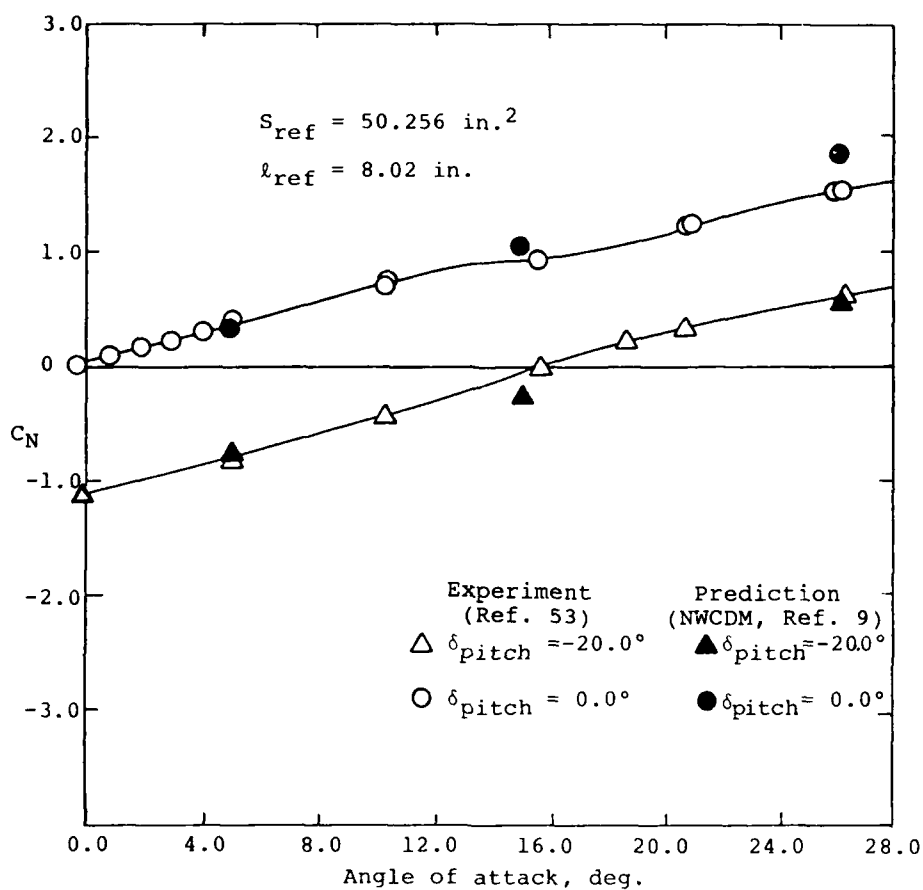
(a) Fin normal-force coefficient

Figure 30.- Loads acting on left horizontal tail fin with tail pitch control;  $\phi_{roll} = 0 \text{ deg}$ ,  $M_\infty = 1.6$ .



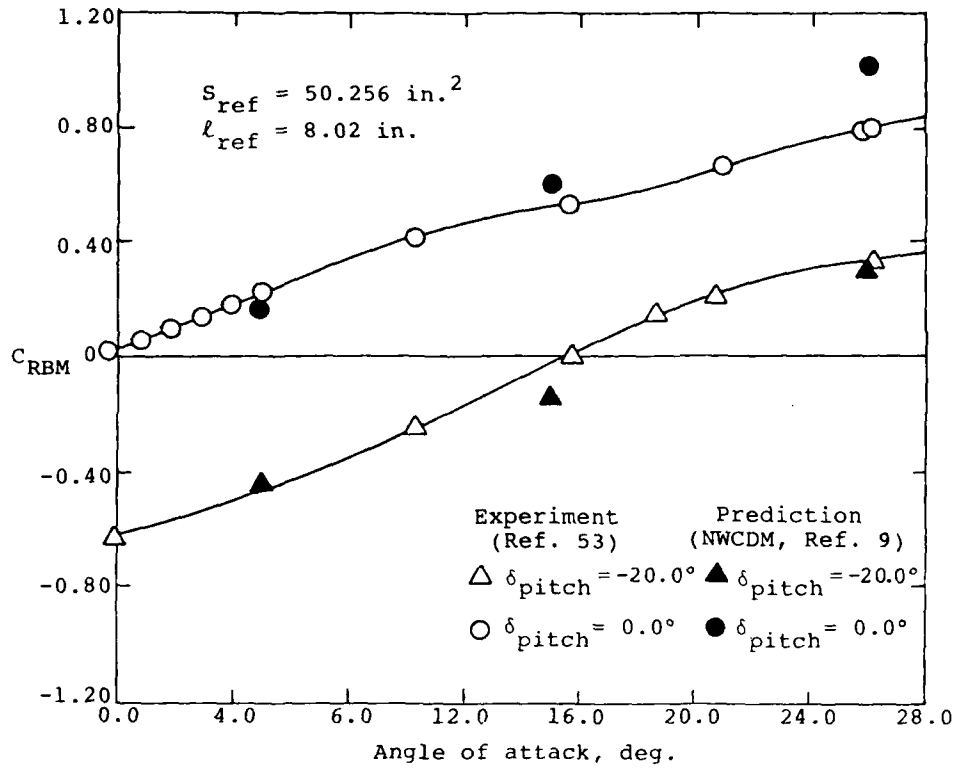
(b) Fin root-bending moment coefficient

Figure 30.- Concluded.



(a) Fin normal-force coefficient

Figure 31.- Loads acting on left horizontal tail fin with tail pitch control,  $\phi_{roll} = 0 \text{ deg}$ ,  $M_\infty = 2.2$ .



(b) Fin root-bending moment coefficient

Figure 31.- Concluded.



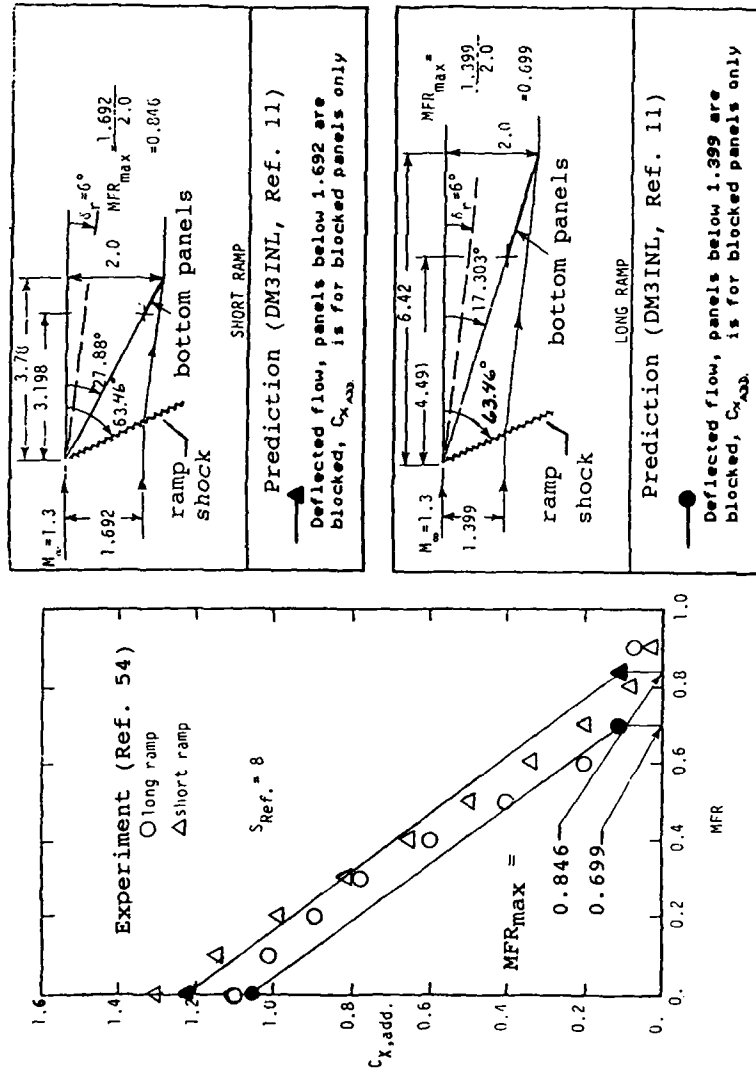


Figure 32.- Additive drag of two rectangular inlets as a function of mass flow ratio;  $M_\infty = 1.3$ ,  $\alpha = 0$  deg,  $\delta_{ramp} = 6$  deg,  $\beta = 0$  deg.

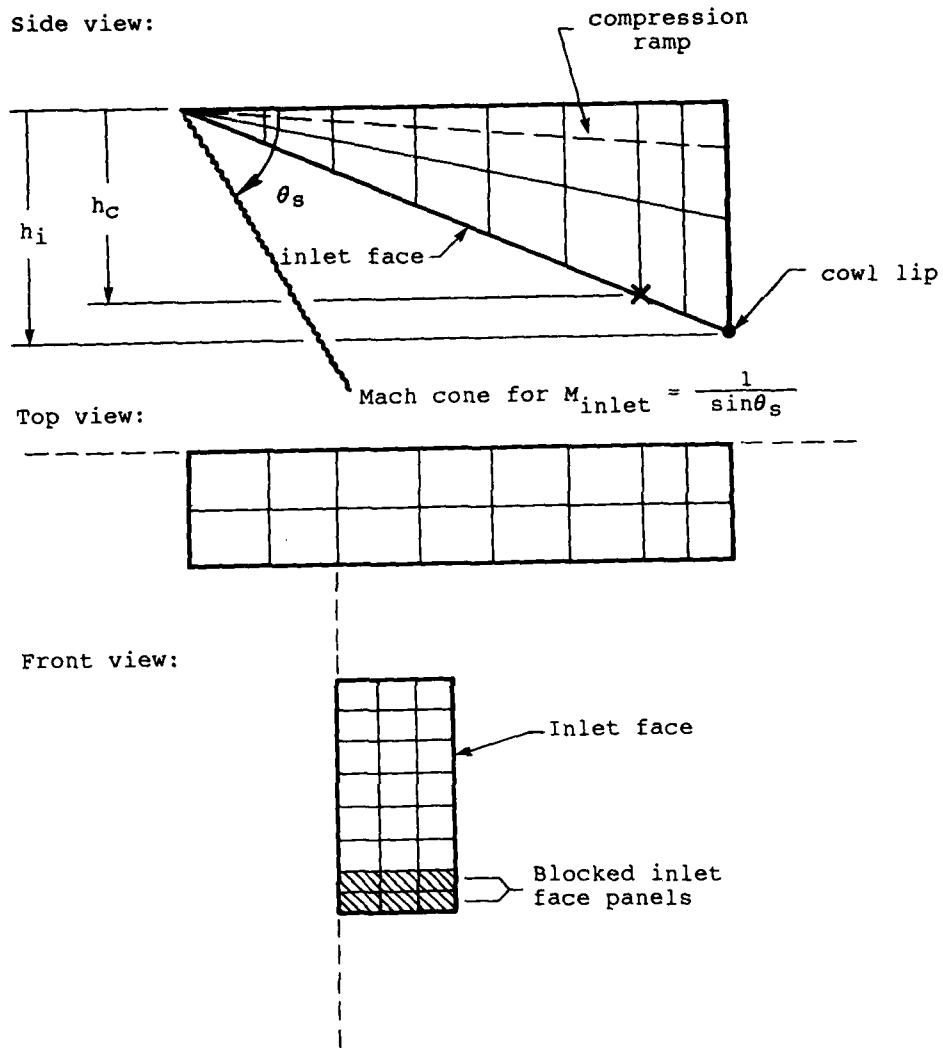


Figure 33.- Typical panel layout for modeling minimum additive drag of a rectangular inlet.

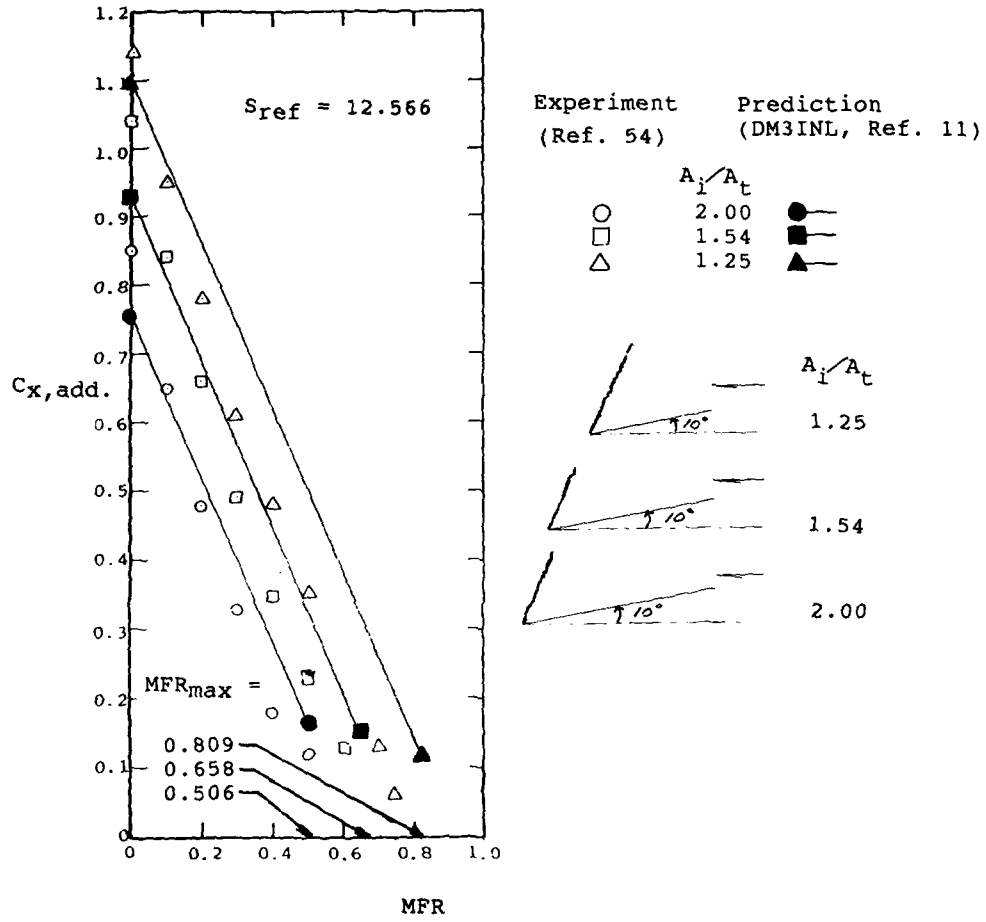


Figure 34.- Additive drag of an axisymmetric inlet as a function of mass flow ratio;  $M_{\infty} = 1.1$ ,  $\alpha = 0$  deg,  $\delta_{cone} = 6$  deg,  $\beta = 0$  deg.

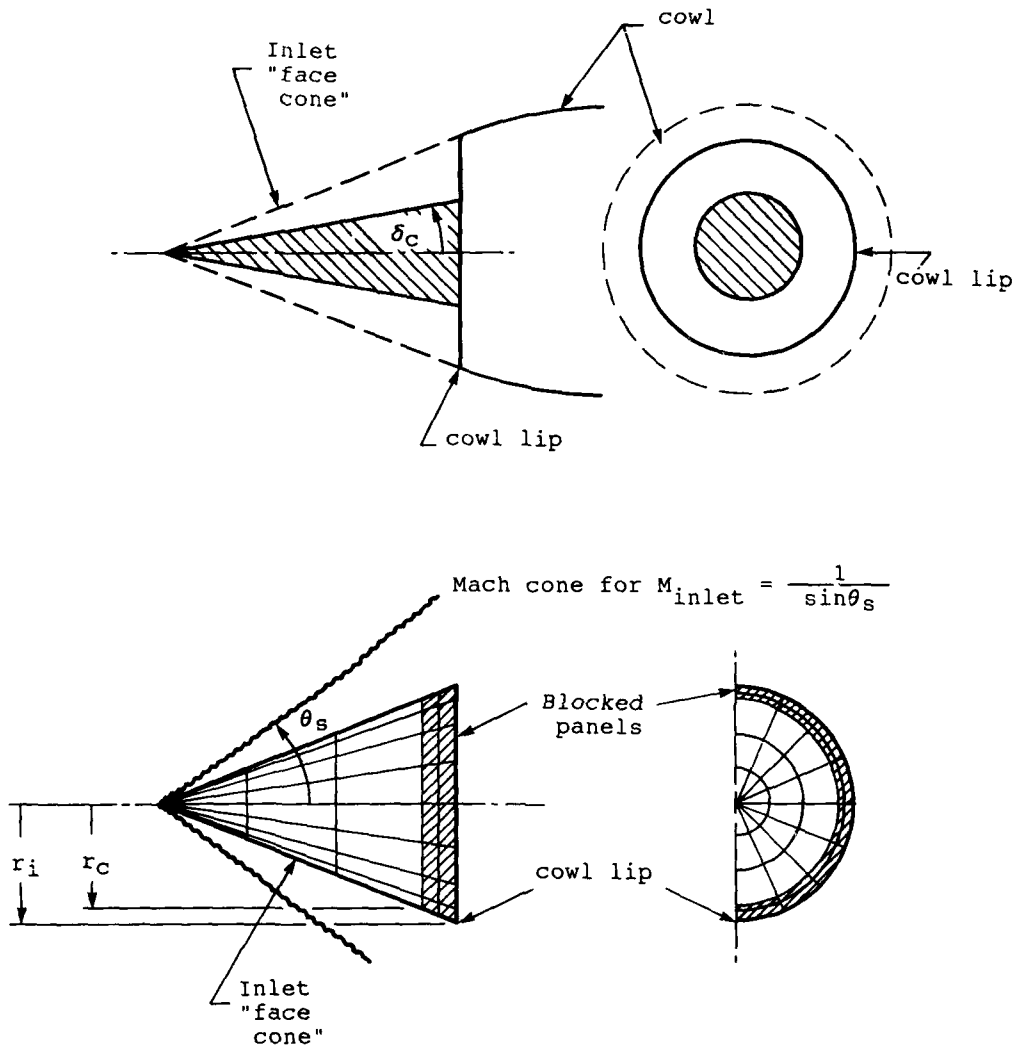


Figure 35.- Example panel layout for modeling minimum additive drag of an axisymmetric inlet.

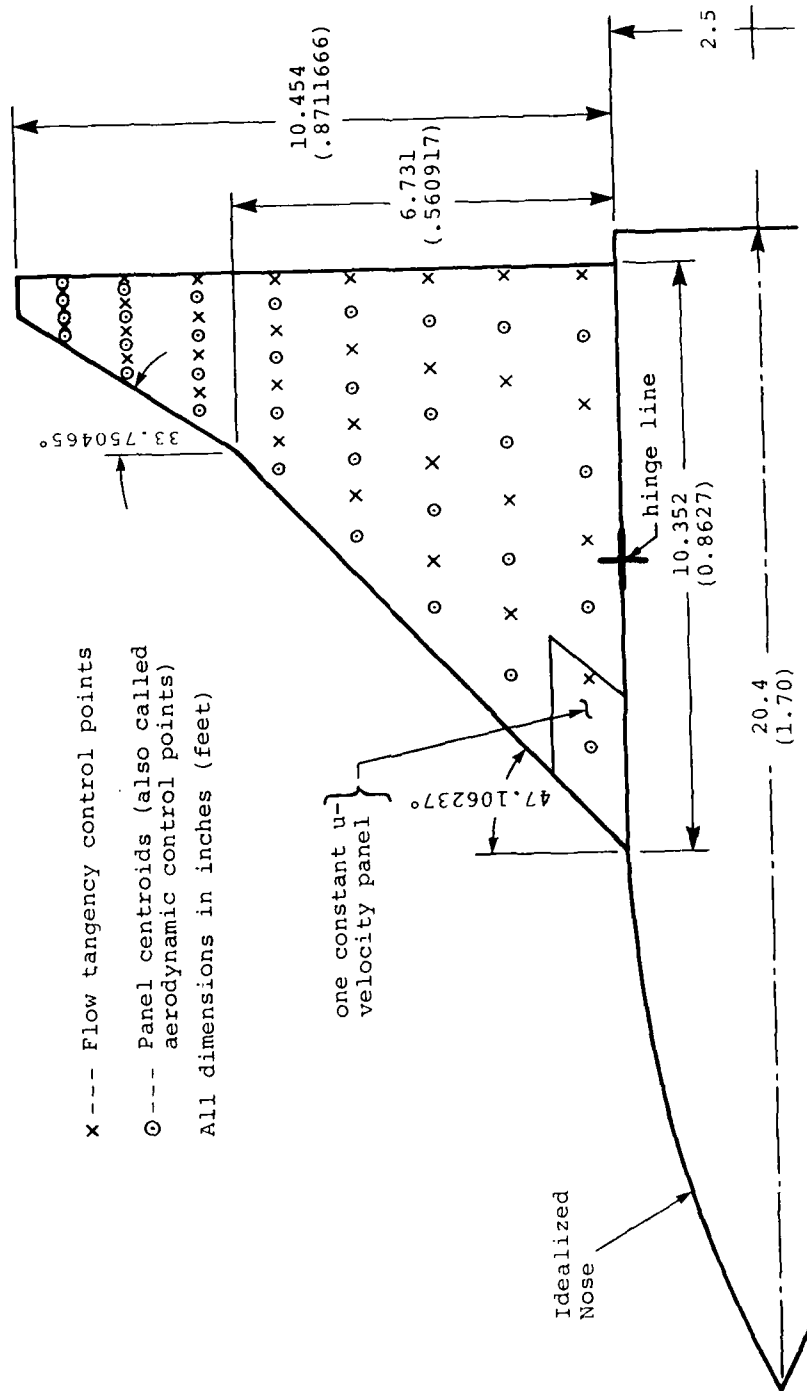


Figure 36.- Fin mounted on axisymmetric body.

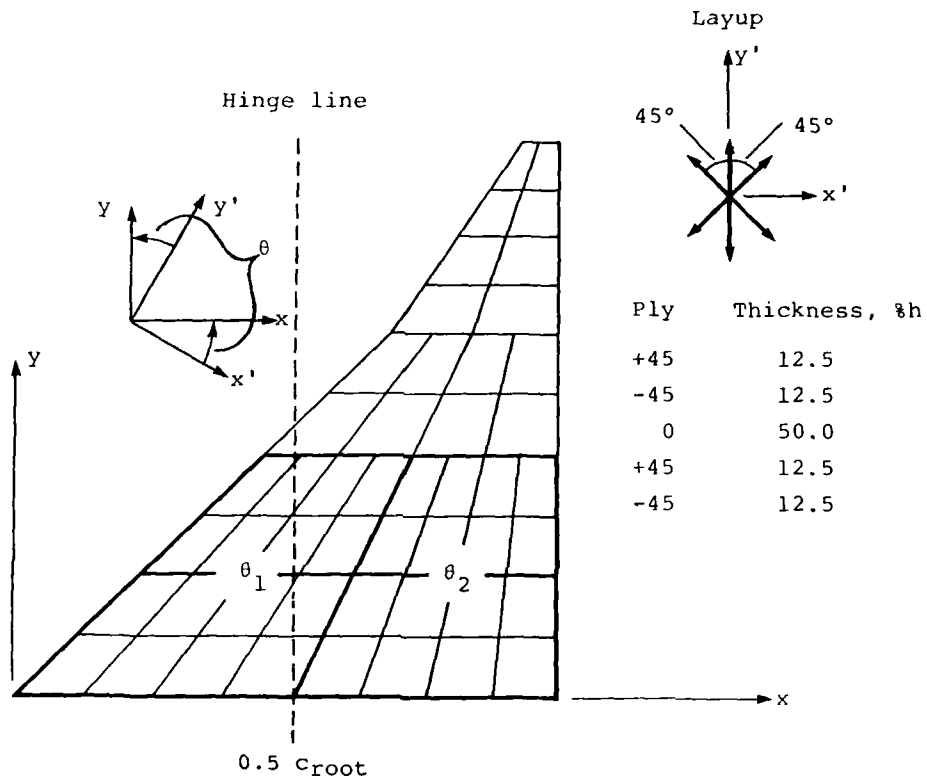


Figure 37.- Structural layout of example fin, with principal-axes directions defined by  $x'$  and  $y'$ .

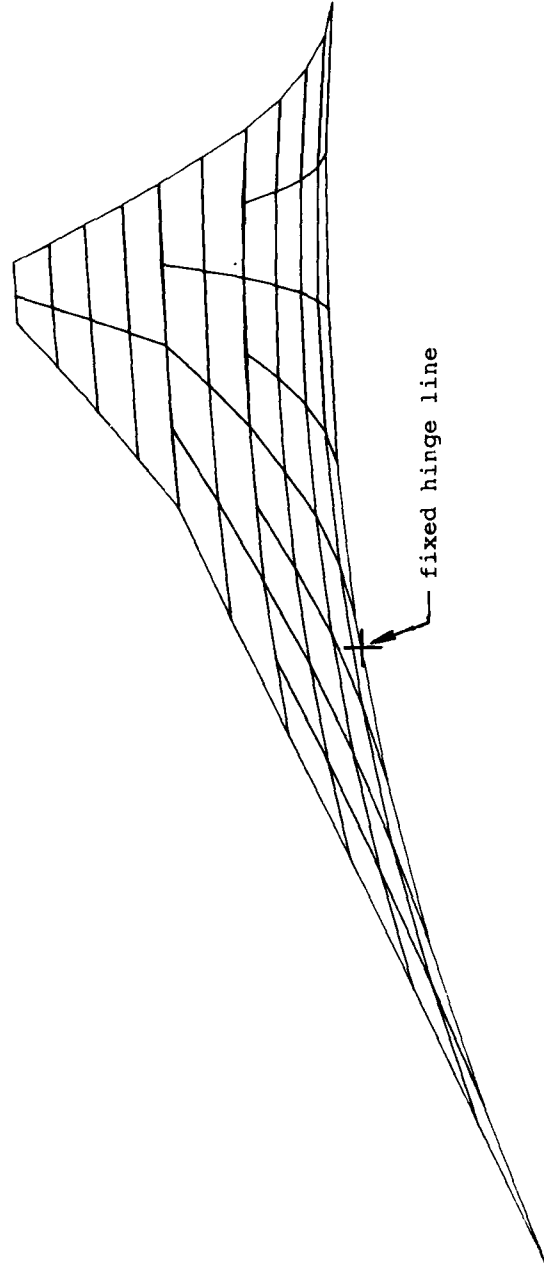


Figure 38.- Spanwise view of deformed composite fin;  
 $\theta_1 = \theta_2 = 45$  deg;  $M_\infty = 1.6$ ,  $\alpha = 15.4$  deg,  
altitude  $h = 30,000$  ft.

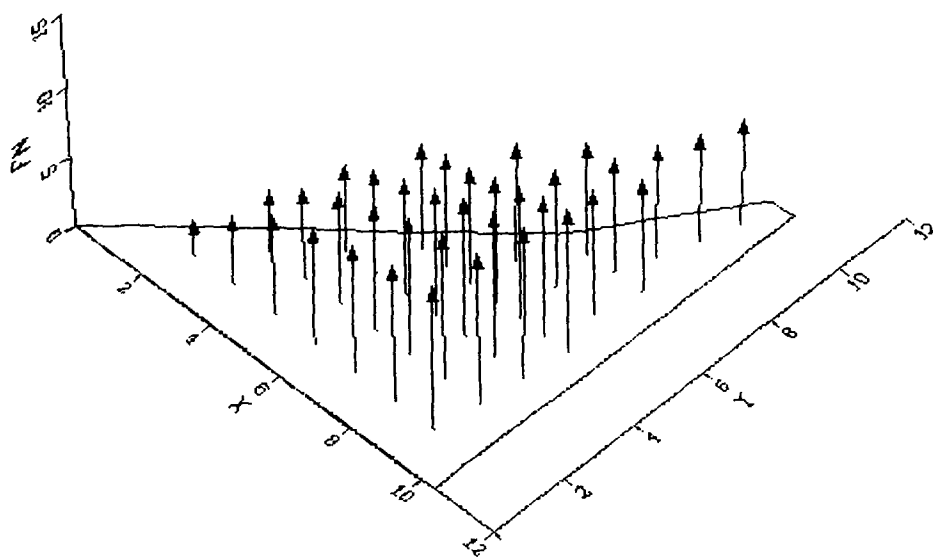


Figure 39.- Predicted distribution of forces on deformed fin;  
 $\theta_1 = \theta_2 = 45$  deg;  $M_\infty = 1.6$ ,  $\alpha = 15.4$  deg,  
altitude  $h = 30,000$  ft.



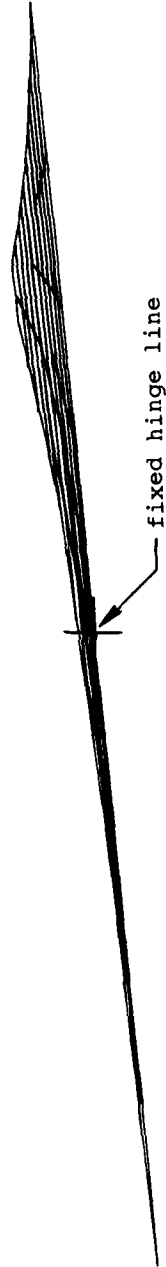


Figure 40.- Spanwise view of deformed aluminum fin;  
 $\theta_1 = \theta_2 = 45$  deg;  $M_\infty = 1.6$ ,  $\alpha = 15.4$  deg,  
altitude  $h = 30,000$  ft.

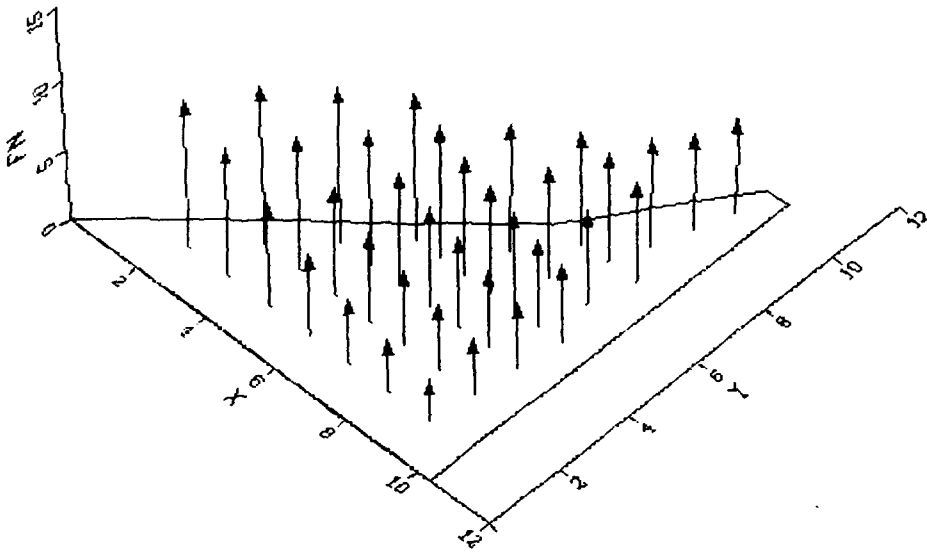


Figure 41.- Predicted distribution of forces on deformed aluminum fin;  $\theta_1 = \theta_2 = 45$  deg;  $M_\infty = 1.6$ ,  $\alpha = 15.4$  deg, altitude  $h = 30,000$  ft.

SEMI-EMPIRICAL METHODS FOR CONVENTIONAL  
AND UNCONVENTIONAL MISSILES

by  
Michael J. Hensch  
PRC Kentron  
303 Butler Farm Road  
Hampton, Virginia 23666  
USA

## SUMMARY

In the development and use of semi-empirical methods for prediction of the aerodynamic characteristics of modern missiles, one fact is exploited more than any other: the slenderness of the airframes and of the flows surrounding them. The first mathematical attempts to use this fact were made over thirty years ago and resulted in classical slender-body theory and the universally-known Pitts, Nielsen and Kaatari method for conventional missiles. In this lecture, it is shown that invoking slenderness for a missile in supersonic high angle-of-attack flow yields similarity forms which correlate data for affine bodies and wings in a particularly useful way. The equivalent angle-of-attack concept which is rooted in classical slender body theory is also presented together with extensions required for flows with high cross-flow Mach number, one of the similarity variables. Finally, it is shown that the classical two-term fits to normal-force and center-of-pressure-location data for isolated wings and bodies are inferior to one-term power-law fits to the data in similarity form.

## NOMENCLATURE

|                             |  |
|-----------------------------|--|
| $a$                         | = body radius  |
| $A$                         | = power-law coefficient for normal force   |
| $AR$                        | = aspect ratio of the wing alone   |
| $B$                         | = power-law exponent for normal force  |
| $b$                         | = span   |
| $c_D$                       | = pressure coefficient   |
| $c_r$                       | = centerline chord   |
| $C_m$                       | = pitching-moment coefficient  |
| $C_N$                       | = normal-force coefficient   |
| $C_{N_B}, C_{N_T}, C_{N_W}$ | = normal-force coefficient for the body alone, tail alone, and wing alone, respectively  |
| $C_{N_B(T)}, C_{N_B(W)}$    | = normal-force coefficient increment for the body in the presence of the tail and wing, respectively                                     |
| $C_{N_{BWT}}$               | = normal-force coefficient for complete wing-body-tail configuration   |
| $C_{N_F(B)}$                | = normal-force coefficient for a fin on a body   |
| $C_{N_T(B)}$                | = normal-force coefficient for the tail in the presence of the body  |
| $C_{N_W(B)}$                | = normal-force coefficient for the wing in the presence of the body;   |
| $k_1$                       | = similarity parameter, $\delta \cot \alpha$   |
| $k_2$                       | = similarity parameter, $M_\infty \sin \alpha$   |
| $k_3$                       | = similarity parameter, $\tan \alpha / AR$   |
| $k_B$                       | = body carryover factor for wing deflection  |
| $K_B$                       | = body carryover factor for wing undeflected   |
| $k_w$                       | = wing interference factor for wing deflection   |
| $K_w$                       | = wing interference factor for wing undeflected  |
| $K_\phi$                    | = wing interference factor for combined angle of attack and sideslip   |
| $l$                         | = body (or wing) length  |
| $LE$                        | = leading edge   |
| $L_\alpha$                  | = lift-curve slope   |
| $m_{22}$                    | = apparent mass for motion in the $Z_0$ direction  |
| $M_l$                       | = local Mach number  |
| $M_\infty$                  | = freestream Mach number   |
| $p$                         | = static pressure  |
| $p'$                        | = nondimensionalized static pressure, $p/q_\infty \sin^2 \alpha$   |
| $p_\infty$                  | = freestream static pressure   |
| $q_l$                       | = local dynamic pressure   |
| $q_\infty$                  | = freestream dynamic pressure  |
| $S_f$                       | = fin planform area  |
| $S_{ji}$                    | = planform area of fin $i$ , which is influenced by fin $j$  |
| $s_m$                       | = semispan of fin including the body   |
| $SR$                        | = reference area; planform for wings, base area for bodies   |
| $TE$                        | = trailing edge  |
| $u, v, w$                   | = flow velocity components in cylindrical coordinates  |
| $u', v', w'$                | = nondimensional flow velocity components, $u/U_\infty \cos \alpha$ , $v/U_\infty \sin \alpha$ , $w/U_\infty \cos \alpha$ , respectively |
| $U_\infty$                  | = freestream velocity  |
| $x, r, \phi$                | = cylindrical coordinates aligned with the body axis with origin at nose tip   |
| $x', r', \phi'$             | = nondimensionalized coordinates, $x/l$ , $r/b$ , $\phi$ , respectively  |
| $\bar{x}$                   | = axial or chordwise center-of-pressure location   |
| $x_0, y_0, z_0$             | = unrolled body coordinate system  |

|                  |  |
|------------------|--|
| $\bar{x}_w$      | = chordwise center-of-pressure location for wing alone                           |
| $\bar{x}$        | = chordwise center-of-pressure location for the wing in the presence of the body |
| $W(B)$           | = angle of attack  |
| $\alpha$         | = angle between body axis and wind velocity vector                               |
| $\alpha_c$       | = equivalent angle of attack   |
| $\alpha_{eq}$    | = equivalent angle of attack with no fins deflected                              |
| $\gamma$         | = ratio of specific heats  |
| $\delta$         | = wing or tail deflection angle; also slenderness parameter, $b/l$               |
| $\delta_j$       | = deflection angle for fin $j$   |
| $\epsilon$       | = semi-apex angle of delta wing  |
| $\Delta\alpha_v$ | = effective angle of attack due to the vortex field                              |
| $\phi$           | = bank angle   |
| $\Lambda_{ji}$   | = fin deflection factor  |
| $\rho$           | = density  |
| $\rho_\infty$    | = freestream density   |
| $\rho^*$         | = nondimensionalized density, $\rho/\rho_\infty$                                 |

## 1. INTRODUCTION

The timely design and analysis of modern, high-performance conventional and unconventional missiles require the use of rapid and accurate procedures for determining their aerodynamic stability, control and drag characteristics over a wide Mach number and angle-of-attack range. Despite impressive advances in computational fluid mechanics, the only methods which meet the above criteria are semi-empirical. By semi-empirical methods, we mean those calculational procedures which are based on a judicious combination of rational flow models and experimental and computational data bases. The first rational flow model for missiles was developed over thirty years ago as an extension of classical slender-body theory (SBT)<sup>1-3</sup>. That model is universally known as the Pitts, Nielsen and Kattari method (PNK)<sup>2,4</sup>. The PNK method was the first semi-empirical method which could be applied to all conventional missile configurations through the subsonic/transonic/supersonic speed regime for stability and control predictions. It uses SBT to properly add together the empirical results for the individual missile components. In the last decade, as demands for high-angle-of-attack performance have increased, the original PNK method has been modified and extended in a wide variety of approaches (e.g., see ref. 5-12). It is the purpose of this lecture to review the mathematical structure developed so far which underlies high angle-of-attack slender-body aerodynamics and to demonstrate some of the useful consequences of those results for semi-empirical methods. The primary emphasis of the lecture is on stability and control.

In the first part of the lecture, the slender-body reduction of the Euler equations for high-angle-of-attack hypersonic flow as given by V.V. Sychev<sup>13</sup> will be presented. Empirical correlations will be used to demonstrate that the similarity results obtained are valid for most supersonic flows of interest and for subsonic flows as well. The second part of the lecture will cover the equivalent-angle-of-attack concept (EAAC) and its origins in the component build-up approach and classical slender-body theory as combined in the PNK method. Results from the similarity analysis of the first part of the lecture will be used to show how to further extend the EAAC to handle nonlinear flow fields resulting from high cross-flow Mach numbers. The third part of the lecture will examine the application of high angle-of-attack similarity to improving the fitting of body-alone and wing-alone data.

## 2. HIGH ANGLE-OF-ATTACK SIMILARITY

The analysis given in this section is taken primarily from the papers by Sychev<sup>13</sup>, Hemsch<sup>14</sup>, and Barnwell<sup>15</sup>. The nomenclature primarily follows Sychev.

### 2.1 Near Field

Since the body and flowfield of interest are slender, we introduce the following dimensionless independent variables in cylindrical coordinates (see figure 1):

$$\begin{aligned} x' &= x/l & (1a) \\ r' &= r/b & (1b) \\ \phi &= \phi & (1c) \end{aligned}$$

and the dimensionless dependent variables

$$\begin{aligned} u' &= u/U_\infty \cos \alpha & (2a) \\ v' &= v/U_\infty \sin \alpha & (2b) \\ w' &= w/U_\infty \sin \alpha & (2c) \\ p' &= p/q_\infty \sin^2 \alpha & (2d) \\ \rho' &= \rho/\rho_\infty & (2e) \end{aligned}$$

All of the dimensionless variables are of order one. By substituting relations (1) and (2) into the governing steady-flow Euler equations and dropping higher-order terms in  $\delta = b/l$ , we obtain the following approximate set for a perfect inviscid gas with constant ratio of specific heats,  $\gamma$ ,<sup>13</sup>

$$\delta \cot \alpha \frac{\partial v'}{\partial x'} + v' \frac{\partial v'}{\partial r'} + \frac{w'}{r'} \frac{\partial v'}{\partial \phi'} - \frac{w'^2}{r'} = - \frac{1}{2\rho'} \frac{\partial p'}{\partial r'} \quad (3a)$$

$$\delta \cot \alpha \frac{\partial w'}{\partial x'} + v' \frac{\partial w'}{\partial r'} + \frac{w'}{r'} \frac{\partial w'}{\partial \phi'} + \frac{v'w'}{r'} = - \frac{1}{2\rho' r'} \frac{\partial p'}{\partial \phi'} \quad (3b)$$

$$\delta \cot \alpha \frac{\partial \rho'}{\partial x'} + v' \frac{\partial \rho'}{\partial r'} + \frac{w'}{r'} \frac{\partial \rho'}{\partial \phi'} + \rho' \left( \frac{\partial v'}{\partial r'} + \frac{1}{r'} \frac{\partial w'}{\partial \phi'} + \frac{v'}{r'} \right) = 0 \quad (3c)$$

$$\delta \cot \alpha \frac{\partial}{\partial x'} \left( \frac{\rho'}{\rho' \gamma} \right) + v' \frac{\partial}{\partial r'} \left( \frac{\rho'}{\rho' \gamma} \right) + \frac{w'}{r'} \frac{\partial}{\partial \phi'} \left( \frac{\rho'}{\rho' \gamma} \right) = 0 \quad (3d)$$

for the four unknowns  $v', w', p'$  and  $\rho'$ .

The approximate boundary condition on the surface of the body  $r' = r'(x', \phi')$  is given by

$$v' - \frac{w'}{r_1'} \frac{\partial r_1'}{\partial \phi} = \delta \cot \alpha \frac{\partial r_1'}{\partial x'} \quad (4)$$

The quantity

$$k_1 = \delta \cot \alpha \quad (5)$$

is the Sychev parameter relating thickness (or span) ratio and angle of attack. For missile flows, the value of this parameter is order one. The above derivation involved no assumptions regarding Mach number. Hence, equations (3) and (4) govern the near field solutions of all inviscid slender-body flows, regardless of Mach number.<sup>15</sup> (Note that  $u'$ , if needed, can be determined from Bernoulli's equation.) Slender-body theorists will recognize  $k_1$  as the inverse of the parameter introduced by J.H.R. Smith for delta wings with leading-edge separation.<sup>16</sup> Since the transport of vorticity is dominated by convection rather than dissipation, we can expect the above equation to govern slender vortical flows as long as the separation lines are only weakly dependent on Reynolds number.

## 2.2 Far Field

Sychev demonstrated that the shock relations also reduce to a set of four equations in the same four unknowns for shock waves which lie close to the body surface. The reduced shock equations depend only on  $\gamma$ ,  $k_1$ , and a second similarity parameter

$$k_2 = M_\infty \sin \alpha \quad (6)$$

Missile aerodynamicists will recognize  $k_2$  as the crossflow Mach number introduced by H.J. Allen.<sup>17</sup> Barnwell<sup>15</sup> has demonstrated that the above far-field analysis holds for

$$M_\infty \sin \alpha > 1 \quad (7)$$

He also shows that the Sychev formulation holds for subsonic values of the cross-flow Mach number if the flow is hypersonic and the body is sufficiently slender, i.e.,  $M_\infty \delta = O(1)$ .

If the independent variable  $x$  is replaced by the fictitious time variable

$$t = \frac{x}{U_\infty \cos \alpha} \quad (8)$$

the approximate relations (3) and (4) transform into the differential equations and boundary conditions determining unsteady two-dimensional flow in a cross-flow plane moving downstream at the rate  $U_\infty \cos \alpha$ . For this reason, it is conjectured that the above analysis holds for sufficiently slender bodies for any cross flow Mach number as long as  $M_\infty \cos \alpha > 1$ . Empirical correlations given by Hemsch<sup>18</sup> for both sharp-edged wings and smooth bodies bear out the conjecture.

## 2.3 Similarity

### 2.3.1 Pressure

For a perfect gas, the approximate relations (3) and (4) involve only the parameters  $k_1$ ,  $k_2$  and  $\gamma$  which demonstrates for affine bodies in the same perfect gas that all of the dimensionless dependent variables are equal at corresponding points of the

field if the similarity parameters  $k_1$  and  $k_2$  have the same values for the two cases. For example, since we have

$$p' = p'(x', r', \phi', k_1, k_2) \quad (9)$$

it is easy to show for perfect gases that  $p/p_\infty$  and  $c_p/\sin^2 \alpha$  are also similarity variables and are functions only of  $x', r', \phi', k_1$  and  $k_2$  (and  $\gamma$ ).

Miller and Wood<sup>18</sup> obtained an extensive set of supersonic leeside surface pressure data for thin sharp-edged delta wings which are useful for checking similarity. Data for three different delta wings with a two-fold aspect-ratio range are compared in figure 2 for nominal values of  $k_1$  and  $k_2$  of 3.9 and 0.40 respectively. The flow type is that of a classic vortex<sup>18</sup>. Note that the hoped-for collapse is evident when the data are plotted in similarity (scaled) form. Data for a different flow type are shown in figure 3. Two delta wings are compared for nominal values of  $k_1$  and  $k_2$  of 4.1 and 0.67 respectively. The flow type is that of a separation bubble plus cross-flow shock.<sup>18</sup> Again, the data in similarity form collapse as desired. These results are strong evidence that similarity holds for subsonic as well as supersonic crossflow Mach numbers.

### 2.3.2 Forces and moments.

For semi-empirical methods, we prefer to work with integrated forces and moments. Integrating the pressure relationship (9) over the body surface gives

$$\frac{C_N}{\sin^2 \alpha} = f_1(k_1, k_2) \quad (10)$$

$$\frac{C_m}{\sin^2 \alpha} = g_1(k_1, k_2) \quad (11)$$

where  $C_N$  and  $C_m$  are referred to the projected planform area.

Relations (10) and (11) are somewhat inconvenient for correlations since the left-hand sides tend to infinity for small angles of attack. It is also more convenient for comparison of different families of affine bodies to use the parameter

$$k_3 = \frac{\tan \alpha}{AR} = \frac{\text{constant}}{k_1} \quad (12)$$

Multiplying equation (10) by  $k_3$  and replacing  $k_1$  with  $k_3$ , we have the more convenient result

$$\frac{C_N}{AR \sin \alpha \cos \alpha} = f_2(k_2, k_3) \quad (13)$$

and dividing equation (11) by equation (10) gives

$$\frac{\bar{x}}{t} = g_2(k_2, k_3) \quad (14)$$

Equations (13) and (14) prove particularly useful for correlating experimental data. They also suggest an improved method for curve-fitting data for a single body as will be shown in section 4.

Hemsch<sup>14</sup> presents correlations based on equations (13) and (14) for five affine families of sharp-edged thin wings and smooth bodies. One of the wing correlations is given in figure 4. It is surprising to note that the correlations hold for an eight-fold range of aspect ratio up to an aspect ratio of four. Another surprising result of the correlations is that they can be represented accurately by a one-term power-law expression (straight-lines on a log-log plot), i.e.,

$$\frac{C_N}{AR \sin \alpha \cos \alpha} = A (\tan \alpha / AR)^B \quad (15)$$

and

$$\bar{x}/t = C (\tan \alpha / AR)^D \quad (16)$$

where  $A$ ,  $B$ ,  $C$  and  $D$  are functions of cross-flow Mach number. Hence, all of the data for  $\alpha = 0-60^\circ$ ,  $M_\infty = 1.60-4.63$ , and  $AR = 0.5-4.0$  can be represented by four functions of cross-flow Mach number. Those functions are given in figure 5 for the data of figure 4.

The advantage of using similarity cannot be overemphasized. Normally, one would attempt to fit the data for each wing with a two-term expression in  $\sin \alpha \cos \alpha$  and  $\sin^2 \alpha$ . Each coefficient would be a function of aspect ratio and  $M_\infty$  resulting in eight functions of Mach number rather than two in crossflow Mach number. Furthermore, the results enhance interpolation and extrapolation in both aspect ratio and Mach number.

Another advantage of using similarity variables is that  $C_N$  and  $\bar{x}$  data can apparently always be well represented by simple power-law expressions. This also makes it easier to extrapolate the data to higher values of  $M_\infty$ . Finally, it is important to note that using similarity allows a drastic reduction in the amount of testing needed for developing the necessary wing and body data bases for use in the component buildup method.

### 2.3.3 Vortex strengths and positions.

Semi-empirical methods for missiles require data bases for vortex strengths and positions. From the similarity results above, it is clear that the positions of vortices over affine bodies are related in the cross flow plane by

$$\begin{aligned}y_V' &= y_V'(x', k_1, k_2) \\z_V' &= z_V'(x', k_1, k_2)\end{aligned}$$

Furthermore, the circulation for the contour  $C$  in the cross flow plan is given by

$$\Gamma = \int_C \vec{q}_C \cdot d\vec{s} \quad (18)$$

where  $\vec{q}_C$  is the cross flow velocity vector and  $d\vec{s}$  is an infinitesimal arc length on  $C$ . Normalizing  $\vec{q}_C$  and  $d\vec{s}$  according to relations (1) and (2) gives

$$\begin{aligned}\Gamma' &= \int_C \vec{q}_C' \cdot d\vec{s}' \\ &= \Gamma'(x', k_1, k_2) \text{ for } c'\end{aligned} \quad (19)$$

where  $\Gamma' = \Gamma/U_\infty \sin \alpha$  and  $c'$  is the scaled contour for integration.

A more familiar scaling is obtained if we divide  $x'$  by  $k_1$  to get

$$\frac{\Gamma}{U_\infty b \sin \alpha} = F\left(\frac{x}{b}, -\tan \alpha, \delta \cot \alpha, M_\infty \sin \alpha\right) \quad (20)$$

For very slender bodies,  $\delta \cot \alpha \rightarrow 0$ , and equation (19) tends to the familiar form for the impulsive flow analogy (e.g., see reference 9).

Unfortunately, due to the excessive cost of obtaining quantitative flow field information, the author has been unable to verify equation (20) with experimental data. However, an extensive set of solutions for leading-edge separation from thin delta wings has been obtained at NASA Langley Research Center by J.M. Luckering for incompressible flow<sup>19</sup>. The code used models both the surface of the wing and the rolled-up leading-edge vortex with linearly varying doublet panels<sup>20</sup>. The strength of the vortex core, its position in the cross-flow plane and the chordwise loading distribution are plotted in similarity coordinates in figure 6 for  $\tan \alpha/AR=0.25$ . Note that even though the loading distribution does not exhibit similarity due to the violation of the slenderness criterion at the trailing edge, the vortex parameters do.

The results obtained in this section demonstrate that for supersonic flows, at least, any semi-empirical method must be consistent with the similarity relations given above. Barnwell<sup>15</sup> has shown that, for subsonic flows,  $k_1 = \delta \cot \alpha$  and  $M_\infty$  are the correct similarity parameters so that equation (10) is replaced, for example, by

$$\frac{C_N}{\sin^2 \alpha} = f_3(k_1, M_\infty) \quad (21)$$

## 3. EQUIVALENT ANGLE-OF-ATTACK

### 3.1 INTRODUCTION

Before describing the equivalent angle-of-attack concept (EAAC), it is useful to review the component buildup method as developed by Pitts, Nielsen and Kattari<sup>4</sup>. The account given here will necessarily be brief. A detailed account can be found in reference 21. As its name indicates, the component buildup method consists of summing up the aerodynamic characteristics of the major airframe parts in isolation (e.g., body, wing, tail, etc.) and then tacking on to those sums the loads produced by component interference. For tactical missile designs, the interference effects are often first order and nonlinear. The key to developing a successful method lies in adequately estimating the interference effects. The authors of the PNK approach used slender-body theory to develop interference coefficients so that empirical results for component loads could be used directly.

It is convenient to illustrate the ideas discussed in this section by considering the wing-body-tail configuration shown in Fig. 7. The configuration is shown in the

"plus" attitude and is composed of an axisymmetric nose, a cylindrical afterbody, and two sets of in-line cruciform fins. Either set of fins can be used for control as long as the fins are all-movable. In practice, the component buildup method is also applied to airframes composed of nonaxisymmetric bodies and noncruciform fins placed anywhere around the body circumference.

Historically, the normal-force coefficient for the case illustrated in Fig. 7 has been broken down as in equ. (22)

$$C_{NBWT} = C_{NB} + C_{NW(B)} + C_{NB(W)} + C_{NT(B)} + C_{NB(T)} + C_{NT(W)} \quad (22)$$

The subscripts are defined as follows:

BWT = complete wing-body-tail configuration  
 B = body alone  
 W(B) = wing in the presence of the body  
 B(W) = increment for the body due to the presence of the wing  
 T(B) = tail in the presence of the body  
 B(T) = increment for the body due to the presence of the tail  
 T(W) = tail in the presence of the wing

Because of the high speeds of modern tactical missiles, the influence of the tail on the wing (W(T) term) can be neglected unless the two sets of fins are very closely coupled. Only static contributions will be considered in this section. Unsteady effects can be included, if necessary, in a straightforward manner. To develop the main ideas, it is sufficient to consider the normal force only. Complete details of the approach can be found in references 2, 4-6, 9, 11, 12, and 21-25.

It is convenient to think of the terms in equ. (22) as arising from a linear superposition of flowfields, which is strictly true, of course, only if the equations governing the flow are linear. This was indeed the case for early missile airframes that flew at low-to-moderate supersonic speeds and small angles of attack. However, the notion is useful far beyond the linear range<sup>5</sup>. It is, in fact, the key to consistent and comprehensive extensions of the component buildup method to missiles with nonlinear aerodynamic characteristics<sup>21-25</sup>.

The body-alone term in equ. (22) is defined as that load which would act on the body if it were isolated in the freestream at the angle of incidence seen by the complete configuration,  $\alpha_c$ . The W(B) term represents the load acting on the exposed wing panels in the  $X_0-Y_0$  ("horizontal") plane. The body acts as a sort of imperfect reflection plane for the panels. Hence, it is convenient to think of the panels as halves of a wing alone (see figure 7)<sup>26</sup>. If the body diameter is very small relative to the wingspan, then two opposing exposed panels essentially act as if they constitute an isolated wing in the freestream. If the body diameter is very large relative to the wingspan, the body acts as a reflection plane for each panel and, again, it is appropriate to consider a wing alone composed of two exposed panels joined at their root chords. However, because of the disturbance of the freestream flowfield by the body, the angle of attack experienced by this "wing along" is not equal to the body angle of attack plus the fin deflection angle.

The B(W) term can be thought of as resulting from "carryover" to the body of the pressure field created by the wing panels. For linear conditions on the "plus" configuration and the nose sufficiently upstream of the wing, the B(W) term is proportional to the W(B) term<sup>2</sup>. For the case where vorticity is shed from the body, the effect of the wing on the development of that vorticity may have to be taken into account.

The T(B) and B(T) terms are similar to those for the wing, but the T(W) term is quite different. The wing, in the presence of the body, generates a change in the flow-field which would otherwise be seen by the tail panels if the wing were not present. For small angles of attack, that change can usually be represented by the flowfields of partially or fully rolled-up vortex sheets shed from the wing panels<sup>2</sup>. If vorticity is shed from the body, the effect of the wing on that flow field near the tail may have to be accounted for.

The PNK component buildup approach yielded the following equation for  $C_{NBWT}$

$$C_{NBWT} = C_{NB} + [(K_W + K_B)\alpha_c + (k_W + k_B)\delta]_{wing} \frac{\partial C_{NW}}{\partial \alpha} \Big|_{\alpha=0} + [(K_W + K_B)\alpha_c + (k_W + k_B)\delta + (1 + \frac{K_B}{K_W})\Delta\alpha_v]_{tail} \frac{\partial C_{NT}}{\partial \alpha} \Big|_{\alpha=0} \quad (23)$$



where the interference coefficients are defined by

$$K_W = C_{N_W(B)}/C_{N_W}; \quad \alpha_c \neq 0, \delta_f = 0 \quad (24a)$$

$$K_B = C_{N_B(W)}/C_{N_W}; \quad \alpha_c \neq 0, \delta_f = 0 \quad (24b)$$

$$k_W = C_{N_W(B)}/C_{N_W}; \quad \alpha_c = 0, \delta_f = 0 \quad (24c)$$

$$k_B = C_{N_B(W)}/C_{N_W}; \quad \alpha_c = 0, \delta_f = 0 \quad (24d)$$

All of the above interference coefficients are functions of the span-to-body diameter ratio only for the SBT approximation. In the usual application of the PNK approach, the wing-alone and tail-alone normal-force coefficient slopes are obtained from linear theory or experimental data. The wing-carryover interference coefficients,  $K_W$  and  $k_W$  are given by SBT, and the body-carryover interference coefficients are obtained for SBT for subsonic and transonic flow. For supersonic flow a linear-theory estimate for  $K_B$  is obtained assuming the body to be a flat-plate extension of the wing panels and  $k_B$  is assumed to be equal to  $K_B^2$ .

The  $\Delta\alpha_v$  is obtained by assuming that the wing trailing and/or leading edge vorticity is fully rolled up at the wing trailing edge and travels in the freestream direction to the vicinity of the tail section. Several different methods based on reverse-flow theory<sup>4,26</sup> have been developed to determine the  $\Delta\alpha_{eq}$  acting on each tail fin due to the presence of the wing vortices.

Equation (22) is not limited to missiles with bodies with circular cross sections. However, to use it for general shapes, one must compute the necessary slender-body interference coefficients. This is a straight-forward albeit messy task since it is only necessary to solve the two-dimensional Laplace equation for the incompressible flow about the shape of the body in the cross-flow plane. Recent examples of such solutions are given by Stahara<sup>27</sup> who used analytic transformations to get solutions, Sigal and Lapidot<sup>28</sup> who used the Schwarz-Christoffel transformation and Beall<sup>29</sup> who used surface singularities. In order to break out the individual interference factors,  $K_W$ ,  $K_B$ ,  $k_W$ , and  $k_B$ , it is necessary to obtain the full SBT solutions. However, for simple stability analysis for low supersonic speeds or less, it is often sufficient to obtain the combined quantity  $K_{WB} = K_W + K_B$ . Fortunately, this is a fairly straight-forward procedure if the apparent-mass method is used<sup>28</sup>. It can be shown from the analysis by Sacks<sup>30</sup> that the SBT lift-curve slope for an axial section of an arbitrary slender body is given by

$$L_a = U_\infty^2 [(m_{22})_{x=x_2} - (m_{22})_{x=x_1}] \quad (25)$$

where  $m_{22}$  is the apparent mass for the cross section translating in the  $Z_a$  direction (wind plane). The quantity  $m_{22}$  has already been computed for many shapes.

A simple calculation for a conventional unrolled missile will illustrate the use of equ. (25). By definition

$$\begin{aligned} K_{WB} &= \frac{(L_a)_{WB}}{(L_a)_W} \\ &= \frac{[(m_{22})_{TE} - (m_{22})_{LE}]_{WB}}{(m_{22})_{TE,W}} \end{aligned} \quad (26)$$

From reference 2, we can determine the necessary apparent masses for a thin wing-circular cylinder combination

$$(m_{22})_{TE} = \pi \rho_\infty [a^2 + (s_m^2 - a^2)/s_m^2] \quad (27)$$

$$(m_{22})_{LE} = \pi \rho_\infty a^2 \quad (28)$$

$$(m_{22})_{TE,W} = \pi \rho_\infty (s_m - a)^2 \quad (29)$$

Substituting (27)-(29) into (26) gives

$$K_{WB} = (1 + a/s_m)^2 \quad (30)$$

It is interesting to note that  $m_{22}$  can be computed from the residue of the transformation which maps the missile cross section into a circle<sup>2</sup>. Skulsky<sup>31</sup> developed a simple mapping technique which yields a truncated Laurent series for the transformation. Since the coefficient of the leading term in the series is the residue, Skulsky's technique should prove useful in obtaining  $m_{22}$  for arbitrary shapes.

In the next subsection, it is shown that nonlinear wing effects can be handled if  $K_W$  and  $K_B$  are known separately. In this case the simplest procedure is to estimate  $K_W$  by computing the average upwash a fin would see in the presence of the body-alone flowfield and then using equ. (26) to get  $K_B$ .

### 3.2 Equivalent Angle-of-Attack Concept

Equation (23) is a useful expression for the linear range and has been applied successfully for more than 30 years. The key to extending it into the nonlinear range is to consider the wing and tail panel (fin) loads separately from those acting on the body. The following analysis will apply to either finned sections in the "plus" attitude. The coefficient for the normal force acting on one of the (horizontal) wing panels of the configuration in Fig. 7 is given by

$$C_{N_{W(B)}} = (K_W a_c + k_W \delta + \Delta a_v) \left. \frac{\partial C_{N_W}}{\partial a} \right|_{\alpha=0} \quad (31)$$

where  $\Delta a_v$  represents the effect of any vortices generated upstream of the finned section. If we define an equivalent angle of attack as

$$\alpha_{eq} = K_W a_c + k_W \delta + \Delta a_v \quad (32)$$

then a reasonable nonlinear extension of equ. (31) would be to write  $C_{N_{W(B)}}$  as a function of  $\alpha_{eq}$ ,

$$C_{N_{W(B)}} = C_{N_W}(\alpha_{eq}) \quad (33)$$

Equation (33) yields eq. (31) for the linear range of the  $C_{N_W}$  curve and extends the method into the nonlinear range in a reasonable manner. Equ. (33) is illustrated in figure 8. If Eq. (33) is to be a useful nonlinear extension of modified slender-body theory, it should correlate fin-on-body data. Normal-force data for a set of moderate aspect-ratio fins mounted at the shoulder of a 3-caliber tangent-ogive nose plus cylindrical afterbody are presented in figure 9 as a function of  $\alpha_{eq}$  for two different Mach numbers. The body vortex and nose effects are small for these cases. Clearly, the correlations are adequate for engineering estimates. For very large angles of attack the  $\alpha_{eq}$  definition equ. (32) should be modified as described in a later section.

To obtain the body carryover load corresponding to the fin load given by equ. (33), we assume that the load ratio is given by the SBT value, i.e.,

$$\frac{C_{N_{B(W)}}}{C_{N_{W(B)}}} = \left[ \frac{C_{N_{B(W)}}}{C_{N_{W(B)}}} \right]_{SBT} = \frac{K_B}{K_W} \quad (34)$$

Hence, once the fin normal force has been found [using equ. (33)], the body carryover normal force due to that fin load is given by equ. (34). However, because the preceding carryover was derived using the small angle approximation, it is probably better to take into account the effect of fin deflection by assuming that only the component of the fin normal force which is perpendicular to the body axis actually contributes to the body carryover load.

Estimation of the coordinates of the fin center of pressure is a different matter. Such information is essential, of course, for hinge-moment calculations. Since  $C_{N_{W(B)}}$  was correlated successfully with  $\alpha_{eq}$ , it seems reasonable to try the following:

$$\frac{\bar{x}_{W(B)}}{c_r} = \frac{\bar{x}_W(\alpha_{eq})}{c_r} \quad (35)$$

Since it has already been shown that  $C_N$  can be correlated with  $\alpha_{eq}$ , it should be possible to correlate center-of-pressure data as a function of the fin normal-force coefficient; i.e.,

$$\bar{x} = \bar{x}(C_N) \quad (36)$$

The present correlation does not account for strong body vortex effects. However, this should not be a problem for most situations. Several correlations are presented in figure 9 for  $\bar{x}$  for a set of rectangular fins mounted horizontally about 10 diameters aft of the nosetip of a tangent-ogive cylinder combination<sup>21</sup>. This particular set of data was chosen for illustration because rectangular fins experience very large chordwise excursions of  $\bar{x}$ . Note that the correlations are adequate for engineering use except for the region of incipient stall for  $M_\infty = 0.8$  and for the smaller values of  $C_N$  which have fairly large error bands for  $\bar{x}$ . Similar results are obtainable for the lateral location of the center of pressure<sup>5, 21</sup>.

### 3.3 Extension to Include Effects of Bank

The analysis presented so far has been concerned only with the longitudinal characteristics of a configuration which is symmetric about the plane containing the velocity vector and the body axis. That information is useful for estimates early in the design process for cruise and turning performance. However, a more general analysis must include the effects of bank and arbitrary fin deflections.

For the case with no fin deflection and no effects of vorticity, it can be shown<sup>2, 5</sup> that the load on fin 4 is given by

$$C_{NF(B)} = (K_W a_c \cos \phi + \frac{2}{AR} K_\phi a_c^2 \sin 2\phi) \frac{\partial C_{NW}}{\partial \alpha} \Big|_{\alpha=0} \quad (37)$$

where  $\phi$  is the fin bank angle as shown in figure 11. The subscript F is used to denote a fin rather than W because of the loss of symmetry with arbitrary bank and fin deflections. The slender-body values of  $K_\phi$  are dependent only on the  $a/s_m$  ratio and are given in figure 12.

The slender-body effects of arbitrary fin deflection at zero angle of attack have been computed by Nielsen et al.<sup>27</sup>. The result for the equivalent angle of attack induced on fin i by the deflection of all of the fins is

$$(\alpha_{eq\delta})_i = \sum_{j=1}^4 \Lambda_{ji} \delta_j \quad (38)$$

The slender-body values of the control effectiveness parameter  $\Lambda_{ji}$  are dependent only on the  $a/s_m$  ratio and are given in Fig. 11 for fin 4 deflected only. The quantity  $\Lambda_{44}$  is less than unity because the body is an imperfect reflection plane. Note that the carryover to adjacent and opposite fins decreases as the fin span decreases relative to the body diameter. Using equ. (37) and (38), we find that the expression for  $\alpha_{eq}$  for fin i with arbitrary bank and fin deflection is

$$\alpha_{eq_i} = K_W a_c \cos \phi_i + \frac{2}{AR} K_\phi a_c^2 \sin 2\phi_i + \sum_{j=1}^4 \Lambda_{ji} \delta_j + \Delta \alpha_{v_i} \quad (39)$$

For increasing supersonic Mach numbers, the Mach lines are swept more sharply downstream. Consequently, the influence of one fin on the other in the same finned section decreases as  $M_\infty$  increases (for  $M_\infty > 1$ ). An approximate analysis based on linear theory for estimating this effect is given in ref. 27, Appendix D. The method determines the area of fin i which is influenced by fin j, and it is assumed that the slenderbody theory estimate for fin influence,  $\Lambda_{ji}$ , should be reduced by the ratio of that area to the fin planform area, i.e.,

$$\Lambda_{ji}(M_\infty) = \Lambda_{ji} \Big|_{\text{SBT}} \frac{S_{ji}(M_\infty)}{SF} \quad (40)$$

Formulas for determine  $S_{ji}$  are given in ref. 27.

It should be noted that the method described above is based on inviscid linear theory. In real flows, the influence of fin j on fin i will depend nonlinearly on the state of the body incidence and bank angles, as well as  $M_\infty$ . No engineering methods exist for estimating these non linear effects.

The equivalent angle-of-attack formulation of equ. 39 was obtained by linearly adding the contributing angle-of-attack components. It is basically a small angle-of-attack formulation and should not be used for configuration angles of attack greater than about 30 degrees. A nonlinear formulation can be obtained by linearly adding the velocity components rather than the angles of attack. The result is<sup>5</sup>

$$\tan \alpha_{eq_i} = K_W \tan \alpha_c \cos \phi_i + \frac{2}{AR} K_\phi \tan \alpha_c \sin \alpha_c \sin 2\phi_i + \tan \Delta \alpha_{v_i} \quad (41)$$

and

$$\alpha_{eq_i} = \alpha_{eq_i} + \sum_{j=1}^4 \Lambda_{ji} \delta_j \quad (42)$$

where  $\alpha_{eq}$  is the equivalent angle of attack for no fin deflection.

#### 3.4 Effect of High Cross-Flow Mach Number

Up to this point, it has been assumed that the nonlinear effects of high angle-of-attack flows can be accounted for in a component buildup method by using the equivalent angle-of-attack formulas together with data for the wing-alone characteristics. Furthermore, we have implicitly assumed that (1) the interference factors  $K_W$ ,  $K_R$ , and  $K_\phi$  do not change with angle of attack, and (2) the dynamic pressure and Mach number of the flow near the fins are nearly equal to their freestream values. These implicit assumptions are true, of course, for the linear theory from which the present approach has been derived. However, as the missile's Mach number and angle of incidence relative to the freestream increase, the two implicit assumptions become increasingly less valid. Fortunately, proper accounting for the changes will allow extension of the FAAC for  $M_\infty \sin \alpha > 1$ . This is important for analysis of high-q turns at high altitude.

The effect of body incidence angle on  $K_W$  is shown in fig. 13 for a typical case. The  $AR = 1$ ,  $\lambda = 0.5$  fins are mounted at the base of a 10-caliber body in the "plus" attitude and are not deflected. The  $a/s_m$  ratio is 0.5. The fin-on-body data were taken from the vortex-free data tables compiled by Nielsen et al.<sup>32</sup>. The wing-alone data used to compute the  $a_{eq}$  values were taken from the data base compiled by Baker<sup>33</sup>. The curves of Fig. 13 can be collapsed into a single line as shown in Fig. 14 if the similarity variable  $k_2 = M_\infty \sin \alpha$  is chosen for the independent variable (see section 2). The success of this correlation suggests that compressibility is the primary culprit in the loss of favorable body-fin interference.

Additional data showing the degradation of favorable interference with increasing  $k_2$  are presented in figure 15 for another body-tail configuration with  $AR=0.5$ ,  $\lambda=0.5$  cruciform fins. The  $a/s_m$  ratio is 0.5 and the fins are undeflected. Data for two roll angles,  $\phi=0$  ("plus") and 40 deg. are given. Wing-alone data were taken again from Baker's data base<sup>33</sup>. The fin-on-body data were taken from ref. 34. For this case, the vortex effects have not been subtracted out. Fig. 15 shows the effect of  $M_\infty \sin \alpha$  on the full normal force generated by the addition of the fins normalized by the normal force which would be generated by the wing alone at the body incidence angle. In addition to the degradation of favorable interference as seen previously in Fig. 14, a strong effect of roll angle is apparent.

A similar kind of dependence on  $k_2 = M_\infty \sin \alpha$  is exhibited by the fin control effectiveness. A dramatic way of demonstrating this is to plot the variation of yaw-control effectiveness with respect to  $k_2$  for the "plus" attitude. The  $a_{eq}$  formulation of Eqs. (41) and (42) would predict no variation of  $C_{NF(B)}$  at  $\phi=+90$

deg. with body incidence angle. The results shown in Fig. 16 for cruciform fins mounted near the base of a 12-caliber ogive-cylinder body demonstrate otherwise. The control effectiveness at  $\phi=-90$  degrees (leeward meridian) of the fin which is deflected 20 degrees begins to decrease at  $k_2 = 0.3$  and eventually becomes negligible. On the other hand, the control effectiveness of the fin at  $\phi=90$  degrees (windward meridian) increases beyond  $k_2 = 0.3$  to as much as four times the value for  $\alpha_c = 0$ .

Additional insight into the effect of high cross-flow Mach number on control effectiveness can be obtained by considering the change in  $C_{NF(B)}$  with bank angle

for a given body incidence angle and freestream Mach number as shown in Fig. 17 for  $k_2=1.54$ . The configuration is the same as that of Fig. 16. The fin of interest is deflected 0, +20, and +40 degrees, and the others are undeflected. A strong variation in control effectiveness with bank angle is apparent. This deviation from SBT (Eqs. (41) and (42)) is shown in reference 6 to be a very strong function of  $k_2 = M_\infty \sin \alpha$ . This is due to the local dynamic pressure,  $q_\ell$ , and local Mach number,  $M_\ell$ , changes seen by the fins. For small values of  $k_2$ ,  $q_\ell$ , and  $M_\ell$  are nearly equal to  $q_\infty$  and  $M_\infty$  respectively. But for values of  $k_2$  on the order of one or greater, compressibility effects cause  $q_\ell$  and  $M_\ell$  to vary significantly in the flow field surrounding the body.

It turns out that the EAAC and Eqs. (41) and (42) can still be used if  $q_\ell$  and  $M_\ell$  are taken into account<sup>6</sup>. To do this, i.e., to obtain the  $a_{eq}$  for a given fin condition, the normal-force coefficient must first be normalized to an appropriately averaged  $q_\ell$  obtained from body-alone data or finite-difference solutions. The, in solving Eq. (33) for  $a_{eq}$ , the wing-alone curve for an appropriately averaged  $M_\ell$  must be used rather than  $M_\infty$ . An example of the success of this approach can be seen in figure 18 in which  $A_{ij}$  has been extracted from the data of figure 17 using average  $q_\ell$  and  $M_\ell$  values obtained from Euler finite-difference solution<sup>6</sup>. It can be seen that, except for a small region near the leeward meridian, the  $A_{ij}$  extracted from the data of figure 17 are properly independent of fin deflection and bank angle. It is suspected<sup>6</sup> that the bank angle dependence near the leeward meridian is due to problems with the finite-difference solver (probably, insufficient grid resolution).

It should be noted from the results of section 2 that  $q_\ell$  and  $M_\ell$  are not direct functions of  $k_2 = M_\infty \sin \alpha$ . In terms of dependent variables which are functions of  $k_2$ ,  $q_\ell$  is given by

$$\frac{q_\ell}{q_\infty} = \rho' [(u'^2 + v'^2) \sin^2 \alpha + w'^2 \cos^2 \alpha] \quad (43)$$

and  $M_\ell$  is given by

$$\left[ \frac{M_\ell^2}{M_\infty^2} \right] = \frac{q_\ell / q_\infty}{p_\ell / p_\infty} \quad (44)$$

where  $p_\ell / p_\infty$  is a function of  $k_2$  (see section 2).

## 4. COMMENTS ON METHODS FOR ISOLATED BODIES AND WINGS

In order to use the component build-up method for missiles, it is essential that accurate procedures be available for computing the aerodynamic characteristics of isolated bodies and wings for the Mach number and angle-of-attack ranges of interest. The most-often used approaches are based on either the cross-flow drag concept or a two-term fit to the variation of each parameter with angle of attack. Cautionary comments on the crossflow drag concept are given by means of an example in section 4.1. In section 4.2 it is shown that fitting data in similarity form is superior to the standard quadratic fits.

## 4.1 Cross-flow drag concept

The cross flow drag concept uses the following form for the normal-force coefficient

$$C_N = C_{N\alpha} \sin\alpha \cos\alpha + c_{dC} \frac{S_D}{S_R} \sin^2\alpha \quad (45)$$

The cross flow drag coefficient,  $c_{dC}$ , is supposed to be given by the drag acting on a two-dimensional cylinder with the same cross-section as the body of interest. Since the flow model is 2-D, it is expected that  $c_{dC}$  is a function of Reynolds

number and cross-flow Mach number only. The quantity  $c_{dC}$  for 2-D circular cylinders has been tabulated from an extensive data base by Jørgensen<sup>10</sup>. Jørgensen also suggested a way to use the circular cylinder data for other shapes<sup>10</sup>. This method is based on Newtonian flow theory.

The cross-flow-drag concept usually works adequately well for slender bodies with relatively short noses and boattails and long circular-cylinder sections. However, for bodies of moderate fineness ratio, it can give serious errors. The problem can be illustrated by considering a data set obtained by Landrum for a 6 2/3 caliber tangent-ogive-cylinder<sup>35</sup>. The body is shown in figure 19. The data were obtained for  $-4^\circ \leq \alpha \leq 60^\circ$  and  $1.60 \leq M_\infty \leq 4.63$ . The cross-flow drag coefficient has been extracted from the data and is shown in figure 20. Note that there is essentially no correlation. Similar results occur for moderate aspect-ratio wings. Clearly, the crossflow drag concept should be used with caution for all but very slender, nearly cylindrical, bodies.

## 4.2 Two-Term Fits

The classic two-term fits for longitudinal aerodynamic characteristics are

$$C_N = C_{N\alpha} \alpha + K_1 \frac{S_D}{S_R} \alpha |\alpha| \quad (46)$$

and

$$C_N = C_{N\alpha} \sin\alpha \cos\alpha + K_2 \frac{S_D}{S_R} \sin^2\alpha \quad (47)$$

Equation (46) is simply a quadratic fit in  $\alpha$  while equation (47) is based on the crossflow concept. The  $C_{N\alpha}$ ,  $K_1$ , and  $K_2$  coefficients are presumed to be functions of body or wing shape and free-stream Mach number only.

For center-of-pressure-location fits, the two-term form corresponding to equation (46) is

$$\bar{x} = \bar{x}_{\alpha=0} + K_3 |\alpha| \quad (48)$$

where  $\bar{x}_{\alpha=0}$  and  $K_3$  are presumed to be functions of body or wing shape and  $M_\infty$  only. For the crossflow concept, the force corresponding to the first term of equation (47) is assumed to act at  $\bar{x}_{\alpha=0}$  while the force corresponding to the second term is assumed to act at the area centroid.

Landrum's<sup>35</sup> data can be used again to check equation's (46) and (47) for moderate fineness ratio bodies. For the  $C_N$  data at  $M_\infty=1.60$ ,  $C_{N\alpha}$  was extracted by a

least-squared fit to the data points in the  $-4^\circ \leq \alpha \leq 4^\circ$  range. The coefficients  $K_1$  and  $K_2$  were then extracted by least-squares fits to the differences between  $C_N$  and the first terms of equation (46) and (47) respectively. The results are shown in figure 21. At first glance, the fits appear to be good with equation (47) giving somewhat better results for the higher angles of attack. However, figure 21 is misleading because of the large scale needed to show the high angle-of-attack data. The actual errors given by the fits are shown in figure 22. Note that the fits give very large errors for the low-to-moderate angle-of-attack range.

It appears from the results of reference 14 and section 2 that the natural way to express data fits for slender bodies is in similarity form. In fact, the correlations obtained in reference 14 suggest using the power-law forms of equation (15) and (16) to produce the fits. To check on this idea, Landrum's data<sup>35</sup> for  $M_\infty=1.60, 2.30, 2.96$  and 4.63 were used to extract the A, B, C and D coefficients. The results are given

in figure 23. The resulting normal-force fit for  $M_\infty=1.60$  is compared with the fits of equ. (46) and (47) in figures (21) and (22). Note large reduction in error for all angles of attack. Comparisons of the power-law fit for normal-force for the other three test Mach numbers are given in figure 24. Results for the center-of-pressure-location fit are given in figure 25. The fit of equ. (48) for  $M_\infty=1.60$  is shown for comparison. Note that the power-law fit is very good for both  $C_N$  and  $\bar{x}$ . As a bonus, of course, the power-law fits can be used to extend the test data to other affine bodies because the variables are in similarity form.

Although the results of reference 14 and this section represent only a small sample of shapes, it does appear that fitting  $C_N$  and  $\bar{x}$  data in natural similarity variables produces better fits. Since four functions are required for each approach examined above, the power-law-similarity method appears to be superior. It should be pointed out, however, that the above results have been obtained for supersonic flows only.

## REFERENCES

1. Ward, G.N., "Supersonic Flow Past Slender Pointed Bodies", Quarterly Journal of Mechanics and Applied Mathematics, Vol. 2, 1949, pp. 75- 97.
2. Nielsen, J.N., Missile Aerodynamics, McGraw-Hill Book Co., New York, 1960.
3. Ashley, H., and Landahl, M., Aerodynamics of Wings and Bodies, Addison-Wesley, 1965.
4. Pitts, W.C., Nielsen, J.N., and Kaatari, G.E., "Lift and Center of Pressure of Wing-Body-Tail Combinations at Subsonic, Transonic, and Supersonic Speeds," NACA Rept. 1307, 1957.
5. Hemsch, M.J., and Nielsen, J.N., "Equivalent Angle-of-Attack Method for Estimating Nonlinear Aerodynamics of Missile Fins," Journal of Spacecraft and Rockets, 20, July-Aug. 1983, pp. 356-362.
6. Hemsch, M.J. and Nielsen, J.N., "Extension of Equivalent Angle-of-Attack Method for Nonlinear Flow Fields," Journal of Spacecraft and Rockets, 22, May-June 1985, pp. 304-308.
7. Stahl, W.H., "Aerodynamics of Low Aspect Ratio Wings," AGARD Lecture Series No. 98, "Missile Aerodynamics," Feb. 1979.
8. Esch, E., "Bodies", AGARD Lecture Series No. 98, "Missile Aerodynamics", Feb. 1979.
9. Wardlaw, A.B., Jr., "High-Angle-of-Attack Missile Aerodynamics," AGARD Lecture Series No. 98, "Missile Aerodynamics," Feb. 1979.
10. Jorgensen, L.H., "Prediction of Static Aerodynamic Characteristics for Slender Bodies Alone and with Lifting Surfaces to Very High Angles of Attack", NASA TR R-474, Sept. 1977.
11. Vukelich, S.R., "Aerodynamic Prediction of Elliptically-Shaped Missile Configurations Using Component Build-Up Methodology," AIAA Paper No. 85-0271, Jan. 1985.
12. Stoy, S.L., and Vukelich, S.R., "Prediction of Aerodynamic Characteristics of Unconventional Missile Configurations Using Component Build-up Techniques," AIAA Paper 86-0489, Jan. 1986.
13. Sychev, V.V., "Three-Dimensional Hypersonic Gas flow Past Slender Bodies at High Angles of Attack," J. App. Math. Mech., 24, pp. 296-306, 1960.
14. Hemsch, M.J., "Engineering Analysis of Slender-Body Aerodynamics Using Sychev Similarity Parameters," AIAA 87-0267, Jan. 1987.
15. Barnwell, R.W., "Extension of Hypersonic, High Incidence, Slender-Body Similarity to Lower Mach Numbers," submitted to AIAA J.
16. Smith, J.H.B., "A Theory of the Separated flow from the Curved Leading Edge of a Slender Wing," A.R.C. R.&M No. 3116, Nov. 1957.
17. Allen, H.J., "Estimation of the Forces and Moments acting on Inclined Bodies of Revolution of High Fineness Ratio," NACA RM A9126, 1949.
18. Miller, D.S., and Wood, R.M., "Lee-Side Flow over Delta Wings at Supersonic Speeds," NASA TP 2430, June 1985.
19. Luckring, J.M., Private Communication.
20. Tinoco, E.N., Lu, P., and Johnson, F.T., "An Improved Panel Method for the Solution of Three-Dimensional Leading-Edge Vortex Flows, Vol. II - User's Guide and Programmer's Document," NASA CR 3279, July 1980.

21. Hemsch, M.J., and Nielsen, J.N., "The Equivalent Angle-of-Attack Concept for Engineering Analysis," Chapter XI in Tactical Missile Aerodynamics, ed: M.J. Hemsch, and J.N. Nielsen, Vol. 104 in AIAA Progress in Astronautics and Aeronautics.
22. Hemsch, M.J., Nielsen, J.N., Smith, C.A., and Perkins, S.C., Jr., "Component Aerodynamic Characteristics of Banked Cruciform Missiles with Arbitrary Control Deflection," AIAA Paper 77-1153, Aug. 1977.
23. Smith, C.A., Nielsen, J.N., and Hemsch, M.J., "Prediction of Aerodynamic Characteristics of Cruciform Missiles to High Angles of Attack," AIAA Paper 79-0024, Aug. 1979.
24. Stoy, S.L. and Vukelich, S.R., "Extension of the Equivalent Angle of Attack Prediction Method," AIAA Paper 84-0311, Jan. 1984.
25. Herring, P.G.C., "A Computer Program Which Evaluates the Longitudinal Aerodynamic Characteristics of Typical Weapon Configurations," AGARD CP-336, Feb. 1983.
26. Morikawa, G., "Supersonic Wing Body Lift," Journal of the Aeronautical Sciences, Vol. 18, April 1951, pp. 217-228.
27. Stahara, S.S., and Spreiter, J.R., "Calculative Techniques for Transonic Flows About Certain Classes of Wing-Body Combinations," NASA CR-2103, Aug. 1972.
28. Sigal, A., and Lapidot, E., "The Aerodynamic Characteristics of Configurations Having Bodies with Square, Rectangular and Circular Cross-Sections at a Mach Number of 0.75," to be presented at the AIAA Atmospheric Flight Mechanics Conference, Aug. 1987.
29. Beall, B.W., "Application of Slender Body Theory to Missiles with Arbitrary Shape Cross Sections, AIAA Paper 86-0488, Jan. 1986.
30. Sacks, A.H., "Aerodynamic Forces, Moments, and Stability Derivatives for Slender Bodies of General Cross Section," NASA TN 3283, Nov. 1954.
31. Skulsky, R.S., "A Conformal Mapping Method to Predict Low-Speed Aerodynamic Characteristics of Arbitrary Slender Re-Entry Shapes. J. Spacecraft and Rockets, Vol. 3, No. 2, Feb. 1966, pp. 247-253.
32. Nielsen, J.N., Hemsch, M.J., and Smith, C.A., "A Preliminary Method for Calculating the Aerodynamic Characteristics of Cruciform Missiles to High Angles of Attack Including Effects of Roll Angle and Control Deflection," Office of Naval Research CR 215-226-4F, Nov. 1977.
33. Baker, W.B., Jr., "Static Aerodynamic Characteristics of a Series of Generalized Slender Bodies with and without Fins at Mach Numbers from 0.6 to 3.0 and Angles of Attack from 0 to 180 Degrees," AEDC-tR-65-124, Vols. I & II, May 1976.
34. Shaw, D.S. et al., NASA TM to be published.
35. Landrum, E.J., and Babb, C.D., "Wind-Tunnel Force and Flow-Visualization Data at Mach Numbers From 1.6 to 4.63 for a Series of Bodies of Revolution at Angles of Attack From -4° to 60°," NASA TM 78813, March 1979.

#### Acknowledgement

Preparation of this lecture was sponsored by the High Reynolds Number Aerodynamics Branch of NASA Langley Research Center.

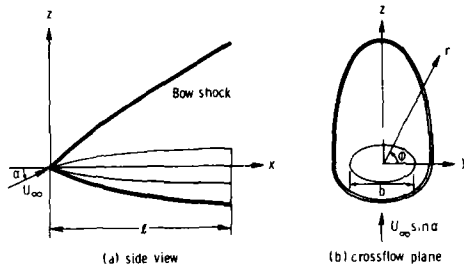


Fig. 1 Coordinate system for similarity analysis.

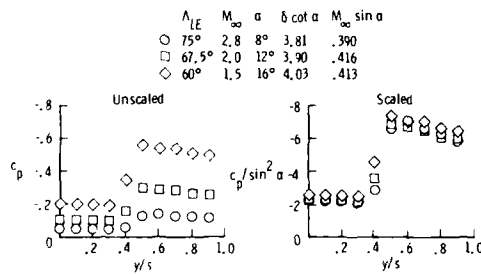
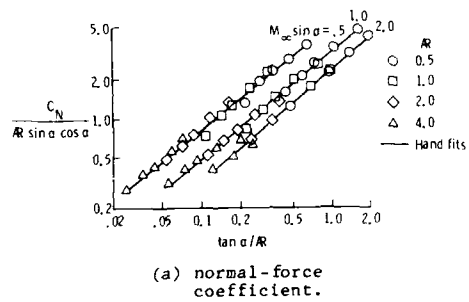
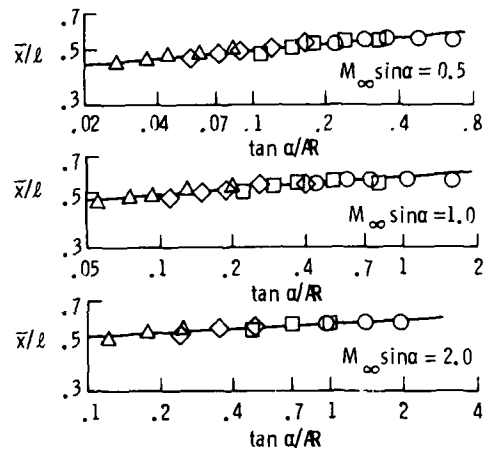


Fig. 2 Correlation of leeside surface pressure data<sup>18</sup> for delta wings for classical vortex case.



(b) axial location of the center of pressure.

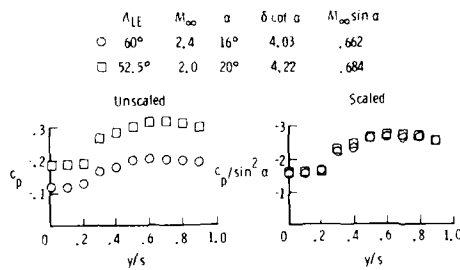


Fig. 3 Correlation of leeside surface pressure data<sup>18</sup> for delta wings for separation bubble case.

Fig. 4 Similarity correlations for clipped delta wings with taper ratio of one-half.



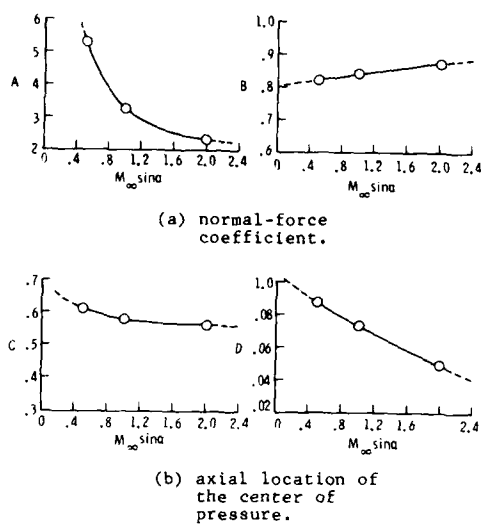


Fig. 5 Power-law coefficients for similarity correlations for clipped-delta-wing data.

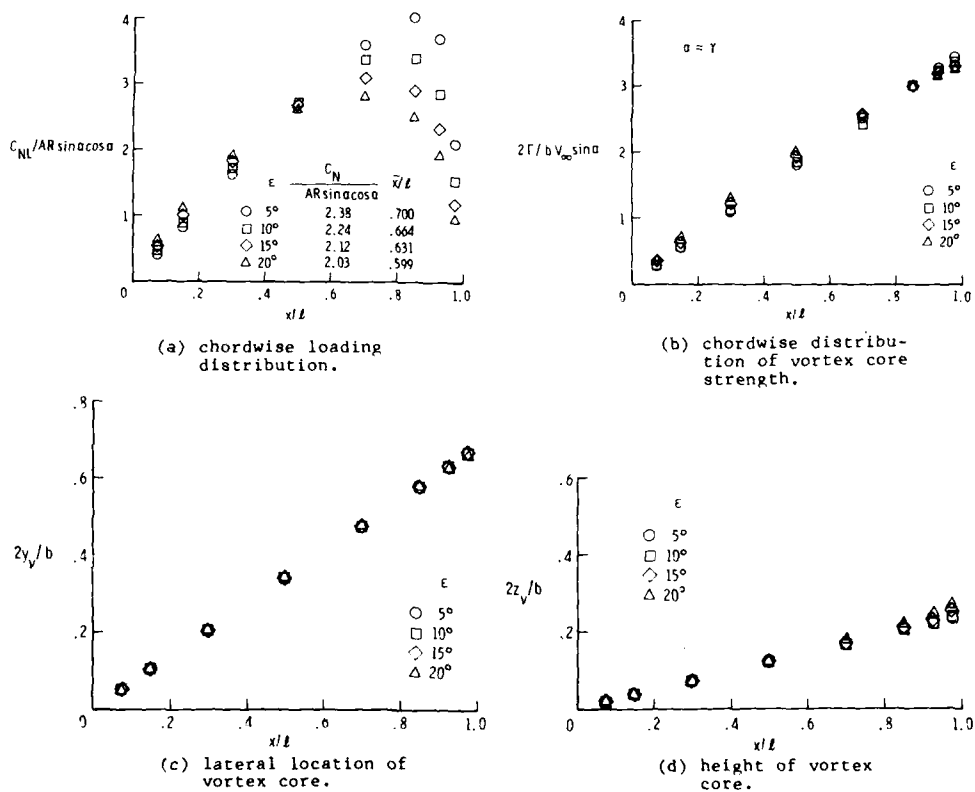


Fig. 6 Similarity correlations of computed results for thin delta wings in incompressible flow for  $\tan \alpha / AR = 0.25$ .

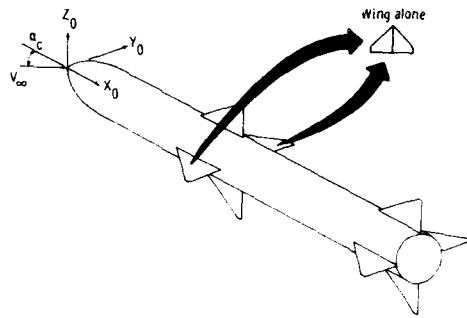
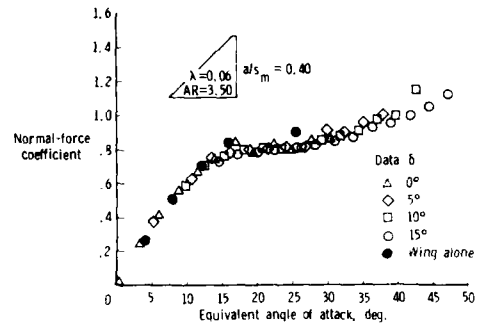


Fig. 7 Conventional wing-body-tail missile.



(a)  $M_\infty = 0.8$

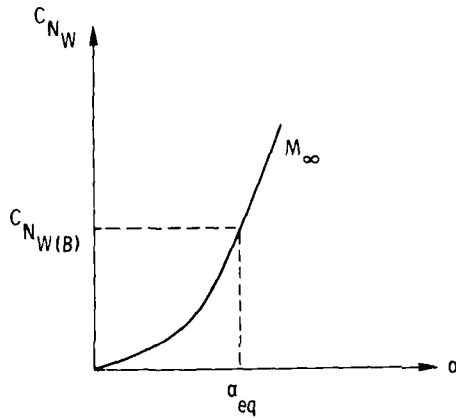
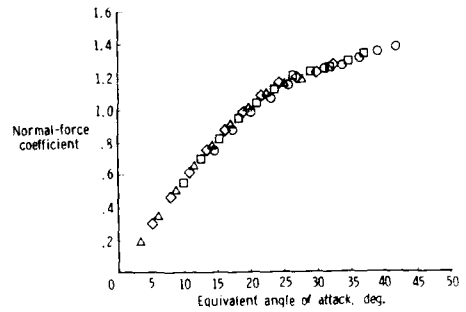


Fig. 8 Illustration of the equivalent angle-of-attack concept.



(b)  $M_\infty = 1.3$

Fig. 9 Correlation of fin normal-force data using EAAC.

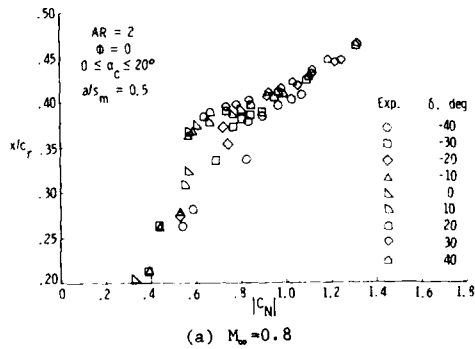
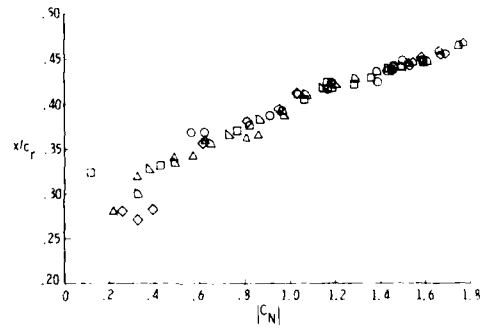
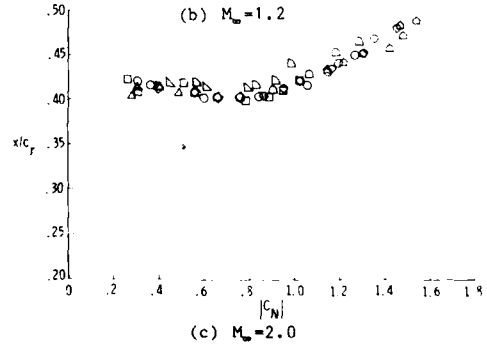


Fig. 10 Correlation of chordwise location of center of pressure for rectangular fins using EAAC.



(b)  $M_\infty = 1.2$



(c)  $M_\infty = 2.0$

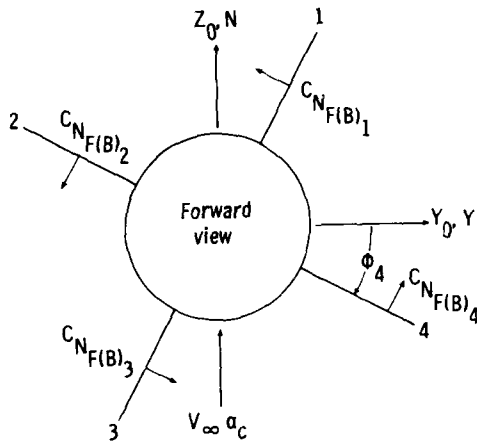


Fig. 11 Fin coordinate system.

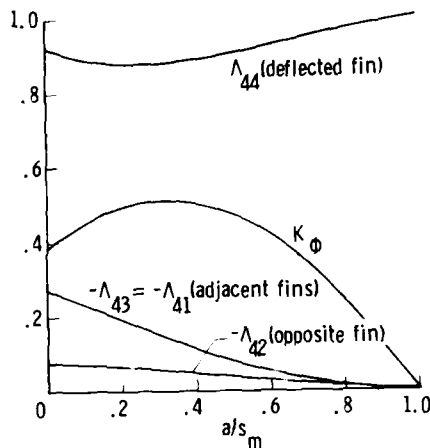


Fig. 12 Slender-body-theory values for sideslip and fin deflection factors for cruciform fins (see sign convention in figure 11).

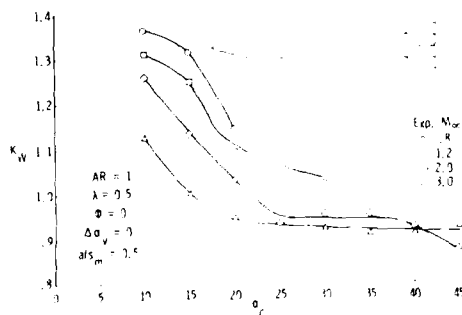


Fig. 13 Effect of body incidence on  $K_W$  for clipped delta fin.

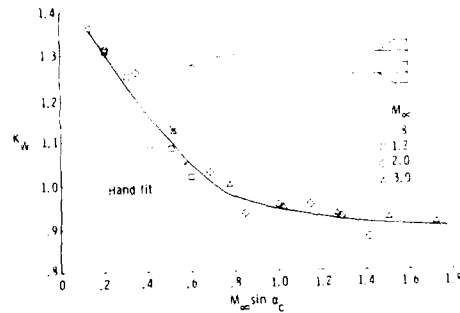


Fig. 14 Correlation of data of figure 13.

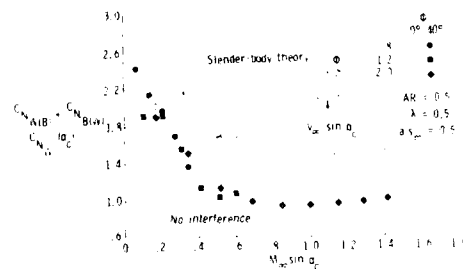


Fig. 15 Effect of cross-flow Mach number on fin-generated normal force.

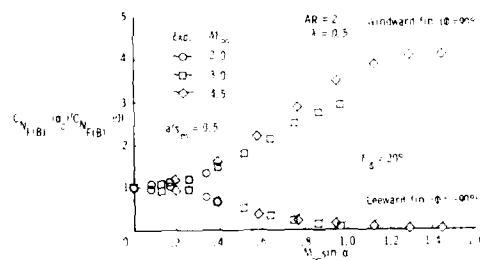


Fig. 16 Correlation of control effectiveness for leeward and windward fin positions.

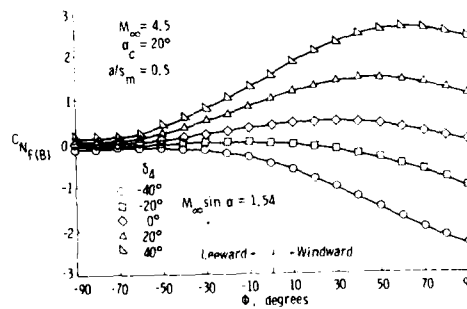


Fig. 17 Variation of fin normal force with bank angle for high cross-flow Mach number.

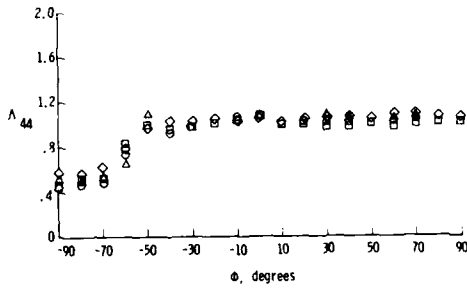


Fig. 18 Correlation of control fin data of figure 17 using EAAC and  $q_L$  and  $M_L$ .

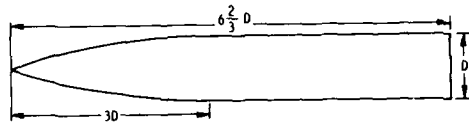


Fig. 19 Landrum's tangent-ogive-cylinder

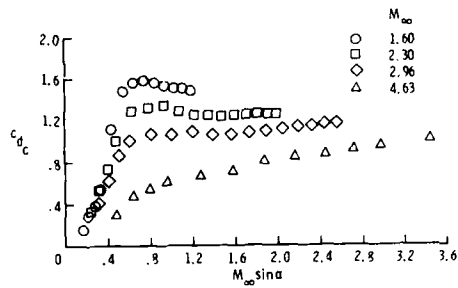


Fig. 20 Crossflow drag coefficients deduced from normal-force coefficient data for tangent-ogive cylinder of figure 19.

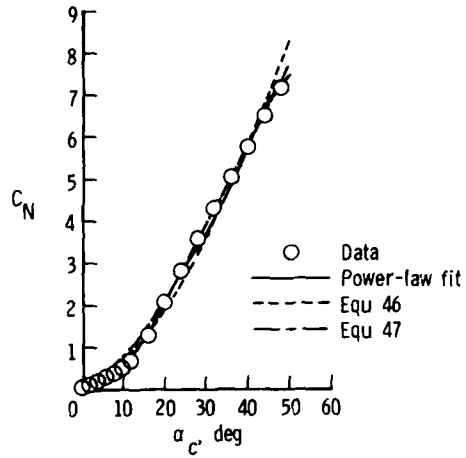


Fig. 21 Two-term least squares fits for tangent-ogive cylinder data at  $M_\infty = 1.60$ .

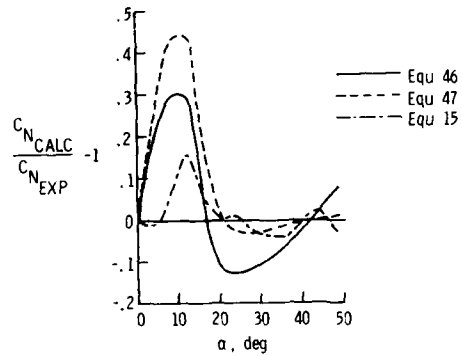


Fig. 22 Error for two-term least squares fits for tangent-ogive-cylinder data at  $M_\infty = 1.60$ .

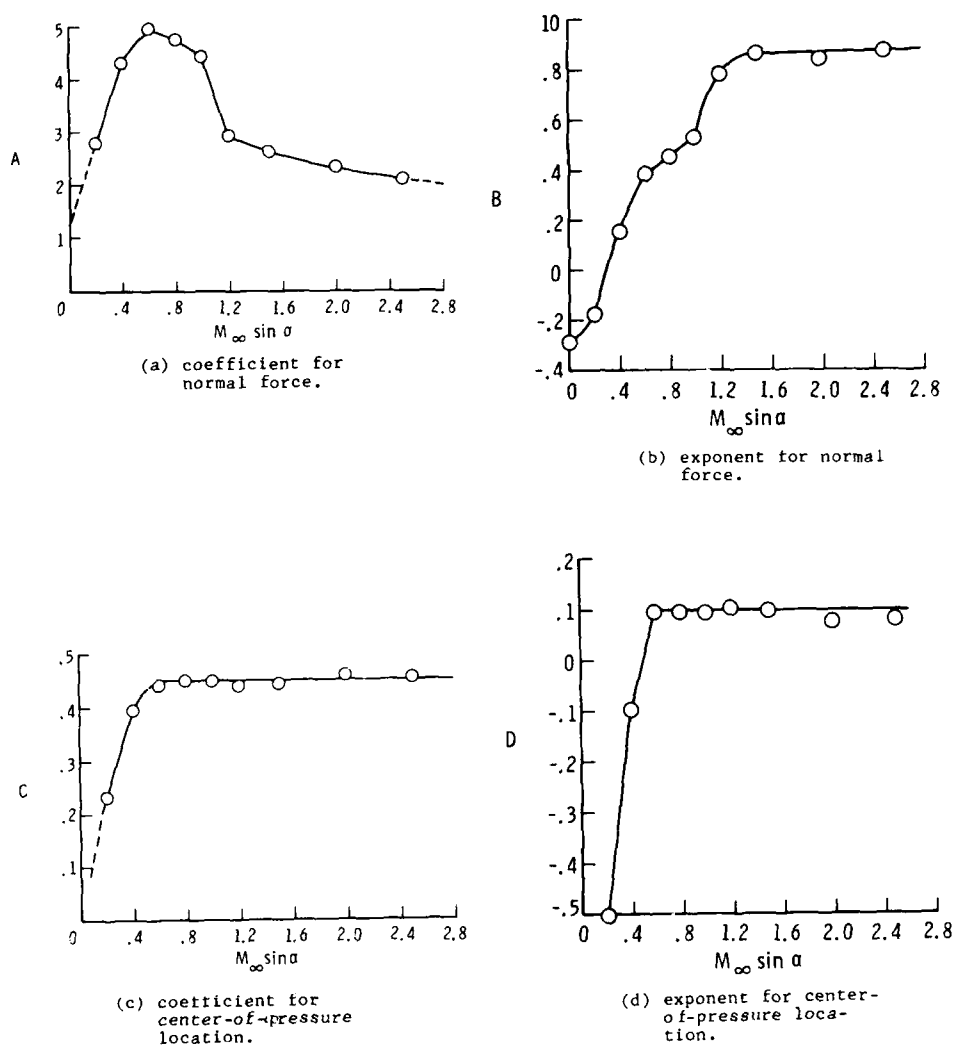


Fig. 23 Power-law fit for tangent-ogive-cylinder data.

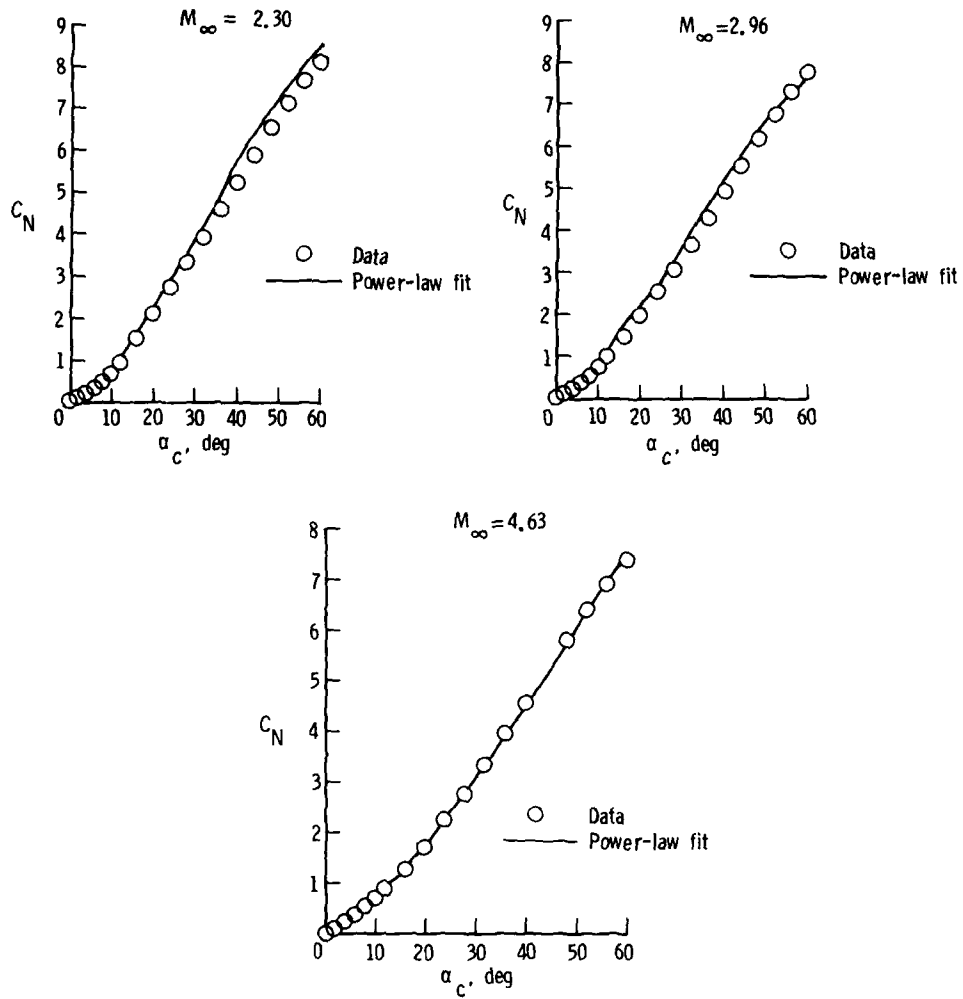


Fig. 24 Comparison of power-law fit and data for normal-force coefficient for tangent-ogive-cylinder.

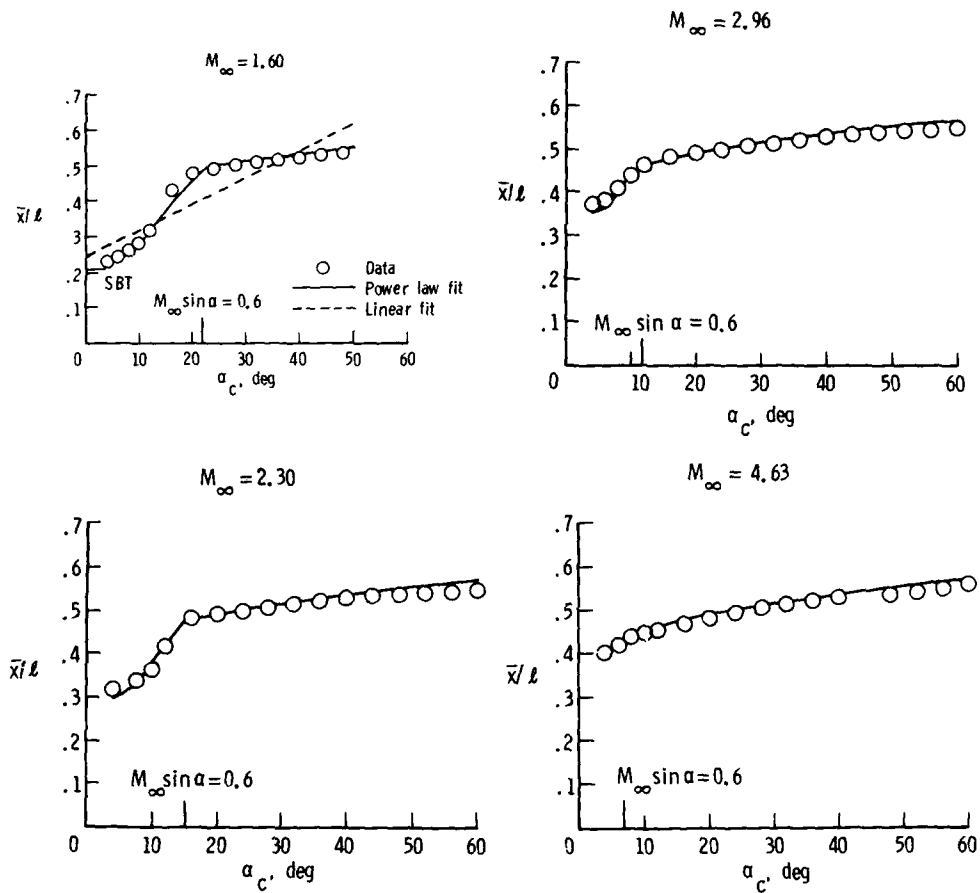


Fig. 25 Comparison of power-law fit and data for axial center-of-pressure location for tangent-ogive-cylinder.

## SPACE MARCHING EULER SOLVERS

Andrew B. Wardlaw, Jr.  
 Naval Surface Weapons Center  
 Silver Spring, Maryland, USA 20903-5000

## SUMMARY

This paper focuses on space marching Euler solvers for tactical missiles. These solvers are applicable to missiles in supersonic flight provided that the flow field remains supersonic everywhere. The introductory section outlines progress to date and is followed by a discussion of numerical methods which have been used to compute the flow about tactical missiles. Four different codes are described which are available for treating missile shapes. Results from these computational methods are presented for body-alone, body-wing and body-wind-tail cases. Force coefficients, surface pressures and flow field predictions are compared to experiment. Reasonable agreement is obtained, illustrating the feasibility of using these methods in the design process. The limitation of the Euler equations are also discussed.

## SYMBOLS

|                                      |   |
|--------------------------------------|---|
| $C_L$                                | - roll moment   |
| $C_N$                                | - normal force coefficient                                      |
| $C_m$                                | - yaw moment  |
| $C_M$                                | - pitching moment coefficient                                   |
| $C_p$                                | - pressure coefficient  |
| $C_Y$                                | - yaw force   |
| $D$                                  | - diameter  |
| $E$                                  | - source term, Eq. (4)  |
| $\vec{E}, \vec{F}, \vec{G}, \vec{H}$ | - flux definitions, Eqs. (1, 3, 4, 6) respectively              |
| $G, \vec{G}, G$                      | - flux definitions, Eqs. (3, 4, 6) respectively                 |
| $h$                                  | - enthalpy  |
| $H_0$                                | - stagnation enthalpy   |
| $J$                                  | - transformation Jacobian; Eq. (6)                              |
| $K$                                  | - slope limiter adjustment, Eq. (11)                            |
| $K$                                  | - smoothing adjustment, Eq. (10)                                |
| $L$                                  | - body length   |
| $M$                                  | - Mach number   |
| $\vec{n}$                            | - vector normal to cell edge                                    |
| $p$                                  | - pressure  |
| $q$                                  | - dynamic pressure  |
| $r$                                  | - radial coordinate, Fig. 2                                     |
| $s$                                  | - entropy   |
| $u_1, u_2, u_3, u_4$                 | - components of $U$   |
| $u, v, w$                            | - x, y, z velocity components, respectively                     |
| $u, v, w$                            | - r, $\phi$ velocity components                                 |
| $\vec{U}, U, \vec{U}, U$             | - vector of advanced quantities, Eqs. (1, 3, 4, 6) respectively |
| $x, y, z$                            | - cartesian coordinates, Fig. 2                                 |
| $X, Y, Z$                            | - computational coordinates                                     |
| $\alpha$                             | - angle of attack   |
| $\beta$                              | - yaw angle   |
| $\delta$                             | - flow direction in x - z plane, $\tan^{-1}(u/w)$               |
| $\phi$                               | - azimuthal angle, Fig. 2                                       |
| $\theta$                             | - angle between the shock and the z axis                        |
| $\mu^s$                              | - mach angle, $\sin^{-1}(1/M)$                                  |
| $\rho$                               | - density   |

## Subscripts:

|            |   |
|------------|---|
| P, Q, R, S | - points in Fig. 7  |
| +, -       | - two sets of conditions for the supersonic Riemann problem |
| n, m       | - indices for mesh point $(X_n, Y_m)$                       |

## Superscripts:

|                 |                      |
|-----------------|----------------------|
| k               | - step number        |
| c               | - corrector value    |
| *               | - predictor value    |
| (r, $\phi$ , z) | - partial derivative |



## 1. INTRODUCTION

The inviscid flowfield about a missile in supersonic flight can be approximated by numerically solving the Euler equations. The resulting solutions predict aerodynamic coefficients, load distributions including fin loads and hinge moments, and velocity profiles at an inlet face (excluding boundary-layer effects). These computational methods do not rely on a data-base and can provide predictions of items such as flow profiles, which are expensive to measure and difficult to predict empirically. Viscous phenomena, such as body vortices, are outside the scope of the Euler equations and must be modeled in an ad hoc manner.

The Euler equations are most easily solved for steady, supersonic flow. Under these conditions disturbances can only propagate downstream. Given a cross-flow plane near the missile nosetip on which the flowfield is defined, it is possible to generate the flowfield at any other cross-flow plane farther from the nosetip. This is accomplished in a series of steps, each of which advances the solution into a cross-flow plane located a small distance farther down the missile axis. Solutions generated in this manner are known as space-marching solutions and are feasible only if the computed flowfield is supersonic everywhere. In subsonic or transonic flow, disturbances can propagate upstream and a marching procedure is not permissible since it precludes any upstream influence in the flowfield. In general, the computer resources required to solve a three-dimensional supersonic flow problem are comparable to those necessary to solve an inviscid two-dimensional subsonic or transonic problem. The advent of high speed computers has made it feasible to apply three-dimensional, steady flow calculations to tactical missile design.

Numerical solutions for two-dimensional supersonic flow (i.e., axisymmetric or planar) have been applied to engineering design since the early 1900s. The earliest solution technique is the method of characteristics which was accomplished graphically or by using a mechanical calculator.<sup>1,2</sup> Such solutions were used in the design of supersonic wind tunnel nozzles, compressor blades, two-dimensional airfoils, and axisymmetric bodies. By the early 1960s, method of characteristics computer programs were available for calculating flows containing strong shocks and expansions.<sup>3</sup> Special procedures were included for detecting and tracking shocks as well as treating shock interactions.

Interest in solving the Euler equations for three-dimensional supersonic external flow arose in the early 1970s in conjunction with the study of hypersonic atmospheric re-entry. The geometries of concern varied from blunted cones with flaps and cuts to the Space Shuttle with blunted, highly swept wings. A sampling of the work from this period is given in Refs. 4-11. The solution strategy which evolved by the mid-1970s replaced the method of characteristics, which was cumbersome to implement in three dimensions, by a finite difference solution of which the most popular choice was MacCormack's explicit method.<sup>12</sup> The numerical solution was obtained only for the shock layer (i.e., the flowfield between the body and bow shock). The bow shock location, which constituted the outer boundary of the computational domain, was determined as part of the solution using a shock fitting procedure which satisfied the Rankine-Hugoniot relations. It became clear by this time that accurate computations on complicated configurations required careful treatment of shock and body boundaries. Two competing philosophies developed concerning the treatment of embedded shocks, or shocks occurring within the shock layer, which had a major impact on solution procedure. One approach was to fit embedded shocks<sup>5,8,9</sup> while the other was to capture such shocks, which is most accurately accomplished using the Euler equations in conservation form.<sup>7,10,11</sup> Shock fitting involves application of a special treatment at the shock surface, while capturing automatically resolves a shock as part of the numerical solution. Fitted shock solutions are more accurate, but their implementation becomes difficult on problems with complex shock structures.

By the late 1970s several different inviscid procedures had been developed which were capable of handling a variety of bodies.<sup>4-11</sup> When applied to relatively simple and smooth configurations, extremely accurate yaw and pitch force and moment predictions could be obtained at re-entry Mach numbers (i.e., Mach > 8) and incidences up to about 30°. At the higher angles of attack, the computed inviscid leeside flowfield was not an accurate representation of the viscous re-entry flowfield. However, due to the high freestream Mach number, pressures on the leeside were such a small fraction of those on the windward side that their actual value had little influence on the calculated forces. For configurations that were not simple or smooth, such as cones with extended flaps or thin-winged configurations, difficulty was often encountered in obtaining a solution. Special procedures were developed to model the flow near geometry discontinuities. These often involved the addition of artificial viscosity, but the amount needed had to be determined by trial and error on a case-by-case basis.

During the 1980s, inviscid computations have been performed on complete winged configurations.<sup>13-18</sup> A major issue has been the type of mapping to be used: multiple zone as opposed to a single conformal transformations. In addition, upwind schemes have been applied to winged configurations. These methods alter differencing

throughout the flow field to correctly account for the domain of dependence of the governing equations. Upwind schemes exhibit improved robustness and artificial viscosity is usually not needed.

Application of the Euler equations to tactical missile configurations introduces several issues that do not occur in the case of hypersonic re-entry vehicles. These problems can be appreciated by considering the sketch of a missile at incidence shown in Fig. 1. This configuration features thin, sharp-edged wings. At angle of attack the flow separates from both the wing edges and the body, rolling up to form leeside vortices which have a strong effect on vehicle aerodynamic characteristics. The large influence of vortex structures on missile aerodynamics is a reflection of the fact that tactical missiles operate in the supersonic rather than hypersonic speed range, and pressures on the leeside cannot be neglected. To treat missile configurations effectively, it is necessary to handle geometries with sharp edges and to model vortices. Vortex modeling is more easily accomplished with the Euler equations than with potential formulations. The Euler equations allow rotational flow and hence can convect vorticity without the addition of ad hoc structures (e.g., point vortices) to the flowfield.

This paper provides an overview of space-marching methods for missiles in supersonic flight. Background information on computational techniques is presented, four different computational algorithms are outlined, and their application is demonstrated on body-alone, body-wing and body-wing-tail missiles. The background information stresses techniques methods to be used later in the paper. The illustrated application of these techniques is to realistic missile configurations.

## 2. NUMERICAL METHODS FOR STEADY SUPERSONIC FLOW

This section provides a brief explanation of computational methods applicable to missiles in supersonic flight. The techniques used to generate the results presented in this chapter will be highlighted, but alternative approaches will also be indicated.

### 2.1 Euler's Equations for Steady Supersonic Flow

Using the coordinates of Fig. 2, the Euler equations for steady flow arise from balancing mass and momentum fluxes through the control volume illustrated in Fig. 3. This results in the following set of equations:

$$\bar{U}_{n,m}^{n+1} = \bar{U}_{n,m}^n - \bar{F}_{n+1/2,m} + \bar{F}_{n-1/2,m} - \bar{F}_{n,m+1/2} + \bar{F}_{n,m-1/2} \quad (1)$$

where:

$$\bar{U}_{n,m}^n = A_{n,m}^n \begin{bmatrix} \rho w \\ \rho w^2 + p \\ \rho w u \\ \rho w v \end{bmatrix}_{i,j} \quad \bar{F}_{n+1/2,m} = \begin{bmatrix} \rho v \\ \rho w v + n_{x,p} \\ \rho u v + n_{x,p} \\ \rho v v + n_{x,p} \end{bmatrix}_{i+1/2,j}$$

$$V = n_{n+1/2,m} \cdot (u,v,w)_{n+1/2,m}$$

For steady supersonic flow, the energy equation reduces to a constraint on the stagnation enthalpy:

$$H_0 = (u^2 + v^2 + w^2)/2 + h \quad (2)$$

Here  $H_0$  is a constant and the enthalpy,  $h$ , is evaluated from the perfect gas relations:

$$h = \frac{\gamma p}{(\gamma - 1) \rho}$$

Eqs. (1) are integral relations for the control volume illustrated in Fig. 3. Taking the control volume to be the cube ( $\Delta x$ ,  $\Delta y$ ,  $\Delta z$ ) and allowing the dimensions of the control volume to go to zero yields the associated partial differential equation in cartesian coordinates:

$$\frac{\partial \hat{U}}{\partial z} + \frac{\partial \hat{F}}{\partial x} + \frac{\partial \hat{G}}{\partial y} = 0 \quad (3)$$

where:

$$\hat{U} = \begin{bmatrix} \rho w \\ p + \rho w^2 \\ \rho w u \\ \rho w v \end{bmatrix}; \quad \hat{F} = \begin{bmatrix} \rho u \\ \rho u w \\ p + \rho u^2 \\ \rho v u \end{bmatrix}; \quad \hat{G} = \begin{bmatrix} \rho v \\ \rho v w \\ \rho v u \\ p + \rho v^2 \end{bmatrix}$$

Alternatively, the Euler equations in cylindrical coordinates  $(r, \phi, z)$  can be derived by considering the control volume  $(\Delta r, \Delta \phi, \Delta z)$  and taking the limit  $(\Delta r, \Delta \phi, \Delta z) \rightarrow 0$ :

$$\frac{\partial(r\bar{U})}{\partial z} + \frac{\partial(r\bar{F})}{\partial r} + \frac{\partial\bar{G}}{\partial\phi} = \bar{E} \quad (4)$$

where:

$$\bar{U} = \begin{bmatrix} \rho\tilde{w}^2 + p \\ \rho\tilde{u} \\ \rho\tilde{v} \end{bmatrix}; \quad \bar{F} = \begin{bmatrix} \rho\tilde{u} \\ \rho\tilde{u}\tilde{u} + p \\ \rho\tilde{u}\tilde{v} \end{bmatrix}; \quad \bar{G} = \begin{bmatrix} \rho\tilde{v} \\ \rho\tilde{v}\tilde{u} \\ \rho\tilde{v}\tilde{v} + p \end{bmatrix}; \quad \bar{E} = \begin{bmatrix} 0 \\ 0 \\ \rho\tilde{v}\tilde{u} \\ -\rho\tilde{v}\tilde{u} \end{bmatrix}$$

Nonconservation forms of Eqs. (3) and (4) can be obtained by a nonlinear change of the dependent variables which are the components of  $U$ . For example, in terms of the dependent variables:

$$Q = (p, \tilde{u}, \tilde{v}, w)^t$$

Eq. (4) takes the nonconservation form

$$A \frac{\partial Q}{\partial z} + B \frac{\partial Q}{\partial r} + \frac{C}{r} \frac{\partial Q}{\partial\phi} = \frac{\bar{E}}{r} - \bar{F} \quad (5)$$

where  $A$ ,  $B$ , and  $C$  are the Jacobian matrices  $\partial\bar{U}/\partial Q$ ,  $\partial\bar{F}/\partial Q$ , and  $\partial\bar{G}/\partial Q$ , respectively.  $Q$  can be any set of independent variables as long as  $A$  is nonsingular for  $w^2 > a^2$ .

Although Eqs. (1), (3), (4) and (5) are all analytically equivalent, they can produce different numerical solutions even when the same numerical technique is applied. Eqs. (1) are the integral or finite volume form of Euler's equations, Eqs. (3) and (4) are in conservation form, while Eqs. (5) are in nonconservation form. Eqs. (1), (3) and (4) follow directly from the integral conservation law, and are valid even when shocks or contact discontinuities are present. This is not true for Eqs. (5) and the resulting solutions do not represent strong shocks realistically. Accordingly, when Euler's equations in nonconservative form are applied to a flow field containing shocks, shock fitting procedures are needed.

The Euler equations are hyperbolic with  $z$  the time-like direction when  $w^2 > a^2$ . This implies that the numerical solution of the flowfield can be determined by marching in the  $z$  direction. The basic marching algorithm is a procedure for determining numerical approximations to the flow variables  $\rho$ ,  $r$ ,  $p$ ,  $u$ ,  $v$ , and  $w$  at  $z = z_0 + \Delta z$  using the known values of these quantities at  $z = z_0$ . For missile applications where the bow shock is fitted, the advanced quantities also include  $c$ ,  $c_\phi$ , and  $c_z$  which describe the bow shock. The calculation is started at an initial data plane,  $z = \text{constant}$ , near the nosetip where the flowfield is known (Fig. 2). On sharp-tipped bodies the initial data plane is commonly determined using a conical flow solution, while on blunted configurations, a transonic blunt body calculation of the type described in Refs. 20 and 21 is used. By repeated application of the marching algorithm, the flowfield is advanced from the initial data plane to any desired  $z$  location. The most popular methods for advancing the flowfield are finite-difference and finite volume techniques to which this paper is restricted. Other approaches include the method of characteristics (e.g., Ref. 22).

## 2.2 Mesh Generation

A principal issue in the development of a marching algorithm is the definition of the mesh which is computed separately for each crossflow plane. The mesh structure places body surfaces, wing surfaces, and usually the bow shock along constant computational coordinates lines. Changes in the body geometry and the shock location as a function of axial location mandates recomputing the mesh at each computational step. Accordingly, simple mesh generation procedures must be used to avoid devoting an excessive amount of computational effort to mesh generation. For this reason computational methods such as elliptic mesh generators have not been applied to the supersonic marching problem.

In the crossflow plane, missile type geometries can be simple, featuring just a circular body, or complex with cruciform fins extending from a noncircular body. Low radar cross sectional shapes may feature blended bodies with inlets and thick wings. The most appropriate type of mapping is dependent on the computational shape being considered. For simple circular bodies, only stretching in the radial direction is necessary<sup>4,5,8,10</sup>:

$$Z = z, \quad X = \frac{(r - b(\phi, z))}{(c(\phi, z) - b(\phi, z))}, \quad Y = \phi$$

where  $b(\phi, z)$  and  $c(\phi, z)$  describe the wall and bow shock locations as indicated in Fig. 2. Mappings based on the above are well suited for bodies that are approximately circular, but are not appropriate for winged configurations. Fig. 4a illustrates the resulting mesh in physical space when such a transformation is applied to a wing-body shape. Here, a clustering in the  $\phi$ -coordinate direction has been applied near the fin

surface. The skewness of the mesh in the vicinity of the fins causes computational problems and a large number of mesh points are needed to adequately resolve cross sections with several fins present. An improvement on this approach is the use of more sophisticated transformations that produce a nearly rectangular mesh in physical space. Generalized conformal transformation techniques have been developed which accomplish this for relatively arbitrary cross sections.<sup>23</sup> As depicted in Fig. 4b, the resulting mesh is appropriate since it clusters points about the fin tips and thus allows the tip to be resolved more accurately. Such methods have been applied (e.g., Refs. 6, 9, and 16) and are viable for tackling many missiles, particularly those with thick wings. Possible drawbacks to this approach are solution sensitivity to small variations in the transformations and difficulty in controlling mesh point locations throughout the flowfield on complicated configurations. When a complicated transformation is used, a significant portion of the computation is associated with its implementation.

A different type of transformation is obtained using a multiple-zone approach, as illustrated in Fig. 4c. This entails dividing each cross section into several nonoverlapping regions and mapping each region separately into individual rectangles. The multiple zone approach is most appropriate for missiles with thin fins. Originally, this type of method was used to develop shock fitting algorithms. In these applications, the embedded shocks are taken as interfaces separating adjacent zones. The multiple zone concept can also be applied to missile geometries where fin and inlet cowl surfaces become convenient zone boundaries.<sup>14,15,17,18</sup> Fig. 4c illustrates the application of a two-zone approach to a wing-body configuration. The geometry of each zone is sufficiently simple that generally only a stretching transformation is required in each direction. The great advantage of the multiple-zone approach is its flexibility and relative ease of application. Its disadvantage is that it requires a more complicated computer program to implement. This is primarily due to bookkeeping and special numerical techniques required to treat points along the interfaces between adjacent zones.

Transformations used in supersonic space marching from cartesian space  $(x,y,z)$  to computational space  $(X,Y,Z)$  usually have the form:

$$X = X(x,y,z); \quad Y = Y(x,y,z); \quad Z = Z(z)$$

In the case of cylindrical coordinates, these become:

$$X = X(r, \phi, z); \quad Y = Y(r, \phi, z); \quad Z = Z(z)$$

As shown in Fig. 2,  $z$  is the marching direction. Partial differential equations in conservation form, such as Eqs. (3) or (4), can be transformed into conservation form in computational space under this generalized transformation. For example, Eq. (4) becomes:

$$\frac{\partial U}{\partial Z} + \frac{\partial F}{\partial X} + \frac{\partial G}{\partial Y} = \tilde{E} \quad (6)$$

where

$$F = X_z U + [r X_r \tilde{F} + X_\phi \tilde{G}] / J,$$

$$G = Y_z U + [r Y_r \tilde{F} + X_\phi \tilde{G}] / J,$$

$$U = r \tilde{U} / J,$$

$$J = X_r Y_\phi - X_\phi Y_r$$

### 2.3 Numerical Schemes

Numerical schemes applied to supersonic marching should be second order accurate in the marching direction as well as in the crossflow plane. For this reason, the MacCormack scheme has been a common choice.<sup>4-11, 13-15</sup> When treating complex configurations, it is also advantageous to capture shocks and slip lines generated by wings and Euler's equations are usually cast in conservation form.<sup>7,10,11,14-18</sup> The alternative is to combine a non-conservative formulation with shock fitting; however, shock fitting is difficult to implement in three-dimensions. The fitting procedure adds additional program complexity and requires the detection of shocks which form during a calculation. To ensure stability, it is necessary to apply tracking to nascent shocks before they reach a finite strength.<sup>24</sup>

Implicit schemes, such as the Beam-Warming algorithm<sup>25</sup>, have generally not been used for supersonic marching calculations. The chief advantage of these methods is unconditional stability which removes, at least in terms of linear stability analysis, any marching step size restriction. However, the necessity of maintaining accuracy in the marching direction precludes using extremely large step sizes. Implicit schemes are much more expensive per step than are explicit methods and it is usually not economical to apply implicit methods. An exception might be calculations featuring a very small mesh spacing in a portion of the computational domain which would result in an extremely small explicit step size.

Viable alternatives to the MacCormack explicit method are upwind differencing schemes. Such methods attempt to accurately account for the domain of dependence of the partial differential equations. To illustrate, consider the case where the crossflow velocity component is supersonic. In this situation, an upwind scheme would use one-sided differences that accept only information which is upwind with respect to the crossflow velocity in the crossflow plane. This reflects the fact that in supersonic flow a point is only influenced by upstream conditions. In contrast, the MacCormack scheme always uses information from all directions in the computational plane. The first upwind scheme used for supersonic steady flow calculations was the  $\lambda$  scheme developed by Moretti.<sup>26</sup> This scheme differences characteristic relations in a one-sided direction determined by the associated characteristic slopes and is the non-conservative. A different non-conservative upwind scheme, termed the split-coefficient method, has also been applied to supersonic steady flow.<sup>19</sup> Here, appropriate one-sided differences are introduced by splitting the coefficient matrices that appear in a non-conservation form of the equations according to the sign of their eigenvalues. The  $\lambda$  scheme and the split-coefficient methods have exhibited improved robustness when compared to the MacCormack scheme.<sup>19,26</sup> Flux vector splitting,<sup>27</sup> the Osher scheme<sup>28</sup> and Godunov methods<sup>29</sup> are conservative upwind schemes which have been developed for unsteady gas dynamics. These schemes are more robust and capture stronger shocks with less smearing than standard methods, but require more computational effort to apply. The application of Godunov methods to tactical missiles is described in Refs. 17 and 18.

The following paragraphs describe the explicit MacCormack and Godunov scheme. Both methods are used to generate the results presented later in the paper. The MacCormack scheme will be classed in a finite difference form while the Godunov scheme is a finite volume scheme.

### 2.3.1 The MacCormack Scheme

The MacCormack predictor-corrector algorithm, when applied to Eqs. (6), is given by:

$$U_{n,m}^* = U_{n,m}^k - \Delta Z \left[ \frac{F_{n+1,m}^k - F_{n,m}^k}{\Delta X} + \frac{G_{n,m+1}^k - G_{n,m}^k}{\Delta Y} - \left( \frac{\tilde{E}}{J} \right)_{n,m}^k \right] \quad (7a)$$

$$U_{n,m}^{k+1} = 1/2 \left[ U_{n,m}^k + U_{n,m}^* - \Delta Z \left( \frac{F_{n,m}^* - F_{n-1,m}^*}{\Delta X} + \frac{G_{n,m}^* - G_{n,m-1}^*}{\Delta Y} - \left( \frac{\tilde{E}}{J} \right)_{n,m}^* \right) \right] \quad (7b)$$

Here

$$U_{n,m}^k = U(x_n, y_m, z^k), \quad F_{n,m}^* = F(U_{n,m}^*, x_n, y_m, z^{k+1}),$$

etc. Eqs. (7a) and (7b) are the predictor and corrector steps, respectively. At the end of each step,  $U$  is decoded to determine predicted or corrected values of  $p$ ,  $\rho$ ,  $u$ ,  $v$ , and  $w$ . Relations for these quantities follow from the definition of  $U = (u_1, u_2, u_3, u_4)^T$ , Eqs. (6), and the equations of state. For a perfect gas these are given by:

$$w = \frac{u_2 [\gamma + \sqrt{1-\phi}]}{u_1 (1+\gamma)}, \quad \phi = (\gamma^2 - 1) \left( H - \frac{u_1}{u_2} \right)^2 - 1,$$

$$\tilde{H} = 2H_\infty - \frac{u_3^2 + u_4^2}{u_1^2}, \quad \rho = J(u_2 - u_1 w) / r,$$

$$\rho = Ju_1 / (rw), \quad u = u_3 / u_1, \quad v = u_4 / u_1 \quad (8)$$

The step size  $\Delta Z$ , which appears in Eqs. (7), must be picked to satisfy the CFL condition for the MacCormack scheme. This condition is derived using a locally linearized form such as Eqs. (5).<sup>10</sup> The CFL condition requires that the domain of dependence of the partial differential equations be contained within the domain of dependence of the finite-difference equations.

The flowfield about a tactical missile may contain shocks, slip surfaces, vortices, and other flow structures which are difficult to resolve computationally. As a result, nonphysical oscillations may occur in the numerical solution which can become sufficiently large to cause the demise of the calculation. To improve the robustness, or reliability, of a difference scheme, a smoothing procedure is sometimes applied which adds numerical dissipation. Smoothing can be implemented in many different ways. Two of the most commonly used methods are the fourth-order dissipative term<sup>16,30</sup> and the switched Schuman filter.<sup>31,32</sup> The switched Schuman

filter is implemented following the corrector step. The advanced quantities calculated in the corrector step, denoted by  $U^C$ , are modified as follows:

$$U_{n,m}^{k+1} = U_{n,m}^C + (U_{n+1,m}^C - U_{n,m}^C) S_{n+1/2,m} - (U_{n,m}^C - U_{n-1,m}^C) S_{n-1/2,m} \\ + (U_{n,m+1}^C - U_{n,m}^C) S_{n,m+1/2} - (U_{n,m}^C - U_{n,m-1}^C) S_{n,m-1/2} \quad (9)$$

Here, the switch  $S$  is defined using the local gradients of some flow quantity, usually  $p$  or  $\rho$ . A density switch can be defined by

$$S_{n+1/2,m} = \frac{[\rho_{n+1,m} - \rho_{n,m}] \hat{K}}{(\rho_{n+1,m} + \rho_{n,m})}; \\ S_{n,m+1/2} = \frac{[\rho_{n,m+1} - \rho_{n,m}] \hat{K}}{(\rho_{n,m+1} + \rho_{n,m})}. \quad (10)$$

Here  $\hat{K}$  is an adjustable parameter used to control the level of smoothing. To eliminate any unnecessary influence of the smoothing operator, it is common practice to set  $K$  to zero in regions of the flowfield where numerical difficulties are not expected.

### 2.3.2 Godunov's Method

Godunov's method<sup>29</sup> is a finite volume technique which is based on the Riemann problem. For steady supersonic flow the Riemann problem represents the confluence of two, two-dimensional, supersonic streams as is illustrated in Fig. 5. At the point of stream intersection, shocks or expansions form which turn both streams to a common direction. The appropriate direction is the one producing the same pressure in both streams. The two final streams need not feature the same density or velocity and a slip line generally forms between them. The resulting solutions feature constant properties along any line passing through the point initial stream intersection.

Solution of the Riemann problem is accomplished by guessing the slip line orientation and computing the pressure on each side of it using the oblique shock or Prandtl-Meyer expansion relations (see Ref. 33 for these relations). The slip line orientation is adjusted by some iterative procedure to achieve equal pressures on both sides of the slip line. The non-linearity of the shock and expansion relations precludes a closed form solution to the Riemann problem. Fortunately, linear versions of the Riemann problem can be used in smooth flow regions and approximate Riemann problems can be defined for all conditions.<sup>34</sup>

Godunov's method advances the flow field by using the Riemann problem to evaluate the fluxes,  $F$ , appearing in Eqs. 1. For the first order method, properties within each control volume are assumed constant. This results in a piece-wise constant description of the flow field which is discontinuous at cell edges. For two-dimensional flow, this is illustrated in Fig. 6. The two sets of properties at cell edges are used as the two initial states of the Riemann problem. The solution of the Riemann problem features constant properties along any line intersecting the point of stream intersection. The fluxes,  $F$ , appearing in Eqs. 1 are computed using the set of properties along the line with the same orientation as the cell edge, as shown in Fig. 6. In three-dimensional flow, a reference plane must be selected on which the two-dimensional Riemann problem is solved. Typically, this is taken to be the plane normal to the cell edge which contains the marching direction.

The first order Godunov's method can be extended to second order by assuming linear property variations within each control volume and adding a predictor step.<sup>35</sup> This general recipe has been applied to three-dimensional steady supersonic flow in Refs. 18 and 34. In determining the property slopes within each control volume, limiters are used which reduce slope values in the vicinity of strong shocks and expansions. For example, to compute the slope in the  $x$  direction on a two-dimensional, uniform mesh (see Fig. 6), the following formula is applied:

$$\frac{\partial f}{\partial x} = \frac{F}{\Delta x} \text{MIN} \left[ \frac{|f_{n+1} - f_{n-1}|}{2}, K|f_{n+1} - f_n|, K|f_n - f_{n-1}| \right] \quad (11)$$

$$F = \begin{cases} 0 & \text{if } (f_{n-1} - f_n)(f_n - f_{n-1}) < 0 \\ 1 \text{ sign}(f_{n+1} - f_{n-1}) & \text{otherwise} \end{cases}$$

The above derivative is second order accurate in smooth flow regions and zero near extrema. The parameter  $K$  is set between 1 and 2. It is generally not necessary to re-adjust  $K$  on new problems.

### 2.3 Boundary Conditions

A basic problem which arises in treating boundary points is determining the relations that should be satisfied at these points. In addition to the governing equations, which of themselves are sufficient to determine all of the unknowns, specific boundary conditions must be enforced. For example, at a solid surface the flow must be tangent to the wall, while at a shock the Rankine-Hugoniot relations must be satisfied. To avoid overspecifying the problem, some but not all of the information contained in the governing equations must be used. The valid information at the boundaries which is contained in the governing equations can be determined using the theory of characteristics.

To fix ideas, consider the case of steady, two dimensional supersonic flow. Here three independent relations are needed to determine flow field properties. As is shown in Fig. 7, the characteristics consist of two Mach lines,  $C_+$ ,  $C_-$  and the streamline,  $C_0$ . On each of these lines, a compatibility relation holds which is an ordinary differential equation. Consider the point on a surface  $P: (x_0, z_0)$ , illustrated in Fig. 7, and trace the three characteristic lines through this point in the negative  $z$  direction. The compatibility relations associated with the  $C_-$ ,  $C_0$  characteristics lie within or on the boundary of the flow field for  $z < z_0$  and represent admissible information. The remaining  $C_+$  compatibility relation is not admissible since the associated characteristic lies outside of the flow field for  $z < z_0$ . It is replaced by the tangent flow boundary condition yielding the required three independent relations at  $P$ :

$$\begin{aligned} dp - \frac{\gamma M^2}{(M^2-1)^{1/2}} d\delta &= 0 \quad \text{along } C_- \\ ds &= 0 \quad \text{along } C_0 \\ \tan(\delta_P) &= \text{wall slope at } P \end{aligned} \quad (12)$$

These relations are satisfied discretely using upstream properties on the  $C_-$  and  $C_0$  characteristics. For example:

$$p_P = p_R - \frac{(\gamma M^2)}{(M^2-1)^{1/2}} (\delta_R - \delta_P) \quad (13a)$$

$$s_P = s_S \quad (13b)$$

where points  $R$  and  $S$  are located on the  $C_-$  and  $C_0$  characteristics as shown in Fig. 7.

At a shock point  $Q: (x_1, z_1)$ , only the  $C_+$  compatibility relation is admissible and it must be augmented by the oblique shock relations giving the equations:

$$\begin{aligned} dp + \frac{\gamma M^2}{(M^2-1)^{1/2}} d\delta &= 0 \quad \text{along } C_+ \\ \frac{p_Q}{p_\infty} &= \frac{2\gamma M_\infty^2 \sin^2 \theta_s - (\gamma-1)}{(\gamma+1)} \\ \frac{\rho_Q}{\rho_\infty} &= \frac{(\gamma+1)M_\infty^2 \sin^2 \theta_s}{(\gamma-1)M_\infty^2 \sin^2 \theta_s + 2} \\ \tan \delta_Q &= \frac{M_\infty^2 \sin 2\theta_s - 2\cot \theta_s}{2 + M_\infty^2 (\gamma + \cos 2\theta_s)} \end{aligned} \quad (14)$$

The oblique shock relations introduce the additional unknown of shock slope,  $\theta_s$ , and four equations are required at the shock. Solution of the above equations within the method of characteristics framework is iterative and requires discretization of the  $C_+$  compatibility equation.

In three-dimensional flow the situation becomes more complex. Here there are two families of characteristic surfaces: stream surfaces and Mach surfaces. The former are generated by streamlines while the latter are everywhere tangent to the local Mach cone. The compatibility relations holding on these surfaces are now partial differential equations in two-dimension. The analysis of this situation can be made analogous to the two-dimensional case using the reference plane method of characteristic.<sup>36</sup> Here the problem is analyzed from a two-dimensional point of view, with derivatives in the third direction being treated as source terms. For example, choosing the  $x$ - $z$  plane to be the reference plane, characteristic relations can be written in a manner similar to those of Fig. 7. However, a source term appears on the right side of each equation which contains  $y$  derivatives. Also an additional compatibility relation applies along the streamline. The basic idea of admissible information carries over directly from the two-dimensional case.

The treatment of boundary points as indicated above occurs naturally in algorithms based on the method of characteristics. The remainder of this section discusses the implementation of boundary conditions within the framework of finite volume and finite difference methods.

### 2.3.1 Finite Difference

A direct implementation of the method of characteristics at boundaries requires interpolation from the finite difference mesh to determine properties on characteristics. Kentzer<sup>37</sup>, in the context of unsteady flow, has suggested casting the admissible characteristic relations in terms of spatial derivatives. For example, the characteristic relations in Fig. 7 can be expressed as:

$$\frac{\partial p}{\partial z} + \tan(\delta \pm u) \frac{\partial p}{\partial x} \pm \frac{\gamma p M^2}{(M^2 - 1)^{1/2}} \frac{\partial \delta}{\partial z} + \tan(\delta \pm u) \frac{\partial \delta}{\partial x} = 0 \quad \text{on } C_{\pm} \quad (15)$$

$$\frac{\partial s}{\partial z} + \tan(\delta) \frac{\partial s}{\partial x} = 0 \quad \text{on } C_0$$

The same technique is applied at shocks. By differentiating the oblique shock relations to obtain differential equations, it is possible to compute shock properties without iteration. To illustrate, Eq. 14, after differentiation, becomes:

$$\frac{dp_0}{dz} = \frac{\partial p}{\partial z} + \tan \theta_s \frac{\partial p}{\partial x} = \frac{p_\infty}{(\gamma + 1)} 2\gamma M_\infty^2 \sin^2 \theta_s \frac{d\theta_s}{dz} \quad (16)$$

From a mathematical point of view, the finite difference implementation of the method of characteristics is well founded. However, this approach is not robust near shocks, where characteristic analysis itself must be augmented with shock tracking in order to be applicable.

Other finite difference methods for treating the boundary conditions have also been used which are not a direct implementation of the method of characteristics. These are reviewed and compared to the characteristic approach in Ref. 38 for two-dimensional, steady flow. Commonly used methods in three-dimensional flow apply the interior point difference scheme at the boundary followed by an ad hoc means of satisfying the boundary conditions. For a body surface, Kutler et al.<sup>7</sup> used the standard MacCormack predictor followed by a two-dimensional, isentropic turn which "corrects" the flow variables to satisfy the flow tangency condition. To treat bow shocks, Thomas et al.<sup>4</sup> and Kutler et al.<sup>7</sup> used the interior-point scheme to advance temporary properties behind the shock of which only the pressure is assumed correct. The other flow variables and the shock geometry are then determined from the pressure using the shock relations.

### 2.3.2 Finite Volume

Finite volume methods do not advance points along the boundaries. However, during each computational step, it is necessary to compute a flux at the cell edges adjacent to boundaries. Application of the method of characteristics to compute these fluxes would require interpolation from the underlying computational mesh. Also, it would be necessary to store property values from the previous step in order to supply upstream information for the  $C_0$  characteristic.

An alternative is to extrapolate computed properties to the boundary. This set of values will not satisfy the boundary conditions. An operation is then applied which satisfies the boundary conditions. At surfaces an oblique shock or Prandtl-Meyer expansion is used to turn the velocity vector to satisfy the tangent flow boundary condition. In two-dimensional smooth flow, the oblique shock or Prandtl-Meyer expansion relations reduce to the characteristic compatibility relation, Eq. 13a. Thus, the method of characteristics is effectively being applied, and only admissible information is being used. In three-dimensional flow, the discrete characteristic compatibility relations contain a source term which is multiplied by distance along the characteristic ray. By extrapolating properties to the location at which the shock or expansion term is applied, the distance between points R, S and P (see Fig. 7) goes to zero and the source term disappears. Thus, the method of characteristics is applied. A similar procedure can be used at shocks. Here, the extrapolated properties at the downstream side of the shock and the freestream conditions define a Riemann problem. The solution of this problem features an angular orientation which separates the free-stream properties from other states. That orientation is taken as the shock slope.<sup>17,18,34</sup>

## 2.4 Separation Modeling

The Euler equations allow rotational flow and thus can convect vorticity. This permits modeling of body and wing-tip vortices which feature reversals of the velocity in the crossflow plane, but not in the axial direction. Solutions to the Euler equations contain mechanisms such as shocks for generating vorticity. However, the inviscid character of these solutions precludes accounting for viscous vorticity



generation, caused by factors such as separation. This type of mechanism creates the bulk of the flow field vorticity in many cases, of which the slender body, high incidence flow field is an example. To simulate vorticity generated by viscous phenomena, vorticity must be added to the inviscid flow field in an empirical manner.

Numerical solutions of Euler's equations can also generate vorticity through numerical error. Inadequate resolution can lead to errors in the computed entropy. For steady supersonic flow with constant stagnation enthalpy, Crocco's theorem states that:

$$T \nabla S = -\nabla x (\nabla x \nabla)$$

Thus errors in entropy result in vorticity production.

Crossflow vortices have been observed in Euler solutions which do not contain shocks.<sup>39</sup> This has occurred for both smooth shapes and those featuring sharp corners. In the case of smooth shapes, vortices have been obtained near delta wing tips as shown in Fig. 8 and are similar in location and size to those which are observed experimentally. However, careful numerical experiments have shown that as the mesh is refined, such vortices disappear.<sup>40</sup> This is to be expected since mechanisms for generating vorticity, other than shocks, are not present in Euler equations. As more accurate solutions are obtained, the flow field structure should become consistent with the properties of the Euler equations.

Geometries featuring sharp corners produce vortices on sharp delta wing which do not disappear as the mesh is refined.<sup>40,41</sup> Furthermore, measured surface pressure, vortex location and total pressure losses are well predicted. This is surprising since the Euler equations omit viscosity which should be central to simulating separation.

Panel methods provide a precedent for accurately modeling leading edge vortex separation using inviscid models.<sup>42</sup> Here a Kutta condition is enforced at the leading edge and vorticity within the flow field is modeled using a singularity distribution (e.g., vortex filaments). An analogous procedure should be possible with the Euler equations. The Euler equations can convect vorticity and singularity distributions are not needed. However, a Kutta condition should be necessary. This is contrary to the results of Refs. 40, 41, discussed above, which achieved accurate vortex modeling without a Kutta condition. It has been postulated that the dissipative nature of numerical schemes imposes a smoothness constraint on the computed pressure. This is equivalent to applying the Kutta condition.

The loss of total pressure within a vortex core has been attributed to numerical dissipation which smears shear layers over several mesh points.<sup>43</sup> Consider a smeared shear layer across which the stagnation enthalpy is constant, and on either side of which the total pressure is constant. This implies that on both sides of the shear layer the velocity magnitude is constant, but of different direction. Dissipation is effectively an averaging operation and near the middle of the shear layer, the velocity vector will equal the average of the velocity vectors on either side of the shear layer. This average velocity vector is of smaller magnitude than either of the adjacent velocity vectors. To maintain constant stagnation enthalpy throughout the shear layer, the enthalpy at this point must increase which presumably increases the entropy. This increase in entropy decreases the total pressure at the center of the shear layer.

The flowfield about a slender, circular body at incidence separates to form two strong leeside vortices. By contrast, the Euler solution to this problem features a crossflow shock which generates sufficient vorticity to form two weak leeside vortices, as shown in Fig. 9. To generate a more realistic flow pattern, vorticity must be explicitly added to the flow field. This is usually accomplished by modeling the separation region directly. Sufficient experimental data exist for circular bodies to develop an empirical relation describing the separation angle in the cross-flow plane as a function of incidence, Mach number, and axial location.<sup>44</sup> At the predicted separation point, special conditions are applied which simulate separation. These conditions are based on the concept of a slip line which originates at the separation point. Across the slip line the pressure is assumed to be continuous and the velocity normal to it is zero. On both sides of the slip surface, entropy is conserved along the streamlines, but is discontinuous across the surface. In Ref. 45, the slip surface is assumed to be tangent to the body surface. At the point of tangency, conditions windward of the slip line are determined using standard body boundary treatment while the leeward cross-flow velocity is set to zero. The slip surface emanating from the separation point is actually fit. Other treatments of the separation region have been less elaborate. In Ref. 46, a single set of properties is calculated at the separation point. At this location, pressure and density are determined by averaging property values at the two adjacent points while the direction of the velocity vector is set empirically. Ref. 32 uses a similar procedure, but orients the velocity at the separation point along the separation line.

The pressure distribution near the prescribed separation point is often not smooth. An alternative procedure which produces a smooth pressure variation is to

reduce the crossflow velocity over a broad area.<sup>47</sup> This adds circulation to the crossflow plane and can be accomplished by setting an upper crossflow velocity limit. Crossflow velocity magnitudes in excess of this limit are reduced to this value and the axial velocity is redefined to satisfy the stagnation enthalpy constraint. This procedure is referred to as clipping.

### 3. SUPERSONIC TACTICAL MISSILE CODES

Four Euler solvers applicable to tactical missile in supersonic flight are described. These are the SWINT, MUSE, ZEUSL and ZEUS codes, which feature the following common characteristics:

1. Multiple zone structure with a simple algebraic mesh.
2. Solution of Euler's equation in conservation form using explicit schemes.
3. Bow shock fitting and the capturing of all other internal shocks.
4. The mesh does not conform to fin tips and surfaces interior to the computational domain may appear and disappear during the calculation. illustrated in Fig. 10.

The multiple zone structure combined with the simple algebraic mesh and approximate resolution of fin edges makes it convenient to treat missiles with thin, sharp edged fins. The user must only ensure that body and fin surfaces coincide with edges of the different zones. As is illustrated in Fig. 10, points on the edges of zones may change from interior to surface points from one step to the next and vice-versa. A leading edge point is one which changes from interior to surface type during a step, while a trailing edge point changes from a surface to interior type.

In many respects these solvers differ, some being finite difference and others being finite volume. Also, different integration schemes are used. The following section outlines the attributes of each.

#### 3.1 SWINT (Supersonic Wing INlet Tail)

The SWINT code, which is described in detail in Ref. 32, solves the Euler equations in conservation form using cylindrical coordinates (i.e., Eqs. 4). Integration of interior points is accomplished using MacCormack's explicit scheme (Eqs. 7). Kentzer's approach is applied to points on the body or fin surfaces and to fit the shock. An abbreviated version of the multiple-zone approach is used which restricts code application to thin fins, located near  $\phi = \text{constant}$  surfaces. Here, the correct fin slope is applied to the fin center line rather than at its true location, as shown in Fig. 11.

To increase robustness and accuracy near fin edges, a local analysis is applied at leading and trailing edge points. The computational algorithm proceeds by completing the step in which the fin edge is encountered without taking the fin edge into account. The resulting flow properties are taken to be the conditions immediately upstream of the leading edge. A local analysis is applied to satisfy the boundary conditions at the fin edge. In the case of a leading edge, the flow downstream of the fin edge should be parallel to the fin surface. If the flow component normal to the leading edge is sufficiently supersonic, an oblique shock or expansion can be used to satisfy this boundary condition. Otherwise, a truly local analysis is not appropriate and an empirical procedure must be used.

Downstream of a trailing edge the streamlines from the upper and lower wing surfaces must feature the same pressure and direction in a plane perpendicular to the fin edge. If the velocity component normal to the trailing edge on both fin surfaces is sufficiently supersonic, this is equivalent to the supersonic Riemann problem cast in a plane perpendicular to the fin trailing edge. Otherwise, a purely local analysis is not appropriate. For simplicity, the SWINT code averages the properties from the two streamlines passing over and under a fin to determine properties downstream of the fin trailing edge.

The presence of surface and interior points along the same zone edge requires the introduction of special differencing procedures. In addition, physical considerations have motivated other adjustments to the differencing used at both fin and interior points located next to the fin edge. The special procedures introduced are as follows:

1. Alteration of the differences at points adjacent to a fin tip. The types of points under consideration are A, B, and C of Fig. 11. The MacCormack scheme at C must be modified since there are two different sets of adjacent flow values (i.e., points A and B). In addition, a discontinuity may be located at the fin edge, and it often is not advisable to difference across the fin edge.
2. Suppression of surface normal derivatives near a leading edge. A discontinuity often exists at a leading edge and differences normal to the surface are not meaningful. Use of such quantities in the finite difference equations leads to non-physical pressure oscillation. Damping such derivatives near the leading edge improves results.

3. Application of smoothing to interior, body and fin points. In computations featuring body separation or highly swept wings at high incidence, large vortex structures develop in the flow field. Under these circumstances, application of smoothing is often necessary to keep the computation from failing. This is accomplished at interior points by applying a switched Schuman filter with a density switch as is described in the previous section (i.e., Eqs. 9 and 10). At the body and fin surfaces, a modified Schuman filter can be applied along the surface to advance these quantities. Smoothing of the fin-tip points is implemented by averaging the fin-tip quantities with those at adjacent fin points.

4. Simulating Cross-flow Separation. Flow separation on a circular body is modeled using an empirical correlation to prescribe the line of separation on the model surface. At the point of separation, the velocity vector is aligned with the separation line. Calculation of highly swept wings produces a leeside vortex irrespective of the treatment applied at the fin tip. However, the strength of the leeside vortex is influenced by the type of differencing applied here.

### 3.2 MUSE (Multiple-zone Steady Euler)

The MUSE code solves Euler's Equations in cartesian coordinates (Eqs. 3) using the explicit MacCormack Method. Ref. 48 provides a detailed description of this computational approach. Using the same methods applied in the SWINT code, it treats the boundaries using Kentzer's technique, applies a local analysis at the leading and trailing edges, and is supplemented with the same special procedures. It differs from SWINT by being cast within a full multiple zone framework. Each zone is a quadrilateral as shown in Fig. 12 and may abut to any other zone. This allows complex geometries featuring items such as a tail located at the wing semi-span (see Fig. 13) or detached inlets to be treated. It also removes the thin fin assumption and places the fin surface at its true location.

### 3.3 ZEUSL (Zonal Euler Solver, Lower order)

The ZEUSL code is a first order Godunov scheme cast in a finite volume formulation. Conservation of mass, momentum and energy within a finite control volume (see Fig. 3) is used to determine the flow field (i.e., Eqs. 1). A detailed description of this technique is available in Ref. 17. The quadrilateral zones of Fig. 12 are used, however, zones can only abut along edges 2 and 4. This formulation removes the thin fin assumption, but does not allow treatment of the range of configurations which can be handled with MUSE.

The ZEUSL code does not advance points located on the boundary and boundary conditions are imposed through the fluxes at cell edges located on the boundary. Such fluxes are determined by applying an operation to the properties of the cell on which the edge borders, which satisfies the necessary boundary condition. At a surface, the shock or expansion relations are used to turn the cell velocity vector tangent to the surface. This procedure is a natural truncation of the Riemann problem to the situation where the final streamline direction is known. The fluxes at this cell edge are computed using the pressure resulting from the shock or expansion. The bow shock is fitted by constructing a Riemann problem along cell edges adjacent to the free-stream. The initial states of this problem are the free-stream conditions and the properties of the adjacent cell. The solution to the Riemann problem specifies a direction which separates free-stream condition from other states. This direction is taken to be the shock slope.

The wall pressure predicted by the above procedure is used to advance the solution. However, these values are only locally first order in smooth regions, and a more accurate surface pressure estimate is needed for evaluating the aerodynamics coefficients. This is accomplished using the reference plane method of characteristics described in Ref. 17.

The special procedures applied in the SWINT code are not needed. The finite volume formulation removes the ambiguity associated with advancing cells adjacent to fin tips (i.e., points A, B, C of Fig. 11). The robustness of the Godunov scheme allows leading and trailing edge points to be directly computed without a local analysis or derivative damping. Artificial viscosity is not needed and the final code formulation does not contain any adjustable parameters.

Near leading and trail edges, accurate treatment of fin geometry is important. Here, a solid surface may cover only a portion of a cell edge. Such edges are divided into two sections: one containing the edge area adjacent to the surface and the other edge area adjoining another element. Separate estimates are made of the fluxes acting on each section and these are added to determine the total edge flux.

### 3.4 ZEUS (Zonal Euler Solver)

The ZEUS code is a second order version of ZEUSL. A predictor step has been added and linear property variations are computed within each control volume, which yields second order accuracy. The predictor step is applied to the Euler Equations in non-conservation form and determines cell property values at  $z^n + \Delta z/2$ . Here,  $\Delta z$  is

the step size. The linear property slopes are determined using the limited differences of Eq. 11. This allows the properties at the cell edge mid-point to be determined by extrapolation. A Riemann problem is constructed at each cell edge using the two predicted edge property sets from the adjacent cells. Near strong shocks, the limiters reduce derivatives to zero and the first order Godunov algorithm is recovered. A detailed description of ZEUS is provided in Ref. 34.

The ZEUS code does not require any special procedures other than the special treatment of cell edges which are partially covered by a surface. Here, the same procedure used in ZEUSL is applied. The only free parameter in the ZEUS code is the limiter constant  $K$ . However, the same value of  $K$  has been successfully used for all the problems.  $K$  is set to unity at interior cells, 2 at cells adjacent to a smooth surface, and 0 at cells adjoining a discontinuous one.

#### 4.0 RESULTS

This section presents the results obtained with SWINT, MUSE, ZEUSL, and ZEUS codes, with emphasis on the SWINT calculations. This code was released in 1982 and has been widely used. The MUSE, ZEUSL and ZEUS codes produce results which are similar to those of SWINT. Unless otherwise stated, all calculations are started using the approximate conical solution of Ref. 33. Computational details for the presented cases can be found in Refs. 17, 32, 34, and 48 for the ZEUSL, SWINT, ZEUS and MUSE codes, respectively. In most cases, a  $36 \times 36$  mesh was used for the winged portion of the computation. Complete configurations can be computed in several minutes on a CRAY 1. All of the reported calculations could also have been completed on a VAX 11-780.

##### 4.1 Body Alone

It has been experimentally observed that the flow over a slender, circular body separates near the model shoulder and rolls up into leeside vortices. The numerical solution to this problem instead features a crossflow shock on the leeside of the body, as illustrated by the ZEUSL results in Fig. 9. Behind the shock, a small vortex may form as a result of the entropy gradient produced by the shock. However, the location and strength of this vortex is not in agreement with experiment. At low Mach numbers, the crossflow shock is positioned near the shoulder of the model and with increasing Mach number, it moves leeward. Windward of the experimental separation point and the numerical crossflow shock, predicted and measured surface pressures follow the same trend. Leeward of this point they do not, as shown in Fig. 1 and 15, using the SWINT results of Ref. 47 and 49. The greatest discrepancy between calculation and experiment occurs at the lower Mach numbers. At the higher Mach numbers, both calculation and experiment feature low pressures over most of the leeside of the model. As illustrated in Table 1, the inviscid normal force is within 5% to 10% of the measured one. On short bodies ( $L/D < 10$ ), the normal force is under-predicted, while the computed center of pressure is aft of the measured one.

The separation modeling procedures described in the last section reduce the qualitative difference between the experimental and the computed flow field. These techniques add vorticity to the flow field, forming a strong leeside vortex that destroys the crossflow shock, as illustrated in Fig. 16, using clipped ZEUS results. This raises the pressure on the leeside of the body, but does not bring computation into agreement with experiment. Figs. 14 and 15 demonstrate the application of clipping<sup>48</sup> and prescribed separation<sup>32</sup> respectively. Table 1 indicates that separation modeling does not have a large influence on the calculated forces and moments. However, its use produces a more realistic model of the flow field which may improve calculated fin loads.

The SWINT code has also been applied to the elliptic body-alone shape shown in Fig. 17. This figure illustrates the circumferential pressure variation at three different incidences. At all incidences, good agreement is obtained between computation and experiment without use of separation modeling options. Calculated and measured force and moment were compared for a similar body in Ref. 50 and agree well with experiment over a broad range in Mach number.

##### 4.2 Body-Wing Models

Fin surface pressures calculated with the ZEUS code are shown in Fig. 18 for a cruriform delta configuration in the plus roll orientation. Experimental data is from Ref. 51 and were measured at a Mach number of 3.7, and incidence of  $7.8^\circ$ . For these conditions, attached shocks or expansions occur at the fin leading edges. The calculated surface pressure agrees well with experiment over most of the fin surface. The crossflow velocity vectors and pressure contours at an axial station near the fin mid-cord are given in Fig. 19. Shocks can be seen attached to the fin edges.

Calculations have been performed on the two swept-wing configurations shown in Fig. 20 using the ZEUS code. These bodies were tested in Ref. 52 at an incidence of  $6^\circ$  and Mach numbers of 2.5 and 4.5. Calculated and measured wing surface pressures are shown in Fig. 20 and agree well in most cases. However, near the wing leading

edge, computed values are larger than measured ones. Fig. 21 provides measured and calculated surface pressures on the windward and leeward side of the body. Calculated surface pressures generally agree well with experiment, however, discrepancies occur on the aft end of the body at Mach 4.5. On the windward side, the pressure rise due to the presence of the wings is computed to occur downstream of the measured one, while on the leeside, predicted pressures exceed experimental values. However, these calculated results are in excellent agreement with those computed in Ref. 48 and thus, these discrepancies are likely due to viscous effects. The crossflow pressure contours are shown in Fig. 22 at three axial stations featuring the wing at Mach 2.5 and 4.5 for the thick wing case. A detached shock is visible below both wings and, at higher Mach numbers, it is positioned closer to the wing surface. This produces the strong wing surface pressure gradients which are visible at this Mach number in Fig. 20.

The pressure distribution along the windward ray of a cruciform missile in the X configuration is shown in Fig. 23 for several Mach numbers. This figure is taken from Ref. 53 where it is noted that the windward measured pressure is nearly independent of Reynolds number. Reasonable agreement is shown between experiment and SWINT calculations at incidences less than  $20^\circ$ . At higher incidences, subsonic pockets form at the body-wing juncture and the computation cannot be completed. Figs. 24 illustrate the measured and calculated surface pressure at an axial station downstream of the fin for both + and X roll positions. Considering the complexity of the flow field, which contains both shocks and vortices, reasonable agreement is obtained with experiment.

The swept wing model tested in Ref. 54 is depicted in Figs. 25 and 26. Also shown are SWINT calculated body and wing surface pressures for the incidence of  $8.8^\circ$  and Mach numbers of 2.3. The calculated wing surface pressures are generally in good agreement with experiment over most of the wing. On the body, the pressure pulse, due to the presence of the wing, is accurately predicted. Fig. 27 illustrates the calculated crossflow plane surface pressure slightly forwards of the wing trailing edge. A detached shock is positioned below the wing. The absence of the wing thickness in this figure is a consequence of the thin fin assumption applied in the SWINT code.

Calculated and measured flow field data have been compared in Ref. 55 for the wing-body combination shown in Fig. 28. Here, Mach number, total pressure, local angle of attack and yaw angle are shown along circumferential and radial paths through the flow field at Mach 3.94 and incidences of  $\pm 10^\circ$ . The computed results are in reasonable agreement with experimental data, which itself exhibits some scatter. The best comparison occurs at  $+10^\circ$  (see Fig. 28a and b) where measuring stations were located on the windward side of the body. The leeside measurements, taken at  $-10^\circ$ , do not compare nearly as closely (see Fig. 28c). Ref. 55 examines additional cases at varying Mach numbers and on different bodies. The accuracy of these predictions is similar to those shown.

Figure 29, taken from Ref. 56, provides experimental data for individual fin loads as a function of roll angle on the illustrated cruciform model at an incidence of  $12^\circ$ . Also shown are SWINT calculated fin loads obtained with and without fin deflection. This figure illustrates that the prescribed separation option (at least for this configuration) has little effect, and deflected fin loads can be accurately predicted at all roll orientations. Fig. 30 compares calculated and measured normal force, pitching moment at a roll angle of zero, while Fig. 31 illustrates roll moment as a function of roll angle. All these quantities are reasonably well predicted.

The measurements of Ref. 57 provide the center of pressure at low incidence and  $C_{No}$  for a range of Mach numbers on a cone-cylinder-tail body. SWINT calculations reported here are compared with experiment in Fig. 32. Good agreement with experiment is obtained in the Mach number range of 2 to 3, with best results occurring at the higher Mach numbers.

#### 4.3 Body-Wing-Tail

The wing-body tail configuration of Ref. 58 is shown in Fig. 33 and features a highly swept wing with a subsonic leading edge normal Mach number. The normal force and center of pressure calculated with the ZEUSL code is shown at Mach 2.86 and agrees well with experiment. The computed crossflow field velocity and pressure contours near the wing trailing edge and at the middle of the tail are shown in Fig. 34. A large leeside vortex is visible near the wing trailing edge. It is convected leewards as it passes over the tail. Below the horizontal tail surface, a strong shock wave is evident.

The calculated and measured normal force on an elliptical body with and without a wing and tail is illustrated in Fig. 35 at Mach 2.5. The calculations were performed using the SWINT code and are taken from Ref. 49 while the data is from Ref. 59. Good agreement is obtained both with and without lifting surfaces. In addition, the calculated surface pressures are in reasonable agreement with experiment.<sup>49</sup>

Fig. 36 illustrates normal force and pitching moment as a function of incidence for the depicted circular body with canards and a tail. Here, SWINT calculations are compared with experiment in Ref. 49 using data from Ref. 60 at a free-stream Mach number of 2.5. The normal force and center of pressure are in good agreement with experiment for the body alone and body-canard-tail configuration.

The accuracy of the SWINT predicted roll moment for the configuration of Fig. 36 is shown at Mach 2.5 in Fig. 37. Here, the horizontal canards have been deflected of 5°. Good agreement with experiment is obtained on a body-canard model up to incidences of 10°. When the tail is added, predictions agree with experiment only at low incidences. This discrepancy at higher incidences suggests that the vortices generated by the deflected wing are not producing the correct induced effects on the tail.<sup>49</sup>

A comparison of the SWINT calculated<sup>61</sup> and measured forces and moments on the configuration of Fig. 36 at 26.6° roll is shown in Fig. 38. The free-stream Mach number is 2.5 and all the fins are deflected 5° to produce a roll moment. Reasonable agreement is obtained between calculation and experiment.

A swept wing configuration configuration with vertical tail located on the wing is shown in Fig. 39. The calculation of this configuration was carried out with the MUSE code using a four zone model. The tail thickness was neglected in order to simplify the geometry description. The calculated normal force and center of pressure shown in Fig. 39 agree well with experimental data of Ref. 62. Crossflow velocities and pressures at an axial station slightly forward of the wing trailing edge are given in Fig. 40 along with those for a similar configuration without a vertical tail. The presence of the tail is seen to produce large changes in the leeward flow field. A detached shock can be seen lying below the outboard section of the wing.

The SWINT code has also been used in Ref. 57 to predict the pitch damping coefficient,  $C_m$ . The varying local incidence experienced by a pitching body is simulated by curving the body and wings as is shown in Fig. 41. Calculations were made in Ref. 54 over a Mach number range of 2 to 4 for both a Basic Finner model and a three finned flechette. Good agreement between experiment and computation was achieved on both configuration. The Basic Finner model results are illustrated in Fig. 41.

## 5. CONCLUDING REMARKS

Missile aerodynamic characteristics traditionally have been predicted by empirical methods or determined from experiment. In cases where an extensive database is available, empirical predictions may be as accurate as computational methods and attainable at a fraction of the cost. However, the computational approach is independent of experimental data and is, therefore, applicable to a broader range of configurations, including new designs. Furthermore, computational methods calculate all flow field properties, information which cannot be predicted empirically and that is extremely costly to measure. Flow field predictions facilitate the design optimization of components such as inlets and fins. For example, knowledge of the dynamic pressure about a missile body suggests fin locations which will produce maximum effectiveness. The recovery pressure distributions and flow profiles indicate the optimal location for inlets.

This paper outlines a strategy for treating missiles in supersonic flight which feature sharp leading edges. Four different computational methods are described: two which use the finite-difference MacCormack explicit scheme and two based on the Godunov finite-volume approach. A comparison of these methods is given in Table 2, while a detailed discussion of the advantages of each approach is available in Ref. 63. All methods produce similar results. However, the MacCormack schemes are not robust and artificial viscosity must often be added along with special procedures at wing edges. While the Godunov methods are slower, they are also more robust and do not require special procedures.

Reasonable agreement can be obtained between calculation and experiment over a broad range of missile configurations. However, problem areas do exist, particularly on the leeside of missiles. Here the physics of viscous flow departs from that of the inviscid equations under considerations. Viscous flow fields can feature extensive vorticity production from boundary layer separation, a mechanism absent from the inviscid model. Leeside vortices, which are experimentally observed to develop on a circular body at incidence, provide an example of a flow field where vorticity generated by boundary layer separation has a great impact on flow field structure. The inviscid solution to the same problem instead features a crossflow shock which generates only a weak vortex. The relation of predicted inviscid to measured separation from sharp edges needs to be examined. Such leading edge separation has a dramatic influence on wing lift and can induce large changes on tail surface aerodynamics. Although successes have been reported in calculating lift on wings featuring leading edge separation, it remains to be established that accurate predictions can be achieved over a broad range of conditions. These physical considerations, rather than numerical ones, constitute the primary obstacle to improved Euler predictions for supersonic tactical missiles.

## REFERENCES

- <sup>1</sup>Shapiro, A. H. and Edelman, G. M., "Method of Characteristics for Two-Dimensional Supersonic Flow - Graphical and Numerical Procedures," Journal of Applied Mechanics, Vol. 14, No. 2, 1949, pp. A154-A162.
- <sup>2</sup>Shapiro, A. H., Compressible Fluid Flow, Vol. 1, The Ronald Press Co., New York, 1953.
- <sup>3</sup>Sorcnsen, V. L., "Computer Program for Calculating Flow Fields in Supersonic Inlets," NASA TN D-2897, July 1965.
- <sup>4</sup>Thomas, P. D., Vinokur, M., Bastianon, R. and Conti, R. J., "Numerical Solution for Three-Dimensional Inviscid Supersonic Flow," AIAA Journal, 10, July 1972, pp. 887-894.
- <sup>5</sup>Moretti, G., Grossman, B. and Marconi, F., "A Complete Numerical Technique for the Calculation of Three-Dimensional Inviscid Supersonic Flow," AIAA Paper 72-192, 1972.
- <sup>6</sup>Marconi, F. and Salas, M., "Computation of Three Dimensional Flows About Aircraft Configurations," Computers and Fluids, 1, June 1973, pp. 185-195.
- <sup>7</sup>Kutler, P., Reinhardt, W. A. and Warming, R. F., "Multishocked, Three-Dimensional Supersonic Flowfields with Real Gas Effects," AIAA Journal, 11, May 1973, pp. 657-664.
- <sup>8</sup>Kyriss, C. L. and Harris, T. B., "A Three-Dimensional Flow Field Computer Program for Maneuvering and Ballistic Re-entry Vehicles," Tenth USN Symposium on Aeroballistics, July 1975.
- <sup>9</sup>Marconi, F., Salas, M., and Yaeger, L., "Development of a Computer code for Calculating the Steady Super/Hypersonic Inviscid Flow Around Real Configurations, Vol. 1, Computational Techniques," NASA CR 2675, April 1976.
- <sup>10</sup>Solomon, J. M., Ciment, M., Ferguson, R. E., and Bell, J. B., "Inviscid Flowfield Calculations for Reentry Vehicles with Control Surfaces," AIAA Journal, 15, Dec. 1977, pp. 1742-1749.
- <sup>11</sup>Chausee, D. S., Holtz, T., and Kutler, P., "Inviscid Supersonic/Hypersonic Body Flow Fields and Aerodynamics from Shock Capturing Technique Calculations," AIAA Paper 75-837, 1975.
- <sup>12</sup>MacCormack, R. W., "The Effect of Viscosity in Hypervelocity Impact Cratering," AIAA Paper 69-354, April 1969.
- <sup>13</sup>Moretti, Gino, "Calculation of Three Dimensional Inviscid, Supersonic, Steady Flows," Polytechnic Institute of New York, Report No. 81-25, Dec. 1981.
- <sup>14</sup>Wardlaw, A. B. Jr., Solomon, J. M., and Baltakis, F. P., "Supersonic Inviscid Flow Field Computations of Missile Bodies," AIAA Journal, 19, July 1981, pp. 899-906.
- <sup>15</sup>Priolo, F. J., Wardlaw, A. B. Jr., Baltakis, F. P., and Solomon, J. M., "Inviscid Multiple Zone Strategy Applied to Complicated Supersonic Tactical Missile Configurations," AIAA Paper 85-1813.
- <sup>16</sup>Klopfer, G. H. and Nielsen, J. N., "Euler Solutions for Wing and Wing-Body Combination at Supersonic Speeds with Leading-Edge Separation," AIAA Paper 80-0126, Jan. 1980.
- <sup>17</sup>Wardlaw, A. B. Jr., Baltakis, F. P., Martin, F. M. and Priolo, F. J., "A Godunov Method for Supersonic Tactical Missiles," Journal of Spacecraft and Rockets, 24, 1, Jan-Feb 1987, pp.40-48
- <sup>18</sup>Wardlaw, A. B., Jr. and Davis, S. F., "A Second Order Godunov Method for Tactical Missiles," AGARD FLUID DYNAMICS PANEL symposium on Applications of Computational Fluid Dynamics in Aeronautics, AIX-EN-PROVENCE, FRANCE, April 7-10, 1986.
- <sup>19</sup>Daywitt, J. E., Szostowski, D. J., and Anderson, D. A., "A Split Coefficient/Locally Monotonic Scheme for Multishocked Supersonic Flow," AIAA Journal, 21, June 1983, pp. 871-880.
- <sup>20</sup>Hsieh, T. and Priolo, F. J., "Generation of the Starting Plane Flowfield for Supersonic Flow Over a Spherically Capped Body," NSWC TR 84-484, May 1985.
- <sup>21</sup>Rakich, J. V., Bailey, H. E., and Park, C., "Computation of Nonequilibrium Three-Dimensional Inviscid Flow Over Blunt Nosed Bodies Flying at Supersonic Speeds," Paper presented at AIAA 8th Fluid and Plasma Dynamics Conference, A75-835, Hartford, CT, June 1975.

- 22 Ransom, V. H., Hoffman, J. D. and Thompson, H. D., "A Second Order Bicharacteristic Method for Three-Dimensional Steady, Supersonic Flow," AIAA Journal, 10, Dec. 1972, pp. 1573-1581.
- 23 Moretti, G., "Conformal Mappings for Computation of Steady, Three-Dimensional, Supersonic Flows," Numerical/Laboratory Computer Methods in Fluid Mechanics, ASME, December 1976, pp. 13-28.
- 24 Moretti, G., "Thoughts and Afterthoughts About Shock Computations," PIBAL Rept. 72-37, 1972.
- 25 Warming, R. F. and Beam, R. M., "On the Construction and Application of Implicit Factored Schemes for Conservation Laws," SIAM-AMS Proceedings, 1978, pp. 85-129.
- 26 Moretti, G., "The  $\lambda$ -Scheme," Computers and Fluids, Vol. 7, Sept. 1979, pp. 191-205.
- 27 Steger, J. L., and Warming, R. F., "Flux Vector Splitting of the Inviscid Gas Dynamic Equations with Application to Finite Difference Methods," J. Comp. Physics, 40, 1981, pp. 263-293.
- 28 Osher, S. and Solomon, F., "Upwind Difference Schemes for Hyperbolic Conservation Laws," Mathematics of Computation, 38, 158, Apr. 1982.
- 29 Godunov, S. K., "A Difference Method for Numerical Calculation of Discontinuous Solutions of the Equations of Hydrodynamics," Mat. Sb., 47, (1959), 271-306 (in Russian).
- 30 Baldwin, B. S. and MacCormack, R. W., "Interaction of Strong Shock Wave with Turbulent Boundary Layer," Proceedings of the Fourth International Conference on Numerical Methods in Fluid Dynamics, Springer-Verlag Lecture Notes in Physics, No. 35, June 1974, pp. 51-56.
- 31 Harten, A. and Zwas, G., "Switched Numerical Schuman Filters for Shock Calculations," Journal of Engineering Mathematics, Vol. 6, No. 2, April 1972, pp. 207-216.
- 32 Wardlaw, A. B. Jr., Baltakis, F. P., Solomon, J. M., and Hackerman, L. B., "An Inviscid Computational Method for Tactical Missile Configurations," NSWC TR 81-457, Dec. 1981.
- 33 "Equations, Tables and Charts for Compressible Flow," NACA 1135, 1953.
- 34 Wardlaw, A. B. Jr. and Davis, S. F., "A Second Order Godunov's Method for Supersonic Tactical Missile Computations," NSWC TR 86-506, April 1987.
- 35 van Albada, G. D., van Leer, B., and Roberts, W. W. Jr., "A Comparative Study of Computational Methods in Cosmic Gas Dynamics," Astro. Astrophys., 108, 76, 1982.
- 36 Rakich, John V., "A Method of Characteristics for Steady Three Dimensional Supersonic Flow with Application to Inclined Bodies of Revolution," NASA TN D-5341, October, 1969.
- 37 Kentzer, C. P., "Discretization of Boundary Conditions on Moving Discontinuities," Proceedings of the 2nd International Conference on Numerical Methods in Fluid Dynamics, Lecture Notes in Physics, 8, Springer-Verlag, 1971, pp. 108-113.
- 38 Abbett, M. J., "Boundary Condition Calculation Procedures for Inviscid Supersonic Flowfields," Proceedings of the AIAA Computational Fluid Dynamics Conference, Palm Springs, CA, 1973, pp. 153-172.
- 39 Newsome, R. W. and Kandil, O. A., "Vortical Flow Aerodynamics - Physical Aspects and Numerical Simulation," AIAA Paper 87-0205.
- 40 Newsome, R. W., "Euler and Navier-Stokes Solutions for Flow over a Conical Delta Wing," AIAA Journal, April 1986, pp. 552-561.
- 41 Murman, E. M., Powell, K. G., Goodsell, A. M., Landahl, M., "Leading-Edge Vortex Solutions with Large Total Pressure Losses," AIAA Paper 87-0039.
- 42 Hoeijmakers, H. W. M., "Computational Vortex Flow Aerodynamics," Aerodynamics of Vortical Type Flows in Three Dimensions, AGARD CP-342, Paper No. 18, July 1983.
- 43 Powell, K., Murman, E., Perez, E. and Baron, J., "Total Pressure Loss in Vortical Solutions of the Conical Euler Equations," AIAA Journal, 25, 3, pp. 360-8, March 1987.
- 44 Wardlaw, A. B. Jr., "High Angle of Attack Missile Aerodynamics," AGARD LS-98, March 1979.



- 45Nielsen, J. N., Kuhn, G. D., and Klopfer, G. H., "Euler Solutions of Supersonic Wing-Body Interference at High Incidence Including Vortex Effect," NEAR TR 263, Aug. 1982.
- 46Marconi, F., "The Spiral Singularity in the Supersonic Inviscid Flow Over a Cone," AIAA Paper 83-1665, 1983.
- 47Baltakis, F. P., Wardlaw, A. B. Jr., Allen, J. M., "Leeside Crossflow Modeling in Euler Space Marching Computations," NSWC TR 86-342.
- 48Wardlaw, A. B. Jr., Priolo, F. J., and Solomon, J. M., "A Multiple Zone Method for Supersonic Tactical Missile," NSWC TR-85-484, July 1986.
- 49Allen, J. M. and Townsend, J. C., "Application of the SWINT Code to Wing/Body/Tail Geometries," AIAA Paper 85-1811.
- 50Shereda, D. F., Amidon, P. F., Dahlem, V., Brown-Edwards, E., "Pressure Test of Three Elliptical Missile Body Configurations at Mach 1.5 to 5.0," AFWAL-TM-84-236-FIMG, Dec. 1984.
- 51Jackson, C. M., Jr., and Sawyer, W. C., "A Method for Calculating the Aerodynamic Loading on Wing Body Combinations at Small Angles of Attack in Supersonic Flow," NASA TN D-6441, 1971.
- 52Lamb, M., Sawyer, W. B., Wassum, L. L., and Babb, C. D., "Pressure Distribution on Three Different Cruciform Aft-Tail Control Surfaces of a Wingless Missile at Mach 1.6, 2.36, and 3.78," Vol. II and III, NASA TM 80097, Aug. 1979.
- 53Agnone, A. M., "High Angle of Attack Aerodynamics of a Cruciform Missile," AIAA Paper 84-507.
- 54Jernell, L. S., "Comparison of Theoretical and Experimental Pressure Distributions Over a Wing-Body Model at Supersonic Speeds," NASA TN D-6480, Sep. 1971.
- 55Sobel, D. R., "Assessment of Three Dimensional Flow Field Codes for Application to Wing-Body Configurations," UTRC Draft Report R86-956257-1, June 1986.
- 56Hodges, J., Ward, L. C., "The RAE Experimental Data-Base for Missiles at High Mach Number and its Use in Assessing CFD Methods," AGARD Paper No. 32, Aerodynamics of Hypersonic Lifting Vehicles, 60th Meeting of the Fluid Dynamics Panel, Bristol, U.K., April 6-9, 1987.
- 57Evans, J. R., "Calculation of Supersonic Pitch Damping Coefficients for Missile Shapes Using the SWINT Euler Code and an Equivalent Bent Body Assumption," 12th Meeting of TTCP WTP-2 Panel, Adelaide, Australia, Oct. 1986.
- 58Spearman, M. L., and Sawyer, W. C., "Longitudinal Aerodynamic Characteristics at Mach Numbers from 1.6 to 2.86 for a Fixed-Span Missile with Three Wing Platforms," NASA TM 74088, Nov. 1977.
- 59Graves, E. B., and Fournier, R. H., "Effect of Nose Bluntness and Afterbody Shape on Aerodynamic Characteristics of a Monoplanar Missile Concept with Bodies of Circular and Elliptical Cross Sections at a Mach Number of 2.50," NASA TM-80055, 1979.
- 60Blair, A. B., Jr., Allen, J. L., and Hernandez, G., "Effect of Tail-Fin Span on Stability and Control Characteristics of a Canard-Controlled Missile at Supersonic Mach Numbers," NASA TP-2157, 1983.
- 61Mansfield, F. A., Naval Weapons Center, California, Private Communication.
- 62Lamb, M., Sawyer, W., and Thomas, Jr., "Experimental and Theoretical Supersonic Lateral-Directional Stability Characteristics of a Simplified Wing-Body Configuration with a Series of Vertical Tail Arrangements," NASA TP 1978, Aug. 1981.
- 63Priolo, F. and Wardlaw, A. B., "A Comparison of Inviscid Computational Methods for Tactical Missiles," AIAA Paper No. 87-0113.

## ACKNOWLEDGEMENTS

This paper summarizes collaborative efforts between the author and J. M. Solomon, F. Baltakis, F. Priolo, S. Davis, all of NSWC. The author would like to thank G. Allen (NASA Langley), J. Hodges (RAE, Bedford), J. Evans (DREV), D. Sobel (UTRC) and W. Estes (NWC) for allowing their results to be included in the paper.

Table 1. 3 Caliber T/O Nose

| Body Length<br>(L/D) | M    | $\alpha$ | $C_N$ |       |      | $Z_{cp}$ |      |      |
|----------------------|------|----------|-------|-------|------|----------|------|------|
|                      |      |          | exp.  | inv.  | sep. | exp.     | inv. | sep. |
| 10.0                 | 1.98 | 10°      | .63   |       | .61  |          |      |      |
|                      |      | 15°      | 1.74  |       | 1.67 |          |      |      |
| 6.67                 | 2.30 | 16°      | 1.46  | 1.33  | .34  | .479     | .503 | .522 |
| 6.67                 | 2.90 | 15°      | 1.45  | 1.33  | 1.36 | .482     | .512 | .514 |
| 10.0                 | 3.88 | 10°      | .93   | .967  | 1.02 | .455     | .447 | .433 |
| 6.67                 | 4.63 | 20°      | 1.71  | 1.517 | 1.60 | .477     | .515 | .506 |

Table 2. Comparison of Euler Solvers

| Code Name           | 1ST ORDER<br>GODUNOV                   | 2ND ORDER<br>GODUNOV                       | MacCORMACK<br>+   |   |
|---------------------|--|--|---|---|
|                     | CHARACTERISTIC BOUNDARY CONDITIONS     |  |   |   |
| ROBUSTNESS          | ZEUSL                                  | ZEUS                                       | SWINT   | MUSE  |
|                     | GOOD                                   |  | NEEDS IMPROVEMENT   |   |
| APPLICATION         |  | BODY ALONE<br>BODY-WING-TAIL<br>BODY-INLET |   | BODY ALONE<br>BODY-WING-TAIL<br>BODY-INLET<br>BODY-WING W/VERTICAL TAIL<br>BODY-WING W/DETACHED INLET |
| SMOOTHING           | NONE                                   | NONE                                       | NECESSARY FOR SEVERE CASES  |   |
| SPECIAL PROCEDURES  | NONE                                   | LIMITER<br>ADJUSTMENT                      | LEADING EDGE JUMPS<br>TRAILING EDGE JUMPS<br>FIN EDGE DIFFERENCING<br>BOUNDARY CONDITION FORM<br>DERIVATIVE DAMPING |   |
| SPEED<br>(RELATIVE) | 1.4* - 2.3                             | 1.6* - 2.5                                 | 1   | 1.75  |
| ACCURACY            | LESS ACCURATE<br>ON EQUIVALENT<br>MESH |  | COMPARABLE  |   |

\* VALUE OBTAINED USING THE APPROXIMATE RIEMANN SOLVER OF REF. 34.

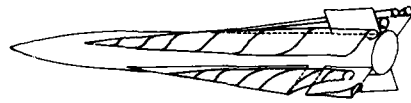


Figure 1. Typical Missile Flow Field .

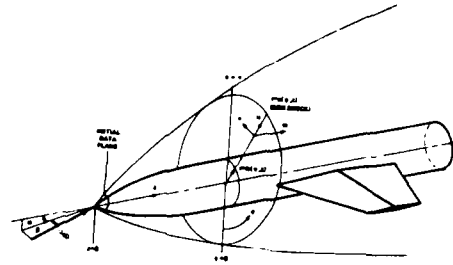


Figure 2. Cartesian and Cylindrical Coordinates.

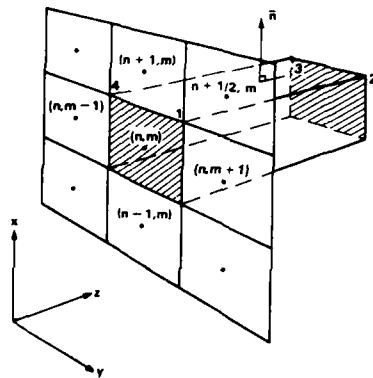


Figure 3. Control Volume.

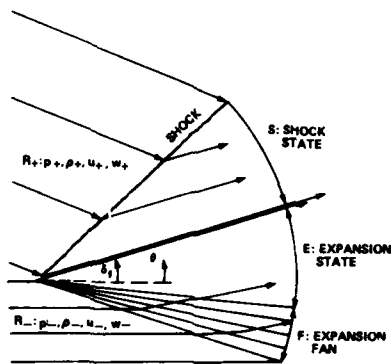
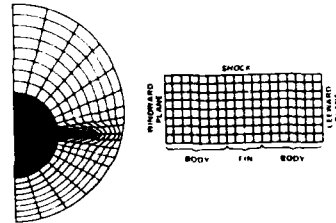
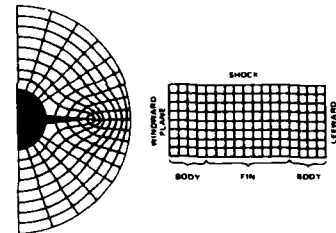


Figure 5. Supersonic Riemann Problem.

a) stretched mesh



b) wrap-around mesh



c) multiple zone mesh

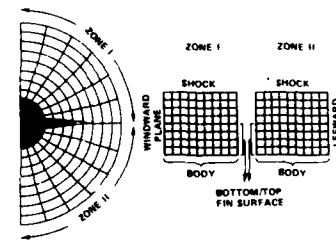


Figure 4. Computational Meshes for Finned Bodies.

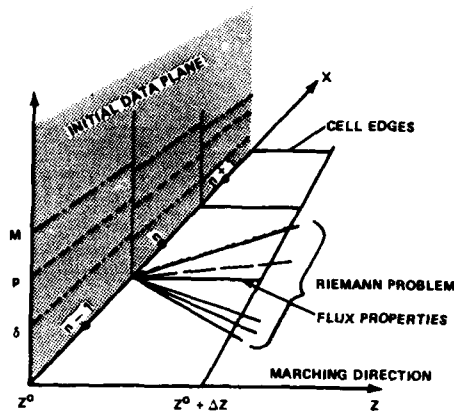


Figure 6. The Godunov Method Assumes Constant Properties Within a Cell and Uses the Riemann Problem to Determine Properties Along Cell Edges.

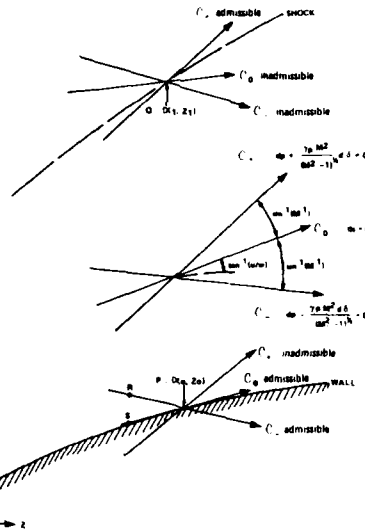


Figure 7. Characteristics for Two-Dimensional Steady Supersonic Flow.

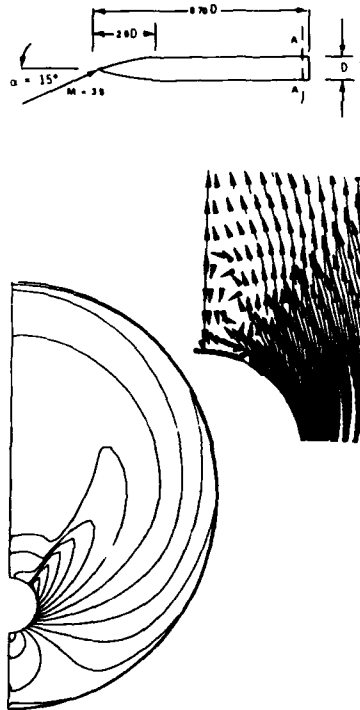


Figure 9. Calculate Crossflow Velocities and Pressures at Section A-A Using the ZEUSL Code.

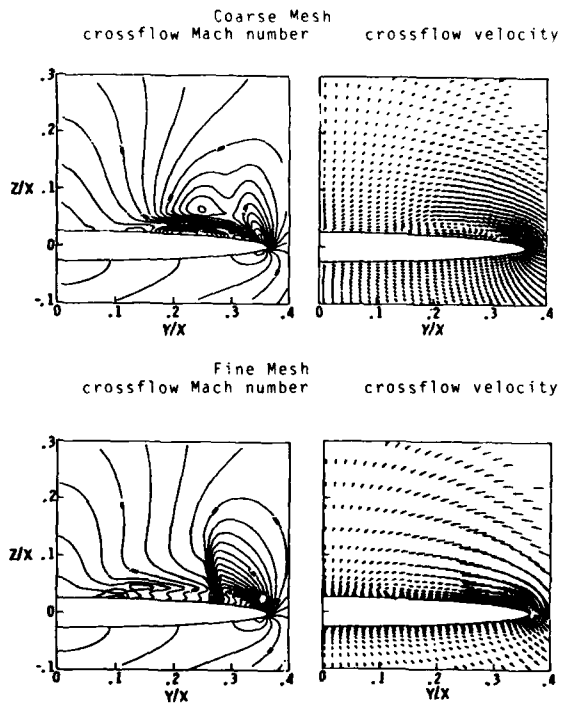


Figure 8. Elliptic Cone Calculations from Ref. 40.

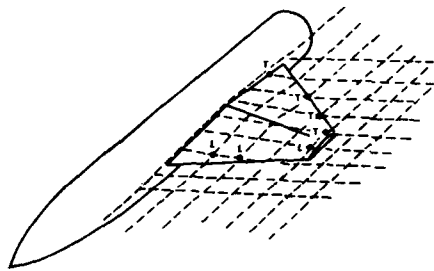


Figure 10. Points on Zone Edges may change Type During a Calculation L - Leading Edge; T - Trailing Edge Points.

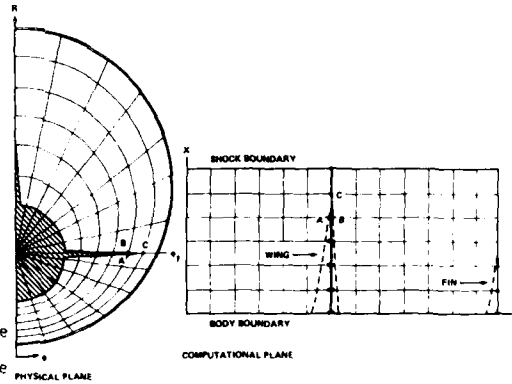


Figure 11. The SWINT Code Applies the Surface Slope at the Fin Centerline

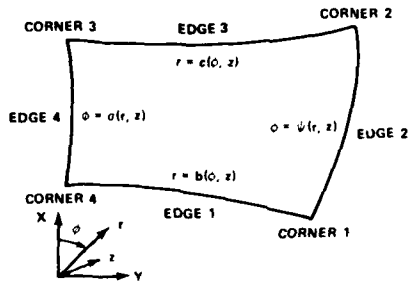


Figure 12. Generalized Quadrilateral Zone

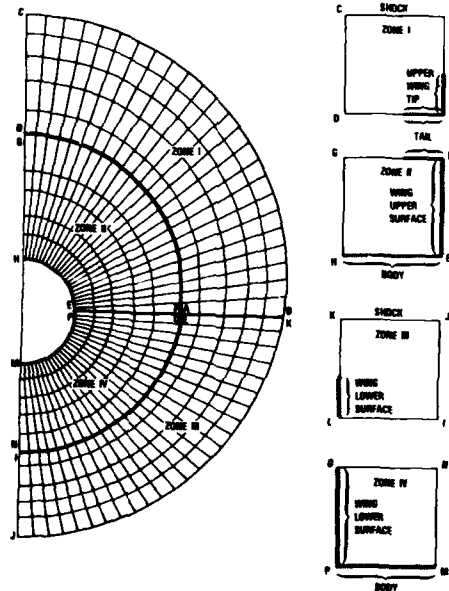


Figure 13. Zone Structure for a Body-Wing with a Vertical Tail Outboard on the Wing.

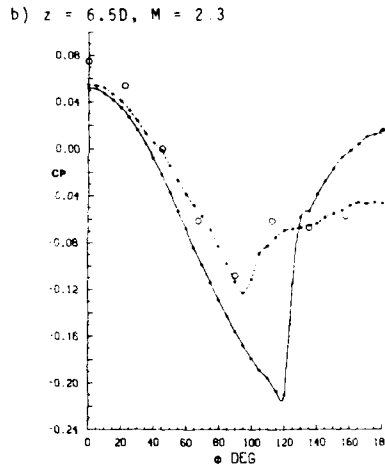
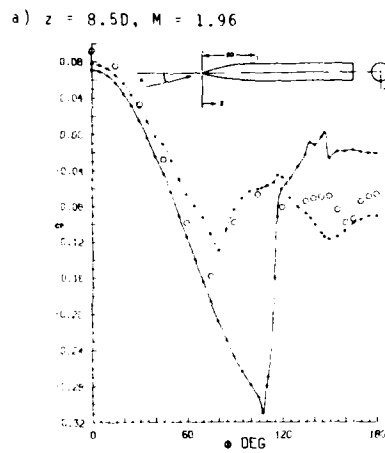
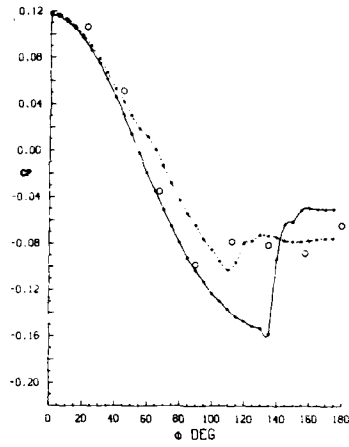


Figure 14. Circumferential Pressure Distribution on a Tangent Ogive. ○ Data; — Inviscid Calculation; --- Viscous Calculation.

c)  $z = 6.5D, M = 2.96$



d)  $z = 6.5D, M = 4.63$

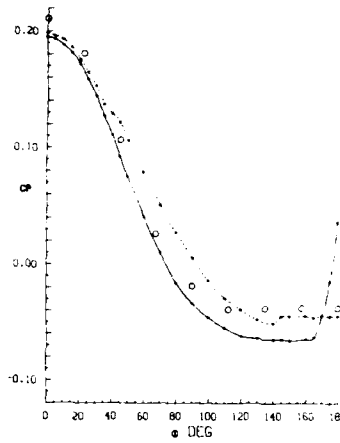


Figure 14. (Continued)

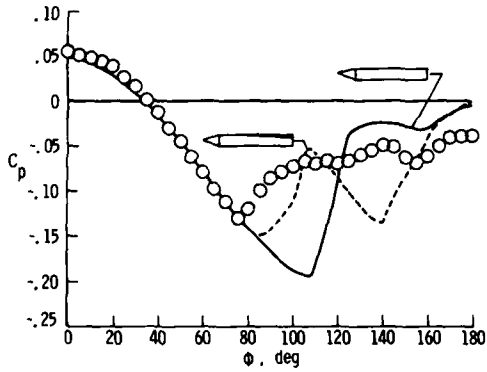


Figure 15. Circumferential Pressure Distribution.  $\circ$  Data, — SWINT inviscid, --- SWINT Prescribed Separation.

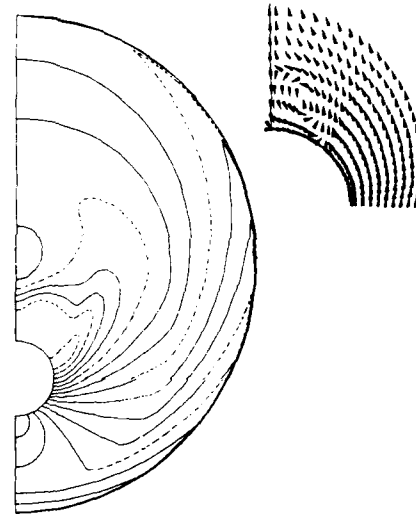


Figure 16. Crossflow Plane Pressure and Velocity on Model of Fig. 9 at Station A-A. Calculated with ZEUS Using Clipping.

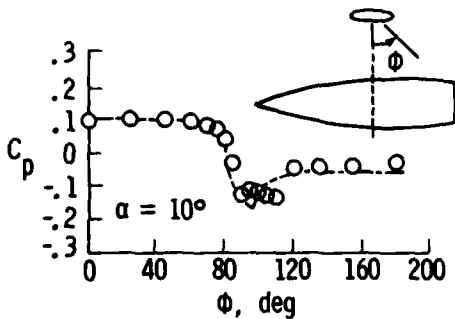
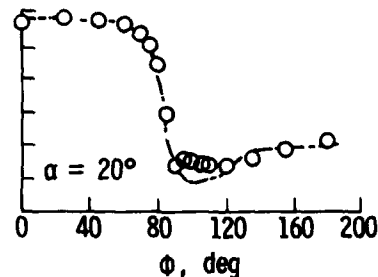
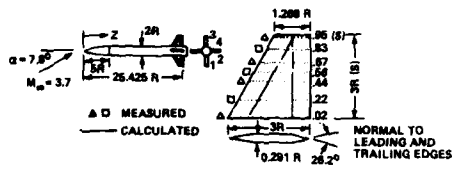
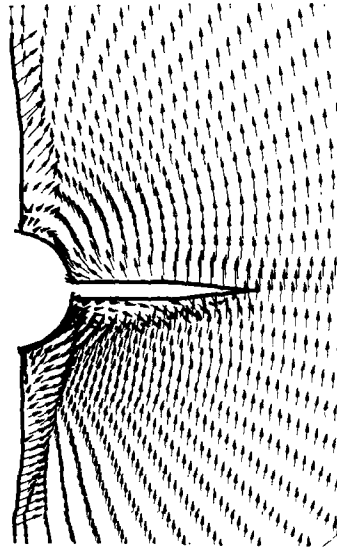
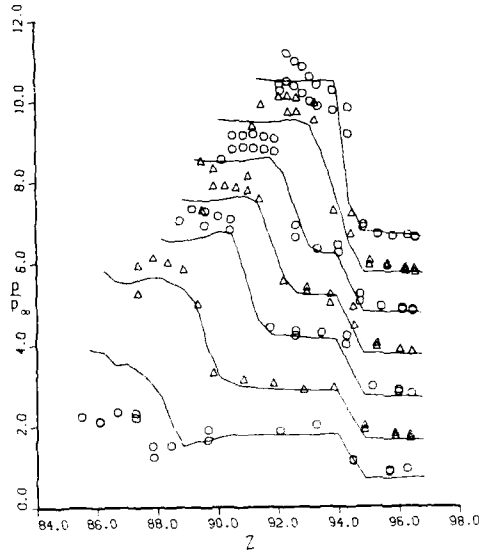


Figure 17. Circumferential Pressure Distribution on an Elliptic Body at  $M = 2.5$  and  $z = .6L$ . From Ref. 49. — SWINT,  $\circ$  Data.





a) Fin Surface 2.



b) Fin Surface 4.

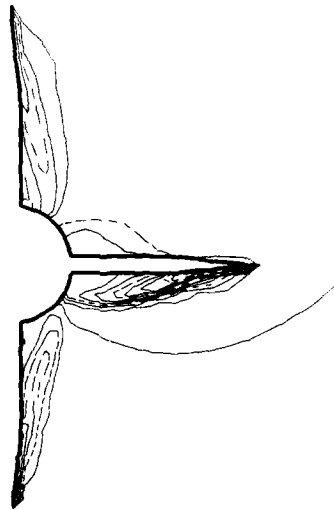
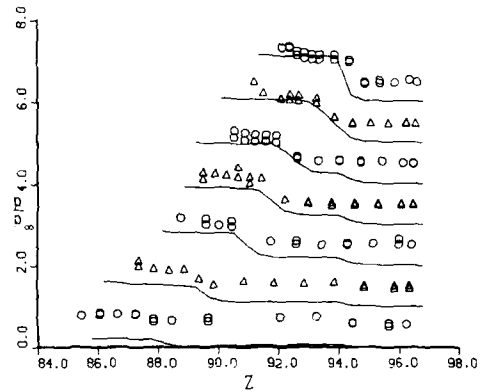


Figure 18. Calculated and Measured Pressure on a Clipped Delta Configuration. Symbols are Measurements and Lines are ZEUS Calculations. Reference 0 Shifted by 1 on Each Successive Curve.

Figure 19. Computed Crossflow Velocities and Pressures at  $z = 24.8R$ .

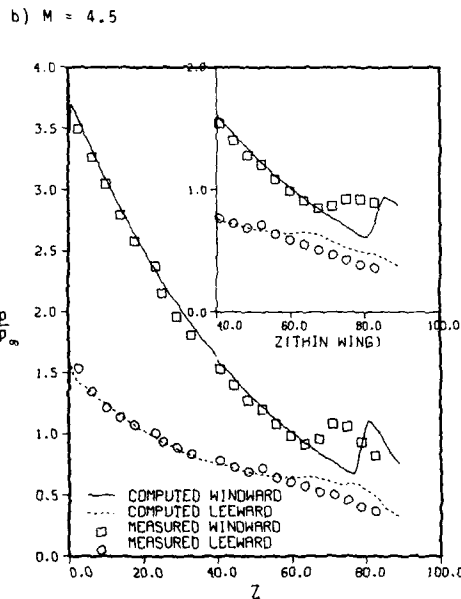
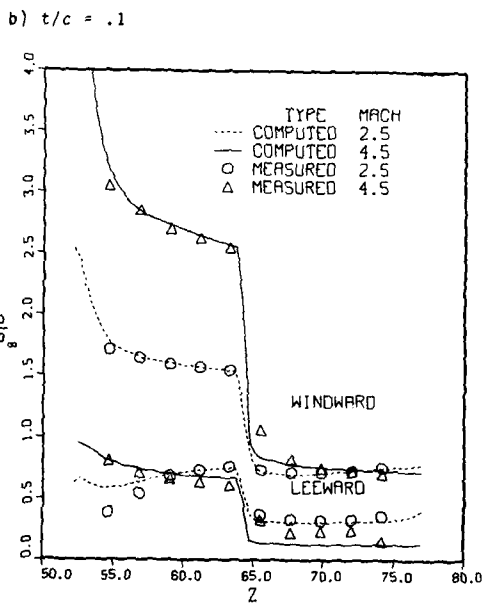
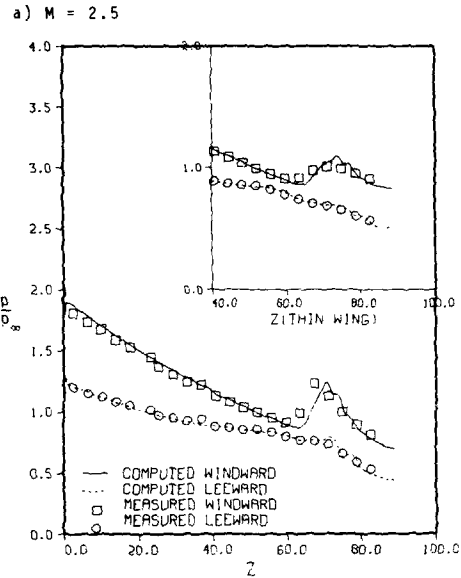
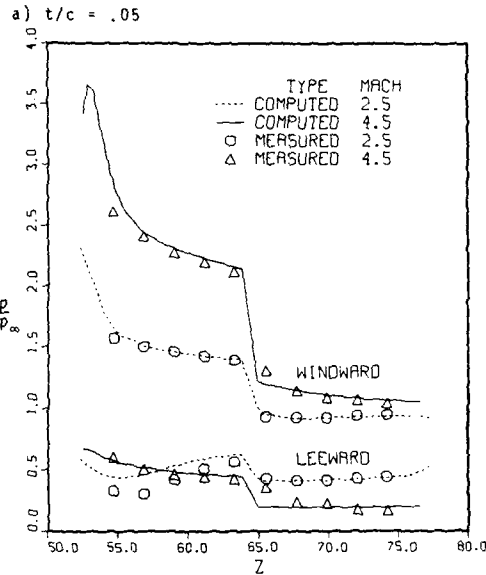
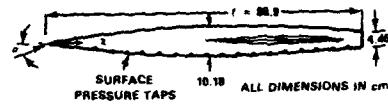
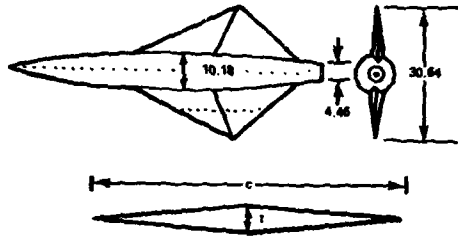


Figure 20. Wing Surface Pressures at  $\alpha = 6^\circ$  Figure 21. Body Surface Pressure at  $\alpha = 6^\circ$



a)  $M = 4.5$

b)  $M = 2.5$

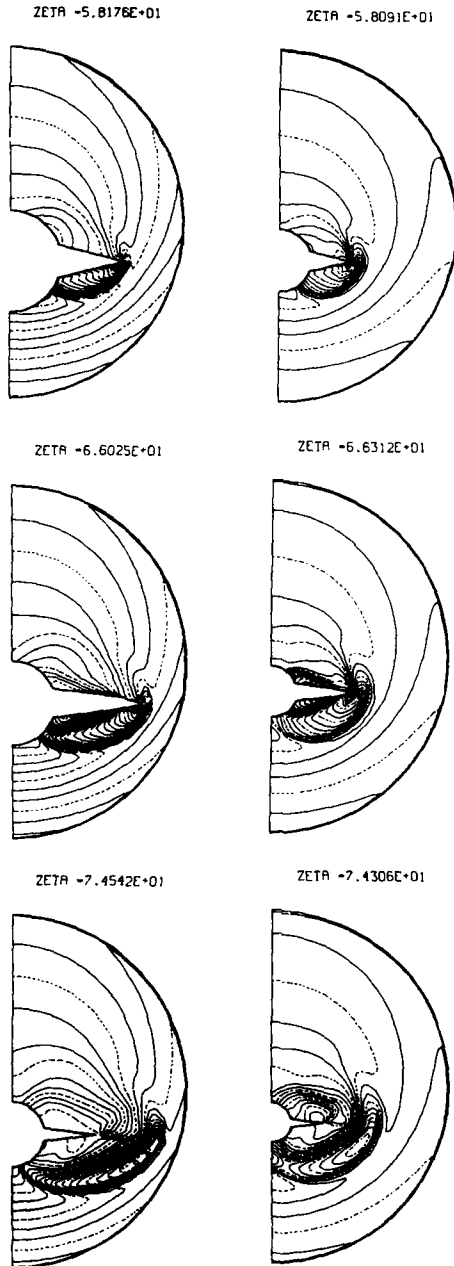


Figure 22. ZEUS Calculated Crossflow Plane Pressure for the Configuration of Fig. 20 and 21 at  $\alpha = 6^\circ$ .

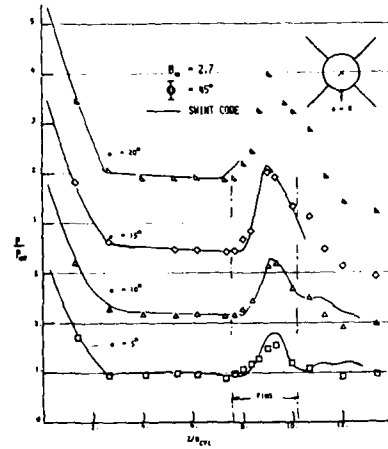
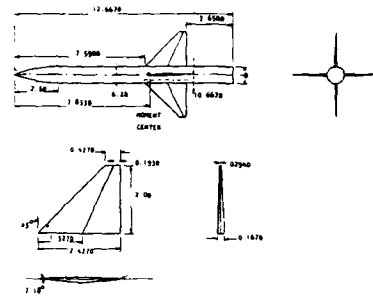


Figure 23. SWINT Calculated and Measured surface pressure along the windward ray. Ordinate shifted by 1 for each successive curve. Taken from Ref. 53.

a) + configuration

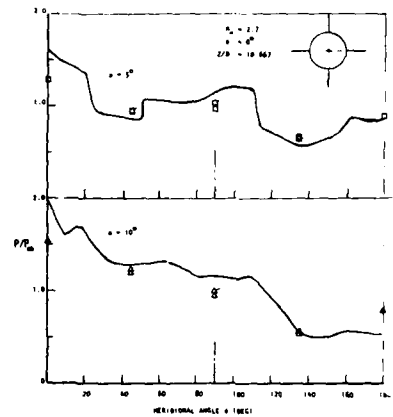


Figure 24. SWINT Calculated and Measured Circumferential Pressure at  $z = 10.67D$ . Lines are Calculations, Symbols are Experiment. Taken from Ref. 53.

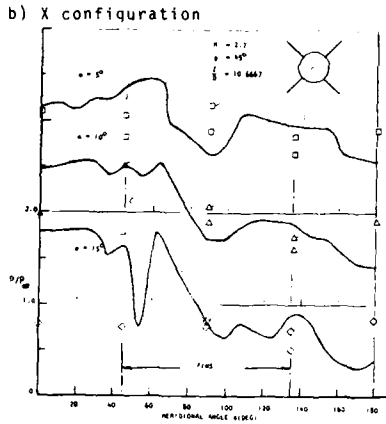


Figure 24. (Continued)

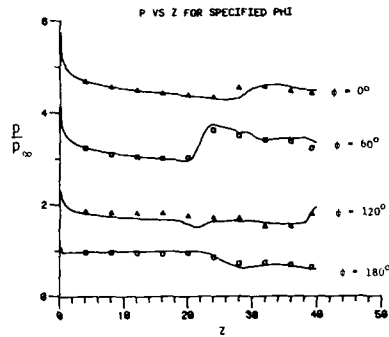


Figure 26. SWINT Calculated and Measured Body Surface Pressures on the Configuration of Fig. 25, at  $M = 2.30$  and  $\alpha = 8.6^\circ$ . Ordinate Shifted by 1 for Each Successive Curve.

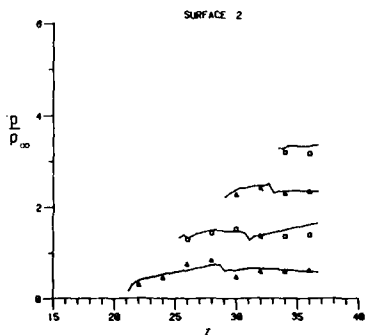
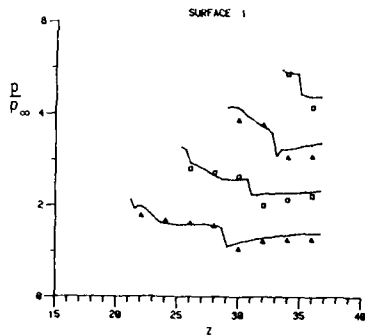
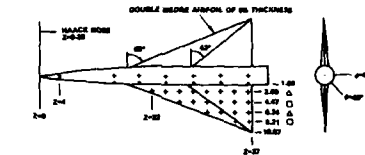


Figure 25. SWINT calculated and Measured Wing Surface Pressure on the Illustrated Model at  $M = 2.3$  and  $\alpha = 8.8^\circ$ . Ordinate Shifted by 1 on Each successive curve.

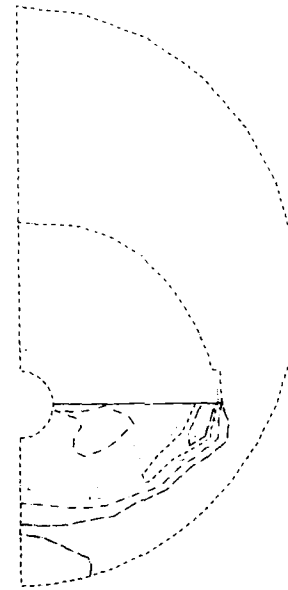
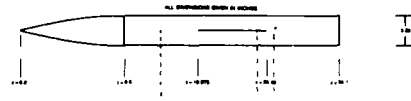
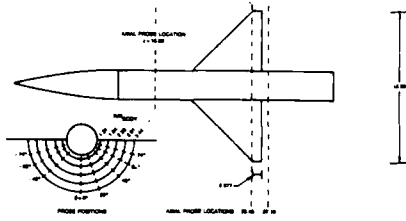


Figure 27. SWINT Calculated Crossflow Plane Pressure on the Configuration of Fig. 25.



a) circumferential variation,  $\alpha = 10.4^\circ$ ,  
 $R/R_B = 1.84$ .

b) radial variation,  $\alpha = 10.4^\circ, \theta = 62^\circ$

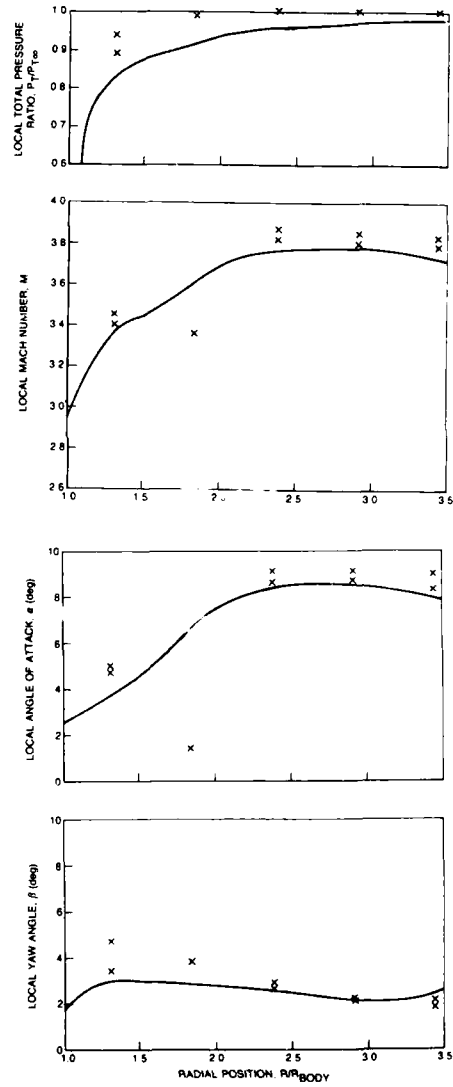
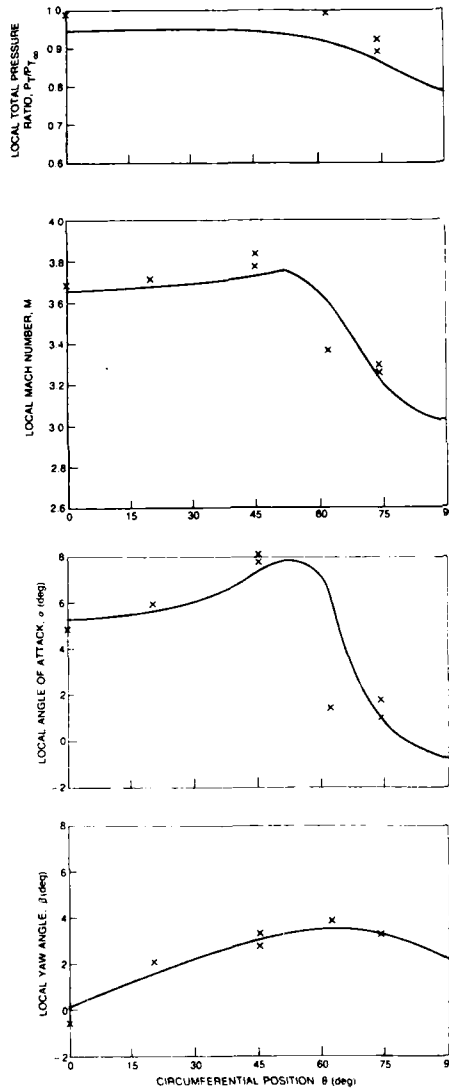


Figure 28. SWINT Calculated and Measured Variations of Total Pressure, Mach Number, and local values of  $\alpha, \beta$  at  $z = 25.5$  inches. Taken from Ref. 55. x experiment; — calculation

c) radial variation,  $\alpha = -10.2^\circ$ ,  $\theta = 62^\circ$

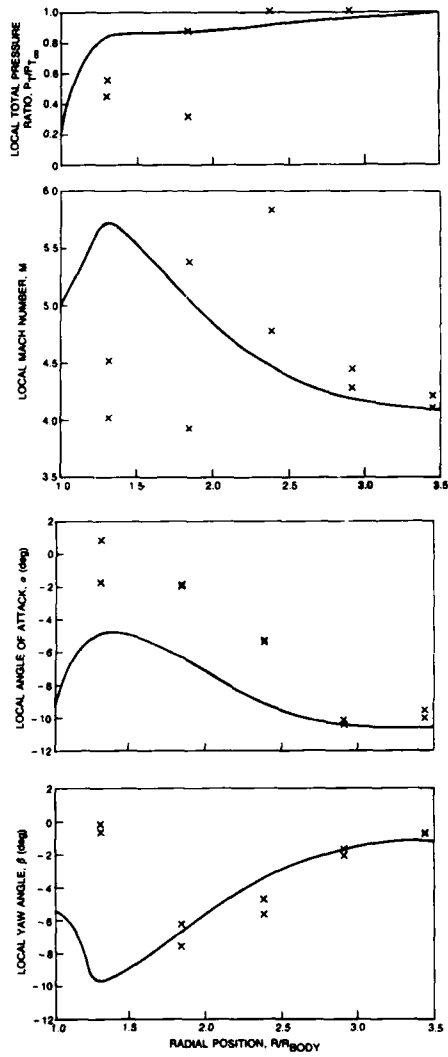


Figure 28. (Continued)

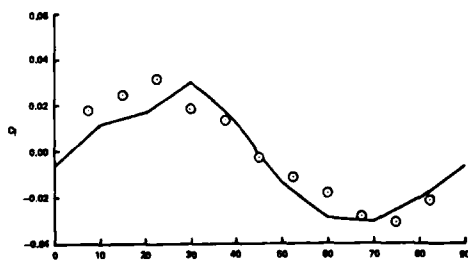


Figure 31. Calculated and Measured  $C_l$  versus roll angle on the model of Fig. 29. Taken from Ref. 56,  $M = 3.5$ ,  $\alpha = 10^\circ$ .

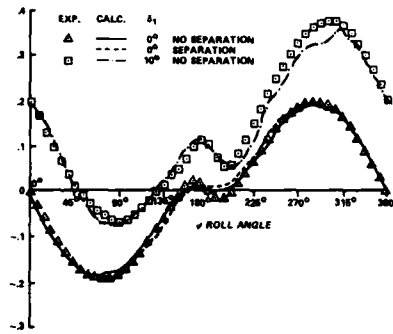
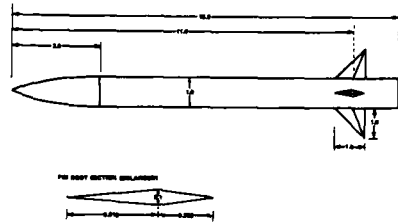


Figure 29. Fin Normal Force as a Function of Roll Angle. Taken from Ref. 56,  $M = 3.5$ ,  $\alpha = 12^\circ$ ,  $\delta_t$  is the Fin Deflection.

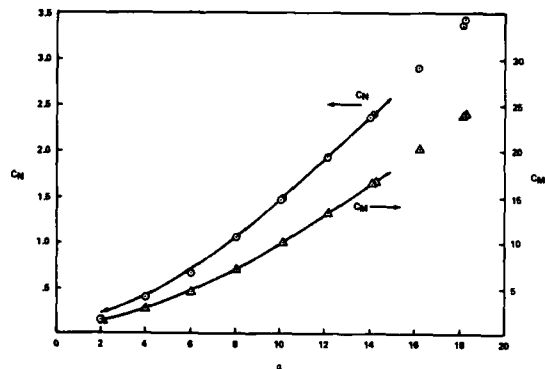


Figure 30. Normal Force and Pitching Moment on the Configuration of Fig. 29 at  $M = 3.5$ . Taken from Ref. 56.

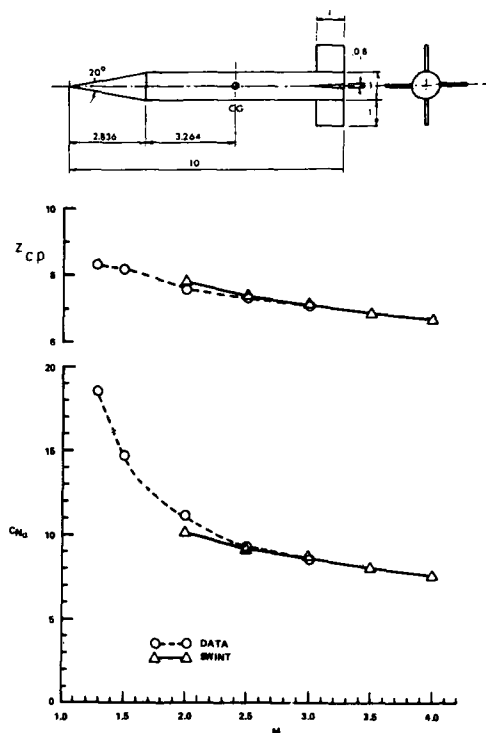


Figure 32.  $C_N$  and  $z_{cp}$  as a Function of Mach Number.  $\circ$  Data;  $\triangle$  SWINT. From Ref. 57.

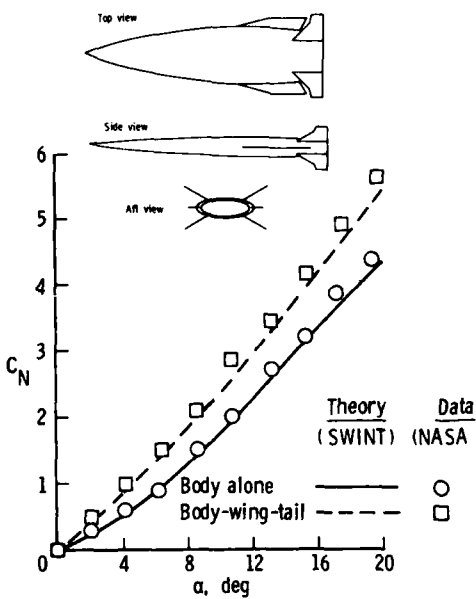


Figure 35.  $C_N$  on an Elliptic Body With and Without Fins. Taken from Ref. 49.

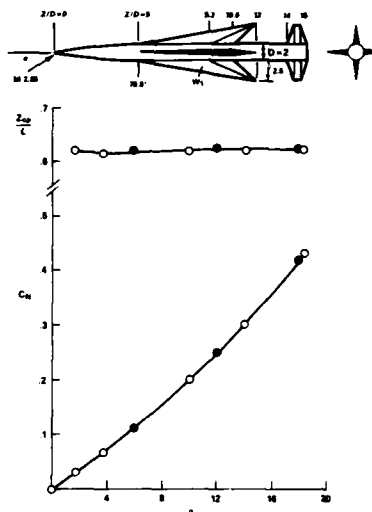


Figure 33. SWINT ( $\bullet$ ) and Measured ( $\circ$ )  $C_N$  and  $z_{cp}$ .

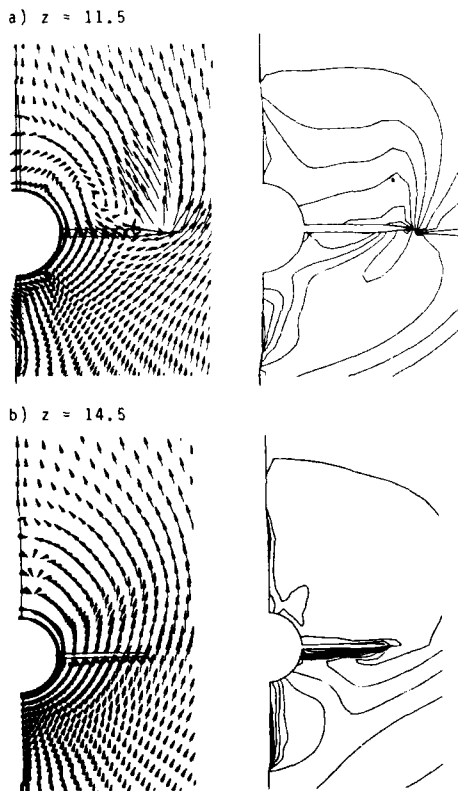


Figure 34. Crossflow Velocity and Pressure on the Model of Fig. 33.

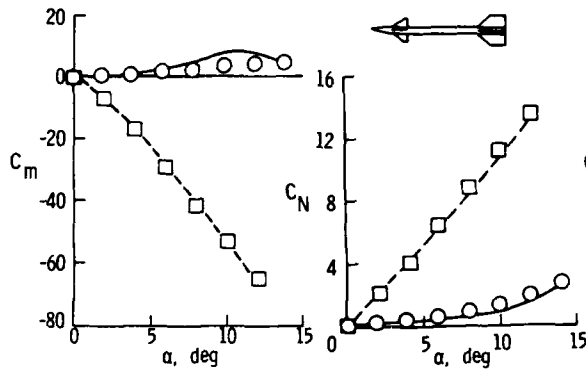


Figure 36. Normal Force and Pitching Moment on a Body-Wing-Tail Configuration at  $M = 2.5$ . Taken from Ref. 49. — SWINT,  $\circ$  Body-Alone;  $\square$  Body-Wing-Tail

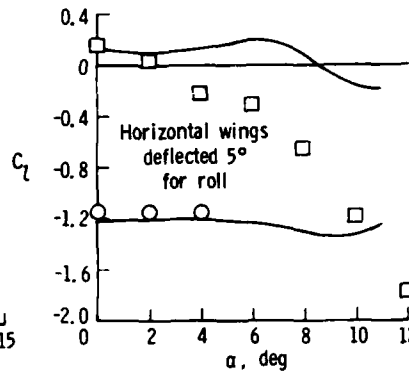


Figure 37. Rolling Moment for Model of Fig. 36 With and Without a Tail. Taken from Ref. 49. — SWINT ;  $\circ$  Body-Wing;  $\square$  Body-Wing-Tail.

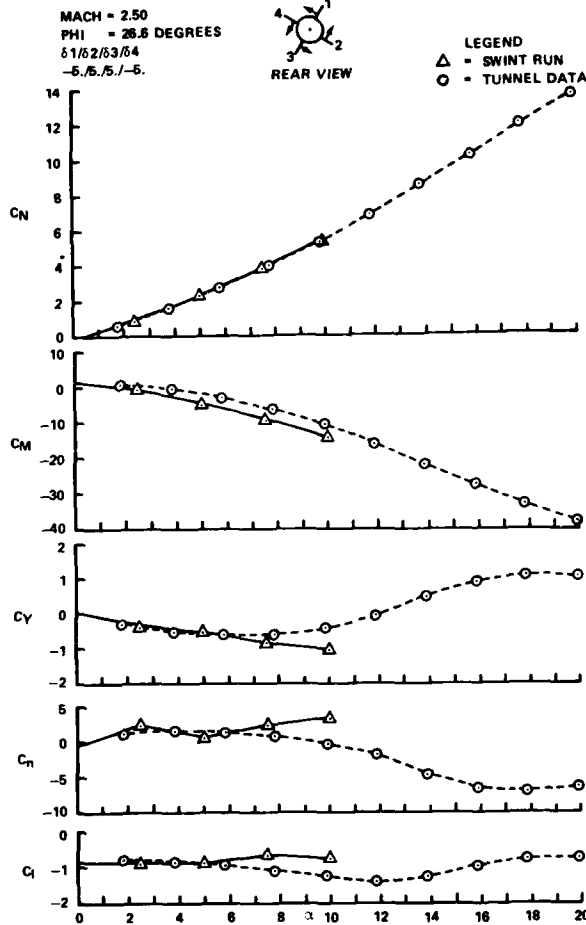


Figure 38. Force and Moment Characteristics for the Model of Fig. 36 at a Roll Angle of 22.5°, and tail Deflection of 5°.

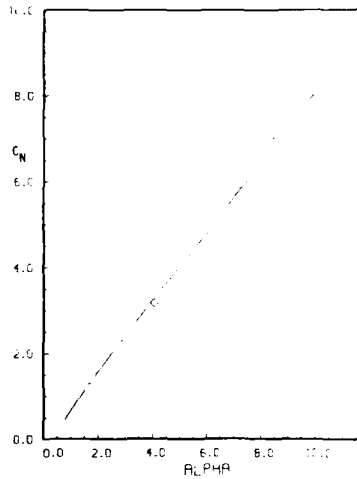
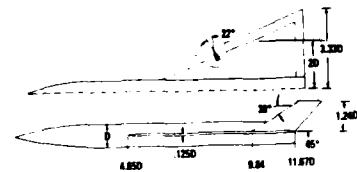


Figure 39. MUSE calculated and measured  $C_N$  and  $z_{cp}$  for a Body-Wing-Tail model at  $M = 2.86$

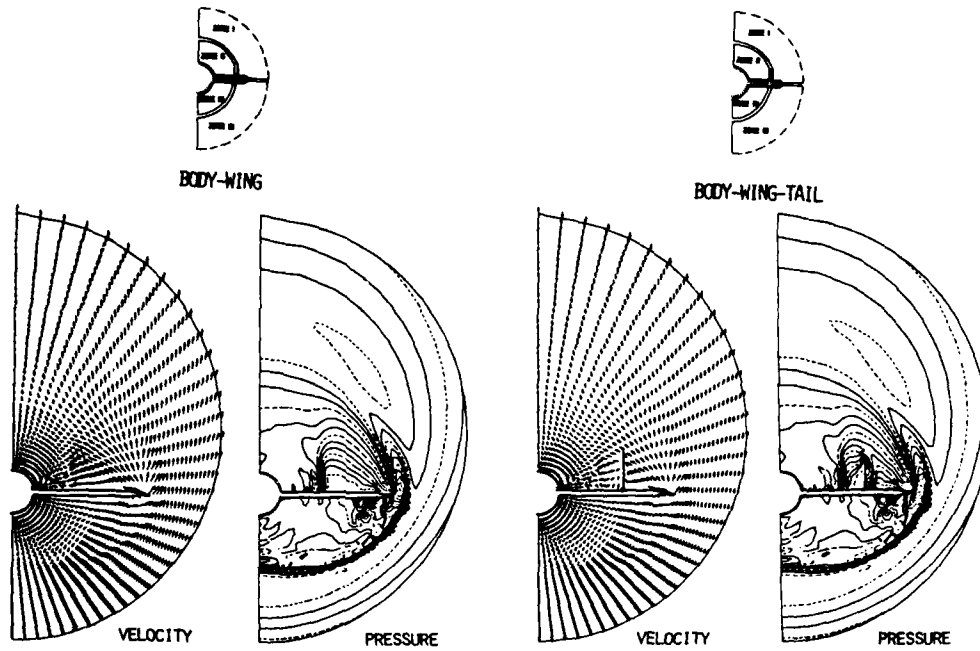


Figure 40. Crossflow Velocities and Pressures on the Body-Wing and Body-Wing-Tail Model of Fig. 39 at  $M = 2.86$ ,  $\alpha = 8.47^\circ$ ,  $z = 11D$ .

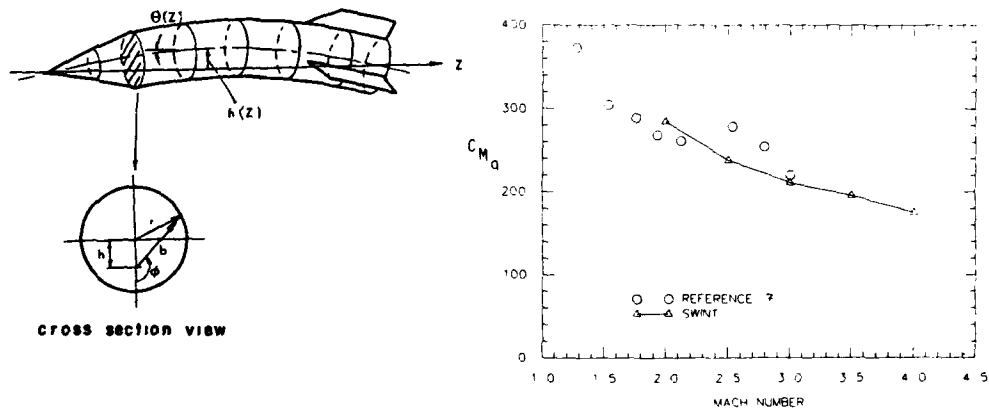


Figure 41.  $C_{M_a}$  as a Function of Mach number.  $\Delta$  SWINT;  $\circ$  Data. Taken from Ref.57.

## NUMERICAL METHODS : EULER TIME DEPENDENT SOLVER

J.J. CHATTOT

MATRA, 37, avenue Louis Bréguet, 78146, Villacoublay, France

## SUMMARY

The EULER time dependent solver of MATRA is described and the fundamental problem of separated flow simulation with an inviscid model is addressed, in particular separation on a smooth surface. The last part of the paper is devoted to applications pertinent to missile aerodynamics, ranging from simple configurations to complete missiles flow simulations.

## INTRODUCTION

Important progress has been made in the solution procedures for solving the three-dimensional EULER equations. In addition, the access to fast vector computers makes large scale EULER simulation feasible and cost-effective, thus opening a new way for the prediction of the aerodynamic characteristics of missiles and introducing a powerful tool in the hands of the design engineers. Care must be exerted, however, since the model does not account for the viscous effects and the domain of validity of the simulation must be assessed whenever a new problem is tackled. Viscous-inviscid coupling methods and Navier-Stokes solvers will eventually overrule the present approach, but one may have to wait for more efficient algorithms and a new step in computer technology. In the mean time, the EULER codes will be developed and improved to provide valuable input for the projects of the coming decade.

Missile aerodynamics is primarily concerned with three-dimensional steady flows with shocks and vortex structures. The Mach number ranges from zero to 3 or more and shock waves appear in the transonic-supersonic regime. Vortex interactions between the lifting surfaces and the body or between the lifting surfaces themselves make separate element flow analysis pointless. The flow is assumed steady since in general, for an isolated missile, no aeroelastic coupling is observed, although, with the introduction of composite materials and the tendency to decrease the size of the cross section, this situation may be encountered in the future.

The EULER equations represent the most complete set of equations modeling the evolution of a non-viscous and non-conducting fluid. They admit weak solutions with jumps, among which physical discontinuities are modeled such as shock waves and vortex sheets.

Since the focus is on steady flow, the use of an unsteady EULER solver must be seen as a means to drive the solution, from an arbitrary initial state, to its asymptotic steady state, regardless of the local subsonic or supersonic flow regime. Thus, unsteady EULER codes can be applied at all Mach numbers and permit a continuous description of the speed range. This is in contrast to the steady approach or space marching methods which can be used only when the flow is everywhere supersonic.

The unsteady EULER solvers are based either on the full unsteady or the pseudo-unsteady formulation. In the latter, the unsteady energy equation is replaced by the steady BERNOULLI's equation, compatible with the full EULER steady state solution [1]. It constitutes the basis of the method developed at MATRA and presented below.

The system reads as follows:

$$\frac{\partial \mathbf{U}}{\partial t} + \text{div } \overline{\mathbf{F}}(\mathbf{U}) = 0$$

where  $\mathbf{U}$  and  $\overline{\mathbf{F}}$  are the following vector and matrix:

$$\mathbf{U} = \begin{bmatrix} \rho \\ \rho u \\ \rho v \\ \rho w \end{bmatrix} \quad \overline{\mathbf{F}} = \begin{bmatrix} \rho u & \rho v & \rho w \\ \rho u^2 + p & \rho uv & \rho uw \\ \rho uv & \rho v^2 + p & \rho vw \\ \rho uw & \rho vw & \rho w^2 + p \end{bmatrix}$$

and the algebraic relation holds:

$$H_1 = \frac{\gamma}{\gamma-1} \frac{p}{\rho} + \frac{|\vec{V}|^2}{2} \quad \text{where } \vec{V} \text{ is the velocity vector,}$$

$H_1$  is the uniform total enthalpy and  $\gamma$  is the ratio of specific heats. The boundary conditions associated with the EULER equations are only known by their number. A mathematical analysis of the characteristic surfaces indicates that the various situations can be found:

- Upstream supersonic boundary: all the variables are specified (4 conditions)
- Downstream supersonic boundary: all the variables are computed from the interior of the domain (0 condition)
- Upstream subsonic boundary: the entropy and the flow direction can be specified (3 conditions)
- Downstream subsonic boundary: one variable i.e. pressure, can be specified (1 condition)
- Solid wall boundary: the tangency condition  $\rho \vec{v} \cdot \vec{n} = 0$  is imposed (1 condition).

A review and discussion of the various methods used in missile aerodynamics, in particular EULER solvers, can be found in the paper of KLOPPER and NIELSEN [2].



## THE EULER TIME DEPENDENT SOLVER OF MATRA

Several classical and well established numerical schemes have been tested, that is the explicit schemes of Mac Cormack, Runge-Kutta and Lax-Wendroff. The study has been carried out with the acceleration technique by multigrid. We found that the one-step Lax-Wendroff scheme was the most robust and cheap to run.

The EULER time dependant solver developed at MATRA is based on the finite volume Lax-Wendroff scheme associated with an efficient multigrid method proposed by NI[3]. It has been extended to three space dimensions by KOECK[4]. Various applications to complex three-dimensional flows have been presented in [5-7].

A brief description of the scheme is given and the details are to be found in [4].

*Numerical scheme. Multigrid technique*

Let  $i$  be an interior node of the mesh and  $C(i)$  be the set of cells sharing the node  $i$ . The unknowns  $U_i$  are located at the nodes and a staggered grid is introduced, defining control volumes  $C_i$  surrounding each node, with volume  $V_i$ . The updating formula is:

$$U_i^{n+1} = U_i^n + \frac{\Delta t}{V_i} \cdot \delta U_i^n$$

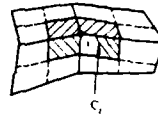
$\Delta t$  is the time step.

$\delta U_i^n = \delta_1 U_i^n + \delta_2 U_i^n$  is composed of a first order contribution  $\delta_1 U_i^n$  and a second order correction  $\delta_2 U_i^n$

$\delta_1 U_i^n = \frac{1}{8} \sum_{C(i)} \left\{ \Delta U_c^n \right\}$  is the mean value of the flux over the cells  $C(i)$  where

$$\Delta U_c^n = - \int_C \bar{F}(U) \cdot \bar{n} \, ds$$

$$\delta_2 U_i^n = - \frac{\Delta t}{2V_i} \int_{C_i} \frac{d\bar{F}}{dU} \cdot \Delta U_c \cdot \bar{n} \, ds$$



The Jacobian matrix  $\frac{d\bar{F}}{dU}$  is assumed constant in each cell. The contour integrals are evaluated with value of the integrand obtained by interpolation from the nodal values. Area vectors are defined as half the cross product of the diagonal vectors [4].

The multigrid acceleration technique can be best described in the case of two grids:

- Compute the total flux  $\delta U_i^n$  on the basic grid  $G_h$ ,
- Compute the first order flux  $\Delta U_{c,2h}$  from  $\delta U_i^n$  on the grid  $G_{2h}$  via the restriction operator  $R_h^{2h}$ :

$$\Delta U_{c,2h} = R_h^{2h} \delta U_{i,h}^n$$

- Compute the second order corrections on  $G_{2h}$ :

$$\delta_2 U_{i,2h}^n = - \frac{\beta \Delta t}{2V_i} \int_{C_{i,2h}} \frac{d\bar{F}}{dU} \cdot \Delta U_{c,2h} \cdot \bar{n} \, ds$$

- Compute the total flux:

$$\delta U_{i,2h}^n = \frac{1}{8} \sum_{C(i),2h} \left\{ \Delta U_{c,2h}^n \right\} + \delta_2 U_{i,2h}^n$$

- Interpolate the result on the grid  $G_h$  via the operator  $I_{2h}^h$  and update the solution

$$U_i^{n+1} = U_i^n + \frac{\Delta t}{V_i} \left( \delta U_{i,h}^n + \omega I_{2h}^h \delta U_{i,2h}^n \right)$$

The interpolation and restriction operators are bi- or trilinear operator and the full weighting operator respectively.  $\omega$  may be considered as an over-relaxation factor which allows an improvement of the convergence.  $\omega$  and  $\beta$  have been optimized by means of a Fourier mode analysis and found to be  $\omega = 1.7$  and  $\beta = 1.4$ .

The time step  $\Delta t$  is computed with the Courant-Friedrichs-Lewy stability criterion. To ensure and stabilize the capture of shocks, a non-linear second-order and a linear fourth-order artificial viscosity term is added when updating the unknowns.

### Boundary condition implementation

#### Inflow and outflow boundaries.

At a supersonic inflow boundary, all the variables are set to the free-stream values. On the other hand, if the upstream flow is subsonic, three boundary conditions must be specified:

$$\begin{aligned} \text{total pressure } p_t &= p_{t\infty} \\ \text{velocity direction } \frac{\bar{V}}{|\bar{V}|} &= \frac{\bar{V}_\infty}{|\bar{V}_\infty|} \end{aligned}$$

At a supersonic outflow boundary, no condition is required; and if the flow is subsonic, one condition is necessary: the average static pressure is driven to its free-stream value.

$$\frac{1}{S} \int_{\text{Outflow boundary}} p dS = p_\infty$$

This condition allows sufficient freedom for the vortex structures to be convected past the outer boundary.

The tangency condition can be imposed in strong form, as mentioned in [4], or specified in weak form as done in finite element methods based on the potential formulation [8].

In weak form, the velocity  $\bar{V}_w^{n+1}$  on the wall is computed with the scheme described above but for which the general flux expression.

$$\bar{F}(\mathbf{U}) \cdot \bar{n} = \begin{bmatrix} \rho \bar{V} \cdot \bar{n} \\ \rho \bar{V}(\bar{V} \cdot \bar{n}) + p \bar{n} \end{bmatrix}$$

reduces to:

$$\bar{F}(\mathbf{U}) \cdot \bar{n} \Big|_{\text{wall}} = \begin{bmatrix} 0 \\ p \bar{n} \end{bmatrix}$$

and the second order flux contributions:

$$\left[ \frac{d\bar{F}}{d\mathbf{U}} \cdot \Delta \mathbf{U} \right] \cdot \bar{n} = \begin{bmatrix} \Delta(\rho \bar{V} \cdot \bar{n}) \\ \Delta[\rho \bar{V}(\bar{V} \cdot \bar{n})] + \Delta(p \bar{n}) \end{bmatrix}$$

reduce to:

$$\left[ \frac{d\bar{F}}{d\mathbf{U}} \cdot \Delta \mathbf{U} \right] \cdot \bar{n} \Big|_{\text{wall}} = \begin{bmatrix} 0 \\ \Delta(p \bar{n}) \end{bmatrix}$$

To account for the zero mass flux across the solid boundary.

In the strong form, after the step corresponding to the weak form, the normal velocity component is set to zero:

$$\bar{V}^{n+1} \cdot \bar{n} = \bar{V}_w^{n+1} \cdot \bar{n} = (\bar{V}_w^{n+1} \cdot \bar{n}) \bar{n}$$

The strong form requires the computation of the normal to the surface at the nodes whereas in the weak form only the normal to the integration volume sides is needed. Both forms have been implemented in the code.

#### Programming aspects

The code has been developed in the framework of a multidomain approach. The mesh structure is of block type, with each block composed of a well-ordered (i, j, k) regular mesh system. Two blocks can share a coordinate surface as boundary. If the boundary is not a material one, the matching condition is easily obtained upon adding contributions coming from each block to a node and enforcing the continuity by setting the double point to the same common value.

This approach has been found to be both efficient, since the multigrid procedure can be employed across the complete domain, and sufficiently flexible to allow treatment of complicated geometries.

The code runs on the CRAY IS. The storage requirement is of 800 K words. The solution is stored on disks and the files are read-in and written-out as the computation proceeds. A typical run with a 120 000 node mesh system requires one hour of total computing time including 20 minutes of CPU and 40 minutes of wait time for I/O, for 300 iterations.

## SEPARATION WITH THE EULER EQUATIONS

The analysis of three-dimensional flow fields pertinent to missile aerodynamics indicates that separation occurs in various places: at trailing edges and other sharp edges of lifting surfaces, on smooth surfaces and at the base. The prediction of such flows is not in the realm of a perfect fluid model since viscosity plays a major role in most cases; however, separation strongly affects the outer inviscid flow in charge of convecting the vortex sheets, and of supporting their interactions with the body. In that sense, the EULER model must be able to represent that part of the physics associated with an a priori knowledge of the lines of separation on the surface of the body.

We shall consider below only the case of open separation, that is the situations in which the vortex sheets are wetted on both sides by the incoming flow. Separation bubbles and recirculation regions, as found at the base of a body or in two-dimensional flows, require, we believe, a special attention, since vorticity is no longer concentrated in thin layers, but distributed in the volume, situation which cannot be handled in principle, with the EULER equations. There exists a link between, say, a two-dimensional separation bubble behind a cylinder and the three-dimensional open separation on the leeward side of an ogive-cylinder configuration, but the path from one to the other is not yet clear [9].

The open separation mechanisms under consideration are either separation at a sharp edge (leading edge or trailing edge) or separation on a smooth surface.

*Separation at a sharp edge*

The first situation is the most familiar one and corresponds to the occurrence of a vortex sheet trailing a wing. Fig. 1 depicts the flow past the AFV-D Wing of ONERA at  $M = 0.84$  and  $\alpha = 4^\circ$  [10].

Separation occurs at the trailing edge in the numerical solution as in the real flow, without the need of introducing a Kutta-Joukowski condition. This is believed to be the result of the dissipative character of the numerical scheme which enforces, through artificial viscosity effects, the same condition as the true viscosity. The side edge of the vortex sheet rolls up to form a concentrated tip vortex.

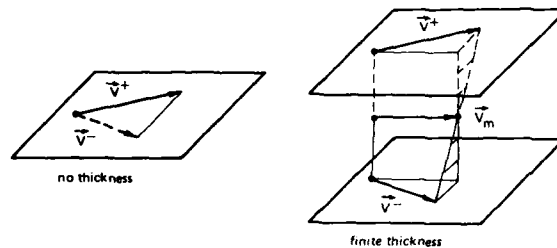
More relevant to missile aerodynamics, separation at the sharp leading edge of a low aspect ratio delta wing at incidence creates a strong vortical structure on the upper part of the wing which noticeably shapes the pressure distribution and increases the lift coefficient. The non-linear coupling between vortex intensity and location is characteristic of strong vortex interaction. Fig. 2 and 3 concern the EULER solution corresponding to the DILLNER Wing at  $M = 0.7$  and  $\alpha = 15^\circ$ , ref. [4].

From the results presented, it can be concluded that the EULER solver captures the vortex sheets emanating from the sharp contours of the geometry. However, the numerical representation appears quite different from a tightly rolled up structure. Furthermore, the total pressure in the vortex is quite different from the upstream infinity value, even in absence of shock waves.

The two remarks call for an answer:

- the capture of vortex sheets is always accompanied by a spreading of the discontinuity by the artificial viscosity. This effect, much like the true viscosity, distributes the vorticity in the cells adjacent to the sheet, until a balance between convection and diffusion is achieved. This aspect is mesh-dependent, and depends also on the magnitude of the artificial viscosity term. In other words, the shape and the location of the vortex structure evolves as the discretization parameters vary.
- conversely, the minimum value of the total pressure is rather independent of the discretization. It seems to depend only on the flow parameters, Mach number, incidence, etc... An explanation of the total pressure loss mechanism has been proposed by POWELL et Al. [11].

The spreading of the contact discontinuity is accompanied by the occurrence of a total pressure minimum inside its finite thickness structure. "This minimum total pressure is dependant only upon the strength of the sheet as measured by the jump in tangential velocity across it, and not upon the thickness of the sheet or the tangential velocity distribution within it" [12].



In the case of simple shear flow as depicted above, the minimum pressure is associated with the value  $\bar{v}_m = \frac{1}{2} (\bar{v}^+ + \bar{v}^-)$  obtained inside the sheet of finite thickness. In a more general situation, such as the DILLNER wing flow, it is not possible to evaluate the pressure loss.

### Separation on a smooth surface

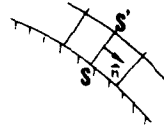
Separation on a smooth surface can occur spontaneously in rotational flow. This is the case with the transonic flow past a circular cylinder in two space dimensions as studied by SALAS [13]. At  $M = 0.5$ , a supersonic zone develops near the top of the cylinder (fig. 4), terminated by a recompression shock. Behind the shock the flow is rotational and the total pressure decreases from the undisturbed value on the streamlines above the shock to a minimum behind the normal shock on the cylinder. Thus the flow separates before reaching the downstream stagnation point.

The three-dimensional counterpart is found in the flow past an ogive-cylinder combination at  $M = 2$  and  $\alpha = 15^\circ$ . The cross flow Mach number is close to 0.5 and embedded shock waves are present in the solution. Asymptotically, as one moves along the cylinder in the downstream direction, the solution resembles the two-dimensional one.

For the computation, a fine  $65 \times 245 \times 33$  mesh system is used, fig. 5; the cross flow velocity field and isobar lines are shown fig. 6 and fig. 7. The shock-induced inviscid separation is visible, but the vortex intensity is weak. The iso Mach lines on the body and in the plane of symmetry are presented on fig. 8.

In order to simulate a viscous separation occurring earlier on the body, a Kutta-Jonkowski (K-J) condition has been implemented at a prescribed location  $S$  along the cylinder. A zero mass flux is imposed across the cell  $SS'$  departing from the wall:

$$\rho \vec{V} \cdot \vec{n} = 0$$

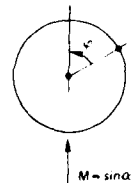


All the variables are continuous along  $SS'$  forcing a capture rather than a fitting of the vortex sheet.

The solution is noticeably different from the previous one, fig. 9 - 10, with a weaker shock and a stronger vortex.

The lift coefficient is dependant on the existence of a vortex structure on the leeward side of the body, and in the case of forced separation, on the location of the separation line  $S$ . Different values of the azimuthal angle have been investigated. The results are summarized in the table below. The configuration is based on the GARTEUR body composed of a three diameter circular tangent ogive and a seven diameter cylinder.

| $M = 2$                           |           | $\alpha = 15^\circ$ |     |
|-----------------------------------|-----------|---------------------|-----|
| Shock induced inviscid separation | $C_N$     | 1.3                 |     |
| Forced inviscid separation        | $\varphi$ | 50°                 | 90° |
|                                   | $C_N$     | 1.7                 | 2.3 |



The lift coefficient does not include the viscous contribution due to the friction drag of the transverse flow. A data base used at MATRA yields a total value of the normal force coefficient for the given flow condition  $C_N = 1.5$ . This indicates that the real flow corresponds to an intermediate situation between the shock-induced inviscid separation ( $\varphi = 35^\circ$ ) and the forced inviscid separation ( $\varphi = 50^\circ$ ).

### APPLICATIONS

The earlier applications of three-dimensional EULER solvers have dealt with simple geometries, isolated wing, body of revolution, etc..., in order to validate the model and its ability to predict the lift of low aspect ratio configurations. The results have been very encouraging, even in the case of strong vortex interaction (DILLNER WING). Non-linearities associated with shock waves and vortex sheets are well predicted when the viscous effects can be neglected or modeled in a simple manner.

This first phase has been followed by a phase of validation on more realistic configurations such as a wing-body combination, and of applications to practical situations for which the classical semi-empirical methods of predictions were not able to yield useful answers, or gave only global results when local knowledge was required. The examples of applications selected below are an illustration of the use that can be made of the numerical simulation to predict and analyse complex aerodynamic systems with a view to improving and, in the long run to optimize, the design of missiles.

#### "Long-wing" missile configuration [5]

"Long-wing" missiles are equipped with very low aspect ratio wings, with a span comparable to the body diameter and a chord extending approximately over half of the body length. This aerodynamic configuration is well suited for high angles of incidence with large capabilities of manoeuvring.

When the missile is at incidence, the wing is the siege of a vigorous vortex, interacting with the upper surface and the body : a typical non-linear situation in term of lift.

In the simulation the wing has no thickness. The mesh system is axisymmetric. It is constructed in a meridian plane, taking into account the wing planform in a multi-domain approach fig. 11, then it is rotated about the missile axis. The "long-wings" are contained in a double plane and surface tangency conditions are specified on the wings, continuity conditions (matching conditions) elsewhere.

The upper and lower subdomains contain each  $73 \times 17 \times 29$  nodes.  $73 \times 33$  nodes are located on the body and  $33 \times 17$  nodes are located on each side of the wing. Only half of the flow field is computed for reason of symmetry. The results are displayed on fig. 12-13 for  $M = 1.5$  and  $\alpha = 10^\circ$ . The cross-flow velocity field and the isobaric curves clearly exhibit the presence of the vortical structure responsible for the non-linear effects.

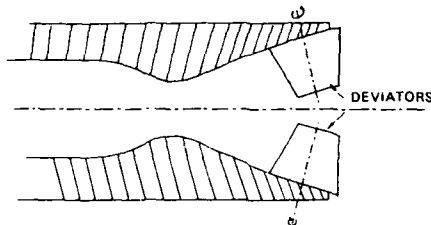
A comparison of the experimental and theoretical lift coefficients at  $M = 0.7$  demonstrates a remarkable agreement up to incidences of 25 degrees, fig. 14.

The advantage of the numerical simulation is to permit access to the local pressure coefficient and thus to evaluate the resulting forces, element by element, as needed for the structural design. The velocity field on the missile is also used as input for the heat transfer analysis.

#### Application to a jet-deviator system [6]

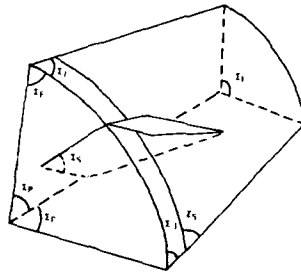
When fired from ground or sea surface, the velocity of the missile is not sufficient to allow piloting with the aerodynamic control surfaces during the early part of the trajectory. For this reason, small orientable lifting surfaces are placed in the nozzle exit of the motor. These jet deviators, by modifying the thrust vector, can create a roll and pitching moment during the propulsive phase of the flight.

The evaluation of the performance of this system is not easy with simple formulae, for example using linearized supersonic theory. Indeed, the blades are placed in a non-uniform supersonic flow, and three-dimensional effects are important at the blade tip and at the blade foot where the nozzle wall interacts with the blade flow.



In order to reduce the computational work in the simulation, use is made of the supersonic character of the flow and of the absence of blade to blade interaction, to be confirmed later. The efforts on the four deviators are obtained by four separate calculations when symmetry arguments do not hold.

The study does not take into account the jet interaction with the external flow. The nozzle flow is slightly underexpanded and it has been assumed that, on the boundary  $\Sigma_j$  located outside the nozzle, the pressure is constant and equal to the external pressure.



$\Sigma_I$  is the inlet boundary. The variables are specified from an axisymmetric converging-diverging nozzle computation. The deviator trailing edge is contained in the exit boundary  $\Sigma_j$ . No condition is necessary on  $\Sigma_j$  since the flow is supersonic.

$\Sigma_S$  is the nozzle and blade walls. The tangency condition is applied on the solid surfaces.

$\Sigma_P$  are orthogonal meridian planes located between the jet deviators. Conditions of symmetry or periodicity are used on  $\Sigma_P$ .

The mesh system is made up of two (i, j, k) blocks, fig. 15. The total number of points is 57 000 ; 1 000 points are located on the deviator.

The iso mach lines on the nozzle wall are presented on fig. 16. The flap angle varies from  $4^\circ$  to  $25^\circ$ . The shock wave and the expansion fan are clearly seen. A perspective view of the flow is presented on fig. 17. At the trailing edge of the deviator, two values of the velocity vector are obtained.

The hypothesis of no blade to blade interaction is validated in the following manner. A first computation is performed using symmetry conditions on  $\Sigma_P$ . A second computation is made with conditions of periodicity. The corresponding situations for the complete system are depicted on fig. 18. The iso-Mach curves on the wall and the flap indicate that the results are identical and can be superimposed fig. 19.

The drag and lift coefficients obtained by subtracting the drag and lift contributions of the single deviator system and the corresponding values for the quarter nozzle alone, are presented on fig. 20. The ratio of the lift of the nozzle to the lift of the flap is negative and varies from -2.5 % to -3 % with the flap angle as it increases from zero to 25 degrees.

The efficiency of the jet deviator system, as measured by the thrust angle to the flap angle, is found numerically to be 22 %. In the experiments it was equal to 21 % at 5 degrees and 23 % at 17.5 degrees of flap incidence. The comparison with experimental data is very satisfactory as far as lift is concerned. As expected, the drag coefficient is largely underestimated by the inviscid simulation.

For this complex piloting system, the numerical simulation with the EULER equations yields useful answers for the project engineer, at very reasonable cost.

#### Application to a complete configuration at MATRA [5]

A numerical simulation campaign has been carried out in favor of a new missile developed by MATRA, in order to investigate a number of peculiarities in the aerodynamics.

The missile is of canard type with orientable flaps in the front part and curved, deployable wings in the rear part. The body is represented by a two diameter conical ogive and an eighteen diameter cylinder. The missile is rotating during its flight. Simulation have been carried out with the missile fixed without rotation. Lift, lateral force and pitching moment have been considered. The rotation rate has been computed at zero incidence with a version of the EULER code written in a frame of reference in rotation with the missile.

The mesh system is composed of approximately 140 000 points. 8 500 points are located on the body and the lifting surfaces, fig. 21. Due to the absence of plane of symmetry, the complete space about the missile has been discretized. The forward flaps have been set at angles  $\delta_m$  varying between zero and 20 degrees.

The mach numbers correspond to the supersonic nozzle mach numbers of the C4 LRBA wind tunnel ( $1.2 < M_\infty < 2.43$ ). The incidence range is between zero and 12 degrees. The roll angle is arbitrary.

The isobar lines exhibit the shock waves and expansion fans on the body and the lifting surfaces at  $M_\infty = 2.12$ ,  $\alpha = 10^\circ$  and  $\delta_m = 10^\circ$  (fig. 22-24). The flow is symmetric in the front part as seen on the cross flow velocity plot at the trailing edge of the flaps, fig. 25. In the rear part, the wings introduce asymmetric effects due to their curvature as depicted fig. 26.

The comparisons of the theoretical results and the experiments exhibit important discrepancies attributable to the lack of viscous modelisation in the simulation. Indeed, for a configuration with a very long body and small lifting surfaces, the friction forces on the cylinder are of the same order of magnitude as the inviscid lift, even at low incidences.

The viscous effects have been included in the evaluation of the lift and pitching moment coefficients for the body alone configuration. This has been done with a simple correction formula due to ALLEN and JORGENSEN [14-15]. The inviscid lift and pitching moments are supplemented by viscous contributions due to the cross-flow drag as :

$$C_N \text{ total} = C_N \text{ inviscid} + C_N \text{ viscous}$$

$$C_m \text{ total} = C_m \text{ inviscid} + C_m \text{ viscous}$$

where :

$$C_N \text{ viscous} = \frac{4}{\pi} \frac{(\lambda - x_0)}{D} C_{DT} \sin^2 \alpha$$

$$C_m \text{ viscous} = \frac{4}{\pi} \frac{(\lambda - x_0)}{D} \frac{(\lambda + x_0)/2 - x_G}{D} C_{DT} \sin^2 \alpha$$

$\lambda$  is the total length of the missile  
 $x_0$  is the length of the ogive  
 $x_G$  is the abscissa of the center of gravity

$C_{DT}$  is the drag coefficient of the cylinder. It depends on Reynolds number and Mach number. The magnitude of the corrections from the inviscid coefficients to the experimental ones (fig. 27), lead us to adopt the following value for  $C_{DT}$  :

$$C_{DT} = 0.3 + 0.25 M, \quad M > 1$$

with this choice, the global coefficients are well reproduced, fig. 28-29, for the two Mach numbers  $M_\infty = 1.2$  and  $M_\infty = 2.43$ , for the body alone.

This correction has been applied to the complete configuration. Viscous corrections on the lifting surfaces have been neglected. The results are presented, fig 30-33, for  $M_\infty = 1.2$  and  $M_\infty = 2.12$  and for  $\delta_m = 0^\circ$  and  $20^\circ$ . The bumps observed in the experimental pitching moment curves for  $\delta_m = 20^\circ$  and  $\alpha < 3^\circ$  correspond to the interaction of the flap vortex sheet with the wings. In the numerical simulation the vortex sheet is spread and the phenomena are attenuated. A finer mesh system would be needed to model more accurately this mechanism, especially because the lifting surface are so wide apart.

The overall agreement is fair and for practical purposes, the equilibrium incidence is found within one degree of accuracy and the error in the location of the center of pressure is less than a half caliber.

As mentioned previously, the EULER equations have been written in a rotating frame of reference in the hypothesis of constant rothalpy, and at zero incidence. In this coordinate system there exists a steady solution for a given rotation rate  $p$ . The corresponding rolling moments have been evaluated. The curve  $C_l$  is drawn on the fig. 34. In the experiments, the value  $C_l(0)$  is measured with the model fixed on a balance, and the derivative  $\frac{dC_l}{dp}(p)$  is explored with a special equipment ; the  $C_{lp}$  value is found constant

in the range of interest. The calculated auto-rotation rate  $p^*$  is in good agreement with experiments.

In conclusion, the EULER solver appears as a powerful analysis tool for a complex three-dimensional flow, extending the capabilities of the empirical methods. The non-linear inviscid mechanisms are accurately modeled. The viscous effects may be evaluated, as in the present case, with a simple correction. The lateral force and rolling moment can be calculated without having to recourse to expensive wind tunnel tests.

*Application to a complete configuration at aerospatiale [18]*

The Aerospatiale Tactical Missile Division is using an unsteady EULER solver for the simulation of aerodynamic problems. The code developed at ONERA [17], is based on a non-centered finite volume scheme of Van Leer, and has been applied by Aerospatiale to the ASTER project. The ASTER missile is equipped with a "long wing" and non-linear vortex interactions are expected to affect the aerodynamic coefficients. An illustration of the vortical flow structure is given, fig. 35, with the isobar lines on the missile and in a transverse plane, for the Mach number  $M = 2.5$  and the incidence  $\alpha = 10$  degrees. Fig. 36 compares theoretical and experimental pressure coefficients on a line drawn along the wing chord for three values of the angle of attack:  $\alpha = 0^\circ$ ;  $4^\circ$  and  $10^\circ$ . The agreement is considered very satisfactory on the lower as well as the upper surface, and in a zone close to the edge where pressure varies rapidly.

The mesh system for this simulation consists of 300 000 points for a half missile. Since the flow is everywhere supersonic, the computation is performed with a pseudo-unsteady marching procedure in which the steady solution is obtained in a plane using an upwind scheme and driving the time derivatives to zero, then proceeding to the next plane, sweeping the domain in the flow direction. In this way, the memory requirement is kept to a minimum, as in a steady marching method. The computing time is of 30 minutes CPU.

#### CONCLUSION

Simulations based on the EULER equations have reached a sufficient state of maturity to yield useful informations in the prediction of missile aerodynamics. At the present time they are used to access the local flow properties and to analyse complex flow features.

Progress must be made in the handling of the exact geometry and of the mesh generation possibly with CAD/CAM tools, and in introducing viscous effects in a more rigorous manner.

In the near future, the aerodynamic simulation will be used to optimize missile configurations.

#### REFERENCES

- [1] Viviani H. et Veuillot J.P., Méthodes pseudo-instationnaires pour le calcul d'écoulements transoniques, ONERA TP n° 1978-4, 1978.
- [2] Klopfer G.H. and Nielsen J.N., Computational Fluid Dynamic Applications to Missile Aerodynamics, in Missile Aerodynamics, AGARD CP n° 336, feb. 1983.
- [3] NI R.H., A multiple-grid scheme for solving the Euler equations, AIAA Paper n° 81-1025, June 1981.
- [4] Koeck C., Computation of three-dimensional flow using the Euler equations and a multiple-grid scheme, International Journal For Numerical Methods in Fluids, vol 5, 483-500, 1985.
- [5] Chattot J.J., Koeck C. and Elsaesser E., Solution of the Euler equations for missiles configurations, Notes on Numerical Fluid Mechanics, Vol 13, VIEWEG, 1986.
- [6] Bredif M., Chattot J.J., Koeck C. and Werle P., Simulation d'un système de déviation de jet à l'aide des équations d'Euler, AGARD CP n° 412, 1986.
- [7] Bredif M., Chattot J.J., Erhart M.L. et Lupieri A., Comparaison théorie-expérience pour le calcul de missiles, 23ème colloque d'Aérodynamique Appliquée, Modane, France, 12-14 novembre 1986.
- [8] Bredif M., A multigrid finite-element method for transonic potential flow, AIAA Paper n° 83-0507, 1983.
- [9] Chattot J.J., Numerical solutions of the Euler equations with separation, proceedings of High Speed Aerodynamics, Prof. A. Nastase Ed., Haag Herchen, 1987.
- [10] Chattot J.J., Boschiere M., Koeck C., Méthodes numériques de prédiction de l'aérodynamique des missiles, Missile Aerodynamics, AGARD CP n° 336, feb. 1983.
- [11] Powell K., Murman E., Perez E., and Baron J., Total pressure loss in vortical solutions of the conical Euler equations, AIAA Paper n° 85-1701, 1985.
- [12] Murman E. and Rizzi A., Applications of Euler equations to sharp edge delta wings with leading edge vortices, AGARD Conference Proceedings n° 412, november 1986.
- [13] Salas M.D., Recent developments in transonic Euler flow over a circular cylinder, Mathematics and Computers in Simulation XXV, pp. 232-236, 1983.
- [14] Allen H., Estimation of the forces and moments acting on inclined bodies of revolution of high fineness ratio", NACA RM A 9126, 1949.
- [15] Jorgensen L.H., Prediction of aerodynamic characteristics for slender bodies alone and with lifting surfaces to high angles of attack, AGARD Conference on High Angles of Attack Aerodynamics, Norway, 4-6 october, 1978.
- [16] Lordon J., Guillen P., Mortel P. et Lacau R.G., Calcul d'écoulements supersoniques autour de missiles tactiques, 23ème colloque d'Aérodynamique Appliquée, Modane, France, 12-14 novembre 1986.
- [17] Borrel M. et Montagne J.L., Numerical study of a non-centered scheme with applications to aerodynamics, AIAA Paper n° 85-1497.

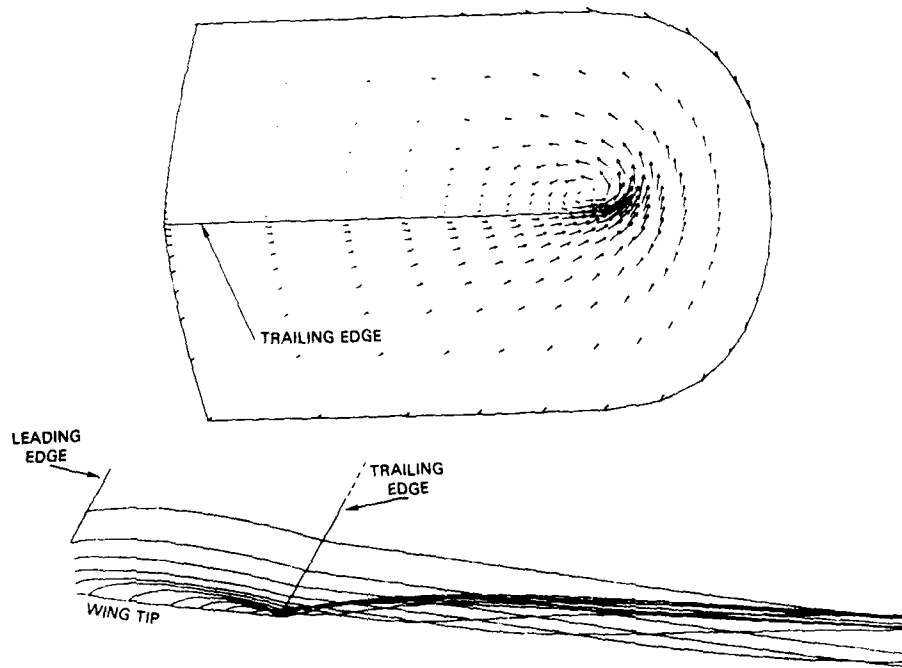


Figure 1. Vortex sheet trailing the ONERA AFV-D wing  $M_\infty = 0.84$   $\alpha = 4^\circ$



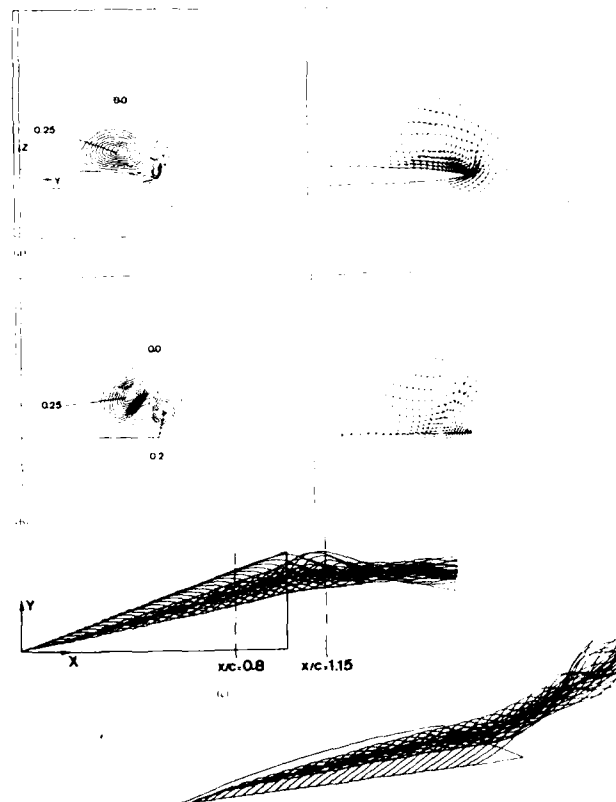


Figure 2. Vortex flow around the Dillner wing;  $M = 0.7$ ,  $\alpha = 15^\circ$ : (a) total pressure loss and cross-flow velocities (wing co-ordinates) at  $X/C = 0.80$ ; (b) total pressure loss and cross-flow velocities (free-stream co-ordinates) at  $X/C = 1.15$ ; (c) computed streamlines

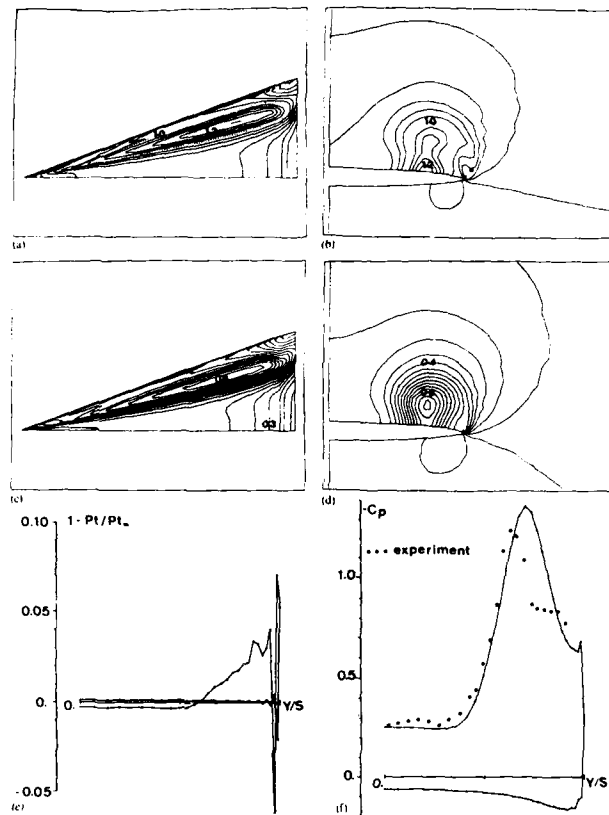


Figure 3. Dillner wing;  $M = 0.7$ ,  $\alpha = 15^\circ$ : (a) isomach lines on the upper surface; (b) isomach lines at  $X/C = 0.8$ ; (c) isobars of normalized pressure on the upper surface,  $C_p = 0.171$ ,  $C_L = 0.678$ ; (d) isobars at  $X/C = 0.8$ ; (e) total pressure loss on the wing at  $X/C = 0.8$ ; (f)  $C_p$  distribution on the wing at  $X/C = 0.8$

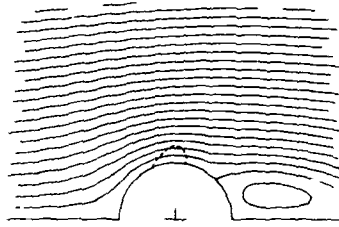


Figure 4. Streamline pattern of the flow past a cylinder,  $M = 0.5$ . Sonic lines and shock shown as a dashed line. From ref. [13].

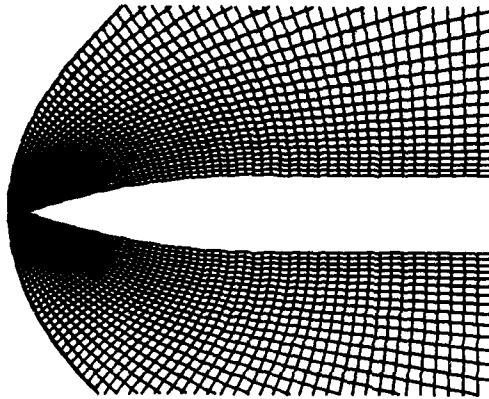


Figure 5. 65 x 245 x 33 mesh system (partial view in a meridian plane)

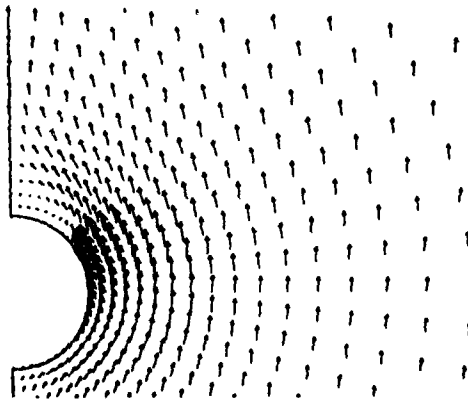


Figure 6. Cross-flow velocity plot. No K-J condition  $M = 2$ ,  $\alpha = 15^\circ$

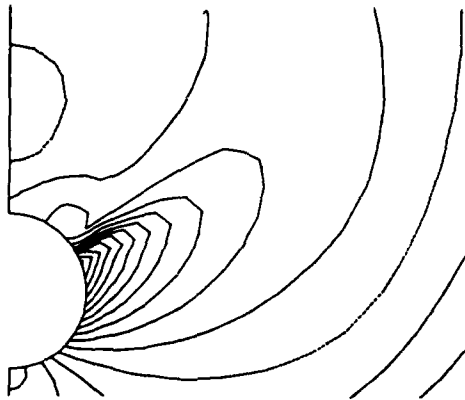


Figure 7. Isobar lines in a cross-flow plane. No K-J condition.  $M = 2$ ,  $\alpha = 15^\circ$

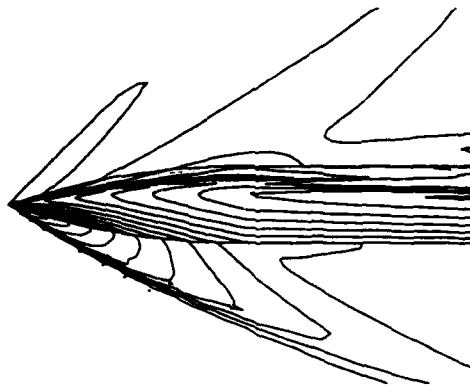


Figure 8. Isomach lines on the body and in the plane of symmetry.  $M = 2$ ,  $\alpha = 15^\circ$

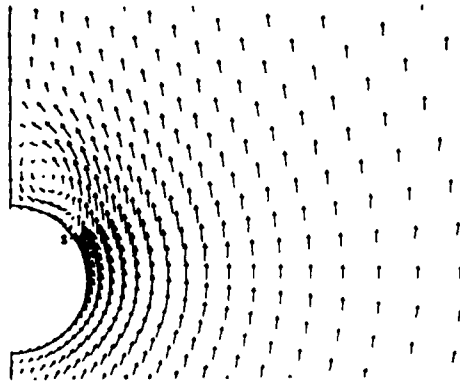


Figure 9. Cross-flow velocity plot. With K-J condition.  $M_\infty = 2$ ,  $\alpha = 15^\circ$

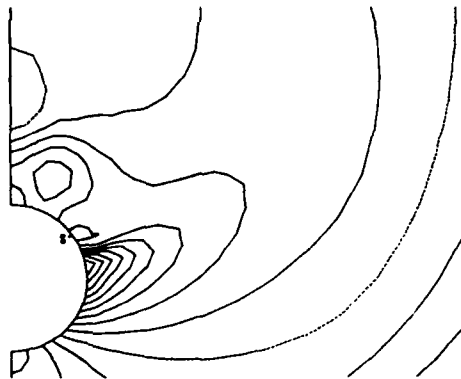


Figure 10. Isobar lines in a cross-flow plane. With K-J condition.  $M_\infty = 2$ ,  $\alpha = 15^\circ$

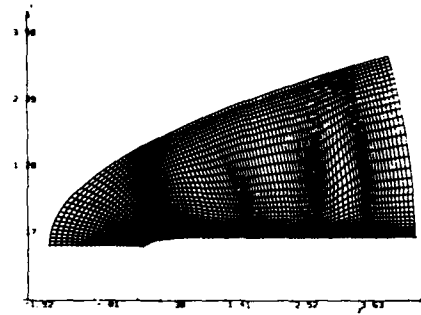


Figure 11. View of the mesh in a meridional plane

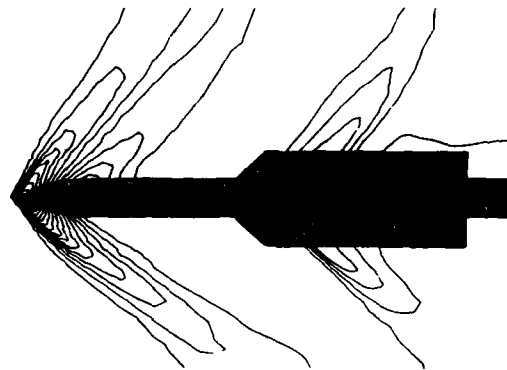


Figure 12. Isobar lines on the body and in the plane of symmetry  $M = 1.5$ ,  $\alpha = 10^\circ$

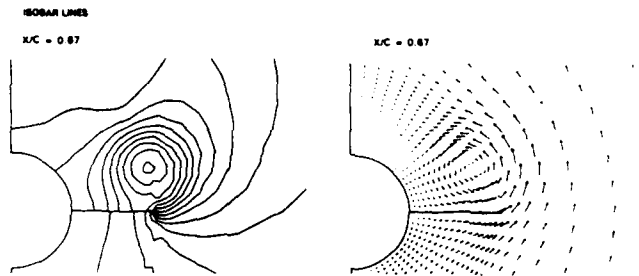


Figure 13. Isobar lines and velocity vector plot in a cross-flow plane  $M = 1.5$ ,  $\alpha = 10^\circ$

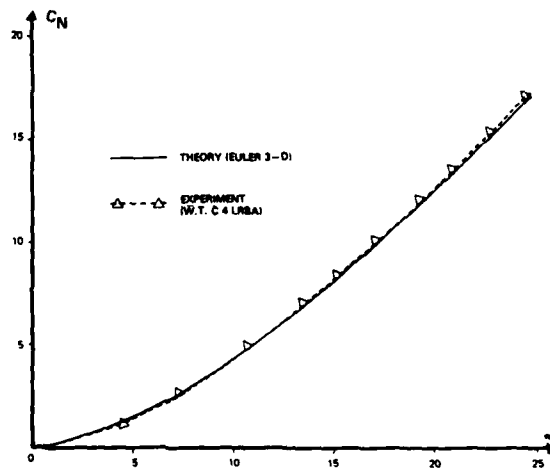


Figure 14. Comparison of lift coefficients  $M = 0.7$

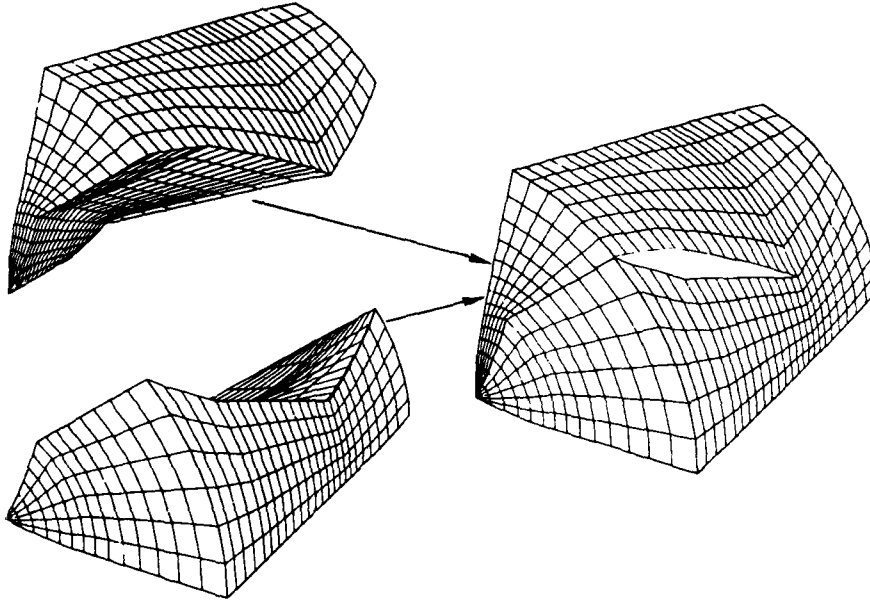


Figure 15. The two-blocks mesh system

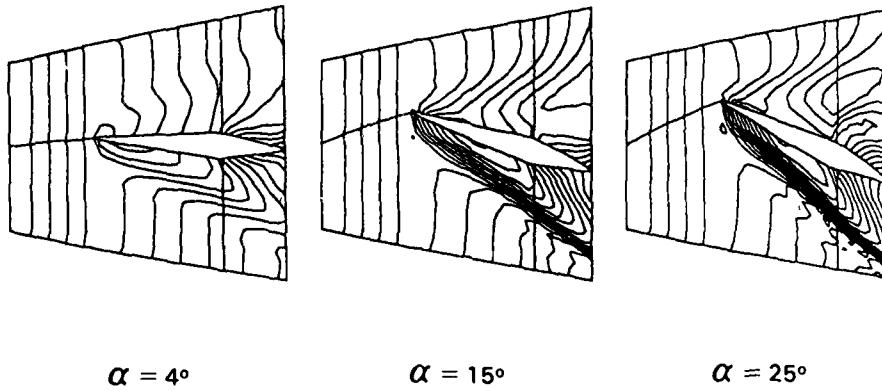


Figure 16. Isomach lines on the nozzle wall



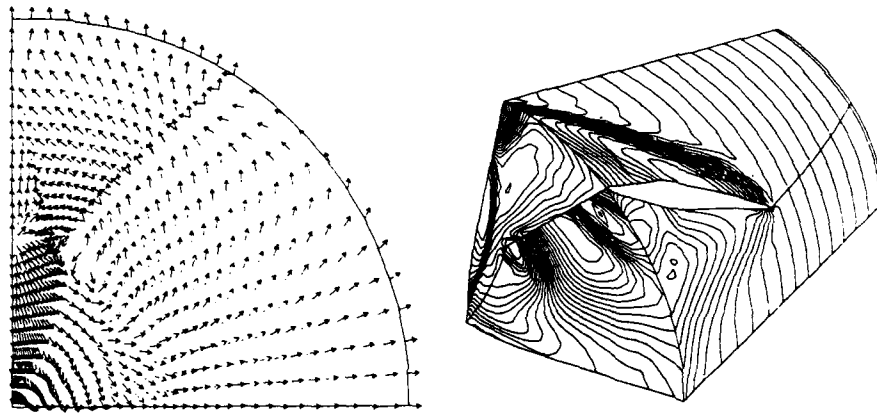


Figure 17. Cross-flow velocity vector plot on the exit surface. Perspective view of the isomach lines

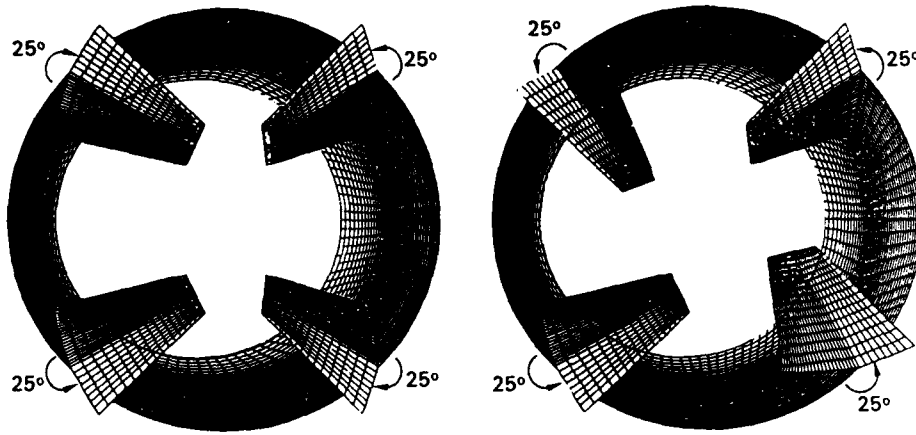


Figure 18. Configurations computed when symmetry or periodic boundary conditions are used

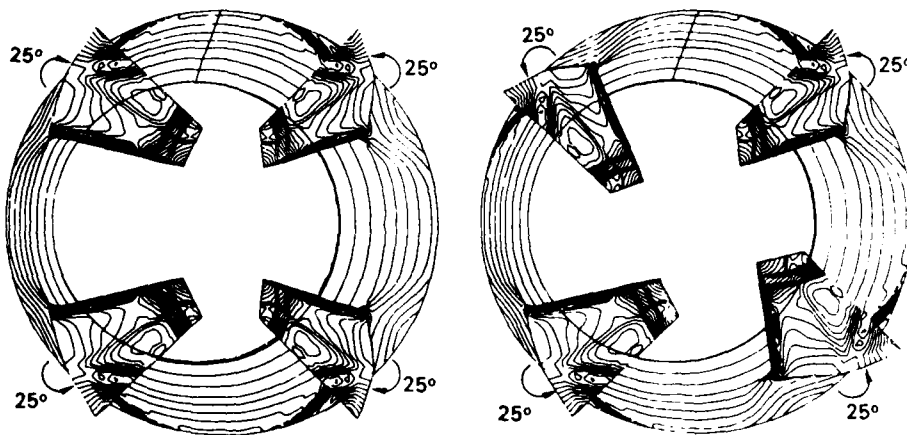


Figure 19. Isomach curves on the solid boundaries with symmetry and periodic boundary conditions

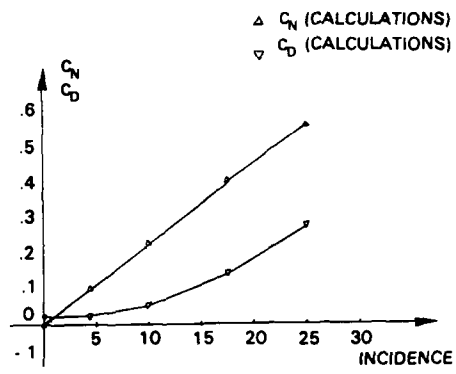


Figure 20. Lift and drag coefficients

Figure 21. Mesh distribution on the missile

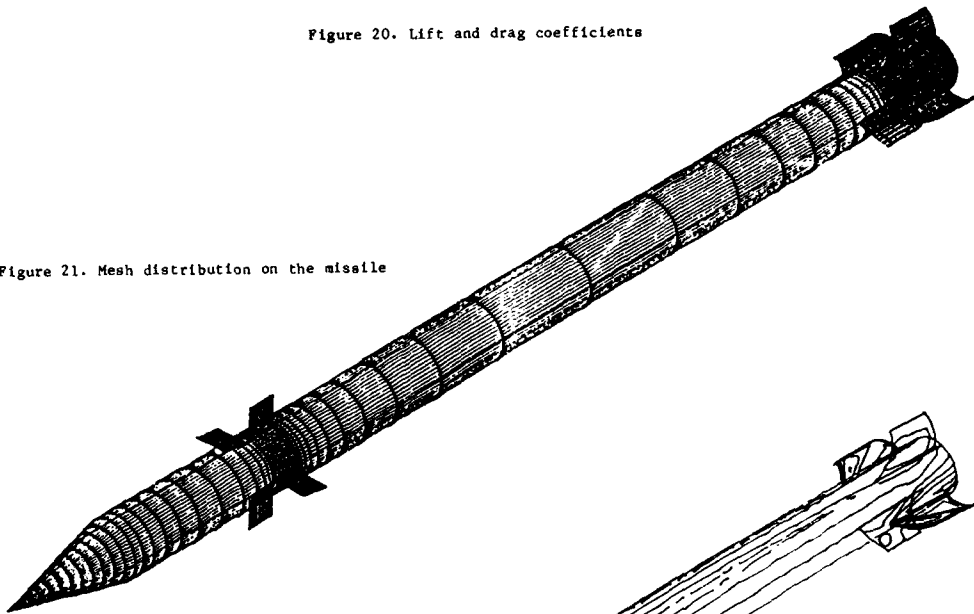
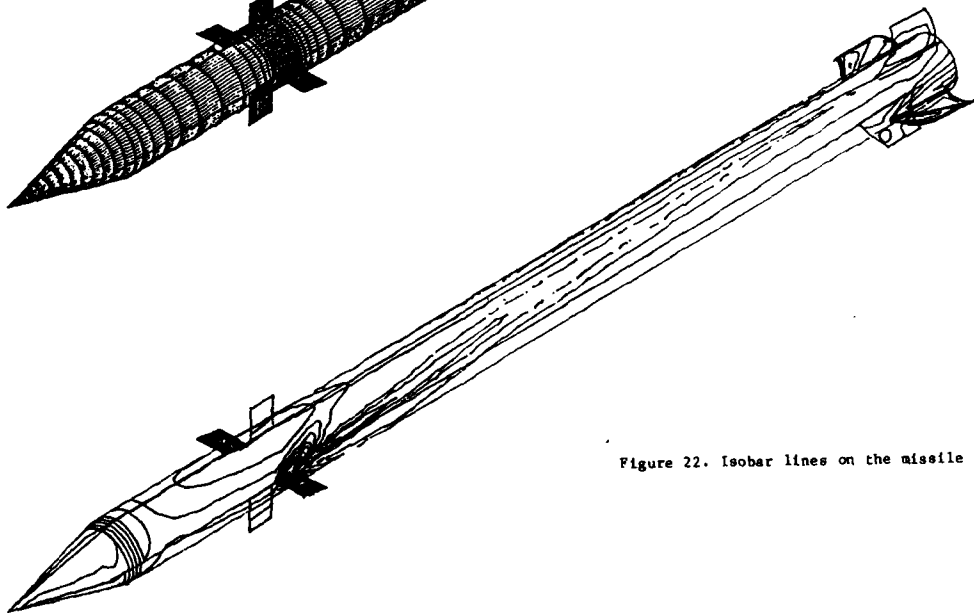


Figure 22. Isobar lines on the missile



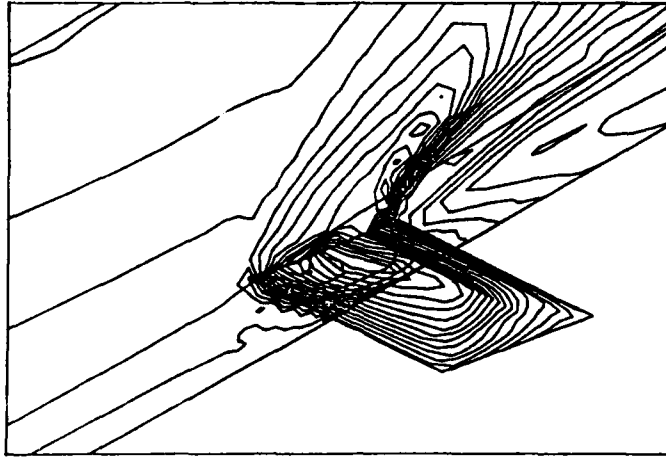


Figure 23. Isobar lines on the flap ( $\delta_m = 20^\circ$ )

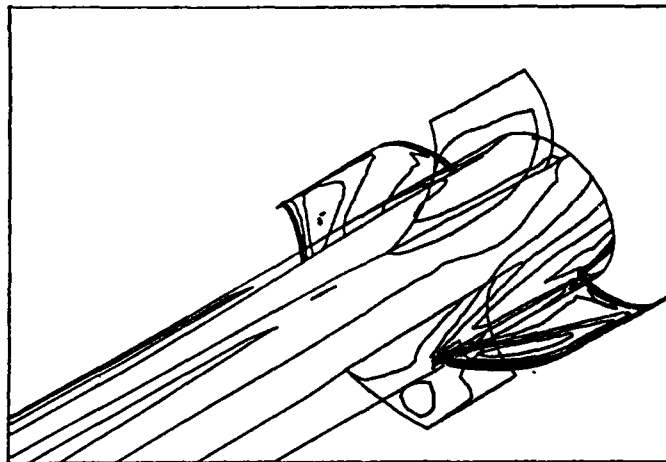


Figure 24. Isobar lines on the wings

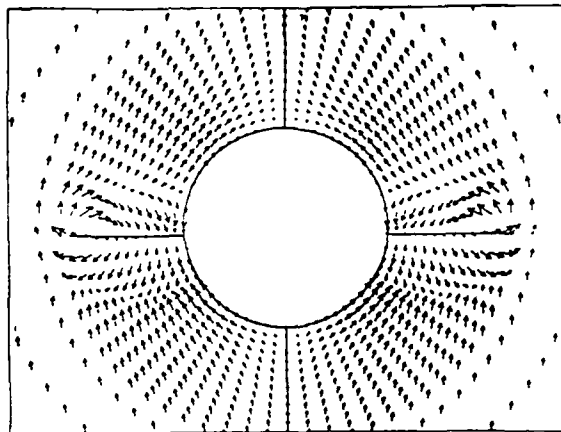


Figure 25. Cross-flow velocity field near the flaps

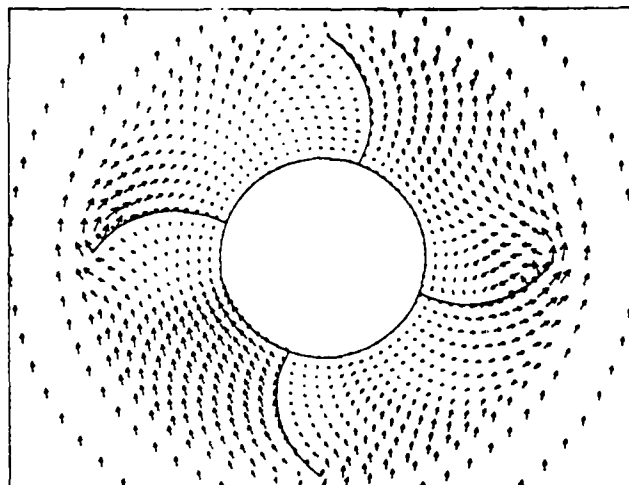


Figure 26. Cross-flow velocity field near the wings

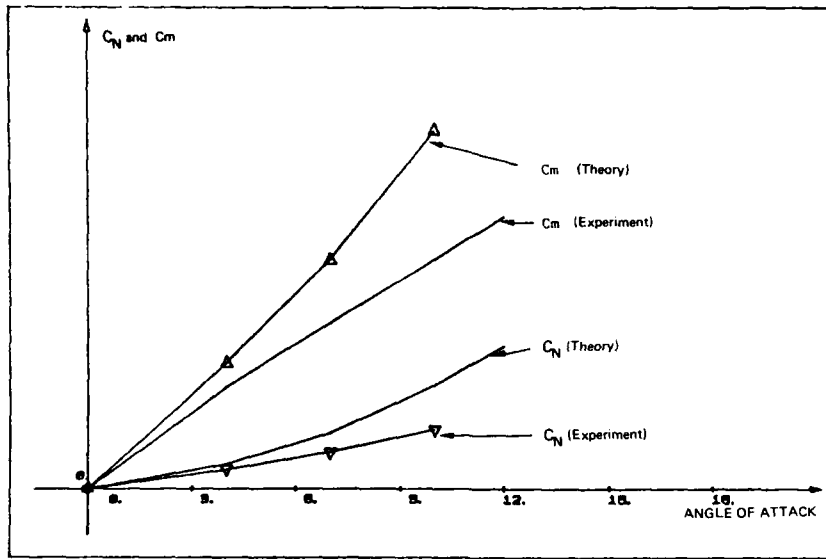


Figure 27. Comparison of the normal force and pitching moment coefficients for the body alone,  $M = 2.12$

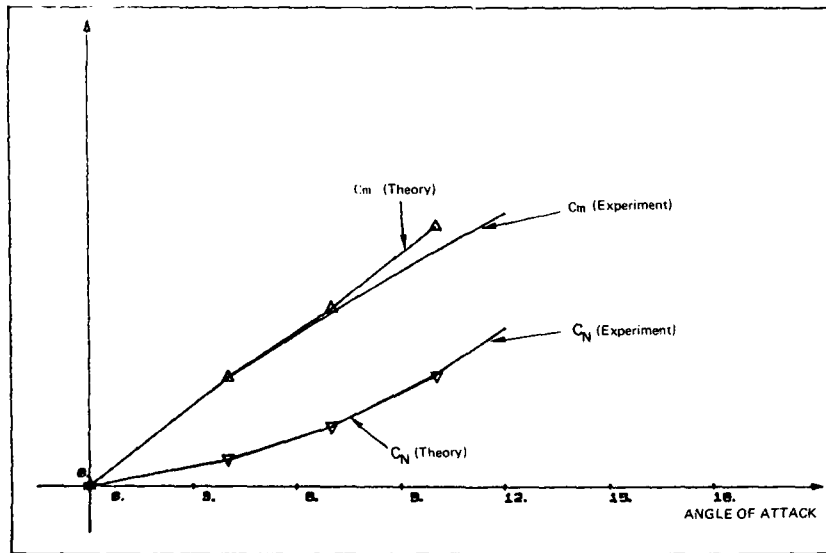


Figure 28. Comparison of the normal force and pitching moment coefficients for the body alone, with correction term,  $M = 1.2$

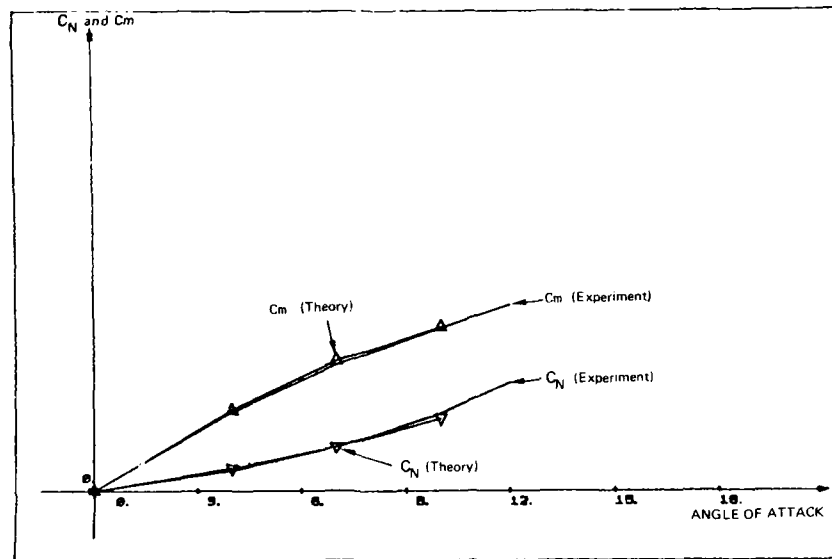


Figure 29. Comparison of normal force and pitching moment coefficients for the body alone, with correction term,  $M_\infty = 2.43$

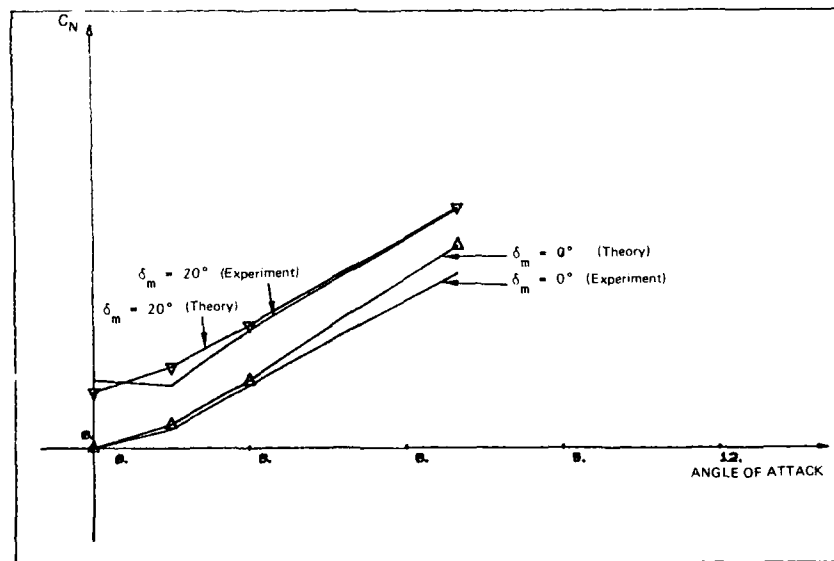


Figure 30. Comparison of the normal force coefficients for the complete configuration with the correction term,  $M_\infty = 1.2$

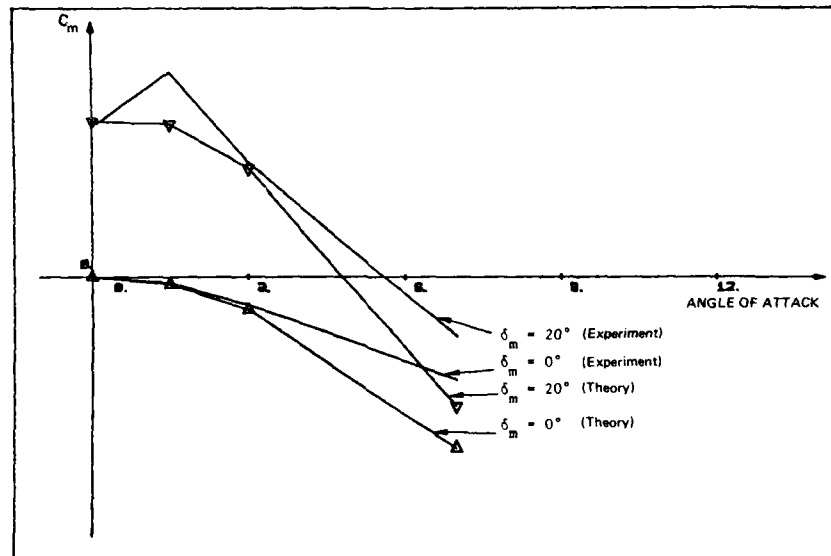


Figure 31. Comparison of the pitching moment coefficient for the complete configuration, with correction term,  $M_\infty = 1.2$

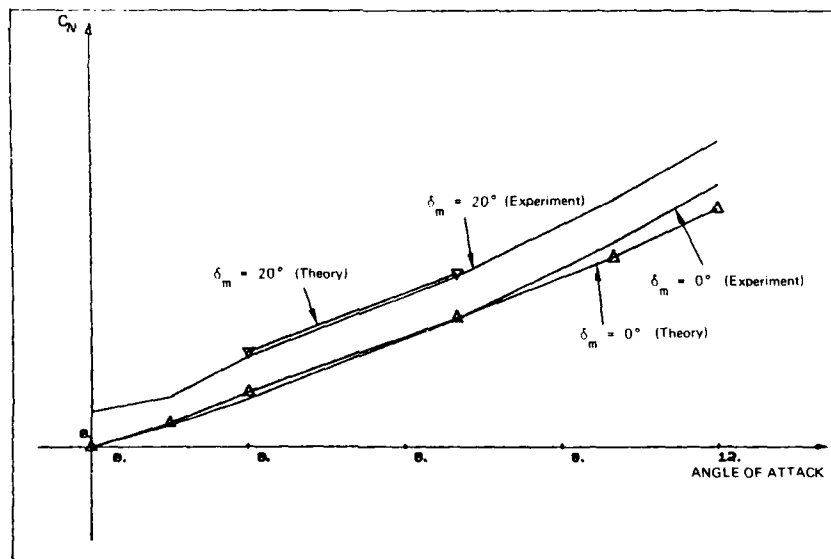


Figure 32. Comparison of the normal force coefficients for the complete configuration, with correction term,  $M_\infty = 2.12$



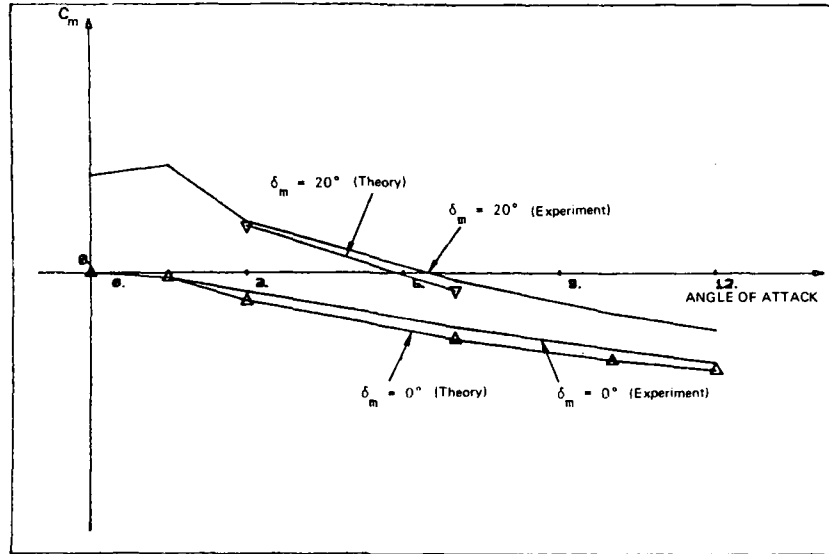


Figure 33. Comparison of the pitching moment coefficients for the complete configuration, with the correction term,  $M_\infty = 2.12$

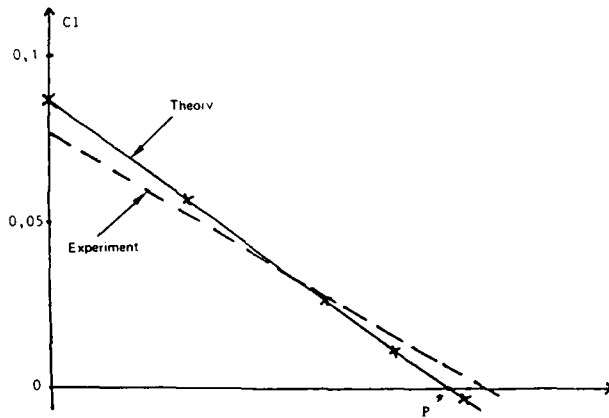
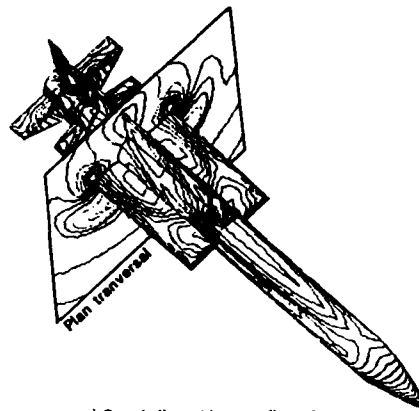
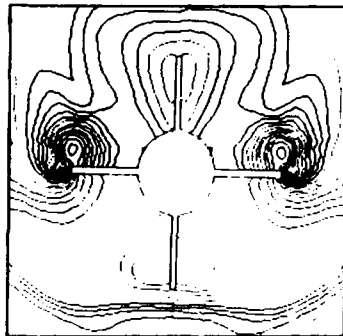


Figure 34. Comparison of the rolling moment coefficients  $M_\infty = 2.12$ ,  $\alpha = 0^\circ$



a) On missile and in cross flow plane



b) In cross flow plane

Figure 35. ASTER Missile  $M_\infty = 2.5$ ,  $\alpha = 10^\circ$  Iso-bar lines

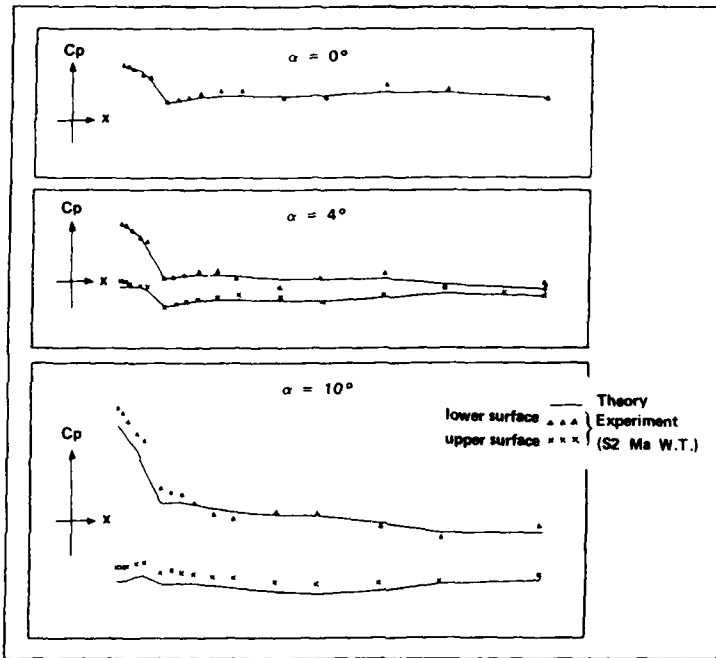
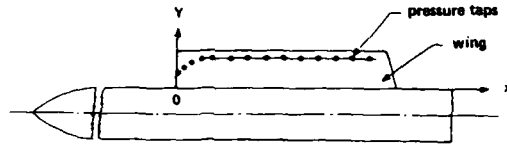


Figure 36. ASTER Missile  $M = 2.5$ . Pressure distribution along the wing

## PREDICTION OF DYNAMIC DERIVATIVES

by

Heinz Fuchs and Rolf Kapp, Dornier GmbH, Abt. BF 20, Postfach 1420, D-7990 Friedrichshafen, FRG

SURVEY

The dynamic derivatives are introduced by their mathematical definition derived from the general expansion of aerodynamic functions with respect to the relevant independent fluid motion variables. The common classification of the dynamic derivatives is evaluated in accordance with the definitions used at flight mechanical applications. This is shown with the examples of nonstationary motion types creating dynamic derivative effects.

The paper in hand shows some basic aspects of a semiempirical method for the calculation of dynamic derivatives of missile configurations or military aircrafts. Results of the computer program 'DYNAM', developed at Dornier within the recent years, are presented in comparison with experimental results of different test rigs. This computer program is based upon the 'USAF Stability and Control Datcom' and updated by semiempirical methods. With the assumptions of attached-flow conditions, at small and moderate angles-of-attack the results are for subsonic speeds derived from potential theory and for supersonic speeds from linearized theory.

For higher angles of attack the linear theory for the calculation of the derivatives with respect to  $q$  is extended by a cross-flow assumption using the cross-flow drag coefficient  $C_{Dc}$ . This extension of the theory quite well succeeds with slender body configurations whereas for the wing parts some kind of uncertainty is introduced by the variation of the cross-flow drag coefficients with the wing shape parameters.

In addition to the semiempirical prediction method of total missile or aircraft configurations there are nonstationary panel methods which are useful for the determination of dynamic derivatives of harmonic oscillating wings or wing-rudder systems. The assumptions of the panel method are very close related to the assumptions of experimental tests of harmonic oscillating models in wind tunnels. This is shown by a quite similar way of identification of the different dynamic derivatives from the unsteady pressure distribution where the harmonic elongation is proportional to the static lift curve slope and the angular velocity is proportional to a 90-deg time-lag in phase with the damping derivatives.

From this kind of prediction methods the second part of the paper goes on to the experimental methods for dynamic derivatives. Primarily, an overview of the different dynamic test rigs is given which are in use at the different aerodynamic test laboratories of FR Germany, especially of the DFVLR. These dynamic test rigs are of forced-oscillation type for subsonic and transonic speeds and of free oscillation type at higher supersonic speeds. Today, the prominent test equipments are of a one degree-of-freedom oscillation rather than of higher dof motions for reasons of higher test accuracy instead of the additional information of more complex multi-dof equipments. Test results of a Dornier standard missile configuration are discussed.

At last, an outlook upon future activities on the evaluation methods of the dynamic test rigs at the high angle-of-attack region is given. This considerations raised from experiences of MOD dynamic tests in the Dornier wind tunnel with a fighter aircraft configuration.

## 1. INTRODUCTION

Dynamic derivatives are the derivatives of an aerodynamic function like lift  $L$  or pitching moment  $M$  with respect to the independent variables of the flow acceleration. There are different derivatives with respect to translational acceleration of the fluid flow as well as with respect to the angular velocity.

These derivatives represent the coefficients of a Taylor series expansion of the aerodynamic force or moment of some configuration to small perturbations of the independent flow variables. Among the well known static derivatives with respect to the angle-of-attack  $\alpha$  (i.e.  $C_{Z\alpha}$ ,  $C_{m\alpha}$ ), the dynamic derivatives due to the rate-of-change  $\dot{\alpha}$  of the angle-of-attack are included as well as the derivatives with respect to the angular velocity  $\dot{\omega} = (p, q, r)$  i.e.  $C_{Zq}$ ,  $C_{mq}$ ,  $C_{Yr}$ ,  $C_{nr}$ ,  $C_{lp}$  etc.

The dynamic derivatives become their flight mechanical relevance when the missile undergoes motions of accelerated type i.e. when curved flight paths are performed with angular velocity or when translational accelerations cause a rate-of-change of the stationary angle-of-attack or the angle-of-sideslip.

We distinguish between general nonstationary motions and motions of harmonic oscillating type. Within flight-mechanical application it is convenient to use the dynamic derivatives derived from harmonic oscillation modes also for general unsteady motions. This is valid under the assumption that the harmonic oscillation is performed with a slow enough reduced frequency. Most of the theoretical prediction techniques for the dynamic derivatives assume a harmonic time dependent flow-field except some real-time unsteady Euler solver methods.

The interest in the development and verification of appropriate methods for predicting dynamic derivatives has been stimulated with increased manoeuvrability of missiles and fighter aircraft and with more sophisticated guidance systems. Especially, dynamic derivatives are needed for the determination of flight envelopes and the design of control systems. With the design of missiles operating at moderate to high angle-of-attack range also the need for the extension of dynamic prediction methods at higher angles-of-attack increased.

These methods may be experimental ones as they are available for instance in West-Germany at the test facilities of the DFVLR or the aircraft industries or may be theoretical ones as they are used and developed in different forms in the national or industrial research institutes.

## 2. DYNAMIC STABILITY DERIVATIVES

### 2.1 Definition and classification of dynamic derivatives

The dynamic derivatives are per definitionem the partial derivatives of an aerodynamic function (like lift-function  $L$ ) with respect to independent flow variables, especially to the variables combined with the acceleration of the fluid flow.

For the introduction of dynamic derivatives one has to begin with some general assumptions of the mathematical description of functions describing the aerodynamic forces on a configuration.

Following the definitions of [1] the simplifying assumption is useful that an aerodynamic function  $L$  is only a function of the instantaneous values of the variables  $u, v, w, p, q, r$  and possibly of the derivatives of these variables with respect to time. This is the common assumption of a quasi-stationary approach of aerodynamic functions which is valid for attached-flow conditions and for motions of the missile which are sufficiently slow. With the assumptions above, function  $L$  is steady and multiple derivatives exist. Let us now consider a Taylor series expansion of the aerodynamic function  $L$  with respect to small perturbations  $\Delta u, \Delta v, \Delta w, \dots$  of the variables up to quadratic order. Then one has a form of eq. (A.1), see Appendix A.

In the planar case of  $L = L(u, w, q)$  the Taylor series reduces to

$$\begin{aligned} L(u+\Delta u, w+\Delta w, q+\Delta q) &= L(u, w, q) + \\ &+ \frac{\partial L}{\partial u} \Delta u + \frac{\partial L}{\partial w} \Delta w + \frac{\partial L}{\partial q} \Delta q + \\ &+ \frac{1}{2} \frac{\partial^2 L}{\partial u^2} \Delta u^2 + \frac{1}{2} \frac{\partial^2 L}{\partial w^2} \Delta w^2 + \frac{1}{2} \frac{\partial^2 L}{\partial q^2} \Delta q^2 \\ &+ \frac{\partial^2 L}{\partial u \partial w} \Delta u \Delta w + \frac{\partial^2 L}{\partial u \partial q} \Delta u \Delta q + \\ &+ \frac{\partial^2 L}{\partial w \partial q} \Delta w \Delta q \end{aligned} \quad \text{eq. (2.1)}$$

Some of the terms of eq. (2.1) are vanishing small as shown below:

$$\frac{\partial L}{\partial u} \Delta u \ll 1:$$

$$L = Ku^2 \quad \frac{\partial L}{\partial u} \Delta u = 2Ku\Delta u = 2L \frac{\Delta u}{u} \ll 1$$

$$\frac{\partial^2 L}{\partial u \partial w} \Delta u \Delta w \ll 1:$$

$$\begin{aligned} L &= Ku^2 \quad \frac{\partial^2 L}{\partial u \partial w} \Delta u \Delta w = \frac{\partial}{\partial w} \left( \frac{\partial L}{\partial u} \right) \Delta u \Delta w = \\ &= 2 \frac{\partial L}{\partial w} \Delta w \frac{\Delta u}{u} \ll 1 \end{aligned} \quad \text{eq. (2.2)}$$

The terms

$$\frac{\partial^2 L}{\partial u \partial q} \Delta u \Delta q \quad \text{and} \quad \frac{1}{2} \frac{\partial^2 L}{\partial u^2} \Delta u^2$$

are vanishing for the same reason. Using the relation

$$\frac{\partial L}{\partial w} \Delta w = \frac{1}{V} \frac{\partial L}{\partial \alpha} \Delta \alpha = \frac{\partial L}{\partial \alpha} \Delta \alpha \quad \text{eq. (2.3)}$$

the following terms of the Taylor series remain:

$$\begin{aligned} L(u+\Delta u, w+\Delta w, q+\Delta q) &= L(u, w, q) + \\ &+ \frac{\partial L}{\partial \alpha} \Delta \alpha + \frac{\partial L}{\partial q} \Delta q + \frac{1}{2} \frac{\partial^2 L}{\partial \alpha^2} \Delta \alpha^2 + \frac{\partial^2 L}{\partial \alpha \partial q} \Delta \alpha \Delta q + \frac{1}{2} \frac{\partial^2 L}{\partial q^2} \Delta q^2 \end{aligned} \quad \text{eq. (2.4)}$$

Introduction of the additional independent variables  $\dot{u}$ ,  $\dot{w}$ ,  $\dot{q}$  leads to equation (A.2) which is shown in the Appendix A.

In an analogous way the lateral terms of an equivalent Taylor series are obtained assuming function L to be dependent from the variables  $v$ ,  $p$ ,  $r$ ,  $\dot{v}$ ,  $\dot{p}$ ,  $\dot{r}$ . The lateral series expansion of function L is shown in eq. (A.3) of the Appendix A.

What terms of aerodynamic coefficients are derived from eq. (A.2) and eq. (A.3) is determined by phenomenological experience. Especially the question where the Taylor series can be truncated without loss of significant accuracy is determined by the experimental and free flight experience. By this reason, a lot of terms of equations (A.2) and (A.3) can be omitted because they are neglectably small.

On the other hand the physical significance of higher order terms cannot be predicted a priori in all cases of applications so some higher order terms are usually truncated because of insurmountable difficulties of their precise determination.

If function L is identified with the aerodynamic pitching moment M equation (A.2) is

$$\begin{aligned}
 & M(V_\infty + \Delta u, \alpha + \Delta\alpha, q + \Delta q, \dot{V}_\infty + \Delta\dot{u}, \dot{\alpha} + \Delta\dot{\alpha}, \dot{q} + \Delta\dot{q}) = \\
 & M(V_\infty, \alpha, q, \dot{V}_\infty, \dot{\alpha}, \dot{q}) + \\
 & + \frac{\partial M}{\partial \alpha} \Delta\alpha + \frac{\partial M}{\partial q} \Delta q + \frac{\partial M}{\partial \dot{\alpha}} \Delta\dot{\alpha} + \frac{\partial M}{\partial \dot{q}} \Delta\dot{q} + \\
 & + \frac{1}{2} \frac{\partial^2 M}{\partial \alpha^2} \Delta\alpha^2 + \frac{\partial^2 M}{\partial \alpha \partial q} \Delta\alpha \Delta q + \frac{1}{2} \frac{\partial^2 M}{\partial q^2} \Delta q^2 + \\
 & + \frac{1}{2} \frac{\partial^2 M}{\partial \dot{\alpha}^2} \Delta\dot{\alpha}^2 + \frac{1}{2} \frac{\partial^2 M}{\partial \dot{q}^2} \Delta\dot{q}^2 + \frac{\partial^2 M}{\partial \dot{\alpha} \partial \dot{q}} \Delta\dot{\alpha} \Delta\dot{q}
 \end{aligned} \tag{2.5}$$

The dimensionless form of equation (2.5) is obtained by the following definitions

$$\begin{aligned}
 C_{m_\alpha} &= \frac{\partial C_m}{\partial \alpha} = \frac{\partial M}{\partial \alpha} \frac{1}{\rho/2 V_\infty^2 S l} && \text{static pitching} \\
 &&& \text{moment slope} \\
 C_{m_q} &= \frac{\partial C_m}{\partial (q \frac{1}{V_\infty})} = \frac{\partial M}{\partial q} \frac{1}{\rho/2 V_\infty S l^2} && \text{pitch damping} \\
 &&& \text{derivativum} \\
 C_{m_{\dot{\alpha}}} &= \frac{\partial C_m}{\partial (\dot{\alpha} \frac{1}{V_\infty})} = \frac{\partial M}{\partial \dot{\alpha}} \frac{1}{\rho/2 V_\infty S l^2} && \text{pitching moment due} \\
 &&& \text{to the rate of change} \\
 &&& \text{of } \alpha \text{ with time} \\
 C_{m_{\dot{q}}} &= \frac{\partial C_m}{\partial (\dot{q} (\frac{1}{V_\infty})^2)} = \frac{\partial M}{\partial \dot{q}} \frac{1}{\rho/2 S l^3} \\
 C_{m_{\alpha^2}} &= \frac{\partial^2 C_m}{\partial \alpha^2} = \frac{\partial^2 M}{\partial \alpha^2} \frac{1}{\rho/2 V_\infty S l^2} && \text{static quadratic} \\
 &&& \text{pitching moment} \\
 &&& \text{derivativum} \\
 C_{m_{\alpha q}} &= \frac{\partial^2 C_m}{\partial \alpha \partial (q \frac{1}{V_\infty})} = \frac{\partial^2 M}{\partial \alpha \partial q} \frac{1}{\rho/2 V_\infty S l^2} \\
 C_{m_{q^2}} &= \frac{\partial^2 C_m}{\partial (q \frac{1}{V_\infty})^2} = \frac{\partial^2 M}{\partial q^2} \frac{1}{\rho/2 S l^3} \\
 C_{m_{\dot{\alpha}^2}} &= \frac{\partial^2 C_m}{\partial (\dot{\alpha} (\frac{1}{V_\infty})^2)} = \frac{\partial^2 M}{\partial \dot{\alpha}^2} \frac{1}{\rho/2 V_\infty^2 S l} \\
 C_{m_{\dot{q}^2}} &= \frac{\partial^2 C_m}{\partial (\dot{q} (\frac{1}{V_\infty})^2)^2} = \frac{\partial^2 M}{\partial \dot{q}^2} \frac{V_\infty^2}{\rho/2 S l^3} \\
 C_{m_{\dot{\alpha} \dot{q}}} &= \frac{\partial^2 C_m}{\partial (\dot{\alpha} \frac{1}{V_\infty}) \partial (\dot{q} (\frac{1}{V_\infty})^2)} = \frac{\partial^2 M}{\partial \dot{\alpha} \partial \dot{q}} \frac{V_\infty}{\rho/2 S l^3}
 \end{aligned}$$

Equivalent coefficients can be derived for the aerodynamic Z-force (i.e.  $C_{Z\dot{\alpha}}$  and  $C_{Zq}$ ) where all conversion factors of the formula above have to be multiplied by  $l$  (= reference length).

Thus, the aerodynamic coefficients

$$C_{Zq} = \frac{\partial C_Z}{\partial (q \frac{l}{V_\infty})} = \frac{\partial Z}{\partial q} \frac{1}{\rho/2 V_\infty S l}$$

$$C_{Z\dot{\alpha}} = \frac{\partial C_Z}{\partial (\dot{\alpha} \frac{l}{V_\infty})} = \frac{\partial Z}{\partial \dot{\alpha}} \frac{1}{\rho/2 V_\infty S l}$$

are introduced.

By this way, the dynamic derivatives are defined by series expansions of the aerodynamic forces and moments with respect to small perturbations of the governing variables.

We distinguish different classes of dynamic derivatives depending on the different use of the longitudinal or the lateral equations [eq. (2.6) and eq. (2.7)] with respect to the component of the aerodynamic force or the moment which is to be expanded into a Taylor series.

We distinguish between 'damping derivatives', 'cross derivatives' and 'cross-coupling derivatives'.

The damping derivatives are defined by the rule that each vector component of the force  $\vec{F} = (X, Y, Z)$  or the moment  $\vec{M} = (L, M, N)$  is differentiated with respect to the same corresponding vector component of  $\vec{u} = (p, q, r)$  i.e.  $C_{Zq}$ ,  $C_{Lp}$ ,  $C_{Mq}$ ,  $C_{Nr}$  etc.

The cross derivatives are defined by cross-wise correlations of the vector components but with cross-wise relations between longitudinal and lateral components excluded, i.e.  $C_{Lr}$  or  $C_{Np}$ .

The cross-coupling derivatives are defined by cross-wise correlations between the vector components of the function and its derivativum combined with a cross-wise correlation of longitudinal and lateral components i.e.  $C_{Lq}$ ,  $C_{Mr}$ ,  $C_{Mp}$ ,  $C_{Nq}$  (see schematic of Fig. 2.1).

## 2.2 Types of nonstationary motion creating dynamic derivative effects

The dynamic derivatives represent the aerodynamic response of a missile to nonstationary motion. This means that the dynamic derivatives are of interest either for fully nonstationary flight trajectories or for quasi-stationary flight curves like circle flight paths (loopings). For the example of the longitudinal derivatives the damping derivatives  $C_{Zq}$ ,  $C_{Mq}$  and the derivatives  $C_{Z\dot{\alpha}}$ ,  $C_{M\dot{\alpha}}$  are the most common ones.

Their influence to different types of missile motion is illustrated by Fig. 2.2 and Fig. 2.3. Within Fig. 2.2 we assume an accurate looping of a missile flown with constant velocity  $V$  and constant angle-of-attack  $\alpha$  i.e.  $\dot{\alpha} = 0$ . This quasistationary flight motion is only influenced by a dynamic derivative effect due to the angular velocity  $q$  according to the pitching rate

$$q = \frac{d\theta}{dt} = \frac{\theta_2 - \theta_1}{\Delta t}$$

Fig. 2.3 shows the well-known example of a sinusoidal flight path trajectory which is flown by two different types of missile attitude. In the upmost example of Fig.2.3 the missile follows the flight path always in tangential attitude creating sinusoidal history of angle of attitude  $\theta$  with time and  $\dot{\alpha} = 0$  all the time. At this example only  $q$ -derivatives are acting without  $\dot{\alpha}$ -effects.

The second example of Fig. 2.3 shows the opposite situation where the missile follows the flight path with constant angle of attitude (= horizontal to geodetical reference). This creates no  $q$ -effects because of  $q = \dot{\theta} = 0$  during all the time whereas the angle-off-attack varies within time in a sinusoidal way creating aerodynamic  $\dot{\alpha}$ -effects.

The last type of the examples of Fig. 2.3 is a missile flying a straight-lined flight-path but undergoing harmonic oscillations in its angle of attitude. Assuming slow frequency of this motion, identical  $q$ - and  $\dot{\alpha}$ -oscillations are effective.

This type of pitching motions represents the mode which is usually found at the wind tunnel test equipments for the measurement of dynamic derivatives. Because this mode combines the rate of change of the angle-of-attack with that of the longitudinal attitude, with test rigs of that 1 dof pitching motion it is not possible to separate the derivatives with respect to  $\dot{\alpha}$  from that of the derivatives with respect to  $q$ .

## 3. METHODS OF THEORETICAL PREDICTION OF DYNAMIC DERIVATIVES

### 3.1 Overview of existing methods and range of applicability

Besides of the semi-empirical methods (cf. next section) there are some other theoretical approaches: First the indicial function concept derived from the fundamental works of M. Tobak [2].

The advantages of this method are the contributions to the downwash effects from forward positioned wings to after positioned tails and the usefulness of the theory with respect to the rate of change of the angle-of-attack. This is due to the idea of the theory in considering the aerodynamic response to instantaneous changes of the conditions determining the aerodynamic properties at steady flow. Disadvantages are that the theory is derived from potential theory. In recent years there were extensions of the theory to more general assumptions (see Tobak, Schiff [3]). Schneider [4] and Schneider-Nikolitsch [5] applied the indicial function concept especially to missile configurations.

A panel-procedure for the prediction of unsteady airloads was developed at the NLR, Netherland (see [6]). This method has the advantage to be applied for complex configurations because of its flexibility with the representation of geometrical surfaces by panel discretization. The characteristics of the unsteady panel method is that each panel contains a time-varying source distribution. Its solutions can be found in terms of integrals over the source distribution on the surface of the configuration. The integral equations are reduced to a set of algebraic equations similar to the well-known steady panel procedures. In doing so, the strengths of the source distributions are defined by applying boundary conditions of an harmonic oscillating body surface.

This reveals the disadvantages of such procedures with its confinement to the linear angle-of-attack range and also the difficulties in the modeling of wakes. Therefore, the powerful tool of this procedure is in its application to aeroelasticity and flutter problems of rather high frequencies and small amplitudes. Another important field of application is the study of flutter properties of wing deflection flaps. For an application of a panel-method for added masses of underwater vehicles see Appendix B.

### 3.2 Semiempirical method according to 'USAF Stability and Control DATCOM'

#### 3.2.1 Longitudinal derivatives

A computer program, designated DYNAM, has been developed by Dornier for several years to calculate the longitudinal dynamic derivatives. The program follows the DATCOM-methods [7] which have been extended to moderate and higher angles-of-attack by introduction of the  $\alpha$ -dependencies of the static components.

In general, the DATCOM method for calculation of the dynamic derivatives is a semi-empirical method which treats the individual missile components separately. Subsequently, the contributions of the individual components like body and wings are summed up in order to determine the total result of the whole missile configuration. This procedure is quite similar to the DATCOM-methods of the static aerodynamic coefficients.

The method of constructing the total result by the contributions of the different missile components implies that the mutual interference effects between the various missile components can be treated in an analogous way to the treatment of the static aerodynamic coefficients. This is a fundamental assumption of the methods described in DATCOM and is also used in DYNAM. The mutual interference factors which are calculated in the static theory can be transferred to program DYNAM via the input data without changing them (an additional option of DYNAM is to calculate them). The types of missile geometry for which DYNAM can be applied is shown in Fig. 3.1 to Fig. 3.3.

The DATCOM-methods for calculation of the dynamic derivatives are based on lifting-surface theory for the wing contributions and subsonic speeds and linearized theory for supersonic speeds. The body derivatives are determined by slender-body-theory. Thus for low-aspect ratio wings - as usually found at missile configurations - the origin DATCOM-methods are restricted to small angles-of-attack.

This means that the DATCOM formulae are confined to attached flow conditions whereas separate flow phenomena are not included in the theory.

At Dornier, the DATCOM method was extended in such a way that all dependencies on the angle-of-attack were introduced wherever such dependencies exist in the terms describing the theory. By this way, the influence of the angle-of-attack was introduced by the function of the lift curve slope  $C_{Z\alpha} = C_{Z\alpha}(Ma, \alpha, \eta)$  and the slope of the moment curve  $C_{m\alpha} = C_{m\alpha}(Ma, \alpha)$ . The movement of the aerodynamic center  $x_{a.c.}$  with the change of the angle-of-attack was also included.

Within this paper it is not the place to reproduce all DATCOM-formulae of dynamic derivatives, the user is referenced to [7] but the principle of the procedure is shown (see Equ. A.4 and A.5 of Appendix A). Equ. A.4 shows the basic principle of DATCOM-methods composing the result for a total configuration by superposition of the contributions of its different components like wing, body etc. (example of the q-derivatives). The total result may be composed of the canard-component [index (WC)], the component of wing 1 [index (W1)], the component of wing 2 [index (W2)], the body contribution [index (B)] and the component of the interference from canard to wing 1 [index WC(W1)].

The superscript (L) means the linear part and superscript (nl) the nonlinear part. The K-factors of wing-body and body-wing interference are the terms in brackets [e.g.  $[K_{W1(B)} + K_{B(W1)}]$ ] and are acting on the linear part. This is as far congruent to the original DATCOM method where the K-factors are multiplied to the total wing components as the original DATCOM procedure is confined to small angles of attack where the nonlinear parts are vanishing.

Analogous formulae are used for the composition of the  $\dot{q}$ -derivatives (see Equ. A.5) with a slightly more complicated part of the canard-wing 1 interference including the change of the downwash angle ( $\partial\epsilon/\partial\alpha$ ). By their physical nature unsteady downwash effects are represented rather by the  $\dot{q}$ -derivatives than by the q-derivatives. These terms are theoretically described by the indicial function concept of the analysis of unsteady motions where the aerodynamic response of an airfoil to an instantaneous change in the steady aerodynamic flow properties is described. For two wings situated one after the other the time lag of the response of a sudden change of the angle-of-attack to the wing after is evaluated (see [7] and [2], [3]). The principle of superposition of the formulae of Equ. A.4 and Equ. A.5 is applied to all speed ranges



(subsonic to supersonic speeds). The contributions of the different components (e.g. wing contribution) are calculated according to the different theoretical methods which are related to the different speed ranges or other governing parameters (e.g. geometrical ones). The procedure is in principle shown for the wing contribution of the q-derivatives. At subsonic and supersonic speed:

$$\begin{aligned} C_{z_q}^{(1)}(n, \alpha) &= (C_{z_q}^{(1)} + \frac{\bar{x}(n, \alpha)}{l}) (C_{z_\alpha}^{(1)}(n, \alpha) - C_x(n, \alpha)) \\ C_{z_q}^{(n)}(n, \alpha) &= (C_{z_q}^{(n)} + \frac{\bar{x}(n, \alpha)}{l}) C_{z_\alpha}^{(n)}(n, \alpha) \end{aligned} \quad \text{eq. (3.1)}$$

$\bar{x}$  is the distance between the point-of-rotation of angular velocity  $q$  and the aerodynamic center of the wing, positive if a.c. of the wing is after the point of rotation.

Eq. (3.1) shows another basic principle of general mechanics, namely the splitting of a pure rotational motion into a translational and a rotational part. The motion of a wing with point of rotation apart from wing-a.c. is splitted into the rotation about the wing-a.c. position and a corresponding translational motion of the a.c.-point. The calculation of the dynamic derivatives is also splitted into these parts where the rotation of the wing about its a.c.-position is the wing-alone part. At subsonic speed the wing-alone part is given by

$$C_{z_q}^{(1)} = \frac{1}{4} \frac{\bar{x}}{l} (C_{z_\alpha}^{(1)}(n, \alpha) - C_x) \quad \text{eq. (3.2)}$$

and the remaining term of eq. (3.1) is the  $C_z$ -component of the  $\Delta\alpha$ -increment  $\Delta\alpha = q\bar{x}/l$  induced by the q-rotation.

At supersonic speed the wing-alone part is calculated according to the linear supersonic wing theory where the procedure is splitted up into the 'subsonic leading edge' part and the 'supersonic leading edge' part. In these cases the wing alone part is a rather complicated function of the compressibility factor and geometrical parameters like aspect ratio AR and taper ratio  $\lambda$ . In DATCOM [7] these functions are tabulated in diagram form. Examples of these formulæ are given in Appendix A eq. (A.6) to (A.7).

One main attribute of these methods is that the calculation of dynamic derivatives is reduced to static terms like  $C_{z_\alpha}$ . Therefore, these methods can also be updated by use of experimental results for the lift curve slopes so that - as a rule - an increase of accuracy can be realized.

In order to qualify the wing-alone contributions, different other methods were also used (e.g. slender body theories by Nielsen [1] and Burhan [8], lifting surface theory by Garner [9], Otto [10] and Gersten [11]), see Fig. 3.4.

This method of expansion of the original DATCOM formulae turned out to give sufficient results for the dynamic derivatives of the aerodynamic forces whereas the variation of the derivatives  $C_{m_q}$  and  $C_{m_\alpha}$  with the angle-of-attack is considerably underestimated when moderate to higher angles-of-attack are considered. The results of the enlarged DATCOM method - as described above - are of better agreement with test results for body-tail-configurations or configurations with only one wing-segment than they are for wing-body-tail configurations. This is due to wing-body interference and to wing-tail interference effects which also depend on the angle-of-attack when moderate angle-of-attacks are investigated.

Numerical examples of the extended DATCOM method are shown in section 4 with comparison to experimental results.

From experiences with all kinds of dynamic test rigs and flow visualization with models undergoing pitch oscillations of moderate or higher angles of attack it is known that flow separation in combination with reattachment is observed.

These effects cannot be represented by the DATCOM-method outlined above. Therefore, some kind of a cross-flow theory for slender bodies and surfaces was developed at Dornier for the determination of the dynamic derivatives  $C_{z_q}$  and  $C_{m_q}$  (see sec. 3.3).

### 3.2.2 Roll damping derivative

For missiles with bodies of revolution and plus or cross wings the lateral dynamic derivatives are for reasons of symmetry defined by the corresponding longitudinal ones:

$$\begin{aligned} C_{y_r} &= -C_{z_q} \\ C_{n_r} &= C_{m_q} \\ C_{y_\beta} &= C_{z_\alpha} \\ C_{n_\beta} &= -C_{m_\alpha} \end{aligned} \quad \text{eq. (3.3)}$$

So in missile aerodynamics one of the most interesting lateral dynamic derivative is the roll damping  $C_{y_r}$ . This derivative defines the rolling-rate which is often restricted by requirements of the seeker-section (esp. TV-imaging, radar- or IR-seeker). Within theory the roll damping is only defined for wings

$$C_{1p} = \frac{\partial C_l}{\partial \left(\frac{\beta s}{2V_\infty}\right)} \quad (s = \text{wing span})$$

The terminology of missile aerodynamics often uses an arbitrary reference length  $l$  (e.g. body diameter)

$$C_{1p} = \frac{\partial C_l}{\partial \left(\frac{\beta l}{V_\infty}\right)}$$

The physical phenomenon of the roll-damping is a change of the wing lift distribution induced by the roll-rate. The roll-rate  $p$  causes an asymmetric lift distribution as schematically shown in Fig. 3.5. At the wing side which is moved downward an additional increment of lift is induced according to the incremental increase of the angle-of-attack  $\Delta\alpha = \arctan\left(\frac{\beta s}{2V_\infty}\right)$ . At the wing tip moved upward a corresponding decrease of the lift distribution is induced. Assuming attached flow conditions, this change of the lift distribution causes a rolling moment  $\Delta C_l$  which acts against the initial rolling motion. (With flow separation effects there are also cases where the induced rolling moment increases the initial roll rate + i.e. autorotation if the flow suddenly separates at the upper side of the profile. With missiles of small spanned wings autorotation is seldom observed.) By analogy to section 3.2.1 program DYNAM follows the DATCOM-methods with the extension that  $\alpha$ -dependencies are introduced via the lift-curve-slope function. The DATCOM subsonic method is a potential theory based on Bird [12] and De Young [13]. This procedure takes into account parameter effects like lift-curve-slope, induced drag, profile drag and dihedral of the wing. For the  $\alpha$ -effects the knowledge of lift and drag as a function of  $\alpha$  is necessary up to stall angle-of-attack.

The subsonic wing formula for  $C_{1p}$  is:

$$C_{1p} = \underbrace{\left(\frac{\beta C_l}{k}\right)_{C_A=0}}_{\text{linear part}} + \underbrace{\left(\frac{k}{\beta}\right) \frac{(C_{l\alpha})_{C_A}}{(C_{l\alpha})_{C_A=0}}}_{\text{profile part}} \frac{C_{lp}}{(C_{lp})_{C_A=0}} + \underbrace{(\Delta C_{lp})_W}_{\text{drag induced part}} \quad \text{eq. (3.4)}$$

non-linear part

The linear part is given by diagrams of [7] as a function of wing aspect ratio and 2-dimensional lift-curve slope. The governing part of eq. (3.4) is for missile applications the nonlinear part (For more details see [7]). The roll-damping of a total configuration is obtained by superposition of the contributions of the different components. No wing-tail interference is taken into account. Eq. (3.4) represents the contribution of two planar fins. For cruciform wings the body-wing interference is estimated following Nielsen [1] by use of interference factors  $k_{BW}$  and  $k_{BT}$ :

$$C_{1p} = k_{BW} (C_{1p})_{BW} + k_{BT} (C_{1p})_{BT} \quad \text{eq. (3.5)}$$

which are a function of the ratio of body diameter to wing span  $\frac{A}{S}$  (see Fig. 3.6).

For supersonic speed range the DATCOM-method is based upon linear supersonic wing theory (see data sheets [13], Harmon and Jeffreys [15] and Malvestuto et. al. [16]). These theories assume the wings as flat plates neglecting thickness effects of the profile which is valid as long as the Mach lines are far enough from the wing leading edge. The thickness effect is taken into account by empirical corrective terms. The procedure of the supersonic speed is, in general, similar to the subsonic case but much of the material is given by functionals presented in diagrams, for details see DATCOM [7]. Numerical examples are given in section 4.3.2.

### 3.3 Cross-flow method for the q-derivatives at high angle-of-attack

Since some results of the DATCOM-method (see 3.2.1) were in poor agreement with test results at higher angles of attack, another method - based on cross-flow theory - was tried by Dornier. From the work of Jorgensen [17] the cross-flow theory is known to be a useful tool for the prediction of static forces and moments of missiles in the nonlinear  $\alpha$ -range. Extension of this static theory to the calculation of the dynamic q-derivative is outlined in the following where we begin with a cylinder in pitch (see Fig. 3.7).

Due to the pitch rate  $q$  an additional decrement of the normal force  $\Delta N_{(q)}(x)$  acts on every cross-section  $x$  of the body part before the center of rotation. In an analogous way, the body part behind the center of rotation experiences an increment of the normal force.

The static cross-flow normal force  $N$  can be expressed by

$$N = C_{Dc} \frac{S_D}{S} \rho/2 V_n^2 S \quad \text{eq. (3.6)}$$

with  $C_{Dc}$  as the cross-flow drag coefficient referred to the projection area  $S_p$ .

Insertion of the normal velocity  $V_n$  of the pitching body

$$V_n(x) = V_\infty \sin \alpha - qx \quad \text{eq. (3.7)}$$

in equation (3.6) leads to the local cross-flow normal force which acts on an infinitely small cylinder section  $\Delta x$  with the projection area  $\Delta S_D$ :

$$\Delta N(x) = C_{D_C} \frac{\Delta S_D}{S} \rho/2 (V_\infty^2 \sin^2 \alpha - 2 qx V_\infty \sin \alpha + q^2 x^2) S \quad \text{eq. (3.8)}$$

The first term of equation (3.8) represents the part of the normal force due to a static body attitude of angle  $\alpha$  whereas the second term of equ. (3.8) represents the dynamic part due to  $q$  which is of special interest for the derivation of a dynamic derivativum. The third term which is quadratic in  $q$  has been neglected.

By use of the second term of equ. (3.8) one defines the dynamic derivative

$$\Delta C_{N_q}(x) = -2 C_{D_C} \frac{\Delta S_D}{S} \frac{x}{D} \sin \alpha$$

which represent the nonlinear increment or decrement of the normal force for each local body segment at distance  $x$  from the center of rotation.

With the body cross-section  $S = \frac{\pi D^2}{4}$  as reference area and with  $\Delta S = 2\Delta y(x)\Delta x$  it follows:

$$C_{N_q} = -\frac{16 C_{D_C}}{\pi D^2} \sin \alpha \int_{x_L}^{x_U} y(x) x dx \quad \text{eq. (3.9)}$$

$$C_{m_q} = -\frac{16 C_{D_C}}{\pi D^2} \sin \alpha \int_{x_L}^{x_U} y(x) x^2 dx$$

Function  $y(x)$  is the variation of the missile contour. The cylinder contour is  $y(x) = D/2$ , thus

$$C_{N_q} = -\frac{4}{\pi} C_{D_C} \sin \alpha \left\{ \left(\frac{x_U}{D}\right)^2 - \left(\frac{x_L}{D}\right)^2 \right\} \quad \text{eq. (3.10)}$$

$$C_{m_q} = -\frac{8}{3\pi} C_{D_C} \sin \alpha \left\{ \left(\frac{x_U}{D}\right)^3 - \left(\frac{x_L}{D}\right)^3 \right\}$$

Similar formulae are derived for a complete missile configuration (cf. Fig. 3.B). The evaluation of eq. (3.10) is splitted up into different segments according to the partions  $\alpha_0$  to  $\alpha_n$  of Fig. 3.6.

The contour of the nose-part, for instance, is given by  $y(x) = -r_0 + \frac{D}{2} + \sqrt{r_0^2 - (x-x_0)^2}$  so that

$$C_{N_q} = -\frac{4 C_{D_C}}{\pi} \frac{4 I_1}{D^2} \sin \alpha$$

with the integral

$$I_1 = \int_{x_1}^{x_2} y(x) x dx$$

The integration of the wing-part is splitted up to the part from trailing-edge  $x_1$  to the leading-edge kink  $x_2$  with  $y(x) = \frac{s}{2}$  ( $s$  = wing span) and into a second wing leading-edge part  $x_2$  to  $x_3$  (cf. Fig. 3.6) with  $y(x) = px + a$ .

The same procedure is done for the derivative of the moment. The integrals are easily to be evaluated so that more details can be omitted. But it is necessary to use  $C_{D_C}$  as a function of the cross-flow Mach number and the Reynolds number as shown with the diagram of Fig. 3.9.

#### 4. EXPERIMENTAL METHODS FOR THE PREDICTION OF DYNAMIC DERIVATIVES

##### 4.1 Overview of different methods

There are many different techniques in the evaluation of dynamic derivatives from wind-tunnel measurements. (For a comprehensive overview see [18]). Nearly all wind tunnel tests are confined to harmonic oscillations of the model for general unsteady motions cannot be simulated because of the spatial restrictions of the wind tunnel test sections. Forced and free oscillation type test rigs are distinguished. This means that with forced oscillations the harmonic oscillating motion of the wind tunnel model is steadily driven by an outer force generated by a motor moving the model (e.g. by an eccentric driven rod or similar devices). With free-oscillation type test rigs the model is initially put off balance and then

suddenly given free so that an oscillating motion about the state of equilibrium is initiated.

What dynamic derivatives can be evaluated by a dynamic test rig is determined by the degree-of-freedom of the harmonic motion which is performed. A multi-dof motion defines multiple dynamic derivatives of a 1-dof motion corresponding to the multiple aerodynamic coefficients of the Taylor-series (cf. section 2) which are necessary to describe the motion.

When the prescribed motion combines longitudinal and lateral components (for instance by a coning motion of the wind tunnel model one even gets cross-coupling derivatives.) But it should be emphasized that the accuracy of the dynamic derivatives is highly affected by the accuracy of the prescribed motion thus lower dof-motion systems are at least easier to be conducted and in general have the tendency to higher accuracy for the pure damping derivatives.

One common characteristic of all different methods is that the inertial reactions of the motion have to be separated from the aerodynamic inductions (= dynamic derivatives). Therefore, in any case the harmonic oscillation is conducted twice: first, without blowing the wind tunnel measuring the inertial reactions and second, with blowing the wind tunnel thus determining the inertial plus the aerodynamic effects. The aerodynamic reactions are then obtained by the difference of these two independent measurements. The aerodynamic response of the harmonic oscillation contains both types of aerodynamic reaction static derivatives as well as dynamic derivatives.

Different evaluation methods extract the dynamic part from the static one of the aerodynamic function. The aerodynamic response reveals the global time-history of the pressure distribution upon the wind tunnel model. The dynamic pressure distribution is also a harmonic function with time showing certain characteristics of the phase of the aerodynamic response relative to the oscillation.

The main difference between the free and the forced oscillation type test rigs is that in the first case - in addition to the aerodynamic response - one has to measure precisely the time history of the model motion whereas with forced oscillation the model motion is prescribed and thus a priori known.

The evaluation methods for determination of the dynamic derivatives are based upon Fourier- or spectral analysis of the aerodynamic response or some other parameter identification methods like regression theory.

The dynamic test rigs used in FR Germany are shown with missile test results in the next section. Besides the MFD-balance and the Mobile oscillation derivative test rig (MOD) they are all of the 1 dof-type (see Fig. 4.1). Important multi-dof dynamic test rigs are

- in Canada: the forced-oscillation apparatus MKI  
at NAE, Ottawa  
and the NAE Dynamic Calibrator  
(see [18] and [19])
- in U.S.A.: different oscillation apparatus of  
AEDC, Tullahoma  
and NASA Langley
- in U.K. : forced oscill. 3 dof-app.  
of RAE Bedford

#### 4.2 Dynamic test rigs used in the different aerodynamic laboratories of FR Germany

##### 4.2.1 The MFD test-rig of the DFVLR Braunschweig

The first German dynamic apparatus for oscillatory motion was the Multi-degree-of-Freedom Derivative Balance (MFD) for sting mounted models in the 3 m low-speed wind tunnels of DFVLR (see [20]).

Installation of the MFD apparatus in the closed test section of the low-speed wind tunnel at DFVLR Braunschweig is shown in Fig. 4.2. The main features of the mechanical system are a flexible sting with two bending flexures in line, which allow combined pitch and plunge motions in the longitudinal plane (see Fig. 4.3).

The support system allows inclination of the total system to angles of attack up to 40 degrees.

From the sting deflections and the excitation force measured with strain gauges, the dynamic stability derivatives are evaluated by applying the Rayleigh-Ritz energy equations to the vibrating system including generalized aerodynamic reactions to the model (see [20]).

The MFD apparatus was used with a missile model of body diameter  $D = 120$  mm. The model was machined from stainless steel and was of 22 kg weight.

##### 4.2.2 The TRAD apparatus of DFVLR Göttingen

Since 1979 a high-load dynamic derivative balance (German abbreviation TRAD) has been developed for use in the 1 m transonic wind tunnel at DFVLR-AVA Göttingen. A description of the test rig is given in [21], a similar 1 dof dynamic balance was developed at FFA, Bromma, Sweden, (see [22]). Main features of this forced-oscillation apparatus are:

- 1 dof oscillation at fixed amplitude in pitch, yaw or roll
- high rigidity against static loads

- direct parallel measurement of displacement and total static and dynamic loads on the model
- analog data reduction with special vector component resolvers and online data transfer to central computer.

The setup for missile tests in the pitching mode is sketched in Fig. 4.4. The standard  $\alpha$ -traverse of the transonic wind tunnel with perforated walls is used to support the sting balance by means of an angle adaptor enabling remote setting of the angle-of-attack from  $-2$  to  $32$  degs. The sting tip is split into a bifurcation, with a moveable head in between, which is fixed on a pair of cross flexures forming the pitch axis. The one degree amplitude of oscillation is prescribed by an eccentricity at the tip of a rotating shaft within the hollow sting. The shaft is driven by a five-phase step motor, selected for its ability to maintain constant speed at alternating torque.

The TRAD balance was used with a missile model of a body diameter  $D = 50$  mm. The forward body of the missile model was manufactured from carbon-fibre material. By this means a total model weight of  $1.55$  kg was reached and the necessary stiffness was achieved (for more details see [23] and [24]).

The oscillation in roll is conducted by an additional sting which is connected with the driving motor. The motor shaft itself undergoes sinusoidal rotations which are transmitted to the driving shaft within the model sting via a steel loop and a gear of ratio  $1:3.6$ . The maximum roll amplitude is  $2$  degs where an amplitude of  $1$  deg is resolved into  $200$  motor steps.

#### 4.2.3 Free-oscillation apparatus of DFVLR Cologne

The principle of the free-oscillation derivative balance of DFVLR Cologne is shown in Fig. 4.5. The apparatus is specially designed for damping measurements on missiles in the  $0,6$  m blow-down transonic wind tunnel at subsonic and supersonic speeds up to  $Ma = 3,0$  (see [25]).

The model is strut-mounted on a removeable cross flexure, the stiffness of which is appropriate to the model inertia. The free-oscillation motion in pitch is initiated by a tripping device, which is hydraulically pushed into the rear end of the model, deflecting it to the starting position. The time history of the model motion is taken from strain gauges glued to the cross flexure. The stiffness and damping derivatives are evaluated from the response data using Fourier transforms and spectral analysis.

The tests were conducted with a stainless steel manufactured model of a body diameter  $D = 28$  mm.

#### 4.2.4 The 'mobile oscillation derivative balance' MOD

The 'mobile oscillation derivative balance' - in the following designated with the abbreviation MOD - is a dynamic test rig of a two dof-motion of forced oscillation type. The special characteristic of this balance is its movability. This means that the whole support of the MOD dynamic test rig is transportable to various low-speed wind tunnel test sections so that dynamic tests can easily be conducted at different places of experimental laboratories.

The MOD was developed in a joint cooperation of the aircraft industries Dornier and the former VFW-Fokker with the experimental laboratories of the DFVLR and the institute for technics of flight of the TH Darmstadt (see [26]). By this means it was possible that dynamic derivative tests were also conducted at the Dornier wind tunnel. Thus, the dynamic derivatives of a fighter aircraft model were examined.

The MOD is a test rig of forced oscillations where the four independent types of motion (plunging, pitching, yawing motion and rolling motion) can be independently excited. A detailed description of the MOD dynamic test-rig is given in [27]. Figure 4.6 shows the support and the driving rod of the pitch and roll configuration. Also the heave-mechanism is shown creating a pure plunging motion.

For the heaving of the plunging motion the driving rod of the motor is movable inside the mounting strut of the model. Each motion type (pitch and roll, yaw or heave) is driven by an own motor. The whole driving mechanism and vertical sting can be mounted at a curved guide rail of the support so that high angles of attack of the model can be installed. Main features of the mechanical and electrical equipment of the MOD are:

- a five component DMS-balance without measuring the tangential force
- a spring-loaded bending beam clued with DMS-gauges for measuring the deflection angle of the oscillation
- an inductive transmitter of the oscillation elongations and accelerometer for the heave motion
- a pulse generator at the driving motors to measure the rotation rate of the shafts

The evaluation method of the MOD is based upon Fourier - or regression analysis. With Fourier analysis the prescribed oscillation  $\theta(t)$  is expanded according to

$$\theta(t) = \theta_{\sin}^{(1)} \sin \omega t + \theta_{\cos}^{(1)} \cos \omega t \quad \text{eq. (4.1)}$$

as well as the aerodynamic response  $M(t)$

$$M(t) = M_{\sin}^{(1)} \sin \omega t + M_{\cos}^{(1)} \cos \omega t \quad \text{eq. (4.2)}$$

By the common used assumption

$$M(t) = f_0 + f_1 \theta(t) + f_2 \dot{\theta}(t) \quad \text{eq. (4.3)}$$

which means that the aerodynamic response is proportional to the elongation itself (stiffness derivatives) and to the velocity of the motion (damping derivatives), one is able to derive two algebraic equations for the unknown derivatives which are easily solved.

Within this procedure the dynamic derivatives are introduced according to the Taylor series, eg. (sec. 2.2), omitting nonlinear terms.

## 5. MISSILE TEST RESULTS AND COMPARISON WITH THEORETICAL PREDICTION

### 5.1 Missile configurations

For dynamic wind tunnel tests at different Mach numbers and with different test rigs two tail-controlled missiles were selected (configurations see Fig. 5.1). They are composed of a cylindrical body of revolution with 17 calibers body length, blunt base and ogival nose, a cruciform wing and a cruciform tail, both in the plus position. Wing and tail are congruent in geometric shape with a scale factor of two. The lifting surfaces of the wind tunnel models were constructed from flat plates of 2 % profile thickness with wedge angles of 20 degs normal to all outer edges (see also [28]).

### 5.2 Low speed results

With the MFD-balance dynamic tests of the Dorrier missiles (Fig. 5.1) were performed at low wind tunnel speeds ( $Ma = 0.1$  to  $0.2$ ). The results are also reported in [23] and [29]. The oscillation frequencies varied from  $f = 3.5$  to  $7.5$  Hz. The Reynolds number referred to the body diameter was kept constant at  $Re_D = 0.25$  Mio.

Results of the dynamic force damping  $C_{Z_q} + C_{Z_{\dot{\alpha}}}$  of config. RFL 122 are shown in Fig. 5.2. The damping moment  $C_{m_q} + C_{m_{\dot{\alpha}}}$  which is not shown in this paper show a considerably larger spread in reduced frequency. Quasi-steady results of DATCOM theory are represented by the dashed line in Fig. 5.2. Cross-flow improvement has not yet been included which might cause the deviations at higher angles of attack.

### 5.3 Free-oscillation results up to $Ma = 3.0$

Results of pitching moment damping of configuration RFL 122 obtained by the free oscillation apparatus at DFVLR Cologne are shown in Fig. 5.3.

The reduced frequency  $\omega^*$  of the model varied from 0.006 to 0.025 and the Reynolds number  $Re_D$  from 0.4 Mio to 1.5 Mio depending on Mach number. The variation of the measured results with angle of attack is small at subsonic speeds whereas at supersonic speeds a considerable variation is to be found. The dependence of the results on Mach number is in good agreement with the theoretical results at zero angle-of-attack. The results of these experimental tests are summarized in more detail in [25].

### 5.4 Forced-oscillation results at transonic speeds

#### 5.4.1 Longitudinal results

The stiffness and the damping derivatives of normal force and pitching moment were measured at the Mach numbers 0.7/0.9/1.05/1.2 with angles of attack up to 30 degs. The oscillation frequencies varied from 3 to 19 Hz corresponding to the reduced frequencies  $\omega^* = 0.004/0.008/0.016/0.020$ . The Reynolds number was  $Re_D = 0.4$  Mio. A BL strip was positioned 2.5 D behind the nose tip. A comprehensive overview of the longitudinal results is to be found in [23] and [24]. The center of rotation D was at 10.872 D behind the nose at all tests. The measured dynamic derivatives are then transformed to a rotation axis at  $x_{c,r} = 10.5$  D to which all results shown in the figures are referred, too. Some typical results are shown in Fig. 5.4 to Fig. 5.9 in comparison to free-oscillation measurements and theoretical predictions.

At every test point (defined by Mach number, angle of attack and reduced frequency) up to four independent measurements were made to detect the scatter of the resultant derivatives. The spread of the results in the order of 5 % of the maximum value was too small to be drawn. Therefore, the figures given in this paper show averaged values for each reduced frequency.

The angle of attack has large influence on all dynamic derivatives measured with the TRAD. Fig. 5.6 show an unexpected  $\alpha$ -dependence of  $C_{Z_q} + C_{Z_{\dot{\alpha}}}$  which might be explicable from the extremely complicated flow conditions with line vortex shedding of body and vortex interaction phenomena observed in the water tunnels of Dornier [30] and VKI/Belgium [31]. For the general aspects of nonlinear effects at the high angle-of-attack range with respect to insteady aerodynamics see also [32] and [33].

The influence of reduced frequency is almost negligible at  $\alpha = 0$  deg and more pronounced at higher  $\alpha$ , especially for configuration RFL 122 (see Fig. 5.5 and 5.7). The trend of the  $\omega^*$ -influence is different for both configurations. The body-tail configuration RFL 102 shows a decrease with increased  $\omega^*$ , whereas the reverse tendency holds if the cross wing is added.

On the whole, all results show that the extension of the pure DATCOM-methods by the cross-flow method (cf. sec. 3.3) considerably improves the theoretical predictions.

Fig. 5.10 shows results of the static aerodynamic coefficients  $C_Z$  and  $C_m$  obtained by the TRAD-balance. They are in good agreement with the static derivatives which are known for this configuration by conventional static measurements as well as by theoretical prediction.

## 5.4.2 Lateral results

The lateral results of the TRAD-measurements of the Dornier standard missile configuration are outlined in [34] in detail. The roll-damping derivativum  $C_{l\dot{\alpha}}$  is shown in Fig. 5.11 to 5.14 for configuration RFL 122. The roll damping is shown there for  $Ma = 0.5$  and  $0.88$  and for  $\omega^* = 0.004$  and  $0.012$ . In all cases the theoretical and experimental results are in quite good agreement even at higher angles of attack. The measured values represent the sum  $C_{l\dot{\alpha}} + C_{l\dot{\alpha}} \sin \alpha_0$  which turn into the pure  $C_{l\dot{\alpha}}$ -value at  $\alpha_0 = 0$  deg. At  $\alpha_0 = 30$  degs the measured results show a considerable scatter but the accumulation points give a reasonable tendency of the results. At each angle-of-attack four independent measurements were conducted and each result is drawn in the figures by a separate symbol. The scattering of the results at high angles-of-attack reveal the difficulty to measure a pure lateral derivativum like the roll damping when cross-coupling effects occur.

The supersonic results are of the same quality like the subsonic ones and the agreement of experiment and theory is as good for small angles-of-attack. At higher angles-of-attack some deviations occur because the theory does not include  $\alpha$ -effects.

Similar results are shown for the body-tail-configuration RFL 102 (see Fig. 5.15 and 5.16). Because of the small tail span the results are a magnitude smaller than for the wing-configuration. The scatter of the experimental results also increases because the magnitude of the aerodynamic response is at the lower threshold of the measurement range of the balance.

## 6. OUTLOOK WITH RESPECT TO FUTURE ACTIVITIES ON NONSTATIONARY HIGH ANGLE-OF-ATTACK AERODYNAMICS

For improvements of the measurement of dynamic derivatives at high  $\alpha$  (near stall angle) it is certainly necessary to get more insight into the characteristics of the nonstationary pressure distributions of the aerodynamic response to harmonic oscillations.

For that reason we have to look at the unsteady overall lift- or pitching moment functions as they are given as a function of amplitude and reduced frequency of the oscillation (qualitative examples of the MOD test-rig see Fig. 6.1 to Fig. 6.4 where the prescribed motion and the aerodynamic response are shown over one period). Such figures reveal the actual time history and especially the time lag or phase shifting between the prescribed motion and the aerodynamic flow properties which are induced. These figures are taken from dynamic tests of a fighter-aircraft model (pitching mode) which were conducted with the MOD-dynamic balance in the Dornier wind tunnel. Figure 6.1 shows the development of the Z-force over one period as a function of the reduced frequency  $\omega^*$  (variation of  $\omega^*$  is  $0.1/0.18/0.3$ ). Interesting to note is the shift of the point of  $Z = 0$  to smaller times  $t$  with increasing  $\omega^*$ .

The same effect is shown for the aerodynamic pitching moment  $M$  in Fig. 6.2. The test condition was an oscillation amplitude of  $A = \pm 2.5$  degs in both cases at an initial angle-of-attack of  $\alpha_0 = 24$  degs which is just before stall conditions of the configuration studied. Fig. 6.3 shows pitching mode results of the same configuration at  $\alpha_0 = 24$  degs but with  $\omega^* = 0.05$  and the amplitude  $A = \pm 5.2$  degs. At this case the variation with  $\alpha$  certainly goes beyond stall conditions at its variation within the range  $18.8 \text{ deg} \leq \alpha \leq 29.2 \text{ deg}$  as it is known from static examination of this fighter aircraft configuration.

The pitching mode with this great amplitude of  $\Delta\alpha = \pm 5.2$  degs show a systematic nonlinearity of the Z-force and pitching moment curves of one period. This is characterized by the deviation of the measured curves from the first-order Fourier series expansion which is drawn in the figures also. In addition, the phase shifting is even more pronounced with the big pitching amplitude than it is with the smaller ones.

Figure 6.3 in addition shows the clear effect that the induced Z-force is much smaller at the upward phase of the pitch oscillation than it is on the downward phase of the movement.

For comparison Fig. 6.4 shows the case when the pitching oscillation is conducted at zero angle-of-attack  $\alpha_0$ . Then the shifting in phase of the measured results nearly vanishes and the scattering of the measured values is considerably decreased. But this effect could also be due to the smaller amplitude of  $A = \pm 1.42$  deg in the case of Fig. 6.4. The study of these effects is of special interest for delta-winged fighter aircraft configurations as it is also shown in [35].

A new approach for improvements of the evaluation method of forced oscillation type test rigs at high angles-of-attack could make use of the nonlinear  $\alpha^2$ -terms of the lift-curve versus angle-of-attack and moreover of higher order dynamic derivativa terms especially derivatives with respect to  $q$  and  $\dot{q}$ . These terms have to be introduced within the system according to the full Taylor series expansion of section 2. This implies that within the series of equations (4.1) and (4.2) also higher order terms are introduced like  $\sin 2 \omega t$ - and  $\cos 2 \omega t$ -terms. Such a procedure of course leads to an extension of the set of algebraic equations which has to be solved with respect to the unknown derivatives (= algebraic coefficients of the system). By this way, the principle problem with dynamic derivatives is highlighted which is the problem to split up a well known overall function into different terms according to perturbation theory like the concept of aerodynamic coefficients.

## 7. CONCLUSION

From the material outlined in this paper it follows that obviously various different methods are in use for the prediction of dynamic derivatives of missiles and fighter aircrafts. At small angles-of-attack the theoretical methods are well established as also is true for the experimental procedures. Difficulties and questions are still existing at the nonlinear angle-of-attack range and especially in the case of near or past stall conditions which may occur in practice. In recent years this field has become of

more practical interest because of the development of higher sophisticated guidance and control mechanisms which allow to fly at such flow conditions with short duration periods.

The theoretical attempts for such research work shall be continued where for complete configurations with arbitrary wing-body-tail combinations the semiempirical methods certainly will remain of importance for a while compared to other higher sophisticated methods (unsteady Euler solvers and time-dependent Navier-Stokes equations). In addition the results of this paper show that research emphasis should also be placed to the evaluation methods of dynamic test rigs at the high angle-of-attack range.

#### 8. REFERENCES

- [1] J. Nielsen  
Missile Aerodynamics, Mc Graw-Hill Book Comp., New York, 1960, pp. 397-401 and pp. 409-416
- [2] M. Tobak  
The use of the indicial function concept in the analysis of unsteady motions of wings and wing-tail combinations, NACA report 1188, NASA Ames, Moffet Field, Ca, USA
- [3] M. Tobak, L.B. Schiff  
Aerodynamic Mathematical Modeling - Basic Concepts, 1981, AGARD-LS-114, Lect. no. 1, VKI Brussels, Belgium and NASA Ames, Moffet Field, Ca., USA
- [4] C.P. Schneider  
Analytical determination of dynamic stability parameters, 1981, AGARD-LS-114, Lect. no. 12, VKI Brussels, Belgium and NASA Ames, Moffet Field, Ca., USA
- [5] C.P. Schneider, D. Nikolitsch  
"Längsmomentenderivative von Flügeln bei hohen Anstellwinkeln in Unterschallströmung", 1976, BMV-FBWT 76-26
- [6] J.W.G. van Nunen, R. Roos, J.J. Meijer  
Investigation of the unsteady airloads on wing-store configurations in subsonic flow, 1977, NLR MP 77025 U, Amsterdam
- [7] D.E. Hoak, R.D. Finck  
DATCOM USAF Stability and Control Handbook, Wright-Patterson Air Force, Ohio, 1979, sec. 7.1-7.4
- [8] F. Burhan  
"Theoretische Bestimmung instationärer flugmechanischer Derivativa von Deltaflügeln mit kleinem Seitenverhältnis", 1964, Bericht 64/43 des Instituts für Aerodynamik der DLR Braunschweig
- [9] H.C. Garner  
"Multhopp's Subsonic Lifting-Surface Theory of Wings in Slow Pitching Oscillations", 1952, R&M No. 2885
- [10] H. Otto  
"Theoretische Bestimmung instationärer flugmechanischer Derivativa der Nickschwingung von Pfeil- und Deltaflügeln", Braunschweig, 1967, DLR-Forschungsbericht 67 - 26
- [11] K. Gersten  
"Nichtlineare Tragflächentheorie insbesondere für Tragflügel mit kleinem Seitenverhältnis", Ing.-Archiv, Bd. 30, 1961, S. 431 - 452
- [12] Bird, J.D.  
Some Theoretical Low-Speed Span-Loading Characteristics of Swept Wings in Roll and Sideslip 1950, NACA TR 969
- [13] De Young, J.  
Theoretical Antisymmetric Span Loading for Wings of Arbitrary Plan Form at Subsonic Speeds 1951, NACA TR 1056
- [14] Anon.:  
Royal Aeronautical Society Data Sheets-Aerodynamics, Vol. III (Aircraft S.06.03.01), 1957
- [15] Harmon, S.M. und Jeffreys, I.  
Theoretical Lift and Damping in Roll of Thin Wings with Arbitrary Sweep and Taper at Supersonic Speeds. Subsonic Leading and Trailing Edges, 1950, NACA TN 2114
- [16] Malvestuto, F.S. Jr., Margolis, K. und Ribner, H.S.  
Theoretical Lift and Damping in Roll at Supersonic Speeds of Thin Sweptback Wings of Arbitrary Taper and Sweep at Supersonic Speeds. Subsonic Leading Edges and Supersonic Trailing Edges, 1950, NACA TR 970
- [17] L.H. Jorgensen  
"Prediction of Static Aerodynamic Characteristics for Space-Shuttle-Like, and other Bodies at Angles of Attack from 0° to 180°", 1973, NASA-TN-D6996
- [18] Orlik-Rückemann, K.J.  
Review of Techniques for Determination of Dynamic Stability Parameters in Wind Tunnels, 1981 AGARD-LS 114, p. 3.1 - 3.28



- [19] Hanff, E.S.  
Direct Forced-Oscillation Techniques for the Determination of Stability Derivatives in Wind-Tunnels, 1981, AGARD-LS 114, p. 4.1 - 4.23
- [20] E. Schmidt  
"Über die Erprobung der AVA-Derivatивawaage mit einem Alpha Jet-Modell im Göttinger 3m-Windkanal", 1978, BMFT-FB W78-07
- [21] E. Schmidt  
Introductory remarks on a new high-load oscillatory derivative balance for the DFVLR transonic wind tunnel 1981, AGARD-LS-114, comment to Lect. no. 4, VKI Brussels, Belgium
- [22] S.E. Gudmundson, L. Torngren  
"Supersonic and Transonic Wind Tunnel Tests on a Slender Ogive-Cylinder Body Single and in Combination with Cruciform Wings and Tails of Different Sizes", 1971, FFA-Report AV-772
- [23] H. Fuchs, E. Schmidt und F.-J. Niezgodka  
Experimental and Theoretical Prediction of Dynamic Derivatives of Missiles, AGARD CP-336, 1982, p. 25-1 to 25-13
- [24] Fuchs, H.  
Dynamische Derivativa von Flugkörpern (Phase II) Auswertung der Windkanalmessungen und Vergleich mit theoretischen Ergebnissen, 1981, Dornier-Bericht 81BF/158
- [25] F.J. Niezgodka, H. Emunds  
"Nickdämpfungsmessungen an mehreren Flugkörperkonfigurationen" Köln, 1980, DFVLR-Bericht Nr. IB 351-79/K1
- [26] X. Hafer  
"Wind Tunnel Testing of Dynamic Derivatives in W. Germany"  
  
J. v.d. Decken, E. Schmidt, B. Schulze  
"On the Test Procedures of the Derivative Balances Used in W. Germany", AGARD CP-235, 1978, p. 5-1 to 6-17
- [27] O. Determann  
"Ermittlung von dynamischen Derivativen der Längs- und Seitenbewegung mit der mobilen oszillierenden Derivatивawaage und systematische Untersuchungen zum Einfluß einiger Parameter auf die Ergebnisse", Darmstadt, 1978, DGLR-paper 78-115
- [28] H. Fuchs  
"Dynamische Derivativa von Flugkörpern (Phase I), Auswertung der Windkanalmessungen und Vergleich mit theoretischen Ergebnissen", Friedrichshafen, 1979, Dornier-Bericht Nr. Do 79/18
- [29] D. Christ  
"Windkanalmessungen mit der Mehrfreiheitsgrad-Derivatивawaage (MFD) an einem Flugkörpermodell, Dynamische Derivativa der Längsbewegung", Braunschweig, 1979, DFVLR-Bericht IB 157-79C01
- [30] D. Jacob  
"Untersuchungen zur Flugkörperwirbelinterferenz (Phase I), Zusammenfassung und Auswertung der Ergebnisse", Friedrichshafen, 1978, Dornier-Bericht Do 78/198
- [31] St. Hitzel, J. Muylaert  
"Untersuchungen zur Flugkörper-Wirbelinterferenz (Phase II)", Friedrichshafen, 1981, Dornier-Bericht 81 BF/10 B
- [32] K.J. Orlik-Rückemann, E.S. Hanff  
"Dynamic Stability Parameters at High Angles of Attack", 1980, ICAS-80-7.1
- [33] G.N. Malcom  
"Impact of High-Alpha Aerodynamics on Dynamic Stability Parameters of Aircraft and Missiles", 1981, AGARD-LS-114, Lect. no. 2
- [34] E. Schmidt, H. Fuchs  
Rolldämpfungsmessungen an zwei Flugkörper-Konfigurationen im Transkanal der DFVLR-AVA Göttingen, DGLR-Jahrestagung 1985, Vortrag Nr. 85-90, Bonn
- [35] S. Ehekircher, H. Fuchs, H. Muylaert  
"Dynamische Derivativa zukünftiger Kampfflugzeuge", Friedrichshafen, 1981, Dornier-Bericht Nr. BM 20-008/82
- [36] Munk, M.M.  
The aerodynamic forces on airship hulls. NACA Rep. 184, (1923)
- [37] Lamb, H.  
Hydrodynamics. 6th edition, Cambridge University Press, London, New York, (1975) (First edition, 1932)
- [38] Landweber, L.  
On a generalization of Taylor's virtual mass relation for Rankine bodies. Quarterly of Appl. Mathematics 14, pp. 51-56 (1956)

- [39] Hess, J.L.  
Extension of the Douglas-Neumann program for axisymmetric bodies to include calculation of potentials, non-uniform cross-flow, added mass, and conductor problems. Douglas-Company Rep. 31765, AD-776639 (1964)
- [40] Wagner, B., Fuchs, H., Hitzel, St.  
Beschleunigungsabhängige Derivative von Unterwasserprojektilen. Dornier-Bericht 82 BF/38, Friedrichshafen, (1982)

9. APPENDIX A

$$L = L(u+\Delta u, v+\Delta v, w+\Delta w, p+\Delta p, q+\Delta q, r+\Delta r) =$$

$$\begin{aligned} &= L(u, v, w, p, q, r) + \frac{\partial L}{\partial u} \Delta u + \frac{\partial L}{\partial v} \Delta v + \frac{\partial L}{\partial w} \Delta w + \frac{\partial L}{\partial p} \Delta p + \frac{\partial L}{\partial q} \Delta q + \frac{\partial L}{\partial r} \Delta r + \\ &\quad + \frac{1}{2} \frac{\partial^2 L}{\partial u^2} \Delta u^2 + \frac{1}{2} \frac{\partial^2 L}{\partial v^2} \Delta v^2 + \frac{1}{2} \frac{\partial^2 L}{\partial w^2} \Delta w^2 + \frac{1}{2} \frac{\partial^2 L}{\partial p^2} \Delta p^2 + \frac{1}{2} \frac{\partial^2 L}{\partial q^2} \Delta q^2 + \frac{1}{2} \frac{\partial^2 L}{\partial r^2} \Delta r^2 + \\ &\quad + \frac{\partial^2 L}{\partial u \partial v} \Delta u \Delta v + \frac{\partial^2 L}{\partial u \partial w} \Delta u \Delta w + \frac{\partial^2 L}{\partial u \partial p} \Delta u \Delta p + \frac{\partial^2 L}{\partial u \partial q} \Delta u \Delta q + \frac{\partial^2 L}{\partial u \partial r} \Delta u \Delta r + \\ &\quad + \frac{\partial^2 L}{\partial v \partial w} \Delta v \Delta w + \frac{\partial^2 L}{\partial v \partial p} \Delta v \Delta p + \frac{\partial^2 L}{\partial v \partial q} \Delta v \Delta q + \frac{\partial^2 L}{\partial v \partial r} \Delta v \Delta r + \\ &\quad + \frac{\partial^2 L}{\partial w \partial p} \Delta w \Delta p + \frac{\partial^2 L}{\partial w \partial q} \Delta w \Delta q + \frac{\partial^2 L}{\partial w \partial r} \Delta w \Delta r + \\ &\quad + \frac{\partial^2 L}{\partial p \partial q} \Delta p \Delta q + \frac{\partial^2 L}{\partial p \partial r} \Delta p \Delta r + \\ &\quad + \frac{\partial^2 L}{\partial r \partial q} \Delta r \Delta q \end{aligned}$$

Equation A.1

Introduction of the additional independent variables  $\dot{u}, \dot{w}, \dot{q}$  leads to

$$L = L(u+\Delta u, w+\Delta w, q+\Delta q, \dot{u}+\Delta \dot{u}, \dot{w}+\Delta \dot{w}, \dot{q}+\Delta \dot{q}) = L(u, w, q, \dot{u}, \dot{w}, \dot{q}) +$$

$$+ \frac{\partial L}{\partial \alpha} \Delta \alpha + \frac{\partial L}{\partial q} \Delta q + \frac{\partial L}{\partial \dot{u}} \Delta \dot{u} + \frac{\partial L}{\partial \dot{w}} \Delta \dot{w} + \frac{\partial L}{\partial \dot{q}} \Delta \dot{q} +$$

$\underbrace{\hspace{10em}}$   
 = virtual mass term (hydrodynamics)

$$+ \frac{1}{2} \frac{\partial^2 L}{\partial \alpha^2} \Delta \alpha^2 + \frac{\partial^2 L}{\partial \alpha \partial q} \Delta \alpha \Delta q + \frac{1}{2} \frac{\partial^2 L}{\partial q^2} \Delta q^2 +$$

$$+ \frac{1}{2} \frac{\partial^2 L}{\partial \dot{u}^2} \Delta \dot{u}^2 + \frac{1}{2} \frac{\partial^2 L}{\partial \dot{w}^2} \Delta \dot{w}^2 + \frac{1}{2} \frac{\partial^2 L}{\partial \dot{q}^2} \Delta \dot{q}^2 +$$

$$\frac{\partial^2 L}{\partial \dot{u} \partial \dot{w}} \Delta \dot{u} \Delta \dot{w} + \frac{\partial^2 L}{\partial \dot{u} \partial \dot{q}} \Delta \dot{u} \Delta \dot{q} + \frac{\partial^2 L}{\partial \dot{w} \partial \dot{q}} \Delta \dot{w} \Delta \dot{q} + \text{higher order terms}$$

neglected terms

Longitudinal terms of the Taylor series

Equation A.2

Lateral terms of the Taylor series:

$$L(v+\Delta v, p+\Delta p, r+\Delta r, \dot{v}+\Delta \dot{v}, \dot{p}+\Delta \dot{p}, \dot{r}+\Delta \dot{r}) =$$

$$\begin{aligned} L(v, p, r, \dot{v}, \dot{p}, \dot{r}) &+ \frac{\partial L}{\partial v} \Delta v + \frac{\partial L}{\partial p} \Delta p + \frac{\partial L}{\partial r} \Delta r + \frac{\partial L}{\partial \dot{v}} \Delta \dot{v} + \frac{\partial L}{\partial \dot{p}} \Delta \dot{p} + \frac{\partial L}{\partial \dot{r}} \Delta \dot{r} + \\ &+ \frac{1}{2} \frac{\partial^2 L}{\partial v^2} \Delta v^2 + \frac{1}{2} \frac{\partial^2 L}{\partial p^2} \Delta p^2 + \frac{1}{2} \frac{\partial^2 L}{\partial r^2} \Delta r^2 + \frac{1}{2} \frac{\partial^2 L}{\partial \dot{v}^2} \Delta \dot{v}^2 + \frac{1}{2} \frac{\partial^2 L}{\partial \dot{p}^2} \Delta \dot{p}^2 + \frac{1}{2} \frac{\partial^2 L}{\partial \dot{r}^2} \Delta \dot{r}^2 \\ &+ \frac{\partial^2 L}{\partial v \partial p} \Delta v \Delta p + \frac{\partial^2 L}{\partial v \partial r} \Delta v \Delta r + \frac{\partial^2 L}{\partial v \partial \dot{v}} \Delta v \Delta \dot{v} + \frac{\partial^2 L}{\partial v \partial \dot{p}} \Delta v \Delta \dot{p} + \frac{\partial^2 L}{\partial v \partial \dot{r}} \Delta v \Delta \dot{r} + \\ &+ \frac{\partial^2 L}{\partial p \partial r} \Delta p \Delta r + \frac{\partial^2 L}{\partial p \partial \dot{v}} \Delta p \Delta \dot{v} + \frac{\partial^2 L}{\partial p \partial \dot{p}} \Delta p \Delta \dot{p} + \frac{\partial^2 L}{\partial p \partial \dot{r}} \Delta p \Delta \dot{r} + \\ &+ \frac{\partial^2 L}{\partial r \partial \dot{v}} \Delta r \Delta \dot{v} + \frac{\partial^2 L}{\partial r \partial \dot{p}} \Delta r \Delta \dot{p} + \frac{\partial^2 L}{\partial r \partial \dot{r}} \Delta r \Delta \dot{r} + \\ \frac{\partial L}{\partial v} \Delta v &= \frac{\partial L}{\partial \beta} \beta + \frac{\partial^2 L}{\partial v \partial p} \Delta \dot{v} \Delta p + \frac{\partial^2 L}{\partial v \partial r} \Delta \dot{v} \Delta r + \\ \frac{\partial L}{\partial \dot{v}} \Delta \dot{v} &= \frac{\partial L}{\partial \dot{\beta}} \Delta \dot{\beta} + \frac{\partial^2 L}{\partial \dot{v} \partial p} \Delta \dot{v} \Delta p + \frac{\partial^2 L}{\partial \dot{v} \partial r} \Delta \dot{v} \Delta r + \end{aligned}$$

Equation A.3

+ higher order terms

$$\begin{aligned} C_{Zq} &= [K_{W1(B)} + K_{B(W1)}] \times C_{Zq(W1)}^{(1)} + C_{Zq(W1)}^{(n-1)} \\ &+ [K_{W2(B)} + K_{B(W2)}] \times C_{Zq(W2)}^{(1)} + C_{Zq(W2)}^{(n-1)} \\ &+ [K_{WC(B)} + K_{B(WC)}] \times C_{Zq(WC)}^{(1)} + C_{Zq(WC)}^{(n-1)} \\ &+ C_{Zq(B)} \\ &+ (\bar{x}_{WC}/D) \times (C_{Z\alpha}^{WC(W1)}) \end{aligned}$$

$$\begin{aligned} C_{mq} &= [K_{W1(B)} + K_{B(W1)}] \times C_{mq(W1)}^{(1)} + C_{mq(W1)}^{(n-1)} \\ &+ [K_{W2(B)} + K_{B(W2)}] \times C_{mq(W2)}^{(1)} + C_{mq(W2)}^{(n-1)} \\ &+ [K_{WC(B)} + K_{B(WC)}] \times C_{mq(WC)}^{(1)} + C_{mq(WC)}^{(n-1)} \\ &+ C_{mq(B)} \\ &+ (\bar{x}_{WC}/D)^2 \times (C_{Z\alpha}^{WC(W1)}) \end{aligned}$$

NOTE: The terms of  $(C_{Z\alpha}^{WC(W1)})$  are omitted when  $\frac{s_{W1}}{s_{WC}} > 1.5$

DATCOM SECTION 4.5.1.1

The derivatives due to pitch-rate  $q$  contributions of the total missile configuration

Equation A.4

$$\begin{aligned}
 C_{Z_a} &= [K_{W1(B)} + K_{B(W1)}] \times C_{Z_a(W1)}^{(1)} + C_{Z_a(W1)}^{(2)} \\
 &+ [K_{W2(B)} + K_{B(W2)}] \times C_{Z_a(W2)}^{(1)} + C_{Z_a(W2)}^{(2)} \\
 &+ C_{Z_a(B)} \\
 &+ (1/D) \times (\partial e / \partial \alpha) \times \{ [K_{WC(B)} + K_{B(WC)}] \times C_{Z_a(WC)}^{(1)} + C_{Z_a(WC)}^{(2)} + [C_{Z_a}^{(1)}]_{WC(W1)} \}
 \end{aligned}$$

$$\begin{aligned}
 C_{M_a} &= [K_{W1(B)} + K_{B(W1)}] \times C_{M_a(W1)}^{(1)} + C_{M_a(W1)}^{(2)} \\
 &+ [K_{W2(B)} + K_{B(W2)}] \times C_{M_a(W2)}^{(1)} + C_{M_a(W2)}^{(2)} \\
 &+ C_{M_a(B)} \\
 &+ (\bar{x}_{WC} / D^2) \times (\partial e / \partial \alpha) \times \{ [K_{WC(B)} + K_{B(WC)}] \times C_{M_a(WC)}^{(1)} + C_{M_a(WC)}^{(2)} + [C_{M_a}^{(1)}]_{WC(W1)} \}
 \end{aligned}$$

NOTE: The terms of  $[C_{Z_a}^{(1)}]_{WC(W1)}$  are omitted when  $\frac{W1}{WC} > 1.5$

The derivatives due to the rate-of-change of the angle-of-attack  $\dot{\alpha}$

Contributions of the total missile configuration

Equation A.5

SUBSONIC + TRANSONIC

$$C_{Z_q}^{(1)}(n, \alpha) = [(1/4) \times (\bar{c}/D) + \bar{x}(n, \alpha)/D] \times [C_{Z_\alpha}^{(1)}(n, \alpha) - C_X(n, \alpha)]$$

$$C_{Z_q}^{(n.1)}(n, \alpha) = [(1/4) \times (\bar{c}/D) + \bar{x}(n, \alpha)/D] \times C_{Z_\alpha}^{(n.1)}(n, \alpha)$$

SUBPERSONIC

$$C_{Z_q}^{(1)}(n, \alpha) = C_{Z_q}^{(1)}(n, \alpha) + (\bar{x}/D) \times [C_{Z_\alpha}^{(1)}(n, \alpha) - C_X(n, \alpha)]$$

1.  $\beta \cot \Lambda_{LE} < 0$  (subsonic leading edge)

$$\lambda = 0:$$

$$C_{Z_q}^{(1)}(n, \alpha) = f(\beta \cot \Lambda_{LE}, M) + [(d_r - x_{a.c.})/D] \times [C_{Z_\alpha}^{(1)}(n, \alpha) - C_X(n, \alpha)]$$

DATCOM 7.1.1.1-7  
7.1.1.1-8

$$\lambda = 0:$$

$$C_{Z_q}^{(1)}(n, \alpha) = C_{Z_q}^{(1)}(n, \alpha) - [x_{a.c.}(n, \alpha)/D] \times [C_{Z_\alpha}^{(1)}(n, \alpha) - C_X(n, \alpha)]$$

$$C_{Z_q}^{(1)} = -0.5 \frac{\bar{c}}{D} \frac{S}{S_R} C_{L_q}^{(1)}$$

DATCOM 7.1.1.1-9a  
7.1.1.1-9b) f (AR-B,  $\lambda$ )  
7.1.1.1-9c

2.  $\beta \cot \Lambda_{LE} > 0$  supersonic leading edge

$$C_{Z_q}^{(1)} = -0.5 \frac{\bar{c}}{D} \frac{S}{S_R} C_{L_q}^{(1)}$$

DATCOM 7.1.1.1-10a  
7.1.1.1-10k

WING-CONTRIBUTION TO  $C_{Z_q}$

Equation A.6

SUPERSONIC (CONTINUED):

$$C_{Z_q}^{(n.1)}(n, \alpha) = C_{Z_q}^{(n.1)}(n, \alpha) + (\bar{x}/D) \times C_{Z_\alpha}^{(n.1)}(n, \alpha)$$

1.  $\beta \cot \Lambda_{LE} < 0$  subsonic leading edge

$$\lambda = 0:$$

$$C_{Z_q}^{(n.1)}(n, \alpha) = [(d_r - x_{a.c.})/D] \times C_{Z_\alpha}^{(n.1)}(n, \alpha)$$

$$\lambda = 0:$$

$$C_{Z_q}^{(n.1)}(n, \alpha) = -[x_{a.c.}(n, \alpha)/D] \times C_{Z_\alpha}^{(n.1)}(n, \alpha)$$

2.  $\beta \cot \Lambda_{LE} > 0$  supersonic leading edge

$$C_{Z_q}^{(n.1)} = 0$$

Equation A.7

WING-CONTRIBUTION TO  $C_{Z_q}$

**APPENDIX B**

Within the case of incompressible fluid flow that is the field of underwater vehicles (all kinds of submarines or torpedos) one has an important field of application of a nonstationary panel method for the 'added mass'-terms. With submerged underwater vehicles it is well-known from the beginnings of the potential theory [36], [37] that one has to take into account the 'added mass'-terms which are dynamic derivatives from their physical character.

The added mass terms arise from the fact that nearfield neighborhood of the underwater vehicle is accelerated together with the solid body for which an amount of energy is needed which can be interpreted to be equivalent to an 'added mass' or an 'added inertia' of the solid body. With aircraft applications these derivatives are neglectably small because of the smallness of the density of air to the density of the accelerated body.

In a fluid like water these terms may become important. Classical virtual (= added) mass terms are the derivatives with respect to the translational acceleration in or transversal acceleration  $\dot{V}$  (see equ. A.2 of Appendix A). At Dornier a panel-method for the calculation of the most common added mass terms was developed based on [38] and [39].

The underwater configurations which can be treated by this program are shown in Fig. 9.1.

Typical results for an ellipsoid at translational and angular acceleration are shown in Fig. 9.2 and 9.3.

Results of different streamline bodies are given in Fig. 9.4 and Fig. 9.5.

A detailed report of the theory is given in [40].

10. ILLUSTRATIONS

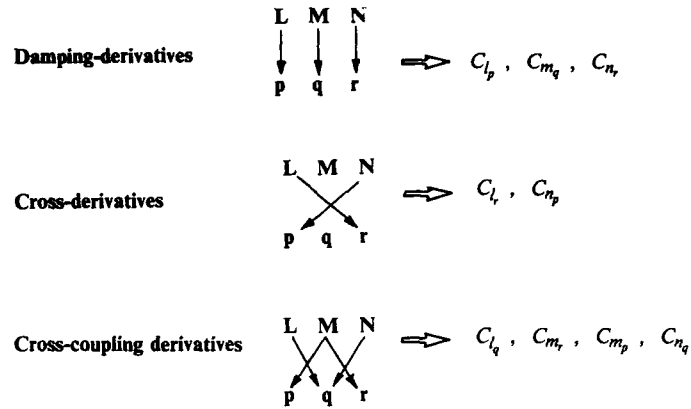
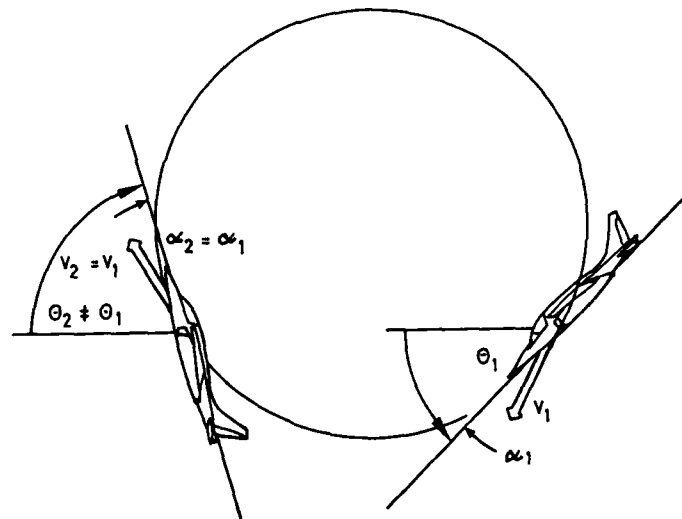


Fig. 2.1: The classification of dynamic derivatives



$\alpha_1 = \alpha_2 = \text{CONST.} \quad \curvearrowright \quad \alpha = \theta$

$V = \text{CONST.}$

CHANGING LONGITUDINAL ATTITUDE

$\curvearrowright$  PITCHING RATE  $q = \frac{d\theta}{dt} = \frac{\theta_2 - \theta_1}{\Delta t}$

Fig. 2.2: Circle flight with constant velocity V



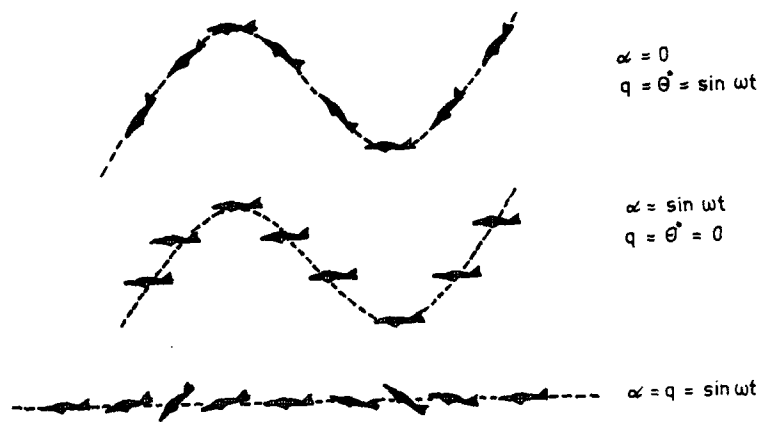


Fig. 2.3: Different flight paths with pitching and  $\alpha$ -motions

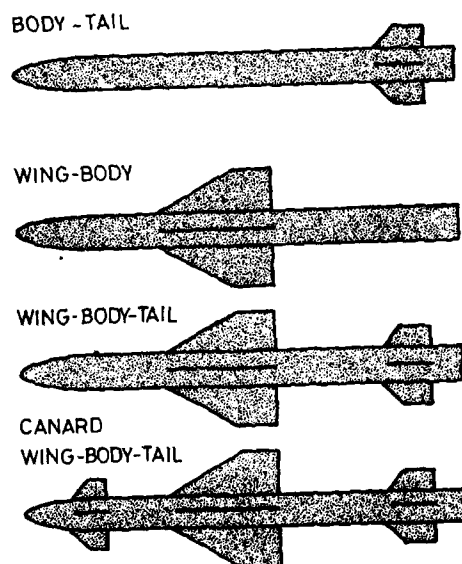


Fig. 3.1: Wing-body combinations applicable to program DYNAM

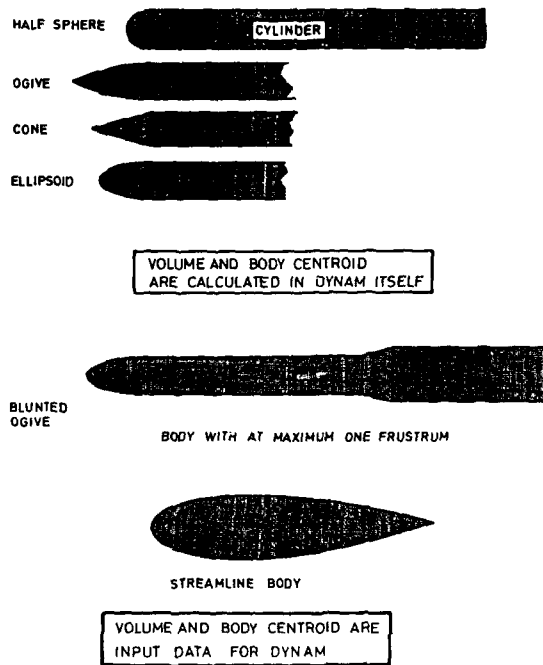


Fig. 3.2: Nose- and body shapes applicable to program DYNAM

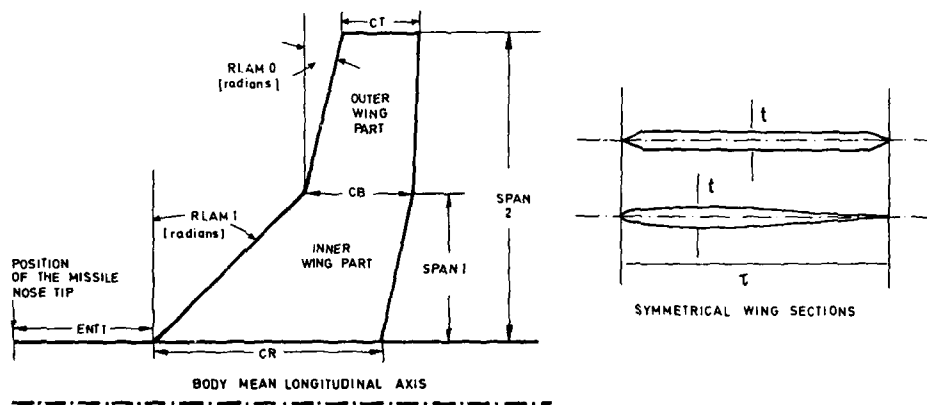



Fig. 3.3: Wing planforms and profiles applicable to program DYNAM

WING SHAPE



|           | F 2  | F 2 exp. | L 2   | L 2 exp. |
|-----------|------|----------|-------|----------|
| $i$       | 6 D  | 5 D      | 3.5 D | 2.5 D    |
| $\lambda$ | 1.0  | 0.857    | 1.11  | 0.857    |
| $\lambda$ | 0.33 | 0.4      | 0.286 | 0.4      |

| DERIVATIVE | WING / TAIL | SLENDER BODY THEORY (NIELSEN) | DATCOM | SLENDER BODY THEORY (BURHAN) | GARNER | GERSTEN SCHNEIDER-NIKOLITSCH |
|------------|-------------|-------------------------------|--------|------------------------------|--------|------------------------------|
| $C_{zq}$   | F 2         | -85.3                         | -33.0  | -104.0                       | -132.0 | -105                         |
|            | L 2         | -26.2                         | -4.7   | -23.0                        | -25.4  | -22                          |
|            | F 2 exp.    | -52.0                         | -21.1  | -53.0                        | —      | —                            |
|            | L 2 exp.    | -6.5                          | -2.4   | -6.6                         | —      | —                            |
| $C_{mq}$   | F 2         | -170.7                        | -51.7  | -183.0                       | -196.7 | -204                         |
|            | L 2         | -41.3                         | -4.1   | -23.8                        | -22.0  | -25                          |
|            | F 2 exp.    | -112.7                        | -33.0  | -83.0                        | —      | —                            |
|            | L 2 exp.    | -7.0                          | -2.1   | -5.2                         | —      | —                            |

Fig. 3.4: Wing-alone contributions according to different theoretical methods

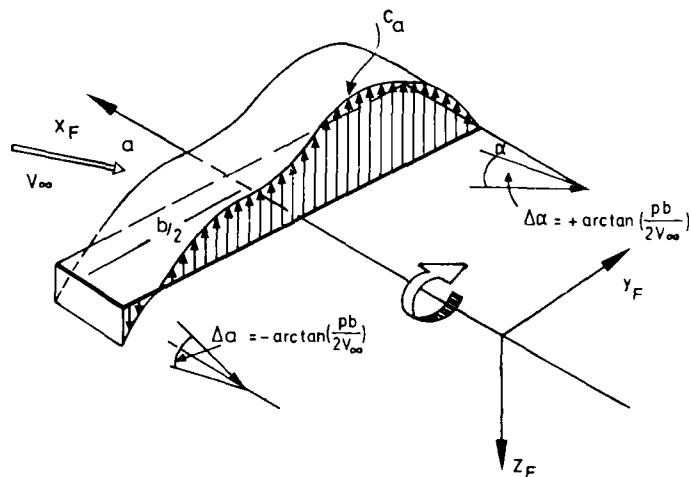


Fig. 3.5: Schematic lift distribution  $c_a$  at a rotating wing

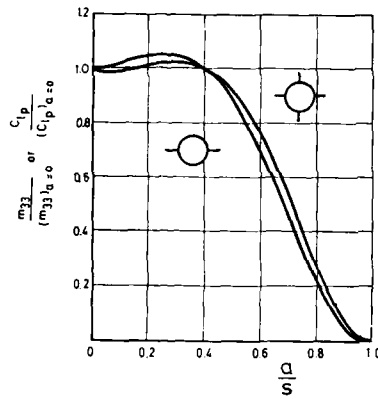
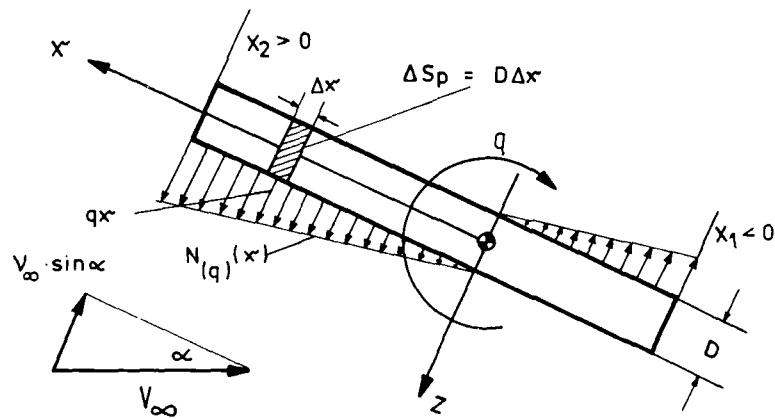


Fig. 3.6: Effect of body radius in roll for fixed span ( acc. to Nielsen /1/ )



$$N = C_{Dc} \frac{S_p}{S} \frac{\rho}{2} V_n^2 S$$

$$V_n = V_\infty \sin \alpha - qx$$

$$\Delta N(x) = C_{Dc} \frac{\Delta S_p}{S} \frac{\rho}{2} (V_\infty^2 \sin^2 \alpha - 2qx V_\infty \sin \alpha + q^2 x^2) S$$

CROSS-FLOW THEORY

Fig. 3.7: Normal force increments induced at a rotating circular cylinder

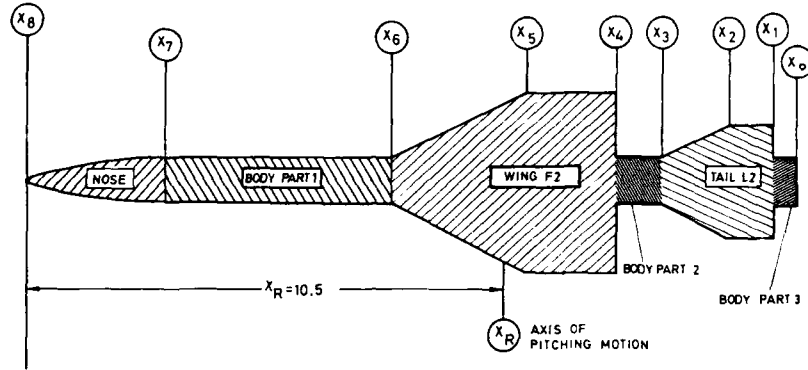


Fig. 3.8: Different missile segments for calculation of cross-flow terms of the derivatives with respect to  $q$

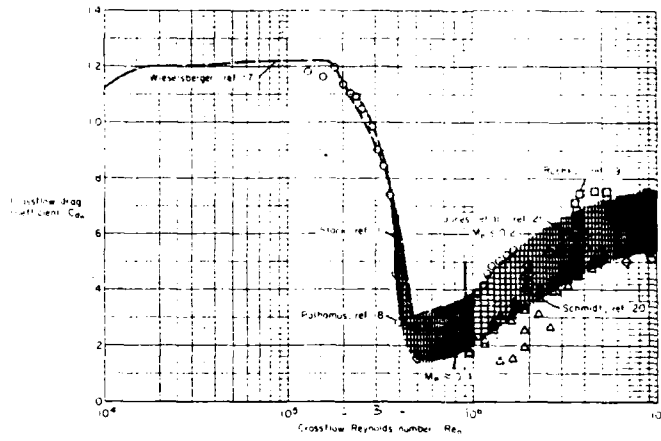


Fig. 3.9: Variation of cross flow Reynolds number for circular cylinders at subcritical crossflow Mach numbers ( $Ma \leq 0.4$ )

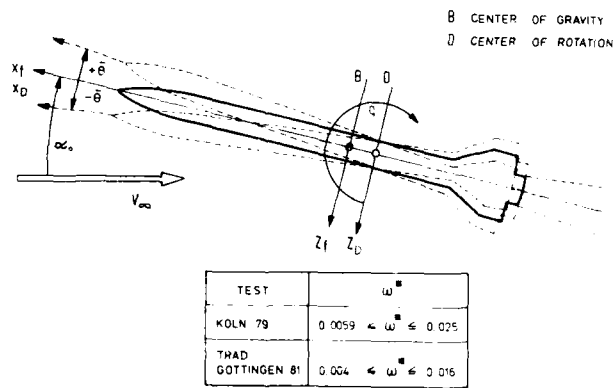


Fig. 4.1: The principle of 1-dof pitching mode

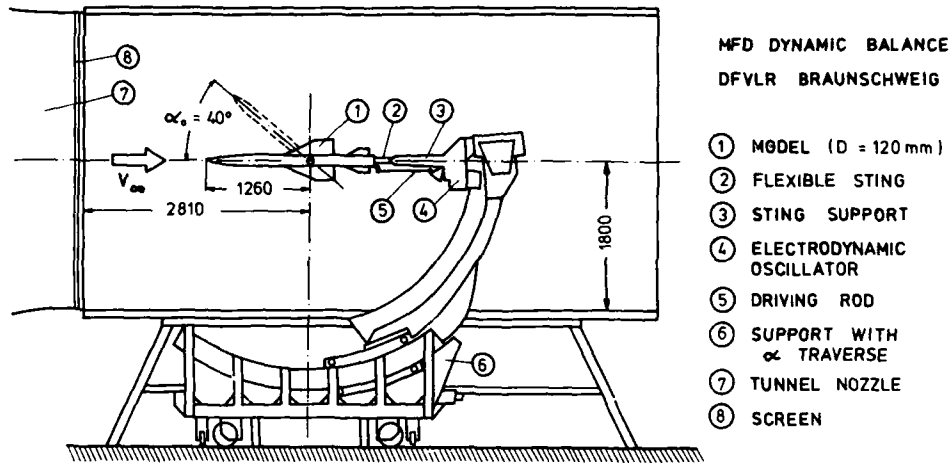


Fig. 4.2: The MFD dynamic test rig of the DFVLR Braunschweig

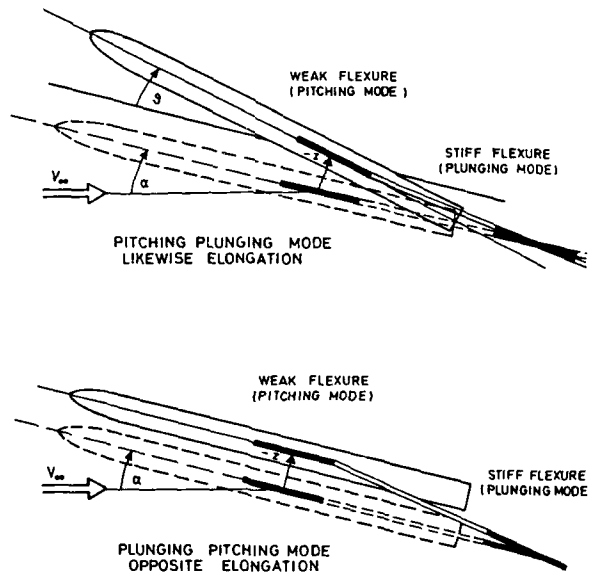


Fig. 4.3: Combined pitching- and plunging excitation of the MFD dynamic test rig ( DFVLR Braunschweig )

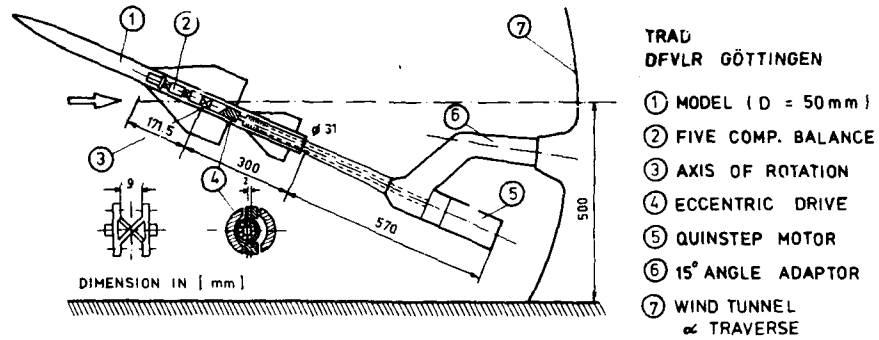


Fig. 4.4: The high-load derivativa balance TRAD of the DFVLR-AVA Göttingen

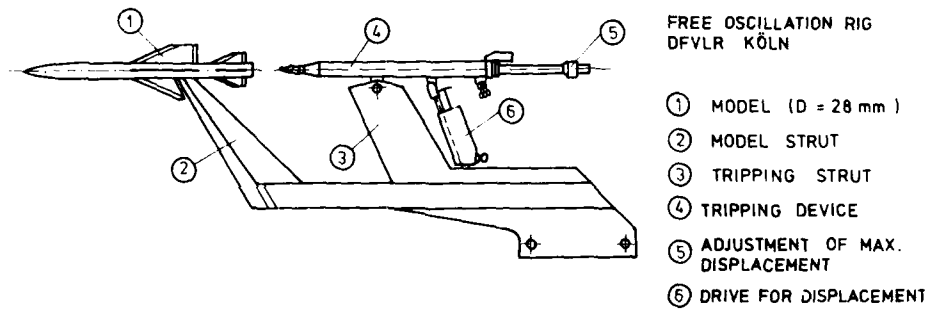


Fig. 4.5: The free oscillation type balance of DFVLR Cologne

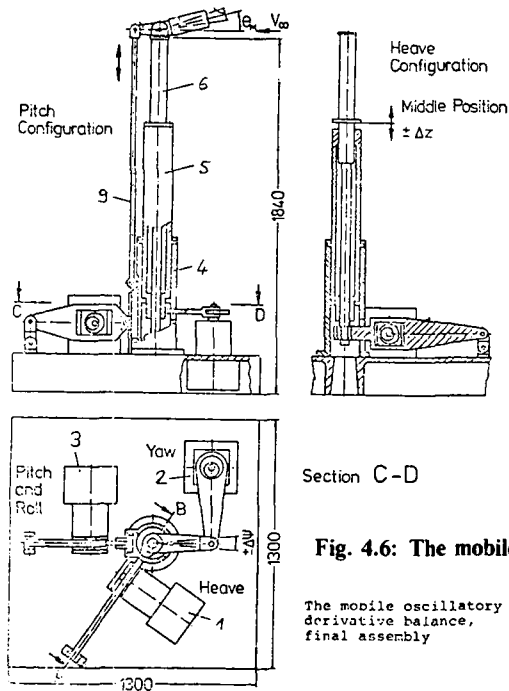
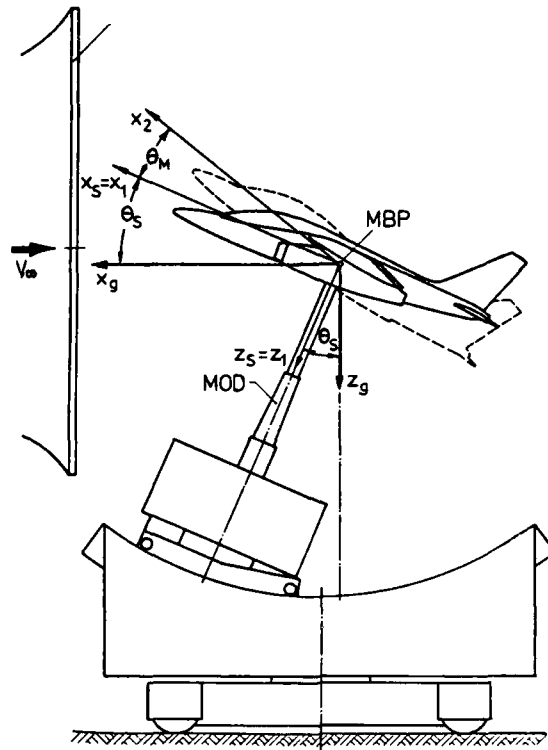


Fig. 4.6: The mobile oscillation derivative balance MOD

The mobile oscillatory derivative balance, final assembly



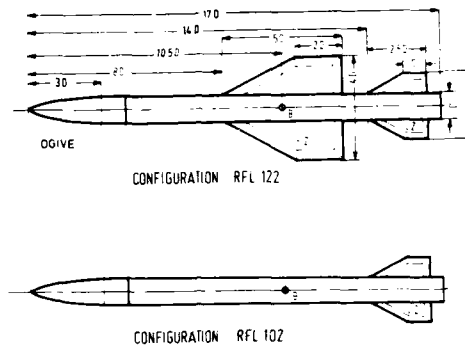


Fig. 5.1: The Dornier standard missile configurations  
Wing-body-tail combination RFL 122  
Body-tail combination RFL 102

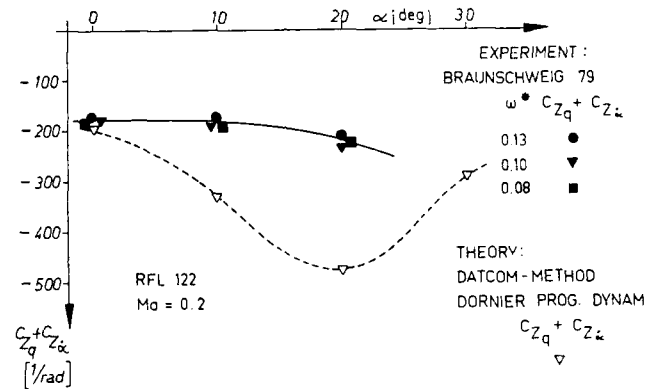


Fig. 5.2: Z-force due to pitching motion measured for the Dornier conf. RFL 122 with the MFD balance at the low-speed tunnel of DFVLR Braunschweig

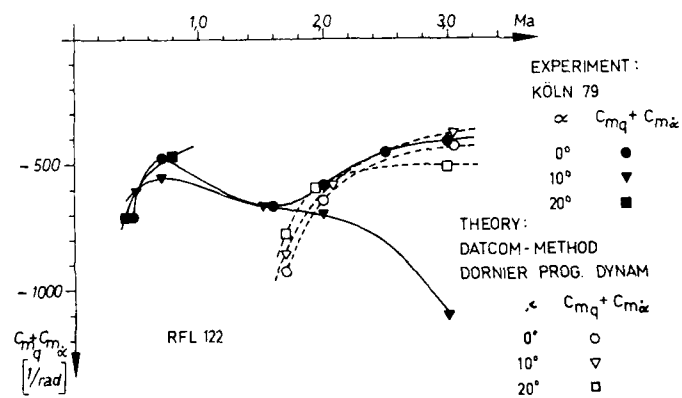


Fig. 5.3: Pitching moment results of the Dornier conf. RFL 122 with free oscillation tests at the supersonic wind tunnel of the DFVLR Cologne

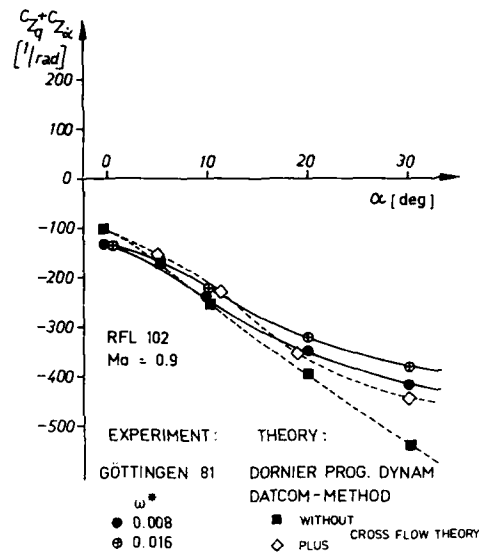


Fig. 5.4: Normal force damping of Dornier conf. RFL102 at Ma=0.9 (TRAD measurement)

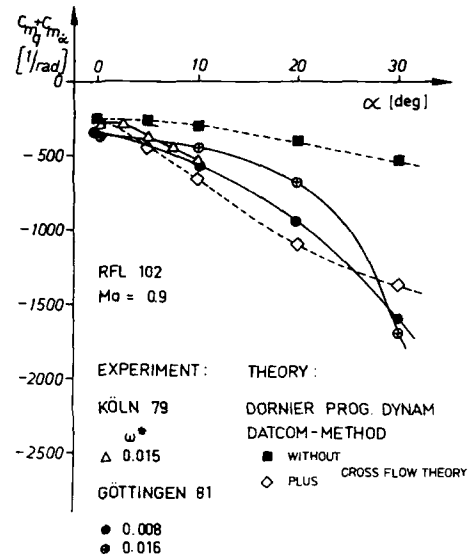


Fig. 5.5: Pitching moment damping of Dornier conf. RFL102 at Ma=0.9 (TRAD measurement)

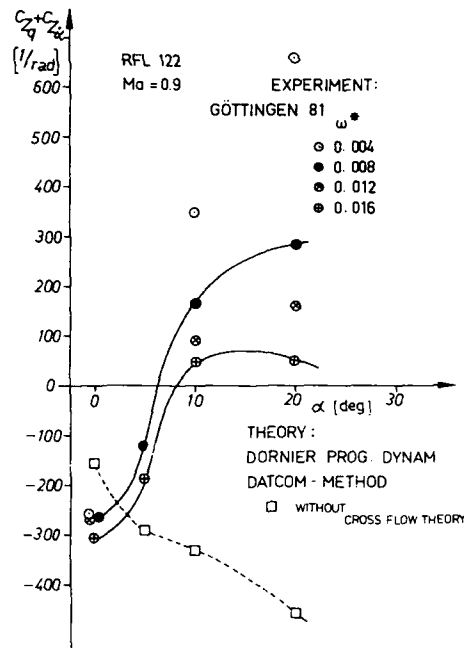


Fig. 5.6: Normal force damping of Dornier conf. RFL122 at Ma=0.9 (TRAD measurement)

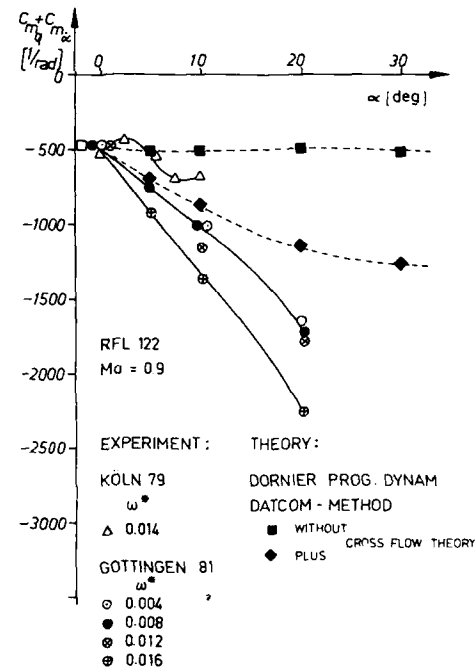


Fig. 5.7: Pitching moment damping of Dornier conf. RFL122 at Ma=0.9 (TRAD measurement)

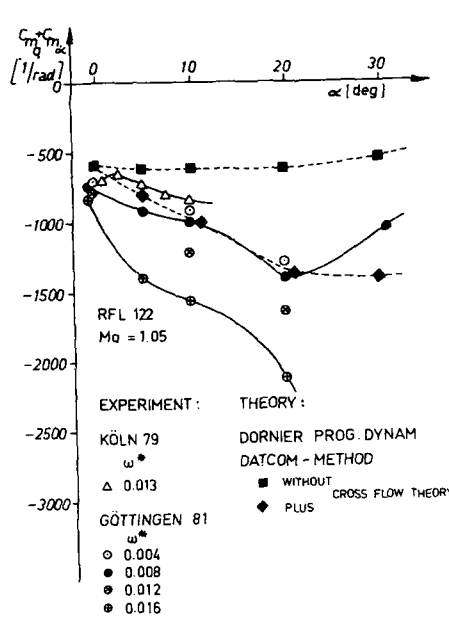


Fig. 5.8: Pitching moment damping of Dornier conf. RFL122 at Ma = 1.05 ( TRAD measurement )

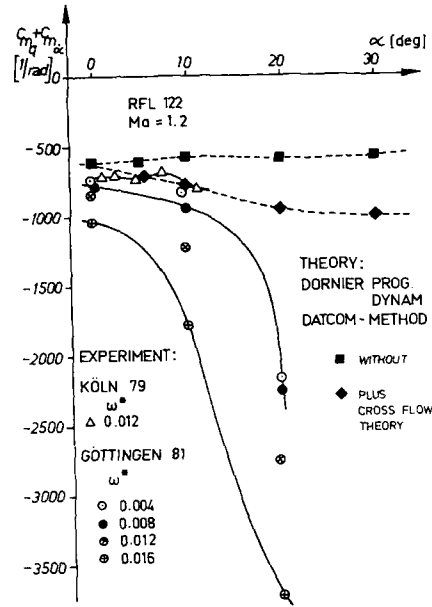


Fig. 5.9: Pitching moment damping of Dornier conf. RFL122 at Ma = 1.2 ( TRAD measurement )

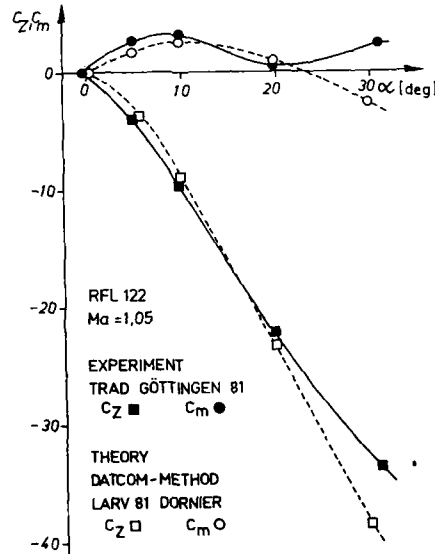


Fig. 5.10: Static aerodynamic coefficients of Dornier conf. RFL122 at Ma = 1.05 ( TRAD measurement )

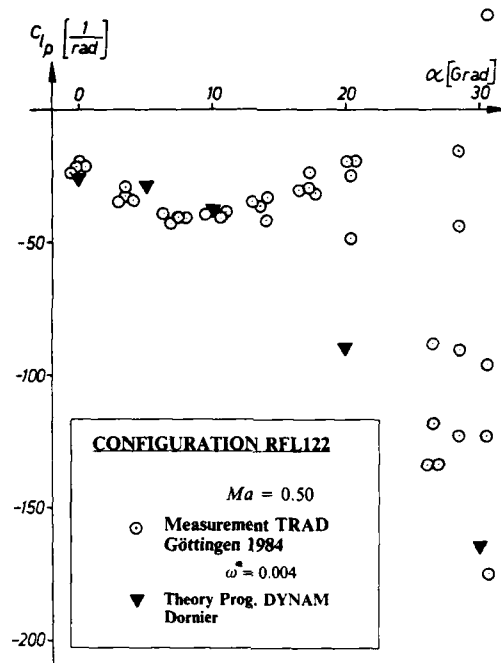


Fig. 5.11: Roll damping coefficient of Dornier conf. RFL122 at  $Ma = 0.50$  and  $\omega^* = 0.004$  (TRAD measurement)

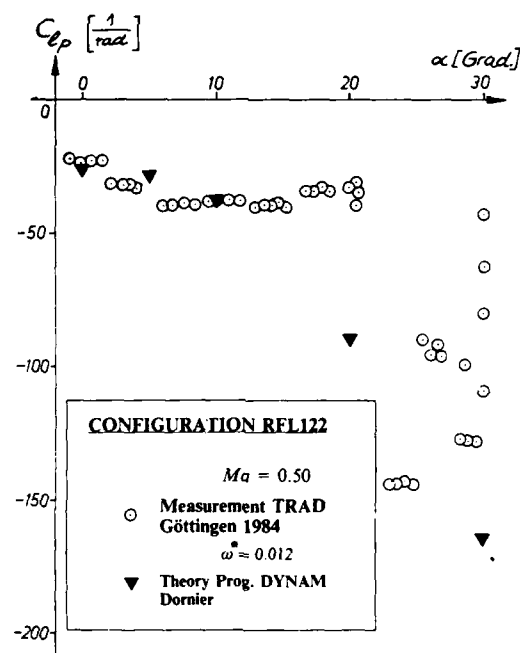
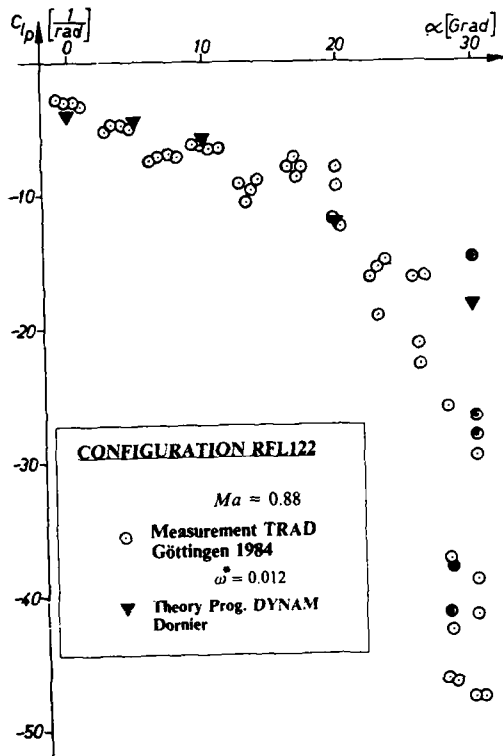
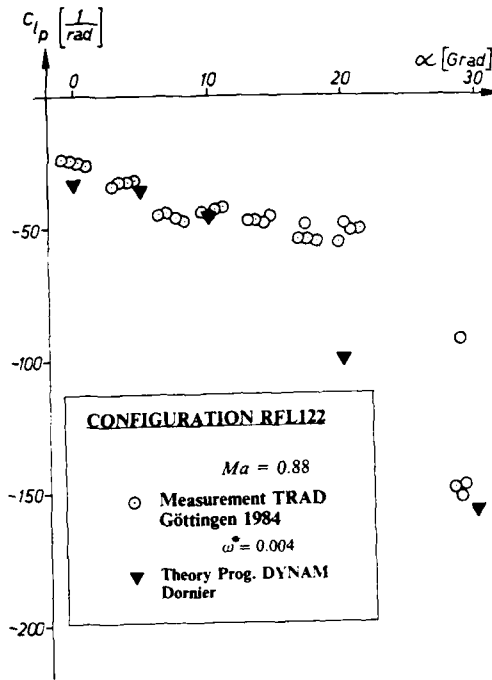


Fig. 5.12: Roll damping coefficient of Dornier conf. RFL122 at  $Ma = 0.50$  and  $\omega^* = 0.012$  (TRAD measurement)

**Fig. 5.13:**  
Roll damping coefficient of Dornier conf. RFL122  
at  $Ma = 0.88$  and  $\omega^* = 0.004$  (TRAD measurement)



**Fig. 5.14:**  
Roll damping coefficient of Dornier conf. RFL122  
at  $Ma = 0.88$  and  $\omega^* = 0.012$  (TRAD measurement)

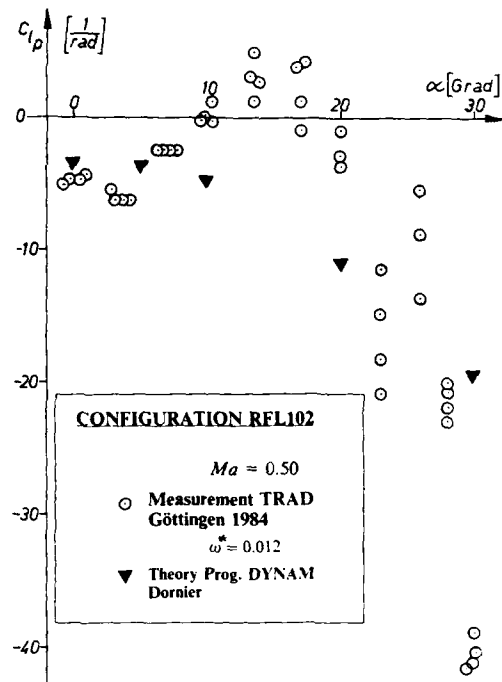


Fig. 5.15: Roll damping coefficient of Dornier conf. RFL102 at  $Ma = 0.50$  and  $\omega^* = 0.012$  (TRAD measurement)

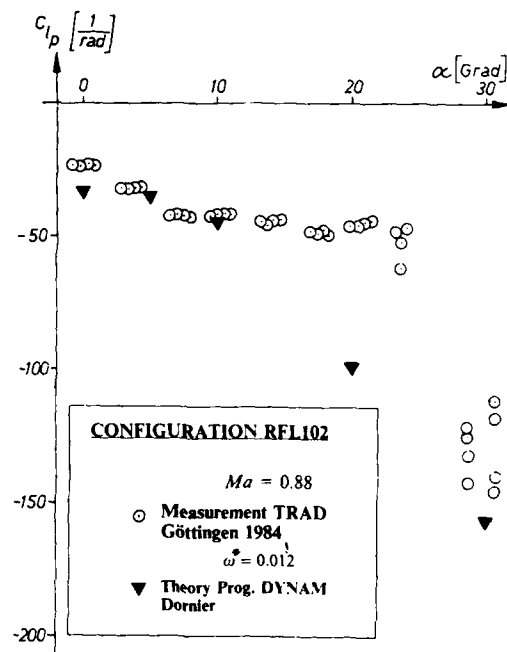


Fig. 5.16: Roll damping coefficient of Dornier conf. RFL102 at  $Ma = 0.88$  and  $\omega^* = 0.012$  (TRAD measurement)

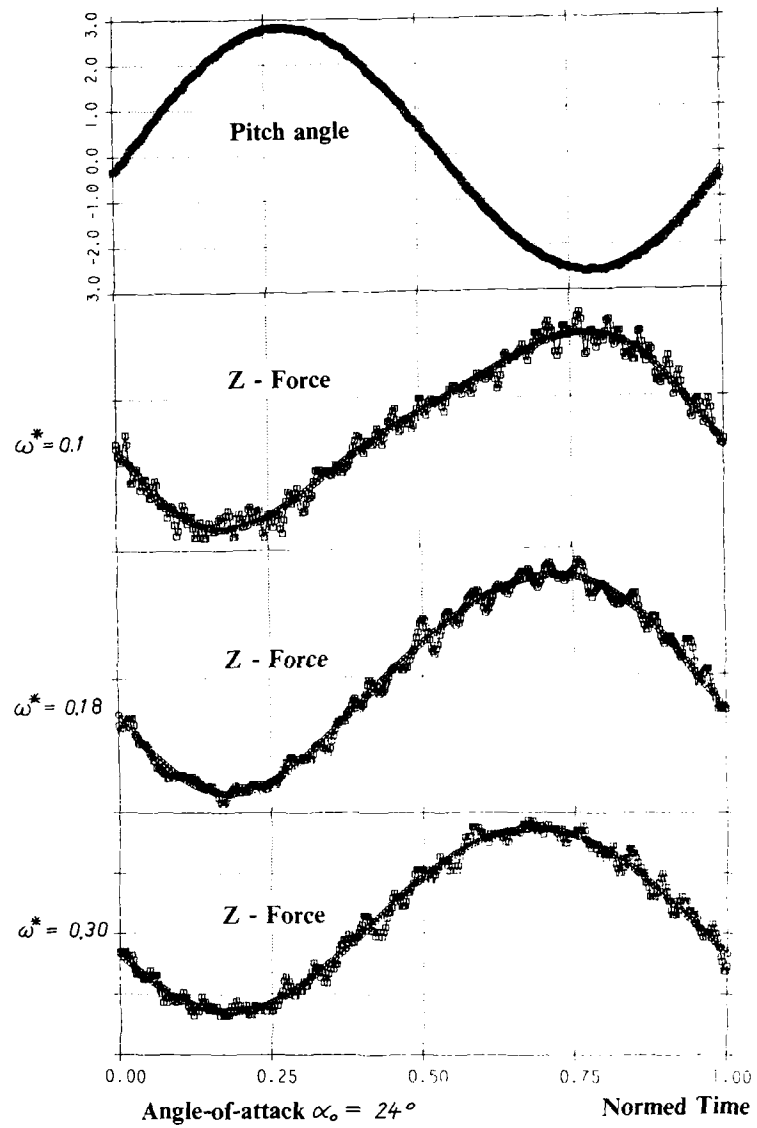


Fig. 6.1: Harmonic Z-force at pitching motion of a fighter aircraft configuration as a function of  $\omega^*$

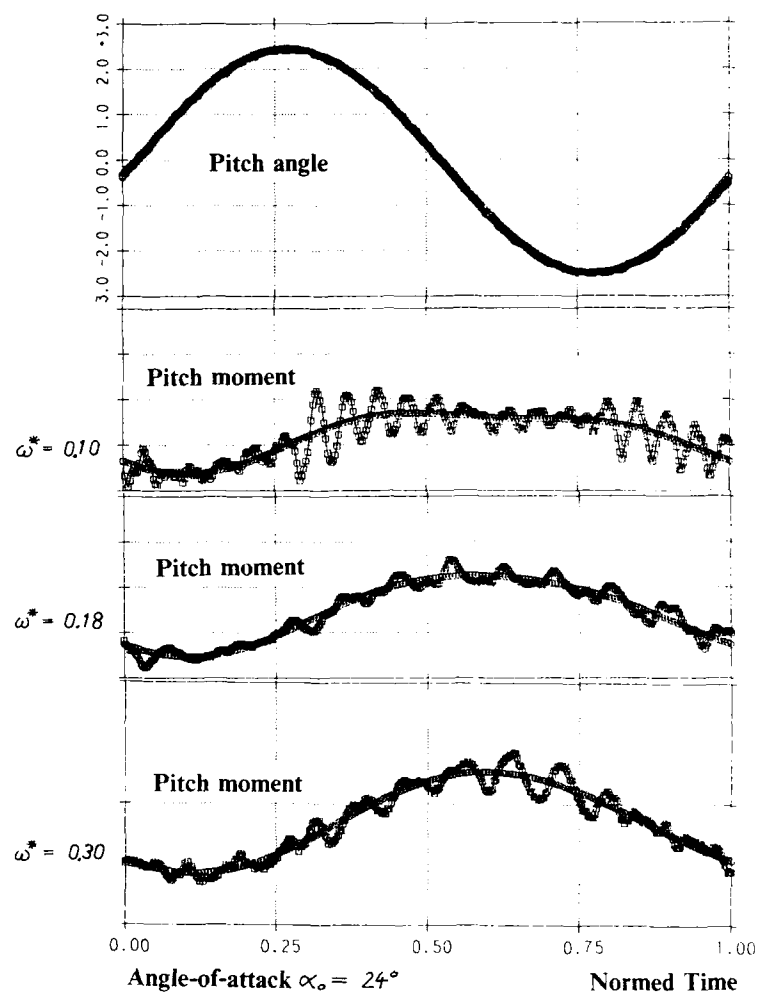


Fig. 6.2: Harmonic longitudinal moment at pitching motion of a fighter aircraft configuration as a function of  $\omega^*$



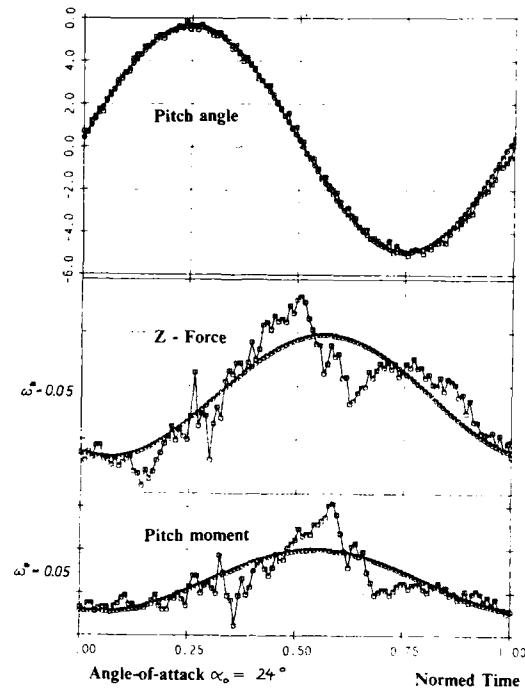


Fig. 6.3: Harmonic Z-force and longitudinal moment at pitching motion of a fighter aircraft configuration as a function of  $\omega^*$

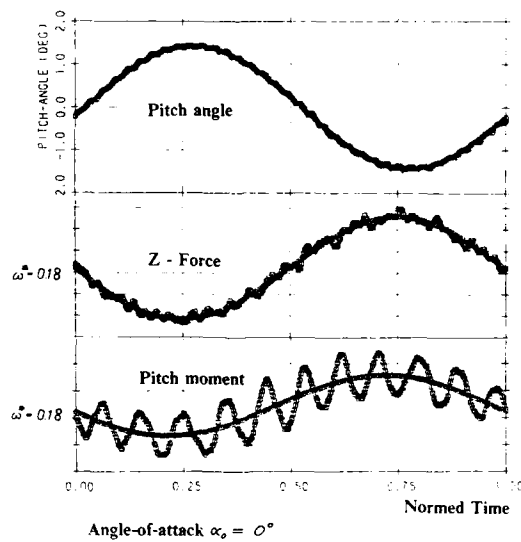


Fig. 6.4: Harmonic Z-force and longitudinal moment at pitching motion of a fighter aircraft configuration at  $\alpha_0 = 0$

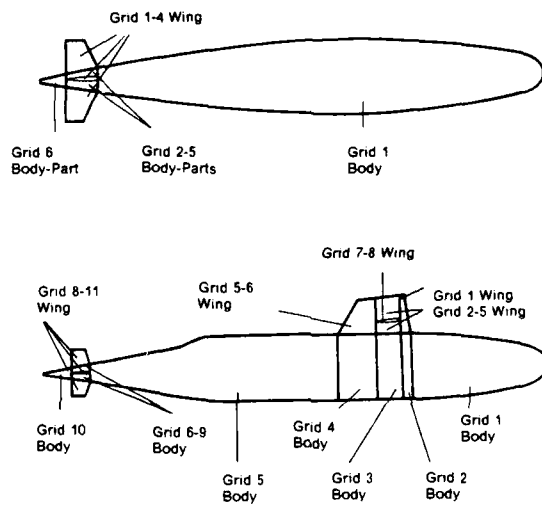


Fig. 9.1: Underwater vehicles to be traected by Prog. ADDMAS

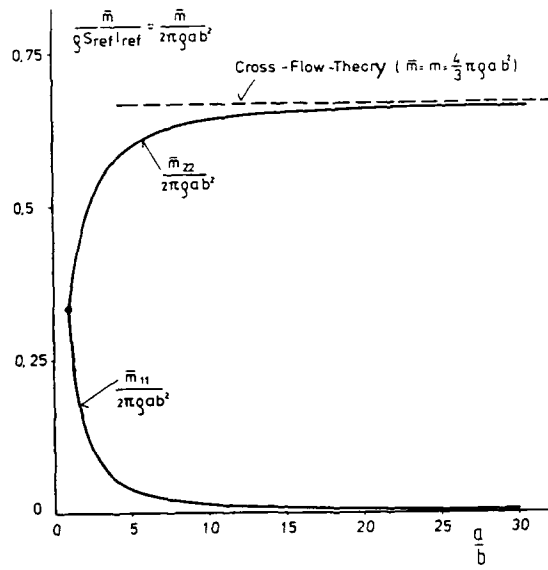


Fig. 9.2: Added mass terms of an ellipsoid

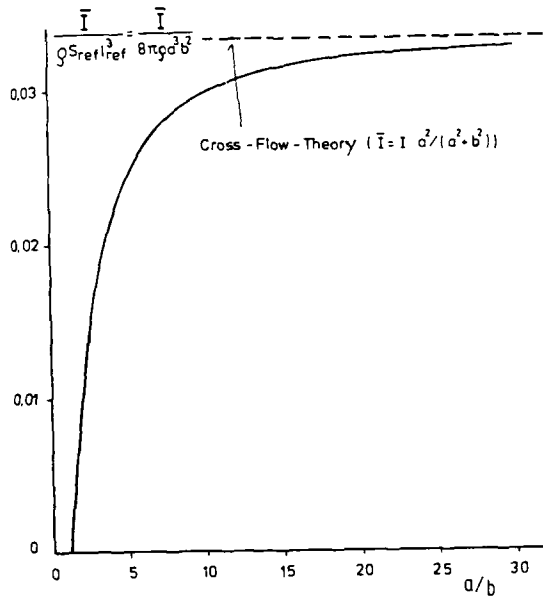


Fig. 9.3: Virtual inertia terms of an ellipsoid

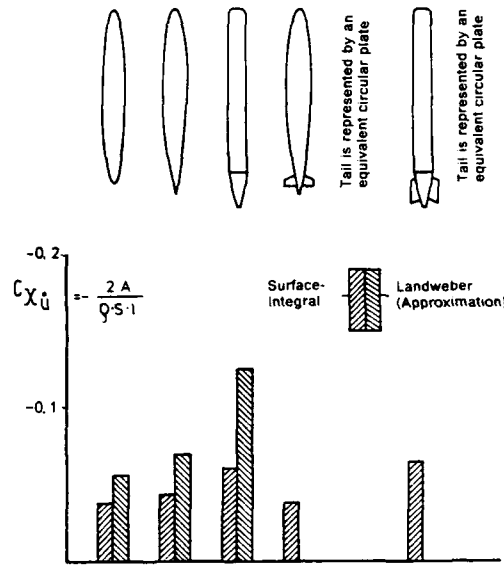


Fig. 9.4: Added mass ( x-onset ) of different configurations program ADDMAS

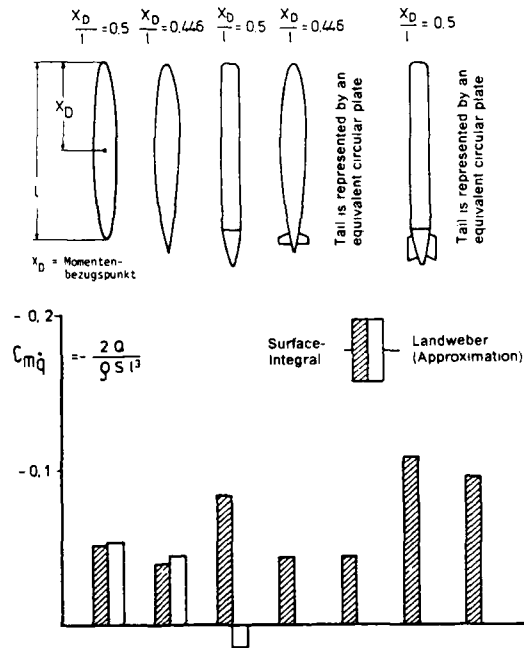


Fig. 9.5: Added mass ( q-onset ) of different configurations program ADDMAS

## AIR INTAKE AERODYNAMICS

by

C. S. Jeil,  
 British Aerospace PLC,  
 Naval and Electronic Systems Division,  
 P.O. Box 5,  
 Filton,  
 Bristol. BS12 7QW  
 ENGLAND

## SUMMARY

The effective operation of airbreathing missiles is strongly dependent on the efficiency of the air intake system and its ability to supply the engine with air of adequate quality at all required flight conditions while minimising any undesirable effects that the intakes may have on the overall aerodynamic characteristics of the missile. This paper describes the role of the intake in the propulsion system of turbojet and ramjet powered missiles and addresses both the internal and external aerodynamic aspects of the induction system. The features of various types of air intake commonly used for subsonic and supersonic operation are discussed. The causes and effects of flow instability and flow non-uniformity at engine entry are considered and the operational relationship between the engine and the intake is shown. Finally three major aspects of intake installation are discussed: namely the influence of the missile body flowfield on internal performance, the forces and moments generated by the internal flow, and the effect of the intakes and their associated fairings on the overall aerodynamic characteristics of the missile.

## 1. INTRODUCTION

The air intake system is an essential component in any air breathing propulsion system. Its purpose is to supply the engine with air from the atmosphere thus providing it with its working fluid. This often involves a change in direction of the airflow in order to turn it into the missile body, and, in general, a reduction in Mach number is required between freestream and engine entry.

From the aerodynamic point of view three aspects are important.

Firstly, to maximise power plant performance, the process of conveying air to the engine should be completed with minimum internal energy losses since the internal efficiency of an air intake is directly reflected by engine performance.

Secondly, the quality of the flow presented to the engine by the air intake must be acceptable in terms of stability and uniformity throughout the flight envelope of the missile. If this is not so, the engine may cease to function correctly, resulting in failure of the missile to complete its mission.

Thirdly, the effect of the air intake system and any associated fairings or nacelles on the overall aerodynamic characteristics of the missile must be acceptable. Drag due to the propulsion system should be minimised and the missile must be controllable and have the response and manoeuvre capability required for the mission.

While the first aspect, that of internal aerodynamic efficiency, is obviously desirable it may need to be compromised in an optimisation of the complete missile system. Factors that may lead to this include complexity, cost, mass and volume limitations, integration with other missile subsystems, and launch platform constraints. The second and third aspects are of course essential, being pre-requisite for the successful operation of the complete missile system.

This paper will discuss the main physical and aerodynamic features of air intake design necessary to fulfil these requirements. Intake design for operation with turbojet and ramjet engines will be considered in the subsonic and supersonic flight regimes as appropriate. Examples are given illustrating how the size of an air intake may be selected for optimum propulsive performance. The response of the intake-engine combination to operational effects, such as changes of missile Mach number, incidence, engine throttle setting and ambient temperature will be shown.

Finally three major aspects of intake installation are discussed: the influence of the missile body flowfield on internal performance, the forces and moments generated by the internal flow, and the effect of the intakes and their associated fairings on the overall aerodynamic characteristics of the missile.

## 2. TYPE OF ENGINE

This paper deals with air intakes for ramjet type engines and turbojet type engines.

Ramjet and Ramrocket (or ducted rocket) propulsion systems, Fig. 1, rely entirely on the effect of forward speed and diffusion of the air through the intake system to provide the necessary pressure rise prior to combustion. Heat is added to the flow by burning fuel at nearly constant pressure and the resulting hot gas is expanded in the nozzle to atmospheric conditions converting the thermal energy to kinetic energy in a propulsive jet. This is the Brayton cycle which may be represented on a temperature-entropy diagram as shown. Although ramjets have been used at high subsonic speeds they are not very effective, due to the small amount of compression available from the air intake. They are generally used in the Mach number range 2 to 5 and require boosting to supersonic speed.

Kerosene or a high density hydrocarbon fuel is employed in a conventional liquid fuel ramjet. In a solid fuel ramjet the solid fuel typically, based on hydroxyl-terminated polybutadiene is located within the ramjet combustion chamber. The surface of this fuel grain burns in the presence of air supplied from the intakes, and the amount of fuel liberated depends on the pressure and mass flux of this air and the surface area of the grain. A Ramrocket uses a solid propellant grain burnt in a rocket type combustion chamber to liberate a fuel rich gas into a ramjet type combustion chamber, where combustion continues in air supplied from the air intakes. In this case the amount of fuel released is independent of conditions within the ramjet combustion chamber. Reference 1 provides a review of ramjet and ducted rocket propulsion systems. Reference 2 particularly deals with the solid fuel ramjet.

A turbojet engine also operates on the Brayton cycle (Fig. 2), but in this case some of the compression prior to combustion is provided by a rotating compressor. Again combustion occurs at nearly constant pressure. Expansion of the hot gas takes place partly through the turbine, which provides the necessary work to drive the compressor and partly in the propulsive nozzle. The air intake plays an important part in contributing to the overall pressure rise under forward speed conditions. This effect of course, increases with increasing flight Mach number.

Turbojets may be used for missile propulsion in both the subsonic and supersonic flight regimes, although their application is much more common in the former area. The turbojet is generally more efficient than the ramjet up to Mach numbers of about 3, above which its performance is reduced by, amongst other factors, the need to limit operating temperatures to avoid component failure. The use of a turbojet for long range supersonic applications may not solely lead to benefits of improved fuel consumption compared with ramjet propulsion. The ability of a turbojet to accelerate a missile from subsonic to supersonic speed may also allow the boost motor to be reduced in size or dispensed with altogether, leading to a reduction in overall missile mass at the expense of increased complexity and cost. Reference 3 describes the development of an expendable turbojet for missile application.

The turbofan is a more complex but more fuel efficient derivative of the turbojet. Its application for missiles is mainly in the subsonic flight regime. It differs from the turbojet in that some of the air after initial compression, is bypassed around the gas generator part of the engine in which combustion takes place. This bypass air is either mixed with the hot gas from the gas generator or exhausted separately from a nozzle situated around the gas generator nozzle. Reference 4 describes the development of a small turbofan engine for missile and drone application.

Intakes for pulsejets are not considered as this type of propulsion is not commonly used for tactical missiles.

### 3. TYPES OF AIR INTAKE

The deceleration, or compression of the airflow to the engine from atmospheric conditions generally takes place partly ahead of the air intake entry and partly within the air intake duct. It is therefore convenient to consider the air intake system as an entry section and a diffuser duct section. The entry section defines the intakes type.

It would probably be helpful at this stage to define some of the common terminology used for various parts of the air intake, by which they will be referred in this paper. These are shown in Fig. 3 for both subsonic and supersonic air intakes.

The intake cowl lip forms the division between the internal flow, passing through the intake entry and the external flow passing around it. It should be designed to allow the division to occur with the minimum of disturbance to either the internal or external stream. The cowl is the external surface of the intake downstream of the entry. The profile has a significant effect on the drag of the intake installation.

Most intakes designed for supersonic operation have compression surfaces situated upstream of the cowl lip to generate a compression shockwave system, as will be seen later. The supersonic intake shown in the sketch is rectangular in section and has swept sidewalls in order to maintain a "two dimensional" entry flowfield.

A major component in any intake is the subsonic diffuser. This is a duct of increasing area where the flow is decelerated subsonically to conditions at engine entry. This normally takes the form of a divergent passage, although a sudden expansion "dump diffuser" may be used.

In the case of a turbojet the entry to the engine, or engine face, is well defined, being the compressor entry. The downstream end of an air intake for a ramjet powered missile is less distinct, especially in the case of multiple intakes. It may be considered to be upstream of the elbow leading to the combustion chamber, or alternatively at a station in the combustion chamber itself downstream of the inlet ports. The inlet air may enter the combustion chamber axially or at any angle between this and the right angle entry.

The dart boundary layer diverter is the passage and fairing between the intake entry and the missile dart. The purpose of this component is to avoid ingestion of the dart boundary layer. The intake afterbody forms a fairing between the cowl lip and the missile body.

### 3.1 Subsonic Air Intakes

#### 3.1.1 The Pitot Intake

The most common type of air intake used in the subsonic flight regime is the Pitot intake (Fig. 4(a)). The entry section of this type of intake is simply a forward facing hole, surrounded by the cowl lip. The cowl has an external profile rather like the upper surface of the leading edge of an airfoil. At high subsonic flight speeds the cowl lip profile should be designed to avoid, if possible, the formation of local regions of supersonic flow caused by the air accelerating over the cowl surface. Recompression shockwaves at the end of these regions may cause increased drag. The Mach number at which the flow first reaches sonic velocity on the surface is known as the critical Mach number. A commonly used family of cowl profiles for subsonic air intakes is the NACA 1-series (References 5 and 6). This was designed according to a criteria of maximising the critical Mach number of the cowl. On a side mounted air intake the part of the entry which is adjacent to the boundary layer diverter is not profiled in this manner.

The internal profile downstream of the entry normally contracts slightly from the highlight of the cowl lip (the most upstream point on the lip) to allow a finite internal lip curvature. The internal profile is usually a radius or an ellipse (typically of 2:1 ratio). The duct contraction ratio (throat area to highlight area) normally lies in the range 1.01 to 1.35.

The entry section is followed by a subsonic diffuser. Since the entry (cowl lip) is usually non-circular and not in line with the engine axis, this diffuser must normally accommodate both a change in cross sectional shape and a longitudinal curvature of the duct centreline.

In an alternative, but less common form of this type of intake, the entry is mounted directly on the body surface, as shown in Fig. 4(b). This configuration is normally only employed if the entry is close to the nose of the missile, where the approaching boundary layer is thin. Fig. 4(c) shows two subsonic, turbojet-powered missiles one having four Pitot air intakes mounted in the cruciform wing roots, the other with a single ventral air intake.

#### 3.1.2 The Flush Intake

Another form of air intake that has been employed in subsonic missiles is the flush intake. The entry section of this intake is completely buried within the surface of the missile body. This type of air intake necessarily ingests some of the approaching boundary layer which degrades the internal performance, relative to that of a Pitot intake not ingesting boundary layer. Performance may be improved, particularly at low mass flow ratios (see Section 4) by profiling the walls of the entry in an ogival, diverging planform as shown in Fig. 5(a). This creates streamwise vortices which sweep the approaching boundary layer around the intake, while at the same time inducing high energy air from the free stream into the intake and inhibiting flow separation on the intake ramp (Fig. 5(b)). This configuration is known as the NACA inlet as it was developed by NACA circa 1947. (Reference 7). It is extensively used on aircraft as a low-drag inlet for air conditioning and cooling systems.

The optimum configuration has a flat ramp of about 7° angle and a width to height ratio of 4 to 1. These proportions are not very practical for an engine air intake, giving a long ramp and an extreme change of cross section in the diffuser duct. A steeper ramp (10 to 15°), possibly curved, and a square entry section to the diffuser are more suitable. A relatively blunt cowl lip is normally used to prevent internal flow separations. Compressibility effects restrict the practical application of this type of air intake to Mach numbers lower than about 0.85.

The flush air intake has the advantage that it does not require folding, in order to fit a launch canister although this may be offset by the large internal volume occupied by the ramp section. Fig. 5(c) illustrates a flush air intake installation on a subsonic turbojet-powered missile.

### 3.2 Supersonic Air Intakes

#### 3.2.1 The Pitot Intake

The Pitot air intake, described in Section 3.1, may also be employed effectively at low supersonic speeds (e.g. to Mach 1.4 or 1.6). Under these conditions a normal

shockwave will form ahead of the intake through which the flow will decelerate from supersonic to subsonic speed, as shown in Fig. 6. A sharp cowl lip may be preferred for supersonic operation since it allows this shockwave to attach to the cowl lip giving reduced intake drag in comparison to that incurred by a blunt cowl of the subsonic type. The sharp lip suffers the disadvantage that it may encourage internal flow separation at subsonic speeds or high incidence when these conditions are coupled with high mass flow rates. This will result in a degradation of internal performance and flow quality, as discussed in Section 4 and 9. External flow separation may occur at low mass flow conditions giving high intake drag.

### 3.2.2 The External Compression Intake

As flight Mach number is increased the loss in internal performance incurred by compression through the normal shockwave of a Pitot intake becomes unacceptably high. It is more efficient to reduce the Mach number in the flow ahead of the cowl lip and upstream of the normal shockwave to a low supersonic value (say 1.3 to 1.6), by turning the flow through one or more shockwaves. These are generated by compression surfaces situated upstream of the cowl, as shown in Fig. 7. Supersonic compression at the design conditions takes place ahead of the cowl lip and external to the intake duct. The compression is completed at subsonic speeds in an increasing area duct, or subsonic diffuser. The subject of shock losses is discussed more fully in Section 4.1.

The compression surfaces, which are normally planar, conical, or part conical in form, are generally positioned so that the shockwaves are focused onto the cowl lip at a given flight Mach number. Thus, a shock system generated by planar compression surfaces will have a straight cowl lip, while one generated by conical compression surfaces will have a circular entry.

The cowl is normally aligned so that its internal surface is parallel to, or forms a slight compression with the local flow direction. Care must be taken to ensure that the flow turning by the cowl, both internal and external, are insufficient to cause cowl shock detachment in the Mach number range of interest, since this will result in increased drag.

### 3.2.3 Types of External Compression Intake

The supersonic external compression intake may take many forms. Commonly used variants are the 'two-dimensional', or ramp compression intake, as shown in Fig. 8(a), the half axisymmetric intake as shown in Fig. 8(b) and the full axisymmetric intake, commonly used in nose installations, which is shown in Fig. 8(c).

These intakes are widely employed because their external compression flowfield is mathematically two-dimensional, allowing the optimum position of the shock generating surfaces and the cowl lip to be determined to suit a given flight condition, and estimates to be made of the intake internal performance and drag. Many different versions of these types have been tested both in wind tunnels and in flight so that their behaviour is well understood.

Efficient supersonic external compression intakes do not have to fall into these categories, however. Indeed, alternative types may be forced on the intake designer by system constraints, such as the need to package the missile in a certain size of container prior to launch, or from the overall system performance point of view (e.g. integration of the intake(s) into the airframe to give low overall drag!).

A less common type of external compression intake that has been used in an air breathing missile is the scoop intake (Fig. 8(d)). In this configuration the flow is compressed supersonically by turning it towards the body, resulting in a shorter intake duct and low intake drag. Problems may arise with this type of intake, however, due to shock-boundary layer interaction and rapid flow quality deterioration as missile incidence is increased.

Some typical installations of several common forms of external compression air intakes on proposed missiles are shown in Fig. 9. Examples of two-dimensional air intakes are given in References 8 and 9, half-axisymmetric intakes in References 10 and 11, full axisymmetric intakes in References 12 and 13 and the scoop intake in Reference 14. These report the results of various wind tunnel tests on such configurations.

### 3.2.4 The Mixed Compression Intake

At Mach numbers higher than about 3, the turning necessary to decelerate the flow to a low supersonic Mach number ahead of the cowl lip becomes large. This results in the need for a steep cowl angle giving a correspondingly high cowl wave drag.

The cowl angle may be reduced in two ways. The external supersonic turning may be reduced, resulting in a stronger cowl shock and decreased internal performance. Alternatively the external supersonic turning may be reduced and supersonic compression continued internally, the flow being turned back by the cowl lip.

The latter arrangement is known as a mixed external-internal compression intake and is shown in Fig. 10. It promises high internal performance coupled with low intake drag, at high flight Mach number. The internal supersonic compression part of the duct



contracts, while the subsonic diffuser area must increase. Therefore a minimum area "throat" is formed within the intake duct.

Maximum internal performance is achieved when the normal shockwave at the end of the supersonic region of the flow is positioned just downstream of the throat, with the area chosen so that the Mach number at this station is close to unity. This shock cannot remain in stable equilibrium within the duct upstream of the throat, and if it is disturbed from its downstream position may be expelled suddenly to form a detached normal shock ahead of the cowl lip. This occurrence is called "unstart" and will result in an instantaneous reduction in intake internal performance, coupled with a sudden increase in intake drag. It is therefore not a desirable event. Unstart may be caused by engine malfunction, reduction in flight Mach number, or incidence effects due to gusts or manoeuvring.

To exploit the full potential of this type of air intake, variable geometry and extensive internal boundary layer control are required (Reference 15), however such devices are not normally practicable in a tactical missile intake. The operation of a mixed compression intake is described more fully in Section 4.4.2.

#### 4. AIR INTAKE INTERNAL PERFORMANCE

##### 4.1 Pressure Recovery

The internal performance of an air intake may be described by the variation of total pressure recovery, with flow conditions (mass flow, Mach number) existing at some station within the intake duct.

Pressure recovery is defined as

$$\sigma_1 = \frac{P_1}{P_\infty} = \frac{\text{mean total pressure at engine entry}}{\text{freestream total pressure}}$$

Thus pressure recovery is a measure of the available pressure energy at engine entry, compared with that existing in the flow at freestream conditions.

The mean value should be that obtained by replacing the non-uniform flow at engine entry with a calculated uniform flow of the same mass flow, enthalpy flux and stream force. This is tedious and in most cases little difference will result from using a more convenient area weighted mean value.

Engine performance directly reflects the pressure available at engine entry and hence pressure recovery. A reduction of 1% in pressure recovery may typically yield a 1% to 2% reduction in nett thrust and an increase in specific fuel consumption of the order of 1/3 to 1%.

The inevitable loss of total pressure in a practical intake may stem from a number of sources, depending mainly on the flight regime, as shown in Fig. 11. At very low speeds "entry" losses dominate, at higher subsonic speeds the main source of loss is almost entirely the subsonic diffuser, while at supersonic speeds shock losses and shock-boundary layer interaction effects become important.

##### 4.1.1 Entry Losses

These are only significant at speeds below which most missiles operate. They are, however, described here for completeness.

If an air intake is sized for efficient operation at high subsonic, or supersonic speeds and the engine is run at high power setting at low forward speed, air will be drawn into the intake from around the cowl lip. If the cowl lip is "sharp" it cannot sustain the suction force necessary to turn the flow into the air intake without separation. Separation will occur internally and losses will ensue due to this and the subsequent effect on the flow in the subsonic diffuser. The entry loss for sharp lips has been evaluated theoretically by Fradenburg and Wyatt (Reference 16) as a function of inlet mass flow (ratio-ed to that required to choke the entry in the absence of viscous effects) and freestream Mach number, as shown in Fig. 12. It can be seen that the loss reduces as mass flow is reduced or as flight Mach number is increased.

The entry losses will also reduce as the lip is blunted. In this case experiment must be used to determine their magnitude. The work of Blackaby and Watson (Reference 17) is notable in this field. They measured the variation of pressure recovery with engine face Mach number in an axisymmetric intake with cowl lips of different radii, ranging from a sharp lip to a bellmouth entry. Fig. 13 illustrates some of the trends of this work. At zero forward speed, increasing the cowl lip radius by increasing the contraction ratio of the entry yielded a significant increase in intake pressure recovery, the effect increasing as the flow through the intake is increased. Even with a contraction ratio of 1.24 considerable entry losses were incurred, as shown by comparison with the pressure recovery of the duct with a bellmouth fitted at entry.

At low forward speed (Mach 0.33) the effect of lip radius is still significant, although as would be expected, not as great as at zero forward speed.

#### 4.1.2 Diffuser Losses

The loss of total pressure in the subsonic diffuser of an air intake is due to skin friction effects on the duct walls and to turbulent mixing of the flow during its passage from diffuser entry to exit. The magnitude of the diffuser loss is largely dependent on the behaviour of the internal boundary layer. This is subjected to an adverse pressure gradient within the diffuser, and is prone to thickening and separation, with a consequent reduction in diffuser performance.

Diffuser losses are therefore closely related to the condition of the flow at entry (Mach number, uniformity, state of boundary layer) and to the geometry of the diffuser (overall entry/exit area ratio, length, centreline curvature (or offset), cross sectional area, longitudinal area distribution, struts, excrescences, surface roughness). In general large rates of diffusion, and any departure from an axisymmetric shape, will increase the diffuser losses, as will the presence of a thick boundary layer or non-uniform flow at entry.

The experiments of Scherrer and Anderson (Reference 18) on a family of circular cross section diffusers illustrate many of these effects.

The diffusers were designed to the following criteria for operation with near-sonic inlet (or throat) velocities:

- (a) Initial (throat) wall angle close to zero to avoid high pressure gradients at near-sonic conditions, which could cause boundary layer separation.
- (b) Gradual initial area increase to avoid the formation of local supersonic flow regions near the wall.
- (c) Maximum wall slope limited by the avoidance of boundary layer separation in the diffuser using theoretical criteria to predict this. The maximum slope thus depends on the condition of the boundary layer at entry.
- (d) Exit wall slope less than maximum in order to maintain attached boundary layer by reducing the pressure gradient.

The walls of the diffusers were therefore reflex in profile. All of the diffusers had a fixed exit to entry area ratio of approximately 2. Diffusers were designed for two boundary layer thicknesses selected as being representative of typical thick and thin entry boundary layers. These basic diffusers had a maximum total wall divergence of 8 and 13.5 degrees respectively. The diffusers under test were mounted between a bellmouth at entry and a pipe leading to a flow measuring device, a flow control valve and a suction plant. Conditions at the diffuser throat were measured using a traversing Pitot probe and at the diffuser exit by means of a flow survey rake of multiple Pitot and static probes. The mass flow through the duct was varied up to sonic velocities (choking) at the duct throat and the pressure recovery of the diffuser measured.

The effect of increasing the maximum divergence angle from 8 to 13.5 degrees, giving a shorter diffuser, is shown in Fig. 14. A slight reduction in pressure recovery results, the difference increasing as the mass flow through the duct approaches the choking value. It is also noticeable that the pressure recovery of both diffusers decreases rapidly as sonic velocities are approached in the diffuser throat. A mass flow ratio of 0.9 approximately corresponds to a midstream throat Mach number of 0.7. This is characteristic of the behaviour of most types of subsonic diffuser and consequently operation with high throat Mach numbers should be avoided if possible.

Fig. 15 illustrates the effect of increasing entry boundary layer thickness at a fixed diffuser exit Mach number. The boundary layer thickness is expressed in terms of the ratio of momentum thickness to duct radius at entry. The range covered is representative of that which might exist in the throat of a supersonic air intake diffuser. As might be expected the diffuser pressure recovery falls as boundary layer thickness increases.

If the boundary layer at the entry to the subsonic diffuser is separated it is beneficial to have a constant, or very slowly diverging section of duct at diffuser entry. The low initial rate of diffusion reduces the pressure gradient in this region, reducing the losses due to mixing, with favourable effects on both pressure recovery and flow steadiness. This has been observed in Reference 18 for an artificially separated boundary layer and in Reference 19 for a supersonic intake with shock-induced separation.

Fig. 16 illustrates the effect of extending the duct at diffuser entry, when a separated boundary layer is present. The extension had a total divergence of two degrees to compensate for boundary layer growth. Increasing the throat length by the equivalent of the duct diameter gave a marked increase in pressure recovery and flow steadiness, particularly at high mass flow ratios. Extending the diffuser throat to three times this value brought further gains in performance. In this case, however, it should be noted that the overall length of the diffuser is doubled.

The effect of offsetting the centreline of a subsonic diffuser, in order, for example to supply an engine buried within a missile body, is shown in Fig. 17. The diffuser pressure recovery losses being approximately doubled by offsetting the outlet centreline, relative to the inlet centreline by an amount equivalent to one throat diameter. Careful development of an 'S' bend diffuser can minimise these losses. Particular attention should be paid to the initial turn of the duct, and if possible turning and diffusion should be separated. It is possible to achieve operating pressure recoveries in the 0.97 to 0.98 range for quite severely offset ducts typical of a Pitot intake installation on a subsonic turbojet powered missile.

Offset diffusers are common in practical air intake installations. In addition it is nearly always necessary to use the diffuser duct to accommodate a change in cross sectional shape between intake entry and exit. This is especially so in the case of a turbojet installation where the diffuser exit is constrained to a circular cross section. For a ramjet installation this may not be necessary. Sketches of some typical diffusers are shown in Fig. 18.

The changes of cross section and the offset, of a practical installation, coupled with possible adverse entry conditions may lead to a boundary layer separation within the diffuser duct (Fig. 19(a)) resulting in a severe loss in performance and an increase in exit flow non-uniformity.

It may be possible to improve the performance in such a case by using vortex generators (i.e. Reference 20) to re-energise the boundary layer, preventing or reducing the extent of the separation as shown in Fig. 19(b). Alternatively, it might be possible to use tangential blowing to maintain an attached boundary layer (Reference 21) as illustrated in Fig. 19(c). The benefits of this must, however, be offset against the performance loss due to providing high energy air for this purpose. A further method of preventing boundary layer separation is the use of boundary layer bleed. This technique is particularly common in supersonic intakes and will be described later in this section. As noted above, careful development of the diffuser may result in acceptable flow quality being achieved without recourse to such devices.

If it is necessary to incorporate parallel ducting, screens, bends or sudden expansions in the intake system, they should be positioned downstream of the subsonic diffuser where the duct velocity is low, since the loss of total pressure in these components increases in proportion to the upstream dynamic head.

#### 4.1.3 Shock Losses

The total pressure loss through the shock system of a supersonic air intake is governed by the Mach number ahead of the intake and the number and angle of the shock generating surfaces. As stated previously, it is more efficient at high flight Mach numbers to decelerate the flow to subsonic speeds through one or more oblique shocks, followed by a normal shockwave at the cowl, rather than through a single normal shockwave as in the case of a Pitot intake. This is illustrated in Fig. 20, for a flight Mach number of 2.0. The variation of Mach number, total pressure and static pressure along typical entry streamlines O to D are shown. It can be seen that pressure recovery losses approaching 30% are incurred through the normal shock of the Pitot intake, while shock losses of only 5% are incurred through the double wedge, three shock system.

Oswatitsch, in Reference 22 shows that, for a given number of compression surfaces, the configuration that gives minimum inviscid shock loss is obtained by compression surface angles which equalise the total pressure loss through each shockwave. To avoid large viscous losses due to shock boundary layer interaction the Mach number upstream of the normal shockwave should be limited to 1.3, as described in the next section. The optimum shock pressure recovery of two dimensional intakes having one, two and three compression surfaces designed to the above criteria for a range of "design" Mach numbers is presented in Fig. 21. The shock pressure recovery for a Pitot intake is shown for comparison.

There will, of course, be a different "optimum" design for each Mach number, for a given number of compression surfaces. For a double wedge, three shock compression system the optimum compression angles are shown in Fig. 22.

The total turning angle for optimum shock pressure recovery increases considerably as flight Mach number is increased and also as the number of compression surfaces are increased to reduce the shock losses. This is illustrated in Fig. 23.

A high degree of turning is not practical in supersonic air intakes as this may lead to a steep cowl angle to avoid cowl shock detachment, with resulting high cowl drag, and to long compression surfaces. For this reason the use of a purely isentropic compression surface (a curved surface giving a reverse Prandtl-Meyer expansion) to decelerate the flow ahead of the cowl shockwave without losses is ruled out. Benefits can, however, be obtained by the use of isentropic compression surfaces between two planar or conical compression surfaces, thus eliminating the intermediate shockwave.

In practice non-optimum compression geometries are generally employed, designed to give the best overall powerplant performance, rather than the best internal performance.

It should be noted that although the foregoing examples referred to a two dimensional air intake, similar results would be obtained for an air intake with conical

compression surfaces. In this case, however, the shock losses and the flow turning angles at the cowl lip would be reduced due to the isentropic compression inherent in the conical flowfield.

#### 4.1.4 Shock-boundary Layer Interaction

The subject of shock-boundary layer interaction is far too large to cover in depth as part of this paper. It has been explored by many investigators over the past 30 to 40 years. The following, therefore, is only intended to outline the causes and effects of such interactions.

The static pressure rise across a shockwave impinging on a boundary layer will cause the boundary layer to thicken. Separation occurs when the boundary layer can no longer withstand the pressure rise across the shockwave. The high pressure feeds forward at separation through the subsonic portion of the boundary layer close to the wall. The pressure difference thus existing across the boundary layer upstream of the shockwave causes it to separate and readjust to a new equilibrium position. The point of separation is therefore upstream of the point of impingement of the shockwave. The separation may reattach, or remain separated, depending on the initial state of the boundary layer, the degree of interaction and the pressure gradient imposed in the downstream region.

Fig. 24 illustrates three common forms of shock induced boundary layer separation.

Fig. 24(a) shows "bridging" of the boundary layer across the angle between two external compression surfaces, caused by the inability of the boundary layer to withstand pressure rise due to the oblique shockwave that would form at their junction. This type of interaction is common at very high altitudes, where the Reynolds number is low enough for the boundary layer to be laminar.

Fig. 24(b) illustrates typical separation of the compression surface boundary layer induced by a strong cowl shockwave. The separation generates oblique shockwaves locally as shown, significantly modifying the shock system from its intended geometry.

The phenomena described above are known as "incident" shock-boundary layer interactions. Another type of interaction which commonly occurs in air intakes is known as the "glancing" shock-boundary layer interaction. In this case the shockwave lies across the boundary layer formed on a surface parallel to the flow direction. Boundary layer separation will occur at a lower pressure ratio than required for incident shock induced separation. This is because the boundary layer is sheared laterally as the flow is turned, parallel to the surface, by the shockwave, as shown in Fig. 24(c).

Reference 23 gives empirically determined pressure ratios at which incipient incident shock-induced separation will occur. These are shown in Fig. 25. It can be seen that a normal shock at a Mach number of 1.3 is sufficient to cause separation according to these criteria. For a laminar boundary layer, of course, a much lower pressure ratio will provoke separation.

For a glancing-shock/boundary layer interaction, Stanbrook (Reference 24) observed that a pressure ratio of 1.5 across an oblique shock was sufficient to cause separation of a turbulent boundary layer.

#### 4.1.5 Boundary Layer Bleed

The internal performance of supersonic air intake intended for high Mach number operation can normally be improved by the provision of boundary layer bleed on, or at the end of the compression surfaces, in the region of any shock/boundary layer interaction. The benefits derive from restoring the shock system to a condition closer to the desired inviscid geometry, and eliminating, or reducing the effects of separated flow on the subsonic diffuser.

The boundary layer may be removed through perforations in the surface of the intake (Fig. 26(a)), a ram scoop (Fig. 26(b)) or a flush slot (Fig. 26(c)).

Distributed bleed through perforations is the most common method for compression surface or sidewall bleed. Ram scoop boundary layer bleeds have been used in the throat of supersonic intakes and are effective at design conditions, though their performance may deteriorate rapidly off design. The wide flush boundary layer bleed slot is well suited to use in the throat of a two dimensional intake (situated between the compression surface and the subsonic diffuser), (Reference 25). This type of bleed is very effective in improving intake internal performance over a wide range of internal flow conditions. Typical internal performance benefits resulting from the use of boundary layer bleed are shown in Fig. 27.

An example of the analytical design of a boundary layer bleed system for a mixed-compression intake is given in Reference 26.

Although boundary layer bleeds are most commonly used to prevent shock induced separation in supersonic air intakes they are occasionally used in subsonic air intakes to improve flow conditions.

#### 4.1.6 Boundary Layer Ingestion Effects

Ingestion of approaching boundary layer from the body of a missile by a side air intake will cause a degradation in flow quality and pressure recovery. This will be due not only to the energy deficit in the ingested boundary layer but to increased mixing losses in the subsonic diffuser, and in the case of a supersonic intake, increased shock-boundary layer interaction. Furthermore Seddon, in Reference 27, shows that thickening and separation of the approaching boundary layer may result from the adverse pressure gradients generated by diffusion in the flowfield ahead of intake entry, as shown in Fig. 28. It is therefore beneficial to move the intake away from the body. The approaching boundary layer may then pass through the gap between the intake and the body and is normally diverted sideways by a wedge shaped fairing as shown in Fig. 29.

The effect on internal performance of immersion of the intake in the body boundary layer is shown in Fig. 30, for a typical half axisymmetric supersonic air intake (Reference 28). Increasing immersion has an adverse effect on both pressure recovery and maximum mass flow.

In determining the height of the boundary layer diverter the effects of incidence on the dart boundary layer should be considered. As will be shown later, for some intake positions the height of the approaching boundary layer is significantly greater when the missile is at incidence than it is at zero incidence.

The diverter passage should, of course be designed so that it does not interfere with the flow entering the intake. For a supersonic intake the included apex angle of the diverter fairing should if possible be less than  $20^\circ$  to avoid upstream influence and to minimise wave drag. The apex should be set back a little from the intake entry and the passage between the intake and the body should diverge slightly laterally and longitudinally to prevent choking. In the case of a half conical intake some interaction may arise between the intake shock system and the body boundary layer ahead of the cowl, reducing the effectiveness of the diverter system. Introducing a swept splitter plate to separate the diverter from the intake pre-entry flowfield, as illustrated in Fig. 29, may prevent this interaction and improve intake performance.

#### 4.2 Mass Flow Ratio

It is convenient to non-dimensionalise the air mass flows entering the intake by referencing them to the mass flow that would pass through a characteristic area if it were placed in the freestream at flight conditions. For convenience the intake entry area  $A_{INT}$  is normally selected as the characteristic area.

Referring to Fig. 31, the mass flow ratio associated with engine air flow, the main duct mass flow ratio, may be defined as:

$$\epsilon_1 = \frac{m_1}{m_{\infty INT}} = \frac{\text{air mass flow at engine entry}}{\text{air mass flow through characteristic area at freestream conditions}} = \frac{A_{\infty ENG}}{A_{INT}}$$

The mass flow ratio associated with any boundary layer bleed, or bypass flow, taken from within the intake may be defined in a similar manner.

$$\epsilon_B = \frac{m_B}{m_{\infty INT}} = \frac{A_{\infty B}}{A_{INT}}$$

The intake capture mass flow ratio will be the sum of the main duct and bleed mass flow ratios.

$$\epsilon_{CAP} = \frac{m_{CAP}}{m_{\infty INT}} = \frac{m_1 + m_B}{m_{\infty INT}} = \epsilon_1 + \epsilon_B = \frac{A_{\infty CAP}}{A_{INT}}$$

Of course, if there is no internal boundary layer bleed flow, then

$$\epsilon_{CAP} = \epsilon_1$$

The mass flow ratio definitions may apply to single intakes as shown, or jointly to multiple intake configurations. The use of freestream reference conditions takes into account any effects due to the body flow flowfield on conditions at intake entry.

If the flow entering the intake is unaffected by the body flowfield, as in the case of a nose intake, or if local conditions ahead of the intake entry are used for reference, then the capture streamtube in supersonic flight will nearly always be less than, or equal to the intake area. Thus the mass flow ratio in this case cannot exceed unity, this value being achieved when the external compression shocks and the final normal shockwave fall on or inside the cowl lip. An exception to this may occur in the case of certain types of intake at incidence. This has the effect of increasing the capture streamtube by increasing the effective intake area (Section 9.2.2).

As shown previously in subsonic flight conditions the streamtube ahead of the intake may be larger than the intake area.

#### 4.3 Engine Airflow Demand

At a given engine "throttle" setting and flight condition both the turbojet and the ramjet engine operate at a fixed value of engine entry Mach number,  $M_1$ . For a given engine this corresponds to the "non-dimensional" mass flow parameter  $m_1 T_1/P_1$  as shown below.

This may be related to the main duct mass flow ratio and intake pressure recovery as follows.

$$\frac{m_1 \sqrt{T_1/P_1}}{m_{\infty INT} \sqrt{T_{\infty}/P_{\infty}}} = \frac{m_1/m_{\infty INT}}{P_1/P_{\infty}} = \frac{\epsilon_1}{\eta_1}$$

Stagnation temperature  $T_1 = T_{\infty}$  since no heat addition.

$$\frac{\epsilon_1}{\eta_1} = \frac{m_1 \sqrt{T_1/P_1}}{Q_{\infty} A_{INT}} = \frac{Q_1 A_1}{Q_{\infty} A_{INT}}$$

where

$$Q = f(M) = \sqrt{\frac{\gamma}{R}} \frac{M}{\left(1 + \frac{\gamma-1}{2} M^2\right)^{\frac{\gamma+1}{2(\gamma-1)}}}$$

and  $\gamma$  = ratio of specific heats  
 $R$  = Universal gas constant

#### 4.4 The Intake Characteristic

The internal performance of an air intake may be described at each flight condition (Mach number, incidence, sideslip or roll angle) by a unique curve, the intake characteristic. A set of such curves are necessary to define intake performance over the flight envelope, taking into account, for example, the variation of flight Mach number and incidence. Any change of intake configuration due to variable geometry, must also be reflected by appropriate intake characteristics.

There are two common forms of intake characteristic:

$\eta_1$  as a function of  $Q_1$   
 $\eta_1$  as a function of  $\epsilon_1$  or  $\epsilon_{CAP}$

The point at which the air intake operates on the characteristic (i.e. the value of mass flow ratio and pressure recovery) is governed by conditions at the downstream end of the intake duct, that is, by the engine airflow demand. This is known as the matched operating point and is given by the appropriate value of  $Q_1$  or  $\epsilon_1/\eta_1$  on the intake characteristic as shown in Fig. 32.

Internal performance characteristics are normally obtained from wind tunnel tests performed using a model of the intake or intakes.

Two types of model are commonly used. An isolated intake model may be used to explore the effect of detail changes of compression geometry on a relatively large scale without the effect of a body flowfield, while full installed performance can only be obtained by using a model in which the internal geometry of the intake, together with any wing or body that may influence the flow entering the intake, are represented.

A typical installed internal performance model is illustrated in Fig. 33. This model is used for general weapon intake research and development purposes and consequently is constructed to allow a wide range of geometry variations to be studied. Different nose lengths and shapes and diverter heights may be tested and components are available to allow various types of intake, different entries into the combustion chamber, and single, twin and four intake installations to be studied.

The main features of the model are as follows:

An array of Pitot tubes, disposed on an equal area basis, or a rotating Pitot rake, is situated at the engine entry station to allow the total pressure recovery of the intake to be deduced and the flow uniformity assessed. One or more high response pressure transducers may be mounted in the surface of the intake duct to allow pressure fluctuations due to flow unsteadiness or instability to be recorded. Downstream of the engine entry station, following a short length of duct, a calibrated choked plug or valve is used to control and measure the flow through the intake. Increasing the throat area of the plug raises "engine face" Mach number, while reducing the throat area has the opposite effect.

The model is mounted on a sting to allow incidence and roll angle to be varied.

For tests at supersonic speeds the full range of simulated engine flow demand may be achieved by exhausting the intake flow into the wind tunnel. For subsonic and transonic testing some form of suction device (generally an ejector) is often necessary to provide representative high mass flows.

A review of some of the techniques used in testing wind tunnel models of air intakes is presented in Reference 29.

The flow behaviour accounting for the shape of the intake characteristic (i.e. how pressure recovery varies with mass flow ratio) follows the same pattern for intakes of similar type. Therefore, although quantitatively the characteristic depends very much on the intake configuration and the flight condition that it represents, the general shape of the characteristic may be qualitatively described for various types of air intake.

#### 4.4.1 Air Intakes at Subsonic Speeds

##### 4.4.1.1 The Pitot Intake

At moderate and high subsonic speeds the flow in the diffuser will be the major factor determining the losses in a Pitot intake. The intake characteristic will therefore take the form shown in Fig. 34(a). The pressure recovery will reduce gradually as mass flow ratio and hence diffuser entry Mach number is increased, falling off rapidly as this approaches sonic conditions.

At low and zero forward speeds, the "sharp lip" loss will dominate, giving a rapid reduction in pressure recovery as mass flow is increased. This is illustrated in Fig. 34(b). The characteristic is plotted against  $Q$ , in this case.  $Q_{CAP}$  will be very large at low forward speeds, as  $Q$  tends to zero at static conditions, and is therefore not a very useful parameter under these circumstances.

##### 4.4.1.2 The Flush Intake

The approaching body boundary layer, thickened or separated due to the adverse pressure gradient on the entry ramp, will form a significant proportion of the mass flow entering the intake at low mass flow ratios. This, coupled with increased diffuser losses due to mixing, will cause the pressure recovery to be depressed, as shown in Fig. 35. As mass flow ratio is increased, the pre-entry pressure gradient will be reduced, with favourable effects on the ingested boundary layer and pressure recovery will rise. Further increasing the mass flow will yield a deterioration in pressure recovery attributable to the approach of sonic conditions at diffuser entry and possible ingestion of the sidewall vortices.

A similar characteristic will be exhibited by any subsonic intake that ingests low energy air from the body boundary layer.

#### 4.4.2 Air Intake at Supersonic Speeds

##### 4.4.2.1 The Pitot Intake

At supersonic speeds the intake characteristic has two distinct regions, dictated by the position of the terminal shockwave.

Consider a Pitot intake operating at supersonic speed (Fig. 36). At low mass flow ratios the normal shockwave that forms at the intake entry, must detach from the cowl lip to allow spillage of excess air to take place between it and the cowl. As engine demand is increased and spillage is reduced, the shockwave moves back towards the cowl lip. During this stage the shock losses remain constant while the diffuser losses increase due to the increasing duct Mach number, resulting in a reduction in pressure recovery.

When the shockwave attaches to the cowl lip forespill cannot take place. The mass flow ratio is therefore limited to this value, which is unity at all flight Mach numbers (when based on conditions ahead of entry).

A further increase in Mach number at the engine entry station will be accomplished by a reduction in pressure recovery. This results from the normal shockwave moving progressively into the subsonic diffuser. As it does this the Mach number ahead of it increases (due to the duct area increase) causing the shock losses to increase. The diffuser losses will also rise due to increasing shock-boundary layer interaction within the duct.

The point at which the normal shockwave attaches to the lip is known as the CRITICAL POINT. The constant mass flow part of the characteristic is the SUPERCRITICAL REGIME of operation, while the varying mass flow region is known as the SUBCRITICAL REGIME.

##### 4.4.2.2 The External Compression Intake

The intake characteristic for an external compression intake, with ramp or conical compression surfaces, is similar to that for the supersonic Pitot intake (Fig. 37).

Increasing interaction between the normal shockwave and the boundary layer on the compression surfaces may, however, occur in subcritical operation due to the effect of the adverse pressure gradient in the pre-entry flowfield. This reduces pressure recovery as mass flow is reduced. By virtue of the more efficient shock compression system the subcritical and critical pressure recovery will generally be higher than that of a Pitot intake at the same Mach number. Also, if the Mach number is lower than that at which the pre-compression shockwaves are focussed onto the cowl lip, the supercritical capture mass flow ratio will be less than unity, since some supersonic foreshock will occur.

In this type of intake the subcritical operating range is limited by an instability known as buzz. The causes and effects of this will be discussed in Section 6.2.

If throat boundary layer bleed is employed, the bleed flow will increase as the intake is driven in the subcritical sense. This is because the pressure in the intake throat increases with reducing throat Mach number, thus increasing the pressure ratio across the bleed system. In this case two characteristics describe the behaviour of the intake, one relating to the main duct mass flow ratio, the other to the capture mass flow ratio, as shown in Fig. 38.

#### 4.4.2.3 The Mixed Compression Air Intake

The mixed compression air intake may exhibit two modes of operation over a range of engine flow demand; "started" and "unstarted". In started operation supersonic internal compression is achieved, resulting in low external drag, with the potential for high pressure recovery. In unstarted operation supersonic internal compression is not achieved and high drag and low internal performance will result.

In considering conditions necessary for started operation it is simpler to observe the operation of a single shock internal compression intake of the classical type (Reference 30), as shown in Fig. 39. For simplicity the flow between the cowl lip and the throat is assumed to be isentropic.

The ability to start the intake at a given flight Mach number depends on the internal contraction ratio, (the ratio of throat to cowl area). For starting to be possible the intake throat must be sized so that it chokes only when the cowl shock is attached to the lip. The terminal shockwave will then be "swallowed" to lie downstream of the throat. This can only occur if the intake contraction ratio lies above line A in Fig. 39, at the flight Mach number of interest. Supersonic flow will exist up to the normal shockwave, decelerating upstream of the throat and reaccelerating downstream of it. Line A is obtained by assuming a normal shock at the cowl and determining the area ratio necessary to achieve sonic flow isentropically from the Mach number downstream of this normal shock.

This is given by

$$\left(\frac{A_T}{A_L}\right)_A = \frac{\left(\frac{\gamma+1}{2}\right)^{\frac{\gamma+1}{2(\gamma-1)}}}{M_\infty \left(\frac{\gamma+1}{2}\right)^{\frac{\gamma+1}{2(\gamma-1)}} \left(1 + \left(\frac{\gamma-1}{2}\right) M_\infty^2\right)^{\frac{1}{2}} \left(\gamma M_\infty^2 - \frac{\gamma-1}{2}\right)^{1/\gamma-1}}$$

Maximum internal performance is achieved when the normal shockwave is situated just downstream of the throat and the throat Mach number is just supersonic. This condition can only be achieved from the started condition by reducing the contraction ratio. It will occur just above line B in Fig. 39. This represents the limit of started operation. It is the area ratio necessary to achieve sonic conditions in the absence of a shock at the cowl lip, assuming isentropic flow.

$$\left(\frac{A_T}{A_L}\right)_B = M_\infty \left(\frac{\gamma+1}{2}\right)^{\frac{\gamma+1}{2(\gamma-1)}} \left(1 + \left(\frac{\gamma-1}{2}\right) M_\infty^2\right)^{\frac{1}{2}} \left(\frac{\gamma+1}{2}\right)^{\frac{\gamma+1}{2(\gamma-1)}}$$

Since the shock cannot remain in equilibrium upstream of the throat a further reduction in contraction ratio, a reduction in engine demand, or a reduction in flight Mach number will cause unstart to occur.

If the throat chokes before the cowl shock attaches to the lip started operation is not possible, since increasing engine demand cannot then affect the external shock structure, but only increase losses in the subsonic diffuser by the formation of a second shockwave downstream of the throat. This will occur in the region below line A.

In practice viscous effects and shockwaves occurring in the contracting section of the duct would slightly increase the limiting contraction area ratio given by line B.

Starting area ratios for a mixed compression intake may be computed in a similar manner, using the Mach number ahead of the cowl shock and downstream of the external oblique shock system.



Operation of a mixed compression intake at a Mach number at which starting is possible (i.e. above line A) is shown in the intake characteristic of Fig. 40.

In supercritical operation the intake is started. As engine flow demand is reduced the shockwave will move closer to the throat of the intake. When this is reached a further reduction in engine flow demand will result in unstart, giving a sudden reduction of mass flow and pressure recovery. If engine flow demand is now increased the intake will remain unstarted until maximum capture is attained.

In the regime of high internal performance, i.e. just above line B in Fig. 39, variation of engine demand will result in an intake characteristic of the type shown in Fig. 41. Assuming started supercritical operation, reducing engine flow demand will result in unstart occurring as the shockwave reaches the intake throat. A second (unstarted) supercritical region will be encountered as shown. A further reduction in engine demand results in a forward movement of the cowl shock in subcritical operation. An increase in engine demand in this unstarted state will result in the intake remaining unstarted in supercritical operation since, as shown previously, only an increase in contraction ratio or in flight Mach number can restart started operation.

## 5. PREDICTION OF INTAKE PRE-ENTRY FLOWFIELDS

In the initial design of an air intake it is often necessary to predict the pre-entry flowfield (the region over which pre-entry diffusion takes place) in order that estimates may be made of internal performance and intake drag. The following remarks assume that the flow upstream of this region is uniform and known.

### 5.1 Subsonic Intakes

Accurate estimates of the pre-entry flowfield of a subsonic intake may be made using theory based on potential flow, such as that of Reference 31. Such methods will provide detailed information on the flowfield at entry and facilitate the selection of an optimum cowl lip profile. Euler methods may also be used. At the other extreme a one dimensional approach is commonly used to estimate pre-entry drag of this type of intake.

### 5.2 Supersonic Intakes

The ease with which the pre-entry flowfield of a supersonic intake may be predicted depends very much on the intake configuration. The method of characteristics (References 32 and 33), has been employed in the calculation of axisymmetric and two dimensional intakes for many years. More recently the use of shock capturing finite difference Euler techniques (References 34 and 35) have been used for the prediction of three dimensional intake flowfields. These methods do not account for viscous effects. Combined viscous and inviscid analysis may be employed, allowing for boundary layer growth through the intake shock system, as described in Reference 36. Navier Stokes methods will find application in this area as the reach maturity.

The above methods, and many others, are computer based techniques, often requiring large storage and long computation time. Therefore, cruder methods are often employed to determine the intake pre-entry flowfield, and to make first estimates of supersonic air intake performance.

#### 5.2.1 Pitot Intake

The stand-off distance and shape of the normal detached shockwave that forms ahead of a Pitot intake at supersonic speeds and in subcritical operation may be estimated using the method of Moeckel (Reference 37). The relationship between detachment and forespill is presented in Fig. 42.

#### 5.2.2 Two Dimensional Intake

Computation of the pre-entry flowfield for a two dimensional intake is relatively straightforward provided that the compression surface shocks are attached and the intake is operating supercritically, (i.e. without a detached normal shock). Tables or graphs of compressible flow properties such as Reference 38 may be employed to locate the shockwaves and determine shock losses, while the pre-entry streamtube may be traced forward from the cowl lip, being parallel to the wedge surfaces (Fig. 43).

In real intake, however, empirical corrections must be made to correct for boundary layer on the wedge surface and to allow for spillage taking place laterally between the shock system and the sidewall. These considerations are discussed in Reference 39.

Comparison of theoretical and experimental shock positions (Reference 40) revealed that the first wedge shock was positioned at an angle equivalent to a wedge angle 0.75 to 1 degree steeper than the geometric value. This is confirmed by capture mass flow measurements, described in Reference 39. The effect is due to the growth of boundary layer on the compression surface. A correction should therefore be made to the angle of the first wedge in any calculation.

If the effect of sidespill is not allowed for the intake capture mass flow ratio will be over-estimated. The disparity will be increased if the sidewall is cut back or the intake is operating below the shock on lip Mach number.

A correlation has been developed by McGregor in Reference 39 to allow a correction for this effect to be made. This was derived using data from a double wedge intake, over a Mach number range between 1.7 and 2.46.

The loss of capture is related to the correlation parameter G (Fig. 44), where

$$G = \frac{1}{A_{INT}} \left[ A_1 \left( \frac{P_1^{-1}}{P_0} \right) + A_2 \left( \frac{P_2^{-1}}{P_0} \right) \right]$$

where  $P_0$ ,  $P_1$ ,  $P_2$ ,  $A_1$  and  $A_2$  are static pressures and areas defined in Fig. 44.

Subcritical operation of a two dimensional intake is also considered in Reference 39. The method of predicting the detachment distance of the cowl shock was that discussed previously for Pitot intakes. Using this technique and an equivalent Pitot intake, Fig. 45, the stability boundary of the intake was reasonably predicted. This was based on the Ferri Criterion for buzz described in Section 6.2.

### 5.2.3 Axisymmetric Intakes

#### 5.2.3.1 Single Conical Compression Surface

The supercritical pre-entry flowfield of intakes having a single conical compression surface may be calculated relatively easily using tables or charts relating to conical flow. In conical flow conditions are constant along 'rays' emanating from the cone apex, varying with ray angle. Thus, the streamlines through the conical flowfield follow a curved path and the conditions across the intake at the cowl lip are not uniform, as shown in Fig. 46. The critical capture mass flow ratio may be determined by tracing the streamline from the cowl lip from ray to ray to the conical shockwave. Alternatively, Reference 41 provides values calculated for a wide range of intake configurations and flight Mach number. Hermann in Reference 42 indicates that a close approximation to the critical shock pressure recovery is given by assuming the normal cowl shock to occur at the mean of the cowl lip and cone surface Mach numbers.

Subcritical operation might be estimated, if required, using the same method as proposed for the two dimensional intake.

#### 5.2.3.2 Double Conical Compression Surfaces

Flowfields of intakes with two or more axisymmetric compression surfaces are more difficult to compute than single cone flowfields, since the flow is not conical behind the second shockwave. A close approximation to the flowfield, suitable for initial estimates of intake internal performance and drag, may be reached using a technique far simpler than the method of characteristics. It is however, tedious and not really suitable for hand calculation.

To design a double cone intake with the shockwaves focussed on the lip at a given Mach number the following procedure is adopted.

A suitable angle for the first cone is selected and the conical flowfield is computed at the shock-on-lip Mach number. The cowl lip position is fixed on the conical shockwave from the cone apex. The assumption is made that the change of flow direction through the second shock is constant along its length. A suitable angle for this is selected and the second shockwave is computed as the series of oblique elements that will provide this constant turning. These elements span the rays of the conical flowfield, as shown in Fig. 47 and the mean values of the flow properties between the rays are used to provide upstream conditions for the second shockwave. The shockwave is constructed sequentially until it meets the cone surface, which defines the start of the second compression surface.

Conditions at the cowl lip station are calculated on a one dimensional basis between the streamlines in the second flowfield. Shock pressure recovery is obtained by using a suitable mean value of the total pressure recovery of the shock system between centrebody and cowl lip.

At Mach numbers lower than that required for shock-on-lip the flowfield may be constructed in a similar manner, this time working from the cone surface outwards to compute the second shockwave.

## 6. INTAKE-ENGINE COMPATIBILITY

The subject of the acceptability of the flow provided by an air intake to an engine is known, particularly where a turbojet engine is involved, as intake-engine compatibility. It deals with the quality of the flow in terms of uniformity and steadiness.

### 6.1 Uniformity of Flow

#### 6.1.1 Turbojet Engine

Intake flow distortion is a measure of the non-uniformity of the flow presented by the air intake to the engine. Acceptable flow distortion at engine entry is particularly important in the case of a turbojet engine. If a turbojet compressor is presented with non-uniform flow at entry the effective incidence of the blades will vary as they sweep through the flowfield. If the distortion is severe enough some of the compressor blades will stall and engine surge may result. Alternatively, the first stages of a compressor may be lightly loaded in some areas, due to an effective incidence reduction and this may have the effect of increasing the loading on the rear stages, again provoking surge.

Surge is a drastic reduction and possible reversal of flow through the compressor, resulting in high pressure loads on both the engine and the intake structure. Depending on the engine, the operating conditions and the cause, it may be cyclic in nature, or take the form of a single pulse. Flame extinction may or may not occur. It is therefore not a desirable occurrence, especially in an unmanned vehicle where remedial action cannot be taken.

Compressor operation may be represented by the steady state compressor characteristics, Fig. 48. Surge free engine operation is possible below the surge boundary. The position of the engine equilibrium running line is determined by the characteristics of the nozzle, turbine and compressor. As turbine entry temperature is increased, the operating point moves along this line to the right. For surge free operation an adequate margin must be maintained between the running line and the surge boundary. Often the value of "non-dimensional" compressor speed  $N/\sqrt{T}$  is limited to avoid the risk of surge at high altitude, or on cold days. The transient behaviour of the engine during rapid throttle operation must also be taken into account, since the operating point will depart from the steady state running line under these conditions, approaching the surge line during engine acceleration.

An increase in flow distortion will cause the surge line to move towards the engine operating line. If they cross and the engine operating point lies above the surge line, then surge will occur.

Much work has been carried out in the aircraft propulsion field to find a parameter or distortion index which will quantitatively relate the intake flow distortion to the loss in surge margin. It is important to know this so that regions of the flight envelope and engine operating envelope in which surge is likely to occur may be identified from wind tunnel tests on intake models. Curative measures may then be taken at an early stage in intake development.

The engine manufacturer will specify limiting values of flow distortion acceptable to the engine. These will have been determined by testing the engine in a test cell and subjecting it to varying degrees of unsteady and distorted entry flow generated by means of rods, gauzes or plates set across the intake duct. No universal distortion index has yet been found. A certain engine entry flow pattern might produce a large loss of surge margin in the case of a particular engine while causing only a small change for another of a different type or make.

Thus, there are many different distortion indices in use (for example,  $KD$ ,  $KA$ ,  $K_{\theta}$ ,  $DC_{\theta}$ ), each quantifying the non-uniformity in a different way and each having been found suitable for predicting the sensitivity of a given type or make of engine to distortion induced surge.

A common example is the distortion coefficient  $DC_{\theta}$ :

$$DC_{\theta} = \frac{\bar{P}_1 - \bar{P}_{\theta}}{q_1}$$

where  $\bar{P}_{\theta}$  = Area weighted mean total pressure in the sector of the engine face, subtending the angle  $\theta$ , which has the lowest mean total pressure.

$\bar{P}_1$  = Area weighted mean total pressure of the whole engine face.

$q_1$  = Mean dynamic head at the engine face.  
 $\theta$  is normally 60 or 90 degrees.

An example of the variation of this parameter and its relation to the total pressure distribution from which it was derived, is given in Fig. 49. This is for a two dimensional supersonic intake operated at Mach 1.9 at zero and 4 degrees of sideslip.

The use of a steady state distortion coefficient has been shown to be an insufficient criterion to predict the onset of distortion induced surge. Experiments and development tests have shown that the distortion pattern at an engine face is not constant but randomly and rapidly changing. Typically the peak instantaneous distortion index, or dynamic distortion index, may be double the time average value. Peaks of sufficient magnitude can cause engine surge even though they may last for only one engine revolution. The measurement of instantaneous distortion requires 20 to 40 small high response transducers mounted in an array of Pitot tubes at the engine face. High speed recording and processing equipments are necessary and the subsequent computer analysis of the instantaneous distortion at time intervals of the order of a millisecond, is time consuming.

For initial assessment of the intake a statistical or synthesis method may be used to predict peak dynamic distortions from steady state distributions and a measure of the unsteady pressure from a limited number of transducers.

References 43, 44, 45 and 46 deal with the measurement of flow distortion, and other aspects of distortion induced surge.

#### 6.1.2 Ramjet Engine

Although the tolerance of a ramjet engine to flow non-uniformity is obviously greater than that of a turbojet engine, severe maldistribution of the flow at engine entry may cause uneven or inefficient burning and possible flame extinction.

This often occurs in supercritical intake operation where separations are present in the diffuser and conditions of low fuel-to-air ratio make the engine more susceptible to the effects of flow non-uniformity. A solution that has been employed on several ramjet engines is an Aerodynamic Grid. This is a grid formed by streamline struts or holes bored in a plate, situated at the end of the subsonic diffuser. The streamlined nature of the grid has little effect on intake performance at critical and subcritical conditions. At the high diffuser exit Mach numbers associated with supercritical operation the apertures in the grid choke. This has two effects: further downstream movement of the diffuser shock is prevented; and the grid redistributes the flow to a more uniform pattern. Aerodynamic grids are described and their effects illustrated in Reference 47.

With multiple air intakes the non-uniformity of flow entering the combustion chamber due to an imbalance of operating conditions between the intakes will generally have more effect than the flow uniformity at the exit to each of the individual ducts. Such effects not only affect the flame-holding qualities of the combustor but may also lead to local hotspots and damage to the combustor itself.

Severe imbalance is more likely to occur at subcritical intake operating conditions at incidence and may be avoided by careful choice of intake size, or use of the fuel control system to maintain supercritical operation.

#### 6.1.3 Sources of Flow Non-Uniformity

The main sources of low non-uniformity and unsteadiness affecting subsonic air intakes are:

- (a) non-uniform flowfield upstream of intake entry (Vortex, wakes, etc).
- (b) ingested body boundary layer.
- (c) diffuser boundary layer separations.
- (d) cowl lip boundary layer separations at high incidence, high mass flow rates, or low forward speed.
- (e) local transonic effects at high mass flow ratios.

Supersonic air intakes may also suffer from high flow distortion from these sources and in addition from non-uniformity of total pressure due to shockwave intersections in the capture flowfield. This problem often arises at incidence when the shockwaves will not be at the "design" positions. Shock-induced boundary layer separation may also prevail in supersonic intakes under these conditions, where local shock strengthening may occur. Shock induced boundary layer separation often occurs in the subsonic duct of a supersonic intake during supercritical operation, when the strength of the terminal shockwave is high, as noted in Section 4.4.

### 6.2 Intake Flow Instability

#### 6.2.1 Buzz

Buzz is a duct flow instability which occurs in subcritical operation of supersonic intakes with external compression. It is characterised by large cyclic pulsations of mass flow and duct pressure, together with extreme movements of the intake shock system. Duct pressure pulsation amplitudes as much as 50 to 80% of freestream stagnation pressure have been measured in wind tunnel experiments on ramjet intake - engine duct combinations (Reference 48). The onset of buzz may be sudden or gradual but in most cases the amplitude of oscillation increases the further mass flow is reduced past the buzz

boundary. This is not true for all supersonic intakes, however, as some types have been observed experimentally to have distinct regions of buzz type instability, separated by regions of stable flow.

Generally, the first buzz boundary that is encountered as mass flow is reduced marks the limit of practical operation of the intake. Where this occurs in the subcritical region is highly dependent on the intake geometry and the flight Mach number. In some instances, when operating close to the Mach number at which the shock falls on the cowl lip no stable subcritical range of operation will be available. When the Mach number is much less than the shock on lip value a fairly large stable subcritical range may be present.

Operation in buzz would almost certainly cause surge in the case of a turbojet and flame extinction in the case of a ramjet. Interaction between the buzzing air intake and the engine may increase the amplitude of the pressure pulsations. A ramjet engine suffering flame extinction, due to the first buzz pulse, for example, would demand increased mass flow due to the reduction in temperature in the combustion chamber. This could cause the intake to move out of the buzz region, allowing combustion to re-establish itself. The resulting increase in combustion chamber temperature would reduce the mass flow again causing a further pulse to occur.

The probable catastrophic effect of the large pressure pulsations on the engine components and duct structure, together with the large oscillatory aerodynamic loading on the missile caused by the motion of the shock system upstream of intake entry cannot be tolerated.

Fig. 50 illustrates the typical position of the buzz boundary for a supersonic external compression intake and the duct pressure-time history during buzz.

Buzz was first encountered by Oswatitsch, during tests on a wind tunnel model of the intake for an air breathing missile in 1944 (Reference 22). Since that date it has been investigated by many researchers and has been observed to be caused by several factors.

One of the first explanations for the cause of this phenomenon was offered by Ferri (Reference 49) and is illustrated in Fig. 51).

Ferri postulated that buzz was initiated when the vortex sheet, originating from the intersection of the normal shockwave and the oblique or conical shockwave, moves inside of the cowl lip. This will occur as the normal shock moves forward as mass flow is reduced. When the vortex sheet enters the intake it causes a separation on the internal surface of the cowl which brings about a large reduction in effective duct area. Because the Mach number at the throat of the intake is high this causes choking to occur, producing a strong pressure wave which moves upstream and starts the oscillations. The pressure wave causes the normal shock to move forward, away from the cowl. This reduces the mass flow, which in turn reduces the back pressure, causing the shock to move back towards the cowl lip. The shock overshoots the initial position and the vortex sheet moves outside the cowl lip. The process repeats itself cyclically and buzz occurs.

Ferri also showed that buzz could be initiated by a vortex sheet from the intersection of the normal shock and an oblique or conical shockwave generated by a separation on the compression surface. In this case the vortex sheet approaches the cowl from the inside as mass flow is reduced and the separation point moves forward.

Sterbertz and Evvard, Reference 50, apply a theoretical approach for predicting the onset of buzz of a ramjet intake and combustor, which likened the duct to a Helmholtz resonator. They showed that resonance would occur when the intake characteristic had a positive slope of sufficient value. Experimental evidence, however, has shown that instability may occur with zero, or negative slope.

Dailey, Reference 51, suggests that a shock induced separation on the compression surface may choke the inlet entry, causing a reduction in mass flow. This reduces the back pressure, causing the shock system to move back towards the cowl lip, initiating a cyclic buzz oscillation (Fig. 52).

More recently, Hall (Reference 52) provided a criterion for instability produced by low energy regions present in the flowfield approaching the intake (Fig. 53). These could be due to, for example, separated body boundary layer, or the wake of a canard foreplane. Hall states that if the total pressure of a streamtube of air intercepted by the inlet, less any shock losses encountered in the compression process, is not greater than the downstream static pressure, then flow reversal and associated intake instability may occur.

In cases where buzz is caused by the presence of a separation on the compression surface, boundary layer bleed, or vortex generators are often effective in removing this and increasing the stable subcritical range of operation of the intake.

#### 6.2.2 Unsteadiness

Flow unsteadiness generally results from the presence of separated flow within the intake or on the compression surfaces. It is therefore often associated with regions of high distortion. It is often found, for example, in the supercritical region of

operation of a supersonic air intake, increasing in magnitude as engine demand is increased (Fig. 50). The unsteadiness is normally of much higher frequency than buzz and of lower amplitude, 10% of freestream stagnation pressure being a typical high level. It may take the form of random jumps, caused by a shock flicking between two near stable positions, or a continuous fluctuation.

The onset of significant unsteadiness of this type may form a practical supercritical intake operating limit for both turbojet and ramjet installations.

#### 6.2.3 Twin Duct Instability

For certain types of twin duct air intakes, symmetric operation may be impossible under certain operating conditions, even though the individual intake ducts are geometrically identical, and operating under the same aerodynamic conditions (Fig. 54(a)).

This phenomenon is encountered in air intakes having pressure recovery characteristics which rise to a maximum, before falling again as mass flow ratio is increased. Flush intakes, Pitot intakes without diverters and some types of supersonic intake fall into this category.

Martin and Holtzhauser, in Reference 53 demonstrate that the intake system will not be stable in the symmetric mode of operation at mass flow ratios (velocity ratio in incompressible flow) below that for maximum static pressure at the confluence of the ducts. At mass flow ratios above that for maximum static pressure, the system will be stable in this mode.

Fig. 54(b) shows a static pressure recovery characteristic of the type of intake in question, for each of the ducts operating independently. It is assumed that the static pressure in each duct at their confluence is always identical. Thus the mass flow ratios at which the ducts will operate in combination may be determined from lines of constant static pressure recovery. At system mass flow ratios greater than that for maximum static pressure recovery, the requirement for uniform static pressure at the confluence can only be satisfied with equal mass flow rates in each duct. The quantity of flow in each will therefore tend to remain constant. At system mass flow ratios less than that for maximum static pressure recovery, the uniform static pressure requirement may be met by either equal quantities of flow in each duct, or unequal quantities, as shown.

The variation of individual duct mass flow ratio, with total system mass flow ratio is shown in Fig. 54(c). The system mass flow ratio for flow reversal in one duct may therefore be determined.

It can be shown by consideration of the conditions that occur if the system is disturbed, that below the mass flow ratio at which the two modes of operation are possible, the asymmetric mode is preferred. Stable asymmetric flow may occur, even with reversed flow in one duct, resulting in high flow distortion and low pressure recovery. Alternatively the system may oscillate, first one duct, then the other, passing the high mass flow. Neither of these conditions are desirable and if such a configuration is unavoidable, it should not be operated below the mass flow ratio for maximum static pressure. This could occur due to throttling, for example, or a change in flight velocity.

Beke (Reference 54) presents a similar analysis, which allows the onset of flow reversal in one of the ducts to be predicted from individual intake duct characteristics for twin duct supersonic intake systems.

#### 6.2.4 Multiple Duct Instability

The instability phenomenon described above is not only restricted to twin duct configurations but may occur in any multiple intake configuration which shares a common duct at some point downstream of the entry.

If, for example, a supersonic 4 intake system at incidence is throttled it often happens that when one of the intakes reaches the critical point (usually the intake in the most adverse flowfield) that intake will jump to a subcritical state while the other 3 intakes will operate more supercritically to compensate and provide the same value of  $\epsilon/\eta$ . Further throttling will result in 2 intakes going subcritical, while the other two move in the supercritical sense. Further throttling may result in 3 and eventually all 4 going subcritical.

Thus a discontinuous multi-leg intake characteristic as shown in Fig. 55 will result.

Depending on the degree of throttling and the nature of the intake characteristics reverse flow may be present in one or more ducts.

The characteristics of a system of multiple intakes may be predicted by considering the characteristics of the individual ducts, and applying the equal static pressure criterion at the confluence, as described in Reference 55.

The criterion of constant static pressure suggests that the pressure recovery of the multiple intake system will essentially be the same as the pressure recovery of the intake

duct having the lowest pressure recovery (that in the most adverse flowfield) unless there is reverse flow present. This has been borne out by experimental data over a wide range of incidence, roll angle and throttle setting as shown in Fig. 56.

## 7. OPERATION OF AN ENGINE-INTAKE COMBINATION

### 7.1 Turbojet Engine

For a turbojet engine the "non-dimensional" mass flow rate  $m_1\sqrt{T_1}/P_1$  is nearly proportional to the "non-dimensional" compressor speed  $N/\sqrt{T_1}$ . (Note these are not true non-dimensional groups but can be considered as such for a specific engine).

For a fixed throttle setting small turbojets may be operated at constant mechanical compressor speed,  $N$ , with a possible limit on the value of  $N/\sqrt{T_1}$ . The value of  $m_1\sqrt{T_1}/P_1$  will therefore reduce with increasing Mach number as the value of  $T_1$  increases, as shown in Fig. 57. If the thrust of the engine is reduced by reducing fuel flow, the compressor speed will decrease and so too will  $m_1\sqrt{T_1}/P_1$ . Increasing ambient temperature (hot day operation, or a decrease in altitude below the tropopause) will also cause a reduction in  $m_1\sqrt{T_1}/P_1$  unless the engine is operating on the  $N/\sqrt{T_1}$  limit.

At a fixed flight Mach number both throttling or an increase in ambient temperature will cause the intake to spill more, as shown in Fig. 58.

In general, when supplying a turbojet engine at fixed throttle setting, a subsonic intake will spill less as flight Mach number is reduced, while a supersonic intake will spill more.

### 7.2 Ramjet Engine

The flow demanded by a ramjet engine is controlled by the exhaust nozzle. This is normally choked, so that the value

$$Q_N = \frac{m_N \sqrt{T_N}}{P_N \lambda_N} \quad \text{at the nozzle throat is constant (ignoring second order effects).}$$

The total temperature of the flow at this station is governed by the total temperature at entry to the combustion chamber and the rise in temperature due to combustion. The former is dependent only on the flight Mach number and ambient temperature, while the latter is nearly proportional to the fuel-air ratio.

Assuming a fixed choked nozzle, and a typical burner total pressure loss factor, it can be shown that, at a fixed value of fuel-air ratio,  $m_1\sqrt{T_1}/P_1$  will increase as  $T_1$  increases. Therefore, increasing flight Mach number, or ambient temperature, will cause an increase in  $m_1\sqrt{T_1}/P_1$  as shown in Fig. 59.

Thrust reduction by reducing the fuel-air ratio will cause the total temperature of the flow at the nozzle to fall. Because of the constraint of the choked nozzle  $m_N/P_N$  must increase to compensate for this and  $m_1\sqrt{T_1}/P_1$  will follow the same trend. Thus, throttling a ramjet will also cause  $m_1\sqrt{T_1}/P_1$  to increase.

At a fixed Mach number, therefore, both throttling or increased ambient temperature will cause the intake operating point to move in the supercritical sense, as illustrated in Fig. 60.

It should be noted that the behaviour of a ramjet engine is therefore opposite to that of a turbojet, as the engine is throttled or the flight Mach number reduced.

In common with a turbojet, reduction in flight Mach number from the design value generally causes a shift in the intake operating point in the subcritical sense.

## 8. INTAKE DESIGN FOR OPTIMUM PERFORMANCE

During the development of a missile the intake size may be optimised to give maximum propulsive performance, either in terms of maximum thrust or minimum specific fuel consumption, for the missile's intended mission.

### 8.1 Subsonic Missile - Intake Sizing

Varying the entry area of the intake changes the balance between the pre-entry diffusion and the diffusion taking place within the intake duct. This affects the internal performance of the air intake (which reflects in the level of engine thrust and specific fuel consumption that can be achieved) and in the intake total drag (spill, cowl, diverter, nacelle).

Suppose it is required to maximise the overall propulsive force generated by the powerplant of a turbojet missile at a given flight condition. Consider the effect of

operation with each of the three intakes of different areas, shown in Fig. 61(a), at the design flight condition and at maximum throttle setting. The internal performance characteristics and the intake drag characteristics are shown in Fig. 61(b). At the engine demand corresponding to maximum throttle setting, the internal performance will increase due to reduced internal diffusion, as the intake area is increased. The intake drag will also increase due to increased intake size.

The result of these changes on the overall propulsive force on the missile is shown in Fig. 62. The opposing trends due to the effect of pressure recovery and drag combine to give a maximum propulsive force at a given intake area, for the design flight condition. The optimum area can therefore be determined.

If the purpose of the optimisation is to maximise fuel economy, a similar principle could be employed. In this case, however, the procedure would be complicated by the need to consider engine power setting for flight at the design Mach number.

Strictly speaking, of course, any optimisation of this type should be considered in the context of the effect on the total missile system and should reflect changes to the basic missile aerodynamics and to missile mass, due to a change of configuration.

## 8.2 Supersonic Missile

Many factors have a bearing on the optimisation of the powerplant of a supersonic missile. Some of these, such as intake type and position, may clarify themselves at an early stage in the design, from the need to integrate the intake with the airframe to minimise drag and to reduce the effects of missile incidence on engine performance. Others, such as the choice of shock-on-lip Mach number and the choice of intake area, may be more difficult to select, especially if the missile is to operate over a wide range of Mach number, altitude and climatic conditions.

A prime consideration, however, is that areas of unstable powerplant operation must be avoided over the whole coverage envelope of the missile.

### 8.2.1 Shock-on-Lip Mach Number

As we have seen previously, increasing the flight Mach number will cause the shock system ahead of the intake to lean back towards the cowl lip. At the shock-on-lip Mach number the shocks will, if focused, impinge on the cowl lip, reducing the pre-entry drag to zero. At Mach numbers greater than that for shock-on-lip the shock system will enter the intake.

The range of stable subcritical operation diminishes as Mach number is increased below shock-on-lip, and is generally small at this condition. Above the shock-on-lip Mach number, stable subcritical operation may not be possible. Increased shock and interaction losses will cause a reduction in potential peak pressure recovery, as illustrated in Fig. 63, and an increase in flow distortion at the engine.

It is the practice in the design of intakes for supersonic aircraft to avoid operation at Mach numbers above shock-on-lip, because of the effect of the resulting flow distortion on turbojet engine operation. Indeed, the shock-on-lip Mach number is generally chosen to be 0.2 to 0.3 above the maximum design Mach number to give an adequate stable operating range and to allow for unintentional overshoots, atmospheric temperature transients which could result in a rapid increase in flight Mach number, or manoeuvring.

A ramjet engine, however, is not as sensitive to flow distortion and is normally operated in the supercritical regime. It is therefore possible to operate above the shock-on-lip Mach number.

The best shock-on-lip Mach number for a ramjet missile required to operate with a wide Mach number variation will fall somewhere in the middle of this range. This will eliminate pre-entry drag at the higher Mach numbers and minimise it at lower Mach numbers. Cowl drag will also be reduced. The low maximum pressure recovery at Mach numbers above shock-on-lip will be of no consequence, since the choice of intake size to suit low Mach number operation will generally dictate supercritical operation under high Mach number conditions, as will be seen later.

For a ramjet powered missile controlled to operate at a fixed flight Mach number, the highest potential intake performance will be achieved if the shock system is focused on the cowl lip at that Mach number. This gives the highest possible critical pressure recovery, while reducing pre-entry drag to zero.

### 8.2.2 Intake Size : Ramjet Powered Missile

For a missile required to fly the major part of its mission at a fixed flight Mach number and altitude, the intake size may be optimised to maximise certain aspects of overall powerplant performance, such as fuel economy. This will result in operation close to the intake critical point, at the required engine flow demand and the flight Mach number in question. A margin must be allowed to avoid operation in buzz if the engine demand is increased due to throttle activity.



A common role for a ramjet powered missile is surface to air. This requires maximum thrust to give maximum acceleration and to counteract the effects of induced drag during manoeuvres. This may be achieved by operating the engine at a fuel-air ratio which gives the highest thrust while maintaining stable and efficient operation. The Rayleigh pressure, as measured by a Pitot tube mounted on the missile, will imitate the trends of supercritical mass flow variation through the air intake over a wide range of flight Mach number, altitude and incidence. Therefore, by setting the fuel flow to be a function of this pressure, an approximately constant fuel-air ratio may be obtained.

Temperature limitations on the missile structure and overall system limitations dictate that the missile speed should be limited. This limit may be based on stagnation temperature, with the fuel-air ratio being reduced, pro rata, if it is exceeded.

A missile controlled in this way will therefore operate over a wide range of flight Mach number, this varying with both altitude and climatic conditions.

Fig. 64 shows the internal performance characteristics of the air intake(s) of a hypothetical ramjet powered missile over a flight Mach number/altitude profile expected to be encountered during a mission. This varies between the Mach number at end of boost at one extreme, to the higher values obtained at altitude and during cold day operation, at the other.

The critical points occur where the kinks appear on the intake characteristics. To the right of this is the supercritical regime, while to the left is the subcritical region and the region of unstable operation encountered to the left of the buzz boundary. In many cases stable subcritical operation may not be possible, even at the lower end of the Mach number range, in which case the critical point forms the limit to stable intake operation.

At a fixed fuel-air ratio and intake area, for the same flight profile, the intake operating point may be determined from the engine characteristics, and plotted on the appropriate intake characteristic. Increasing the size of the intake will cause this matched point to move to the left, in the subcritical sense, while decreasing the size will cause more supercritical operation.

The intake size which gives maximum thrust is that which allows the engine to operate at as high a pressure recovery as possible without causing the intake to operate in regions of instability. This is most likely to occur on a cold day, when the engine flow demand at a given fuel-air ratio is reduced, and at incidence, when the critical pressure recovery of the intake is depressed and the stable subcritical margin is reduced.

Taking account of these factors the intake size may be selected so that the cold day, maximum fuel-air ratio matched intake operating point gives the minimum required margin to instability. This choice of intake size then sets the matched intake operating points at the other Mach numbers. Operation on hotter days, or at lower fuel-air ratios, will move this operating line to the right.

Several other factors might be taken into account in a design study. The effect of ramjet exhaust nozzle throat area, which controls engine air flow demand, might be studied, for example. Fuel flow scheduling, or autopilot incidence limitations, might also be considered to avoid operation in areas of instability.

Again, any optimisation should be considered in the context of overall weapon system performance.

### 8.2.3 Turbojet Powered Missile

Intake size for a supersonic turbojet powered missile may be chosen in the same manner as that for a subsonic vehicle. Optimum performance will be achieved at, or near the critical point at the design Mach number. As discussed previously, a shock-on-lip Mach number slightly higher than this normally considered necessary.

Fig. 65 shows the variation of maximum capture mass flow ratio with Mach number for a supersonic air intake. Also shown is the buzz boundary. A typical variation of required mass flow ratio, which depends on the subcritical intake pressure recovery variation, engine throttle setting and altitude is illustrated. At Mach numbers below the design value the intake will match subcritically, while above the design Mach number supercritical operation will result.

Operation on a cold day will move the operating line upwards, while a reduction in fuel flow or an increase in ambient temperature will cause a subcritical shift towards the buzz boundary.

Again, it is worth emphasising that regions of operation where distortion is high, or the flow is unstable, must be avoided throughout the whole operating envelope of the missile.

## 9. INCIDENCE SENSITIVITY

Incidence sensitivity - the reduction in pressure recovery, stable subcritical range and the increase in flow non-uniformity which results from missile incidence - is of prime importance for both turbojet and ramjet powered missiles.

The behaviour of an intake at incidence can determine the size of air intake and so determine the performance of the powerplant over the whole flight envelope. In addition the available thrust will be reduced at incidence, while the induced drag of the missile will increase. The net force available for acceleration of the missile will therefore diminish as incidence increases and deceleration will occur at high incidence. Finally, extreme non-uniformity of the flow at incidence may lead to distortion induced surge in the case of a turbojet engine, or flame extinction in the case of a ramjet engine.

The sensitivity of an air intake to incidence depends mainly on:

- (a) The position of the intake(s) on the body.
- (b) The type of air intake(s).
- (c) The intake operating condition.
- (d) The flight condition.

The incidence requirement of a missile obviously depends on its role and its aerodynamic characteristics. Broadly speaking, however, the ability of the air intakes to operate satisfactorily up to a body incidence of 10 to 20 degrees is desirable for both ramjet and turbojet powered missiles.

### 9.1 Intake Position

The position of the intake on a missile is governed not only by aerodynamic consideration of the flowfield ahead of the intake but also by system requirements, such as guidance and packaging of payload and fuel.

This section will consider some of the aerodynamic aspects of intake position. Several possible locations are illustrated in Fig. 66.

#### 9.1.1 Nose Intake

The nose of a missile is probably the best position for an air intake from the aerodynamic point of view, since it will be unaffected by the flowfield around the missile body. For a subsonic missile a Pitot intake would be employed, while for a supersonic missile the axisymmetric intake would of course, integrate best into a cylindrical missile body. The performance of this type of intake at incidence would be independent of missile roll angle, making it particularly suitable for application to missiles with cartesian control.

Despite the aerodynamic advantages of such an installation there are usually physical disadvantages that may make this type of configuration unattractive. Shortage of space in the nose of the missile may make the installation of a sufficiently large radar dish homing head impossible and the installation of other guidance devices difficult. In addition, the need for a duct through the missile body to transfer air from the intake at the front to the engine which is generally at the rear, takes up considerable internal volume and presents many problems in packaging the payload, electronics and instrumentation packages, and fuel.

#### 9.1.2 The Chin Intake

The chin intake is an air intake mounted very close to, but below the nose. This type of intake would be affected only by the flowfield at the nose of the missile. The asymmetry of the installation would, however, result in the sensitivity of the intake to incidence being dependent on the plane in which the incidence was applied. In a supersonic missile the external compression surfaces of the intake might be integrated into the nose of the vehicle.

The use of a chin intake, rather than a nose intake, allows the nose to be used for a homing head and the internal layout of the missile may be more conventional due to the offset transfer duct.

#### 9.1.3 Side Intakes

In this context, the term "side intake" is used to describe any intake mounted on the surface of a missile body and it therefore includes top and bottom mounted intakes.

The main physical advantage of the side intake is that it leaves the front part of the missile body free for payload, fuel, etc. The behaviour of a side intake depends very much on the flowfield that it is situated in. Since the flowfield around a missile at incidence is very non-uniform the position of the intake relative to the plane at which incidence is applied is a major factor in determining this.

The main features of the flowfield about a body at incidence are illustrated in Fig. 67.

As incidence is applied to a missile the crossflow will cause the boundary layer on the windward side of the body to thin and that on the leeward side to thicken. At incidences greater than about 5 degrees a separation will occur on the leeward side, moving forward as incidence is increased. A pair of stable, symmetric vortices will originate from the separation and form above the body. These sweep the boundary layer into two thickened regions on either side of the body upper surface. Very high incidences (greater than about 25 degrees) will result in an asymmetric vortex formation above the body. The flow outside the boundary layer will be retarded on the windward side of the body, will turn outward in this region and accelerate around the sides of the body, resulting in a high local mach number.

The flow around the body will also have a large effect on the local upwash. On the windward side of the body the flow will tend to be aligned with the body surface, so reducing the local upwash in this region. At right angles to the plane of incidence high upwash angles will be encountered close to the body. These will theoretically reach twice the body incidence angle at the body surface.

These effects are well illustrated by the work of Hasel (Reference 56). Fig. 68 presents the variation of boundary layer thickness and the Mach number at the edge of the boundary layer at various positions around the body measured from the incidence plane. This is for a cylindrical body with a 3.5:1 fineness ratio ogive nose, at 0, 6 and 12 degrees incidence in a Mach 2 stream. Measurements were made 4 body diameters downstream of the nose apex.

Clearly, if an air intake is positioned so that it intercepts the vortices, or the thickened or separated boundary layer produced on the upper surface of the body at incidence, the internal performance will be degraded. Similarly, the increased crossflow angles and local Mach number at the side of the missile would cause a deterioration in the performance at incidence of an intake mounted in that position. An intake mounted on the bottom surface of the body may display improved performance at incidence, due to the lower local Mach number and reduced boundary layer thickness in this region.

The effect of circumferential position on the critical pressure recovery of an air intake is shown in Fig. 69 (from Reference 56). The stable range of operation will also diminish as the intake is moved from the bottom of the body to the top.

Hasel shows a significant effect of forebody length on intake performance at incidence, particularly in the case of a top mounted intake (Fig. 70). Increasing nose length causes a deterioration in intake performance. This work indicates that an increase in boundary layer diverter height to twice the thickness of the boundary layer at zero incidence brings about only a slight improvement in intake performance at incidence.

For a missile which is subjected to major incidence variations in one plane and one direction (i.e. one roll angle) as may be encountered with twist-steer or bank-to-turn control, a single intake mounted on the windward side of the body at incidence is often considered. Twin air intakes may also be mounted so as to take advantage of the beneficial features of the body flowfield at incidence. Fig. 71 illustrates the relative merits, in terms of critical pressure recovery, of two twin intake installations at supersonic speed. Both have rectangular intake entries, with compression surfaces aligned so that increasing incidence will increase the compression. It can be seen that the installation with intakes in the lower quadrant is superior at high incidence for the reasons explained above. At moderate incidence and higher sideslip angles the radially opposed installation is better due to the shielding effect of the body in sideslip, while in negative incidence and sideslip lee-side flow effects cause the performance of intakes in the lower quadrant to deteriorate more.

If a missile has a monoplane wing the effect of incidence may be reduced by mounting the intakes beneath the wing.

#### 9.1.4 Multiple Side Intakes

Missiles with cartesian control, for example most surface to air missiles, will be subject to incidence variation in all planes. Consequently, there is no preferred position for a single intake, except of course the nose, and if a single intake were to be used its incidence sensitivity would vary with the orientation of the incidence plane. To restore symmetry, therefore, multiple side intakes are normally used in this type of configuration. The most common configuration is four intakes, mounted in-line with the wings and control surfaces.

The use of multiple intakes of this type on ramjet powered missiles frees the missile forebody allowing more efficient internal packaging. It also separates the propulsion system from the rest of the missile's systems. The current trend of using the swirl and turbulence generated by opposing streams of air entering the combustion chamber at a large angle in order to stabilise the flame removes the need for a gutter-type flameholder. This may reduce the length of combustion chamber, or alternatively allow an integral rocket boost motor to be installed more readily. The design of a more compact missile is therefore possible.

From previous considerations of the body flowfield it is apparent that each of the individual air intakes will experience different entry conditions when incidence is applied and therefore they will all match at different operating points. The stability of the flow in the combustion chamber may be dictated by the stability of the flow in any of the intakes. The intake having the most sensitivity to incidence will set a limit to powerplant performance.

Rosander, in Reference 57, outlines the development of rear mounted air intakes for a ramjet powered missile. The missile had four side intakes with ducts which entered the upstream end of the combustion chamber in a near axial direction. Pressure recovery was measured some distance downstream of the entry to the combustion chamber. Total system mass flow was also measured.

Fig. 72 illustrates the effect of roll angle on the critical pressure recovery and mass flow ratio of the intake system at 10 and 15 degrees of body incidence. A variation of about 5% on critical pressure recovery and 3% on capture was noted, with roll angle. The intake system was least sensitive to incidence when two of the intakes were close to the incidence plane and most sensitive when they were positioned 20 to 30 degrees from it. This can be attributed to the ingestion of separated forebody boundary layer and body vortices at high incidence.

The basic missile configuration had a four diameters long Von Karman nose, followed by a one diameter parallel section of body ahead of the intakes. It was designed so that vortex separation would not occur ahead of the intakes at incidences lower than 10 degrees. Fig. 73 shows the effect on intake critical point performance of moving the intakes further aft. No effect was observed at lower incidences. At higher incidences a reduction in intake performance was apparent resulting from partial ingestion of the body vortices. This effect was noted to be small in the 0 and 15 degree roll angle positions but quite large in the 30 and 45 degree positions.

Fig. 74 shows the effect of a blunt nose, as might be required to house an infra-red homing head, on intake performance. Blunting the nose produces a reduction in system performance throughout the incidence range.

The basic forebody tested by Rosander produced a local Mach number ahead of intake entry which was higher than freestream. This adversely affects intake performance by incurring increased shock losses. The forebody profile was therefore modified to limit the re-expansion of the flow to retain the freestream Mach number at intake entry. This resulted in a modified Von Karman nose, with a conical surface of 3 degrees slope just upstream of intake entry. A comparison of intake performance with the modified and basic forebodies is shown in Fig. 75. The modification produces an improvement in critical point performance of the intake over a wide incidence and Mach number range.

It is nearly always beneficial from the intake performance point of view to shape the forebody or position the intake, so that the local Mach number at entry is minimized. Such modifications may however, incur penalties in other areas, for example increased drag, and reduced internal volume.

Many other interesting features, such as the effect of intake type and diverter height, the effects of the intakes on missile stability and control, and the choice of a reference pressure signal to control the fuel flow of this type of missile are also presented in this paper.

The deleterious effects of vortex ingestion on intake performance are noted above. Two methods of alleviating this effect have been demonstrated. These are:

- (a) "inverting" the intakes to place the compression surface away from the missile body.
- (b) using strakes on the forebody to modify the body vortex pattern.

Laruelle of ONERA (Reference 58) has shown that "inverting" the intakes to move the compression surface away from the body yields a significant improvement in intake performance at incidence, compared with an intake having its compression surface adjacent to the body. This is because the effect of an ingested vortex or forebody boundary layer in disrupting flow over the compression surfaces is far more damaging to intake performance than if they pass down the intake without effecting the compression surface flow.

This effect has also been noted in tests carried out by RAE assisted by BAE using the model described in Section 4.4. Fig. 76 illustrates the benefit achieved in terms of intake stability due to inverting two types of intake, half axisymmetric and rectangular. The range of stable operation is significantly increased. The marked similarity between the shape and extent of the area of unstable operation and the range of incidence and roll angle over which experiment has indicated that the vortex impinges on the compression surface is also evident.

The effect of intake orientation on intake characteristics is shown in Fig. 77, for operation at a roll angle of 22.5 degrees where one of the upper intakes will ingest one of the forebody vortices at incidence. Inverting the intakes to bring the compression surfaces away from the body yields significant improvement in critical pressure recovery

and stable subcritical operating range at incidence.

It should also be noted that placing the cowl next to the body may allow the diverter height to be reduced giving a reduction in diverter drag.

The use of forebody strakes to prevent forebody vortex ingestion has also been investigated in France and in the United Kingdom.

Laruelle, in Reference 58 gives details of the ONERA geometry in which the strakes are located midway between the intakes as shown in Fig. 78. The beneficial effects of such an arrangement at moderate incidences are also illustrated.

The UK research suggests that strakes located in-line with the intakes may be more beneficial than those located between intakes at higher incidences. Water vapour flow visualisation on a forebody with various configuration of longitudinal strakes at Mach 1.8 have allowed the position of the vortex cores to be established at a typical intake entry station.

Fig. 79 shows how the position of the vortex varies with body roll angle at a constant incidence of 10 degrees. If no strakes are fitted the vortex position remains fixed in space as the body is rolled. When strakes are fitted, however, the vortices tend to roll with the body. Positioning intakes in line with the strakes, as at A or C, avoids vortex ingestion. Positioning the intakes between strakes, as at B, will allow vortex ingestion at this incidence.

The effect of strakes positioned in line with the intake entries on intake performance is shown in Fig. 80 for a roll angle of 22½ degrees. The improvement in intake performance and stable operating range is readily apparent.

## 9.2 Intake Type

Some general remarks may be made about the behaviour of various types of air intake in isolation to incidence or cross flow.

### 9.2.1 Subsonic Intakes

#### 9.2.1.1 Pitot Intake

-----

The deterioration of the flow quality within a Pitot intake at incidence is due to a separation occurring on the internal surface of the windward cowl lip (Fig. 81). In this respect the mechanism is similar to the low speed entry losses described previously and is similarly highly dependent on the internal profile of the cowl lip (or lip bluntness) and the Mach number in the intake throat.

Boundaries between attached and separated flow at the cowl lip are shown for an axisymmetric Pitot intake with a high contraction ratio, from Reference 59. For a given freestream Mach number the incidence at which separation occurs can be increased by reducing the throat Mach number (or the velocity ratio between throat and freestream conditions). This reduces the local peak velocities in the flow accelerating around the cowl lip and the severity of the subsequent recompression.

Reducing the contraction ratio will cause separation to occur at a lower throat velocity ratio (i.e. the curves will shift to the left).

#### 9.2.1.2 Flush Intake

-----

The performance of a flush intake cannot be divorced from the flowfield on the body in which it is mounted.

Assuming the intake to be mounted in the undersurface of a missile body, the pressure recovery will improve in positive incidence, due to the increased "ram" effect and to a reduction in boundary layer thickness on the body surface, as shown in Fig. 82. Negative incidence will have the opposite effect as the boundary layer thickens and an increased amount is ingested by the intake. At higher negative incidences the missile vortex flowfield will sweep the boundary layer away from the path of the intake and this, together with the upwash induced by the vortices will cause the internal performance to improve.

Very little data is available on the effect of cross flows (i.e. sideslip) on this type of configuration, most being concerned with intakes semi-submerged in an aircraft nose (e.g. Reference 60). This indicates a 5% reduction in pressure recovery with a 10 degree cross flow. A bigger reduction might be expected for a fully submerged intake.

### 9.2.2 Supersonic Intakes

At supersonic speeds changes in local flow direction ahead of the intake will affect the geometry and the strength of the intake shock structure, as well as changing the angle the incident flow makes with the cowl lip, or intake sidewall. Since the effect of incidence on maximum capture is generally less than its effect on pressure recovery, the intake operating point will generally tend to move in the subcritical sense as incidence is applied, as shown in Fig. 83.

### 9.2.2.1 Pitot Intake

As with a subsonic Pitot intake this may suffer from internal flow separation from the windward cowl lip at incidence. An increased lip radius will prove beneficial and increased forespill will both decrease velocities around the inside of the cowl lip and reduce the incident flow angle on the cowl lip.

### 9.2.2.2 Two-Dimensional Intake

The sensitivity of this type of intake to cross-flow depends whether the incidence variation is normal to the plane of the compression surfaces, or parallel to it.

#### (a) Incidence Normal to Plane of Compression Surface

In this case, as shown in Fig. 84, incidence variation will result in changes to the intake pressure recovery and capture mass flow ratio due to symmetric or planar movement of the shock system, as the effective compression surface angle changes. The oblique shock strengths will increase with increasing incidence giving a reduced Mach number ahead of the cowl shock, thus causing it to reduce in strength. Maximum capture and critical pressure recovery may increase initially as positive incidence is applied, before falling as the cowl lip shock, and possibly the second oblique shock, detaches. It should be noted that a small positive incidences the value of maximum capture mass flow ratio, based on conditions at intake entry, may exceed unity due to the effective increase in intake entry area at incidence (see Fig. 84).

In negative incidence the deceleration through the oblique shocks will reduce. The increased Mach number ahead of the cowl shock will produce increased losses due to an increase in shock strength and to shock-boundary layer interaction. Capture mass flow ratio will also be reduced.

The deterioration in performance will therefore be greater in negative incidence than in positive incidence.

#### (b) Incidence Parallel to Plane of Compression Surface

If incidence is applied parallel to the intake compression surface (i.e. at right angles to the previous case) the external shock system will be distorted, as shown in Fig. 85. Flow expanding round the windward sidewall will increase the local Mach number in this region, causing the ramp shock to approach the cowl lip, while the opposite sidewall will create a compressive flowfield, and the opposite will occur. The shock patterns that exist under these conditions have been studied experimentally by Nangia (Reference 61).

Reduced performance under these conditions may arise for several reasons. Flow may separate from the sharp swept leading edge of the windward sidewall, which is akin to a delta wing at incidence. Alternatively, separation may occur on the internal surface of this sidewall due to coalescence and strengthening of the distorted shock system in this region. In addition the oblique shock may be deformed sufficiently to enter the intake giving increased shock losses. These features will also cause increased flow non-uniformity and unsteadiness.

A significant improvement in the cross-flow capability of this type of intake may be achieved by removing the sidewall completely, as tested in Reference 62 and illustrated in Fig. 86. This will reduce distortion of the shock system and remove any surface on which boundary layer separation might have occurred. At the same time the diverging flowfield due to lateral spillage will reduce the effective local incidence on the windward sidewall, reducing the likelihood of internal flow separation at this point.

Such a measure would, however, incur a significant increase in intake drag, due to the side spillage, together with a decrease in the pressure recovery at zero incidence.

### 9.2.2.3 Axisymmetric and Half-axisymmetric Intakes

In the absence of effects due to body flowfields the axisymmetric and half-axisymmetric intakes will behave in a similar manner.

The conical shock structure will deform under cross-flow conditions as shown in Fig. 87. The boundary layer will thicken on the leeward side of the cone, and become more prone to separation under the action of the cowl shock. This will result in reduced pressure recovery and stable subcritical operating range, and increased flow distortion and unsteadiness.

### 9.2.2.4 Mixed Compression Intakes

The mixed compression intake will in general behave in a similar manner to its external compression counterpart. Change in the internal shock structure due to incidence, however, is likely to provoke unstart, resulting in a rapid degradation in performance as incidence is increased.

## 10. AERODYNAMIC CHARACTERISTICS OF AIRBREATHING MISSILES

Typically the total intake entry area for an airbreathing tactical missile may be one quarter to one half of the cross sectional area of the missile forebody. Consequently the intakes and their associated nacelles or fairings will provide a significant contribution to the aerodynamic forces and moments acting on the missile.

The missile aerodynamicist needs to be able to quantify these effects to allow realistic estimates of weapon performance to be made in preliminary studies. Because of the large number of possible options for integrating a missile propulsion system, choice of steering policy, etc., it is often necessary to carry out comparative studies in order to determine the best option.

Once a suitable configuration has been selected the aerodynamic characteristics must be defined, and refined if necessary for autopilot design and to allow modelling of the missile and guidance in order to evaluate its performance as part of the weapons system.

Prediction techniques have been evolved for determining forces and moments on airbreathing missiles, particularly at supersonic speeds. Semi-empirical component build-up methods, and computation fluid dynamic techniques are described elsewhere in this course. These techniques have been derived and/or validated using experimental data.

This section of the paper describes some of the techniques used to obtain forces and moments from wind tunnel model tests, notes the details of some of the published and unpublished work, and provides an indication of the trends and salient features of the aerodynamic characteristics so obtained.

### 10.1 Models, Measurements and Corrections

Considerable care is required in the design of a wind tunnel model of an airbreathing missile and in the interpretation of the results obtained to ensure that they are correct and meaningful. Fig. 88 illustrates the main features of a generalised research model.

Flow enters the intakes and passes along an annular passage around the sting to exhaust at the rear of the model. Forces and moments are measured using a six component balance. It is important that the pre-entry flowfield is representative of that on the proposed flight vehicle. This implies high dimensional accuracy in the intake entry geometry and correct intake operation over the complete flight regime or alternatively a known datum operating condition from which corrections may be made. For supersonic missiles supercritical operation is a convenient (and for ramjets usually representative) operating condition.

Intake operating conditions are generally governed by a sonic throat formed by a fixed or variable contraction at the rear of the model. This contraction may either be built into the metric part of the model, or mounted on the sting. It is important that there is adequate flow area to ensure that supercritical operation can be obtained over the required regime of speed, incidence and roll angle.

The internal ducting should be leak free, and designed to minimise total pressure loss through the system. It is important that the flow does not impinge on non-metric components such as the sting in such a way as to generate forces and moments that are not representative and cannot be accounted for in the analysis of results. Hence for the model shown, the sting is protected by a shroud.

The forces and moments measured by the balance will include contributions due to the momentum change of the internal flow in the appropriate direction. Thus for an axial exit the measured normal force:

$$N_{\text{balance}} = N_{\text{ext}} + \dot{m} V_{\infty} \sin \sigma$$

where  $N_{\text{ext}}$  is the normal force excluding intake momentum effects  
 $\dot{m}$  is the intake mass flow  
 $V_{\infty}$  is the freestream velocity  
 $\sigma$  is the incidence

Similarly pitching moment:

$$M_{\text{balance}} = M_{\text{ext}} + \dot{m} V_{\infty} \ell$$

when  $\ell$  is the moment arm of the inlet momentum effects.

This moment arm is difficult to ascertain for most side intake configurations since, taking account of the body flowfield, it is not easy to determine the location of the entry streamtube upstream of the model.

Finally axial force:

$$X_{\text{balance}} = X_{\text{ext}} + X_{\text{int}} + X_{\text{base}}$$

where  $X_{\text{int}}$  is the internal drag and  $X_{\text{base}}$  is the base drag.

Internal drag is obtained from a momentum balance between conditions in the capture streamtube well upstream of the model, and conditions at exit. In the case of the model shown in Fig. 88 an array of Pitot probes, and associated static tappings were mounted on the sting and used to estimate mass flow and stream force at a station close to the exit. This estimate was calibrated to give accurate mass-flow and axial force using the Mach Simulation Tank (MST) at the Aircraft Research Association, Bedford. If a static calibration rig of this type had not been available it would have been necessary to use the stream force estimated at the rake position and correct this to exit conditions by estimating the skin friction drag on the metric part of the duct downstream of the rake position. For a less accurate measurement (often unavoidable on smaller models) the internal momentum loss may be determined from choked exit flow, and upstream Pitot or static pressure measurements.

Base drag must be corrected for since the base geometry of the model will be unrepresentative of the flight vehicle. In the model of Figure 88 static pressure probes, situated in close proximity of the base, were used to determine this. The base was recessed to ensure a near constant pressure distribution across the surface. Axial force due to balance cavity pressure is also included in this term. Incremental drag effects associated with the correct geometric representation of the afterbody, absence of a sting, and the correct jet pressure ratios have to be measured on a separate model if accurate evaluation of drag is essential (e.g. long range missiles, Reference 6)).

Skin friction drag must be corrected from tunnel to flight conditions by deducting estimated wind tunnel values and replacing with estimated flight values.

It should be noted that the force and moment measurements described above will include pre-entry effects (normal force, moment, axial force) existing at the Mach number, incidence, roll angle and intake operating condition at which the tests were conducted.

## 10.2 Longitudinal and Lateral Aerodynamic Characteristics

### 10.2.1 Twin Intake Configurations

Following wind tunnel tests in connection with a range of airbreathing missile programmes the NASA Langley Research Centre developed in 1977 a model that would enable a wide range of airbreathing missile configurations to be tested.

Configurations (Fig. 89) included single and twin axisymmetric and two-dimensional air intakes. The twin intakes could be mounted on the body at 0, 25 and 45 degrees to the horizontal. A monoplane wing could be mounted at various positions and triform and cruciform tail configurations could be adopted. Tests were carried out at subsonic Mach numbers with the intakes faired, and at Mach numbers 2.5 to 3.95 with internal flow. Since the configurations were intended to represent air-to-air missiles with bank-to-turn steering, tests were only carried out at zero and 3 degrees of sideslip.

Results of the tests are contained within References 64, 65, 66, 67 and main points summarised in Reference 68. This reference indicates that the twin intake configurations tested exhibited a trend of near neutral longitudinal stability at low incidences, increasing rapidly at high incidence. Rotating intakes downward about the centreline tended to decrease the longitudinal stability and increase the directional stability, while a cruciform X-tail was found to give overall benefits in stability terms compared with inverted and upright triform tails.

In an attempt to clarify the flow around the model, oil flow visualisation tests were performed for both twin axisymmetric and rectangular intake configurations as described in Reference 69. This work indicated subcritical intake operation at Mach 2.5 with extensive spillage at zero incidence, evidenced by shock impingement on the body, for the axisymmetric intake and signs of subcritical spillage occurring at 6 degrees of incidence for the two dimensional intakes (Both arranged horizontal). Crossflow separation lines were identified on both the forebody and the intake fairings, with a complex vortex pattern establishing itself on the windward as well as the leeside of the intake boattail at incidence. Further work was planned to investigate these using vapour screen techniques.

RAE and British Aerospace have also explored the aerodynamic characteristics of twin intake configurations using the model shown in Fig. 88. This model is of modular construction to allow the representation of various types, sizes, number and location of intakes to be tested, either in conjunction with various wings and tails, or in isolation.

The effect of flow direction for twin half axisymmetric intakes mounted diametrically opposite one another is shown in Fig. 90. At zero roll angle the normal force produced is approximately twice that of the body alone. For rectangular intakes approximately triple the body-alone normal force is produced. It is interesting to note that for a roll angle of 90 degrees (i.e. sideslip) the normal force is lower than that for the body alone due to the streamlining effect that the intakes have an crossflow drag.

The effect of flow direction for twin half axisymmetric intakes mounted ventrally at 45 degrees to the missile axis of symmetry is shown in Fig. 91. For this configuration the normal force is approximately one and a half times that of the body alone, and is



approximately double the body alone value for rectangular intakes. A greater normal force is achieved when the intakes are on the windward side (roll angle zero) compared with the leeward side (roll angle 180 degrees). The small finite normal force at zero incidence is apparent.

The tendency toward reduced stability in pitch and increased stability in yaw, as the intakes are rotated downwards from the opposed to the ventral position, noted by Hayes is also apparent in these results.

#### 10.2.2 Four Intake Configurations

Reference 70 describes a series of wind tunnel tests carried out on  $\frac{1}{2}$  and  $\frac{1}{3}$  scale models of the VOUGHT ALVRJ between 1967 and 1972. Tests were performed at transonic and supersonic speeds up to Mach 3.2, and included component build up tests to evaluate the relative contributions of body, intakes, tail controls and cable ducts. The significant effect of the intake ducts to both normal force and pitching moment is reproduced in Fig. 92. The configuration had four rectangular intakes of total capture area approximately 0.4 of the body cross sectional area, located approximately  $6\frac{1}{2}$  calibres from the nose.

Champigny of ONERA (Reference 71) presents a range of information illustrating the effect of intake span, length, number, type, roll angle and afterbody shape on normal force and centre of pressure position for configurations with three and four intakes at incidences up to 7 degrees. Many of these trends shown by Champigny have been noted in the experimental research carried out by RAE and British Aerospace.

The advantages of sharp cornered rectangular intakes and fairings over rounded half axisymmetric intakes in the generation of normal force is highlighted in Fig. 93. The effect of increasing length of the intake nacelle on normal force and centre of pressure position is shown in Fig. 94. The effect is small at low incidence, as noted by Champigny. At higher incidences, however, the larger intakes give a significantly increased contribution to normal force as the crossflow drag effects dominate.

Fig. 95 illustrates, for a 4 half-axisymmetric intake configuration, the normal force and centre of pressure position of each of the major missile components as incidence is varied.

### 11. DRAG

The contribution of the intakes and associated fairings to the overall zero incidence drag of the missile is large, typically 30 to 40 per cent. The breakdown of drag for a 4 intake ramjet powered missile into main components is shown in Fig. 96. A significant proportion of the intake drag emanates from the cowl, the diverter, and the intake pre-entry flowfield, as noted in Fig. 97.

#### 11.1 Cowl Drag

Cowl drag may be measured using pressure tappings and integrating the pressure distribution over the surface, or more rarely through a component balance. Wind tunnel measurements of cowl drag are described in Reference 72 for rectangular cowls, and Reference 73 for axisymmetric cowls.

A comprehensive discussion of various methods of cowl drag prediction is presented in Reference 74.

#### 11.2 Diverter Drag

The wave drag of a boundary layer diverter system at supersonic speed is a function of diverter wedge angle, local Mach number and boundary layer immersion, as shown in Fig. 98 (Piercy and Johnson, Reference 75). As might be expected the wave drag coefficient increases significantly with increasing diverter wedge angle but is weakly dependent on upstream Mach number. It is also shown that the drag coefficient increases with decreasing boundary layer immersion. (i.e. increasing diverter height relative to the boundary layer). It should be noted that in all cases the drag coefficient is based on the diverter frontal area.

Other drag components associated with the diverter are the skin friction drag and interference drag.

Typically, wave and skin friction drag may contribute about 5% to 10% of the total drag of an air breathing missile. Reference 76, however, suggests that in certain cases the diverter may contribute as much as 30% due to interference of the exit flow with the missile flowfield if care is not taken in the detail design to minimise these effects. (See Section 11.7).

At subsonic speeds, as at supersonic speeds, a slender diverter has been demonstrated to be beneficial in reducing diverter pressure and interference drag and hence overall vehicle drag, as illustrated in Reference 77.

Typically, the overall drag coefficient of a wedge type boundary layer diverter at subsonic speeds is of the order of 0.25 (based on frontal area) as shown in Reference 78.

It can be seen from Section 4 and this Section that a trade-off is possible between the drag of the boundary layer diverter and the effect of internal performance gains reflected by increased thrust. Therefore within the constraints set by the need to maintain a certain level of flow uniformity and steadiness within the air intake, the diverter height may be optimised to maximise powerplant performance.

Typical diverter heights suggested by various sources range from 0.7 to 1.5 of the zero incidence body boundary layer thickness.

### 11.3 Pre-Entry Drag

The propulsive force generated on a ducted body due to the air flow passing through it,  $F_p$ , is equal to the difference between the sum of the momentum and pressure forces acting on planes normal to the internal flow at the entry and exit of the duct. Thus, referring to Fig. 99

$$F_p = m_{ex} V_{ex} + (P_{ex} - P_o) A_{ex} - m_o V_{in} + (P_{in} - P_o) A_{in}$$

The assumption has been made, for the sake of simplicity, that the body is at zero incidence, and that the entry and exit planes are normal to the body axis.

For generality, the propulsive force generated by an air breathing engine is normally expressed as a Nett Thrust,  $X_N$ , this being the exit (gross) thrust less the inlet momentum drag (the momentum of the air entering the engine, when this is at freestream conditions).

$$\text{Thus } X_N = m_{ex} V_{ex} + (P_{ex} - P_o) A_{ex} - m_o V_o$$

$X_N$  and  $F_p$  are only the same when freestream conditions exist right up to intake entry. The difference is the momentum and pressure force change through the pre-entry compression flowfield, between freestream and the intake cowl lip station. It is known as the PRE-ENTRY DRAG.

$$D_{PRE} = m_o V_{in} + (P_{in} - P_o) A_{in} - m_o V_o$$

A similar analysis will show that if compression surfaces are situated upstream of the cowl, as shown in Fig. 100, the pre-entry drag will be given by

$$D_{PRE} = [m_o V_{in} + (P_{in} - P_o) A_{in}] \cos \theta - m_o V_o + F_{comp}$$

where  $F_{comp}$  is the drag force on the compression surfaces upstream of the cowl.

Consider the control volume defined by the pre-entry streamtube, the compression surfaces and planes at the cowl lip and freestream conditions. For this to be in equilibrium the change of momentum of the flow passing through it must equate to the pressure forces acting on it.

$$\text{Thus } D_{PRE} = \int_0^{in} (P_{sL} - P_o) \delta A$$

where  $\delta A$  is the projection of an element of streamtube area acted upon by  $p_{sL}$

The pre-entry drag is therefore equivalent to the force due to the pressure acting on the pre-entry streamtube in an axial direction. It is the drag force associated with spilling excess air around the intake entry.

The magnitude of the pre-entry drag will depend on the flight Mach number and the intake capture mass flow ratio. A typical variation of pre-entry drag with flight Mach number for a supersonic intake operating supercritically is shown in Fig. 101. The spillage of air is, in this case, a result of the position of the external oblique shock system. The degree of spillage reduces as the shockwaves sweep back towards the cowl lip with increasing flight Mach number, resulting in a reduction in pre-entry drag coefficient. When the first shockwave enters the cowl lip, the pre-entry drag will be zero.

At a given flight Mach number the pre-entry drag coefficient of a supersonic air intake will increase rapidly with reducing capture mass flow ratio, as subsonic spillage takes place between the normal shockwave and the cowl lip at a high static pressure. At subsonic speeds the rate of increase will be lower. This is illustrated in Fig. 102.

#### 11.3.1 Calculation of Pre-Entry Drag

Pre-entry drag may be calculated using either of the equations set out in the previous section.

At subsonic speeds the pre-entry drag may best be estimated using the momentum relationship. If external compression surfaces are present the drag on these must be estimated, by using an average pressure, between the apex and the cowl lip, as suggested in Reference 79. Alternatively, experimental results relating to the drag or pressure distribution over cones and wedges may be employed.

For a supersonic intake and critical and supercritical operation, it may be easier to compute the external flowfield, and conditions along the pre-entry streamtube.

This is particularly easy in the case of a two dimensional air intake with attached shockwaves, since the flowfield may be computed using shock tables.

Data sheets presenting the critical internal performance and drag of such an intake are contained in Reference 80, with due allowance for the corrections for sidespill and ramp boundary layer discussed in Section 5.

Tables of values of pre-entry drag coefficient and mass flow ratio for inlets having single conical compression surfaces are presented in Reference 41. These will apply to both half axisymmetric and axisymmetric air intakes.

As shown in Section 5 the flowfield generated by more than one conical compression surface is complex, and computation of the capture mass flow ratio and pre-entry drag would be tedious and not amenable to hand calculation.

For an intake in subcritical operation a knowledge of the terminal shockwave position is pre-requisite for the determination of pre-entry drag. This may be derived as outlined in Section 5. The pressure on the streamline downstream of the normal shockwave will vary between the shock and the lip. The pressure just downstream of the shock may be determined from the shock strength and assumed to act on the streamtube between the shock and the cowl lip. The pressure just downstream of the shock may be determined from the shock strength and assumed to act on the streamtube between the shock and the cowl lip.

Reference 81 notes good agreement between the subcritical pre-entry drag calculated in this manner and wind tunnel measurements. This was for a two dimensional, three ramp, external compression intake.

#### 11.4 Spill Drag

The overall change in the drag of the intake due to reducing mass flow ratio from a datum value is known as spill drag. It is normally attributed to the powerplant, (i.e. a thrust decrement) rather than the airframe, since it may vary with engine operating condition.

For most intake configurations the drag penalty incurred by spilling the approaching air flow around the cowl lip is less than the calculated pre-entry drag. This is because some of the pre-entry drag is cancelled by an increased cowl thrust generated by regions of suction occurring on the cowl leading edge. This is a similar phenomenon to the leading edge suction peaks found on an aircraft wing at incidence. In inviscid, irrotational flow it may be shown that theoretically the cowl thrust will completely cancel the pre-entry drag, resulting in zero spill drag.

Fig. 103 illustrates the typical variation of spill drag coefficient as mass flow ratio is reduced at high subsonic Mach number. Two examples are shown: an axisymmetric air intake with a cowl lip designed for subsonic operation and an air intake with a sharp cowl lip. Also shown is the variation of theoretical pre-entry drag coefficient.

It can be seen that the axisymmetric subsonic intake (typically with a NACA 1-series cowl profile) displays near zero spill drag until low mass flow ratios are reached. This is because the cowl thrust is very nearly equal to the pre-entry drag, i.e. close to the theoretical inviscid condition. A sharp cowl lip, on the other hand, is unable to sustain a large leading edge suction and the cowl thrust is small. The spill drag of this configuration is therefore much closer to the theoretically predicted pre-entry drag.

It should be emphasised that the remarks above refer to an incremental change in drag from a datum condition, often taken as unity mass flow ratio at subsonic speeds and maximum capture mass flow ratio at supersonic speeds.

Reference 82 notes that several investigations have shown that axisymmetric conical compression intakes have less drag than two dimensional ramp inlets with equal throat/capture area ratios and equivalent ramp or cone angle. This characteristic is explained by the relief provided by the three dimensional spillage of the cone resulting in lower flow spillage angles, i.e. the flow deflection is less than the two dimensional configurations, resulting in lower drag.

In order to determine the spill drag of an intake configuration it is necessary to resort to wind tunnel experiment. Methods of measuring spill drag of air intakes at transonic speeds are discussed in Reference 83, while a technique for measuring the cowl and pre-entry drag, using a metric intake entry section, is described in Reference 84. Reference 29 also covers this topic in some detail.

#### 11.5 Normal Force Due to Spill

Intakes which are not symmetric, such as those with two dimensional, or half conical supersonic compression surfaces, will generate a significant normal force towards the compression surface due to spillage. The magnitude of this force may be estimated in the same manner as pre-entry drag but considering the momentum change normal to the intake axis. Again, some alleviation will derive from cowl suction effects.

Therefore, a supersonic missile with this type of intake mounted under the body, or at the side with the compression surfaces facing downwards, will generate spill lift at zero incidence at Mach numbers below shock-on-lip, or when operating in the subcritical regime.

Even a Pitot intake mounted ventrally on a missile body will generate a small spill lift due to the increased pressure imposed on the body by the pre-entry flowfield as mass flow ratio is reduced.

#### 11.6 Internal Boundary Layer Bleed Drag

As shown in Section 4 internal boundary layer bleed may prove to be beneficial in improving the internal performance and flow quality of an intake. There will, however, be a drag penalty from such a system which must be set against the gain in internal performance in any optimisation study. The drag penalty arises mainly from the loss in momentum of the bleed air as it passes through the system from intake entry to bleed exhaust, as shown in Fig. 104.

$$\text{Thus } D_{\text{BLEED}} = m_B V_o - F_{\text{ex}} + D_{\text{FAIRING}}$$

$$\text{where } F_{\text{ex}} = m_B V_{\text{ex}} + (p_{\text{ex}} - p_o) A_{\text{ex}}$$

It may be calculated from a knowledge of the amount of bleed flow, the total pressure loss through the bleed system and conditions existing at the bleed exhaust. Additional drag will arise from the exhaust nozzle fairing,  $D_{\text{FAIRING}}$  and interference of the exit flow with the flow over the missile.

#### 11.7 Interference Drag

Experiment has shown that there may be a significant drag effect arising from interference of the flow between adjacent intakes. Figure 105 illustrates this. Drag was derived from a configuration where no mutual interference was possible, and a four intake configuration where the flow around adjacent intakes could interact.

#### REFERENCES

1. Curran, E.T., Stull, F.D., Ramjet engines - Highlights of past achievements and future promise. 2nd International Symposium on Air Breathing Engines (1974).
2. Myers, T.D., Special Problems of Ramjets with Solid Fuel, AGARD LS 136 (1984).
3. Dengler, R.P., Macioce, L.E., Small, low-cost, expendable turbojet engine. 1 - Design, fabrication and preliminary testing. NASA TM X-3392 (1976).
4. Wills, T.K., Wise, E.P., Development of a new class of engine - the small turbofan. AIAA Paper No. 76-618 (1976).
5. Baals, D.D. et al, The development and application of high-critical-speed nose inlets. NACA Rep 920 (1948).
6. Re, R.J., An investigation of several NACA 1 - SERIES axisymmetric inlets at Mach numbers from 0.4 to 1.29. NASA TM X-2917 (1974).
7. Mossman, E.A., Randall, L.M., An experimental investigation of the design variables for NACA submerged duct entrances. NACA RM A7130 (1947).
8. Simon, P.C., Performance of a double ramp side inlet with combinations of fuselage, ramp and throat boundary layer removal - Mach number range 1.5 to 2.0. NACA RM E56G09a (1956).
9. Brown, C.S., Goldsmith, E.L., Measurement of the internal performance of a rectangular air intake with variable geometry at Mach numbers 1.7 to 2.5. RAE TR 71159 (1971).
10. Wittliff, C.E., Byrne, R.W., Preliminary investigation of a supersonic scoop inlet derived from a conical spike nose inlet. NACA RM E51G11 (1951).
11. Goldsmith, E.L., Brown, C.S., Effect of boundary layer bleed on the internal performance of two half-axisymmetric air intakes with conical compression surfaces at Mach numbers between 1.8 and 2.4. RAE TR 72143 (1972).
12. Goldsmith, E.L., Griggs, C.F., The estimation of shock pressure recovery and external drag of conical centrebody intakes at supersonic speeds. ARC R & M 3035 (1953).
13. Allen, J.L., Mitchell, G.A., Performance of a Mach number 3.0 design axisymmetric double cone external compression inlet in the Mach number range 2.07 to 1.48. NASA Memo 12-222-58E (1958).
14. Comenzo, R.J., Mackley, E.A., Preliminary investigation of a rectangular supersonic scoop inlet with swept sides designed for low drag at a Mach number of 2.71. NACA RM L52J02 (1952).

15. Smeltzer, D.B., Sorensen, N.E., Investigation of a large scale mixed compression inlet system capable of high performance at Mach numbers 0.6 to 3.0. NASA TM X-1507 (1968).
16. Fradenburgh, E., Wyatt, D.D., Theoretical performance characteristics of sharp-lip inlets at subsonic speeds. NACA Report 1193 (1954).
17. Blackaby, J.R., Watson, E.C., An experimental investigation at low speed of the effects of lip shape on the drag and pressure recovery of a nose inlet in a body of revolution. NACA TN 3170 (1954).
18. Scherrer, R., Anderson, W.E., Preliminary investigation of a family of diffusers designed for near sonic inlet velocities. NACA TN 3668 (1966).
19. Goldsmith, E.L., The effect of internal contraction, initial rate of subsonic diffusion, and cowl and centrebody shape on the pressure recovery of a conical centrebody intake at supersonic speeds. Unpublished MOD(PE) material.
20. Brown, A.C., Nawrocki, H.F., Paley, P.N., Subsonic diffusers designed integrally with Vortex generators. AIAA Paper no. 67-464 (1967).
21. Wong, W.F., Application of boundary layer blowing to suppress strong shock induced separation in supersonic inlets. AIAA 77-147 (1977).
22. Oswatitsch, K., Pressure recovery for missiles with reaction propulsion at high supersonic speeds. NACA TM 1140 (1947).
23. Pearcy, H.H., Shock induced separation and its prevention by design and boundary layer control. In: Boundary Layer and Flow Control. Lachmann ed. Pergamon Press (1961).
24. Stanbrook, A., An experimental study of the glancing interaction between a shockwave and a turbulent boundary layer. ARC CP No. 555 (1961).
25. Leynaert, J., Fonctionnement du piege a couche limite interne d'une prise d'aire a compression supersonique externe. In: AGARDagraph 103 (1965).
26. Syberg, J., Koncsek, J.L., Bleed system design technology for supersonic inlets. AIAA Paper 72-1138 (1972).
27. Seddon, J., Boundary layer interaction effects with particular reference to those designed for dual subsonic and supersonic performance. ARC R & M 3565 (1966).
28. Piercy, T.G., Johnson, H.W., A comparison of several systems of boundary layer removal ahead of a typical conical external compression side inlet at Mach numbers of 1.88 and 2.93. NACA RM E53F16 (1953).
29. Carter, E.C., Experimental determination of inlet characteristics and inlet and airframe interference. AGARD-LS-53 Paper 3 (1972).
30. Faro, T.D.V., Keirse, J.L., Ramjet Technology - Section on flow processes and engine performance. TG 610-3B (1967).
31. Geissler, W., Calculation of potential flow about axially symmetric fuselages, annular profiles and engine inlets. NASA TF F 15213 (1973).
32. Ferri, A., Application of a method of characteristics to supersonic rotational flow. NACA RPT 841 (1946).
33. Anderson, B.H., Design of supersonic inlets by a computer program incorporating the method of characteristics. NASA TN 4960 (1969).
34. Kutler, P., Lomax, H., Shock-capturing, finite difference approach to supersonic flows. J. Spacecraft Vol. 8 No. 12.
35. Presley, L.L., Internal flow calculations for axisymmetric supersonic inlets at incidence. AIAA 75 1214 (1975).
36. Reyhner, T.A., Hickcox, T.E., A procedure for combined viscous-inviscid analysis of supersonic inlet flowfields. AIAA 72-44 (1972).
37. Moekel, W.E., Approximate method for predicting form and location of detached shockwaves ahead of plane or axially symmetric bodies. NACA TN 1921 (1949).
38. Rosenhead, L., et al, A selection of graphs for use in calculations of compressible airflow. Oxford University Press (1954).
39. McGregor, I., Some theoretical parameters relevant to the performance of rectangular air intakes with double-ramp compression surfaces at supersonic speeds. RAE TR 71232 (1971).
40. Bryce, J.D., Cocking, B.J., Some effects of Reynolds number on the performance of an air intake proposed for Concorde. NGTE Report R 304 (1968).

41. Mascitti, V.R., Charts of additive drag coefficient and mass flow ratio for inlets utilising right circular cones at zero angle of attack. NASA TN D3434 (1966).
42. Hermann, R., Supersonic inlet diffusers and introduction to internal flow. Minneapolis-Honeywell Regulator Co. (1956).
43. Fuhs, A.E. (ed), Distortion induced engine instability. AGARD-LS-72 (1974).
44. Burcham, F.W., et al, Steady state and dynamic pressure phenomena in the propulsion system of an F-111A airplane. NASA TN D 7328 (1973).
45. Borg, R., A synthesis method for estimating maximum instantaneous inlet pressure distortion based on measured inlet steady state and RMS pressures. AGARD CP 301 (1981).
46. Inlet total pressure distortion considerations for gas turbine engines. SAE AIR 1419 (1983).
47. Bendot, J., et al, Ramjet air induction system design for tactical missile application. AGARD LS 136 (1984).
48. Sterbentz, W.H., Davids, J., Amplitude of supersonic diffuser flow pulsations. NACA RM E52I24.
49. Ferri, A., Nucci, L.M., The origin of aerodynamic instability of supersonic inlets at subcritical conditions. NACA RM L50K30 (1951).
50. Sterbentz, W.H., Evvard, J.C., Criterion for prediction and control of ramjet flow pulsations. NACA RM E51C27 (1951).
51. Dailey, C.L., Supersonic diffuser instability. Journal of the Aeronautical Sciences, Vol. 22 No. 11 (1955).
52. Hall, G.R., A criterion for prediction of airframe integration effects on inlet stability with application to advanced fighter aircraft. AGARD-CP-150 Paper 2 (1974).
53. Martin, N.J., Holzhauser, C.A., Analysis of factors influencing the stability characteristics of symmetric twin-intake air-induction systems. NACA TN 2049 (1950).
54. Beke, A., Criteria for initial flow reversal in symmetrical twin-intake air-induction systems operating at supersonic speeds. NACA RM E55L02a (1955).
55. Krohn, E.O., Triesch, K., Multiple Intakes for Ramrockets. AGARD CP 307 (1982).
56. Hasel, L.E., The performance of conical supersonic scoop inlets on circular fuselages. NACA RM L53I14a (1953).
57. Rosander, G., Development of aft inlets for a ramjet powered missile. 1st International Symposium on Air Breathing Engines (1972).
58. Laruelle, G., Comparaison de Differentes Configurations d'Entree d'Air de Missiles Supersoniques. AGARD CP 307 (supp) (1982).
59. Goldsmith, E.L., Private communication (1978).
60. Braden, J.A., Pierpont, P.K., Pressure and force characteristics at transonic speeds of a submerged divergent-walled inlet on a body of revolution. NACA RM L53C13 (1953).
61. Nangia, R.K., Three dimensional wave interactions in supersonic intakes. 2nd International Symposium on Air Breathing Engines (1974).
62. Brown, C.S., Goldsmith, E.L., Measurement of the internal performance of a rectangular air intake mounted on a fuselage at Mach numbers from 1.6 to 2.0. RAE TR 72136 (1972).
63. Brunner, P.W., et al, Development of the Integrated Propulsion System for the AGM-86A Air Launched Cruise Missile. AIAA 76-916.
64. Hayes, C., Aerodynamic characteristics of a series of single inlet airbreathing missile configurations. NASA TM 84557 (1983).
65. Hayes, C., Aerodynamic characteristics of a series of twin inlet air breathing missile configurations. I - Axisymmetric inlets at supersonic speeds. NASA TM 84558 (1983).
66. Hayes, C., Aerodynamic characteristics of a series of twin inlet air breathing configurations. II - Two-dimensional inlets at supersonic speeds. NASA TM 84559 (1983).
67. Hayes, C., Aerodynamic characteristics of a series of twin inlet air breathing missile configurations. III - Axisymmetric and two-dimensional inlets at subsonic - transonic speeds. NASA TM 84560 (1983).

68. Hayes, C., Aerodynamic Characteristics of a series of air breathing missile configurations. 12th Navy Symposium on Aeroballistics (1981).
69. Stoy, S.L., et al, Correlation and analysis of oil flow data for an air breathing missile model. AIAA 85-0452.
70. Prilliman, F.W., Francis, H.L., Aerodynamic and flight characteristics of the air launched low volume ramjet ALVRJ (vehicles). AIAA 80-0375.
71. Champigny, P., Problemes Lies a l'Aerodynamique Externe des Missiles Aerobies. AGARD CP-336 (1982).
72. Goldsmith, E.L., et al, The internal performance and external drag of some weapon intakes. AGARD CP 307 (supp) (1982).
73. Samanich, N.E., Pressure drag of axisymmetric cowls having large initial lip angles at Mach numbers from 1.190 to 4.90. NASA Memo 1-10-59E
74. Goldsmith, E.L., Some aspects of engine and airframe integration for ramjet and ramrocket powered missiles. AGARD LS136 (1984).
75. Piercy, T.G., Johnson, H.W., Experimental investigation at Mach numbers 1.88, 3.16 and 3.83 of pressure drag of wedge diverters simulating boundary-layer-removal systems for side inlets. NACA RM E53L146 (1954).
76. Campbell, R.C., Kremzier, E.J., Performance of wedge type boundary layer diverters for side inlets at supersonic speeds. NACA RMF E54C23 (1954).
77. Peake, D.J., Rainbird, W.J., Aerodynamic drag resulting from 3-D separations caused by boundary layer diverters and nacelles in subsonic and supersonic flow. In AGARD-CP-124 (1974).
78. Davenport, C., A further investigation of the drag at subsonic speeds of side intake boundary layer diverters. Ministry of Technology S & T Memo 7/68 (1968).
79. Neale, M.C., The drag variable ramp intakes at high subsonic speeds. Unpublished MOD(PE) material.
80. Performance data for the critical operation of nominally two-dimensional double ramp supersonic intakes. ESDU Item No. 75005 (1975).
81. Kamman, J.H., Hall, C.L., Effects of selected design variables on three ramp, external compression inlet performance. NASA CR 2485 (1975).
82. Antonatos, P.P., Surber, L.E., Stava, D.J., Inlet/Airplane interference and integration. AGARD-LS-53 Paper 2 (1972).
83. Thornley, S.A.M., Carter, E.C., The measurement of the transonic spillage drag of a supersonic intake. AGARD-CP-150 Paper 3 (1974).
84. Callahan, C.J., An experimental investigation of the component drag composition of a two-dimensional inlet at transonic and supersonic speeds. AGARD-CP-150 (Paper 4) (1974).

#### ACKNOWLEDGEMENT

The author is indebted to his colleague Mr. C.J. Richards of British Aerospace P.L.C. Naval and Electronic Systems Division, and to Dr. I. McGregor of RAE, Bedford for their help in the preparation of this paper.

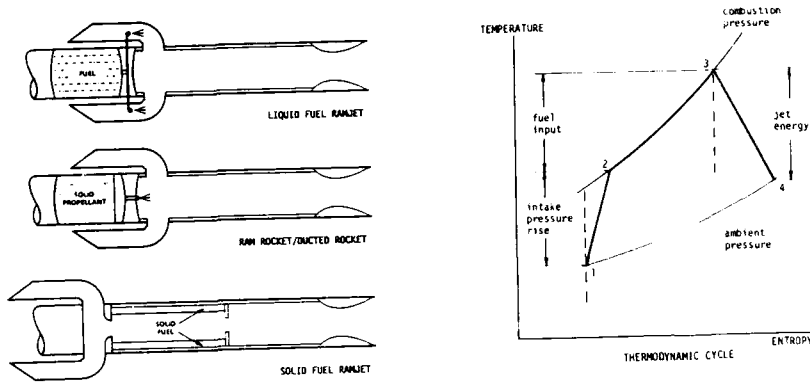


Fig. 1: RAMJET TYPE ENGINES

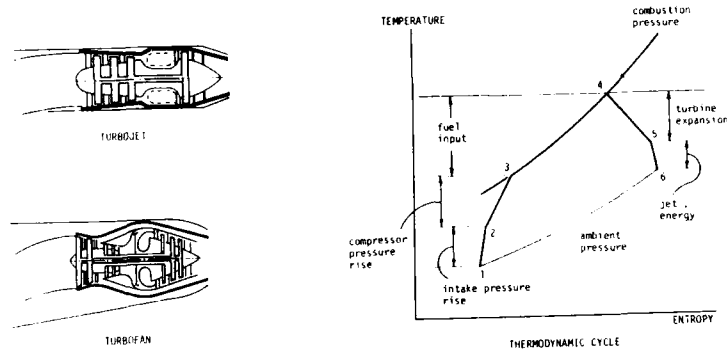


Fig. 2: TURBOJET TYPE ENGINES

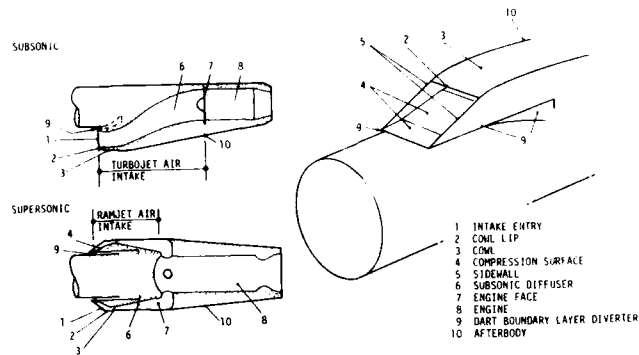


Fig. 3: MAIN FEATURES OF INTAKE SYSTEMS

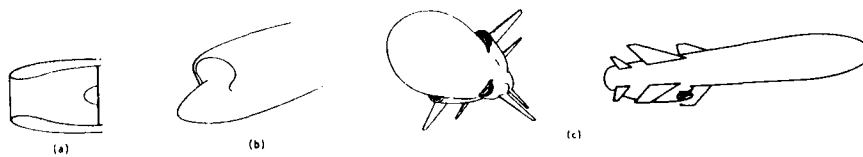


Fig. 4: THE PITOT INTAKE



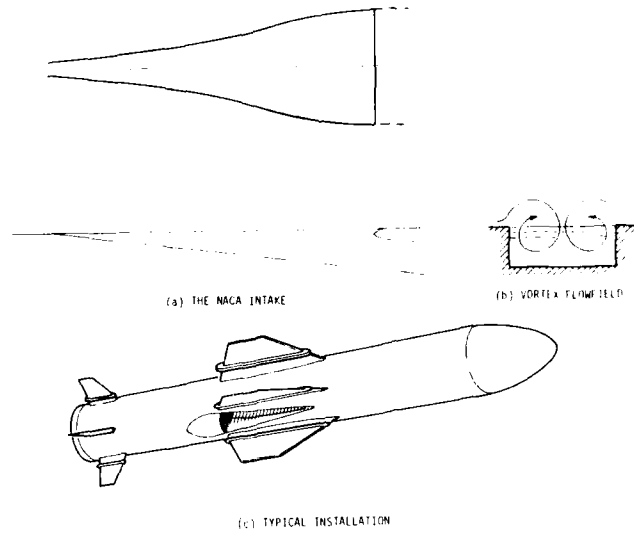


Fig 5: THE FLUSH INTAKE

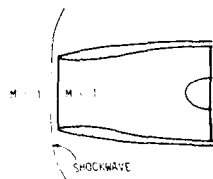


Fig 6: THE PITOT AIR INTAKE AT SUPERSONIC SPEEDS

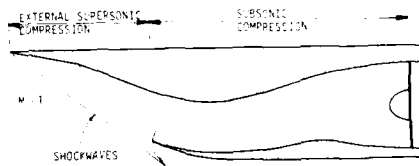


Fig 7: THE EXTERNAL COMPRESSION INTAKE

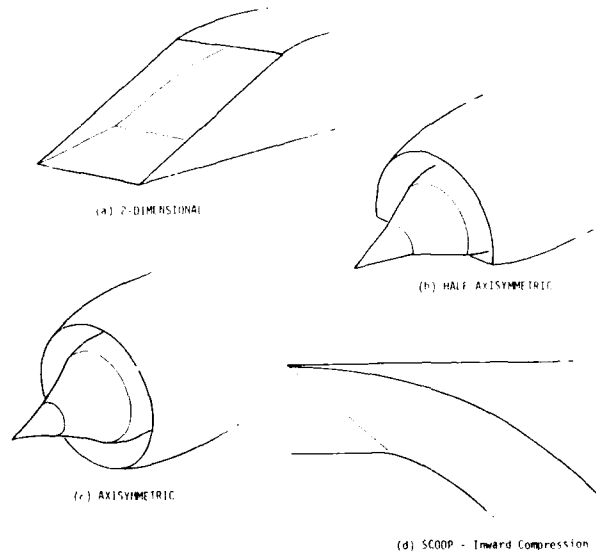


Fig 8: SOME COMMON TYPES OF EXTERNAL COMPRESSION INTAKE

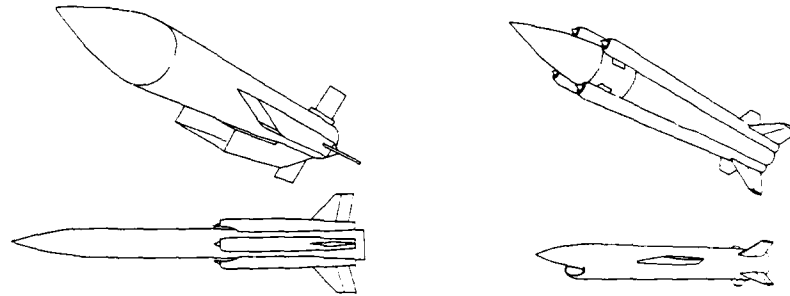


Fig 9: SUPERSONIC INTAKE INSTALLATIONS

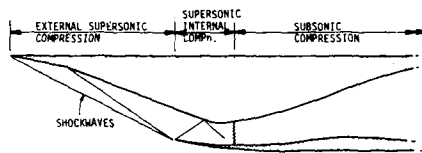


Fig 10: THE MIXED COMPRESSION AIR INTAKE

| LOSS                             | SPEED | LOW SUBSONIC | SUBSONIC | SUPERSONIC |
|----------------------------------|-------|--------------|----------|------------|
| ENTRY ("Sharp Lip")              |       | ●            | ○        |            |
| DIFFUSER                         |       | ○            | ●        | ○          |
| SHOCK                            |       |              |          | ●          |
| SHOCK-BOUNDARY LAYER INTERACTION |       |              |          | ○          |
| BOUNDARY LAYER INGESTION         |       | ○            | ○        | ○          |

Fig.11: MAIN SOURCES OF LOSS OF TOTAL PRESSURE IN INTAKE SYSTEMS

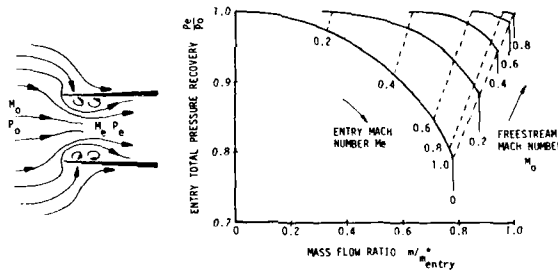


Fig 12: SHARPLIP ENTRY LOSS (Fradenburg & Wyatt, Ref.16)

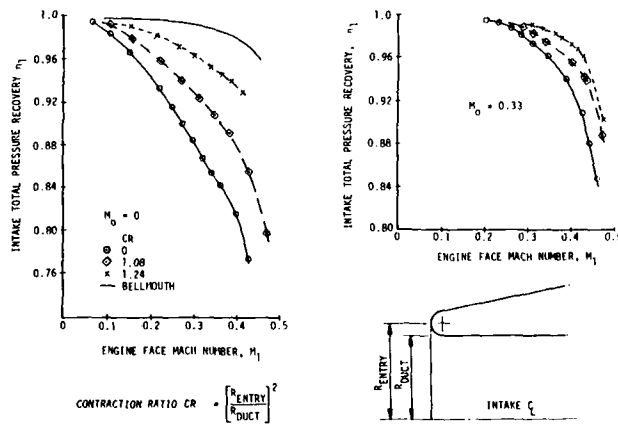


Fig.13: EFFECT OF LIP RADIUS ON LOW SPEED ENTRY LOSSES (Blackaby & Watson, Ref 17)

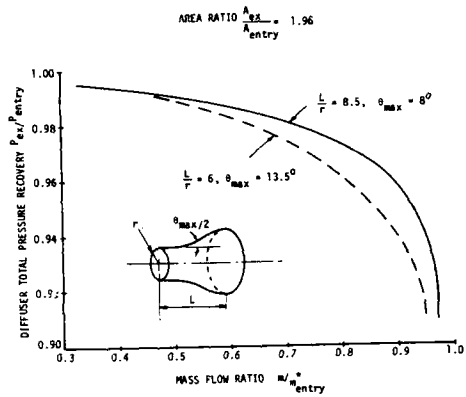


Fig. 14: EFFECT OF MAXIMUM WALL ANGLE ON DIFFUSER PERFORMANCE (Ref.18)

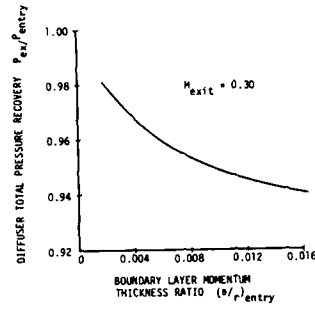


Fig. 15: EFFECT OF ENTRY BOUNDARY LAYER ON DIFFUSER PERFORMANCE (Ref.18)

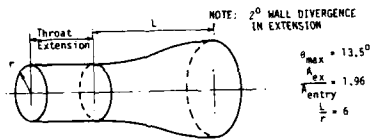
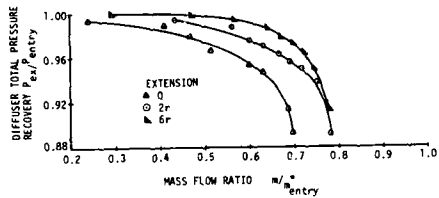


Fig. 16: EFFECT OF THROAT EXTENSION ON PERFORMANCE OF DIFFUSER WITH SEPARATED ENTRY BOUNDARY LAYER (Ref.18)

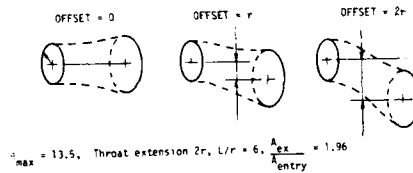
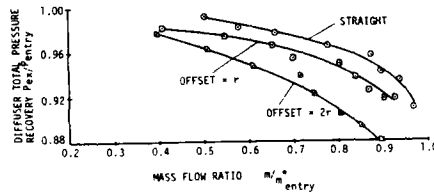


Fig. 17: EFFECT OF DUCT OFFSET ON DIFFUSER PERFORMANCE (Ref.18)

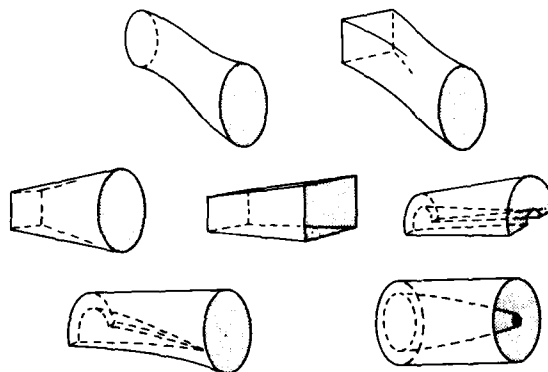


Fig. 18: TYPES OF SUBSONIC DIFFUSER

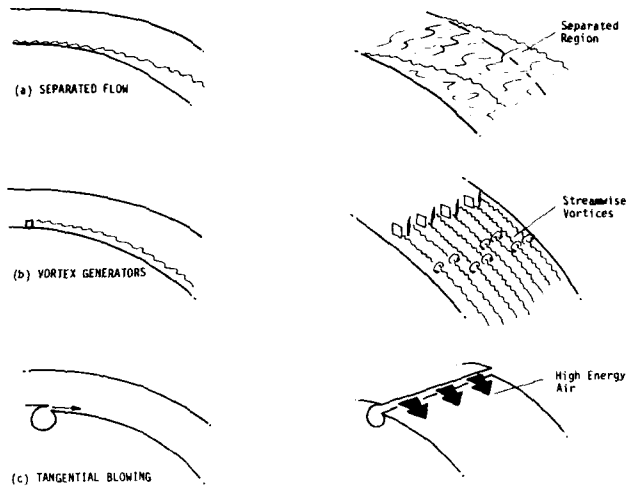


Fig 19: METHODS OF PREVENTING FLOW SEPARATION

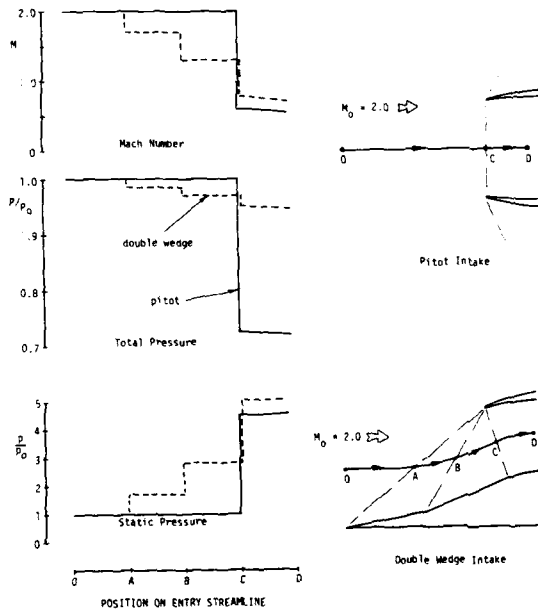


Fig.20: FLOW PROPERTIES THROUGH SHOCK SYSTEM OF A PITOT AND A DOUBLE WEDGE AIR INTAKE

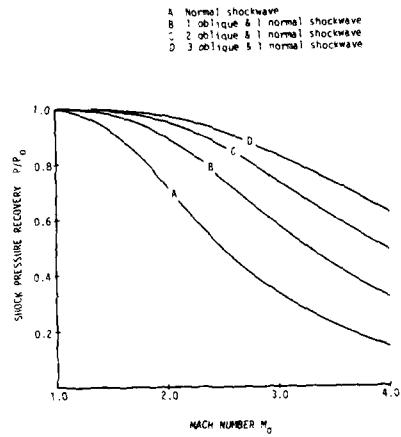


Fig.21: 'OPTIMUM' SHOCK PRESSURE RECOVERY OF TWO-DIMENSIONAL AIR INTAKES (Ref.22)

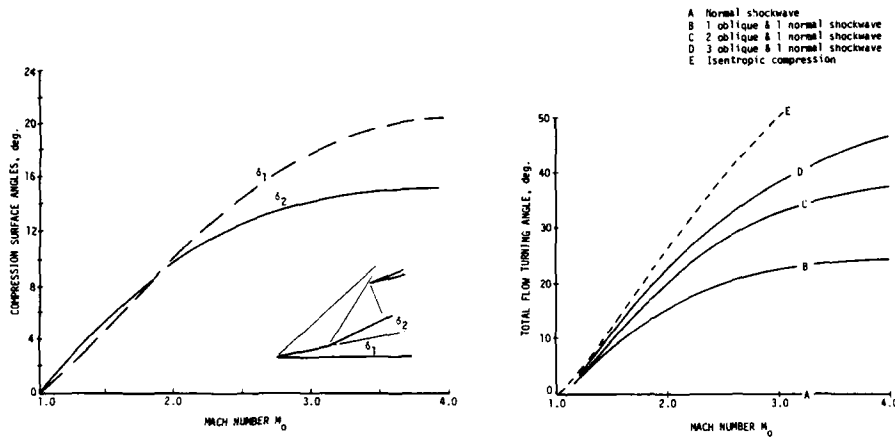


Fig.22: 'OPTIMUM' COMPRESSION SURFACE ANGLES FOR THREE SHOCK TWO-DIMENSIONAL AIR INTAKES

Fig.23: TOTAL FLOW TURNING ANGLE FOR 'OPTIMUM' TWO-DIMENSIONAL AIR INTAKES

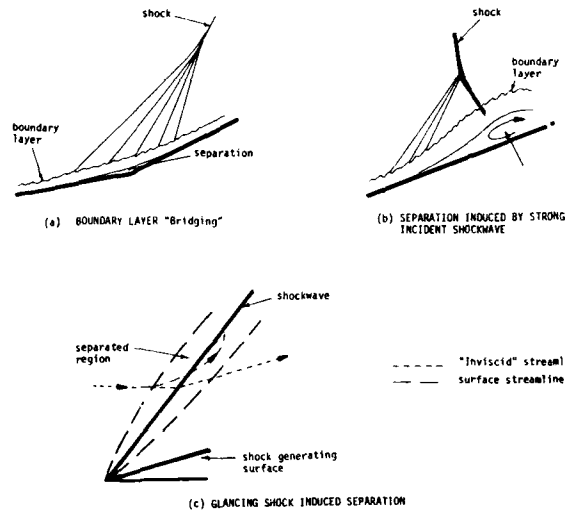


Fig.24: SHOCK INDUCED BOUNDARY LAYER SEPARATION

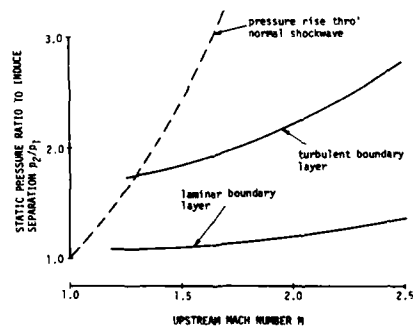


Fig.25: PRESSURE RATIO FOR INCIPIENT INCIDENT - SHOCK INDUCED SEPARATION (Ref.23)

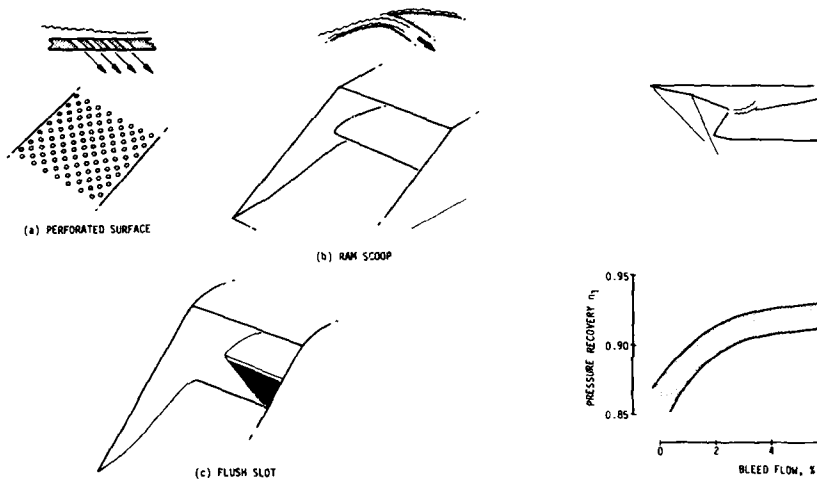


Fig. 26: TYPES OF BOUNDARY LAYER BLEED

Fig. 27: TYPICAL EFFECT OF THROAT BOUNDARY LAYER BLEED IN A TWO-DIMENSIONAL INTAKE AT MACH 2.0

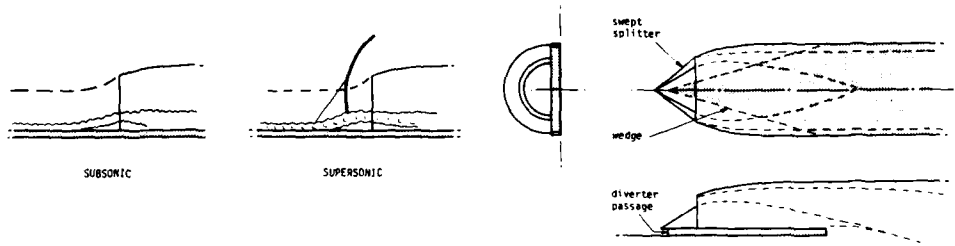


Fig. 28: SEPARATION INDUCED BY PRESSURE GRADIENTS IN THE PRE-ENTRY FLOWFIELD (Ref. 27)

Fig. 29: WEDGE TYPE BOUNDARY LAYER DIVERTER

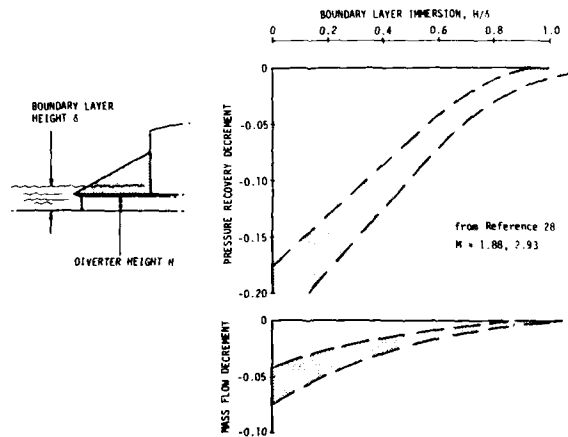


Fig. 30: TYPICAL EFFECT IF INGESTING BODY BOUNDARY LAYER ON SUPERSONIC INTAKE INTERNAL PERFORMANCE

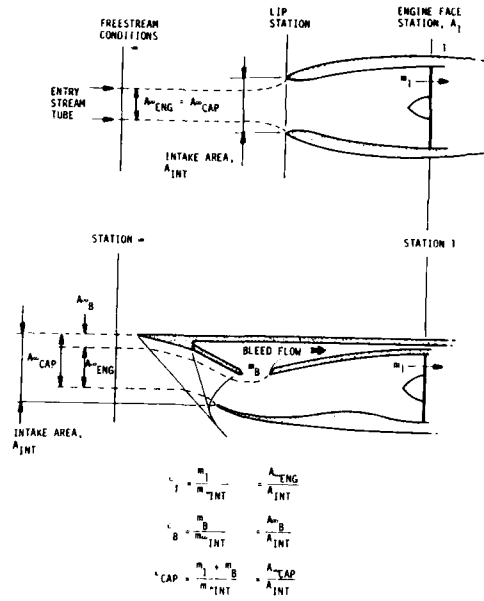


Fig. 31: DEFINITION OF INTAKE MASS FLOW RATIO

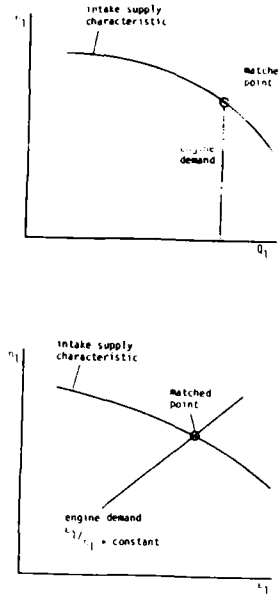


Fig. 32: MATCHED OPERATING POINT ON INTAKE CHARACTERISTIC

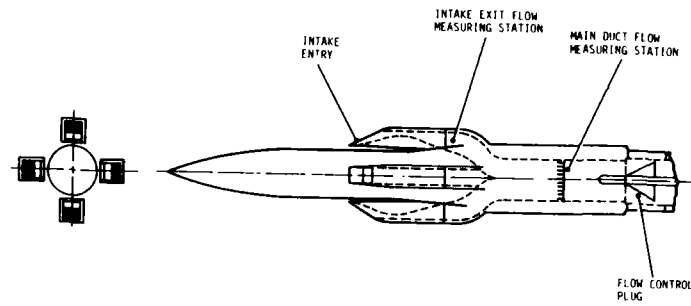


Fig. 33: SKETCH OF TYPICAL WIND TUNNEL MODEL FOR INTAKE INTERNAL PERFORMANCE MEASUREMENTS

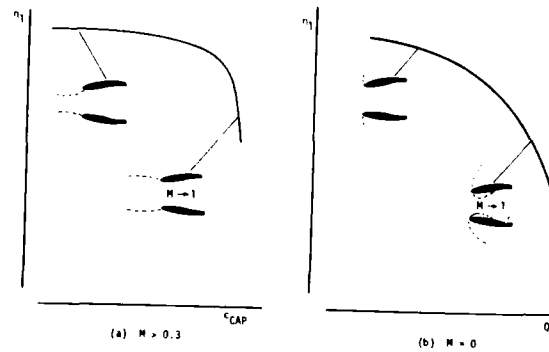


Fig. 34: TYPICAL CHARACTERISTIC FOR SUBSONIC PITOT INTAKE

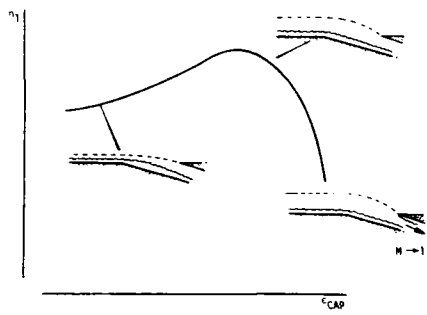


Fig.35: TYPICAL CHARACTERISTIC FOR FLUSH AIR INTAKE

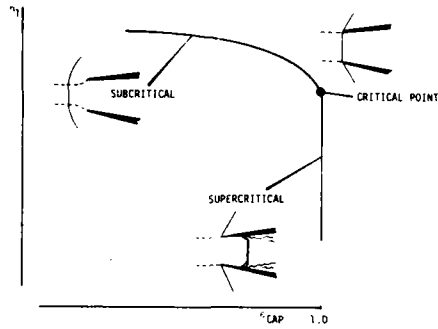


Fig.36: TYPICAL CHARACTERISTIC FOR SUPERSONIC PITOT INTAKE

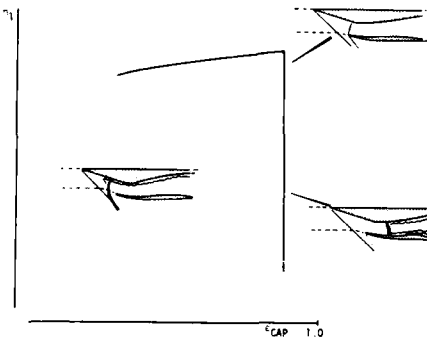


Fig.37: TYPICAL CHARACTERISTIC FOR EXTERNAL COMPRESSION INTAKE

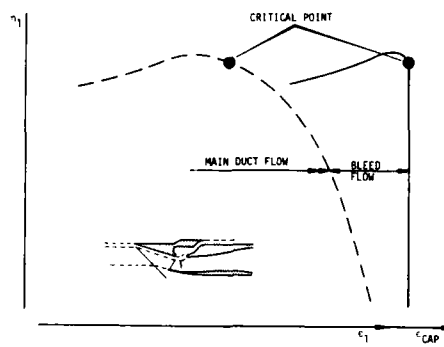


Fig.38 TYPICAL CHARACTERISTIC FOR EXTERNAL COMPRESSION INTAKE WITH THROAT BOUNDARY LAYER BLEED

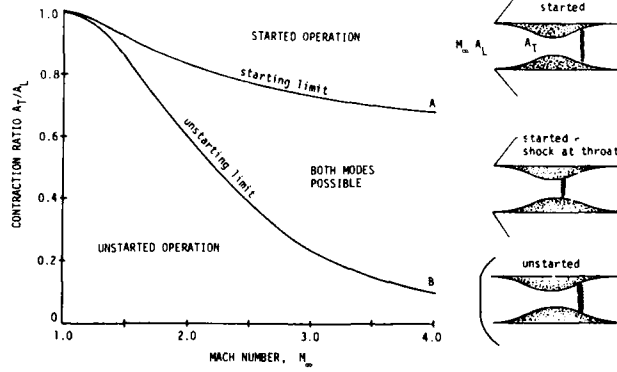


Fig.39: THROAT CONTRACTION RATIOS FOR STARTED AND UNSTARTED OPERATION OF INTAKES WITH INTERNAL COMPRESSION



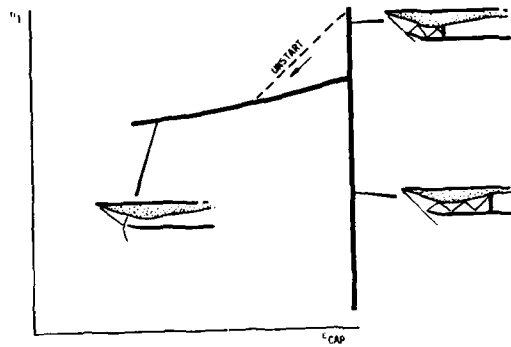


Fig.40: TYPICAL CHARACTERISTIC FOR MIXED COMPRESSION INTAKE - CONTRACTION RATIO ABOVE STARTING LIMIT

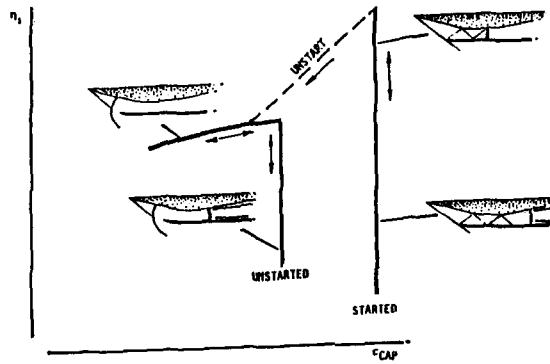


Fig.41: TYPICAL CHARACTERISTIC FOR MIXED COMPRESSION INTAKE - CONTRACTION RATIO BELOW STARTING LIMIT

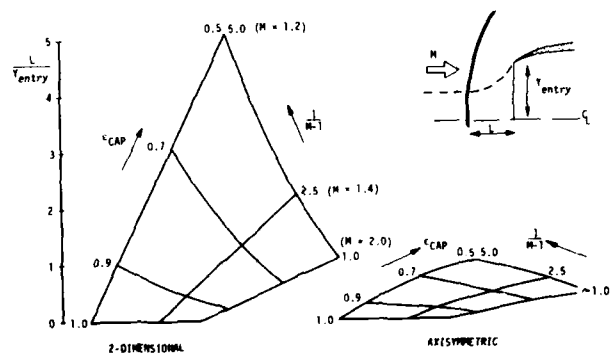


Fig.42: VARIATION OF SHOCK DETACHMENT DISTANCE WITH MASS FLOW RATIO FOR PITOT INTAKE (Moekel, Ref.37)

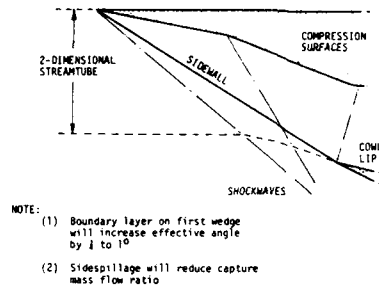


Fig.43: PRE-ENTRY FLOWFIELD FOR TWO-DIMENSIONAL INTAKE OPERATING CRITICALLY

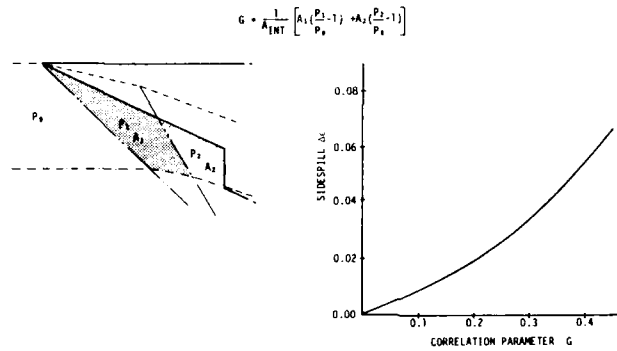


Fig.44: SIDESPILLAGE FROM TWO-DIMENSIONAL SUPERSONIC AIR INTAKE (Ref.39)

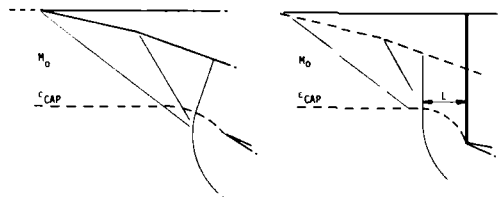


Fig.45: EQUIVALENT PITOT INTAKE FOR ESTIMATING STABILITY BOUNDARY OF TWO-DIMENSIONAL INTAKE (Ref.39)

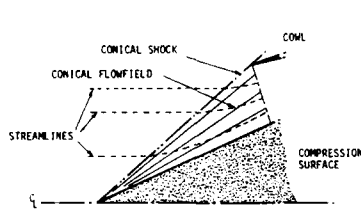


Fig.46: PRE-ENTRY FLOWFIELD FOR INTAKE WITH SINGLE CONICAL COMPRESSION SURFACE

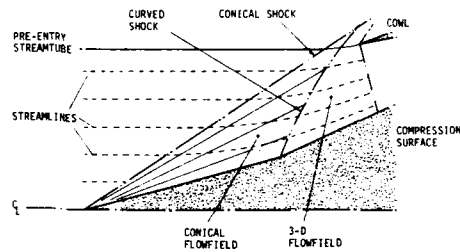


Fig.47: PRE-ENTRY FLOWFIELD FOR INTAKE WITH DOUBLE CONICAL COMPRESSION SURFACES

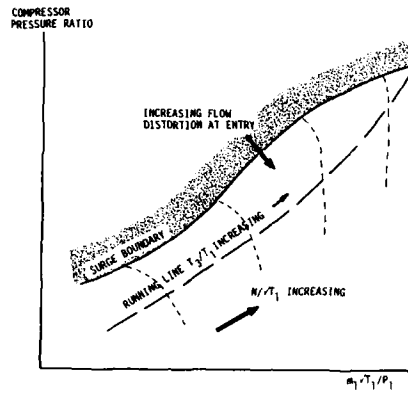


Fig.48: TURBOJET COMPRESSOR CHARACTERISTIC

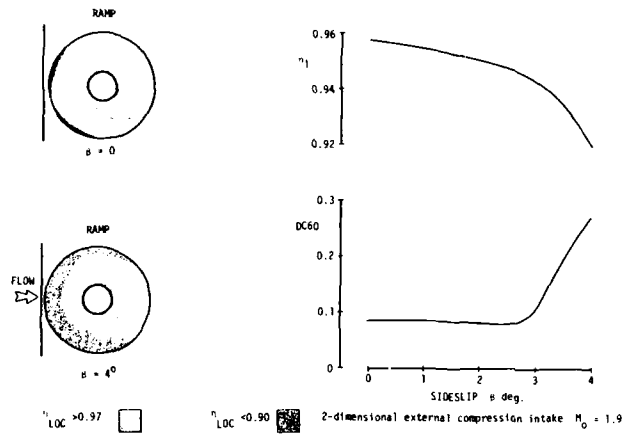


Fig.49: ENGINE FACE FLOW DISTORTION

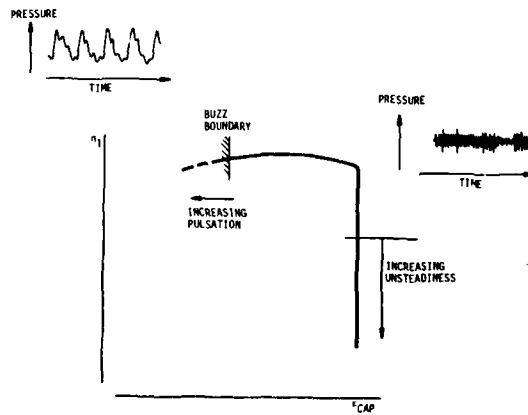


Fig.50: INTAKE BUZZ AND FLOW UNSTEADINESS

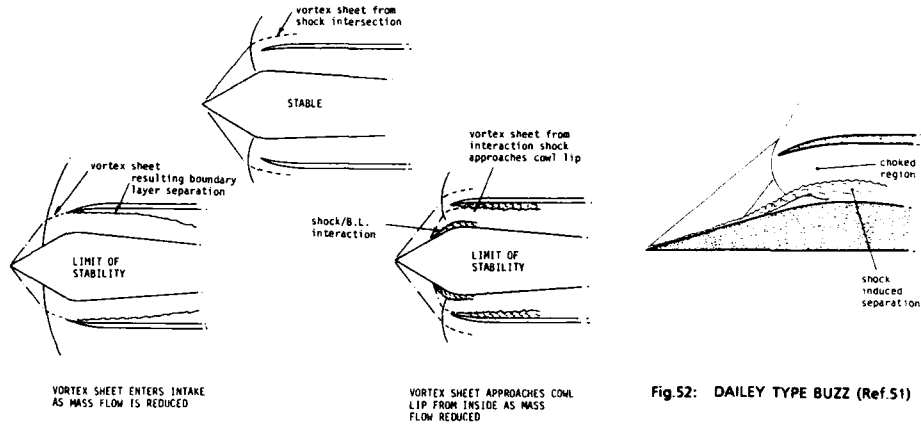


Fig.52: DAILEY TYPE BUZZ (Ref.51)

Fig.51: FERRI CRITERION FOR BUZZ (Ref.49)

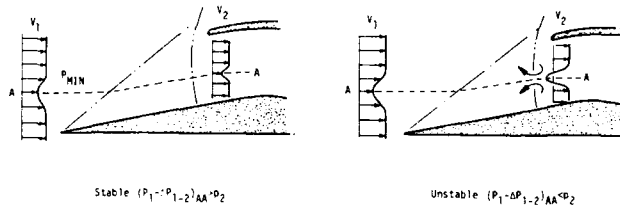


Fig.53: INSTABILITY DUE TO INGESTION OF LOW ENERGY AIR (Hall, Ref.52)

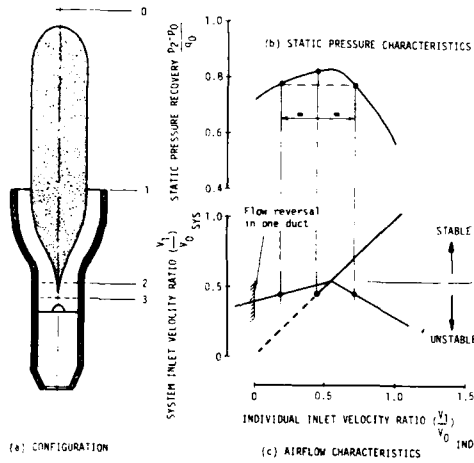


Fig.54: TWIN DUCT INSTABILITY (Ref.53)

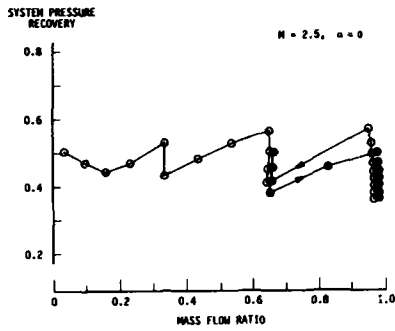


Fig. 55: MULTIPLE INLET INSTABILITY (Ref. 55)

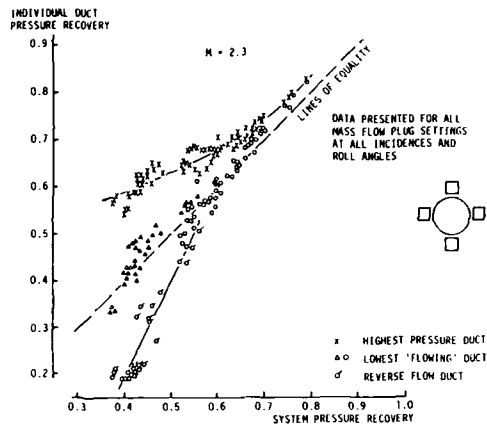


Fig. 56: RELATIONSHIP BETWEEN INDIVIDUAL AND SYSTEM PRESSURE RECOVERY

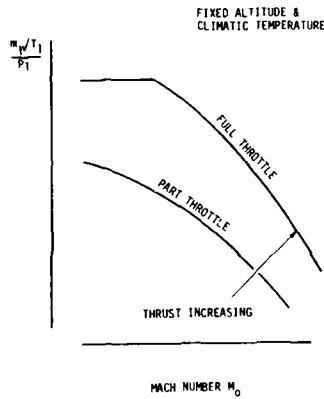


Fig. 57: TURBOJET AIRFLOW REQUIREMENT

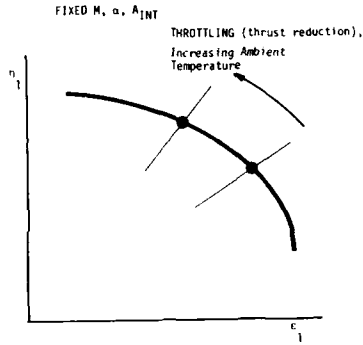


Fig. 58: EFFECT OF THROTTLING TURBOJET ON INTAKE MATCHED OPERATING POINT

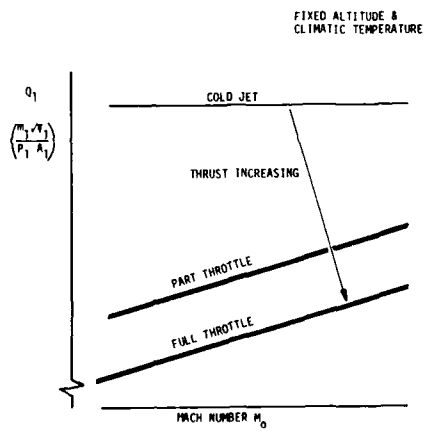


Fig. 59: RAMJET AIRFLOW REQUIREMENT

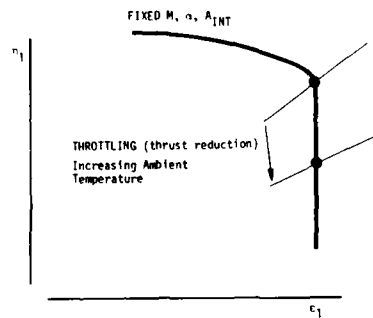


Fig. 60: EFFECT OF THROTTLING RAMJET ON INTAKE MATCHED OPERATING POINT

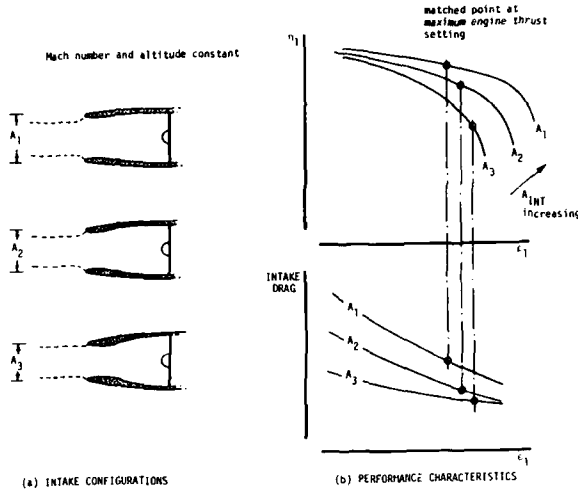


Fig. 61: EFFECT OF INTAKE AREA ON INTERNAL PERFORMANCE AND DRAG

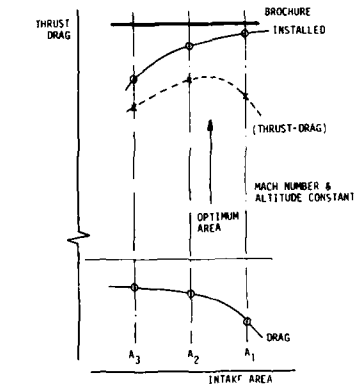


Fig. 62: EFFECT OF INTAKE AREA ON MAXIMUM NETT PROPULSIVE FORCE

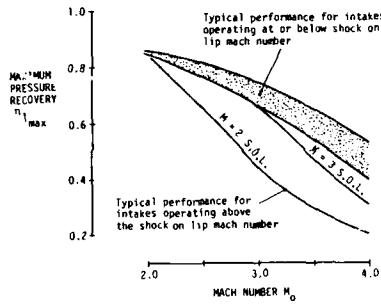


Fig. 63: INTAKE PRESSURE RECOVERY ABOVE AND BELOW SHOCK-ON-LIP ON LIP MACH NUMBER

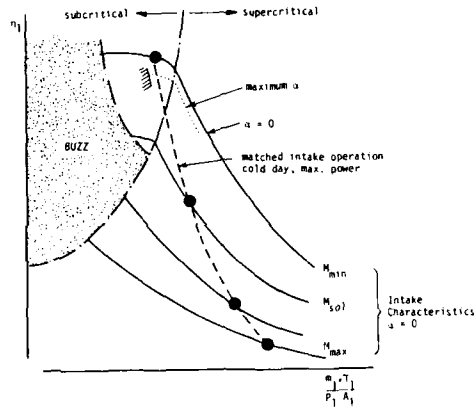


Fig. 64: RAMJET INTAKE SIZING

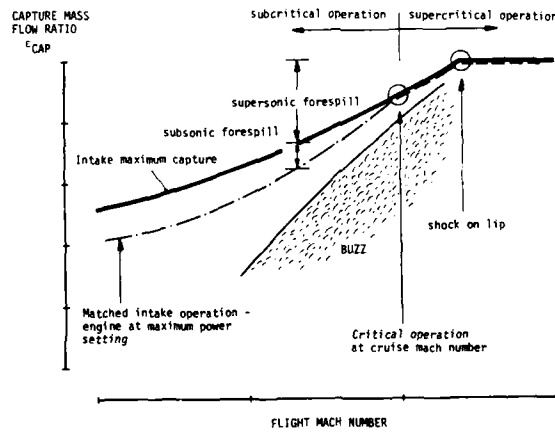


Fig. 65: SUPERSONIC TURBOJET INTAKE SIZING

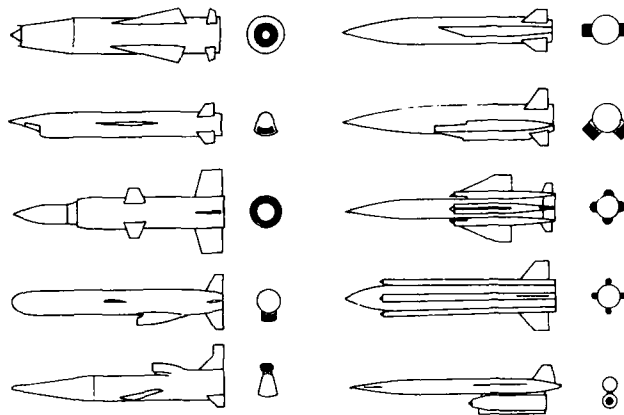


Fig. 66: INTAKE POSITIONS

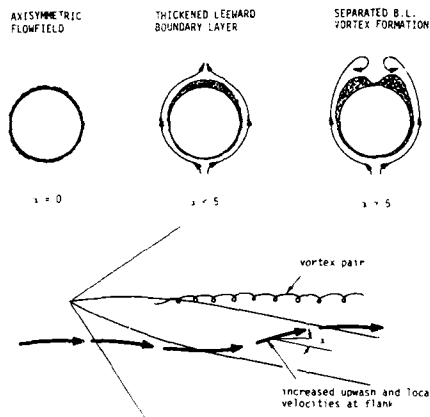


Fig. 67: MAIN FEATURES OF FLOW AROUND A MISSILE BODY AT INCIDENCE

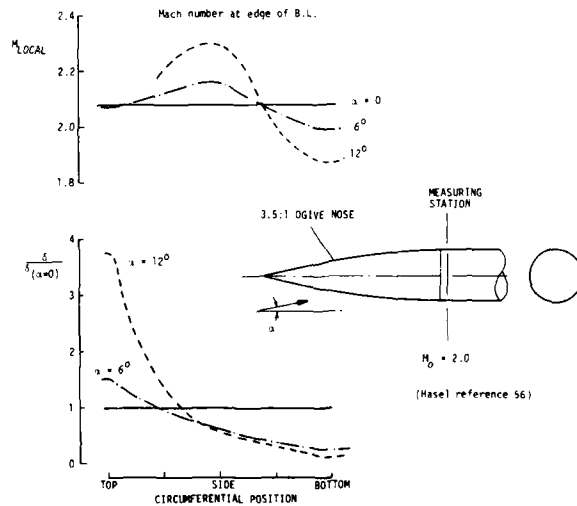


Fig. 68: EFFECT OF INCIDENCE ON LOCAL MACH NUMBER & BOUNDARY LAYER ON MISSILE TYPE BODY

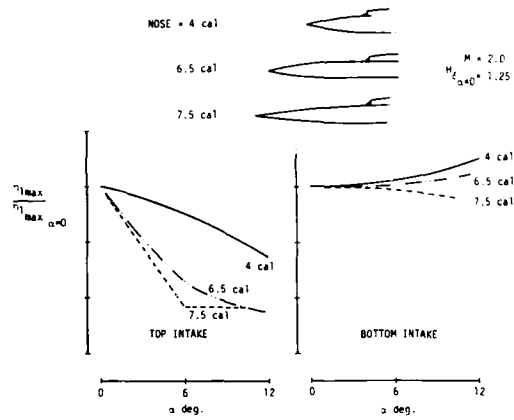
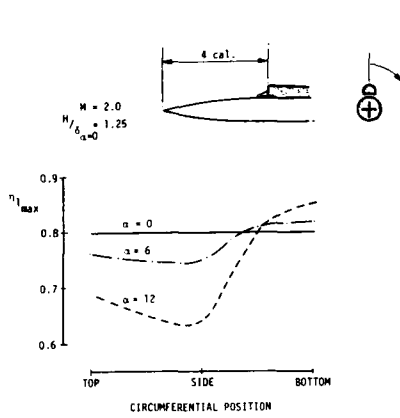


Fig. 69: EFFECT OF CIRCUMFERENTIAL POSITION ON PRESSURE RECOVERY OF AN INTAKE ON A MISSILE BODY AT INCIDENCE (Ref. 56)

Fig. 70: EFFECT OF FOREBODY LENGTH ON THE PERFORMANCE OF AN INTAKE MOUNTED ON A MISSILE TYPE BODY (Ref. 56)

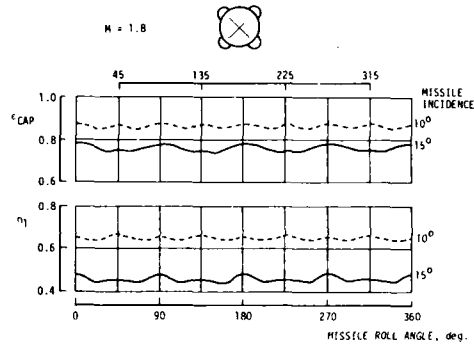
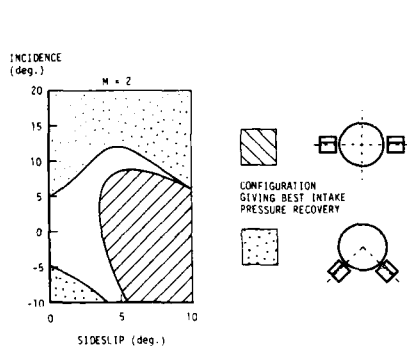


Fig. 71: COMPARISON OF INTERNAL PERFORMANCE OF TWO TWIN INTAKE CONFIGURATIONS

Fig. 72: EFFECT OF ROLL ANGLE ON FOUR-INTAKE SYSTEM PERFORMANCE (Rosander, Ref. 57)

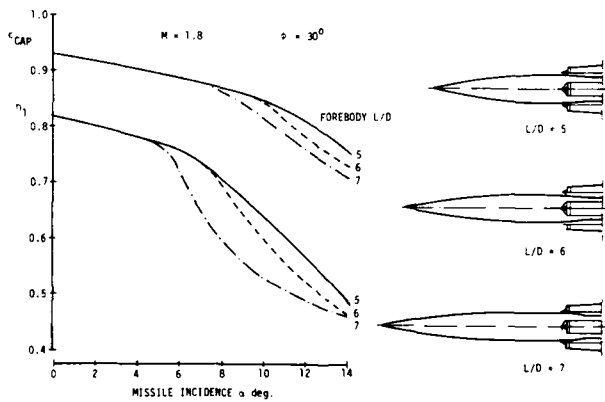


Fig. 73: EFFECT OF NOSE LENGTH ON FOUR-INTAKE SYSTEM INCIDENCE PERFORMANCE (Ref. 57)



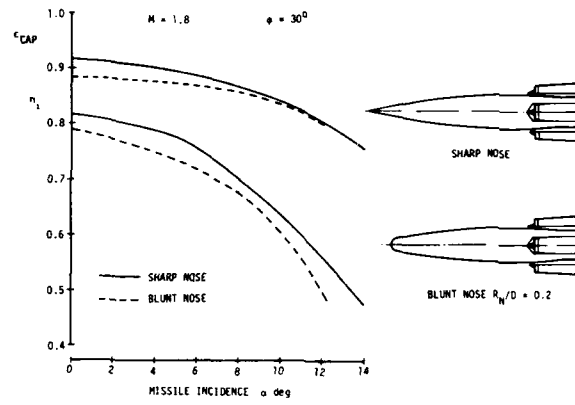


Fig.74: EFFECT OF NOSE BLUNTNES ON FOUR-INTAKE SYSTEM INCIDENCE PERFORMANCE (Ref.57)

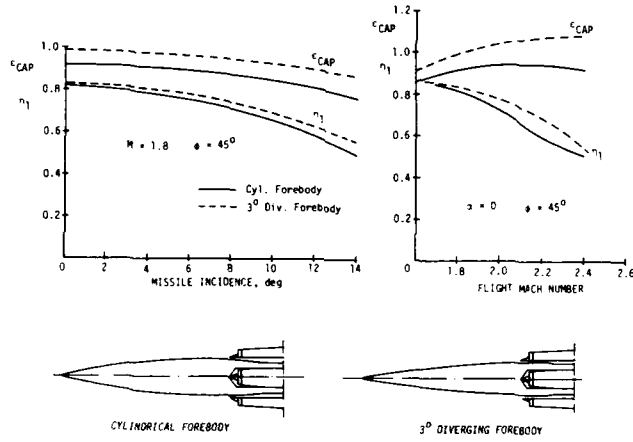


Fig.75: EFFECT OF FOREBODY DIVERGENCE (Ref.57)

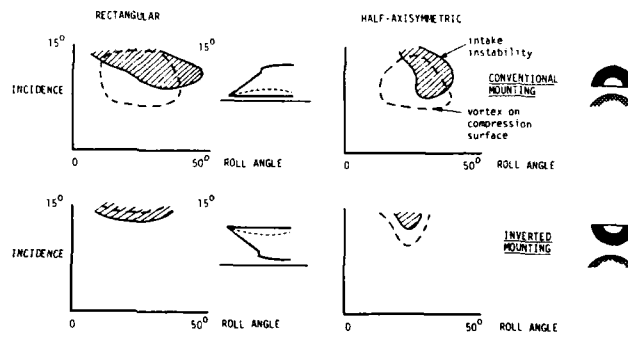


Fig.76: EFFECT OF INVERTING INTAKES ON STABILITY - FOUR-INTAKES, MACH 2.0

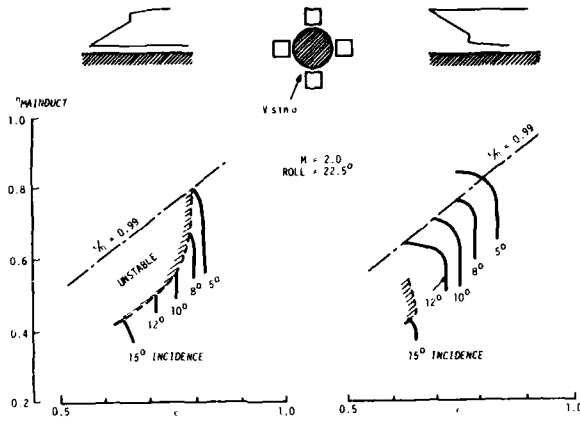


Fig. 77: EFFECT OF INTAKE ORIENTATION ON INTAKE CHARACTERISTICS

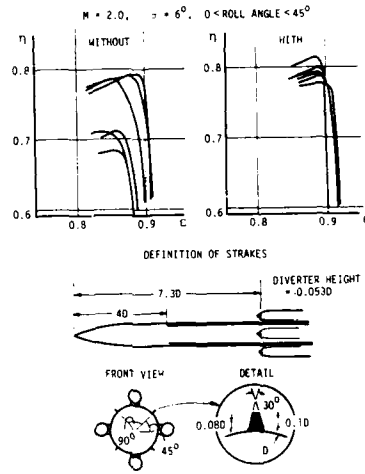


Fig. 78: EFFECT OF STRAKES BETWEEN INTAKES (Ref. 58)

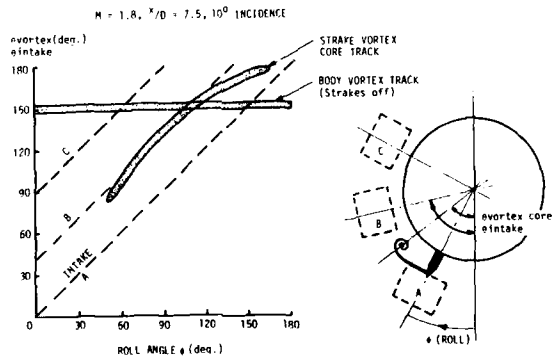


Fig. 79: POSITION OF FOREBODY VORTICES WITH AND WITHOUT STRAKES

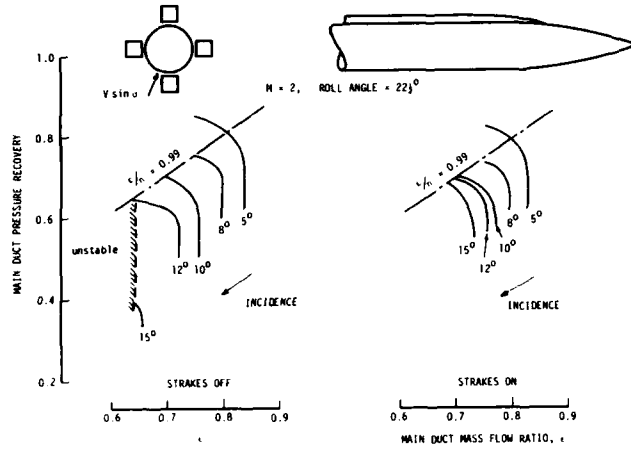


Fig.80: EFFECT OF IN-LINE STRAKES ON INTAKE CHARACTERISTICS

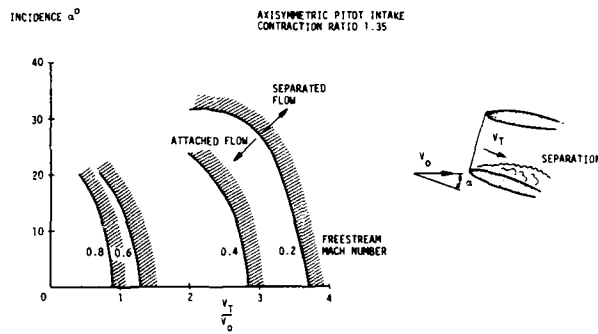


Fig.81: BOUNDARIES BETWEEN ATTACHED AND SEPARATED FLOW AT THE COWL LIP OF A PITOT INTAKE AT INCIDENCE (Ref.59)

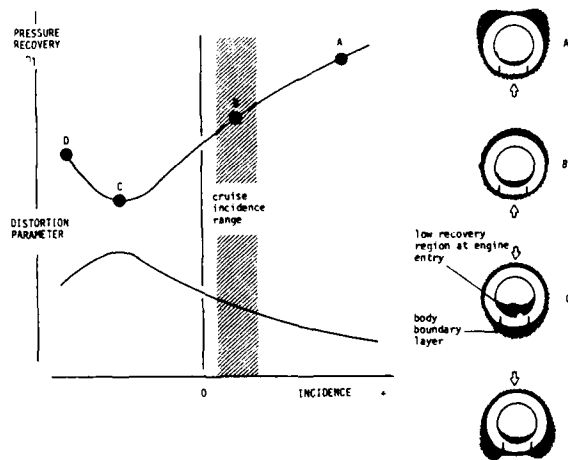


Fig.82: BEHAVIOUR OF VENTRAL FLUSH INTAKE WITH MISSILE INCIDENCE

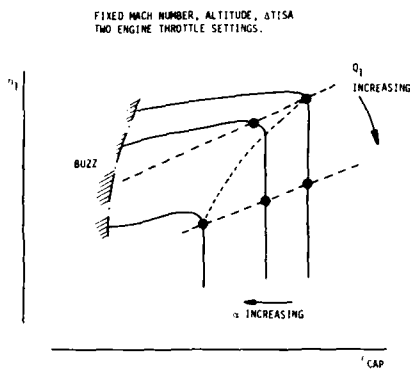


Fig.83: EFFECT OF INCIDENCE ON MATCHED OPERATING POINT

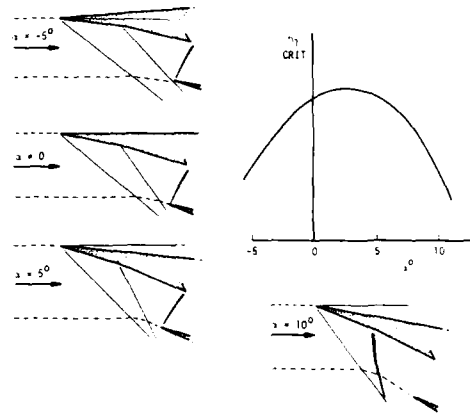


Fig.84: EFFECT OF INCIDENCE VARIATION NORMAL TO THE RAMPS OF A TWO-DIMENSIONAL SUPERSONIC AIR INTAKE (Ref.62)

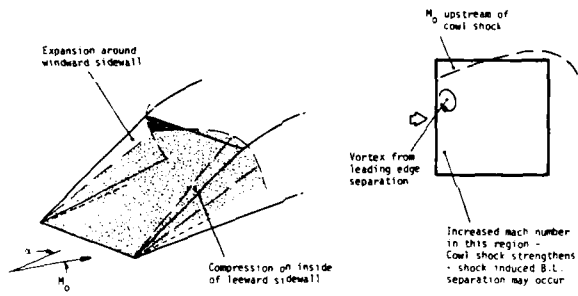


Fig.85: FLOW FEATURES AT ENTRY OF A TWO-DIMENSIONAL INTAKE WITH SWEEPED SIDEWALLS WITH INCIDENCE PARALLEL TO RAMPS

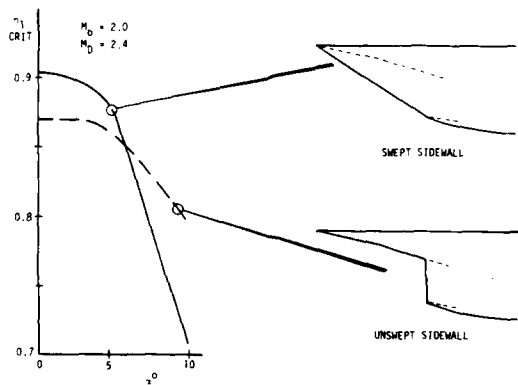


Fig.86: EFFECT OF INCIDENCE VARIATION PARALLEL TO THE RAMPS OF A TWO-DIMENSIONAL, SUPERSONIC AIR INTAKE (Ref.62)

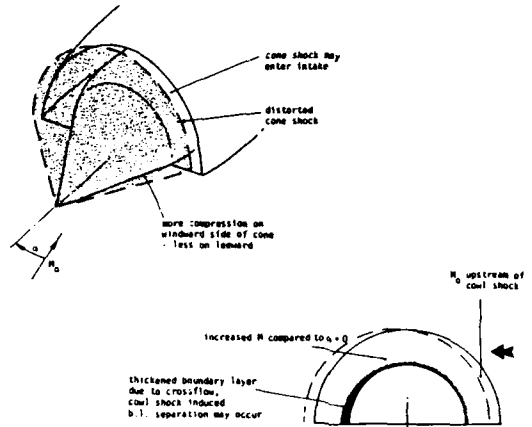


Fig.87: FLOW FEATURES AT ENTRY TO PART-AXISYMMETRIC OR AXISYMMETRIC INTAKE AT INCIDENCE

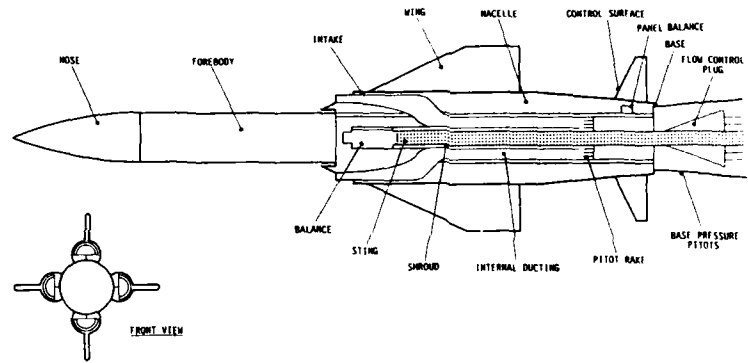


Fig.88: WIND TUNNEL MODEL OF AIRBREATHING MISSILE

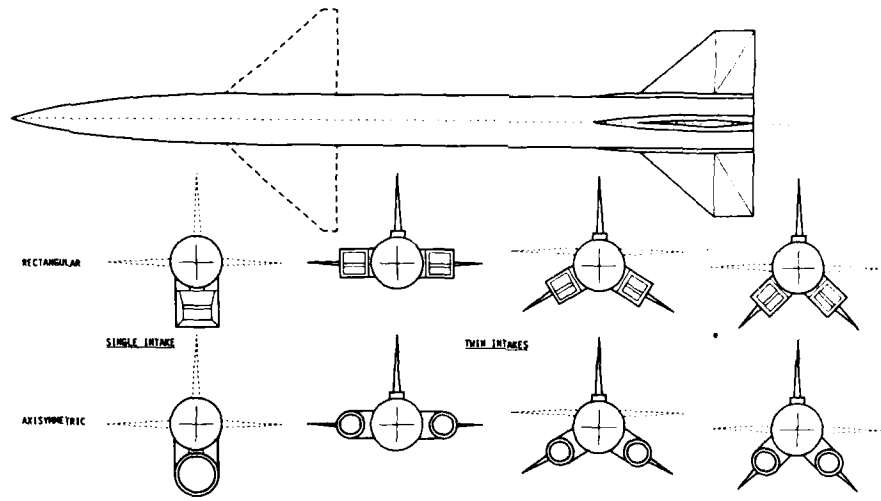


Fig.89: NASA AIRBREATHING MISSILE WIND TUNNEL MODEL (Ref.64 to 68)

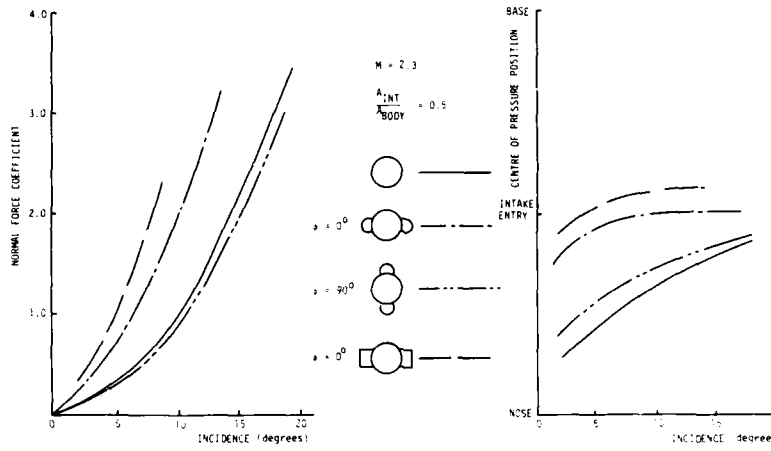


Fig.90: EFFECT OF ROLL ANGLE - TWIN OPPOSED INTAKES

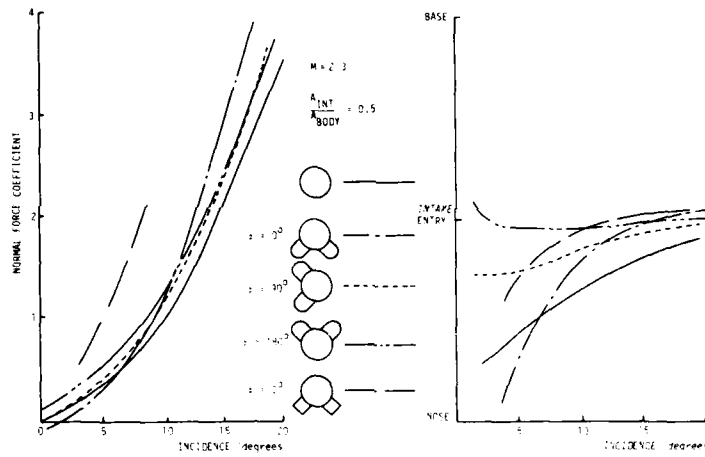


Fig.91: EFFECT OF ROLL ANGLE - TWIN VENTRAL INTAKES

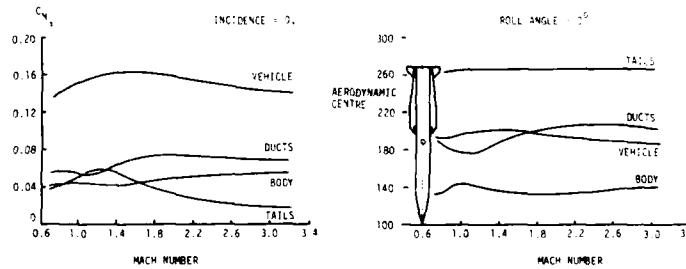


Fig.92: VOUGHT ALVRJ - COMPONENT EFFECTS ON NORMAL FORCE AND AERODYNAMIC CENTRE (Ref.70)

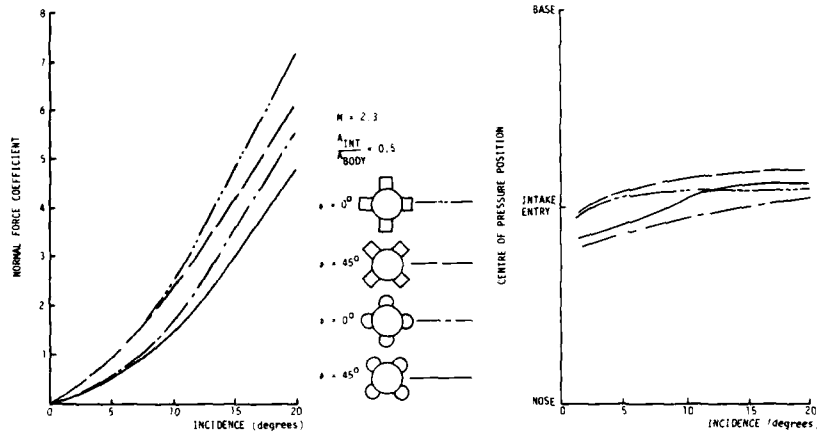


Fig. 93: EFFECT OF INTAKE TYPE - FOUR INTAKES

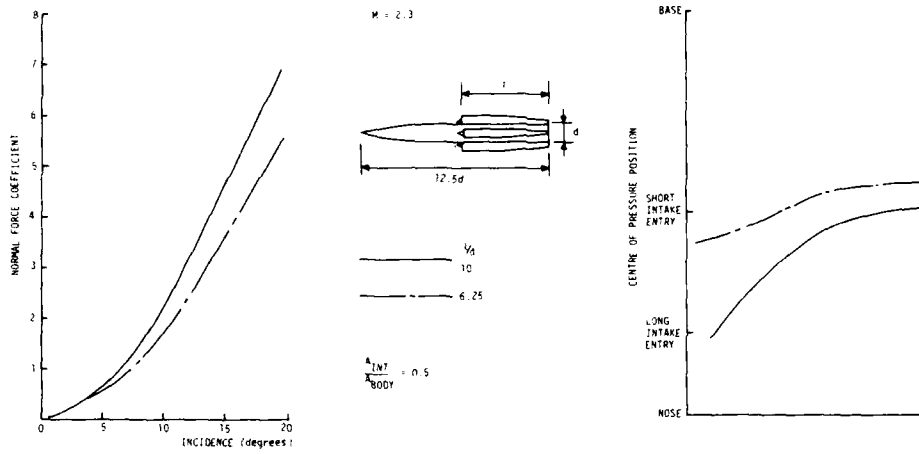


Fig. 94: EFFECT OF INTAKE LENGTH - FOUR HALF AXISYMMETRIC INTAKES

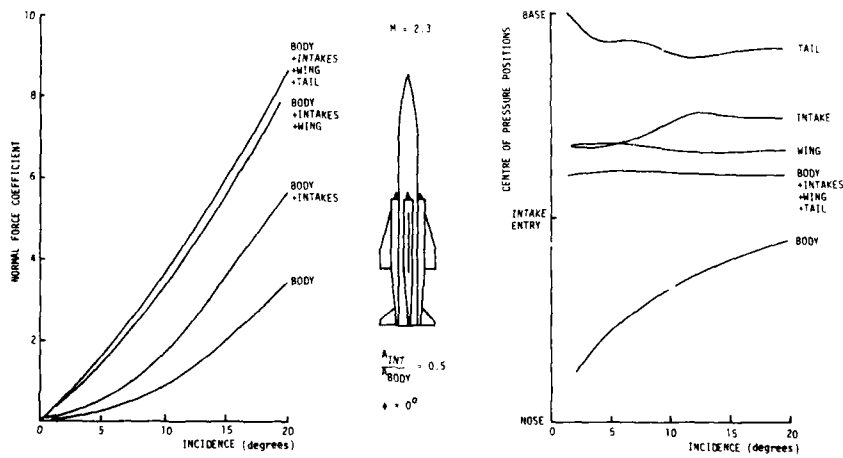


Fig. 95: COMPONENT CONTRIBUTIONS TO NORMAL FORCE & CENTRE OF PRESSURE POSITION

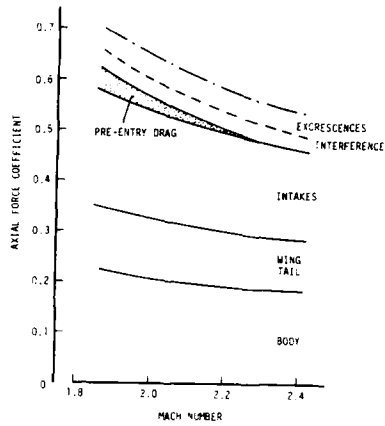


Fig.96: TYPICAL COMPONENT CONTRIBUTIONS TO ZERO INCIDENCE DRAG - FOUR INTAKE CONFIGURATION

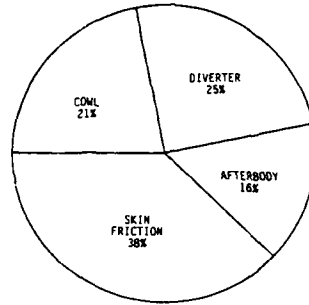
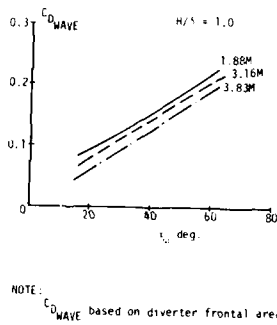


Fig.97: NACELLE DRAG CONTRIBUTIONS



NOTE:  $C_{D\_WAVE}$  based on diverter frontal area

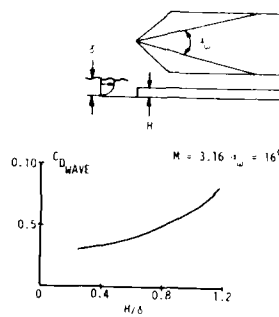
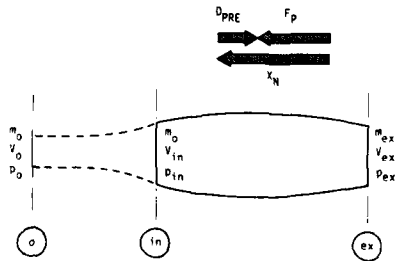


Fig.98: WAVE DRAG OF WEDGE TYPE DIVERTERS (Piercy & Johnson, Ref.75)



Engine Thrust (by definition)

$$X_N = [m_{ex} V_{ex} + (p_{ex} - p_o) A_{ex}] - m_o V_o$$

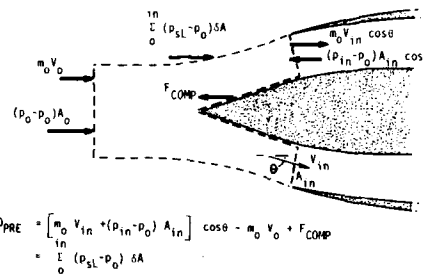
Propulsion Force on Body

$$F_P = [m_{ex} V_{ex} + (p_{ex} - p_o) A_{ex}] - [m_o V_o + (p_{in} - p_o) A_{in}]$$

Pre-entry Drag

$$D_{PRE} = [m_o V_o + (p_{in} - p_o) A_{in}] - m_o V_o$$

Fig.99: PRE-ENTRY DRAG



$$D_{PRE} = [m_o V_o + (p_{in} - p_o) A_{in}] \cos \theta - m_o V_o + F_{COMP}$$

$$= \int (p_{sl} - p_o) \delta A$$

Fig.100: PRE-ENTRY DRAG FOR INTAKE WITH EXTERNAL COMPRESSION SURFACE



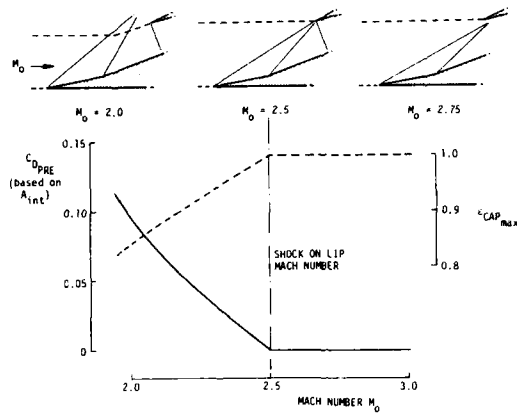


Fig. 101: SUPERCRITICAL PRE-ENTRY DRAG

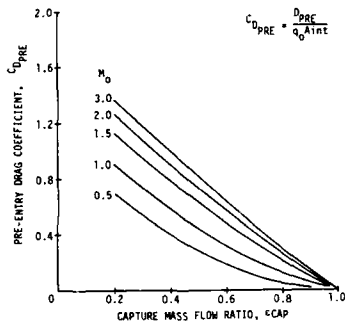


Fig. 102: THEORETICAL PRE-ENTRY DRAG FOR PITOT INTAKE

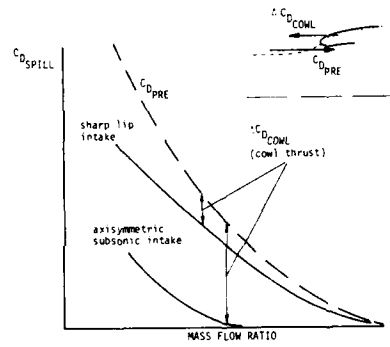
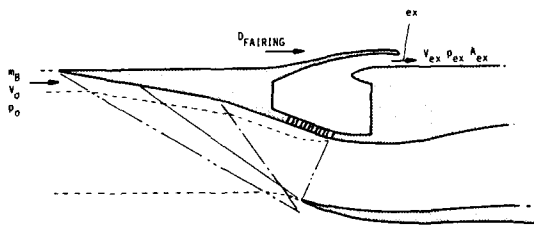
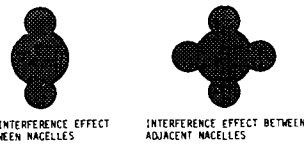


Fig. 103: SPILL DRAG



BLEED DRAG:  

$$D_b = \dot{m}_b V_0 - [\dot{m}_b V_{ex} + (\rho_{ex} - \rho_0) A_{ex}] + D_{FAIRING}$$

Fig. 104: BOUNDARY LAYER BLEED DRAG

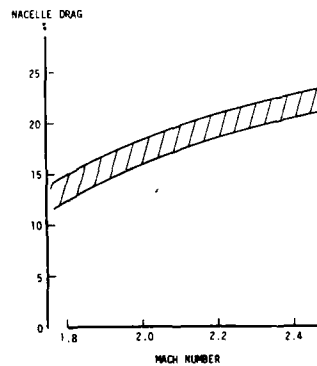


Fig. 105: INTERFERENCE DRAG BETWEEN NACELLES

## SEMIEMPIRICAL METHODS FOR AIRBREATHING MISSILES

J. E. Williams  
 Unit Chief - Technology  
 and  
 R. J. Krieger  
 Chief - Technology  
 McDonnell Douglas Astronautics Company  
 P.O. Box 516, St. Louis, MO 63166  
 USA

## ABSTRACT

A computer-aided design procedure is described for use in conceptual design for sizing and shaping supersonic non-circular missiles with turbojet or ramjet propulsion systems. The theoretical basis for the method which uses a sensitivity derivative approach is developed. Avionics, structures, payload, inlet, engine, fuel, aerodynamic and performance models are described. Inlet/engine sizing, external moldline shaping and interactive graphics design processes are presented. The synthesis procedure overcomes many of the major drawbacks of airbreathing missile synthesis. It has features such as: simple initial geometry setup for body, wings, tails and inlets; modeling of completely arbitrary missile shapes; non-circular subsystem packaging; non-circular and multiple inlet modeling; aerodynamic and performance shaping; low cost, short duration computer sessions; rapid convergence; and accurate aerodynamic predictions. Two example configuration shapings are provided to depict the sizing process.

## NOMENCLATURE

|                    |                                      |
|--------------------|--------------------------------------|
| a                  | = speed of sound                     |
| b                  | = exponent - propulsion weight       |
| c                  | = exponent - propulsion volume       |
| C <sub>A</sub>     | = axial force coefficient            |
| C <sub>D</sub>     | = drag coefficient                   |
| C <sub>L</sub>     | = lift coefficient                   |
| C <sub>m</sub>     | = pitching moment coefficient        |
| C <sub>N</sub>     | = normal force coefficient           |
| D                  | = drag                               |
| e                  | = fuel packaging efficiency          |
| h                  | = altitude                           |
| L/D                | = lift-to-drag ratio                 |
| M                  | = Mach number                        |
| q                  | = dynamic pressure                   |
| Re                 | = Reynolds number                    |
| R <sub>ge</sub>    | = range                              |
| r <sub>i</sub>     | = local radius at point i            |
| SFC                | = specific fuel consumption          |
| S <sub>ref</sub>   | = reference area                     |
| S <sub>wet</sub>   | = wetted surface area                |
| V                  | = velocity                           |
| V <sub>fuel</sub>  | = volume - fuel                      |
| V <sub>other</sub> | = volume - other (avionics, payload) |
| V <sub>prop</sub>  | = volume - propulsion system         |
| V <sub>str</sub>   | = volume - structure                 |
| V <sub>tot</sub>   | = volume - total vehicle             |
| W                  | = weight                             |
| W <sub>bo</sub>    | = weight - burnout                   |
| W <sub>fuel</sub>  | = weight - fuel                      |
| W <sub>other</sub> | = weight - other                     |
| W <sub>prop</sub>  | = weight - propulsion system         |
| W <sub>str</sub>   | = weight - structure                 |
| W <sub>tot</sub>   | = weight - total vehicle             |
| x                  | = length                             |
| α                  | = angle of attack                    |
| μ                  | = viscosity                          |
| ρ                  | = atmospheric density                |
| ρ <sub>fuel</sub>  | = fuel density                       |
| ∂                  | = partial derivative                 |
| Δ                  | = numerical derivative               |

## SUBSCRIPTS

|     |                               |
|-----|-------------------------------|
| o   | = reference value             |
| i   | = inviscid                    |
| f   | = friction                    |
| des | = propulsion design condition |

## INTRODUCTION

The goal of the missile synthesis process is to develop a configuration which accommodates the payload and achieves the desired performance. For example, a cylindrical-shaped, solid-rocket-powered missile is often synthesized as follows. A body diameter is selected, all required subsystem sizes and

weights are estimated, the length of forebody required to accommodate them is determined, and a length for the booster is guessed. The booster is combined with the forebody, tails and possibly wings are added, structure is sized and weighed, the aerodynamic coefficients are estimated, and the performance during boost is then computed. If the vehicle fails to achieve the desired end-of-boost condition, a new booster size is selected, and the process is repeated until the desired system performance is obtained. The success of this process has been more than adequate<sup>1,2</sup> in the past for circular missiles.

However, when non-circular missiles, such as that shown in the exploded view of Figure 1 are considered, this process becomes much more complicated. Because the body shape is arbitrary, subsystem packages and internal boosters no longer need to be cylindrical and more than one booster can be considered. Therefore, the first step described above of selecting a body diameter is no longer applicable. Now an initial body shape must be selected. This shape is a strong function of the subsystem shapes and sizes because the external missile surface can be "wrapped around" the subsystems. In addition, the size of the configuration is also a strong function of its shape. For example, if the body cross section shape is changed from elliptic to blended, the avionics packaging becomes completely different, and the vehicle overall size changes significantly. Each shape has different aerodynamic characteristics which have a strong effect on booster size. Finally, more aerodynamic characteristics must be considered during early stages of the design process. Parameters such as zero-lift pitching moment and optimum lift-to-drag ratio become important design drivers.

Extending the procedure to arbitrary shaped airbreathing missiles further increases the number of parameters that must be considered in the synthesis process. Ramjet powered missiles require a booster to accelerate them to supersonic speeds where the airbreathing engine can take-over. The take-over condition varies with engine size and the vehicle drag. In addition sufficient fuel must be packaged to achieve the desired performance. For maximum range there is a tradeoff between L/D and fuel loading. In summary, the number of variables which must be considered in the airbreathing missile synthesis process becomes very large.

#### SENSITIVITY DERIVATIVE APPROACH

The concept of aerodynamic sensitivity derivatives is illustrated by answering the question posed on Figure 2: What changes occur when a point on the surface is moved? By inspection, the configuration forces, moments, surface area, and volume are changed, Figure 3. At supersonic speeds, impact theory can be used to calculate the pressure for each quadrilateral on the surface. It is then possible to relate the movement of a given point to a change in pressure on the surrounding quadrilaterals and, therefore, a change in the aerodynamic characteristics of the missile. For this method, the geometry modeling techniques and selected impact pressure methods from the USAF Supersonic/Hypersonic Arbitrary Body Program (S/HABP)<sup>3</sup> were used.

Sensitivity derivatives can be calculated by one of two methods: differentiate the governing equations for the aerodynamic derivatives with respect to moving the point, or physically move the point and recalculate aerodynamic coefficients to obtain a numerical derivative. For this program, the equations were differentiated giving over 70 derivatives which are combined using the chain rule to give the sensitivity derivatives for quadrilateral pressure, area, and volume with respect to moving a surface point radially. A summary of the development of sensitivity derivatives is given in References 4 and 5.

A procedure for arbitrary body synthesis for single stage, rocket-powered vehicles based on a sensitivity derivative approach was developed<sup>6</sup>. This process required the booster to be sized to achieve an end-of-boost velocity requirement. It was implemented in a computer program which makes extensive use of interactive graphics during the sizing and shaping process. This approach included a computer display of subsystem packaging and missile external geometry, easily modified subsystem models, automated booster sizing and interactive reshaping of the external moldline for improved aerodynamics. In the present paper, the method is extended to airbreathers. First the theoretical formulation of airbreather sensitivity derivatives is given, the interactive program characteristics are described and two examples cases given.

#### THEORETICAL FORMULATION

Because of the many possible shapes which are candidates for supersonic arbitrary body airbreathers, design guidelines are needed to guide configuration shaping. For many airbreathers, cruise range is a design driver. Using an extension of a sensitivity derivative approach<sup>7</sup>, a set of guidelines for shaping airbreathers for maximum range has been developed. A summary of this derivation follows.

To guide the shaping of airbreathers, the designer would like to know how a change in the external moldline of the configuration impacts total range. More specifically, if the local surface coordinate is changed at some point on the body, wing, tail or inlet, how much will range change? The following derivation develops this sensitivity derivative,  $\partial R_{ge}/\partial r_i$ .

Consider the classical closed-form range equation<sup>8</sup>,

$$R_{ge} = \frac{V(L/D)}{SFC} \log (W_{tot}/W_{bo}) \quad (1)$$

This equation assumes constant velocity, lift coefficient, an specific fuel consumption. However, altitude is allowed to change during cruise as fuel is burned. For many ramjets and turbojets these assumptions are accurate. The total weight is related to major vehicle component weights through

(2)

$$W_{tot} = W_{str} + W_{fuel} + W_{prop} + W_{other}$$

The burnout weight is given by

$$W_{bo} = W_{tot} - W_{fuel} \quad (3)$$

Equation (1) can be differentiated with respect to local radius change at a point on the vehicle surface to give:

$$\frac{\partial Rge}{\partial r_i} = \frac{Rge}{L/D} \frac{\partial(L/D)}{\partial r_i} + \frac{V(L/D)}{SFC} \left[ \frac{1}{W_{tot}} \frac{\partial W_{tot}}{\partial r_i} - \frac{1}{W_{bo}} \frac{\partial W_{bo}}{\partial r_i} \right] \quad (4)$$

This equation defines the sensitivity of cruise range to changes in local body radius,  $r_i$ . It requires the evaluation of the three derivatives: 1)  $\partial(L/D)/\partial r_i$ , 2)  $\partial W_{tot}/\partial r_i$ , 3)  $\partial W_{bo}/\partial r_i$  described below.

1. L/D - derivative -  $\partial(L/D)/\partial r_i$  - The lift to drag ratio can be defined as:

$$\frac{L}{D} = \frac{C_L}{C_D} \quad (5)$$

where  $C_L$  and  $C_D$  can be expressed in normal and axial force coefficients as

$$C_L = C_N \cos \alpha - C_A \sin \alpha \quad (6)$$

$$C_D = C_A \cos \alpha + C_N \sin \alpha \quad (7)$$

Traditionally, skin friction effects are neglected in the normal force coefficient but the axial force contains both viscous and inviscid terms,

$$C_A = C_{A_I} + C_{A_f} \quad (8)$$

where

$$C_{A_f} = C_f S_{wet}/S_{ref} \quad (9)$$

To evaluate  $C_f$  the cruise altitude must be known. By assuming lift equals weight, which neglects the thrust contribution to lift, the atmospheric density for this condition is

$$\rho = \frac{2W}{C_L S_{ref} V^2} \quad (10)$$

The cruise altitude corresponding to can be determined from standard atmospheric tables which give

$$h = h(\rho) \quad (11)$$

Then Reynolds number and Mach number at that altitude also can be obtained

$$Re/x = \frac{\rho V}{\mu} \quad (12)$$

$$M = V/a(h) \quad (13)$$

and  $C_f$  is then computed using standard methods<sup>9</sup>, to give

$$C_f = C_f(Re, M) \quad (14)$$

Equations (5) through (14), cannot be solved directly given the geometry and weight of the vehicle because the  $C_L$  in Equation (10) is a function of  $C_L$  in Equation (6). However, a constant  $C_L$  with altitude can be assumed by neglecting the viscous axial force contribution to the lift coefficient in Equation (10). This requires that

$$\frac{C_{A_f} \sin \alpha}{C_N \cos \alpha} < < 1 \quad (15)$$

For high L/D configurations,  $\alpha$  is small at maximum L/D and  $C_N$  is typically 10 to 20 times  $C_{A_f}$ . The ratio in Equation (15) is typically 1/100 and  $C_{A_f}$  can be neglected in Equation (6).

Therefore, in Equation (10), the  $C_L$  can be replaced with  $C_{L_I}$  and little error is introduced. As a consequence, Equations (5) through (14) are resolvable directly. First, for a given configuration geometry,  $C_N$ ,  $C_{A_I}$  and  $C_{L_I}$  are computed. Equation (10) is solved for density given vehicle weight. Then  $C_f$  is computed with Equations (11) through (14). At this point,  $C_D$  can be computed from Equation (7) and L/D in Equation (5).

This system of equations can also be differentiated with respect to local radius to give

$$\frac{\partial(L/D)}{\partial r_i} = \frac{1}{C_D} \left[ \frac{\partial C_N}{\partial r_i} \cos \alpha - \frac{\partial C_A}{\partial r_i} \sin \alpha \right] - \frac{C_L}{C_D^2} \left[ \frac{\partial C_A}{\partial r_i} \cos \alpha + \frac{\partial C_N}{\partial r_i} \sin \alpha \right] \quad (16)$$

The axial force derivative in Equation (16) is obtained by differentiating Equations (7) through (14) to obtain

$$\frac{\partial C_A}{\partial r_i} = \frac{\partial C_{A_I}}{\partial r_i} + \frac{\partial C_{A_f}}{\partial r_i} \quad (17)$$

$$\frac{\partial C_{Af}}{\partial r_i} = \frac{S_{wet}}{S_{ref}} \frac{\partial C_f}{\partial r_i} + \frac{C_f}{S_{ref}} \frac{\partial S_{wet}}{\partial r_i} \quad (18)$$

$$\frac{\partial C_f}{\partial r_i} = \frac{\partial C_f}{\partial \rho} \frac{\partial \rho}{\partial r_i} \quad (19)$$

where the first two derivatives are obtained from Equations (8) and (9). Equation (19) is obtained by noting that  $C_f$  is only a function of altitude if velocity is fixed and altitude is a monotonic function of density. Therefore,  $C_f$  can be considered as a function of density. To obtain  $\partial \rho / \partial r_i$ , differentiate Equation (10) to obtain

$$\frac{\partial \rho}{\partial r_i} = \frac{2}{S_{ref} V^2} \left[ \frac{1}{C_{L1}} \frac{\partial W}{\partial r_i} - \frac{W}{C_{L1}^2} \frac{\partial C_{L1}}{\partial r_i} \right] \quad (20)$$

$$\text{where } \frac{\partial C_L}{\partial r_i} = \frac{\partial C_N}{\partial r_i} \cos \alpha + \frac{\partial C_{A1}}{\partial r_i} \sin \alpha \quad (21)$$

Equations (16) through (21) require the following five derivatives,  $\partial C_N / \partial r_i$ ;  $\partial S_{wet} / \partial r_i$ ;  $\partial C_f / \partial \rho$ ;  $\partial W / \partial r_i$ . The first 3 derivatives were developed using quadrilateral geometry models and local flow pressure methods<sup>3</sup>. The derivative  $\partial C_f / \partial \rho$  is not easily computed in closed form. However, using the Van Driest II method<sup>4</sup>, it can readily be evaluated numerically, i.e.,

$$\frac{\partial C_f}{\partial \rho} = \frac{\Delta C_f}{\Delta \rho} \quad (22)$$

The weight derivative in the current scheme is assumed to refer to the average vehicle weight during the cruise,  $W = (W_{tot} + W_{bo})/2$ .

$$\frac{\partial W}{\partial r_i} = \frac{1}{2} \left[ \frac{\partial W_{tot}}{\partial r_i} + \frac{\partial W_{bo}}{\partial r_i} \right] \quad (24)$$

Therefore,

These are the same derivatives required for Equation (4) and are discussed below.

2. Total Weight Derivative,  $\partial W_{tot} / \partial r_i$  - The total weight consists of four components as identified in Equation (2). The W<sub>other</sub> term includes all constant weight systems such as payload and avionics. Therefore, it is constant and

$$\frac{\partial W_{tot}}{\partial r_i} = \frac{\partial W_{str}}{\partial r_i} + \frac{\partial W_{fuel}}{\partial r_i} + \frac{\partial W_{prop}}{\partial r_i} \quad (25)$$

Weight models are needed for each of the three derivatives listed in Equation (25). In the following, simple scaling models are described which allow preliminary estimates of these derivatives. More complex weight models can be used for these and numerical derivatives obtained.

Structure Weight Derivative,  $\partial W_{str} / \partial r_i$  - For many conceptual design applications, the structural weight is assumed proportional to vehicle surface area, i.e.,

$$\frac{W_{str}}{S_{wet}} = \frac{W_{stro}}{S_{wet0}} \quad (26)$$

$$\frac{\partial W_{str}}{\partial r_i} = \frac{W_{stro}}{S_{wet0}} \frac{\partial S_{wet}}{\partial r_i} \quad (27)$$

where the  $S_{wet}$  derivative is known for a given geometry.

Fuel Weight Derivative,  $\partial W_{fuel} / \partial r_i$  - The fuel weight in conceptual design is often calculated by

$$W_{fuel} = V_{fuel} \times \rho_{fuel} \times e \quad (28)$$

The volume of fuel is that volume remaining after all other systems have been packaged.

$$V_{fuel} = V_{tot} - V_{str} - V_{prop} - V_{other} \quad (29)$$

At this conceptual design level the structural volume can be assumed negligible and volumes such as avionics and payloads can be assumed fixed. The fuel weight derivative is then

$$\frac{\partial W_{fuel}}{\partial r_i} = \rho_{fuel} \frac{\partial V_{fuel}}{\partial r_i} e \quad (30)$$

and the volume derivative is

$$\frac{\partial V_{fuel}}{\partial r_i} = \frac{\partial V_{tot}}{\partial r_i} - \frac{\partial V_{prop}}{\partial r_i} \quad (31)$$

The total volume derivative,  $\partial V_{tot} / \partial r_i$ , is easily computed from the quadrilateral formulation<sup>2</sup>. The propulsion volume derivative is obtained from the propulsion model described next.

Propulsion Weight Derivative.  $\partial V_{prop}/\partial r_i$  - The propulsion model at the conceptual design level is often based upon engine/inlet sizing algorithms which relate propulsion system size to vehicle drag at a Mach number, altitude, and angle of attack design point. In equation form, this is

$$W_{prop} = W_{prop0} \times \left(\frac{D}{D_0}\right)^c \quad (32)$$

Where  $D = q_{des} C_{Ddes} S_{ref}$  evaluated at the engine design point. The volume of the propulsion system is often assumed proportional to the weight by

$$V_{prop} = V_{prop0} \left(\frac{W_{prop}}{W_{prop0}}\right)^b \quad (33)$$

For both equations the derivatives with respect to local radius can be computed

$$\frac{\partial W_{prop}}{\partial r_i} = c \frac{W_{prop}}{D} \frac{\partial D}{\partial r_i} \quad (34)$$

$$\frac{\partial V_{prop}}{\partial r_i} = b \frac{V_{prop}}{W_{prop}} \frac{\partial W_{prop}}{\partial r_i} \quad (35)$$

Since the engine design point is fixed in altitude and Mach number,  $C_{Ddes}$  is the only parameter that varies with radius change, i.e.,

$$\frac{\partial D}{\partial r_i} = q_{des} S_{ref} \frac{\partial C_{Ddes}}{\partial r_i} \quad (36)$$

$$\text{where} \quad \frac{\partial C_{Ddes}}{\partial r_i} = \frac{\partial C_{A_{des}}}{\partial r_i} \cos \alpha + \frac{\partial C_{N_{des}}}{\partial r_i} \sin \alpha \quad (37)$$

3. Burnout Weight Derivative.  $\partial W_{bo}/\partial r_i$  - Since  $W_{bo}$  is defined by Equation (3)

$$\frac{\partial W_{bo}}{\partial r_i} = \frac{\partial W_{tot}}{\partial r_i} - \frac{\partial W_{fuel}}{\partial r_i} \quad (38)$$

to summarize, seven derivatives are needed to compute the range derivative. These are

$$\frac{\partial C_N}{\partial r_i}, \frac{\partial C_{A_i}}{\partial r_i}, \frac{\partial S_{wet}}{\partial r_i}, \frac{\partial V_{tot}}{\partial r_i}, \frac{\partial C_{A_{des}}}{\partial r_i}, \frac{\partial C_{N_{des}}}{\partial r_i}, \frac{\partial C_f}{\partial p}$$

All other derivatives are computed from these.

The above derivatives account for changes in lift-to-drag ratio; drag at the engine condition; structural, fuel and propulsion system weight; and fuel and propulsion system volume. These derivatives are readily calculated from the vehicle geometry and atmospheric properties and are the basis for the PICTOS airbreather synthesis program.

#### PROGRAM CHARACTERISTICS

The solid rocket PICTOS program version was modified to include airbreather synthesis based upon these sensitivity derivatives. To speed up the conceptual design process, we have applied interactive computer graphics to the initial sizing process. This approach includes a computer display of major missile subsystems, automated inlet/engine resizing, verification of internal packaging and guidelines for reshaping the external vehicles for improved range and aerodynamic characteristics.

The overall automated sizing process is illustrated in Figure 4 where the initial external geometry of the missile configuration is combined with user selected subsystem sizing models. These subsystem models include inlet/engine, structural weight, payload weight/volume, and avionics weight/volume. The external geometry and subsystem sizes are combined and displayed at the Cathode Ray Tube (CRT) display console. The optimization options are then selected to provide guidelines for improving the vehicle performance by reshaping.

The inlet/engine size is determined by using simple scaling laws to relate propulsion size to thrust, and hence drag requirements. The models are easily replaced if more sophisticated calculations are desired.

Once the inlet/engine and fuel load are sized the user can view a sideview or cross sections to identify any packaging problems or to begin reshaping.

Some typical internal subsystem component layouts are shown in Figure 5. Ramjet combustors can be tapered elliptical frustums. Turbojet engines must be circular. In either case, multiple engines and fuel tanks can be considered. Many of these models are user supplied. For example, the non-propulsion subsystems are often modeled as either tapered elliptical frustums or volume conforming shapes. Options are available for single or multiple inlet configurations. Inlets can have any shape.

The PICTOS airbreathing synthesis program was developed as shown by the flow chart of Figure 6. This flow chart is very similar to most conventional airbreathing missile synthesis procedures. Data are in-

put, aerodynamics are estimated at the engine sizing condition, the propulsion system is sized, subsystems are sized, cruise aerodynamics are estimated and a cruise range estimated. However, at this point instead of a fully automated vehicle sizing iteration scheme, sensitivity derivatives are computed and the user becomes actively involved through interactive graphics to review the design, modify it, and control the design iteration process.

The required initial external geometry definition in terms of body coordinates can be extremely simple. Because coordinate points can be added at each body cross section, new cross sections can be inserted and the entire set of coordinates can be scaled. Only a few critical coordinates need to be input and their scale is irrelevant.

The PICTOS program is in subroutine form so that the user can supply his shown avionics, payload, propulsion, and structural weight models. Typical models used for both the solid rocket and airbreather version are described below.

A typical internal subsystem packaging arrangement is shown in Figure 7. Options are available for single or twin engine configurations with skew angles relative to the missile axis. The subsystems are packaged by positioning the nozzle exit station at the base of the missile followed by the combustor or engine, payload and avionics. Internal ducting of inlets are often modeled by assuming their volume is proportional to the engine volume.

A typical weight model for structure is shown schematically in Figure 8. Structural weight per unit surface area is determined as a function of vehicle length. Typically, the weight per unit area is constant for short length vehicles because of minimum practical material thicknesses. For larger length vehicles, because of the need for stiffeners and bulkheads, weight per unit area increases with vehicle length.

The dimensions of the avionics volume are determined by user inputs as shown in Figure 9. The half-elliptic shape is most useful for flat bottom missiles. An optional weight input overrides the weight calculation and allows the user to account for other subsystems such as hydraulics and fuzes.

Typical payload and engine sizing input parameters are described in Figure 10 and 11 and are similar to the avionics inputs. Both can be tapered, elliptic cylinders. The engine nozzle is assumed conical for packaging purposes.

#### INTERACTIVE GRAPHICS

Once the engine is sized, the configuration is ready, for display and interaction shaping. Figure 12 shows the logic flow chart for viewing the configuration. Although it looks complicated, during actual PICTOS running, most of these options appear as interactive equations on the screen. External and internal sideviews (SIDE) and cross section views (XSECT) are available to the user. The sideviews are used to look for an oversize or undersize airframe and to label each cross section with station numbers. The internal cross section views are given at one of five longitudinal stations: avionics, forward end, avionics aft/payload forward end, payload aft/engine forward end, engine aft end, and nozzle exit. These are viewed to examine local payload interference with the external moldline. Another type of cross section view corresponds to a longitudinal station on the external moldline of the vehicle for which input coordinates were provided. These are the points which define the external moldline and are available for reshaping. This view also includes the sensitivity derivative results available for guiding the aerodynamic shaping of the vehicle. In addition to the range, the aerodynamic coefficients which can be considered are  $C_m$ ,  $C_A$ , and  $L/D$ .

#### EXAMPLE CASES

To illustrate this interactive design process two example cases are presented. The first considers a simple body shape and the second a full configuration.

Case 1 - Figure 13 shows the simple shape and the effect on range and  $L/D$  of varying the height. The body cross section is rectangular. The front half is a wedge. This shape was selected to illustrate the process modeled in PICTOS. For this case, a simple packaging model was assumed. The avionics, payload, fuel and engine packaging was assumed to conform to the body shape. As indicated by the plot, maximum range of approximately 1500 nmi is achieved for a configuration with a relatively low  $L/D$  of 4.2 at a body height of 21 inches. For smaller heights, although  $L/D$  is larger, the fuel carrier is lower as shown in Figure 14. Although fuel increases with increased height, the  $L/D$  decrease and total weight increase offsets the added fuel and range is less. In general, whether or not the best fixed length configuration occurs at the highest  $L/D$  is a function of the packaging and propulsion models.

Case 2 - A more complicated example case involves the initial configuration shown in Figures 15 and 16. The configuration is 195 inches long, has a short spatular nose, twin vertical tails, a larger delta wing, and two-dimensional inlets. The geometry inputs to PICTOS need not be sophisticated because the geometry will be modified during reshaping. Therefore, initial geometry definition can be very rapid and simple geometric shapes are used to define body cross sections. In this case, half-ellipses and rectangles are used.

Because of the crude inputs, some unusual panels exist on the configurations. At Section 2, a large, twisted panel connects this section to the one behind it. This panel will contribute significantly to drag. Section 6 includes a wing section attached to the rectangular body. This rectangular shape is a simple geometry for a first guess.

As an exercise for PICTOS, the goal of the reshaping of this configuration was to maximize range for a fixed length vehicle. The initial ramjet engine sizing and cruise conditions are shown in Figure 17. PICTOS uses this data to develop the initial configuration based upon the flow chart of Figure 6. The initial configuration results are shown in Figure 18. Range is 1372 nmi with 800 lb of fuel. At this point, the designer will display the external cross section views and begin modifying geometry to increase range.

For example, Figure 19 is a display of cross section 2 showing the current and recommended shape for increased range. The recommendations indicate a need to reduce the nose height but expand the side of the vehicle and bulge the bottom. The strong discontinuity results from the highly twisted panel identified in Figure 15. This is exactly why a designer is in the loop. Typically the designer will modify or ignore recommendations like these to maintain a realistic configuration. At station 6 in Figure 20, the recommendations for the body are to bulge it in all directions. This will add substantially more fuel without large drag increases.

Each cross-section of the configuration is usually viewed starting at the nose and moving aft. For this case, two reshaping and sizings were needed to achieve a maximum range configurations. Figure 21 shows the maximum range configuration from an isometric view. The reshaping has reduced the angles on the sides of the nose and increased body height.

Figure 22 compares side views of the three configurations. Each one increased in height and the nose was modified. Figure 23 shows the final configuration range of 2690 nmi. The fuel weight is double that of the initial configuration and L/D is over 5.7.

Figures 24 and 25 show the changes of the body cross sections during each iteration. Note the section 2 side wall bulging and the Section 5 bottom and top bulging. These allow more fuel to be carried with lower drag. Also notice at Station 5, the maximum range configuration has developed an off-centerline maximum height. This shape may not be desirable in the final design because of structural or carriage constraints.

#### SYNTHESIS CODE DEVELOPMENTS

The PICTOS code described in this paper has been used successfully to perform sizing and shape optimization of advanced missile configurations. The methods incorporated are appropriate for supersonic missiles that cruise at Mach numbers between 1.5 and 4.0 and altitudes to 120,000 feet. We have enhanced the code to a vehicle synthesis and optimization code with methods that are applicable from subsonic to hypersonic speeds. New analysis methods have been incorporated in the following six areas: aerodynamics, trajectory simulation, propulsion, structures, thermodynamics, and packaging.

The massive addition and replacement of methods required a significant change in the optimization methods. In the earlier code, vehicles were optimized using closed-form sensitivity derivative equations to minimize computer time. This approach demanded simplified methods that were required to be in mathematically differentiable form. This was impossible for the complicated models. Therefore, the main program logic and optimization techniques were redesigned. The most significant change is that the sensitivity derivatives are calculated numerically by physically moving a point and calculating the vehicle parameters and resulting derivatives. A summary of the upgrades is given in Figure 26 and the PICTOS design system in Figure 27.

#### SUMMARY

A missile synthesis approach for arbitrary-body shapes with airbreathing engines and subject to a variety of constraints is presented. By using interactive graphics, simple subsystem and performance models, low cost aerodynamic prediction techniques, and aerodynamic sensitivity derivatives a rapid, accurate and inexpensive approach to airbreather conceptual design is obtained. The technique is flexible because the user supplies the various subsystem and propulsion sizing algorithms consistent with his design problem. It can also be started with very simple geometries, which are completely different than the final shape. The resulting configurations are compatible with conceptual design level of accuracy and detail.

#### REFERENCES

1. S. Rinn and R. Bithell, Development of a Rapid Approach for Missile Synthesis, AIAA Paper 80-0259, January 1980.
2. A. J. Roch, Missile Integrated Design Analysis System (MIDAS), AIAA Paper 81-0285, January 1981.
3. A. E. Genetry, D. M. Smyth, W. R. Oliver, The Mach IV Supersonic/Hypersonic Arbitrary Body Program, AFFDL-TR-73-159, November 1973.
4. R. J. Krieger, A Technique for Developing Low Drag Nose Shapes for Advanced Supersonic Missile Concepts, AIAA Paper 80-0361, January 1980.
5. R. J. Krieger, An Aerodynamic and Signature Shaping Technique for Developing Advanced Supersonic Missile Concepts, AIAA paper 82-0373, January 1982.
6. R. J. Krieger, and L. J. Mockapetris, "Interactive Design Technique for Arbitrarily Shaped Missile Configurations", AIAA Paper 84-0390, January 1984.
7. R.J. Krieger, "An Aerodynamic and Signature Shaping Technique for Developing Advanced Supersonic Missile Concepts", AIAA Paper 82-0373, January 1982.



8. R. J. Krieger et al, "Aerodynamic Configured Missile Development - Final Report, Volume II - Configuration Development, Appendix B - Relations Between Aerodynamic Characteristics and Performance", AFWAL-TR-80-3071, July 1980.
9. E. R. Van Driest, "Calculation of the Stability of the Laminar Boundary Layer in a Compressible Fluid on a Flat Plate with Heat Transfer", J. Aero Science, Vol. 19, December 1952, pp 801-812.

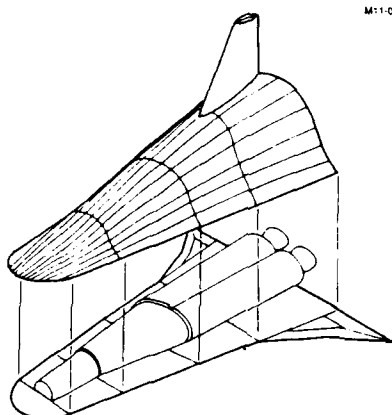


FIGURE 1. EXPLODED VIEW OF TYPICAL PACKAGING ARRANGEMENT

M11-07623

M11-5438C-1

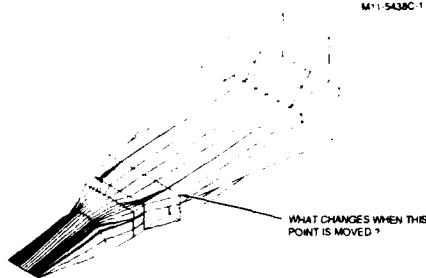


FIGURE 2. SENSITIVITY DERIVATIVE APPROACH

SURFACE ELEMENT

11-5553-1

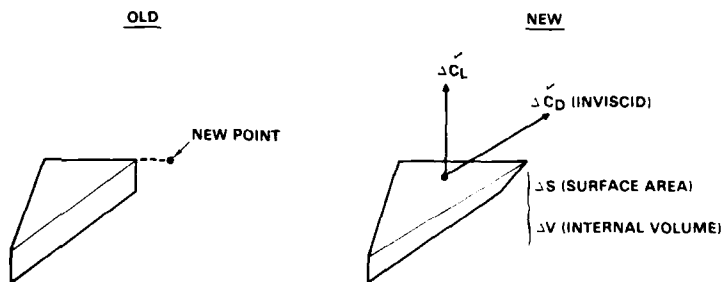


FIGURE 3. SENSITIVITY DERIVATIVE CONCEPT

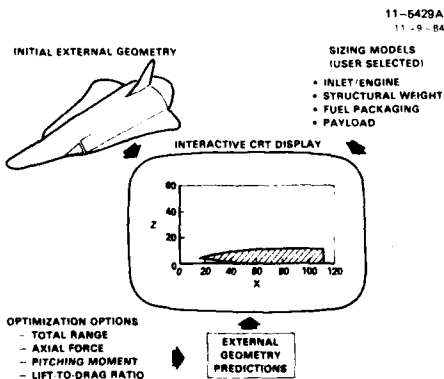


FIGURE 4. INTERACTIVE PICTOS DESIGN SYSTEM FOR AIRBREATHERS

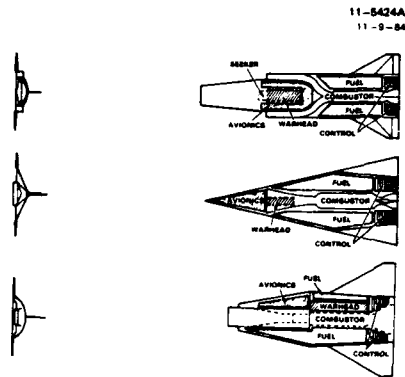


FIGURE 5. TYPICAL SUBSYSTEM INTERNAL LAYOUTS

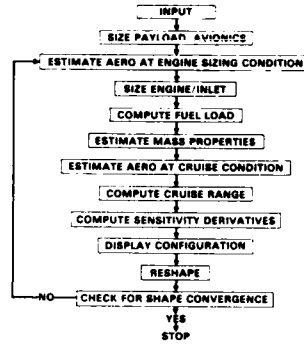


FIGURE 6. FLOWCHART OF SHAPING LOGIC

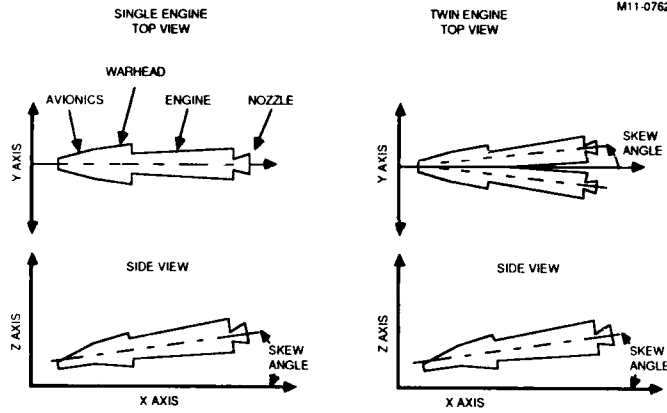


FIGURE 7. TYPICAL INTERNAL COMPONENT MODEL

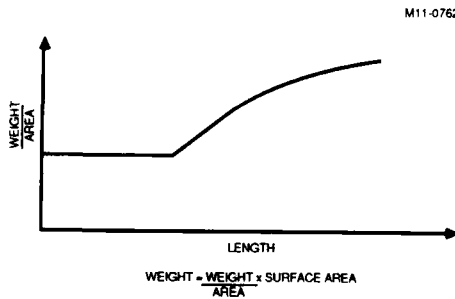


FIGURE 8. TYPICAL STRUCTURAL WEIGHT MODEL

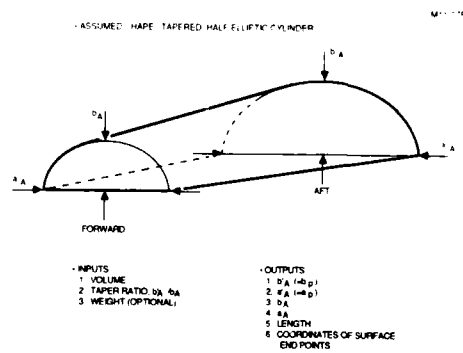


FIGURE 9. TYPICAL AVIONICS SIZING MODEL

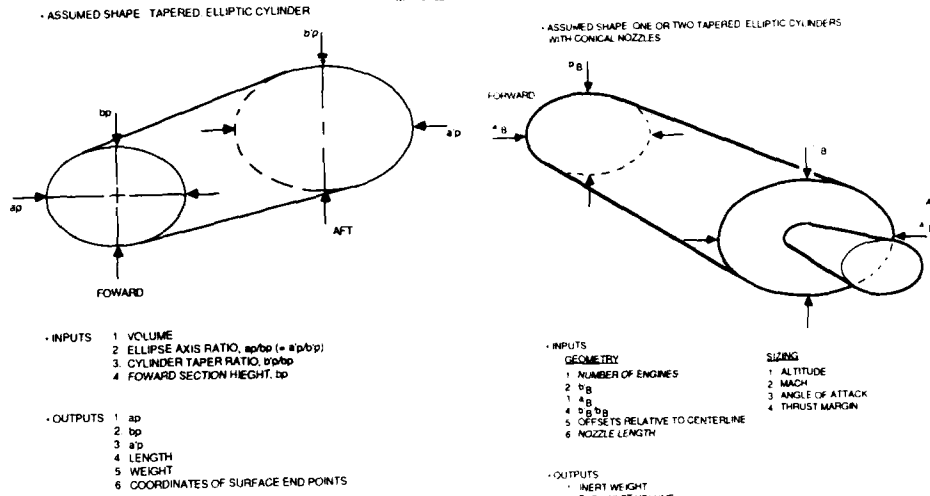


FIGURE 10. TYPICAL PAYLOAD SIZING MODEL

FIGURE 11. TYPICAL PROPULSION SIZING MODEL

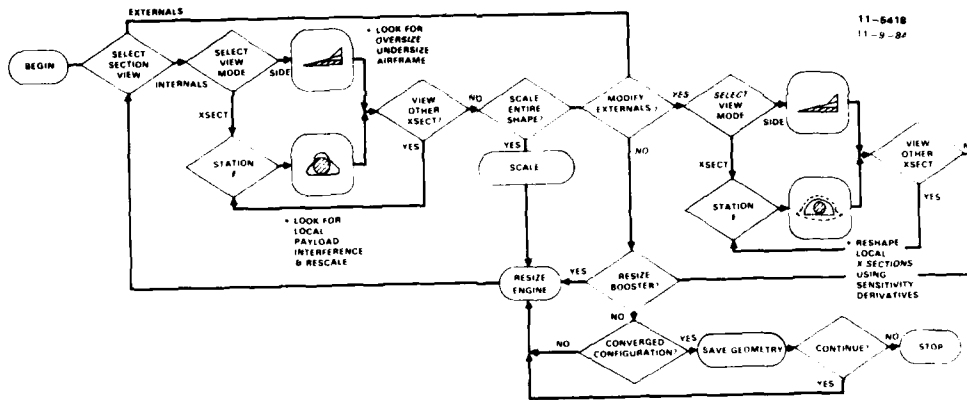


FIGURE 12. INTERACTIVE LOGIC

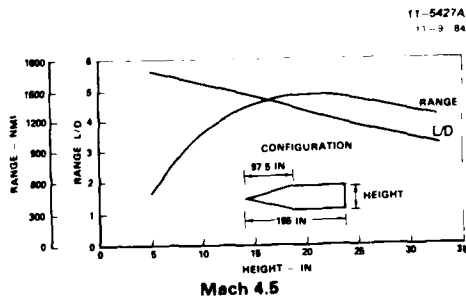


FIGURE 13. SENSITIVITY OF RANGE AND L/D TO MISSILE HEIGHT

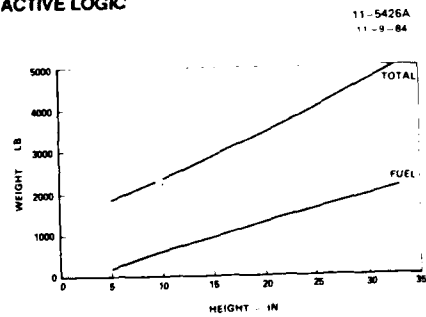


FIGURE 14. SENSITIVITY OF TOTAL AND FUEL WEIGHT TO MISSILE HEIGHT

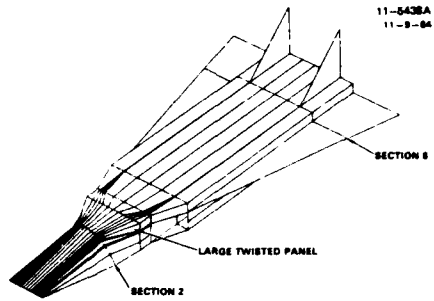


FIGURE 15. INITIAL CONFIGURATION ISOMETRIC VIEW

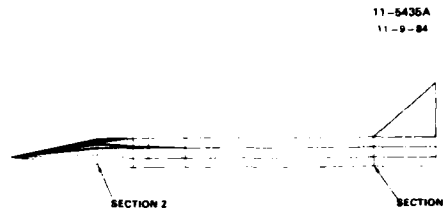


FIGURE 16. INITIAL CONFIGURATION SIDE VIEW

11-07629

| MISSILE DATA (CONSTANT)          |        |
|----------------------------------|--------|
| ENGINE SIZING CONDITIONS         |        |
| MACH NUMBER                      | 2.5    |
| ALTITUDE (FT)                    | 0      |
| ANGLE OF ATTACK (DEG)            | 0.0    |
| CRUISE CONDITIONS                |        |
| FREESTREAM VELOCITY (FT/SEC)     | 4426.9 |
| ANGLE OF ATTACK (DEG)            | 0.0    |
| PAYLOAD WEIGHT (LB)              | 354    |
| AVIONICS WEIGHT (LB)             | 300    |
| SPECIFIC FUEL CONSUMPTION (1/HR) | 3.70   |

FIGURE 17. INITIAL INPUT DATA

11-7750

| MISSILE DATA (INITIAL CONFIGURATION) |        |
|--------------------------------------|--------|
| RANGE (NM)                           | 1372.1 |
| ALTITUDE (FT)                        | 103471 |
| LIFT TO DRAG RATIO                   | 5.26   |
| FUEL WEIGHT (LB)                     | 800    |
| ENGINE WEIGHT (LB)                   | 294    |
| TOTAL VEHICLE WEIGHT (LB)            | 2598   |

FIGURE 18. INITIAL CONFIGURATION SIZING DATA

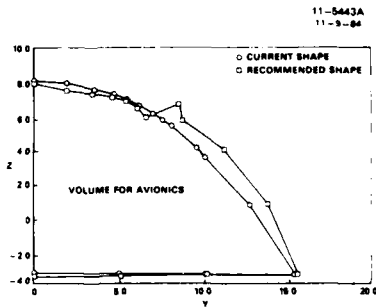


FIGURE 19. INITIAL CONFIGURATION SECTION 2 DISPLAY

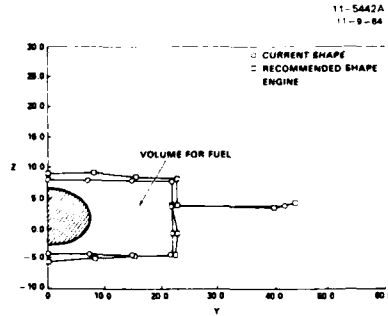


FIGURE 20. INITIAL CONFIGURATION SECTION 6 DISPLAY

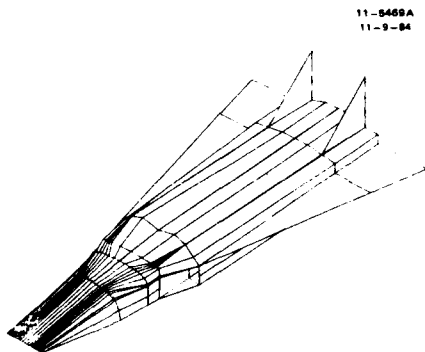


FIGURE 21. MAXIMUM RANGE CONFIGURATION ISOMETRIC VIEW

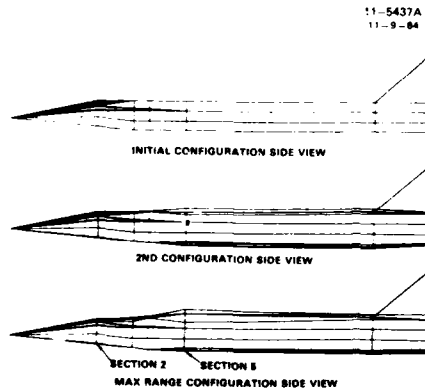


FIGURE 22. COMPARISON OF CONFIGURATIONS

**MISSILE DATA  
(FINAL CONFIGURATION)**

|                           | MAXIMUM RANGE CONFIGURATION |
|---------------------------|-----------------------------|
| RANGE (NM)                | 2880.0                      |
| ALTITUDE (FT)             | 98323                       |
| LIFT TO DRAG RATIO        | 5.72                        |
| FUEL WEIGHT (LB)          | 1854                        |
| ENGINE WEIGHT (LB)        | 245                         |
| TOTAL VEHICLE WEIGHT (LB) | 3408                        |

11-07831

11-5441A  
11-9-84

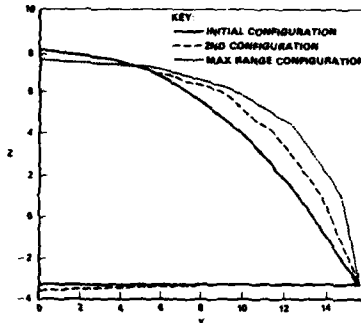


FIGURE 23. FINAL CONFIGURATION SIZING DATA

FIGURE 24. COMPARISON OF SECTION 2 SHAPES

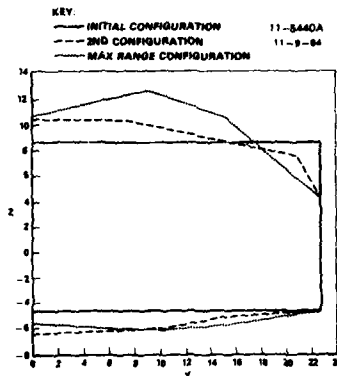


FIGURE 25. COMPARISON OF SECTION 5 SHAPES

M11-07832-1

| CATEGORY                | PRIOR CAPABILITY   | UPGRADE   | ADVANTAGE DUE TO UPGRADE   |
|-------------------------|--|---|--|
| SENSITIVITY DERIVATIVES | CLOSED-FORM EQUATIONS  | REPLACED WITH NUMERICAL DIFFERENTIATION                                   | MORE COMPLEX TECHNOLOGY MODELS POSSIBLE                                |
| TRAJECTORY SIMULATION   | RETURNING CLINE OR PROCKET EQUATIONS   | ADDED ARBITRARY TRAJECTORY PATHS  | REALISTIC FLIGHT PATHS. SIMULATE FLIGHT FROM TAKE-OFF TO END OF FLIGHT |
| PROPULSION              | ROCKETS, RAMJETS, TURBOJETS  | ADDED SCRAMJETS   | HYPERSONIC VEHICLES  |
| STRUCTURES              | MONOCOQUE STRUCTURES   | REPLACE WITH SHELL MODELS   | DETAILED STRUCTURE SIZES   |
| THERMODYNAMICS          | (NONE)   | SURFACE TEMPERATURE MAPS  | SIZE THERMAL PROTECTION SYSTEMS  |
| GEOMETRY MODELING       | POINT/PANELS MOVABLE   | POINT/PANELS GIVEN ATTRIBUTES   | CAN FIT LOCAL GEOMETRY OR CONTROL MATERIAL USED                        |
| PACKAGING               | 4 PACKAGES IN BODY<br>FIXED CROSS SECTION SHAPES<br>1 PACKAGE PER BODY SECTION | 16 PACKAGES CAN BE LOCATED<br>PACKAGES CAN OVERLAP OR CROSS BODY SECTIONS | COMPLICATED PAYLOAD/FUEL TANKAGE CONFIGURATIONS                        |

FIGURE 26. SUMMARY OF PICTOS UPGRADE

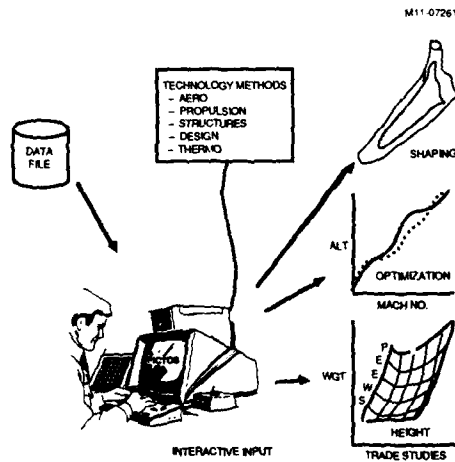


FIGURE 27. PICTOS DESIGN SYSTEM

## AERODYNAMIC HEATING OF MISSILES

by  
 R. Kapp, H. Mathauer, H. Rieger  
 DORNIER GMBH  
 Postfach 1420  
 D-7990 Friedrichshafen  
 F. R. G.

### SUMMARY

This paper presents the results of investigations of the aerodynamic heating of missiles. First the applied basic semiempirical methods to determine the flow field about the isolated components of missiles are described and some possibilities to calculate the heat flux in the boundary layer are specified for different pointed or blunted body noses, such as conical, ogival and hemispherical noses. The methods are valid for laminar and turbulent flow properties and in the transition region between laminar and turbulent. The calculated heattransfer factors or Stanton numbers are compared with experimental results. The agreement between theoretical and measured values is good.

In the second part of the paper a theoretical method for the calculation of the flow field around missile configurations is presented. This method is based on the parabolization of the compressible, stationary Navier-Stokes equations (PNS-eq.) and limited to supersonic Mach numbers. The quality of the results is demonstrated by comparison to corresponding test results of other authors.

Finally a computational method is described to calculate the local time-dependent temperatures at the surface or inside the body. The configuration is divided into a number of volume elements, thus permitting numerical solution of the time varying equation of heat transfer. The resulting temperatures for some special configurations are plotted and when possible compared with experimental results.

### 1. INTRODUCTION

The knowledge of aerodynamic heating of missile-surface and of the corresponding increase of missile temperature may be very important during the design of missiles. The heating of the missile-body is very often a determining factor in the selection of materials, in order to ensure that the structure and the internal equipment of the missile, such as seeker, guidance control, power supply, warhead or propellant will not become too warm during its mission. Aerodynamic heating even may become critical for the operational efficiency of a missile, especially for an air-to-air-missile with an infrared-seeker and Mach numbers up to 4 and sometimes even more.

Figure 1 shows the theoretical stagnation temperature as a function of Mach number and altitude, indicating a large increase of stagnation temperature  $T_0$  with increasing Mach number  $M$  and a slight decrease of  $T_0$  with increasing altitude  $H$ . These stagnation temperatures represent a rough measure of the maximum temperatures induced by aerodynamic heating, the real maximum temperatures however are fortunately below the stagnation temperatures. By real gas effects the exact stagnation temperatures are lower than the values of fig. 1, which is valid for ideal gas.

The prediction of aerodynamic heating is possible by wind tunnel tests or by computational methods which include a wide spectrum of methods from approximate empirical methods to exact solutions of the full Navier-Stokes equations. A survey and introduction on common methods used to predict aerodynamic heating of missiles is given by Neumann and Hayes in [0], describing semiempirical methods, theoretical methods and test methods.

### 2. CALCULATION OF AEROKINETIC HEATING AND FLOW PROPERTIES

#### 2.1 Semiempirical Method

The method to determine the heat flux between the boundary layer and the missile-surface is based on the assumption that the calculation may be applied to isolated components of the missile. The body is considered as a cylinder with either a hemispherical, conical or ogival nose, where the cone or the ogive may be pointed or blunted. The wing and tail are considered as flat plates with wedged or hemicylindrical noses. A summary of the possible configurations and the different flow states is shown in figure 3.

The considered velocities may be from subsonic up to hypersonic, but the results will be the better, the higher the Mach number is. The applied methods are valid for the range from zero up to about twenty degrees incidence with the restriction that no vortex or shock induced change of the heat transfer is considered.

It is important to note that at the junction between body and wing or tail, the induced vortices and shocks develop very high rate of kinetic heating. However, this effect is not considered in this method.

The heat flux  $\dot{q}$  between the surrounding flow and the surface of a missile is induced by the gradient of the fluid temperature at the solid wall  $(\partial T/\partial y)_{y=0}$  according to Fourier's law of heat conduction  $\dot{q} = \lambda (\partial T/\partial y)_{y=0}$ . Figure 2 shows characteristic temperature profiles in the boundary layer with cooled, adiabatic and heated wall. Instead of using  $\partial T/\partial y$ , the heat flux can be expressed by the difference  $T_r - T_w$  between the adiabatic wall temperature  $T_r$  (= recovery temperature) and the actual wall temperature  $T_w$  as  $\dot{q} = \alpha_w(T_r - T_w)$ . The semiempirical method presented in this paper is based on this equation. To calculate the heat flux it is necessary to determine the quantities listed in figure 4. In order to avoid the complicated boundary layer calculations, empirical approximations are used for the estimation of the flow parameters  $T_r$ ,  $\alpha_w$ ,  $T_\delta$ ,  $M_\delta$ .

In figure 4 the subscript  $\delta$  indicates a boundary layer condition, whereas the subscript  $w$  denotes a wall condition. The most important quantities to determine the heat flux are the heat-transfer factor  $\alpha_w$  or the corresponding, nondimensional, so called Stanton number  $St$  and the recovery factor  $r$ , which is the ratio of temperature increase due to friction to the increase due to compression. To calculate the Stanton number we must determine the flow field and especially the pressure distribution in the nearfield of the body. In figure 5 some methods to calculate the local pressure distribution for several configurations can be seen. For the most interesting case of supersonic and hypersonic Mach numbers we calculate the pressure distribution by the following methods:

For blunt bodies and pointed bodies with detached nose shocks we determine the pressure of the body surface by the so-called "modified Newtonian theory", which supplies very good results over the forward portion, but predicts free stream pressure at the shoulder.

Therefore we use the so-called "blast wave analogy" near the shoulder. This method is not applicable either in the nose region, where the details of the flow are important or far downstream where the shock wave decays to a Mach wave. The limiting value between the modified Newtonian theory and the blast wave theory is that point on the surface from which on the Newtonian pressure is less than the blast wave value. Farther downstream we use the blast wave theory as long as the pressure is higher than the ambient pressure.

For pointed bodies with attached nose shock we use equations, tables and charts for compressible flow (i. e. see [1]) in the nearfield of the stagnation point. Near the junction between nose and cylindrical body we determine the surface pressure from tables of supersonic flow over cone cylinder (i. e. see [2]).

A very important criterion for the heat flux is the physical effect whether the flow is laminar or turbulent. This difference determines the size of the Stanton number, which for turbulent flow may be up to ten times the value for laminar flow, whereas the recovery factors differ only slightly ( $r \approx 0.82$  up to  $0.85$  for laminar flow and  $r \approx 0.88$  for turbulent flow). The ratio between turbulent and laminar heat transfer factors increases with increasing Reynolds number. This means that for many configurations the heat transfer factor has its highest value far downstream from the stagnation point. This might be surprising in the first moment, but we should keep in mind this physical fact, when we later calculate the temperature distribution on the surface of the body.

The beginning of flow transition is influenced by several parameters. Some of the governing parameters are the flight Mach number, the local Mach number and the local Reynolds number at the outer edge of the boundary layer, but besides these there are additional parameters such as pressure gradient in the flow direction, geometrical shape of the nose, surface roughness or temperature ratio between surface and flow. In the literature we often find the local momentum thickness  $\theta$  and the displacement thickness  $\delta^*$  instead of the local Mach- and Reynolds numbers.

In our digital program we use experimental results from H. Schlichting [3], K. F. Stetson [4], R. W. Detra [5], K. R. Czarnecki [6] and L. D. Wing [7] for the beginning of flow transition. Moreover we have to remember that the extent of the transition region between laminar and full turbulent flow increases rapidly with increasing Mach number, where the transition region is usually considered to be characterized by the intermittent appearance of turbulent spots which grow as they move downstream until they finally merge into one another to form the turbulent boundary layer. This "spot theory" from H. W. Emmons [8] is extended to flows on blunt bodies by K. K. Chen and N. A. Thyson [9] and is fitted in the computer program.

To calculate the local Stanton number and recovery factor we use a procedure from L. D. Wing [10] for ogival noses and a method from E. R. Van Driest [11] for all other configurations. According to Van Driest's method the Stanton number depends on the geometrical shape and on the local Reynolds number, which is determined with the flow parameters at the outer edge of the boundary layer. The Stanton number is inversely proportional to the square root of the Reynolds number in laminar flow and also inversely proportional to the fifth root of the local Reynolds number in turbulent flow. It should be noted here that Van Driest's method neglects real gas effects.

A typical result for the Stanton number on a flat plate is shown in figure 7, where the local flow parameters in the boundary layer are varied. In figure 8 we see the local heat flux for laminar turbulent flow state and in the transition region of a sphere.

For a pointed tangent ogive nose with attached shock the flow parameters are calculated by subdividing the ogival nose into a short pointed conical region followed by several truncated cones. The boundary layer heat transfer rate and shear stresses at the wall are calculated by means of the Eckert and Tewfik [12] adaption of Lee's momentum integral

equation and the use of Reynolds analogy for the laminar case, and the flat plate reference enthalpy method described in [13] (also applying Reynolds analogy) for the turbulent boundary layer case.

## 2.2 Theoretical Method (PNS-Method)

Theoretical calculations of flow fields around solid bodies at high supersonic or hypersonic speeds and the calculation of heat transfer at all Mach numbers must be based on the complete conservation equations, including viscous effects and careful treatment of the boundary layer. The consideration of complex vortex- and shock-systems is important, as they may effect extremely high local heat flux to the body surface. Figure 9 gives a classification of approximation levels of theoretical methods for the calculation of flow fields. Heat transfer calculations are possible only by the methods of level 1 to 3.

Full 3-D Navier-Stokes calculations of flow fields around realistic configurations are almost impossible with the available generation of computers. Therefore it is reasonable that efficient theoretical methods are based on approximations to the Navier-Stokes equations.

The "Thin-Layer"-approximation is able to give very good results [18], [19], but needs big computers [20] and has some problems with viscous effects at curved walls [21]. The computational expenditure is close to that of full Navier-Stokes solutions, using time-step-integration.

Using the parabolized Navier-Stokes equations (PNS) the amount of needed CPU-time and store capacity can be reduced to reasonable values. PNS-approximations are limited to supersonic flow calculations without recirculation, open flow separations however (vortex sheet separation) are included. Compared to methods solving the complete time-dependent conservation equations, the advantage of PNS-methods is given by the spatial integration in direction of the main flow.

Successful applications of PNS-methods, based on the approximations of Vigneron et al. [22] and Schiff and Steger [23] include 3-D flow calculations for simple reentry bodies [24], for the US space shuttle [25], [26], [27], and for a supersonic fighter [28]. All cited applications used PNS-methods based on finite difference discretization. The presented Dornier method by Rieger [29] is based on a finite volume formulation.

Starting with the integral form of the conservation equations (s. figure 10), the finite volume formulation of the conservation equations is defined (see fig. 11, 12; notation after [30]). The system of equations has to be completed by the equations of a perfect gas, of Fourier's-law for molecular transfer of energy (heat conduction), and of Newtonian fluid (specification of Newtonian stress tensor). The influence of the temperature on the dynamic viscosity is used after Sutherland.

Details of the mathematical formulations and of the parabolization of the equation system are given by Rieger [29]. Figure 13 gives a characterization of the purpose, problem and measures of the parabolization. It has been proofed [22] that a good approximation of the pressure gradient in the subsonic layer is important and necessary for accurate results, except for some hypersonic problems [31].

In the "sublayer"-method (see fig. 14), extended by Schiff and Steger [23] to non-iterative PNS-methods, the pressure gradient in integration direction of the subsonic layer is taken from the bordering supersonic flow. This assumption seems to cause a consistency problem and a limitation of the minimum integration intervals for numeric stability (see [23], [32], [33]).

Therefore the Dornier PNS-method is based on the Vigneron-approximation [22], using a portion of the pressure gradient which gives no mathematical problems and no limitation of the minimum integration interval. This is important for the accurate flow field calculation at pointed body noses.

In order to reduce the amount of CPU-time and of store capacity, the presented PNS-method assumes (see fig. 15) that the planes  $x^1 = \text{const.}$  of the curved coordinate system  $x^i = (\xi, \eta, \zeta)$  with  $(i = 1, 2, 3)$  are identical with the planes  $x^{i'} = \text{const.}$  of a fixed cartesian coordinate system  $x^{i'} = (x, y, z)$  with  $(i' = 1', 2', 3')$ .

## 2.3 Results of Aerokinetic Heating and Flow Field Calculations

### Semiempirical method:

Figure 16 shows calculated heat transfer factors or Stanton numbers for a sphere ( $M_\infty = 8.9$ ) compared with experimental results. The agreement between the two theoretical methods and between theory and experiment is good. In figure 17 we see the results for a blunted cone ( $M_\infty = 7.0$ ). Here we have great difference between the same methods as in figure 16, especially in the region of the junction from spherical to conical body. Compared with measurements, we can see that the presented method is better than Lee's method. In figure 18 we see a blunted conical nose followed by a cylindrical body, the so-called AGARD-calibration-model HB-1. The agreement between calculated and experimental values is very good. In figure 19 the heat transfer factor is shown for a pointed ogive nose followed by a cylindrical body. The angle of incidence is varied from -10 degrees up to



10 degrees. Near the stagnation point the heat transfer factor decreases downstream, but behind the station, where the transition begins, we recognize a very high increase in the heat transfer. The increase on the windward side is much higher than on the leeward side. The differences between windward and leeward sides are relatively weak on the cylindrical body. The agreement between theoretical and experimental results of the ogive nosed body is also good.

#### PNS-method:

For testing the PNS-method some typical configurations were used. Figure 20 shows calculated pressure coefficients compared to test results for the NASA-forebody No. 4 (after [34]) at  $M = 1.7$ ,  $\alpha = -5^\circ$ . The agreement between theoretical and test results is good. Comparisons of PNS-results and TNS-results of Haase [35] for a flat plate in supersonic flow ( $M = 3.0$ ) proof good accuracy of the PNS-method (see fig. 21, 22). Figure 24 shows the comparison of the present PNS-method results with test result of Holden and Moselle [36], and with theoretical results of Hung and McCormack [37] and Lawrence et al. [38] for a hypersonic compression ramp defined in figure 23.

An important testcase is given by the calculations for a pointed cone (at  $M = 7.95$ ;  $\alpha = 12^\circ, 24^\circ$ ) which has been tested by Tracy [39]. Figure 35 shows the shock position in the solution adaptive coordinate system after Haase [40] which agrees very well with the test results of Tracy. The pressure coefficients and the heat transfer coefficients (see fig. 26, 27) versus the circumferential angle are in very good agreement with the test results.

Figure 28 shows the geometry of an ogive for which some results of the time dependent temperature distribution are available [17]. Heat flux calculations by the Dornier-PNS-method and by the semiempirical method proof a good agreement of the calculated results (fig. 29) at  $M = 1.99$  and  $\alpha = 0^\circ$ , confirming the good experience with the semiempirical method.

### 3. CALCULATION OF LOCAL TEMPERATURES

#### 3.1 Calculation method

If the Stanton numbers and the recovery factors are determined, the local time-dependent temperatures at the surface or inside the missile can be calculated. Therefore the configuration is divided into a number of volume elements, thus permitting numerical solution of the time varying equations of heat transfer. There is a physical requirement in the method, that the temperature is constant within a volume element. The temperature of an element depends on heat transfer, heat convection, picked up and reflected heat radiation, internal heat conduction and from internal losses. For any volume element the heat balance is expressed (see figure 30) and we obtain a system consisting of a number of first order differential equations.

For steady state flows, we can determine the temperatures by solving the system of equations iteratively. For intermittent states of flow, which are typical in missile flights, we solve the system of ordinary nonlinear differential equations by a fifth order Runge-Kutta-method. The computational organization of the digital program provides that the heat transfer factors  $\alpha_w$  and the corresponding recovery temperatures  $T_{rec}$  for several Mach numbers and angles of attack are determined in a first step. The results will be used in form of input data in the second step, the computation of local temperatures. This simplification requires that the influence of temperature on the heat transfer factor is negligible.

It should be noted here that the time for computation of the local temperatures depends first of all on the number of volume elements. With 24 volume elements and a duration of flight of about 30 seconds in an example, we had about two minutes of computation time whereas the semiempirical calculation of aerodynamic heating runs very much quicker.

#### 3.2 Results of Local Temperature Calculations

In figure 31 we see the time varying local temperatures on the surface of a spherically-nosed cylindrical body. The appropriate Mach-time-curve is typical for an air-to-air missile. The most important facts in this figure are that the station with the highest temperature of the body is not the stagnation point, but the station of the beginning of transition and that the maximum value comes chronologically clearly after the maximum of Mach number. Besides these effects we should notice that those stations with high heating during acceleration of the missile lose more temperature when the Mach number decreases. The heating of the cylindrical regions is weak compared with that of the stagnation region.

Figure 32 shows time-dependent temperatures at the stagnation point for one-layer-model and five-layer-model calculations. Here we can see that it is extraordinarily necessary to use a multi-layer-model. With an one-layer-model we determine temperatures which are too low during acceleration and too high during a following speed retardation. If we want to know the exact surface temperatures or internal temperatures the multi-layer-model is necessary except the heat conduction is relatively good (see figure 14). But we should remember that the materials of body noses are usually glass or something like that especially if we have infrared seekers.

The results in figures 31, 32 and 33 are valid for axisymmetric flow. In figure 34 the angle of incidence is 20 degrees. The temperature on the windward side is up to about 150 degrees higher than on the leeward side. This statement is only valid during acceleration of the missile. When the Mach number decreases, the temperature decreases too, where the reduction in temperature is higher for areas of higher temperature during accelerated flight.

In figure 35 some theoretically determined temperatures of a pointed tangent ogive nose are compared with experimental results, where the Mach number was constant for about half a minute. First of all we have to note that the differences between calculated and experimental results are not greater than about twenty degrees, which means a good agreement. It is nearly impossible to specify the reasons for the differences, but it seems important to show that the theoretical recovery temperatures after a relatively long time of mission are too low in the stagnation- and transition region, whereas more downstream (element C in figure 35) the agreement is very good.

#### 4. REFERENCES

- [0] Hensch, M. J.; Nielsen, J. N.:  
Tactical Missile Aerodynamics.  
Progress in Astronautics and Aeronautics, Volume 104,  
American Institute of Aeronautics and Astronautics, Inc. (1986)
- [1] Equations, tables and charts for compressible flow.  
NACA-Report 1135 (1953)
- [2] Clippinger, R. F.; Giese, J. H.; Carter, W. C.:  
Tables of supersonic flow about cone-cylinders. Part I: Surface Data  
Ballistic Research Lab., Report 729 (1950)
- [3] Schlichting, H.; Truckenbrodt, E.:  
Aerodynamik des Flugzeugs, 2. Band.  
Springer-Verlag Berlin/Göttingen/Heidelberg (1960)
- [4] Stetson, K. F.:  
Boundary-layer transition of blunt bodies with highly cooled boundary layers.  
J. Aerospace Sci. 27, p. 81 - 91 (1960)
- [5] Detra, R. W.; Hidalgo, H.:  
Generalized Heat Transfer Formulas and Graphs for Nose Cone Re-Entry into the  
Atmosphere.  
ARS Journal (March 1961)
- [6] Czarnecki, K. R.; Sinclair, A. R.:  
An investigation of the effects of heat transfer on boundary-layer transition  
on a parabolic body of revolution (NACA RM-10) at a Mach number of 1.61.  
NACA Report 1240 (1956)
- [7] Wing, L. D.:  
Aerodynamic Heating for Wedge/Wedge or Cone/Cone at angles of attack from  
zero to approximately 40°.  
Fairchild Hiller Corporation, Report No. ER-116 (1968)
- [8] Emmons, H. W.:  
The Laminar-Turbulent Transition in a Boundary Layer - Part I.  
Journal of the Aerospace Sciences, Vol. 18, No. 7, p. 490 - 498 (July 1951)
- [9] Chen, K. K.; Thyson, N. A.:  
Extension of Emmons' Spot Theory to Flows on Blunt Bodies.  
AIAA Journal 9, p. 821 - 825 (May 1971)
- [10] Wing, L. D.:  
Tangent Ogive Nose Aerodynamic Heating Program: NQLDW 019.  
NASA TN X-65540 (1971)
- [11] Van Driest, E. R.:  
The problem of aerodynamic heating  
Aeronautical Engineering Review 15, No. 10, p. 26 - 41 (1956)
- [12] Eckert, E. R. G.; Tewfik, O. E.:  
Use of Reference Enthalpy in Specifying the Laminar Heat Transfer Distribution  
Around Blunt Bodies in Dissociated Air.  
Journal of the Aero/Space Sciences, Vol. 27, No. 6 (1960)
- [13] Libby, P. A., Cresci, R. J.:  
Evaluation of Several Hypersonic Turbulent Heat Transfer Analyses by Comparison  
with Experimental Data.  
WADC Technical Note 57-72 (July 1957),  
ASTIA DOC. No. AD 118 093

- 14] Cox, R. N.; Crabtree, L. F.:  
Elements of hypersonic aerodynamics.  
Academic Press, New York/London, p. 132 ff (1965)
- 15] Lees, L.:  
Laminar heat transfer over blunt-nosed bodies at hypersonic flight speeds.  
Jet Propulsion 26, p. 259 - 269 (1956)
- 16] Schepers, H. J.:  
Wärmeübergangsuntersuchungen an rotationssymmetrischen Flugkörpermodellen bei  
Hyperschallanströmung mittels des Infrarot-Meßverfahrens.  
DLR Mitteilung 71-19 (1971)
- 17] Steinheil, E.; Hamer, E.:  
Allwettertauglicher Wärmeschutz für Flugkörper.  
Forschungsbericht aus der Wehrtechnik, Dornier-Bericht 71514 (1980)
- 18] Pulliam, T. H.; Steger, J. L.:  
On Implicit Finite-Difference Simulations of Three Dimensional Flow.  
AIAA-78-10 (1978)
- 19] Steger, J. L.:  
Implicit Finite Difference Simulation of Flow About Arbitrary Geometries with  
Application to Airfoils.  
AIAA-77-665 (1977)
- 20] Baldwin, B. S.; Lomax, H.:  
Thin Layer Approximation and Algebraic Model for Separated Turbulent Flows.  
AIAA-78-0257 (1978)
- 21] Blottner, F. G.:  
Significance of the Thin-Layer Navier-Stokes Approximation.  
Third Symposium on Numerical and Physical Aspects of Aerodynamic Flows,  
California State University, Long Beach, California, Jan. 21 - 24, 1985
- 22] Vigneron, Y. C.; Rakich, J. V.; Tannehill, J. C.:  
Calculation of Supersonic Viscous Flow over Delta Wings with Sharp Subsonic  
Leading Edges.  
AIAA-Paper: 78-1137 (1978)
- 23] Schiff, L. B.; Steger, J. L.:  
Numerical Simulation of Steady Supersonic Viscous Flow.  
AIAA-Paper: 79-0150 (1979)
- 24] Chaussee, D. S.; Patterson, J. L.; Kutler, P.; Pulliam, T. W.; Steger, J. L.:  
A Numerical Simulation of Hypersonic Flows over Arbitrary Geometries at High  
Angle of Attack.  
AIAA-Paper: 81-0050 (1981)
- 25] Chaussee, D. S.; Rizk, Y. M.; Buning, P. G.:  
Viscous Computatin of a Space Shuttle Flow Field.  
NASA-TM-85977 (1984)
- 26] Prabnu, D. K.; Tannehill, J. C.:  
Numerical Solution of Space Shuttle Orbiter Flow Field Including Real Gas Effects.  
AIAA-Paper: 84-1747 (1984)
- 27] Balakrishnan, A.:  
Computation of Viscous Real Gas Flow Field for the Space Shuttle Orbiter.  
AIAA-Paper: 84-1748 (1984)
- 28] Chaussee, D. S.; Blom, G.; Waj, J. C.:  
Numerical Simulation of Viscous Supersonic Flow over a Generic Fighter  
Configuration.  
NASA-TM-86823 (1985)
- 29] Rieger, H.; Mathauer, H.:  
Thermische Aufheizung von Flugkörpern bei hohen Geschwindigkeiten.  
Dornier-Bericht. BF 7/86 B (1986)
- 30] Flügge, W.:  
Tensor Analysis and Continuum Mechanics.  
Springer-Verlag, Berlin (1972)
- 31] Lin, T. C.; Rubin, S. G.:  
Viscous Flow over a Cone at Moderate Incidence.  
Computer & Fluids, Vol. 1, p: 37 - 57 (1973)
- 32] Mitchell, A. R.; Griffiths, D. F.:  
The Finite Difference Method in Partial Differential Equations.  
John Wiley & Sons, Chichester (1980)

- [33] Kaul, U.; Chaussee, D. S.:  
A Comparative Study of the Parabolized Navier-Stokes Code Using Various Grid  
Generation Techniques.  
AIAA-Paper: 84-0459 (1984)
- [34] Townsend, J. C.; Howell, D. T.; Collins, F. K.; Hayes, C.:  
Surface Pressure Data on a Series of Analytic Forebodies at Mach Numbers from  
1.7 to 4.5 and Combined Angles of Attack and Sideslip.  
NASA-TM-80062, June 1979
- [35] Haase, W.; Wagner, W.; Jameson, A.:  
Development of a Navier-Stokes Method Based on Finite Volume Solution Techniques  
for the Time-Dependent Euler Equation.  
Proc. of GAMM-Conf. on Numerical Methods in Fluid Mechanics, in: Notes on Numerical  
Fluid Mechanics, Vol. 7, Vieweg-Verlag (1984)
- [36] Holden, M. S.; Moselle, J. M.:  
Theoretical and Experimental Studies of the Shock Wave - Boundary Layer Interaction  
on Compression Surfaces in Hypersonic Flow.  
CALSPAN, Buffalo, N. Y., Rep. AF-2410-A-1 (1969)
- [37] Hung, C. M.; MacCormack, R. W.:  
Numerical Solutions of Supersonic and Hypersonic Laminar Compression Corner Flows.  
AIAA-Journal, Vol. 14, p. 475 - 481 (1976)
- [38] Lawrence, S. L.; Tannehill, J. C., Chaussee, D. S.:  
Application of the Implicit MacCormack Scheme to the Parabolized Navier-Stokes  
Equations.  
AIAA-Journal, Vol. 22, p. 1755 - 1763 (1984)
- [39] Tracy, R. R.:  
Hypersonic Flow over a Yawed Circular Cone.  
Ph.D.-Thesis, California Institute of Technology, Graduate Aeronautical Lab.  
Memo 69, Aug. 1963
- [40] Haase, W.; Misegades, K.; Naar, M.:  
Adaptive Grids in Numerical Fluid Dynamics.  
Int. Journal for Numerical Methods in Fluids, Vol. 3, p. 515 - 528 (1985)

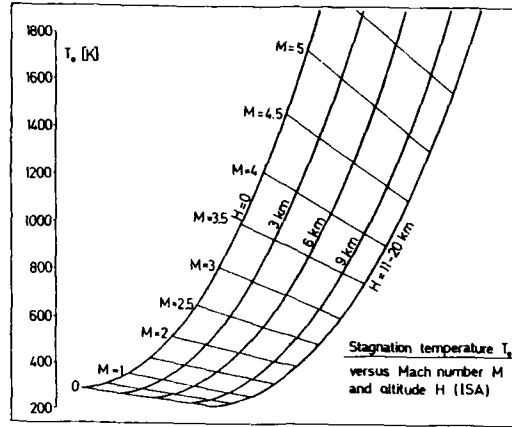


Figure 1

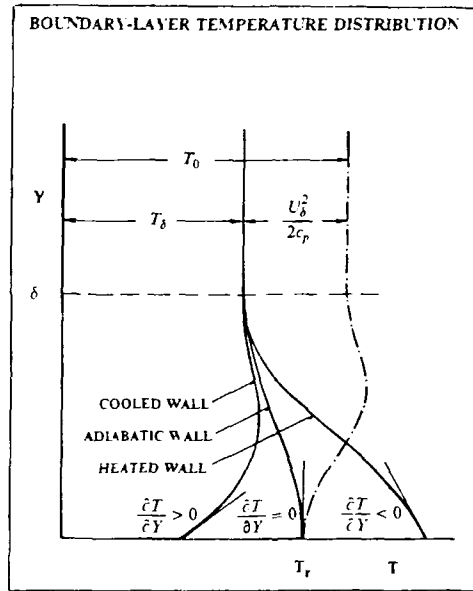


Figure 2

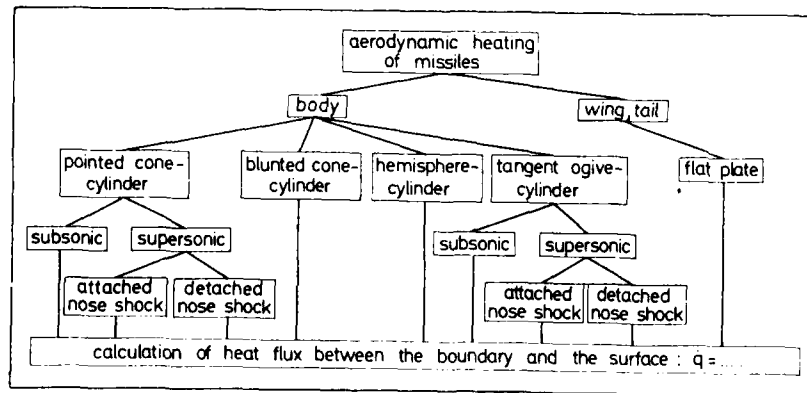


Figure 3

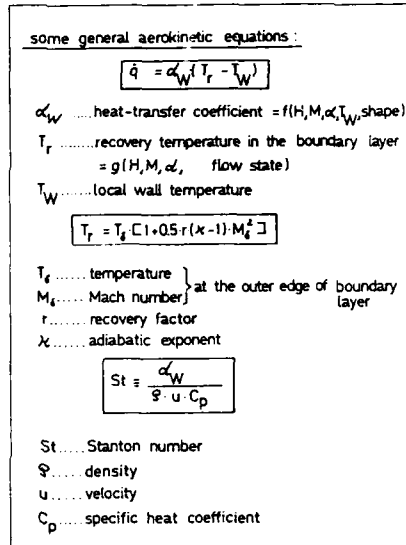


Figure 4

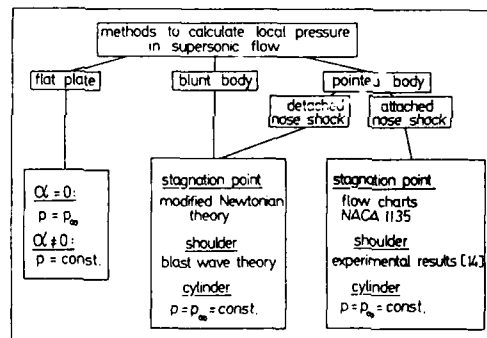


Figure 5

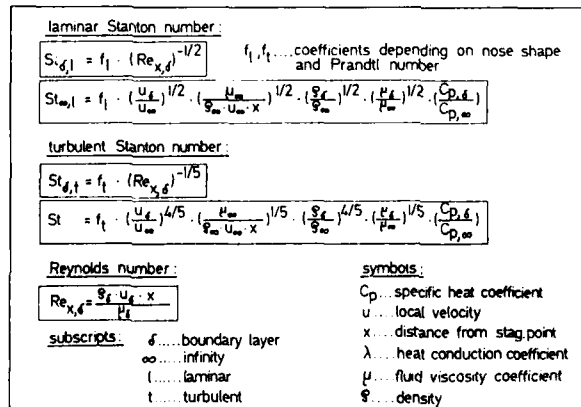


Figure 6

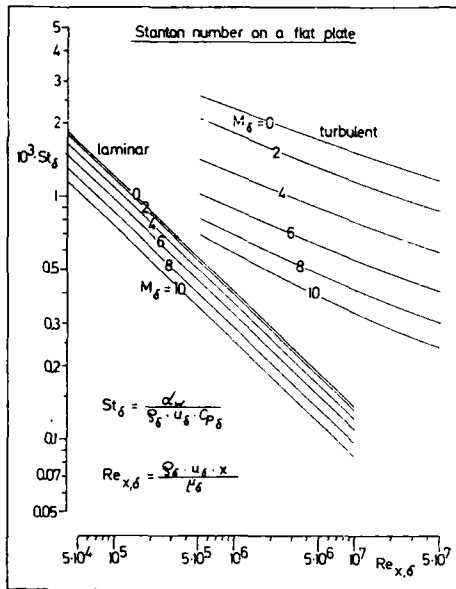


Figure 7

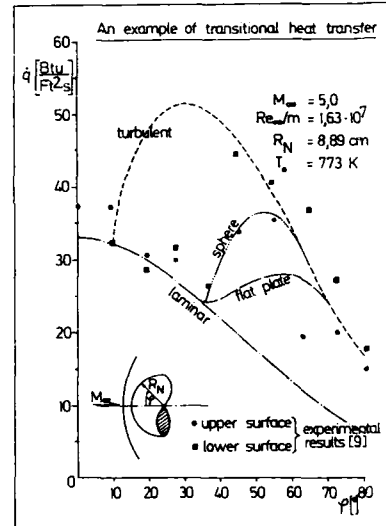


Figure 8

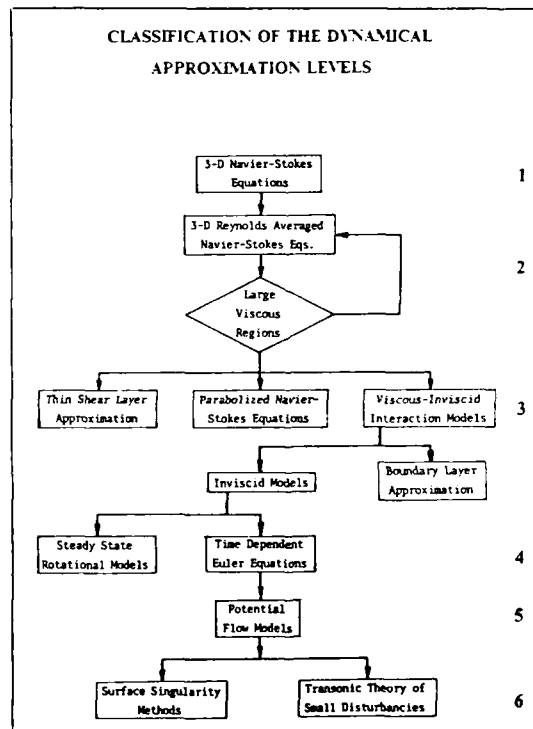


Figure 9

STEADY STATE FORMULATION  
OF CONSERVATION EQUATIONS

$$\int_S (\underline{A}v + B) \cdot \underline{n} dS = 0$$

CONSERVATION OF MASS :  $A \equiv \rho$  ;  $B \equiv 0$

CONSERVATION OF MOMENTUM :  $A \equiv \rho \underline{v}$  ;  $B \equiv -\underline{g}$

CONSERVATION OF ENERGY :  $A \equiv E_{\text{tot}} = \rho e + \frac{1}{2} \rho (\underline{v} \cdot \underline{v})$   
 $B \equiv -\underline{g} \cdot \underline{v} + \underline{q}$

Figure 10

DIRECT FINITE VOLUME DISCRETIZATION

CONSERVATION OF MASS  $\int_S \rho v^{1'} dS_{1'}^k = 0$

MEAN VALUE THEOREM OF INTEGRAL CALCULUS

$$\int_S \rho v^{1'} dS_{1'}^k = \sum_{k=1}^3 \Delta_k [\overline{\rho v^{1'}} \delta S_{1'}^k] = 0$$

$$\Delta_k [\bar{E}^{i'} \delta S_{i'}^k] = [\dots]_+ - [\dots]_-$$

Figure 11

DIRECT FINITE VOLUME DISCRETIZATION

CONSERVATION OF MOMENTUM  $\left\{ \sum_{k=1}^3 \Delta_k [(\rho v_{1'} v^{m'} + p \delta_{1'}^{m'} - \sigma_{1'}^{m'}) \delta S_{m'}^k] \right\} \underline{e}^{1'} = 0$

CONSERVATION OF ENERGY  $\sum_{k=1}^3 \Delta_k [([E_{\text{tot}} + p] v^{m'} - \sigma_{1'}^{m'} v^{1'} + q^{m'}) \delta S_{m'}^k] = 0$

ASSUMPTIONS: PERFECT GAS  
 VALIDITY OF FOURIER LAW  
 NEWTONIAN FLUID  
 DYN. VISCOSITY DEPENDS ON TEMPERATURE AFTER SUHTHERLAND

Figure 12



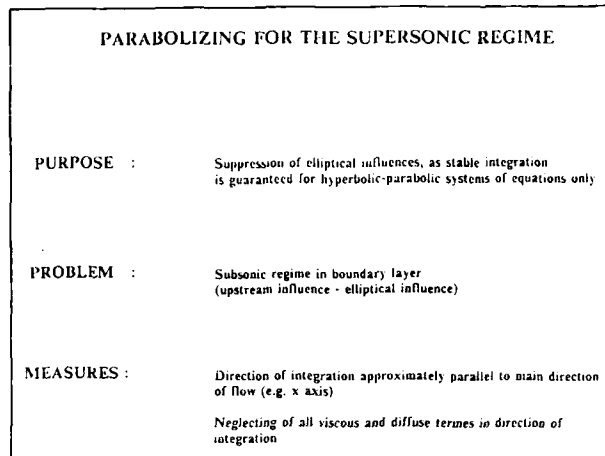


Figure 13

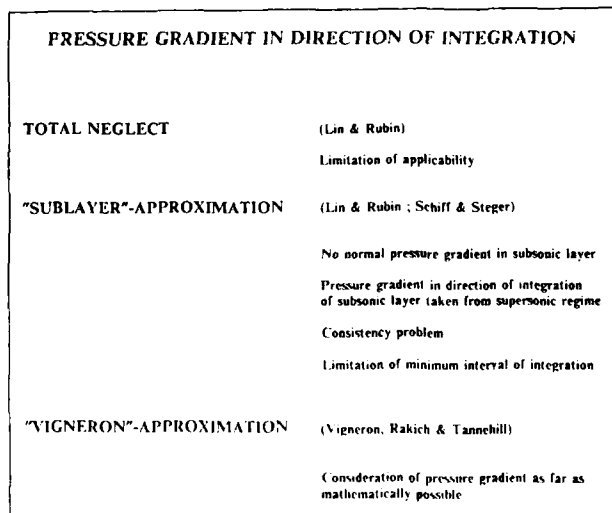


Figure 14

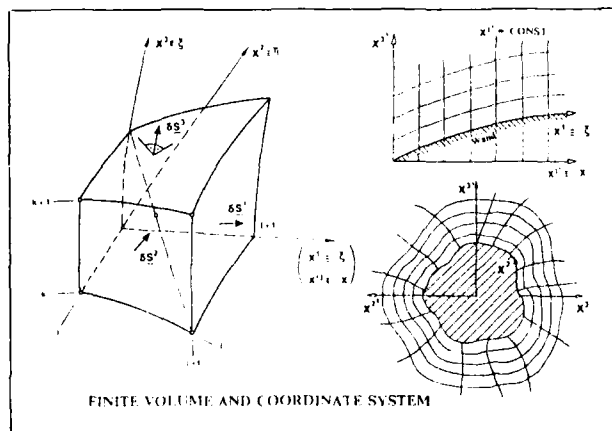


Figure 15

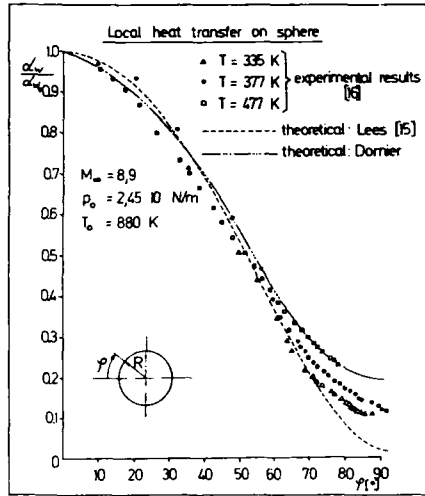


Figure 16

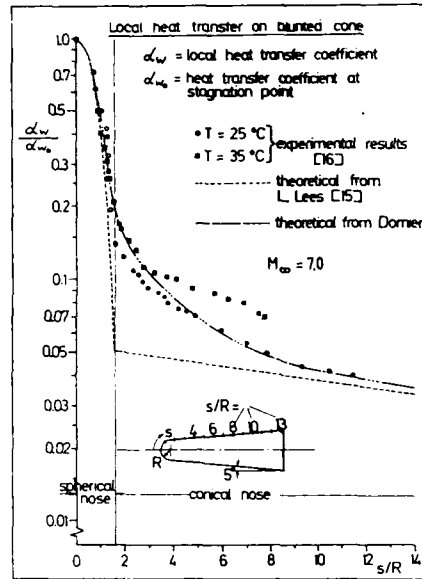


Figure 17

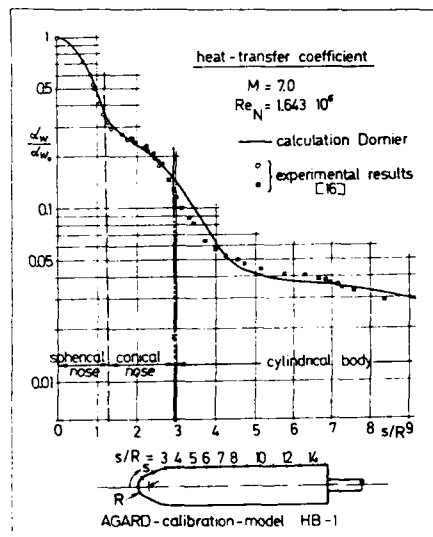


Figure 18

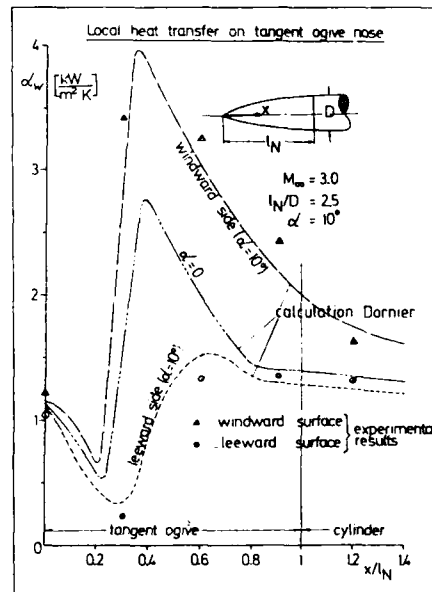


Figure 19

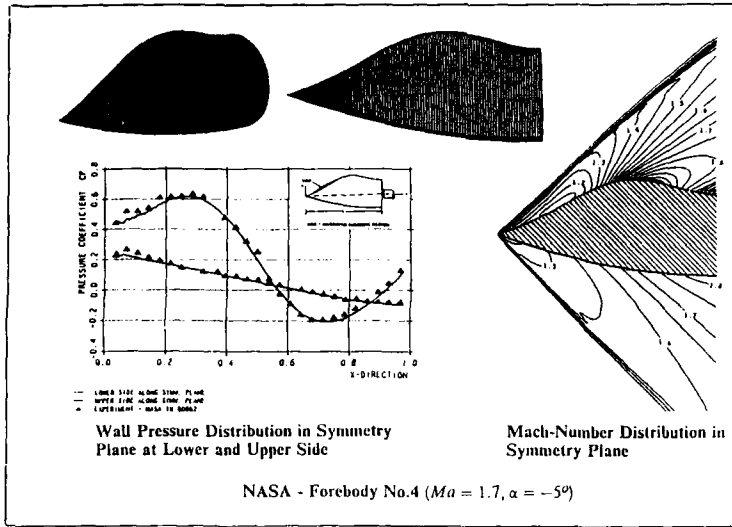


Figure 20

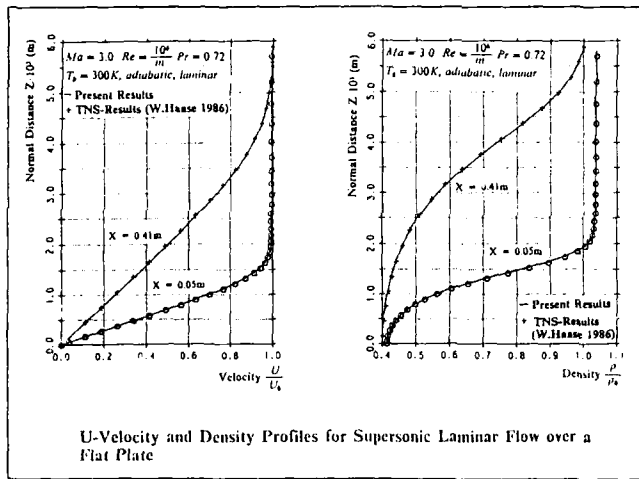


Figure 21

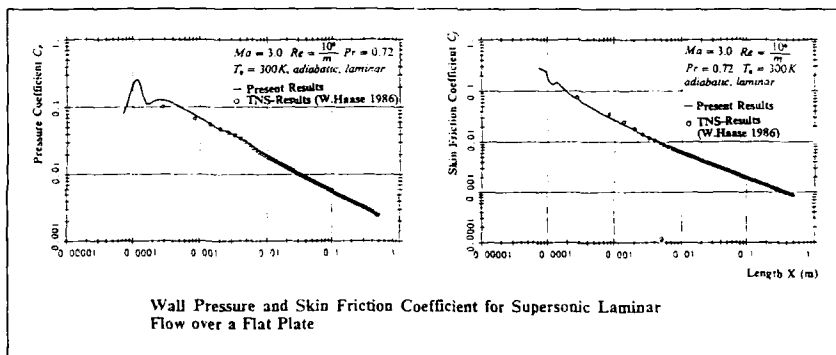


Figure 22

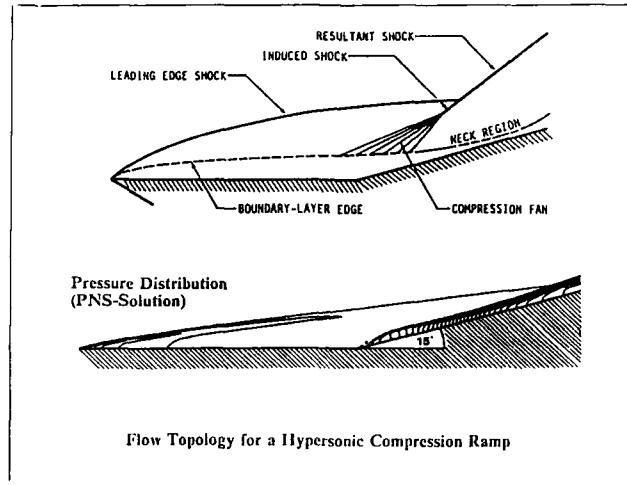


Figure 23

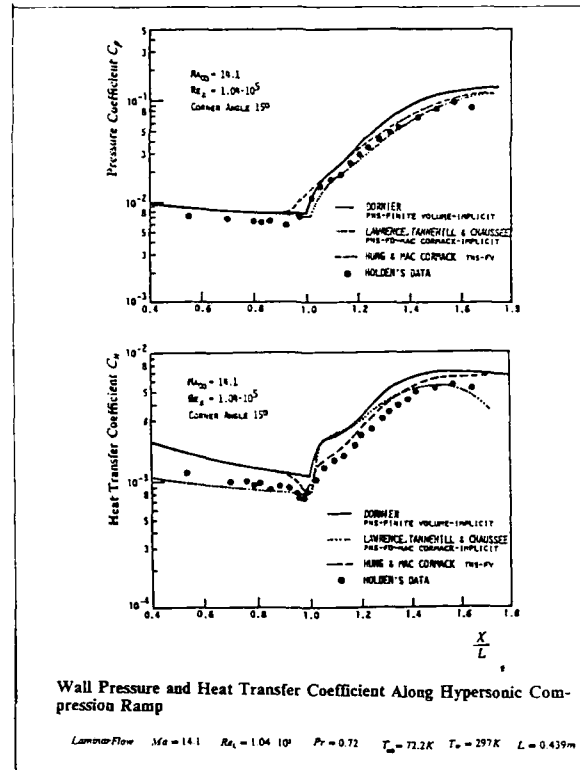


Figure 24

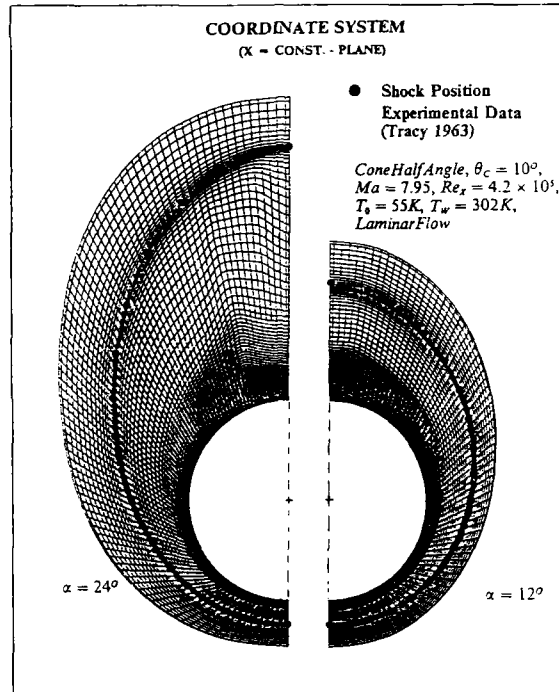


Figure 25

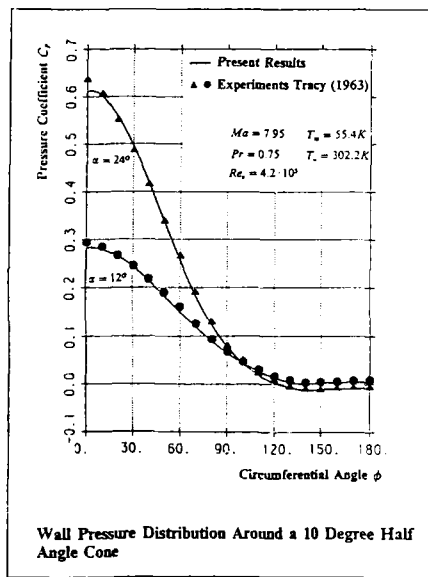


Figure 26

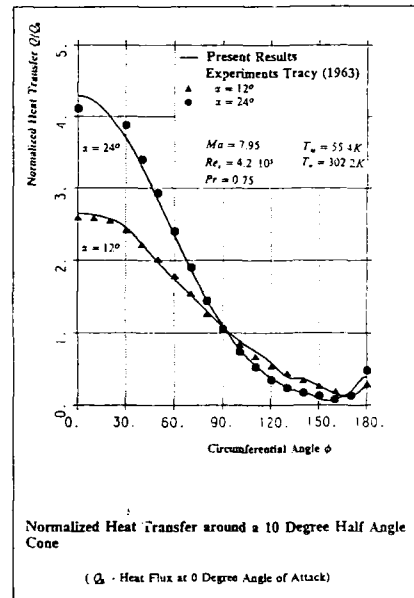


Figure 27

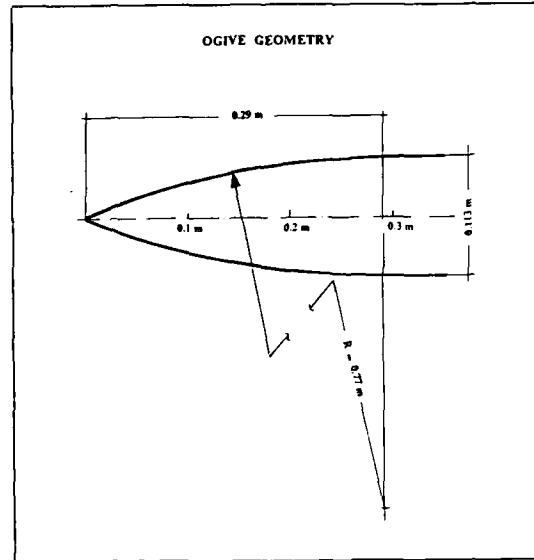


Figure 28

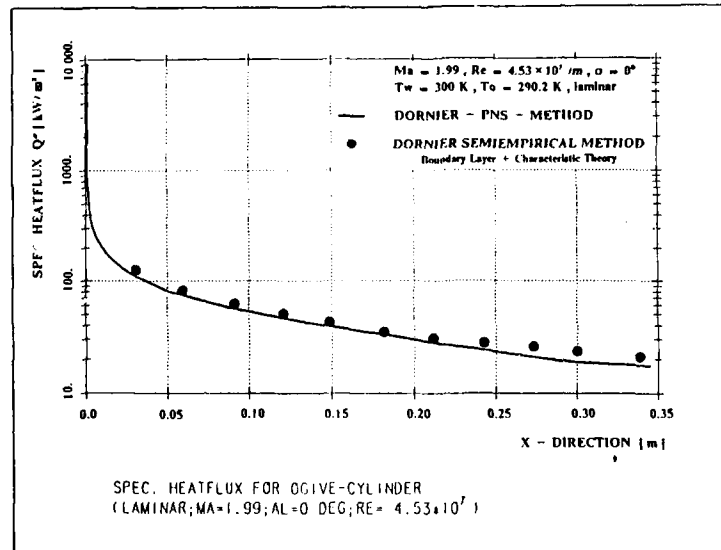


Figure 29

heat balance for a volume element  $i$ :

$$m_i \cdot C_{p_i} \cdot \frac{dT_i}{dt} = \epsilon_i \cdot F_i \cdot \sigma \cdot \left[ \sum_{j=1}^n B_{ij} \cdot T_j^4 \right] - \epsilon_i \cdot F_i \cdot \sigma \cdot T_i^4 + \sum_{j=1}^n d_{ij} (T_j - T_i) + \dot{q}_{aero,i} + \dot{q}_V$$

the physical meaning of these terms is:

- $\epsilon_i \cdot F_i \cdot \sigma \cdot \left( \sum_{j=1}^n B_{ij} \cdot T_j^4 \right)$  ..... picked up heat radiation
- $-\epsilon_i \cdot F_i \cdot \sigma \cdot T_i^4$  ..... reflected heat radiation
- $\sum_{j=1}^n d_{ij} \cdot (T_j - T_i)$  ..... heat conduction
- $\dot{q}_{aero,i}$  ..... heat transfer
- $\dot{q}_V$  ..... internal losses

Figure 30

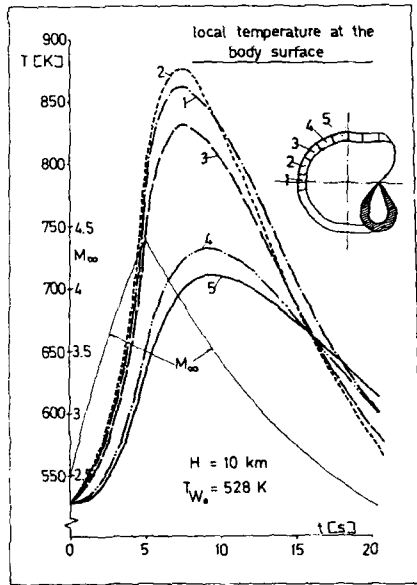


Figure 31

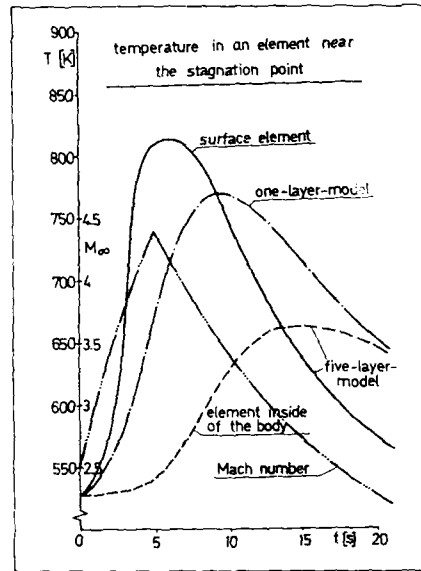


Figure 32

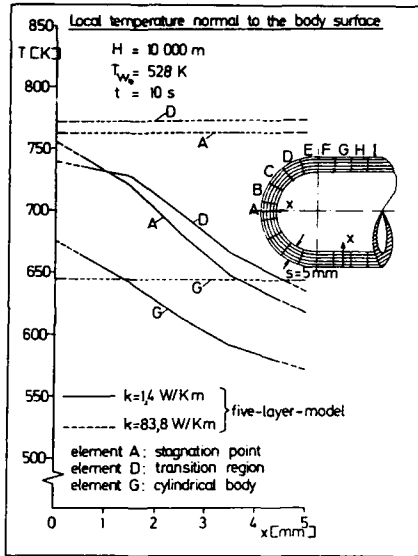


Figure 33

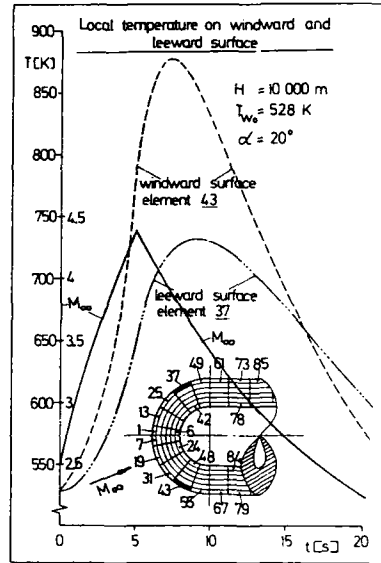


Figure 34

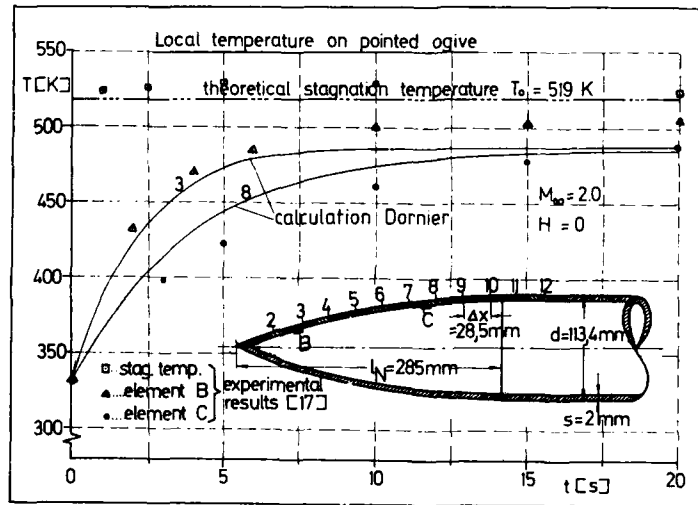


Figure 35



PREDICTION OF BASE-FLOWS

By

J. DELERY

ONERA - 92320 CHATILLON - France

and

R.G. LACAU

aerospatiale - DIVISION ENCHS TACTIQUES - 92320 CHATILLON - France

**SUMMARY**

The base region of a missile or a launcher is the seat of complex phenomena which can have important repercussions on vehicle performance. The fields they concern are many : afterbody drag, heat transfer, interaction between external stream and the base, etc. Thus prediction of these phenomena is of great practical interest for missile design.

The present lecture is mainly centered on a presentation of the basic principles underlying most of the methods currently used to compute base-flows. These methods belong essentially to the following three categories : In the Inviscid/Viscous Interactive approach, the outer inviscid flow and the viscous regions are computed together and made compatible along a common boundary. In the Multi-Component approach, the flowfield is decomposed into a limited number of regions which are treated by approximate methods and then patched together. This approach has led to the development of a large variety of practical methods which are still routinely used in industry. The last approach, much more recent, consists in solving the time averaged Navier-Stokes equations. Base-flows in the jet-off and jet-on situations are now computed by solving the full Navier-Stokes equations or the thin layer approximation of these equations. Although still costly in computer time and not always in good agreement with experiment because of the difficulty of modeling turbulence in such complex flows, the Navier-Stokes approach is particularly promising. It appears also as the most straightforward way to extend prediction capability to three-dimensional flows.

The presentation of these different approaches is illustrated by applications as well as comparisons with experiment.

**TABLE OF CONTENTS**

SUMMARY

- 1 - INTRODUCTION
- 2 - PHYSICAL DESCRIPTION OF BASE-FLOWS
  - 2.1. - Base-flow without propulsive jet
  - 2.2. - Base-flow with propulsive jet
- 3 - THEORETICAL METHODS FOR BASE-FLOW PREDICTION
  - 3.1. - Introduction to the problem of base-flow modeling
  - 3.2. - Basic principles of Inviscid/Viscous Interactive and Multi-Component methods
  - 3.3. - Inviscid/Viscous Interactive methods
    - 3.3.1. - Introductory remarks
    - 3.3.2. - Formulation of the problem
    - 3.3.3. - Method of solution
    - 3.3.4. - Applications to base flow problems
  - 3.4. - Multi-Component methods
    - 3.4.1. - The basic flow model
    - 3.4.2. - The isobaric turbulent mixing
      - Representation of compressibility effect
      - Representation of axisymmetry effect
      - Representation of initial boundary-layer effect
    - 3.4.3. - Determination of the Dividing Streamline and of the Stagnation Streamline
    - 3.4.4. - Problem of the reattachment criterion
    - 3.4.5. - Practical method of calculation. Balance equations for mass and energy
    - 3.4.6. - Base-flow models for supersonic external stream
      - 3.4.6.1. - Missile in jet-off situation
      - 3.4.6.2. - Missile in jet-on situation
        - The different flow models
        - Base-flow with plume induced separation
    - 3.4.7. - Base-flow models for subsonic external stream
      - 3.4.7.1. - Missile in the jet-off situation
      - 3.4.7.2. - Missile in the jet-on situation
    - 3.4.8. - Application to multi-nozzle configurations
      - 3.4.8.1. - General description of phenomena
      - 3.4.8.2. - The different flow models
  - 3.5. - Solution of the Navier-Stokes equations
    - 3.5.1. - The Navier-Stokes equations
    - 3.5.2. - Methods of numerical solution
      - 3.5.2.1. - Computational domain and co-ordinate system
      - 3.5.2.2. - The boundary conditions
      - 3.5.2.3. - The technique of numerical integration
    - 3.5.3. - The problem of turbulence modeling
      - 3.5.3.1. - Algebraic turbulence models
      - 3.5.3.2. - Transport equation models
    - 3.5.4. - Application to base-flow calculations
- 4 - CONCLUSION
- 5 - REFERENCES

## 1 - INTRODUCTION

The phenomena taking place in the base region of a missile or a launcher can have important repercussions on its performance and consequently on its design. These complex phenomena involve in fact both aerodynamic and thermodynamic problems, including chemistry and radiative processes.

The first point of interest for base flows is certainly that of **base-drag** prediction. Indeed, at subsonic as well as at supersonic speeds, the pressure  $p_B$  that establishes itself in the "dead-air" region in contact with the base of a projectile or a missile is almost always noticeably lower than the pressure  $p_\infty$  of the unperturbed upstream flow. There results a drag force, proportional to the base area and representing an important fraction of the total drag when this area is close to that of the maximum cross section. Thus for a classical missile in powered flight, base drag represents nearly 30% of the total drag at subsonic and transonic Mach numbers and 25% at supersonic speeds. This fact is illustrated in Fig. 1 which shows the base drag contribution for three tactical missiles in the Mach number range 0.2 - 2.2. In a particularly unfavorable case, as for an unpowered rocket or an artillery shell at transonic Mach number, the base drag can contribute up to 50% of the total drag, as shown in Fig. 2.

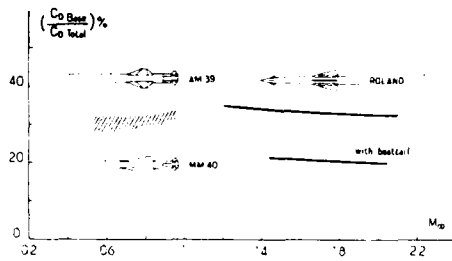


Fig. 1 - Typical base-drag of tactical missiles

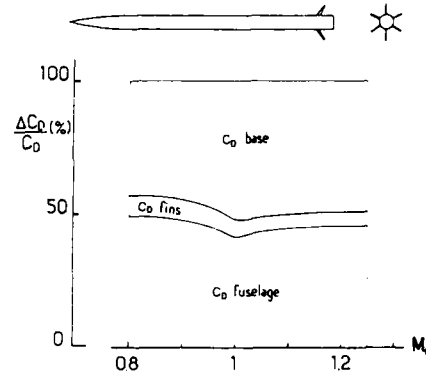


Fig. 2 - Contribution to drag of the different parts of an unpowered missile

On the other hand, for a strongly **underexpanded** nozzle, as occurs at high altitude where the pressure  $p_{0j}$  in the nozzle exit plane is much higher than  $p_\infty$ , the exhaust jet expands abruptly at the nozzle lip. The resulting obstacle effect produces a rise in the base pressure  $p_B$  which can become superior to the pressure  $p_{0F}$  on the fuselage upstream of the base. In this circumstance, the pressure ratio  $p_B/p_{0F}$  across the shock-wave which then forms at the base corner at supersonic Mach number can be high enough to separate the boundary-layer on the fuselage. Such a situation, sketched in Fig. 3a, may lead to several nefast consequences.

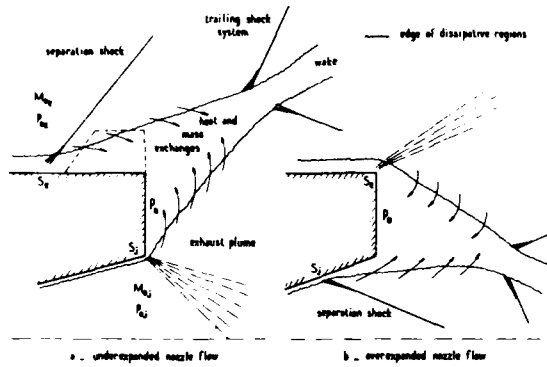


Fig. 3 - Base flow with separation on the fuselage or inside the nozzle

Thus, if the separation point  $S$  moves well upstream of the base corner, fins mounted in the aft part of the fuselage will be immersed in a low energetic separated flow. They will then lose their effectiveness rendering the control of the missile trajectory difficult if not impossible. Furthermore, plume induced separation often leads to severe stability problems, the situation being worsened by the frequently unsymmetrical character of separation, even at zero incidence.

In addition, due to the intense turbulent mixing process developing along the frontiers of the separated flows (external stream and exhaust jet, see Section 2.2. below), hot gases coming from the propulsive jet are fed into the separated region and can be in contact with the unprotected missile fuselage.



Fig. 4 - Plume induced separation on a boattailed afterbody (Agrell and White, 1974)

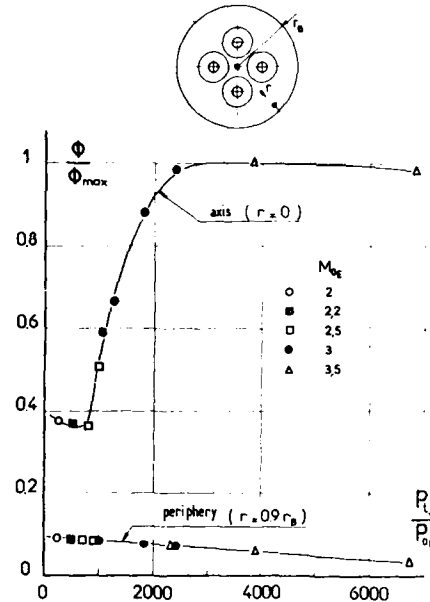


Fig. 5 - Heat transfer at the base for a multi-nozzle configuration (Musial and Ward, 1961)

Plume induced separation can also happen at lower altitude if the afterbody is equipped with a boattail in order to reduce afterbody drag. In this case, at supersonic Mach number, the pressure on the boattail being lower than  $p_\infty$  and the base area reduced, separation at the base corner is more likely to occur. Figure 4 shows this type of separation in a wind tunnel test (Agrell and White, 1974). The figure is a composite picture made of a schlieren photograph of the flowfield and a photograph of surface flow visualization showing the separation line on the boattail.

A similar situation may happen for an overexpanded nozzle. Now, as sketched in Fig. 3b, separation takes place inside the nozzle. However, such a situation is more likely to occur in an aircraft nozzle at low altitude than in a missile nozzle.

Another extremely important problem of interest in the base region of a powered missile is the risk of post-burning of incompletely burned exhaust gases by mixing with the outer air in the dead-air region. Occurrence of this phenomenon provokes a dramatic increase of heat transfer rate at the base. Also the resulting existence of a high temperature spot in contact with the base can facilitate detection of the missile by infra red sensors or perturb missile guidance by laser beam system.

Concerning multi-nozzle launch vehicles at high altitude, the dynamics of the flow in the region of jet mutual impingements results in strong recirculating currents of hot gases flowing towards the base of the launcher. This phenomenon, considered in more detail in Section 3.4.8, is the cause of an abrupt rise of heat transfer rate in the base central region as illustrated by the example shown in Fig. 5.

Base flow phenomena are also of importance in the development of plumes whose emissive and radiative properties are key elements of detection capabilities.

To conclude this probably incomplete list of problems involving base-flow, let us mention some techniques actively developed to reduce base drag by means of fluid injection into the dead-air region. Indeed, injection of a small amount of fluid through the base of a projectile results in a noticeable increase of the base pressure. The effect is largely magnified if the fluid injected burns by mixing with the outer air. In this case the base pressure  $p_b$  can become practically equal to the upstream pressure  $p_\infty$  resulting in a nearly complete cancellation of base drag (for information on base drag reduction techniques, see "Aerodynamics of Base Combustion", 1976).

Before entering into the presentation of methods allowing the calculation of base-flows, it can be worthwhile to give a short physical description of such flows. The essential purpose of this description, which does not claim to be complete, is to provide the physical bases of the theoretical models considered hereinafter. The many aspects of base-flow phenomena will not be envisaged, neither shall we discuss here the role of the different parameters influencing the flow in the base region. Such information can be found elsewhere (see for example Détery and Sirieix, 1979). On the other hand, there exists a huge quantity of data on base-flows and a thorough review of the literature on this subject would be a formidable task.

Here we shall focus our attention on detailed descriptions of typical and "basic" base flows by examination of carefully made experiments.

## 2 - PHYSICAL DESCRIPTION OF BASE-FLOWS

### 2.1 - Base-flow Without Propulsive Jet

Let us first consider the flow at the base of a cylindrical afterbody without jet for a subsonic incoming stream. The separation structure depends, in this case, little on compressibility effects so we shall use as first elements of analysis, the results provided by visualization in the water tunnel.

The photographs reproduced in Figs. 6a and 6b were obtained with different exposure times. In Fig 6a, where the exposure time is about 1 second, the tracers consist of fine air bubbles in suspension in the water and can be observed in a thin section containing the axis. A rather good definition of the mean flow structure can be deduced. This perfectly reproducible flow is organized around a toroidal main vortex located within a domain bounded by the (j) streamline. Separation occurs practically at the corner S, a mixing process develops along (j) and the fluid entrained during this process flows back into the closed zone under the effect of the compression taking place in the vicinity of the stagnation - or reattachment - point R.

In the photograph of Fig. 6b (whose exposure time is much shorter-about 0.01 second), the unsteady character of the turbulent dissipative layer is clearly shown as well as the mechanism of formation of large structures entrained within the mixing layer and later evacuated downstream in a quasi-periodic manner.

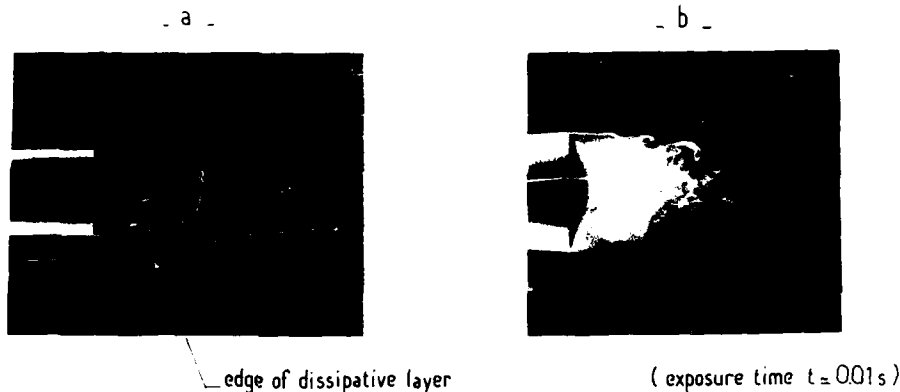


Fig. 6 - Hydrodynamic visualization of base flow (Werle, 1970)

As regards the mean field, detailed explorations by Laser Doppler Velocimetry of the separated zone and its surroundings provide data complementing those obtained by visualizations.

The example given in Figs. 7a to 7c (Bernier, 1986), in the case of a low speed flow at  $M_\infty = 0.35$ , reveals the structure of the mean field behind a cylindrical afterbody by means of streamwise velocity profiles, vector plot and tracing of the streamlines in a meridian plane. The following features can be remarked in particular :

- the rapid development and transverse expansion of the mixing layer starting from the separation point S at the base shoulder ;
- the relative compacity of the separated zone whose length is slightly greater than one caliber ;
- the importance of negative reverse velocities (shaded area in Fig. 7a) in the dead-air region. These velocities can reach 30% of the external velocity ;
- lastly, the rather continuous evolution of the streamwise velocity profiles and their gradual passage from a situation of mixing layer type with back flow to a situation of wake type and velocity increasing on the axis. This evolution can be characterized by the definition of a one - or two-parameter - family of profiles whose utilization will be examined in the Sections of this paper dealing with calculation methods.

During this process, a strong production of turbulence occurs around (j), as shown in Fig. 8 which represents the spatial distributions of both the axial and radial turbulent intensities as well as of turbulent shear-stress. This turbulence diffuses very rapidly towards the wake axis as well as outwards and remains at a rather high level within the separated zone throughout recirculation.

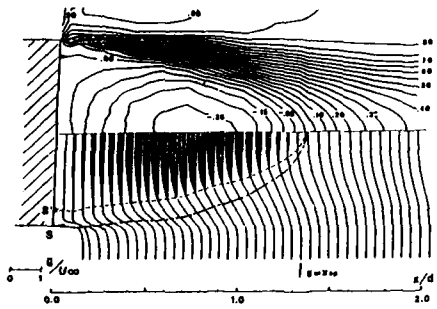
As regards the pressure field, the curve  $\delta^*(x)$  representing the viscous flow displacement effect and which was obtained by integration of the mean velocity field defines the boundary of the obstacle equivalent to the separated flow and wake.

The evolution of the pressure coefficient  $C_p$  plotted in Fig. 9 (Vanwagenen, 1968) shows that this obstacle effect is felt upstream of the base up to a distance of about one diameter.

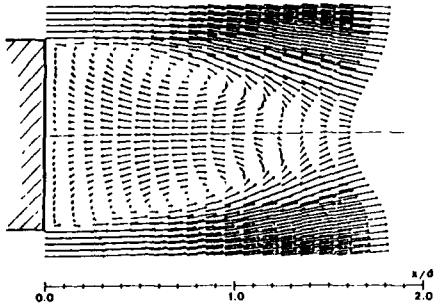
The acceleration of the flow, very marked near the base, ensures the continuous matching of pressures in S on either side of separation.

The axial evolution of pressures behind the base presents the characteristic shape shown in Fig. 9. This evolution with increasing streamwise distance X is first marked by a slight decrease of  $C_p$  up to a minimum value at a distance of about  $X = r_B$ ,  $r_B$  being the base radius. This decrease of  $C_p$  can be associated with the increase of the reverse velocity (see Fig. 7). The recompression that follows is important : it results from the flow confluence on the axis ; the maximum pressure is reached slightly behind the stagnation point R.

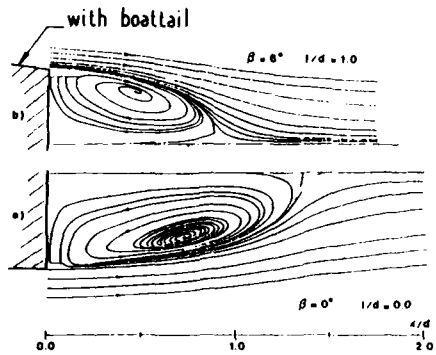
Figure 10 shows the variation of the base pressure coefficient  $C_{pB}$  with the momentum thickness of the boundary-layer at the base shoulder  $\theta_0$ . We can see that  $C_{pB}$  decreases when  $\theta_0$  decreases, in so much as  $\theta_0/r_B$  is smaller. On the other hand, for values of  $\theta_0/r_B$  higher than about 0.02, the base pressure evolution is very small. This tendency is confirmed by other observations (Chang, 1970 ; Rom et al., 1972) and explains the small effect of an appreciable variation of the Reynolds number recorded by experimentalists when the boundary-layer upstream of the base is turbulent and the values of  $\theta_0/r_B$  scanned during the variation of the Reynolds number are higher than 0.02.



a - Streamwise velocity distribution and isovelocity contours

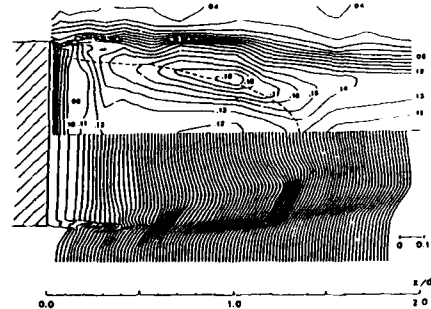


b - Velocity vector field

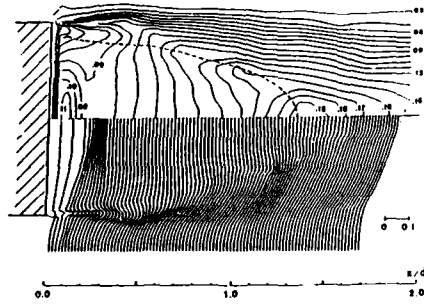


c - Mean flow streamlines

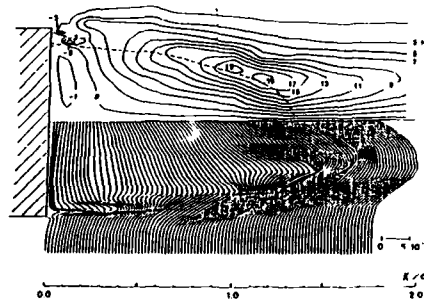
Fig. 7 - Base flow behind a cylindrical afterbody in subsonic flow - Mean flow structure (Berner, 1986)



a - Axial turbulent intensity  $\sqrt{u'^2}/U_\infty$



b - Radial turbulent intensity  $\sqrt{v'^2}/U_\infty$



c - Reynolds shear stresses  $\overline{u'v'}/U_\infty^2$

Fig. 8 - Base flow behind a cylindrical afterbody in subsonic flow - Turbulent field (Berner 1986)

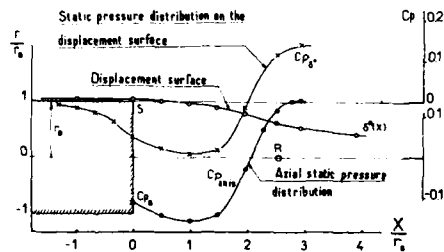


Fig. 9 - Base flow behind a cylindrical afterbody in subsonic flow - Distributions of pressure coefficient (Vanwagenen, 1968)

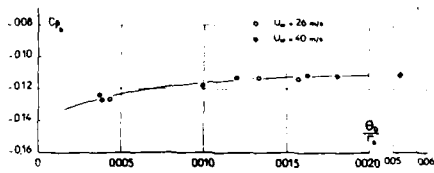


Fig. 10 - Base flow behind a cylindrical afterbody in subsonic flow - Initial boundary-layer effect on base pressure coefficient (Vanwageningen, 1968)

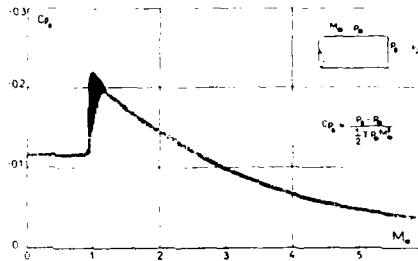


Fig. 11 - Variation of base pressure coefficient with Mach number - Basic curve-Cylindrical afterbody (Love, 1957)

As announced at the beginning of this Section, the Mach number effect is slight. Thus as shown in Fig. 11, the base pressure coefficient  $C_{pB}$  varies only a very little when the upstream Mach number  $M_\infty$  is lower than 0.85. On the other hand, when approaching transonic speeds,  $C_{pB}$  rises rapidly with a relatively large uncertainty in the Mach number range 0.9 - 1.2. Thereafter, the base pressure coefficient decreases steadily when  $M_\infty$  increases.

In the case of a **supersonic** incoming flow, schlieren pictures constitute a privileged means of observation, revealing the main features of flow separation in supersonic régime. Thus the visualizations of Figs. 12a to 12c clearly show

- the quasi-centred expansion at the base corner, which suddenly deviates the flow towards the axis;
- the highly dissipative turbulent mixing layer separating the inviscid flow from the separation bubble;
- the continuous recompression, in the wake neck region, whose waves focalize to form a shock;
- the relatively thick wake that follows this recompression.

First we shall note the disappearance of the upstream interaction effect, the separation in supersonic flow being preceded by an expansion practically centred at the base corner which is often limited by the presence of a weak shock (the so-called "lip shock", Hama, 1966, 1968). Then, in photograph 12b, where exposure time is shorter, we remark the turbulent structures that develop along the mixing layer and in the wake.

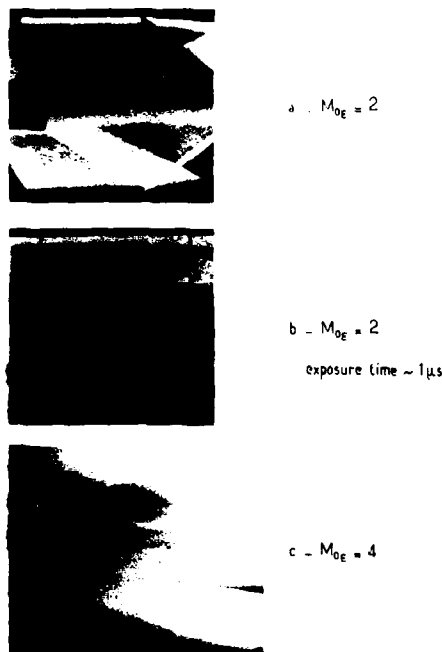


Fig. 12 - Flow visualization downstream of a cylindrical afterbody - Supersonic flow

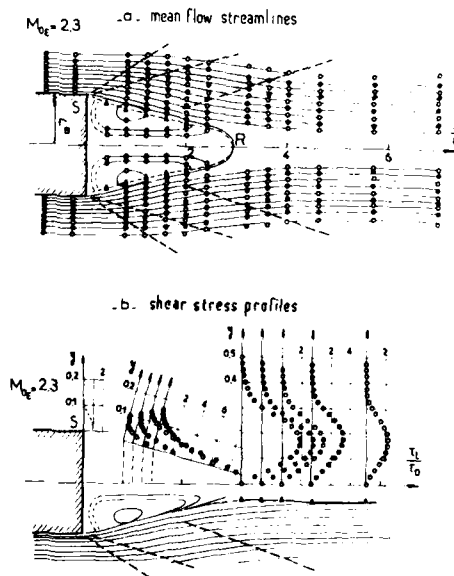


Fig. 13 - Flow structure downstream of a cylindrical afterbody - Supersonic flow (Gaviglio et al., 1977)

As regards mean and turbulent fields, we shall examine the typical elements represented in Figs. 13a and 13b (Gaviglio et al., 1977) which give a very detailed analysis of the flow behind a cylindrical afterbody for an upstream Mach number equal to 2.3.

Figure 13a provides the tracing of the mean flow streamlines in the meridian plane. The pattern of the separated zone differs only from the subsonic case by the separation condition in S, the supersonic separation being characterized by a sudden variation of the velocity direction due to the initial expansion. The velocity profiles that describe the flow within the separated zone and in its vicinity belong to the same family as in subsonic flow. So, apart from scale effects, the difference between the subsonic and supersonic cases concern only the external, non dissipative flow (initial centred expansion, formation of shock-waves, etc...) and intervene at the level of the "coupling" conditions between the dissipative and inviscid parts of the flow (see Section 3.3.2.).

In Fig. 13b are plotted the profile of turbulent shear stress  $\tau_t = -\rho \overline{u'v'}$ , scaled to the wall shear stress of the boundary-layer in S, at various distances behind the base. Effects similar to those observed in subsonic flow are emphasized. We shall note the high levels of  $\tau_t$  measured at the end of the mixing zone. The compressibility influence is in fact expressed by the noticeable variation with Mach number of the turbulent mixing parameter which defines the crosswise scale of the mixing layer downstream of S. This question is more thoroughly discussed in Section 3.4.2. below.

As shown in Fig. 14, the static pressure distribution along the axis behind the base reflects the evolution of the external flow (Siriex et al., 1968). As in subsonic flow, we first note a slight decrease of p, followed by a continuous compression rather rapid at first, then passing by a maximum and decreasing more slowly down to a level almost equal to  $p_\infty$ . This recompression shape, rather different from that observed in the plane two-dimensional supersonic case, is specific to separation at the base of an axisymmetric afterbody. The presence of a nearly isobaric separated zone at the boundary of the external supersonic flow entails a noticeable increase of the inclination angle  $\varphi$  of its local direction when this flow comes closer to the axis (Chapman, 1951). When the flow returns to a direction almost parallel to the axis, this situation contributes to the creation of a compression whose level is higher than the upstream pressure  $p_\infty$  in a manner all the more marked as the Mach number is higher (see Fig. 14).

In the same manner as in subsonic flow, we observe an increase of base pressure when the momentum thickness of the initial boundary-layer increases, this increase rate becoming very low for a given range of  $\theta_0/R_B$  values. So, in most applications, the evolution of the ratio  $p_B/p_\infty$  with the Reynolds number Re can be neglected, at least as long as Re is large enough for relaminarization of the mixing layer not to occur after the initial expansion preceding separation.

With a view to estimations useful for a "project department" we may define in these conditions a base pressure coefficient  $C_{pB}$  practically independent of Reynolds number whose evolution with the upstream Mach number  $M_\infty$  has been given in Fig. 11. The results traced in this figure are the result of compilations produced in particular by Chapman (1951) and Love (1957). Except in the transonic range, the scatter of results is not very great, and this mean curve constitutes an empirical reference allowing one to obtain rather accurate estimates for cases close to the "basic" configuration, i.e., that of a cylindrical afterbody.

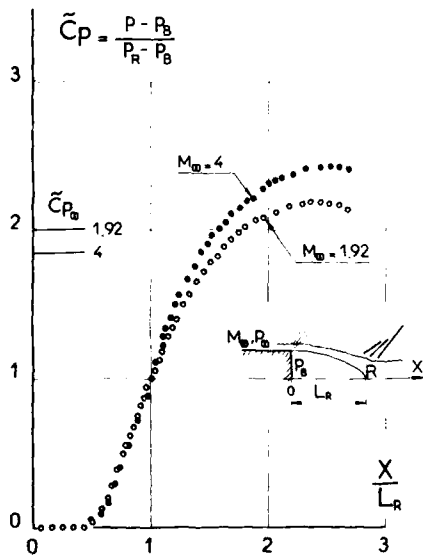


Fig. 14 - Axial pressure distribution - Supersonic flow

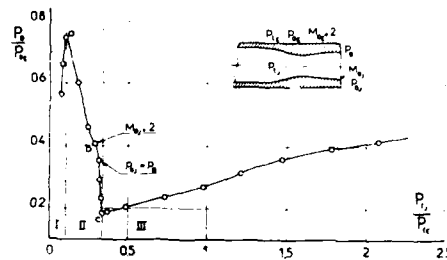


Fig. 15 - Pressure at the base of an afterbody with a propulsive nozzle - Supersonic flow (Reid and Hastings, 1961)

## 2.2 - Base-Flow with Propulsive Jet

We shall now deal with the study of the aspects specific to the powered phase of a missile flight where very complex phenomena come into play, especially during the starting of the exhaust nozzle. These phenomena are created by the confluence of two flows whose stagnation conditions and local state (Mach number, velocity direction, etc...) as well as chemical compositions are very different.

We shall essentially examine the case of supersonic external flows which leads to the most note worthy interaction effects (Reid and Hastings, 1961 ; Carrière, 1961).

Let us first examine a typical example corresponding to the geometric configuration defined in Fig. 15 (Reid and Hastings). The internal and external flows are supplied by air at the same stagnation temperature. The Mach number  $M_{0E}$  of the external flow is uniform upstream of the base and equal to 2, as is the nominal Mach number  $M_{0J}$  of the internal flow.

The curve giving the evolution of the ratio  $p_B/p_{0E}$  ( $p_{0E}$  is the static pressure upstream of the base) with the ratio of the stagnation pressures  $p_{tJ}/p_{tE}$  is plotted in Fig. 15. This curve can be divided into three domains :

- the first domain (I) which corresponds to very small flow rates is marked by a continuous increase of  $p_B/p_{0E}$  up to a maximum value. This evolution of the base pressure corresponds in fact to the **base-bleed** effect which is sometimes considered as a means of reducing base drag of a projectile as mentioned in the introduction ;
- in the second domain (II), we observe a sudden and rapid decrease of the base pressure, down to a very low minimum value. During this phase we observe successively :
  - a) - the nozzle starting from the throat to the outlet (from a to b in Fig. 15) ;
  - b) - the establishment of a régime of confluence of the external flow and the fully supersonic internal flow (from b to c in Fig. 15).
- within domain (III), the base pressure increases continuously when the nozzle expansion ratio increases. The flow is then stable.

The above example shows a rapid but continuous evolution of the phenomena which does not always take place as shown in Fig. 16. These results are relative to a cylindrical afterbody immersed in an external stream with a Mach number  $M_{0E} = 1.87$ . The afterbody is equipped with a conical nozzle whose exit Mach number is equal to 3.29.

With the variation of  $p_B/p_{0E}$ , represented here as a function of expansion ratio  $p_{tJ}/p_{0E}$ , are associated photographs of schlieren visualization of the jet flow which illustrate the various circumstances described above.

We observe in this example that the nozzle starting phase - domain (III) - ends in a discontinuity. Moreover, a hysteresis phenomenon appears. When once the nozzle is started, we decrease the expansion ratio  $p_{tJ}/p_{0E}$ , de-starting takes place for a value of  $p_{tJ}/p_{0E}$  which is different from that corresponding to starting conditions.

These two examples show that during phase (II) the separated zone structure undergoes a true upheaval. This is expressed by the passage from a situation similar to that of Section 2.1. above, comprising an extended separated zone with a stagnation point on the axis and important axisymmetric effects, to a situation of confluence around a reduced separation zone predominantly two-dimensional in structure.

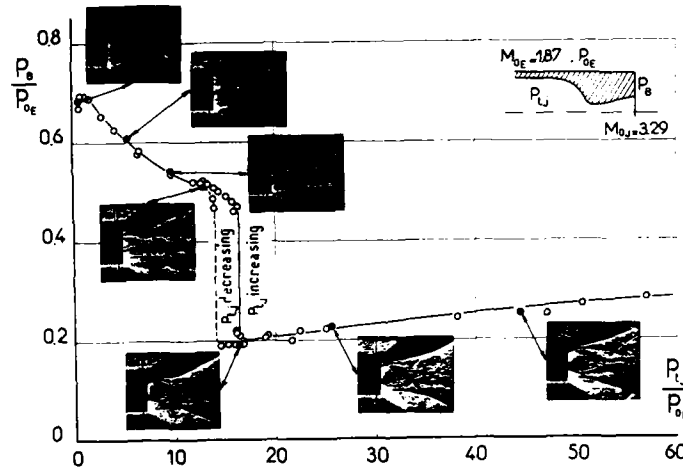


Fig. 16 - Base pressure variation with nozzle expansion ratio (ONERA result)

This later situation is illustrated by the schlieren photograph of Fig. 17a which reveals the essential flow features in the confluence region of a started configuration. In this example, the external flow Mach number is equal to 4 and the nozzle is conical. One observes the following phenomena (see also sketch in Fig. 17b) :

- downstream of the base corner  $S_E$  and of the nozzle lip  $S_J$ , the inviscid streams expand to the base pressure  $p_B$ . They are bounded by nearly isobaric frontiers along which two mixing-zones develop ;
- the two separated flows impinge upon each other in the **confluence region** (R) where recompression leading to the formation of shock-waves  $(C)_E$  and  $(C)_J$  take place in each flow ;
- downstream of the confluence region, the external stream and the nozzle jet are contiguous along a common boundary  $(\Sigma)$  along which a wake develops ;
- the two converging streams imprison the **dead-air** region in which the pressure  $p_B$  is nearly uniform.

A more detailed description of phenomena occurring in the so called dead-air region can be established by considering experimental results obtained in the base region of a cylindrical afterbody equipped with a Mach 2.9 nozzle of diameter  $D_J = 0.15 D_B$  (Lacau et al., 1982). Although these experiments have been made for a subsonic external Mach number ( $M_\infty = 0.85$ ), the features they reveal are also observed for a supersonic external stream.





a - Schlieren photograph

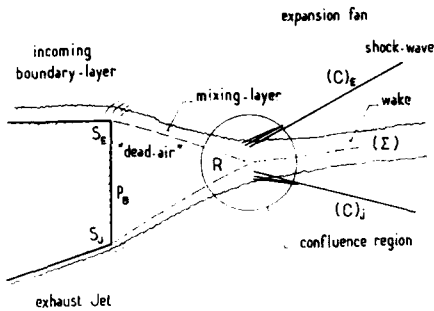


Fig. 17 - Flow confluence behind a base - Supersonic flows

Distributions of the mean streamwise velocity component are shown in Fig. 18 (here  $u$  is scaled to the unperturbed velocity  $u_\infty$  at upstream infinity). Roughly speaking, two regions can be distinguished: in one of these regions, the distributions include a zone where  $u$  is negative; in the other  $u$  is always greater than zero. Starting from the base, the minimum (negative) velocity  $u_m$  first diminishes, reaches a minimum and then increases to vanish at point  $R_c$  of abscissa  $X_c$ .  $R_c$  is the point where the "pocket" containing negative  $u$  components becomes so small as to vanish. It is instructive to plot the ratio  $u_m/u_e$  ( $u_e$  being the local streamwise velocity at the outer edge of the near wake) versus the reduced abscissa  $X/X_c$ . The corresponding evolutions obtained for the cylindrical afterbody as well as for afterbodies of a different shape are plotted in Fig. 19. One sees that there exists a fairly good correlation for the four flows investigated here. This result exhibits a tendency which seems quite general for base-flows. Thus the minimum value of  $u_m/u_e$  is approximately equal to  $-0.3$  for all cases here and this minimum is always reached in the vicinity of  $X/X_c = 0.5$ .

Let us consider now the vertical evolution (along  $r$ , distance from the axis) of the  $u$ -profiles. Starting from the base, the first profiles are characterized by the existence of an outer region where the transverse velocity gradient  $\partial u/\partial r$  is small or moderate. Below this region, there exists a zone of very intense strain which corresponds to the development of a mixing-zone starting from the separation point  $S_E$ . This mixing zone expands rapidly and progressively engulfs the outer region which is in fact the continuation of the initial boundary-layer existing at the base shoulder. Thus, the external and internal flows of initially very different structures and turbulent scales will gradually merge into a unique shear-layer which then evolves to constitute a wake-like flow.

The mean velocity vector field plotted in Fig. 20 clearly shows the structure of the flowfield in a meridian plane, particularly the vertical and streamwise extent of the reversed flow region. Thus one notes the existence of a stagnation point of the flow which streams towards the base. This point is located on the base at a reduced distance  $r/r_B = 0.185$  from the centerline.

From the previous results, it is possible to construct the **streamlines of the mean flow**. It is to be noticed that such streamlines are fictitious since they are relative to a **mean flow** in the sense of statistical turbulence (Reynolds averaging). In reality, the flow is highly turbulent and its instantaneous structure far more complex than the mean organization shown here. However, the streamlines thus constructed are those which would result from a modeling of the flow with the classical time averaged Navier-Stokes equations. Thus the structure of the mean flow is particularly well-visualized by the tracing shown in Fig. 21. One can first distinguish a region where the streamlines are closed curves. This "recirculating bubble" is bounded by a particular streamline ( $S_1$ ) ending at the stagnation point  $R_B$  located on the base. As a consequence of conservation of the mass in the bubble when the regime is steady, the streamline ( $S_1$ ) must necessarily originate at the separation point  $S_E$ , located at the base shoulder. In the absence of jet, ( $S_1$ ) would be on the flow axis and coincide with the reattachment point of the classical flow model for a jet-off configuration (see Section 2.1. above and Fig. 7).

Another line to be remarked is the streamline which delimits the reverse flow region, i.e., the area where the streamwise component  $u$  can become negative. This other particular streamline ( $S_2$ ) passes through point  $R_c$  where its tangent is vertical. The conservation of mass principle imposes that ( $S_2$ ) come from upstream infinity. The streamlines flowing between the wall and ( $S_2$ ) are first turned back towards the base. Then, they are rapidly bent in the downstream direction by the strong entrainment effect of the supersonic jet.

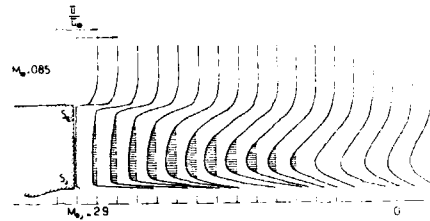


Fig. 18 - Base flow behind a cylindrical afterbody with jet - Streamwise mean velocity distributions (Lacau et al., 1982)

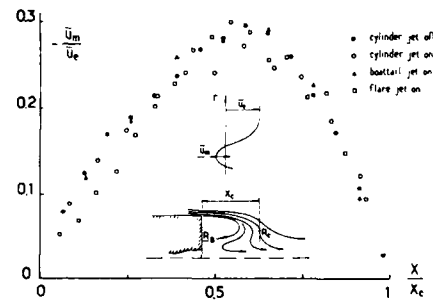


Fig. 19 - Base flow behind a cylindrical afterbody with jet - Streamwise variation of the minimum reverse velocity (Lacau et al., 1982)

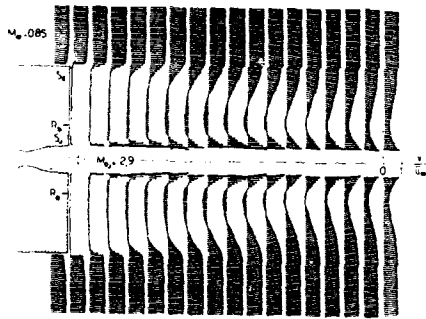


Fig. 20 - Base flow behind a cylindrical afterbody with jet - Velocity vector field (Lacau et al., 1982)

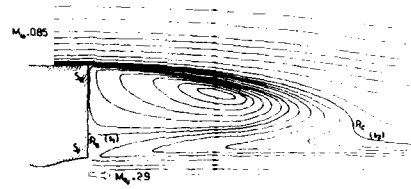


Fig. 21 - Base flow behind a cylindrical afterbody with jet - Mean flow streamlines

It may be hazardous to interpret the observed organization within the framework of the base-flow models presented in the forthcoming Sections. Nevertheless, there is a certain similarity between  $R_r$  and the reattachment point of the classical theory. Thus  $(S_2)$  can be interpreted as the Stagnation Streamline which, by definition, is the streamline stagnating at the reattachment point. On the other hand,  $(S_1)$  can be identified with the Dividing Streamline, the origin of which is at the separation point. The mass flow between  $(S_1)$  and  $(S_2)$  is here extracted by the strong entrainment induced by the high velocity jet. Of course such a comparison is approximate since  $R_r$  is not here a stagnation point, "reattachment" taking place on the base. However, the present flow structure visualizes clearly the mass exchange mechanism which establishes itself between the two flows uniting behind a base.

The spatial distributions of the turbulent kinetic energy and turbulent shear stress are represented in Fig. 22a and 22b by the tracing of contour lines. This representation reveals the very high levels of turbulence in the mixing-layers developing from the base shoulder and the nozzle lip. Turbulence levels remain high also in the so-called dead-air region. They result from large scale turbulence structures which promote exchanges of mass and energy between the two flows. These exchanges play a fundamental role in aerothermodynamics phenomena occurring in the base flow region, including mixing of different species and chemistry.

### 3 - THEORETICAL METHODS FOR BASE-FLOW PREDICTION

#### 3.1 - Introduction to the Problem of Base-Flow Modeling

For a long time, the prediction of base flows has rested upon very crude theoretical models or on purely empirical information. As is well known, in incompressible perfect fluid flow, the classical potential flow theory gives zero drag - hence no base-drag - for any body. On the other hand, in supersonic non-viscous flows, the only drag can result from shock waves produced by the obstacle. However, observation shows that a bluff body experiences an important drag due to the formation behind the body of a separated region whose pressure  $p_B$  can be largely inferior to the upstream pressure  $p_\infty$ . Thus a perfect fluid model is unable to predict, even approximately, a flow containing a separated zone except if the separation point and the base pressure are assumed known. Reasoning on a two-dimensional or axisymmetric configuration for the sake of simplicity, in some circumstances, the separation point is fixed by a discontinuity of the surface, e.g., the base shoulder or the nozzle lip. Thus the separation location can be determined a priori from obvious physical reasons. However, the pressure  $p_B$  existing in the dead-air region remains undetermined: for any value of  $p_B$  (within certain limits) it is possible to construct a perfect fluid solution.

Simple perfect fluid solutions corresponding to base flows in the jet-on situation are represented schematically in Fig. 23. In the first case (Fig. 23a), the pressure  $p_B$  is less than the pressures  $p_{0E}$  and  $p_{0J}$  before separation at the base shoulder and nozzle lip. The main features of the perfect-fluid solution are the centred expansion waves emanating from the separation points  $S_E$  and  $S_J$ , the isobaric boundaries  $(f)_E$  and  $(f)_J$  bounding the constant pressure region at  $p_B$ , the shock-waves  $(C)_E$  and  $(C)_J$  originating from the intersection point  $R_T$  of  $(f)_E$  and  $(f)_J$ , and the slip line  $(\Sigma)$  originating from  $R_T$ .

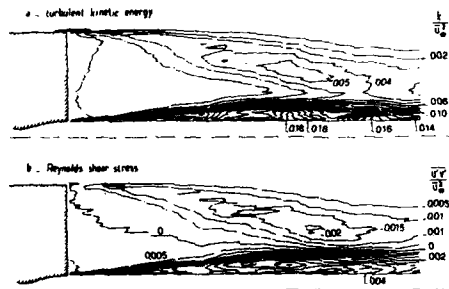


Fig. 22 - Base flow behind a cylindrical afterbody with jet - Turbulent field (Lacau et al., 1982)

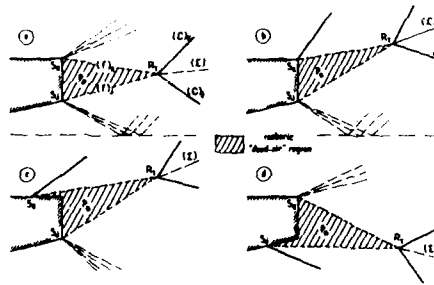


Fig. 23 - Flow behind an afterbody with propulsive jet - Perfect fluid solutions for supersonic incoming streams

In the second case (Fig. 23b),  $p_B$  is higher than  $p_{0E}$ . Then a shock wave emanates from the separation point  $S_E$ .

In the third example (Fig. 23c), separation occurs on the fuselage upstream of the base corner. In this case, the separation point is no longer fixed by a singularity and its location must be furnished in addition to the base pressure  $p_B$  in order to be able to determine the perfect fluid solution.

The last example (Fig. 23d) shows a symmetrical situation where separation takes place inside the nozzle.

In fact, as will be seen in the forthcoming Sections, the uniqueness of the solution, e.g., the value of the base pressure and/or the location of the separation point, is ensured by the consideration of viscous phenomena.

The first theory for predicting pressure drag of blunt bodies in incompressible flow was developed by Kirchhoff (1869). In this perfect fluid theory, the free streamline originating from the separation point extends to downstream infinity. Below the free streamline, behind the body, there is a quiescent fluid whose pressure is assumed equal to that of the unperturbed upstream flow. Thus in this solution  $p_B = p_{\infty}$ . In reality,  $p_B$  is significantly lower than  $p_{\infty}$  and various improvements of the Kirchhoff theory have been proposed to take this fact into account (for details, see Tanner, 1973). However, as emphasized by Tanner, these theories do not predict the base pressure, but rather allow the calculation of body drag once  $p_B$  is known.

More empirical approaches providing evaluation of the base pressure for simple geometry have been followed by Gabeau (1931, 1950), Von Kármán and Moore (1932) and others (see Murthy and Osborn, 1976, for other references). However, the first really convincing and physically realistic base-flow model was proposed in the early 50's by Chapman (1951) and Korst (1956). This theoretical work has been at the origin of a very intense research effort which led to the development of nearly all the practical methods which are still used to predict base-flows behind missiles or projectiles. These methods, usually called **Multi-Component Methods**, are the subject of Section 3.4.

Practically at the same time, Crocco and Lees (1952) inaugurated a somewhat distinct approach which allows, in principle, a more satisfactory representation of a flowfield containing important viscous regions. Although widely used in many domains of aerodynamics, this so-called **Inviscid/Viscous Interactive** approach has been applied relatively seldom in base-flow predictions (methods belonging to this approach are presented in Section 3.3.).

It should be mentioned that with few exceptions, the above methods apply only to **two-dimensional** or **axisymmetric** configurations.

In fact, the most decisive progress in base-flow calculations certainly come from the direct solution of the **Time-Averaged Navier-Stokes Equations**. Although still extremely costly in computer time and not always quantitatively satisfactory, this approach allows a truly realistic prediction of the flowfield structure. It is also probably the most straightforward way to extend the prediction capability to three-dimensional configurations, whereas the extension of "simple" methods to three-dimensional flows appears as extremely hazardous and leads to nearly inextricable difficulties. Navier-Stokes methods applied to base-flow are presented in Section 3.5.

To conclude, it should be said that in spite of the spectacular progress made in base-flow computations, empirical or semi-empirical formulae are still extremely precious in making evaluation of base drag - particularly in situations where theories are either lacking or still unreliable: transonic Mach numbers, flight at angle of attack, afterbody with tails, etc... A relatively large amount of data is available to obtain this information (see in particular Hitchcock, 1951; Baugham and Kochendorfer, 1957; E.S.D.U. publication, 1979; Tanner, 1994, 1986a, 1986b; also ample information can be found in the JANNAF Handbook on base-flows, 1981).

In the following Sections, we shall only consider **turbulent** base-flows, i.e., situations in which the boundary-layers are turbulent upstream of the base. Indeed, these situations are the most likely to occur for current missile applications.

### 3.2. - Basic Principles of Inviscid/Viscous Interactive and Multi-Component Methods

The basic idea of Inviscid/Viscous Interactive Methods and Multi-Component Methods consists in splitting the flowfield into :

- i - an external or outer region where the viscous terms are assumed to play a negligible role ;
- ii - one or several inner region(s) in which viscous effects are essential. These regions are boundary-layers, mixing-zones, wakes, etc.

Thus the external flow satisfies the Euler equations, or the potential equation if it is, in addition, irrotational, whereas the dissipative zones are represented by more or less sophisticated models.

The inviscid and viscous (or dissipative) parts of the flow are computed separately but not independently. They must indeed satisfy appropriate conditions in order to be compatible.

In the so-called **Multi-Component Methods** which apply essentially to flows such as missile base-flows containing large separated regions, the dissipative layers are represented by simplified analyses incorporating a relatively large dose of empiricism. The compatibility of these regions with the contiguous inviscid flow is expressed in a rather coarse manner by satisfying continuity of pressure and velocity at a very limited number of "control points".

This is in contrast with the more sophisticated **Inviscid/Viscous Interactive Methods** in which the compatibility conditions between the inviscid and the viscous flows are satisfied all along a suitably chosen control surface. Such methods require a more refined description of the dissipative part of the flow.

Inviscid/Viscous Interactive methods are now widely used to compute complex flows including separated regions. However, due to their relative complexity, their use in the calculation of base-flows behind missile afterbodies with exhaust jet effects has been very limited. For practical applications, Multi-Component Methods remain the essential predictive tool due to their generally acceptable level of accuracy in the prediction of the most important flow features and their cheap computation cost. As will be seen in Section 3.4., these methods are capable of predicting base-flows including effects of exhaust jet, base-bleed, heat flux, mixing of different species, chemistry, etc...

However, the Inviscid/Viscous Interactive Methods are of considerable interest in the prediction of less complicated situations where they can often give a description of the flow as accurate and as detailed as that furnished by the solution of the full (time-averaged) Navier-Stokes equations. For example, they could be used to predict a base-flow behind a projectile or a missile in the jet-off condition. Thus these methods will be considered in some detail in the following Section.

Some concepts useful to the understanding of the basic principles of both Inviscid/Viscous Interactive Methods and Multi-Component Methods applied to base-flow problems are more clearly introduced by considering the reattachment behind a rearward facing step. A schematic representation of such a flow is shown in Fig. 24 for the case of a supersonic incoming stream. As seen above, the experimental analysis of reattachment in subsonic regime leads to a description of phenomena practically identical to those which will be considered here, except that the pressure gradients are less intense, the flow being of course free of shock-waves. Consequently, conclusions derived for supersonic flows will still hold true at subsonic speeds with only minor changes.

Broadly speaking, the turbulent dissipative flow can be divided into five regions :

- i - the first region I is located in the vicinity of the step shoulder S where the incoming boundary-layer (presently assumed to be thin when compared to the step height  $h$ ) separates. In the pictured situation, the boundary-layer undergoes at S a centered expansion. In other circumstances, for example when a highly underexpanded jet induces separation on the missile fuselage, the boundary-layer at S is submitted to a compression. Thus in supersonic flows, the boundary-layer in region I is subjected to a concentrated pressure gradient acting over a very short streamwise distance. Viscous forces are known to play a negligible role over the major part of the boundary-layer in such a "**Rapid Interaction Process**", the flow being essentially controlled by pressure and inertia forces (Lighthill, 1953). In fact, viscosity is of importance only very close to the wall in a sublayer which is for turbulent regime extremely thin when compared to the total thickness  $\delta$  of the incoming boundary-layer ;
- ii - downstream of S, in region II, a quasi-isobaric turbulent mixing layer develops ;
- iii - region II is followed by a first compression zone III extending to the reattachment point R ;
- iv - the compression continues downstream of R in region IV until some far downstream level is reached ;
- v - in contact with the wall, a recirculating bubble V is trapped, inside which the flow is reversed, feeding the mixing-layer.

At this point, two important concepts must be introduced. Let us examine the behavior of the fluid particles flowing in the mixing zone and approaching the reattachment region. The conservation of the fluid mass contained in what is called the "dead-air" region requires that the streamline (j) issuing directly from the separation point S end up at the reattachment point R (see Fig. 25a). Any streamline below (j) should fold back towards the dead-air due to the existence of the adverse pressure gradient in the vicinity of R. Streamline (j) will be called the **Dividing Streamline** or DSL. The above scheme can be generalized to take into account a possible injection of mass into the dead-air region at a flow rate  $\dot{q}_B$  (see Fig. 25b). Then, the streamline (s) ending up at the reattachment point R, which we shall call the **Stagnation Streamline** (SSL), is distinct from the DSL (j). The conservation of mass for a steady flow regime implies that  $\dot{q}_B$  be equal to the flow rate between (j) and (s). In this case, where  $\dot{q}_B$  is positive, the DSL is above the SSL. On the other hand if suction is performed ( $\dot{q}_B < 0$ ), the SSL is now above the DSL (see Fig. 25c).

When considering a base-flow (two-dimensional or axisymmetric), the above description remains essentially valid. The main difference is that, beyond reattachment, a boundary-like development is replaced by an evolution towards a far-wake situation. In fact, as shown by experiment (D elery and Srieix, 1979), the presence of a wall does not appreciably modify the general flow structure.

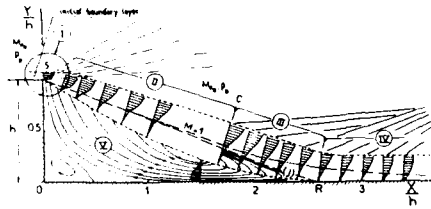


Fig. 24 - Supersonic reattachment downstream of a rearward facing step

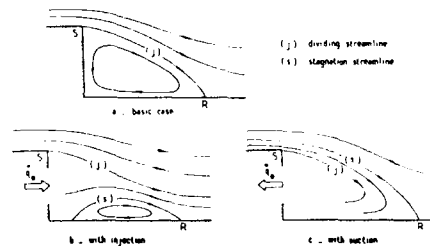


Fig. 25 - Definition of dividing streamline and stagnation streamline

### 3.3. - Inviscid/Viscous Interactive Methods

#### 3.3.1. - Introductory Remarks

In situations where dissipative zones remain thin when compared to a characteristic length of the body (e.g., chordlength of a profile or blade to blade distance of a cascade), their influence on the general flow structure is weak. Thus a simple perfect fluid calculation ignoring any viscous effects can give a good representation of the real flow. In this case, the viscous regions are computed afterwards, the pressure distribution issued from the perfect fluid calculation being prescribed as boundary condition for this calculation. Then a viscous correction is eventually applied to the perfect fluid result.

However, if separation occurs, the role of the dissipative regions in the determination of the flowfield tends to become predominant so that a purely perfect fluid calculation gives a prediction which is too far from reality to be considered even as a first approximation of the solution. In fact, in this case a **strong interaction** mechanism establishes itself between the inviscid and viscous parts of the flow such that these parts can no longer be determined independently. The calculation of the flow requires an **interactive** procedure between the inviscid outer flowfield and the dissipative regions.

The basic principles of the Inviscid/Viscous Interactive approach are contained in the historical paper of **Crocco and Lees** (1952) who applied an interactive method to the calculation of supersonic reattachment behind a rearward facing step.

It is now customary to distinguish two ways to formulate the Inviscid/Viscous Interaction problem :

- i - the first one consists in dividing the flowfield into distinct regions which are separated by a boundary ( $\Sigma$ ) and described by different equations. The two sets of equations are solved independently, their solutions having to satisfy compatibility or coupling conditions along ( $\Sigma$ ). This method is frequently called the **multi-domain** or **patching approach**. It has been applied with success, in particular by Cambier et al. (1981), who coupled Navier-Stokes and Euler domains to compute transonic shock-wave/turbulent boundary-layer interaction and supersonic cascade flows (Cambier et al., 1987) ;
- ii - in the second technique, one considers a continuation of the external inviscid flow into the region normally occupied by the viscous flow. The compatibility conditions are written on a surface embedded in the viscous part. Most often, this surface is the displacement body - i.e., the body surface augmented by the dissipative layer displacement thickness - or the wall itself. Such a technique is called the **matching approach**.

In what follows, we will only consider Inviscid/Viscous Interactive methods using the classical Prandtl equations to represent the dissipative regions (incoming boundary-layers, near-wake and wake in the present application to missile afterbodies). This presentation will also be restricted to iso-energetic and steady flows. Neither do we intend to discuss Inviscid/Viscous Interactive methods in general. These methods involve many problems, the consideration of which would go beyond the scope of the present review paper. Thorough examination of the coupling approach can be found elsewhere (see, in particular, Le Bailleur, 1978, 1984).

### 3.3.2. - Formulation of the Problem

In most cases, the equations starting the description of the dissipative part of the flow are those of the boundary-layer written here for a two-dimensional flow in order to simplify this presentation, viz. :

- continuity

$$(1) \quad \frac{\partial(\rho u)}{\partial x} + \frac{\partial(\rho v)}{\partial y} = 0$$

- x - momentum

$$(2) \quad \rho u \frac{\partial u}{\partial x} + \rho v \frac{\partial u}{\partial y} = - \frac{\partial p}{\partial x} + \frac{\partial \tau_T}{\partial y}$$

- y - momentum

$$0 = \frac{\partial p}{\partial y}$$

The flow being turbulent, all variables are time - averaged variables, the bar being omitted for clarity ; (Oxy) is a local system of co-ordinates with x along the surface of the obstacle, y being perpendicular to x ; u and v are the velocity components along x and y respectively ;  $\rho$  is the density and p the pressure.

Here  $\tau_T$  expresses the total shear stress, sum of the laminar term  $\tau_l$  and of the Reynolds shear stress  $\tau_r = - \rho u'v'$ . For the sake of simplicity, we shall consider the iso-energetic case and assume the stagnation enthalpy  $h_t$  constant, which enables us to ignore the energy equation.

Equation (2) is put into the integral form of Von Kàrmàn :

$$(3) \quad \frac{d\theta}{dx} + \theta \left( 2 + \frac{\delta^*}{\theta} - \frac{2 m_e}{\gamma - 1} \right) \frac{1}{1 + m_e} \frac{dM_e}{dx} = \frac{C_f}{2}$$

where :

-  $M_e$  is the Mach number at the edge of the dissipative layer ;

-  $\delta^*$  the displacement thickness : 
$$\delta^* = \int_0^{\delta} \left( 1 - \frac{\rho u}{\rho_e u_e} \right) dy ;$$

-  $\theta$  the momentum thickness and : 
$$\theta = \int_0^{\delta} \frac{\rho u}{\rho_e u_e} \left( 1 - \frac{u}{u_e} \right) dy ;$$

-  $m_e = \frac{\gamma - 1}{2} M_e^2 ;$

-  $C_f = \frac{2 \tau_w}{\rho_e u_e^2}$  is the skin-friction coefficient,  $\rho_e$  and  $u_e$  being the values of  $\rho$  and  $u$  at  $\delta$ .

In base-flow calculations, the skin friction  $C_f$  is frequently neglected ; this approximation is due to the fact that  $C_f$ , zero at separation or reattachment, is small everywhere within the zone considered whose longitudinal extent is small anyway (a few  $\delta$ ).

To the integral momentum equation is added a complementary relation. Originally, Crocco and Lees proposed a "mixing" or "entrainment" equation of the form :

$$\frac{d\dot{m}}{dx} = C_E \rho_e u_e$$

where  $\dot{m} = \int_0^{\delta} \rho u \, dy$  is the mass flow through the dissipative layer and  $C_E$  an entrainment coefficient. The above equation can also be written in the form :

$$(4) \quad \frac{d(\delta - \delta^*)}{dx} - (\delta - \delta^*) \frac{1 - M_e^2}{1 + m_e} \frac{1}{M_e} \frac{dM_e}{dx} = C_E$$

Other authors have preferred to adopt the integral equation of the first moment of momentum, also called the Mean-Flow Kinetic Energy equation. It is obtained by multiplying Eq. (2) by  $u$  :

$$\rho u^2 \frac{\partial u}{\partial x} + \rho uv \frac{\partial u}{\partial y} = -u \frac{\partial p}{\partial x} + u \frac{\partial \tau_T}{\partial y}$$

whence, after integration in  $y$  from  $y = 0$  to  $y = \delta$

$$(5) \quad \frac{d\theta^*}{dx} + \theta^* \left[ 3 + \frac{2(\gamma - 2)}{\gamma - 1} m_e \right] \frac{1}{1 + m_e} \frac{1}{M_e} \frac{dM_e}{dx} = C_D$$

where :

$$\theta^* = \int_0^{\delta} \frac{\rho u}{\rho_e u_e} \left( 1 - \frac{u^2}{u_e^2} \right) dy \quad \text{is the kinetic energy thickness ;}$$

$$C_D = \frac{2}{\rho_e u_e^3} \int_0^{\delta} \tau_T \frac{\partial u}{\partial y} dy \quad \text{is the shear-work integral coefficient also called the dissipation integral coefficient}$$

A variant, used in particular by Kuhn and Nielsen (1974), consists in multiplying Eq. (2) by  $y$  before integration with respect to  $y$ . It should be noted that the above integral approach which is limited here to the consideration of two integral equations is a particular case of a general integration technique, the so-called Method of Integral Relations developed by Dorodnitsyn (1960) to compute attached boundary-layers. By successively multiplying the local equation (2) by  $n$  different weighting functions  $f$  and then integrating over the thickness of the dissipative layer, one obtains  $n$  integral equations. Then by making appropriate assumptions about the shape of the streamwise velocity distributions  $u/u_e$ , it is possible to reduce these equations to a set of ordinary differential equations. This technique has been used in particular by Holt and Meng (1965) to compute the near wake behind a hypersonic re-entry body.

The fundamental equation ensuring the coupling between the dissipative layer and the contiguous inviscid flow is obtained by integrating the continuity equation (1), which gives :

$$(6) \quad \frac{d\delta^*}{dx} - (\delta - \delta^*) \frac{1 - M_e^2}{1 + m_e} \frac{1}{M_e} \frac{dM_e}{dx} = \frac{v_e}{u_e} = \tan \theta_e$$

where  $\theta_e$  represents here the inclination of the velocity vector  $V_e$  with respect to the body surface at the frontier  $\delta$ .

However, by considering an analytical continuation of the outer inviscid flow towards the wall (or the axis), it is possible to express the coupling condition on any surface comprised between  $y = \delta$  and  $y = 0$  (see Lighthill, 1958 and Le Balleur, 1978). Thus, except the boundary  $\delta$ , the most frequently used coupling surfaces are :

- the displacement surface  $\delta^*$ ; Eq. (6) then becomes :

$$(7) \quad \frac{d\delta^*}{dx} = \tan \theta_e$$

- the wall itself; Eq. (6) then becomes :

$$(8) \quad \frac{d\delta^*}{dx} + \delta^* \frac{1 - M_e^2}{1 + m_e} \frac{1}{M_e} \frac{dM_e}{dx} = \tan \theta_e$$

Equations (3-4-6) or (3-5-6) - Eq. (6) being eventually replaced by Eq. (7) or (8) - constitute the system describing the interaction between the dissipative layer and the external flow.

In the supersonic case, integration can be performed by a forward marching procedure with the external flow being calculated at the same time using, for instance, the Method of Characteristics that provides a relation connecting  $M_e$  and  $\theta_e$ . If this flow is a simple wave,  $M_e$  and  $\theta_e$  are directly linked by the well-known Prandtl-Meyer relation ( $[\theta_e, M_e]$  being a reference state) :

$$\theta_e - \theta_{e0} = \nu(M_e, \gamma) - \nu(M_{e0}, \gamma)$$

where :

$$\nu(M, \gamma) = \sqrt{\frac{\gamma + 1}{\gamma - 1}} \tan^{-1} \sqrt{\frac{\gamma - 1}{\gamma + 1} (M^2 - 1)} - \tan^{-1} \sqrt{M^2 - 1}$$

On the other hand, in a subsonic or transonic situation, computation of the perfect fluid flow requires relaxation or time-marching methods in order to properly take into account the boundary conditions on all the frontiers of the computational domain. In this way, it is no longer possible to fulfill the compatibility conditions by a streamwise progression since outer flow quantities at a station  $x$  depend on downstream conditions. In fact, the boundary-layer and the external inviscid flow have to be computed

**in turn** according to an iterative process which is repeated until convergence is achieved. This iteration procedure leads to a convergence problem which will not be discussed here (for information, see Détery and Marvin, 1986).

In fact, for the differential system to be complete, we must also make an assumption about the dissipation layer velocity profiles so as to be able to express the thicknesses  $\delta$ ,  $\delta^*$ ,  $\theta$ , and  $\theta^*$  as functions of a reduced number of parameters. Most often, we adopt a family using a single shape parameter A, so that :

$$\frac{\theta}{\delta} \equiv H(A, M_e) \quad , \quad \frac{\theta^*}{\delta} \equiv J(A, M_e) \quad , \quad \frac{\delta - \delta^*}{\delta} \equiv Z(A, M_e)$$

are known functions of A and  $M_e$ . Frequently, the "incompressible" shape parameter  $H_i$  is chosen as shape parameter. This parameter is defined by :

$$H_i \equiv \frac{\delta_i^*}{\theta_i} = \frac{\int_0^{\delta} \left(1 - \frac{u}{u_e}\right) dy}{\int_0^{\delta} \frac{u}{u_e} \left(1 - \frac{u}{u_e}\right) dy}$$

The viscous terms (namely, the skin-friction coefficient, the dissipation integral, the entrainment coefficient) are expressed also as functions of  $H_i$  and  $M_e$  (plus, if necessary, the Reynolds number), either from empirical formulae or from the velocity profiles and an assumption about turbulence properties.

Finally the differential system can be written (if Eq. (5) is used) :

$$H \frac{d\delta^*}{dx} + \delta^* \frac{\partial H}{\partial H_i} \frac{dH_i}{dx} + Q_1 \frac{\delta^*}{M_e} \frac{dM_e}{dx} = \frac{C_f}{2}$$

$$J \frac{d\delta^*}{dx} + \delta^* \frac{\partial J}{\partial H_i} \frac{dH_i}{dx} + Q_2 \frac{\delta^*}{M_e} \frac{dM_e}{dx} = C_D$$

$$\frac{d\delta^*}{dx} + Q_3 \frac{\delta^*}{M_e} \frac{dM_e}{dx} = \tan \theta_e$$

Where  $Q_1$ ,  $Q_2$  and  $Q_3$  are functions of  $H_i$  and  $M_e$  that we shall not expound here (see Carrière et al., 1975). The above system can also be written out into the form :

$$(9) \quad \frac{d\delta^*}{dx} = \frac{N_1}{D} \quad , \quad \frac{dH_i}{dx} = \frac{1}{\delta^*} \frac{N_2}{D} \quad , \quad \frac{dM_e}{dx} = \frac{M_e}{\delta^*} \frac{N_3}{D}$$

In the case of a base flow problem, system (9) is usually only applied to a recompression (region III and IV of Fig. 24). Indeed, the isobaric mixing zone preceding reattachment cannot be correctly described by a one parameter velocity profile family. This region can be calculated either by means of approximate analyses similar in spirit to the one presented in Section 3.4 below, or by using a two-parameter profile family (Green, 1966 ; Le Balleur, 1978). An additional equation is thus needed to complete the system of integral equations. Some authors adopt the momentum equation written on the axis ; it is also possible to use an empirical relation linking these two parameters.

### 3.3.3 - Method of Solution

The general principle for solving a reattachment problem thus consists in calculating separately the isobaric mixing and then the recompression, the base pressure  $p_B$  being assumed provisionally known. The two solutions are then matched by ensuring the continuity of some parameters, e.g., the Mach number  $M_e$ , the velocity  $u_f$  on the Dividing Streamline and, for example, the mass flow rate passing above the latter (for more details, see Alber, 1967 and also Alber and Less, 1968).

In the supersonic case starting from an initial state, system (9) can be integrated at the end of the isobaric zone by progressing downstream so as to reach a state of "rehabilitated" boundary-layer downstream of reattachment. This means that if the inviscid outer flow becomes uniform downstream of reattachment, the reattached boundary-layer must tend towards a state compatible with a uniform contiguous inviscid stream interacting weakly with it. In particular this signifies that the incompressible shape parameter  $H_i$  tends towards a typical flat plate value, generally close to 1.3.

Thus the unicity of the solution - namely the up-to-now arbitrary value of the base pressure  $p_B$  - is ensured by the fact that a condition must be satisfied at the downstream extremity of the computation domain. There results a two-point boundary value problem which necessitates an integration technique calling upon either a shooting technique or an overall relaxation procedure. This downstream condition restores the ellipticity of the real separated flow problem which apparently was lost by the use of the integral formulation.

However, in the case of a supersonic turbulent flow, it appears that during integration, the denominator D of Eqs. (9) changes sign if coupling Eqs. (6) or (7) are used. This fact makes the solution singular except if the numerators are zero at the same time (if D and one  $N_i$  are zero at the same time, the others are also zero). The differential system exhibits a singular point K which has in fact a saddle-point behavior. Thus a solution curve starting from A (beginning of recompression) can join B (weakly interacting downstream boundary-layer) only if it passes through the singular point K. Any other solution curve corresponds to a solution physically unacceptable for a reattachment process (appearance of an extremum for A or  $M_e$ ).

The same considerations apply for a base-flow problem. The downstream state now corresponds to the development of a wake whose velocity distributions must also tend towards some "equilibrium" or asymptotic state.

The fundamental consequence of the existence of the singular point K is that it renders the solution from A to K independent of the conditions imposed downstream of K which thus plays a "choking" role in the same way as the throat of a converging-diverging supersonic nozzle. The existence of the critical point was demonstrated for the first time by Crocco and Lees (1952). Moreover, by analogy with subsonic and supersonic flows, the dissipative layer in a reattachment process is said to be subcritical upstream of K and supercritical downstream of K.

In this case, it is the regular passage of the solution through the critical point that ensures the unicity of the solution for the reattachment problem, i.e., the condition defining the base pressure  $p_b$ . This condition constitutes a reattachment "criterion" (the behavior of the solution in the vicinity of K, as well as the integration methods allowing one to verify the regularity in K, are discussed in detail in Ai, 1970 and in Carrière et al., 1975).

This theoretical scheme is obviously very attractive as it seems to interpret perfectly the concept of critical point, experimentally brought to light by Sirieix et al. (1966). However, the location of K and even its very existence are closely related to the coupling equation used. So, the singularity appearing by the zero value of D disappears when we ensure the coupling at the wall (Eq. B) (see Le Bailleur, 1978). The physical meaning of the critical point is thus far from being clear. Presently, most Inviscid/Viscous Interactive methods avoid the occurrence of any singular point by choosing a coupling surface so that this kind of singularity does not exist.

Now we shall briefly survey Inviscid/Viscous Interactive methods which have been proposed for computing base flows. Most of these methods are of a historical interest, few of them having led to practical applications due to the extreme difficulties in extending this approach to real, complex configurations.

### 3.3.4 - Applications to Base-Flow Problems

The initial work of Crocco and Lees has inspired a vast research effort, still actively pursued. We shall not analyze here the many variants of this method published to date. Inviscid/Viscous Interactive techniques have been employed in particular to treat shock-wave/boundary-layer interaction first in laminar flow (Bray et al., 1960; Glick, 1960; Lees and Reeves, 1964), then in turbulent flow (Holden, 1969; Hunter and Reeves, 1971; Le Bailleur, 1982). As already mentioned, these techniques have now reached a high degree of sophistication and allow the computation of complex interacting flows. In what follows, we shall concentrate on applications to separation and reattachment behind a base.

A theory for the laminar near wake of blunt bodies in hypersonic flow was proposed by Reeves and Lees (1965). The method essentially follows the previous work by the authors on shock-induced separation. In the present model, the flow is divided into a constant pressure mixing region followed by a strongly Inviscid/Viscous Interaction region at reattachment and in the wake. The problem is formulated by considering the Momentum and Mean-Flow Kinetic Energy integral equations. However, before  $y$ -wise integration, a compressible-incompressible transformation, similar to the well known Stewartson transformation, is applied to the local equations in order to replace the auxiliary functions  $H$ ,  $J$  and  $Z$  by equivalent "incompressible" functions  $H_i$ ,  $J_i$  and  $Z_i$  independent of the Mach number. These functions are then evaluated by considering the wake-like solutions of the Falkner-Skan equation computed by Stewartson (1954). The outer inviscid flow is computed by assuming a simple wave evolution.

The system of integral equations is integrated by a classical Runge-Kutta technique. The proper solution is determined by the condition of a smooth passage of the solution curve through the Crocco-Lees critical point that exists downstream of reattachment.

The laminar version of the Crocco-Lees model was applied to two-dimensional base flow problems by Rom (1962). Thereafter, Seginer and Rom (1967) extended the model to non-adiabatic flows. For this purpose, an integral energy equation was added to the momentum and entrainment equations and the similar non-adiabatic solutions of Cohen and Reshotko (1956) were used to obtain the additional correlation laws.

Turbulent supersonic reattachment behind a rearward facing step was computed by Alber (1967, see also: Alber and Lees, 1968). This method is in fact an application to the turbulent base flow problem of the already cited Lees-Reeves theory. The velocity distribution in the "incompressible" plane is also given by the similar Stewartson wake-like solutions (for a turbulent wake flow, the velocity distributions are nearly the same as those of a laminar flow), the dissipative terms being evaluated by a simple algebraic turbulence model. Unicity of the solution is ensured by the existence of a critical point.

A method used to compute two-dimensional supersonic reattachment without performing a compressible-incompressible transformation can be found in Carrière et al. (1975). In this method, the stagnation enthalpy is assumed everywhere constant and the functions  $H$ ,  $J$  and  $Z$  are evaluated by using an incompressible velocity family inspired from the well-known law-of-the-wall/law-of-the-wake Coles composite formula (Coles, 1956). Indeed, for an iso-energetic flow at moderate Mach number (less than four), the velocity distributions are practically unaffected by compressibility.

The basic formulation of Crocco and Lees was extended to axisymmetric base flows by de Krasinsky (1966) who also made a very detailed experimental analysis of the near wake region of a cylindrical afterbody. However, the first convincing axisymmetric calculations for turbulent base flows are due to Mehta (1977; see also Mehta and Strahle, 1977).

The flow model adopted by Mehta is represented in Fig. 26: it consists of an external inviscid region, which can be calculated by the Method of Characteristics, and an internal viscous zone to which boundary-layer type equations are applied. The influence of the "lip shock" (Hama, 1968) which usually appears in the immediate vicinity of the separation point S is neglected, an approximation that is probably quite justified as long as the Mach number remains moderate (less than four).

Moreover, following experimental observations clearly showing that, because of the rapid expansion at the base, viscous forces are predominant only in the lowest part of the boundary-layer, Mehta includes in the inviscid region the external part of the initial boundary-layer which is thus considered as a rotational perfect fluid flow.

Because of the axisymmetry effect and also the fact that entropy is not constant (rotational layer), the inviscid flow can not be calculated by the Prandtl-Meyer relation which would constitute here far too rough an approximation. Accordingly, in order to know the conditions at the viscous layer outer edge at each integration step in  $x$ , we must use the Method of Characteristics, formulated in non-isentropic axisymmetric flow. We shall not consider here this classical formulation. So as to save computing time, Mehta implements a simplified procedure which is an improvement of the technique proposed by Webb (1968).



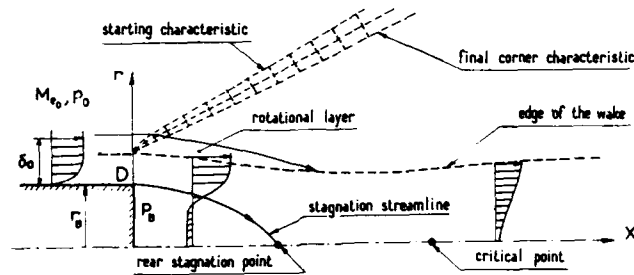


Fig. 26 - Base pressure in axisymmetric supersonic flow - Mehta's inviscid-viscous/interactive method

The dissipative flow is described by boundary-layer type equations which take the form :

- continuity :

$$\frac{\partial(\rho u)}{\partial x} + \frac{1}{r} \frac{\partial}{\partial r} (\rho u r) = 0$$

- streamwise momentum :

$$\rho u \frac{\partial u}{\partial x} + \rho v \frac{\partial u}{\partial r} = - \frac{\partial p}{\partial x} + \frac{1}{r} \frac{\partial}{\partial r} (r \tau r)$$

- radial momentum :

$$0 = \frac{\partial p}{\partial r}$$

- energy :

$$h_t = h + \frac{u^2}{2} = \text{constant}$$

Here  $r$  designates the distance from the symmetry axis.

According to the above approach, the equations applied to the dissipative layer are solved by an integral method using the following three equations :

- continuity (coupling) :

$$\frac{d}{dx} (\rho_e u_e A_1) - \rho_e u_e \delta \frac{d\delta}{dx} = - \rho_e v_e \delta$$

- momentum :

$$\frac{d}{dx} (\rho_e u_e^2 A_2) - u_e \frac{d}{dx} (\rho_e u_e A_1) = - \frac{\delta^2}{2} \frac{dp}{dx} + \delta \tau_\delta$$

- mean flow kinetic energy :

$$\frac{d}{dx} \left( \frac{1}{2} \rho_e u_e^3 A_3 \right) - \frac{u_e^2}{2} \frac{d}{dx} (\rho_e u_e A_1) = - u_e A_u \frac{dp}{dx} - \rho_e u_e^3 R_I + \delta u_e \tau_\delta$$

where  $A_1$ ,  $A_2$ ,  $A_3$  and  $A_u$  are quantities having the dimension of a surface, they are defined by :

$$A_1 = \int_0^\delta \frac{\rho u}{\rho_e u_e} r dr, \quad A_2 = \int_0^\delta \frac{\rho u^2}{\rho_e u_e^2} r dr, \quad A_3 = \int_0^\delta \frac{\rho u^3}{\rho_e u_e^3} r dr, \quad A_u = \int_0^\delta \frac{u}{u_e} r dr$$

$R_I$  is the «dissipation integral» :

$$R_I = \frac{1}{\rho_e u_e^3} \int_0^\delta r \tau r \frac{\partial u}{\partial r} dr$$

$\tau_\delta$  is the shear stress at the edge  $\delta$ , which is non-zero because of the existence of the rotational layer. The terms involving the shear stress are computed by considering an algebraic turbulence model.

Taking his inspiration from the Alber approach, Mehta uses a compressible-incompressible transformation to take into account in a simple way the compressibility effect.

The incompressible equivalent of the integrals  $A_i$  are evaluated by considering the Green profiles close to the base (Green, 1966) and, far from the base, the profiles of Kubota and al. (1964) which are similarity solutions for the axisymmetric wake.

The above system is integrated, along with the calculation of the outer inviscid flow, by a streamwise marching method. This system presents a singularity similar to the Crocco-Lees critical point which makes it possible to ensure, as described in Section. 3.3.3. above, the unicity of solution, i.e., the value of the base pressure  $p_B$ .

By considering profiles with positive velocity in the dead-air region at the initial station in contact with the base, the model is capable of predicting base-bleed effect.

We shall now present some applications of Mehta's theory.

Figure 27 shows the pressure distribution along the wake axis for an upstream Mach number of the order of 2. The theory-experiment agreement is usually good : in particular, the base pressure is accurately predicted. The important discrepancy observed for  $M_\infty = 1.85$  is quite likely due to perturbing effects provoked by the wind tunnel walls. The letters R, K, C and E mean respectively the reattachment point, the critical point, the wake neck ant the sonic point on the axis.

Figure 28 gives the evolution of the base pressure coefficient as a function of the upstream Mach number  $M_\infty$ , and emphasizes the effect of the initial boundary-layer. The prediction can be considered as correct, considering the rather large experimental scatter that does not make it possible to clearly show the influence of the initial boundary-layer. In the case of an axisymmetric base, this parameter seems to play a secondary role anyway, the prime effect for a given geometry arising from the upstream Mach number. Such a tendency is also observed in the case of two-dimensional reattachment where the boundary-layer strongly affects the phenomenon only around the limit case  $\theta = 0$ .

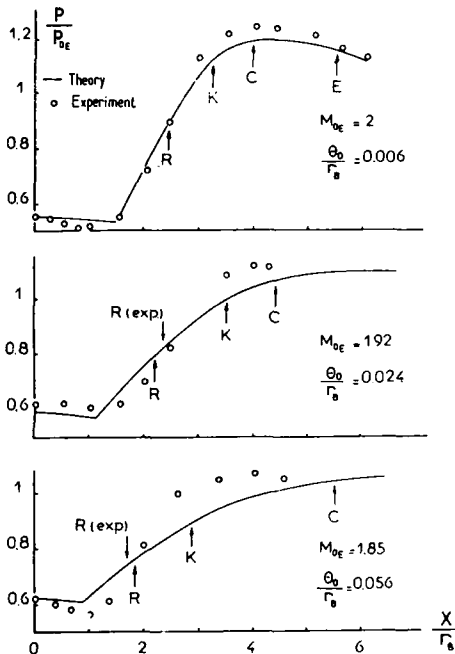


Fig. 27 - Centerline pressure distribution - Mehta's theory

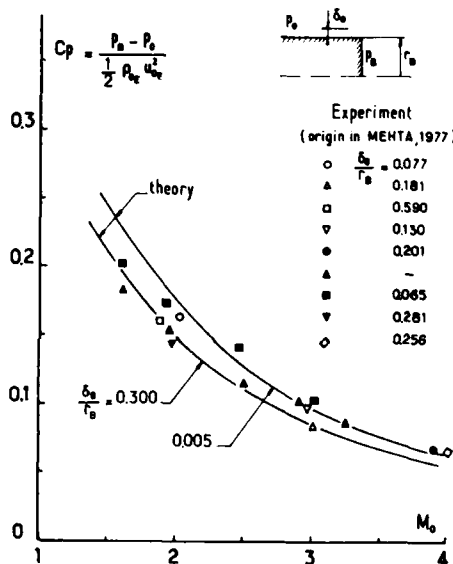


Fig. 28 - Effect of upstream Mach number on base pressure - Mehta's theory

Lastly, Fig. 29 shows the influence of base-bleed. Here, prediction is quite below the experimental level, the slopes of the computed and experimental curves being particularly different around the origin.

Other theories similar in concept to that just described have been proposed to treat the base flow problem in axisymmetric supersonic flow (Peters and Phares, 1976). They essentially differ in the way they treat the expansion effect from  $p_0$  to  $p_B$  on the initial boundary-layer, as well as in the choice of other representations of velocity profiles in the viscous zone.

A variant of the above integral techniques was proposed by Chow (1971 ; see also Chow and Spring, 1975) for modeling the reattachment of a turbulent shear layer. In this formulation, the flow is divided into three successive regions : an isobaric mixing layer, a recompression zone extending down to reattachment and a redevelopment region. The isobaric mixing zone is treated by assuming simplified velocity distribution. The reattachment region is divided into an upper flow above the Dividing Streamline and an inner flow below the Dividing Streamline. This region, as well as the redevelopment region, are computed by using integral equations both for the streamwise and the transverse momentum. The velocity distributions in the different parts of the flowfield are given by simple polynomial laws. Thus in this method special attention is given to the pressure difference across the dissipative layer and the flow redevelopment process is treated as a relaxation of this pressure difference. The system of equations governing the flow produces a saddle point singularity corresponding to the fully rehabilitated asymptotic flow condition.

First applied to supersonic reattachment behind a rearward facing step, the method was further extended to treat incompressible reattachment (Chow and Spring, 1976), axisymmetric supersonic reattachment (Weng and Chow, 1978) and finally, transonic base flows (Liu and Chow, 1979 ; Chow, 1984). In the latter case, the inviscid flowfield is established from the relaxation finite

difference calculation of the full potential equation. This outer flow is computed along an equivalent body made of the body itself augmented by the boundary-layer displacement thickness surface followed by the displacement surface of the viscous flow downstream of the base, i.e., near wake and wake. This last application is specially interesting since, to our knowledge, it is the only "simple" method available for computing the base drag of projectiles within the transonic regime.

Examples of results yielded by this theory are presented in Fig. 30 which shows pressure distributions along an equivalent body (i.e., displacement surface) for a boattailed projectile (a 6 Caliber Secant-Ogive Cylinder Projectile) tested by Kayser and Whiton (1982). Agreement with experiment is generally good except at the ogive cylinder junction at high subsonic Mach number. The average base-pressure within the transonic regime is plotted in Fig. 31.

The problem of base flow with under expanded propulsive jet leading to plume induced separation has been treated by Klineberg et al. (1972). The method is applied to a two-dimensional configuration in the presence of a very small base surface. The turbulent as well as the laminar regimes are considered.

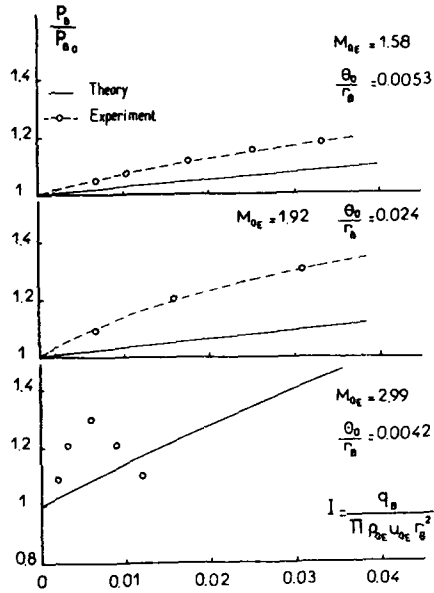


Fig. 29 - Base bleed effect - Mehta's theory

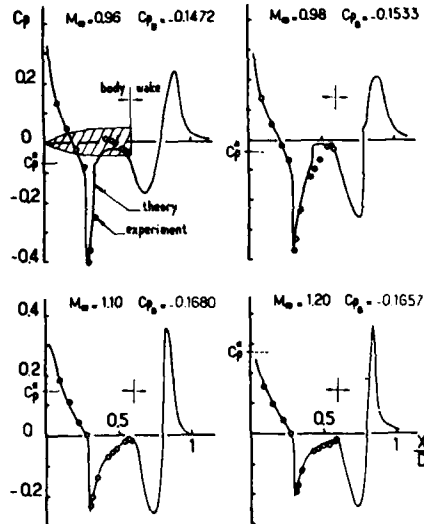


Fig. 30 - Pressure distribution over axisymmetric projectile at transonic speed - Chow's model (1986)

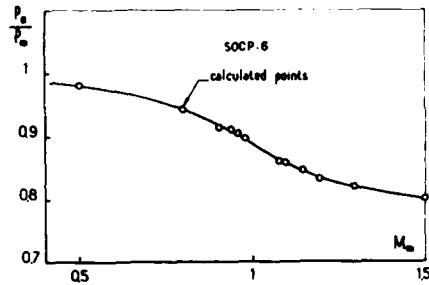


Fig. 31 - Average base pressure within the transonic regime - Chow's model (1986)

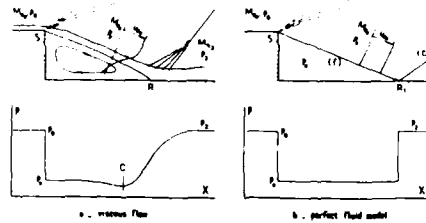


Fig. 32 - Schematization of the flow behind a rearward facing step

### 3.4 - Multi-Component Methods

#### 3.4.1 - The Basic Flow Model

In the most simple Multi-Component Methods, regions I to V of the flow represented in Fig. 24 are depicted by distinct and generally simple models. Most often, only regions I to IV are considered, the flow in V having a secondary and negligible influence on the mechanism determining the main base flow structure. The different regions mentioned above are patched together in an approximate manner in order to satisfy conservation of some global quantities. Most of the considerations which follow apply both to supersonic and subsonic flows, with the essential differences residing in the application method.

In the Multi-Component approach the viscous effects are in fact superimposed on a basic inviscid flow model which is entirely determined if the pressure  $p_j$  in the separated (or dead-air) region is assumed known (see Section 3.1.). Thus as shown in Fig.

32, to the physical model of reattachment behind a rearward facing step in supersonic flow (Fig. 32a) is associated an inviscid flow model such that the pressure  $p_B$  is the same in the two cases (Fig. 32b). Indeed if  $p_B$  is known, the inviscid flowfield can be computed by solution of the Euler equations, prescription of  $p_B$  playing a role similar to the condition of Kutta-Joukowski by ensuring unicity of solution. Thus the inviscid solution constitutes a skeleton upon which the viscous phenomena will be superimposed so as to arrive at the physical constraint which fixes the values of the separated flow properties : namely the pressure  $p_B$  and the temperature  $T_B$  of the dead-air region. The main features of the inviscid model are the isobaric boundary (f) and the recompression shock (C) emanating from the point  $R_T$  where (f) impinges the reattachment wall. In the situation sketched in Fig. 32b, a centered expansion wave originates from the separation point S. This situation corresponds to a pressure  $p_B$  lower than the upstream pressure  $p_0$ . If  $p_B$  is greater than  $p_0$ , then separation is accompanied by a compression giving rise to a separation shock. Such a situation will be met in cases of plume induced separation on the missile fuselage (see Section 3.4.6.2.)

The fundamental model described here was proposed independently by Chapman and Korst in the early 1950's (Chapman, 1951 ; Korst et al., 1955 ; Korst, 1956). The two theories are based on the same fundamental concepts but one, that of Chapman, treats the laminar case, while the other, that of Korst, applies to the turbulent one. So we shall concentrate on the Korst model which inspired most of the methods routinely used to compute base-flows behind missiles. Since that time, many modifications have been proposed to remedy deficiencies of the original Korst model or to improve its range of applicability. These variants will be examined in the forthcoming Sections.

In this model, only regions II and III of the above description are considered (see Section 3.2.). The isobaric mixing-zone has a pressure  $p_B$  which is assumed to be equal to that of the contiguous inviscid flow of Mach number  $M_{rB}$ .

The three fundamental problems arising from this simplified base-flow analysis are thus the following :

- i - to determine the state of the fluid within the isobaric zone ;
- ii - to know the mixing properties at the level of the point where the reattachment phenomenon begins ; to define which is the streamline (s) - i.e., the Stagnation Streamline - that will end up at the reattachment point R ;
- iii - to define a condition which will ensure the unicity of the solution, i.e., which will fix the pressure  $p_B$  which has been arbitrary up to now. This condition is clearly linked to the flow situation on the SSL which stagnates at R. It is the problem of the Reattachment Criterion.

**3.4.2. - The Isobaric Turbulent Mixing**

Let us consider the rectilinear and orthogonal co-ordinate system OXY defined in Fig. 33. The origin of this system coincides with the separation point S. For the sake of simplicity we will assume that separation at S occurs without deviation of the flow, which means that the pressures  $p_0$  and  $p_B$  are the same. The isobaric turbulent mixing zone can be represented by the following equations in which all the quantities are Reynolds averaged values :

- continuity :

$$(10) \quad \frac{\partial(\rho u)}{\partial X} + \frac{\partial(\rho v)}{\partial Y} = 0$$

- momentum :

$$(11) \quad \rho u \frac{\partial u}{\partial X} + \rho v \frac{\partial u}{\partial Y} = \frac{\partial \tau_r}{\partial Y}$$

- energy :

$$(12) \quad \rho u \frac{\partial h_r}{\partial X} + \rho v \frac{\partial h_r}{\partial Y} = \frac{\partial}{\partial Y} (u \tau_r - \phi_r)$$

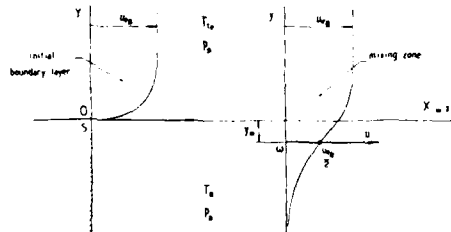


Fig. 33 - Co-ordinate system for mixing zone representation

In the above equations, written with usual notations,  $\tau_r$  designates the turbulent shear-stress (the laminar contribution being negligible),  $h_r$  the stagnation enthalpy and  $\phi_r$  the heat transfer term. Usually,  $\phi_r$  is expressed in the form :

$$\phi_r = - \frac{k_r}{C_p} \frac{\partial h_r}{\partial Y}$$

by introducing the turbulent thermal conductivity  $k_r$ .

If the turbulent shear stress is expressed in terms of the Boussinesq eddy viscosity concept, which leads to the relation :

$$\tau_r = \mu_r \frac{\partial u}{\partial Y}$$

and if the Prandtl number  $Pr_r = \frac{\mu_r C_p}{k_r}$  is assumed to be unity, then Eqs. (11) and (12) can be written :

$$\rho u \frac{\partial u}{\partial X} + \rho v \frac{\partial u}{\partial Y} = \frac{\partial}{\partial Y} \left( \mu_r \frac{\partial u}{\partial Y} \right)$$

$$\rho u \frac{\partial h_r}{\partial X} + \rho v \frac{\partial h_r}{\partial Y} = \frac{\partial}{\partial Y} \left( \mu_r \frac{\partial h_r}{\partial Y} \right)$$

Thus, to any solution  $u(X,Y)$  of Eq. (11) corresponds a solution of Eq. (12) which is of the form (the so-called Crocco relation) :

$$\frac{h_r}{h_{re}} = \frac{h_B}{h_{re}} + \left( 1 - \frac{h_B}{h_{re}} \right) \frac{u}{u_e}$$

where  $h_B$  designates the dead air stagnation enthalpy and  $h_{te}$  the enthalpy in the outer inviscid stream.

By assuming that the fluid is calorically perfect, the stagnation temperature distribution is given by :

$$\frac{T_t}{T_{te}} \equiv \Lambda = \Lambda_B + (1 - \Lambda_B) \varphi$$

in which :  $\Lambda_B = \frac{T_B}{T_{te}}$  and :  $\varphi = \frac{u}{u_{eB}}$

The density profile results immediately from the velocity distribution across the mixing layer :

$$(13) \quad \theta = \frac{Q}{Q_{eB}} = \frac{T_{eB}}{T} = \frac{1 - C_{eB}^2}{\Lambda - C_{eB}^2 \varphi^2} = \frac{1 - C_{eB}^2}{\Lambda_B + (1 - \Lambda_B) \varphi - C_{eB}^2 \varphi^2}$$

where  $C_{eB}$  is the Crocco number defined by :

$$C_{eB}^2 = \frac{\gamma - 1}{2} M_{eB}^2 / \left( 1 + \frac{\gamma - 1}{2} M_{eB}^2 \right)$$

Thus the only problem which remains is to determine the velocity profile  $\varphi = u/u_{eB}$ . This necessitates the solution of Eqs. (10-11) satisfying the following initial and boundary conditions :

$$\varphi(0, Y) = \varphi_0(Y)$$

$$Y \rightarrow -\infty \quad \varphi(0, Y) \rightarrow 0$$

$$Y \rightarrow +\infty \quad \varphi(X, Y) \rightarrow 1$$

$\varphi_0(Y)$  is the (given) velocity profile at  $X = 0$  including possibly the initial boundary-layer profile.

At this step, it is necessary to introduce a model to represent the turbulent eddy viscosity  $\mu_t$ .

The problem of the turbulent isobaric mixing is at the origin of a great number of studies and is now most often solved by means of numerical methods incorporating more or less sophisticated turbulence models frequently based on transport equations for the turbulent quantities (see Leuchter, 1976). However, in Multi-Component Methods containing a relatively large dose of empiricism, the simplified Korst solution is generally used.

To obtain this solution, we define a first co-ordinate orthogonal system OXY whose X axis follows the isobaric boundary (f) of the inviscid separated flow (see Fig. 33), then a second intrinsic system  $\omega xy$  such as :

$$X \equiv x \quad Y = y - y_m(x)$$

The origin shift  $y_m(x)$  is determined in order to satisfy a global conservation equation for the momentum, as will be seen in Section 3.4.3.

If the initial boundary-layer is vanishingly small, this solution takes the simple form :

$$(14) \quad \frac{u}{u_{eB}} \equiv \varphi = \frac{1}{2} (1 + \operatorname{erf} \eta)$$

where  $\eta = \sigma \frac{y}{x}$  is a similarity variable and  $\sigma$  is the turbulent mixing parameter (or jet spreading parameter) which must be provided by experiment. This parameter characterizes the expansion rate of the mixing zone : the greater  $\sigma$ , the slower the growth of the mixing layer.

The above equation constitutes the basic solution for the reference base-flow problem. However, in practical situations, a boundary-layer is always present at the separation point and its existence must be taken into account. We will see below how to represent this effect.

**Representation of Compressibility Effect.** In principle, the velocity distribution given by Eq. 14 is only valid for incompressible flows. But experiment (Crane, 1957 ; Sirieix and Solignac, 1966) shows that the reduced velocity profile  $\varphi = u/u_e$  represented as a function of  $\eta$  is nearly insensitive to Mach number and temperature ratio  $\Lambda_B$  (in so far as  $M_{eB}$  is not too high and  $\Lambda_B$  not very different from unity, the limits being unknown). In fact, the influence of these factors is essentially felt through the turbulent mixing parameter. As already mentioned,  $\sigma$  is an empirical factor whose determination is unfortunately difficult and most often inaccurate. Thus the available experimental values for  $\sigma$  exhibit a rather large scatter. Various laws proposed to represent the evolution of  $\sigma$  with the outer Mach number  $M_{eB}$  (for air  $\gamma = 1.4$ ) and for an iso-energetic flow ( $\Lambda_B = 1$ ), are plotted in Fig. 34. One notes very large differences between the various correlation laws.

Korst and Tripp (1957) suggested the following linear relation to represent the Mach number dependence :

$$(15) \quad \frac{\sigma}{\sigma_0} = 1 + 0.23 M_{eB}$$

where  $\sigma_0$  is the incompressible value of the mixing parameter ; most often the value  $\sigma_0 = 12$  is adopted.

For gases other than air, the following relationship suggested by Page (see Page and Dixon, 1964) is sometimes used :

$$\frac{\sigma}{\sigma_0} = 1 + 0.513 \left[ C_{eB}^2 / (1 - C_{eB}^2) \right]^{1/2}$$

in which  $C_{eB}$  is the Crocco number. For air ( $\gamma = 1.4$ ) this equation is identical to eq. (15).

McDonald (1965) has proposed the following relation :

$$\frac{\sigma}{\sigma_0} = \frac{\left( 1 + \frac{\gamma-1}{2} M_{eB}^2 \right) (1 + 0.35 M_{eB}^2)}{1 + 0.004 M_{eB}^2}$$

In order to take into account both the effects of  $M_{eB}$  and  $\Lambda_B$ , Channapragada and Wolley (1967 ; see also Channapragada, 1963) derived the expression :

$$\frac{\sigma}{\sigma_0} = \frac{1 - 0.5(1 - \Lambda_B) + 0.9 C_{\epsilon B}^2}{0.5(1 - \Lambda_B) - 0.25 C_{\epsilon B}^2}$$

Other formulae inspired from semi-theoretical arguments have been proposed. For example, Bauer (1966) gives the relation :

$$(16) \quad \frac{\sigma}{\sigma_0} = \int_{-\infty}^{\eta_j} \frac{\rho}{\rho_{eB}} \varphi^2 d\eta / \left[ 0.5085 \left( \frac{d\varphi}{d\eta} \right)^2 \right]$$

where j designates conditions on the Dividing Streamline.

Figure 34 also shows the purely empirical correlation of Sirieix and Solignac (1966) deduced from very carefully made experiments. This correlation used in Multi-Component Methods developed at ONERA, is relatively close to the curve resulting from the "Stanford consensus".

The above results having been obtained for air, it is not clear that they are still valid for other gases. Undoubtedly, uncertainty about  $\sigma$  is one of the weakest points of the turbulent mixing calculation. It should be said that more advanced models based on the numerical solution of the local equations are also unable to correctly represent compressibility effects.

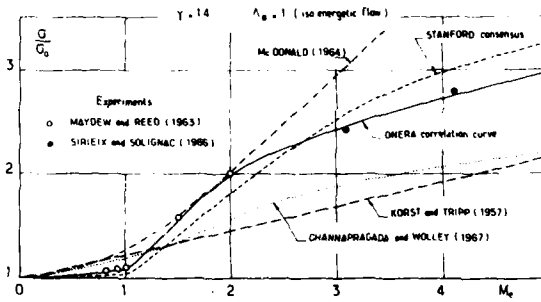


Fig. 34 - Turbulent jet spreading parameter

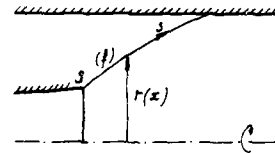
**Representation of Axisymmetry Effect.** The above results have been established for a two-dimensional flow and by assuming that the isobaric boundary (f) of the inviscid jet is rectilinear. Such conditions are generally not encountered in practical situations where, for a missile for example, the outer stream and the jet issuing from the nozzle are axisymmetric (at zero incidence).

To treat the case of an axisymmetric jet, it is generally assumed that the mixing zone is thin when compared to the distance from the axis of the isobaric boundary (f). Then the mixing layer equations are solved in a local system OXY whose longitudinal axis OX is curvilinear and coincides with (f). Furthermore, it is assumed that axisymmetry has no effect on the reduced velocity distribution  $\varphi = u/u_{eB}$ , as function of  $\eta$ ; the non-negligible axisymmetry effect is entirely accounted for by its incidences on the mixing parameter  $\eta$ . From a simplified study of the mixing based on the Prandtl model of turbulence, Déleury (see Solignac and Déleury, 1972) deduced the following relation :

$$(17) \quad \frac{\sigma_{Ax}}{\sigma_{2D}} = \frac{1}{F}$$

in which F is a geometric factor given by the relation :

$$F = \int_0^L \frac{r(x)}{r_{RT}} \frac{ds}{L} \quad (\text{for a two-dimensional flow } F = 1)$$



The integral is computed along the boundary (f), L designates the length of (f) comprised between the separation point S and the point RT where (f) impinges the wall on which the jet reattaches ; s is the curvilinear distance along (f), and r(x) is the local distance from the axis.

For an expanding jet (as the flow issuing from an underexpanded propulsive nozzle), F is less than 1 ; on the other hand for a mixing zone which develops along a jet boundary tending towards the symmetry axis (as is the case for the outer stream), F is greater than 1. Such a more or less rapid thickening of the mixing layer is intuitively understood by considering mass conservation arguments.

Similar formulae for  $\sigma_{Ax}/\sigma_{2D}$  have been proposed by other authors. For example Bauer and Fox (1977) give the relation :

$$(18) \quad \frac{\sigma_{Ax}}{\sigma_{2D}} = \frac{2 r_{RT}}{r_S + r_{RT}}$$

which is equivalent to Eq. (17) if the jet boundary is assumed to be conical.

**Representation of Initial boundary-Layer Effect.** Korst (1954) gave a general solution for the turbulent mixing with an initial boundary-layer present at the separation point S. This solution takes the form :

$$(19) \quad \varphi = \frac{1}{2} \left[ 1 + \operatorname{erf}(\eta - \eta_p) \right] + \frac{1}{\sqrt{\pi}} \int_{\eta - \eta_p}^{\eta} \varphi_0 \left( \frac{\eta - \beta}{\eta_p} \right) e^{-\beta^2} d\beta$$

where  $\eta_p$  is a position parameter equal to zero in the absence of initial boundary-layer (see Korst, 1954).

It has been used by several authors in their Multi-Component model for missile base-flow (Bauer and Fox, 1977 ; Fox, 1979). However, in order to avoid the rather lengthy calculations implied by the use of Eq. (19), a simpler way to take into account the effect of the initial boundary-layer is to adopt the mixing-zone virtual origin concept introduced by Kirk (1959).

According to this concept, the mixing with a boundary-layer at its origin O is assumed to develop in a manner similar to that which would be obtained in the absence of an initial boundary-layer from a virtual origin  $\bar{O}$  located upstream of O, the distance  $\bar{O}O$  depending, as a first approximation, on the momentum thickness of the boundary-layer at O and on the Mach number  $M_{eB}$  of the inviscid external flow contiguous to the mixing layer.

The corresponding distance  $X_0 = \bar{O}O$  can be obtained in various ways. In particular, Sirieix and Solignac (1966) proposed a relation established from the hypothesis that the momentum contained in O within the fictitious mixing layer, above the Dividing Streamline ( $j$ ), be identical to that of the real boundary-layer at the same point. This leads to the relation :

$$\bar{O}O \equiv X_0 = \sigma \theta_0 / I$$

In this expression,  $I$  is the function of the Mach number defined by the integral :

$$I = \int_{\eta_j}^{\infty} \theta \varphi (1 - \varphi) d\eta = \int_{\infty}^{\eta_j} \theta \varphi^2 d\eta \quad (\text{here } \theta \equiv \frac{Q}{Q_{eB}})$$

which can be calculated from the known laws of the isobaric turbulent mixing in the asymptotic state, i.e., with a vanishingly small boundary-layer at its origin.

In the above method the vertical displacement of the virtual origin  $Y_0$  is neglected since its value is always small. However, it can also be computed by similar considerations on global conservation of momentum (see Kirk, 1959).

The above calculations have shown the influence of the initial boundary-layer at the origin of the isobaric mixing. In practical situations, separation at S is generally accompanied by an expansion - or in the case of plume induced separation, a compression - from  $p_0$  to  $p_B$ . Thus arises the question of how to determine in each particular case the velocity distribution of the boundary-layer which has been submitted at S to a rapid change in pressure.

As already mentioned, viscous forces often play a negligible role in the largest part of a turbulent dissipative layer undergoing such a rapid interaction involving either compression or expansion. The phenomenon is controlled essentially by pressure and inertia forces. Consequently, the change in boundary-layer properties can be computed by approximate analyses which are of two kinds :

- i - in the first approach, the boundary-layer evolution through the pressure gradient is modeled by means of simplified forms of the boundary-layer integral equations in which the terms involving shear-stress are neglected. Among these methods, the most popular is certainly that proposed by Reshotko and Tucker (1955) who gave closed form solutions for the change in the boundary-layer global properties (momentum thickness and incompressible shape parameter).
- ii - in the second approach, sometimes termed Inviscid Shear Layer Analysis (Green, 1969), the interacting boundary-layer is considered as a rotational inviscid stream which means that entropy is assumed constant on each streamline. Thus the basic principle of most methods calling upon this principle (Carrière and Sirieix, 1960 ; Nash, 1962 ; Roberts, 1966) is to divide the boundary-layer into N streamtubes of thickness  $\Delta Y$  (this thickness can vary from one streamtube to the other) over which the flow properties are considered as constant. By assuming that each streamtube undergoes an isentropic expansion or compression between Station 0 (upstream of S) and Station 1 (downstream of S), and making use of the continuity relation (conservation of mass), one may construct the downstream velocity distribution at 1 (provided that the static pressure is transversally constant at Stations 0 and 1 which is generally the case). No restrictive assumption has to be introduced concerning the shape of the velocity profiles (in contrast with Reshotko and Tucker's theory which assumes power law profiles) and this technique is rather general in the sense that no boundary-layer approximations are made.

Another approach relying basically on the same assumptions consists in performing an exact calculation of the rotational layer throughout the interaction zone. A calculation of this kind can be made without any special difficulty if most of the shear flow remains supersonic. Then the equations of motion are of a hyperbolic nature and can be solved by a downstream marching process. The Method of Characteristics is very well-suited for such calculations. Of course there is a problem with the subsonic part of the boundary-layer. Nonetheless, if the Mach number of the external inviscid fluid is high enough (say greater than 2), the subsonic region of a turbulent boundary-layer is very thin compared to its total thickness so that the influence of the subsonic inner layer can be neglected in a first level of approximation. This method generally gives excellent results for computing boundary-layer flows submitted to intense pressure gradients (Délery and Masure, 1968).

However, one generally uses simpler methods to compute the change in the boundary-layer properties at S (except maybe for flows with very thick initial boundary-layers). Thus, an easy formula often used is that proposed by Nash (1962) which gives the boundary-layer momentum thickness  $\theta_B$  after expansion - or compression - from  $p_0$  to  $p_B$  :

$$\frac{Q_{eB} u_{eB} \theta_B}{Q_{e0} u_{e0} \theta_0} = \frac{M_{e0}^2}{M_{eB}^2}$$

The concept of virtual origin for the mixing layer becomes questionable when the initial boundary-layer has a thickness comparable to the size of the separated region. In such circumstances, the streamwise development of the mixing layer is insufficient to permit the establishment of an asymptotic profile represented by Eq. 14. In fact, when the boundary-layer is very thick, the separated flow downstream of a rearward facing step exhibits a "multi-deck" structure according to the terminology of Strong Interaction Theories (Lighthill, 1953 ; Stewartson, 1969). This structure can be described as consisting of an "outer deck" which is the separated inviscid external flow, a "main deck" which comprises the major part of the initial boundary-layer and a "lower deck" at the outer edge of the recirculation bubble and in the near wall region of the reattaching viscous layer. The above description is given without any rational justification and the analogy with the "triple deck" structure of Strong Interaction Theories is purely formal. The flow should in fact include more decks.

In what we have called the main deck, viscous forces have negligible influence. The flow is essentially a **rotational inviscid stream** driven only by pressure and inertia forces (see also the description of region I given in Section 3.2.). Viscous effects become predominant in the lower deck where a smooth transition has to take place between the main deck and the low velocity recirculating bubble or zero velocity at the wall. This lower deck is essentially a mixing-layer originating at the separation point S and which develops along the inner boundary of the rotational flow. Thereafter, this layer becomes the viscous sublayer of the reattaching boundary-layer. The initial "boundary-layer" at S is now the very thin viscous sublayer of the incoming boundary-layer. Thus the condition of a small to moderately thick initial boundary-layer is fulfilled and the "classical" mixing theory can be applied to this thin inner viscous flow.

This concept was already checked in the past (Sirieix et al., 1968 ; Détery and Masure 1969) and has been adopted by Mehta (see Section 3.3.4.) as well as by Sinha and Dash (1985). An example is presented here relative to an axisymmetric reattachment behind an annular rearward facing step. The inviscid incoming flow has a Mach number equal to 1.83 and the initial boundary-layer, a thickness  $\delta$  such that  $\delta/h = 3.6$ . It has been assumed that initially the viscous effects are confined within the subsonic part of the boundary-layer. The thickness  $\delta$  of this sublayer is here such that  $\delta/\delta = 0.03$ . The downstream evolution of that part of the flow considered as inviscid has been computed by the rotational Method of Characteristics, the measured wall pressure distribution being prescribed along the flow free boundary. The starting characteristic has been determined from the measured boundary-layer profile just upstream of the separation point.

The overall structure of the computed flow is shown in Fig. 35, which reveals the expansion fan emanating from the separation point S with the separated flow-free boundary (f) and the shock wave forming at reattachment by focalization of compression waves.

The computed Mach number profiles are compared to measured profiles in Fig. 36. There is very good agreement between experiment and computation over the major part of the distributions. This agreement persists well after reattachment. The lower part of the profiles could not be computed because there, the flow is subsonic. This zone also corresponds to the development of the mixing-layer and, downstream of reattachment, to a new sublayer in which it is no longer legitimate to neglect viscosity.

Base pressure computations made with this flow schematization are in excellent agreement with experiment (see Détery, 1983). Thus this method provides a rather simple way to apply the usual theory to situations where thick boundary-layers are present at the base, as is the case for a missile fuselage.

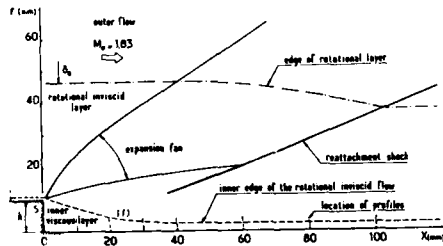


Fig. 35 - Reattachment with thick initial boundary-layer - Computed inviscid flow structure

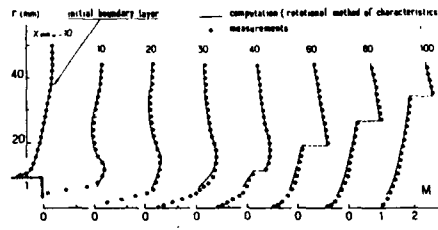


Fig. 36 - Reattachment with thick initial boundary-layer - Mach number profiles

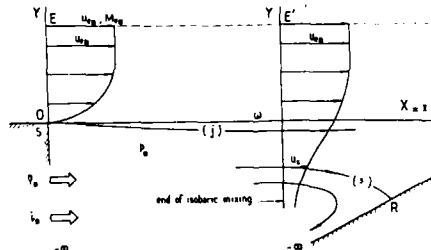


Fig. 37 - Control volume for determination of Dividing Streamline and Stagnation Streamline

**3.4.3. - Determination of the Dividing Streamline and of the Stagnation Streamline.**

By definition, the DSL (j) is the mixing zone streamline originating from the separation point S. Its ordinate  $Y_j$ , is determined by writing the conservation of mass flow between section SE and (j)E' (see Fig. 37) where EE' is a streamline far enough away to be outside the mixing zone. Hence the equation :

$$\int_0^{Y_E} \rho u \, dY = \int_{Y_j}^{Y_{E'}} \rho u \, dY$$

or, by introducing the reduced ordinate  $\eta$  :

$$(20) \quad \frac{\sigma}{X + X_0} \int_0^{Y_E} \frac{\rho u}{\rho_e B u_e B} \, dY = \int_{\eta_j}^{\eta_{E'}} \frac{\rho u}{\rho_e B u_e B} \, d\eta = \int_{\eta_j}^{\eta_{E'}} \theta \varphi \, d\eta$$



In this equation  $\eta$  is defined as  $\eta = \sigma y / (X + X_0)$  which takes into account the origin shift  $X_0$  of the mixing virtual origin.

Equation (20) alone does not permit the determination of  $\eta_j$  since the distributions  $\varphi$  and  $\theta = \rho / \rho_{eB}$  are represented in an intrinsic system of co-ordinates whose ordinate  $y_m(X)$  relative to the physical system OXY is still unknown. Thus, another relation is needed. It is obtained by applying the momentum theorem to the control volume  $[-\infty SEE' - \infty]$  drawn in Fig. 37. The entire volume being isobaric at the pressure  $p_B$ , the shear stress being zero along  $EE'$  and the velocity becoming extremely small in the dead-air region, this theorem leads to the equation :

$$(21) \quad \frac{\sigma}{X + X_0} \int_0^{Y_{E'}} \frac{\rho u^2}{\rho_{eB} u_{eB}^2} dY = \int_{-\infty}^{\eta_{E'}} \frac{\rho u^2}{\rho_{eB} u_{eB}^2} d\eta = \int_{-\infty}^{\eta_{E'}} \theta \varphi^2 d\eta$$

Thus, by forming (20) - (21) :

$$(22) \quad \frac{\sigma}{X + X_0} \left[ \int_0^{Y_{E'}} \frac{\rho u}{\rho_{eB} u_{eB}} \left(1 - \frac{u}{u_{eB}}\right) dY \right] = \int_{-\infty}^{\eta_{E'}} \theta \varphi (1 - \varphi) d\eta - \int_{-\infty}^{\eta_{E'}} \theta \varphi d\eta$$

As the integrals are converging, it is possible to go to the limit  $Y_{E'} \rightarrow \eta_{E'} \rightarrow \infty$ ; in this condition, the integral of the left hand side of (22) becomes equal to the initial boundary-layer momentum thickness  $\theta_B$ . Thus the equation giving  $\eta_j$  is finally :

$$\frac{\sigma \theta_B}{X + X_0} = \int_{-\infty}^{\eta_j} \theta \varphi (1 - \varphi) d\eta - \int_{-\infty}^{\eta_j} \theta \varphi d\eta$$

As we know, the Stagnation Streamline (s) is the mixing zone streamline which stagnates at the reattachment point, thus all the flow entering through section  $[-\infty SE]$  must pass above (s) at the end of the mixing layer. The location of (s) is determined by considering the control volume drawn in Fig. 37. Let us assume that in the dead-air region there is an injection per unit span of mass flowrate  $\bar{q}_B$  which carries a momentum  $\bar{i}_B$ . The application of the conservation theorems leads to the following equations :

- for the mass :

$$(23) \quad \int_0^{Y_{E'}} \rho u dY + \bar{q}_B = \int_{Y_S}^{Y_{E'}} \rho u dY$$

- for the momentum :

$$(24) \quad \int_0^{Y_{E'}} \rho u^2 dY + \bar{i}_B = \int_{-\infty}^{Y_{E'}} \rho u^2 dY$$

Making (23) - (24) and introducing the reduced ordinate  $\eta$  brings one to the relation :

$$\int_{-\infty}^{\eta_s} \theta \varphi d\eta = - \frac{\sigma}{X + X_0} \left[ \int_0^{Y_{E'}} \frac{\rho u}{\rho_{eB} u_{eB}} \left(1 - \frac{u}{u_{eB}}\right) dY + \frac{\bar{q}_B}{\rho_{eB} u_{eB}} - \frac{\bar{i}_B}{\rho_{eB} u_{eB}^2} \right] + \int_{-\infty}^{\eta_s} \theta \varphi (1 - \varphi) d\eta$$

or

$$(25) \quad \int_{-\infty}^{\eta_s} \theta \varphi d\eta = - \frac{\sigma}{X + X_0} \left( \theta_B + \frac{\bar{q}_B}{\rho_{eB} u_{eB}} - \frac{\bar{i}_B}{\rho_{eB} u_{eB}^2} \right) + \int_{-\infty}^{\eta_s} \theta \varphi (1 - \varphi) d\eta$$

Numerical application of the reattachment theory shows that introduction of the total mixing length  $L = X + X_0$  into Eq. (25) leads to a bad prediction of injection effect for high values of  $\bar{q}_B$ . On the other hand, the initial boundary-layer influence is well-predicted, even for large values of the momentum thickness  $\theta_B$ . The reason for this deficiency has not yet been entirely elucidated. Thus for practical applications, in order to obtain quantitatively correct results, it is recommended to determine  $\eta_s$  by the following equation :

$$(26) \quad \int_{-\infty}^{\eta_s} \theta \varphi d\eta = - \sigma \left( \frac{\theta_B}{X + X_0} + \frac{\bar{q}_B}{\rho_{eB} u_{eB} X} - \frac{\bar{i}_B}{\rho_{eB} u_{eB}^2 X} \right) + \int_{-\infty}^{\eta_s} \theta \varphi (1 - \varphi) d\eta$$

The above equation, established by Carrière (1960), allows the introduction of the **Generalized Injection Coefficient** :

$$Cq = \frac{\bar{q}_B}{\rho_{eB} u_{eB} X} + \frac{\theta_B}{X + X_0} - \frac{\bar{i}_B}{\rho_{eB} u_{eB}^2 X}$$

which shows that the initial boundary-layer can be assimilated with an injection (**equivalent bleed concept**).

The above relations localizing the Dividing Streamline and the Stagnation Streamline are strictly valid only for a two-dimensional flow.

As already mentioned, it is generally assumed that the velocity distribution given by (14) is still valid for an axisymmetric flow. However, in this case, the conservation equations should be written by considering an axisymmetric control volume. Thus if  $r(x)$  designates the distance from the axis, the equation determining  $y_j$  becomes :

$$\int_0^{y_E} \rho u r \, dy = \int_{y_j}^{y_E} \rho u r \, dy$$

In fact, if in a confluence problem the distance to the axis does not vary too much between the separation and the reattachment points, the two-dimensional equations can be used without introducing an appreciable error.

#### 3.4.4. - Problem of the Reattachment Criterion

The above relations make it possible to determine the properties of the mixing zone as well as the conditions on the Dividing and Stagnation Streamlines as a function of factors of influence represented by  $C_q$  for a **given value of the base pressure  $p_B$** .

The "closure" of the problem requires the introduction of a complementary law or condition, commonly called "Reattachment Criterion".

Historically, the first criterion proposed is the "Escape Criterion" of Chapman-Korst. It consists first in assuming that between the end of the isobaric plateau and the reattachment point, the viscous forces are negligible in relation to terms of inertia and pressure. Consequently, compression takes place **isentropically on each streamline**.

Then, it is admitted that at the time it reaches reattachment, the stagnation pressure  $p_{rS}$  on the SSL ( $s$ ) is just equal to the static pressure  $p_2$  prevailing in the flow at the end of the compression (see Fig. 32). Thus :

$$(27) \quad p_{rS} = p_2$$

If the flow is iso-energetic (constant stagnation temperature throughout the flowfield), simple calculations show that the Mach number  $M_S$  on the SSL is given by :

$$M_S^2 = \frac{\varphi_S^2 M_{eB}^2}{1 + \frac{\gamma - 1}{2} M_{eB}^2 (1 - \varphi_S^2)}$$

whence :

$$(28) \quad p_{rS} = p_B \left( 1 + \frac{\gamma - 1}{2} M_S^2 \right)^{\frac{\gamma}{\gamma - 1}}$$

Practical application of the theory consists in deciding on a value of the base pressure  $p_B$ . Knowing  $p_B$ , it is possible to determine for given initial boundary-layer and mass flow injection rate into the base region, the location of the SSL (Eq. 26) and accordingly, the stagnation pressure  $p_{rS}$  (Eq. 28). On the other hand, the pressure  $p_2$  after reattachment can be computed from perfect fluid theory (considering either an isentropic compression or an oblique shock at reattachment). We must now make sure that condition (27) is actually fulfilled. If it is not the case, we try a new value of  $p_B$ , the operation being repeated until  $p_{rS} = p_2$ .

The first applications of the theory performed by Korst, considering the boundary-layer as negligible, showed rather good agreement with experiment. In fact, it was observed later that this agreement was fortuitous and was due to the compensation of two errors : the first resulted from the neglecting of the boundary-layer, the second resided in the inaccuracy of the escape criterion (27). Thus it appeared that the stagnation pressure  $p_{rS}$  was always inferior to  $p_2$ .

Many modifications were then proposed to improve the Chapman-Korst criterion. In what follows, we will only mention the most important ones, insisting however on the concept of "Angular Criterion" which is the basis of the methods developed at ONERA for treating base flow problems.

##### Goethert Criterion (Goethert, 1960).

This criterion is a modified Korst's escape criterion formulated as follows : If the Mach number on the Stagnation Streamline is subsonic, then the Korst criterion is applied without any change ; if this Mach number is supersonic, the flow on the Stagnation Streamline is assumed to pass first through a normal shock before regaining its stagnation pressure which must be equal to the static pressure downstream of the reattachment shock.

##### Nash criterion (Nash, 1962).

The flow model used by Nash is basically the same as that of Korst. The essential difference concerns the fact that Nash probably first pointed out that the static pressure at reattachment  $p_R$  is lower than the downstream pressure  $p_2$  which explains the inaccuracy of the Chapman-Korst criterion. To take this observation into account, Nash introduces the ratio :

$$N = (p_R - p_B) / (p_2 - p_B)$$

which would be sought experimentally. The condition  $p_{rS} = p_R$  is maintained, but now  $p_R < p_2$ . The coefficient  $N$  varies with the Mach number  $M_{eB}$  (see Fig. 38a), the evolution being however less noticeable in supersonic flow. For this reason, Nash adopted at first a mean value  $N = 0.35$ . In fact,  $N$  is also a function of the initial boundary-layer (Nash, 1966).

##### Robert criterion (Roberts, 1966)

The reattachment criterion proposed by Roberts is based on a similarity between the pressure variation from  $p_R$  to  $p_2$  in a reattachment and the pressure rise from  $p_0$  to  $p_S$  in a separation process taking place on a smooth surface. For a separating supersonic turbulent boundary-layer, the pressure ratio  $p_S/p_0$  can be computed by using the Reshotko and Tucker discontinuity analysis (See Section 3.4.2.) This ratio corresponds to a ratio of the corresponding Mach numbers  $M_{eS}/M_{e0}$  close to 0.76. Similarly, Roberts introduces a reattachment parameter defined by :

$$R = \frac{M_{e2}}{M_{eR}}$$

and given by the empirical relation :

$$R = 0.799 + 0.156 M_{eB} - 0.08237 M_{eB}^2 + 0.0009564 M_{eB}^3$$

which he deduced from experimental results on supersonic reattachment.

As can be seen in Fig. 38b, the parameter R leads to a better correlation than Nash's coefficient N.

**Mc Donald criterion** (McDonald, 1964)

Although rather different from the Korst method, the McDonald model also follows the multi-component approach. Very briefly, the dissipative zone is divided into three regions :

- isobaric mixing extending down to an abscissa  $X_I$  ;
- reattachment, from  $X_I$  to the abscissa  $X_R$  of the reattachment point R ;
- "rehabilitation" between  $X_R$  and the final state corresponding to a constant pressure equal to  $p_2$ .

From a simplified analysis consisting in neglecting the shear stress after R and in using global conservation relations for mass and momentum, Mc Donald determines the properties of the dissipative reattaching layer at the end of the rehabilitation region for a given pressure  $p_B$ . The solution, i.e., the right value of  $p_B$ , is obtained when the incompressible shape parameter of the boundary-layer in the final state is equal to the value resulting from known flat plate laws.

**Page criterion** (Page et al., 1967).

In this criterion, the significant parameter is the ratio :

$$K = (\theta_R - \theta_B) / (\theta_2 - \theta_B)$$

in which  $(\theta_2 - \theta_B)$  represents the total turning of the outer inviscid flow when it recompresses between  $p_B$  and  $p_2$ , and  $(\theta_R - \theta_B)$  the turning corresponding to the compression up to the physical reattachment point R. The criterion consists essentially in a correlation of K with the dimensionless velocity  $\varphi_S = u_S/u_{cB}$  on the Stagnation Streamline which can be represented by the following analytical expression :

$$K = 0.5 \left[ 1 - \cos(180\varphi_S - 1.8) \right]$$

The condition that the pressure at the reattachment point be equal to the stagnation pressure on the SSL at the end of the isobaric mixing region provides the closure relation enabling the determination of the base-pressure.

**Bauer and Fox criterion** (Bauer and Fox, 1977)

The reattachment criterion proposed by Bauer and Fox (see also Fox, 1979) is based on a correlation law for the pressure distribution at reattachment in the form  $(p - p_B) / (p_2 - p_B)$  as a function of  $(X - X_I) / (X_2 - X_I)$  given by Narayanan et al. (1972). The abscissa  $X_I$  of the end of the isobaric region (see Fig. 39a) is determined assuming that at  $X_I$ , the reversed base flow is turned back through an area equating the approaching area between the SSL and the lower limit of the isobaric mixing-zone whose ordinate  $Y_L$  corresponds to a location where the velocity component  $u$  is practically zero. Thus  $X_I$  is related to  $Y_L$  geometrically whereas the abscissa  $X_2$  of the end of the pressure rise is deduced from a simplified control volume analysis applied in the reattachment region. It is thus possible to position the pressure distribution  $p(x)$  at reattachment in the physical plane i.e., with respect to the isobaric mixing layer.

Then in the plane  $[X, p]$ , one traces the curve representing the stagnation pressure of all streamlines of the mixing zone (see Fig. 39b) which would impinge the reattachment surface. The reattachment criterion is satisfied when the pressure at the intersection point of the two curves coincides with the stagnation pressure of the Stagnation Streamline.

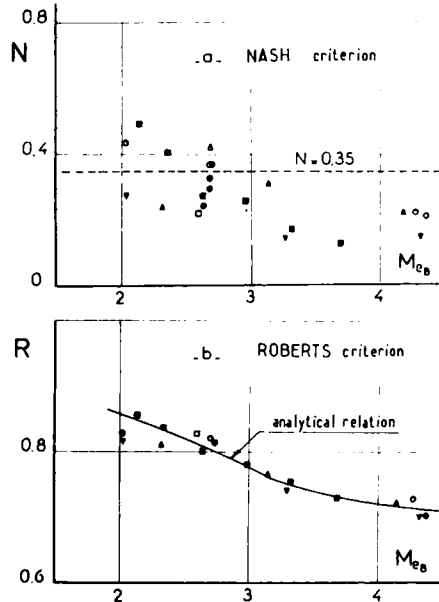


Fig. 38 - Nash and Roberts reattachment criteria

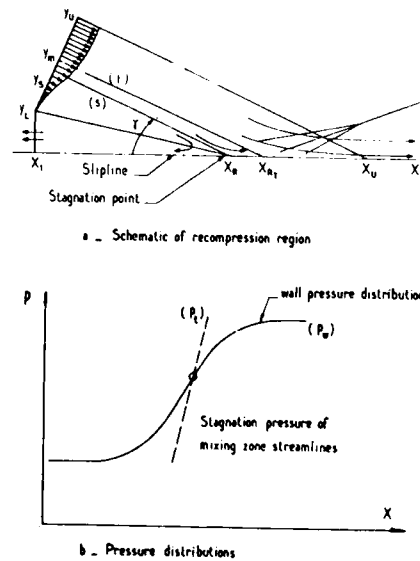


Fig. 39 - Bauer and Fox reattachment criterion

**The Angular Reattachment Criterion** (Carrière and Sirieix, 1960).

The various criteria reviewed above probably have the major drawback of introducing, directly or indirectly, the pressure level  $p_2$ , i.e., conditions prevailing well downstream of the reattachment point. Indeed, during carefully made experiments, Carrière (1965), then Sirieix et al. (1966), clearly brought to light the fact that the pressure downstream of the reattachment point could be perturbed (within certain limits) without the initial part of the reattachment process, - thus the base pressure  $p_B$  - being modified. Such an observation tends to prove that any criterion calling upon state 2 has little chance of giving satisfactory results.

The "Angular Reattachment Criterion" takes this fact into account by retaining as a basic idea the fact that the reattachment process is entirely governed by the state of the dissipative layer when it approaches the reattachment zone. This state can be characterized by :

- the direction  $\psi$  of the inviscid stream relative to the wall (see Fig. 40) ;
- the external Mach number  $M_{eB}$  ;
- the velocity and density distributions within the turbulent mixing layer.

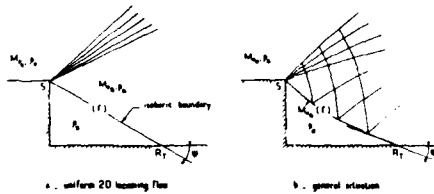


Fig. 40 - Definition of reattachment angle

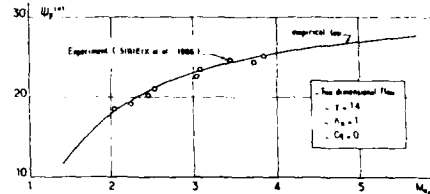


Fig. 41 - Reattachment angle in the reference situation

It is postulated that the reattachment condition is essentially defined by the state of the fluid on the Stagnation Streamline at the end of the isobaric region. Consequently, taking Eqs. (13) and (14) into account leads to the following functional dependence for the reattachment angle :

$$\psi = \psi (M_{eB}, \gamma, \varphi_5)$$

or :

$$\psi = \psi (M_{eB}, \gamma, \eta_5)$$

The results of Section 3.4.3. show that the reduced velocity on the Stagnation Streamline depends on the injection coefficient  $C_q$  and on the temperature ratio  $\Lambda_B$ . Furthermore, experiments have shown that  $\psi$  is also a function of the flow geometry in the axisymmetric case. This effect can be characterized by the factor  $F$  already defined in Section 3.4.2.

Thus we can write :

$$(29) \quad \psi = \psi (M_{eB}, \gamma, F, \Lambda_B, \eta_5) = \psi (M_{eB}, \gamma, F, \Lambda_B, C_q)$$

The reattachment angle will be expressed in the form :

$$(30) \quad \psi = \psi (M_{eB}, \gamma, F, \Lambda_B, C_q) = \psi_{2D} (M_{eB}, 1.4, 1, 1, 0) \\ + \Delta\psi_{Ax} (M_{eB}, 1.4, F, 1, 0) \\ + \Delta\psi_K (M_{eB}, \gamma, 1, \Lambda_B, C_q)$$

In the above expression :

- $\psi_{2D}$  is the reattachment angle in the "reference" case, i.e., for a flow which is two-dimensional ( $F = 1$ ), iso-energetic ( $\Lambda_B = 1$ ), without mass injection nor initial boundary-layer ( $C_q = 0$ ) and whose  $\gamma$  is equal to 1.4 (this is the case of air in nearly ambient conditions).
- $\Delta\psi_{Ax}$  is a correction term representing the axisymmetric effect determined in the conditions :  $\gamma = 1.4$ ,  $\Lambda_B = 1$ ,  $C_q = 0$ . In fact,  $\Delta\psi_{Ax}$  is independent of  $M_{eB}$ , hence  $\Delta\psi_{Ax} = \Delta\psi_{Ax}(F)$  ;
- the last term  $\Delta\psi_K$  takes into account the influence of all the other parameters, namely :  $\gamma$ ,  $\Lambda_B$  and  $C_q$ .

The "reference" reattachment angle has been determined from careful and systematic experiments (Délery, 1965 ; Sirieix et al., 1966). Its evolution with the Mach number  $M_{eB}$  is represented in Fig. 41. For practical application, the following analytical expression can be convenient :

$$\psi_{2D} = 32.6 - 29.2/M_{eB}$$

This correlation is well-established in the Mach number range  $2 < M_{eB} < 4.5$ .

The correction angle  $\Delta\psi_{Ax}$  representing the axisymmetric effect is represented in Fig. 42 as a function of the factor  $F$ . The experimental correlation can be represented by the formula :

$$\Delta\psi_{Ax} = 19.185 - 25.798 F + 6.5088 F^2$$

We have not yet sufficiently reliable and accurate experiments with which can clearly be established the respective influence of the other parameters. Indeed, in most practical situations  $\Lambda_B$  and  $\gamma$  act at the same time since for base-flows behind missiles, the propulsive jet is made of hot combustion gases. However, it seems reasonable to represent the effect of  $\gamma$ ,  $\Lambda_B$  and  $C_q$  by assuming that for the two dimensional case the term :  $\Delta\psi_K$  can be estimated by applying the Korst reattachment criterion.

Thus, we will write :

$$\Delta\psi_K = \psi_K (M_{eB}, \gamma, \Lambda_B, C_q) - \psi_K (M_{eB}, 1.4, 1, 0)$$

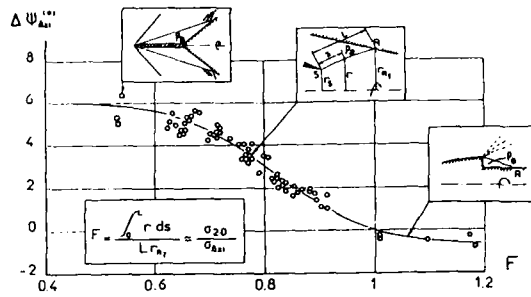


Fig. 42 - Reattachment angle - Correction for axisymmetry effect

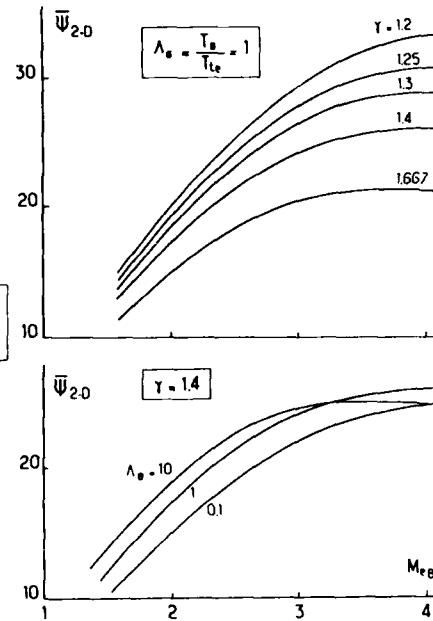


Fig. 43 -  $\gamma$  effect and thermal effect on the reattachment angle

If we assume that the outer inviscid stream undergoes an isentropic simple wave compression during the reattachment process, then :

$$\psi_K = \nu(M_{eB}, \gamma) - \nu(M_{eR}, \gamma)$$

where  $\nu$  is the Prandtl-Meyer function. The Mach number in the external flow at reattachment  $M_{eR}$  is obtained by writing the corresponding static pressure  $p_R$  equal to the stagnation pressure  $p_{t1}$  on the Stagnation Streamline which is confirmed experimentally. The stagnation pressure  $p_{t1}$  results immediately from the properties of the isobaric mixing layer. It depends on  $M_{eB}$ ,  $\Lambda_B$ ,  $\gamma$ , and on  $Cq$  (see Eq. 26).

Inasmuch as  $Cq$  is a small parameter, the Angular Reattachment law (29) is frequently written in the linearized form :

$$(31) \quad \psi = \bar{\psi}(M_{eB}, \gamma, F, \Lambda_B) + Cq \frac{\partial \psi}{\partial Cq}(M_{eB}, \gamma, \Lambda_B)$$

In this case, we are led to determine the two functions :

$$\bar{\psi}(M_{eB}, \gamma, F, \Lambda_B) \text{ and } \frac{\partial \psi}{\partial Cq}(M_{eB}, \gamma, \Lambda_B)$$

The unperturbed reattachment angle which characterizes a reattachment without base bleed and without initial boundary-layer is decomposed into the sum of three contributions by writing :

$$\psi = \bar{\psi}_{2D}(M_{eB}, 1.4, 1, 1) + \Delta\psi_{Axi}(F) + \Delta\psi_K(M_{eB}, \gamma, 1, \Lambda_B)$$

The angles  $\bar{\psi}_{2D}$  and  $\Delta\psi_{Axi}$  are identical to those introduced in expression (30). The third term, which characterizes the effect of  $\gamma$  and  $\Lambda_B$ , is computed by applying the Korst reattachment criterion, as is done above.

The same process can be employed to represent the effect of  $\Lambda_B$ . The curves drawn in Fig. 43 show the influence of  $\gamma$  and  $\Lambda_B$  thus calculated. There is a strong dependence of  $\bar{\psi}_{2D}$  on  $\gamma$ , the effect of  $\Lambda_B$  being weak. These trends are completely confirmed by the experiments of Rougier (1970).

The sensitivity function  $\partial\psi/\partial Cq$  is computed by writing  $\psi$  in the form :

$$\psi(M_{eB}, \gamma, F, \Lambda_B, Cq) = \Delta\psi + \psi_R$$

where  $\Delta\psi$  is the deflection undergone by the external inviscid flow between the beginning of the reattachment process (i.e., the end of the isobaric region) and the physical reattachment point R, and  $\psi_R$  is the residual inclination with respect to the wall of the external flow at R. If we assume that the outer inviscid flow undergoes an isentropic simple wave compression from  $p_B$  to the pressure  $p_R$  at reattachment, then  $\Delta\psi$  can be written :

$$(32) \quad \Delta\psi = \nu(M_{eB}, \gamma) - \nu(M_{eR}, \gamma)$$

Now it is assumed that the dissipative layer at R is hardly sensitive at all to the variations of  $Cq$  (for  $Cq \ll 1$ ), thence  $\partial\psi_R/\partial Cq = 0$ . Finally, taking Eqs. (13), (14), (26) and (32) into account, we find the following expression :

$$\frac{\partial \psi}{\partial Cq} = - \frac{\sigma}{\sqrt{2\pi}} e^{-\eta^2} \frac{M_{eB}^2}{M_{eR}^2} \sqrt{M_{eR}^2 - 1} \left[ 1 + 0.5 (\gamma - 1) M_{eB}^2 \right] / \left[ 1 + 0.5 (\gamma - 1) M_{eR}^2 \right] \times$$

$$\left[ 2\varphi_j \Lambda_B + (1 - \Lambda_B) \varphi_j^2 \right] \left[ \Lambda_B + (1 - \Lambda_B) \varphi_j - 0.5 (\gamma - 1) M_{eB}^2 \varphi_j^2 \right] / \varphi_j \left[ \Lambda_B + (1 - \Lambda_B) \varphi_j \right]^2$$

where  $\varphi_j$  is the dimensionless velocity on the Dividing Streamline (j). The above expression takes into account any thermal effects. In the simpler case of an iso-energetic flow, we have :

$$\frac{\partial \psi}{\partial Cq} = - \frac{\sigma}{\sqrt{\pi}} e^{-\eta^2} \frac{\sqrt{M_{eB}^2 (1 - \varphi_j^2) - 1}}{1 - \varphi_j^2}$$

**3.4.5. - Practical Methods of Calculation - Balance Equations for Mass and Energy**

Most often the computational algorithm for determining the base-flow properties is a shooting technique on the unknown quantities, namely the base-pressure  $p_B$  and the dead-air temperature  $T_B$  (or  $\Lambda_B$ ). For a given couple  $(p_B, T_B)$ , the outer inviscid flow (which in fact does not depend on  $T_B$ ) as well as the location of the Dividing Streamline can be computed. Then, application of the reattachment criterion allows the determination of the Stagnation Streamline (for example, by solving the implicit equation (29) if the angular reattachment criterion is applied). It is thus possible to evaluate the two following balance equations for the dead-air region.

The balance equation for mass involves the mass flow fed into the dead-air region by the outer flow and the mass flow possibly injected from the base (base-bleed), which leads to the equation (for a two-dimensional flow) :

(33)  $\int_{Y_j}^{Y_s} \rho u dY = \bar{q}_B$  ( $\bar{q}_B$  : base-bleed rate per unit span)

Similarly, a balance equation can be established for energy or enthalpy.

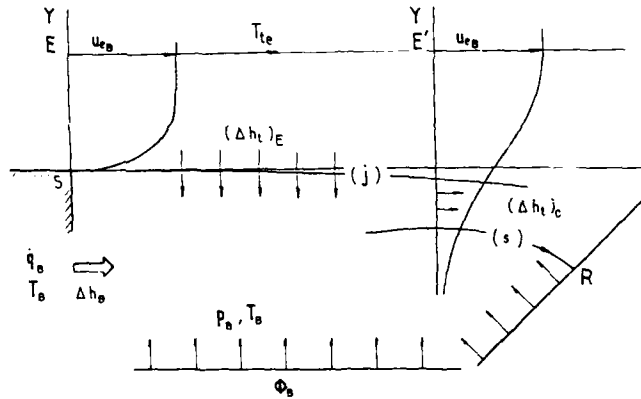


Fig. 44 - Control volume for enthalpy balance equation

By considering the control volume represented in Fig. 44 in which the entrance section is located at the base and the exit section at the extremity of the constant pressure mixing, the different contributions to this equation are (for a two-dimensional flow) :

- the enthalpy transferred to dead-air region by conduction and the work of shear forces along the Dividing Streamline :

$$(\bar{\Delta h}_t)_E = \int_0^{Y_E} \rho u h_{te} dY - \int_{Y_j}^{Y_E} \rho u h_r dY$$

- the enthalpy convected with the mass flow between (j) and (s)

$$(\bar{\Delta h}_t)_C = \int_{Y_j}^{Y_s} \rho u h_r dY$$

- the enthalpy brought by base-bleed :  $\bar{\Delta h}_B$  ( $> 0$  if  $\bar{q}_B > 0$ )

- the heat transferred through the walls :  $\dot{\Phi}_B$  (generally neglected)

Hence the balance equation :

$$(34) \quad \int_0^{Y_E} \rho u h_{re} dY - \int_{Y_j}^{Y_{E'}} \rho u h_r dY + \int_{Y_j}^{Y_s} \rho u h_r dY + \Delta \bar{h}_B + \phi_B = 0$$

In this equation, the stagnation enthalpy is assumed constant across the initial boundary-layer for the sake of simplicity. However, a variable enthalpy can be taken into account without difficulty of principle (see Benay and Déliery, 1986).

Due to the definition of the DSL, the mass flowing through SE is equal to the mass flowing through (j)E' and the energy equation can also be written in the form :

$$\int_{Y_j}^{Y_{E'}} \rho u (h_{re} - h_r) dY + \int_{Y_j}^{Y_s} \rho u h_r dY + \Delta \bar{h}_B + \phi_B = 0$$

Thus the solution is found by iterating on  $p_B$  and  $T_B$  until Eqs. (33) and (34) are simultaneously satisfied,  $q_B$  and  $\Delta h_B$  being known quantities. The procedure is generally accelerated by using a Newton-Raphson technique.

The coming Sections are devoted to applications of the above basic model for computing the flow behind missile afterbodies. The case of supersonic external flow will be first contemplated by considering successively base-flow in the jet-off condition (Section 3.4.6.1) and in the jet-on condition (Section 3.4.6.2). Then the case of an external subsonic flow will be envisaged (Sections 3.4.7.1 and 3.4.7.2). The large majority of the considered methods concern axisymmetric configurations. Extension to multi-nozzle geometries will be dealt with in Section 3.4.8.

### 3.4.6. - Base-Flow Models for Supersonic External Stream

#### 3.4.6.1. - Missile in the Jet-Off Situation.

The determination of the pressure behind an axisymmetric base in the absence of jet raises a particular problem due to the difficulties encountered in the ideal fluid calculation when the flow converges towards the axis. The expedient used to overturn this difficulty consists in imagining that the flow reattaches on a sting materializing the core of the viscous wake : the problem now is to find the diameter of this sting.

The model initially proposed by Mueller (1967 ; see also Mueller et al., 1970) closely follows the Chapman-Korst scheme, but adapts it to the axisymmetric case.

The adapted flow model is represented in Fig. 45. According to the classical approach, the flow is divided into three regions : a) a zone of external inviscid fluid, b) a zone of turbulent mixing, and c) a reattachment zone.

Several assumptions are made :

- i - the initial boundary-layer is neglected, but its nature is turbulent ;
- ii - the inviscid flow, contiguous to the mixing zone, is supposed to develop between S and  $R_T$  along a truncated conical surface of semi-angle  $\varphi$ . This modeling, due to Zumwalt (1959), rests on experimental observations showing that the constant pressure zone along the axis is relatively short, the pressure variation being close to that on a truncated conical afterbody. There results from this assumption that mixing is no longer isobaric and the Mach numbers at S and  $R_T$  are different. The flow on the conical surface is computed by the Method of Characteristics ;
- iii - nevertheless, the velocity profiles in the mixing zone are still represented by Eq. 14. The effect of compressibility and of the gas characteristics on the mixing parameter  $\sigma$  are represented by the Channagragada formula (see Section 3.4.2. above) ;
- iv - recompression at  $R_T$  takes place through an oblique shock that makes the pressure rise to the value  $p_2$ . The origin of the shock is located on the sting whose radius  $r_R$  is given by a correlation proposed by Chapman (1951) in the form  $r_R/r_B$  which is a function of Mach Number  $M_{oe}$ ,  $r_B$  being the base radius (see Fig. 46). In a later version of the method, Roache (1973) determines the value of  $r_R$  according to a criterion consisting in adopting the radius  $r_R$  that makes the base pressure  $p_B$  maximum. Thus, we do away with some experimental information whose character of generality is questionable.
- v - the unicity of the solution is ensured by satisfying the escape criterion of Korst.

In the method, the axisymmetry effect intervenes essentially in the establishment of the balance equations allowing the positioning of the Dividing Streamline. The control volume is limited by two sections respectively located at S and  $R_T$  and by two streamlines E and -E (see Fig. 45) defined in such a way that the cross section exposed presented to the flow remains

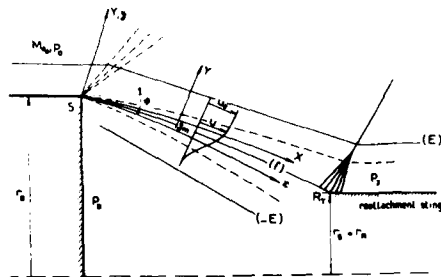


Fig. 45 - Base pressure in supersonic axisymmetric flow - Mueller's model

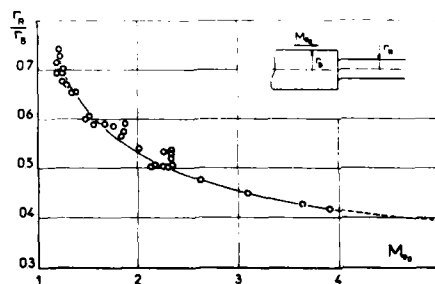


Fig. 46 - Fictitious sting radius (after Chapman, 1951)

almost constant and that the pressure term  $pdA$  can be neglected in the momentum equation. The balance relations thus obtained account for the difference between the Mach number at  $S$  and  $R_T$ . The procedure leads to a rather complicated implicit equation for  $\eta_j$  (or  $\eta_s$ ) at  $R_T$  which will not be given here (see Mueller, 1967).

The method makes it possible to take into account an effect of mass injection at the base.

Figures 47a and 47b show examples of application for a cylindrical base (where the points of experimental comparison are many) and for a boattail base. Agreement with experiment is generally very good.

Figure 48 emphasizes the effect of the nature of the gas for a boattail afterbody. The increase of  $\gamma$  entails an increase of base pressure which is in agreement with the evolution of the reattachment angular criterion experimentally observed (Rougier, 1970).

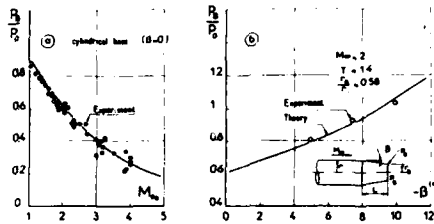


Fig. 47 - Base pressure in supersonic axisymmetric flow - Comparison of calculated and experimental results - Mueller's model

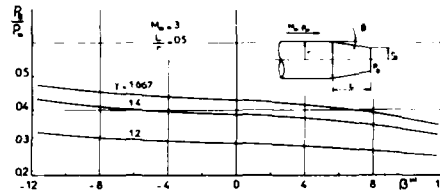


Fig. 48 - Base pressure in supersonic axisymmetric flow - Mueller's model

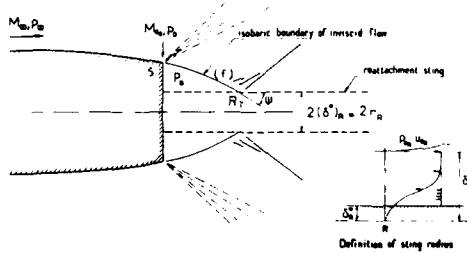


Fig. 49 - Base pressure in supersonic axisymmetric flow - ONERA flow model

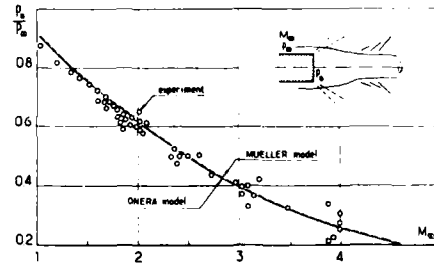


Fig. 50 - Base pressure in supersonic axisymmetric flow - Comparison of calculated and experimental results - ONERA model

The method developed at ONERA (see Dély and Sirieix, 1979) uses the concept of Angular Reattachment Criterion (see Section 3.4.4.). Its essential features are the following (see Fig. 49) :

- i - the turbulent mixing that develops from the separation point is supposed isobaric at the base pressure  $p_B$ . The corresponding frontier of the inviscid separated flow ( $f$ ) is computed by the Method of Characteristics ;
- ii - the axisymmetry effect intervenes essentially by its influence on  $\sigma$ , the balance relations defining  $\eta_j$  , and  $\eta_s$  being written for a two-dimensional flow ;
- iii - reattachment is assumed to occur on a sting of radius  $r_B$  which makes it possible to define the reattachment angle and to apply the reattachment angular law ;
- iv - the radius  $r_R$  is assimilated to the displacement thickness  $\delta^*_R$  of the wake at the level of reattachment  $R$ ,  $\delta^*_R$  being defined by :

$$(35) \quad 2\pi \int_0^{\delta^*_R} Q u r dr = 2\pi \int_{\delta^*_R}^{\delta_R} Q_{eR} u_{eR} r dr$$

where  $Q_{eR}$ ,  $u_{eR}$  are the conditions at the edge  $\delta_R$  of the wake at  $R$  level. These conditions are calculated from  $p_B$  and  $M_{eB}$  assuming an isentropic compression of the flow on the Stagnation Streamline ( $s$ ).

- v - the left hand side of Eq. (35) represents the mass flow rate passing through the wake at the level of the reattachment station. This mass flow rate is assumed equal to the mass flow rate of the mixing zone above the Stagnation Streamline at the end of the isobaric mixing. Thus, by assuming that the velocity profile  $u/u_{eR} = f(y/\delta_R)$  in the wake at the reattachment point  $R$  is universal and given by results obtained in incompressible flow (the compressibility effect on this profile is very weak), it is possible to determine the thickness  $\delta_R$  of the wake at  $R$ . Then the value of  $r_R$  is obtained readily.

The calculation procedure adopted is as follows : we take a priori a set of values for  $r_R$  and we calculate for each of them the base pressure  $p_B$ , taking into account the boundary-layer at  $S$ . The calculation also provides the thickness  $\delta_R$ . The solution corresponds to the value of  $p_B$  ensuring the equality of  $r_R$  and  $\delta_R$ .

Application of this model to the classical cylindrical afterbody is shown in Fig. 50. As was the case with the model of Mueller, agreement with experiment is very good.



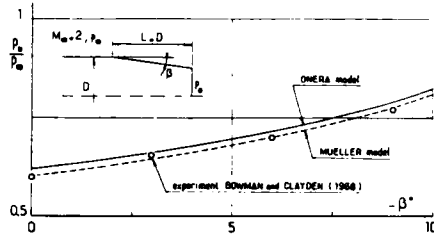


Fig. 51 - Base pressure in supersonic axisymmetric flow - Influence of boattail angle

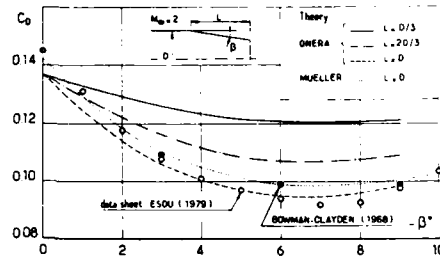


Fig. 52 - Total drag coefficient of a boattailed afterbody

Figure 51 illustrates the influence of a boattail of angle  $\beta$  for a flow with upstream Mach number equal to 2. Agreement with experiments of Bowman and Clayden (1968) is extremely good.

To conclude, Fig. 52 shows calculations of the total drag (i.e., boattail drag plus base drag) of a boattailed afterbody. This kind of application is extremely interesting for optimization purposes. One sees that independently of the boattail length, the optimum boattail angle is very close to 7 deg. This results agrees fairly well with experiment.

Tanner (1980) proposed relatively simple models to predict base pressure both in subsonic and supersonic flows. Let us examine here the supersonic case (the subsonic case is considered in Section 3.4.7.1.).

The basic idea of Tanner's theory rests on the well-known Oswatitsch (1945) theorem which relates the drag of a body to the increase in entropy in the flow :

$$(36) \quad \iint_{\Sigma} (s - s_{\infty}) \rho V_r d\sigma = D \frac{U_{\infty}}{T_{\infty}}$$

In the above equation,  $s$  is the specific entropy,  $V_r$  the velocity component normal to the control surface ( $\Sigma$ ) surrounding the body,  $D$  represents the drag of the body, and  $U_{\infty}$  and  $T_{\infty}$  are the velocity and temperature at upstream infinity. The flow is assumed to be stationary with no heat transfer.

$$\text{Introducing : } \Delta s = \iint_{\Sigma} (s - s_{\infty}) \rho V_r d\sigma$$

$$\text{equation (36) can be written in the more concise form : } \Delta s = D \frac{U_{\infty}}{T_{\infty}}$$

Now let us consider the flow behind the base of a circular cylinder indefinitely long in the upstream direction. As seen above (see Fig. 32), if the base pressure  $p_b$  is known, it is possible to construct the perfect fluid solution which consists essentially of a centered expansion wave at the base shoulder, an isobaric frontier (f) at pressure  $p_b$  and an oblique shock-wave (C) emanating from the point  $R_1$  where (f) intercepts the axis (this kind of perfect fluid solution does not seem to be possible in an axisymmetric flow where the isobaric boundary bends rapidly on approaching the axis and tends to become normal to this axis).

Since in this model the only drag is the base drag  $D_b$ , we have :

$$\Delta s = D_b \frac{U_{\infty}}{T_{\infty}}$$

where  $\Delta s$  is the entropy rise through the reattachment shock (C).

Now let us consider the physical dissipative flow and assume that the base pressure is the same as in the perfect fluid model. If the initial boundary-layer is vanishingly small, the drag reduces to the base drag and is thus equal to the non-viscous drag. However, the entropy production  $\Delta s$  can now be expressed as :

$$\Delta s = \Delta s_1 + \Delta s_2$$

where  $\Delta s_1$  is the increase in entropy resulting from the dissipative phenomena and  $\Delta s_2$  is the increase in entropy due to the reattachment shock (C).

Now it is assumed that  $\Delta s_1$  can be equated to the entropy rise taking place in the perfect fluid model over a height  $H^*$  from the axis.

The entropy rise is evaluated in a section located downstream of the reattachment point where the pressure has recovered the upstream value  $p_{\infty}$ .  $\Delta s_1$  can be written :

$$\Delta s_1 = D_V \frac{U_{\infty}}{T_{\infty}}$$

where  $D_V$  is the viscous drag. Hence, expressing  $D_V$  in terms of the momentum deficit through the viscous wake, one obtains :

$$\frac{\Delta s_1}{R} = \frac{2\pi \rho_{\infty} U_{\infty}^2 H^2}{RT_{\infty}} \int_0^1 \frac{\rho}{\rho_{\infty}} \frac{u}{U_{\infty}} \left(1 - \frac{u}{U_{\infty}}\right) r dr$$

H designates the wake radius and R is the gas constant. Thus, the above Eq. (36) can be written :

$$\frac{\Delta s_1}{R} = \frac{2\pi \rho_\infty U_\infty^2 H^2}{RT_\infty} \int_0^1 \frac{\rho}{\rho_\infty} \frac{u}{U_\infty} \left(1 - \frac{u}{U_\infty}\right) \frac{r}{H} \frac{dr}{H}$$

Now, let us consider the perfect fluid model. If  $M_{eB}$  designates the Mach number along the isobaric frontier (f), and  $\beta$  the deflexion across the reattachment shock (C), then the entropy rise through a section of radius  $H^*$  is given by :

$$\frac{\Delta s_2}{R} = \pi H^{*2} \rho_\infty U_\infty F_2(M_{eB}, \beta)$$

where  $F_2(M_{eB}, \beta)$  results from oblique shock theory (it is assumed that the flows upstream and downstream of  $R_T$  are uniform).

The basic assumption of the model is to equate  $\Delta s_1$  and  $\Delta s_2$  leading to the equation :

$$2\gamma M_\infty^2 H^2 \int_0^1 \frac{\rho}{\rho_\infty} \frac{u}{U_\infty} \left(1 - \frac{u}{U_\infty}\right) \frac{r}{H} \frac{dr}{H} = H^{*2} F_2(M_{eB}, \beta)$$

or :

$$(37) \left(\frac{H^*}{H}\right)^2 F_2(M_{eB}, \beta) = 2\gamma M_\infty^2 \int_0^1 \frac{\rho}{\rho_\infty} \frac{u}{U_\infty} \left(1 - \frac{u}{U_\infty}\right) \frac{r}{H} \frac{dr}{H}$$

Now, if the velocity and density profiles  $u/U_\infty$  and  $\rho/\rho_\infty$  are provided by appropriate equations (for details, see Tanner), and if the ratio  $(H^*/H)$  is assumed known, relation (37) constitutes an equation which can determine the Mach number  $M_{eB}$ ; hence, the base pressure  $p_B$ . In fact,  $(H^*/H)$  is a function of  $M_{eB}$  which must be obtained using experimental data.

The above basic model has received successive empirical refinements to represent effects of initial boundary-layer, boattail, angle of attack, etc...

### 3.4.6.2. - Missile in the Jet-On Situation

**Flow Schematization.** The flow structure downstream of the base of an afterbody equipped with a propulsive jet has been analyzed in the first part of this paper (see Section 2.2). It is extremely complex and the only really practical methods still at our disposal for treating that kind of problem are of the Multi-Component type and rest on a rather rough schematization of the real phenomena. However, most often they provide a good prediction of the main base flow features as will be seen later. To our knowledge, few Inviscid-Viscous Interactive methods have been developed to treat such a problem. Let us mention however the theoretical attempts of Klineberg et al. (1972) and Bogep et al. (1972) to solve the problem of external flow separation caused by the pluming of a greatly underexpanded propulsive jet. Although interesting, these methods have led to severe difficulties of principle in their application to realistic missile afterbody configurations so that their use for routine base-flow evaluations has never been seriously considered. At this level of sophistication, the most straightforward approach solving the full time averaged Navier-Stokes equations seems preferable (see Section 3.5).

The theoretical models that will be presented constitute an extension of methods developed for two-dimensional reattachment on a wall. In fact, the different models which will be reviewed are based on nearly the same schematization.

The basic model adopted to treat base flows with a propulsive jet was first established by Chow (1959) as an application of the Korst theory. The essential features of this model are as follows :

- the dead-air region, roughly limited by the triangle  $S_E R_T S_J$  (see Fig. 53), is at the same pressure  $p_B$  as the two separated external and internal (nozzle jet) streams ;
- the viscous phenomena are superimposed on a perfect fluid structure entirely determined if the base pressure  $p_B$  is known.

For all theories, the first step consists in performing a perfect fluid calculation which provisionally considers the base pressure  $p_B$  as known. The very efficient and very rapid Method of Characteristics is most often used to perform this calculation. Thus it is possible to calculate the inviscid flows separating at points  $S_E$  and  $S_J$  respectively. This calculation provides in particular the constant pressure free boundaries  $(f)_E$  and  $(f)_J$  of the inviscid streams. When  $p_B$  is lower than both  $p_{0E}$  and  $p_{0J}$  (upstream pressure at  $S_E$  and  $S_J$  respectively),  $S_E$  and  $S_J$  are the origin of an expansion fan (a circumstance pictured in Fig. 53). But, as already pointed out (see Section 2.2), this situation is not always met with : for example, if the jet is underexpanded,  $p_B$  can be higher than  $p_{0E}$  and then a shock-wave emanates from  $S_E$ . Conversely, if the jet is overexpanded, a shock can propagate from  $S_J$ .

The two lines  $(f)_E$  and  $(f)_J$  usually meet at the inviscid confluence point  $R_T$  different from the physical reattachment point R. Downstream of  $R_T$ , the two inviscid streams have a common boundary  $(\Sigma)$  - a slip line - on which both flows must have the same pressure and the same direction. These two conditions allow the determination of the initial direction  $\varphi_2$  of  $(\Sigma)$  at  $R_T$  as well as of the common pressure  $p_B$  in the two flows. The calculation of these downstream conditions can be done :

- either by considering that at  $R_T$  each flow is submitted to a compression shock - as sketched in Fig. 53 - which is in principle the most accurate procedure for purely inviscid flows ;
- or by replacing the shocks by isentropic simple wave compressions : indeed, experiments show that the shock-waves form by the focusing of the compression waves at a distance from R. The assumption of an isentropic compression should thus lead to a more accurate evaluation of  $\varphi_2$ .

Having computed the isobaric free boundaries  $(f)_E$  and  $(f)_J$  and, in the non iso-energetic case, assumed a value for the dead-air temperature  $T_B$ , it is possible to determine the properties of the two turbulent mixing layers developing along  $(f)_E$  and  $(f)_J$ , i.e., the velocity and density distributions (see Section 3.4.2).

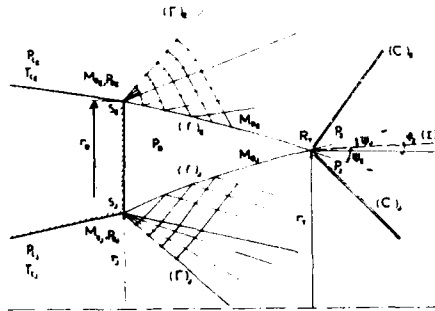


Fig. 53 - Supersonic base flow with propulsive jet - Inviscid flow pattern

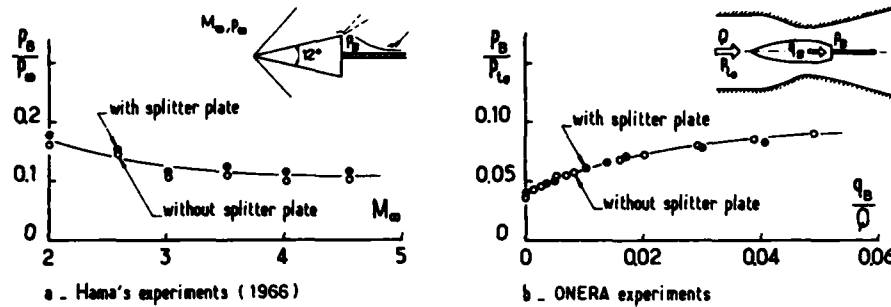


Fig. 54 - Wall type reattachment and wake type reattachment

In the next step which will involve closure relations ensuring the unicity of the solution, the reattachment theory of Section 3.4.4 above is applied to each flow. For this we allow that everything happens as if each stream reattached on a wall materializing the common confluence direction ( $\Sigma$ ). Such an assumption is justified by experimental observations which show that the materialization by a thin plate of the plane of symmetry of a symmetrical near wake introduces only minor effects into the field close to the confluence point R. This behavior can be intuitively understood if one considers that in the dead-air region and also in the vicinity of the reattachment point, the wall friction is very small. Experimental results presented in Fig. 54 show that the base pressure is not noticeably affected by the introduction of a material reattachment wall, even when mass is injected into the dead-air region at low velocity.

Knowledge of the downstream pressure  $p_2$  or the initial direction  $\varphi_2$  of the slip line allows application of one of the above reattachment criteria to the external flow and to the jet (see Section 3.4.4). It is thus possible as explained in Section 3.4.3 to determine the location of the two Stagnation Streamlines ( $\eta_{sE}$  and  $\eta_{sJ}$ ).

The flow being assumed steady, the conservation of mass and energy of the dead-air region leads to the two budget equations. They are written here for an axisymmetric flow by considering the thicknesses of the mixing layers small when compared to the distance to the axis  $r$ :

- for the mass :

$$(38) \quad 2\pi \left\{ \left[ \int_{Y_j}^{Y_s} \rho u r dr \right]_E + \left[ \int_{Y_j}^{Y_s} \rho u r dr \right]_J \right\} = \dot{q}_B$$

- for the total enthalpy :

$$(39) \quad 2\pi \left\{ \left[ \int_{Y_j}^{Y_E} \rho u (h_{te} - h_t) r dr + \int_{Y_j}^{Y_s} \rho u h_r r dr \right]_E + \left[ \int_{Y_j}^{Y_E} \rho u (h_{te} - h_t) r dr + \int_{Y_j}^{Y_s} \rho u h_r r dr \right]_J \right\} + \dot{\Delta}h_B + \dot{\phi}_B = 0$$

where  $\dot{q}_B$  represents the injected mass flow rate in the case of base-bled,  $\dot{\Delta}h_B$  the total enthalpy of the injected gas and  $\dot{\phi}_B$  corresponds to heat transfer through the base wall (most often this term - difficult to estimate - is neglected).

In the equation for the total enthalpy, the influence of the initial boundary-layers has been neglected for the sake of simplicity.

The integrals figuring in the balance equations (38) and (39) represent the flow rate of mass and enthalpy which is exchanged between the two supersonic separated streams and the dead-air region through the mixing process taking place along the frontiers ( $f$ )<sub>E</sub> and ( $f$ )<sub>J</sub>. Thus, in principle these integrals must be evaluated at the end of the isobaric mixing, i.e., at the beginning of each recompression zone. However, the lengths of the isobaric mixing zones are frequently taken to be equal to the lengths  $L_E$  and  $L_J$  of the isobaric inviscid frontiers comprised between the separation points and  $R_7$ . This convention does not strictly correspond to reality, isobaric mixing representing only a fraction of  $L_E$  or  $L_J$ . For this reason, Addy (1970) proposed a modification consisting in the introduction of effective lengths  $L_E^*$  and  $L_J^*$ , determined approximately by locating the meeting point of the two mixing zones. Dixon et al. (1970) take for effective mixing lengths 0.8 times the values obtained from inviscid flow intercepts. Hong (1970) considers that reattachment begins at approximately half the distance between the points of separation and reattachment.

If the distance from the axis  $r(x)$  can be considered as nearly constant in the region of interest - which implies a small dead air region - the above balance equations are frequently written in the form :

- conservation of mass :

$$(40) \quad 2\pi R_T \left\{ \left[ \int_{Y_j}^{Y_s} \rho u \, dY \right]_E + \left[ \int_{Y_j}^{Y_s} \rho u \, dY \right]_J \right\} = \dot{q}_B$$

- conservation of energy :

$$(41) \quad 2\pi R_T \left\{ \left[ \int_{Y_j}^{Y_{E'}} \rho u (h_{te} - h_t) \, dY + \int_{Y_j}^{Y_s} \rho u h_t \, dY \right]_E + \left[ \int_{Y_j}^{Y_{E'}} \rho u (h_{te} - h_t) \, dY + \int_{Y_j}^{Y_s} \rho u h_t \, dY \right]_J \right\} + \Delta h_B = 0$$

where  $R_T$  is the distance to the axis of the confluence point.

In the formulation of the above theoretical model, the base pressure  $p_B$  and the dead-air enthalpy  $h_B$  (or dead-air temperature) are assumed known. This allows the determination of the inviscid streams, the calculation of the mixing zone properties, application of the reattachment criterion, etc... However, for arbitrarily assumed values of  $p_B$  and  $h_B$ , the balance equations (40) and (41) will not in general be satisfied. Thus the principle of solution is an iteration on  $p_B$  and  $h_B$  (or  $T_B$ ) until the two above balance equations are simultaneously satisfied. In most application codes, the iteration process is accelerated by employing a Newton-Raphson method.

Now we will briefly examine the different methods proposed for computing turbulent base flows on an axisymmetric body with a single exhaust jet. In fact, these methods are variants of the above basic theoretical model and it is only minor changes which make them different from each other.

#### The Different Flow Models.

The method proposed by Addy (1969 ; see also Addy et al., 1973) closely follows the general flow model. The inviscid streams are computed by the Method of Characteristics and the pressure downstream of reattachment is determined by assuming oblique shock recompressions. The initial boundary-layers are neglected. Two balance equations for mass and energy are considered. In order to remedy a deficiency of the original Korst reattachment criterion, a modification of this criterion is introduced which consists in writing that the stagnation pressure on the Stagnation Streamline is only a fraction of the downstream static pressure  $p_2$  :

$$\frac{p_{ts}}{p_B} = k \frac{p_2}{p_B}$$

In the above equation,  $k$  is an empirical function of the ratio of radii at  $S_E$  and  $S_J$  :  $r = r_J/r_E$  which can be represented by :

$$k = 0.483 + 1.088 \bar{r} - 0.874 \bar{r}^2 + 0.303 \bar{r}^3$$

The Addy base-flow model has been extensively used to conduct a systematic study of the effect of the different parameters influencing the base pressure (afterbody geometry, Mach numbers, nozzle expansion ratio, gas temperature, etc...). The results of this study can be found in Addy (1969).

The model proposed by Hong (1970) also treats the case of a base-flow with energy exchanges. It very closely follows the basic Korst model.

The method proposed by Dixon et al. (1970) presents significant differences with respect to the two previous methods. Thus, the external inviscid flow is calculated for a real gas using partition functions for the thermodynamic properties, the frontier of this flow remaining linear after initial adjustment to  $p_B$ . This assumption results in an axial pressure gradient through the dead-air region. Then the shape of the internal inviscid flowfield is computed for an ideal gas using as a boundary condition the axial pressure distribution determined from the external flow calculation. According to these authors, the usual assumption of  $p_B$  as constant is not employed because it leads to recompression which did not agree with experimental data.

To represent axisymmetry effect, the similarity coordinate is defined in terms of the Mangler transform, yielding :

$$\eta = \sigma \frac{\bar{y}}{\bar{x}}$$

with :

$$\bar{x} = \int_0^x \left[ \frac{r_f(x)}{r_E} \right]^2 dy \quad \text{and} \quad dy = \frac{r_f(x)}{r_E} y$$

In these expressions,  $r_f(x)$  is the radius of the inviscid frontiers and  $r_E$  (or  $r_J$ ) a reference length. For the external mixing length,  $r_E$  is the afterbody base radius, and for the exhaust jet mixing layer the jet exit radius  $r_J$  is used.

Here the balance equations are written in the form (38) - (39) which more accurately represents the axisymmetry effect. This version of the method does not consider an equation for energy, thus it only applies to iso-energetic flows.

The adopted reattachment criterion is the modified version of the Korst criterion introduced by Goethert (see Section 3.4.4).

In the model developed at ONERA (see Détery and Sirieix, 1979 ; Benay and Détery, 1986), the Angular Reattachment Criterion presented in Section 3.4.4 is applied to the external flow and the jet. For this, the two isobaric inviscid frontiers are computed by the Method of Characteristics up to their intersection point  $R_T$ . Then the inviscid slip line ( $\bar{\Sigma}$ ) is determined by assuming isentropic simple wave compression at  $R_T$ . The two reattachment angles  $\psi_E$  and  $\psi_J$  are defined as the angles between ( $\bar{\Sigma}$ ) and the tangents to ( $f_E$ ) and ( $f_J$ ) at  $R_T$  respectively. Application of the general reattachment law (30) allows the determination of  $(\eta_s)_E$  and  $(\eta_s)_J$ , hence the location of the two Stagnation Streamlines. It is thus possible to compute the flow rates of mass and enthalpy exchanged

between the two mixing layers and the dead-air region and check if the balance equations (40) and (41) are - or are not - satisfied. In this evaluation, the influence of the initial boundary-layer at the separation points is taken into account and its effect on the velocity distributions represented by the virtual origin concept (see Section 3.4.2).

If the linearized form (31) of the Angular Reattachment law is used, the two generalized injection coefficients  $Cq_E$  and  $Cq_J$  are deduced from (31) once  $\psi$  and  $\partial\psi/\partial Cq$  have been determined. The exchange mass flow rates  $\dot{q}_E$  and  $\dot{q}_J$  are then evaluated by :

$$\dot{q}_E = 2\pi R_T \left[ Q_{eB} u_{eB} \right]_E L_E \left( Cq_E + \frac{\theta_{BE}}{L_E + X_{OE}} \right)$$

$$\dot{q}_J = 2\pi R_T \left[ Q_{eB} u_{eB} \right]_J L_J \left( Cq_J + \frac{\theta_{BJ}}{L_J + X_{OJ}} \right)$$

in which the injection of momentum due to bleed has been neglected. The balance equation for mass thus takes the form :

$$\dot{q}_E + \dot{q}_J = \dot{q}_B$$

The following examples of application will give an idea of the validity of the method :

- the first case (see Fig. 55) concerns a cylindrical afterbody in a uniform flow at Mach  $M_{0E} = 1.97$  equipped with a conical nozzle. Two values of the exit Mach number  $M_{0J}$  are considered : 2.0 and 3.0. The results presented show the evolution of the base pressure as a function of the nozzle expansion ratio. These calculations take into account the effect of initial boundary-layers ;
- in the second example, (see Fig. 56), the nozzle exit Mach number is fixed ( $M_{0J} = 2.5$ ) and two values of the external Mach number  $M_{0E}$  are considered : 2.01 and 3.27 (the experiments are those of Agrell and White, 1974) ;
- the third example (see Fig. 57) corresponds to a configuration where the nozzle largely emerges from the afterbody which leads to quite different lengths of jet boundaries ;
- lastly, Fig. 58 represents an application to a case where a mass injection is performed at the base, for several values of the expansion ratio.

There results from all these comparisons between theory and experiment that the method leads to a generally satisfactory prediction of the influence of the various parameters considered.

Thus the method can be used confidently to investigate the influence of parameters affecting base pressure. Examples of such a study are given in Figs. 59 to 63 where the specific effects of the following parameters are considered :

- upstream Mach number (Fig. 59) ;
- nozzle exit Mach number (Fig. 60) ;
- relative size of the exhaust nozzle (Fig. 61) ;
- base to nozzle exit plane distance (Fig. 62) ;
- exhaust jet stagnation temperature (Fig. 63).

Calculated values of the dead-air temperature are represented in Fig. 64 vs. the nozzle expansion ratio for increasing exhaust jet stagnation temperature.

The influence of the various factors considered here on the afterbody drag is summarized in the Table of Fig. 65.

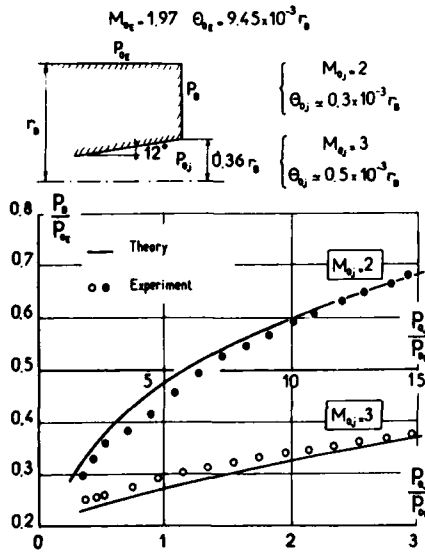


Fig. 55 - Supersonic base flow with propulsive jet - Nozzle Mach number effect - ONERA model

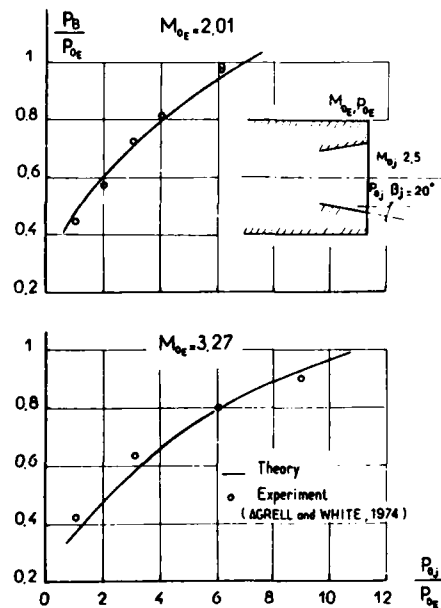


Fig. 56 - Supersonic base flow with propulsive jet - External Mach number effect - ONERA model

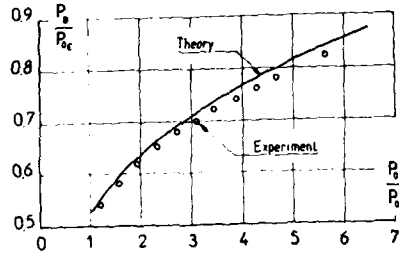
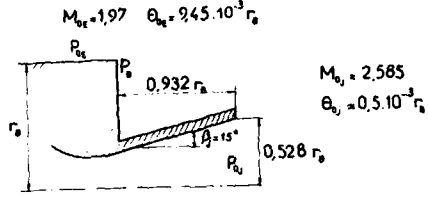


Fig. 57 - Supersonic base flow with propulsive jet - influence of afterbody geometry - ONERA model

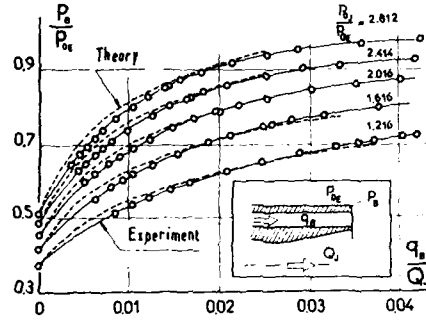
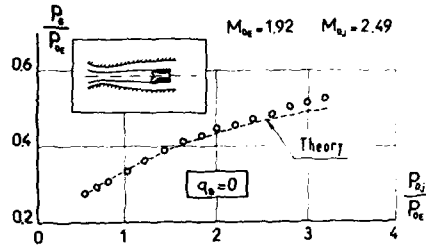


Fig. 58 - Supersonic base flow with propulsive jet - Base bleed effect - ONERA model

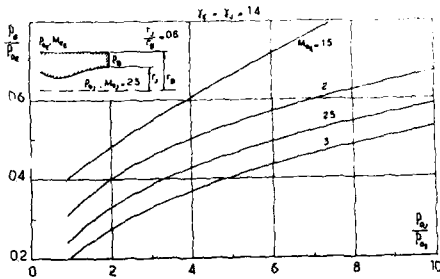


Fig. 59 - Parametric variation of base pressure with external Mach number - ONERA model

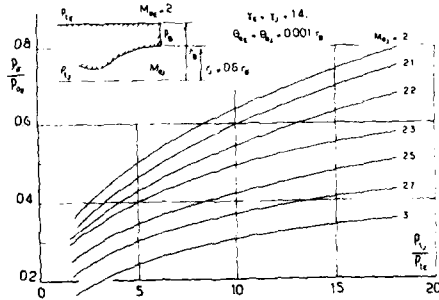


Fig. 60 - Parametric variation of base pressure with nozzle exit Mach number - ONERA model

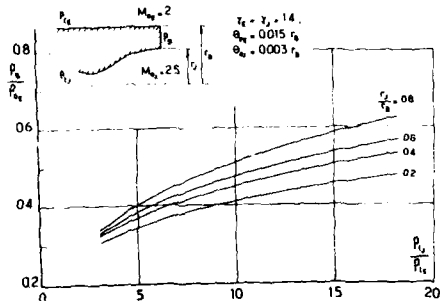


Fig. 61 - Parametric variation of base pressure with nozzle exit radius - ONERA model

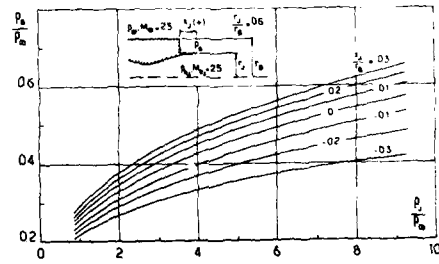


Fig. 62 - Parametric variation of base pressure with nozzle length - ONERA model

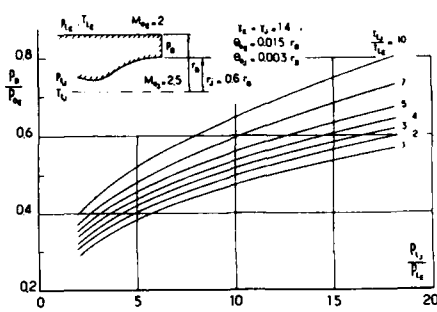


Fig. 63 - Parametric variation of base pressure with jet stagnation temperature - ONERA model

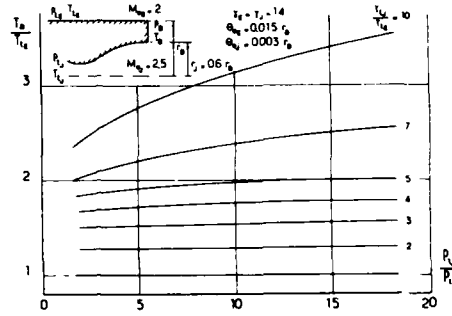


Fig. 64 - Parametric variation of base temperature with jet stagnation temperature - ONERA model

| Varying parameter for fixed nozzle expansion ratio                    | sense of variation | Influence on total drag coefficient C <sub>0</sub> |
|---|--------------------|--|
| - upstream Mach number M <sub>0</sub>                                 | /                  | /  |
| - nozzle exit Mach number M <sub>0e</sub>                             | /                  | /  |
| - nozzle divergence angle β <sub>j</sub>                              | /                  | /  |
| - boattail (or flare) angle β <sub>e</sub>                            | /                  | /  |
| - ratio of specific heats γ <sub>j</sub> (for fixed M <sub>0j</sub> ) | /                  | C <sub>0</sub> = ...                               |
| - ratio of radii r <sub>j</sub> /r <sub>e</sub>                       | /                  | /  |
| - nozzle emergence length x <sub>j</sub> /r <sub>e</sub>              | /                  | /  |
| - boattail length   | /                  | /  |
| - initial boundary-layer momentum thickness θ <sub>0</sub>            | /                  | /  |
| - exhaust jet stagnation temperature                                  | /                  | /  |

Fig. 65 - Supersonic base flow with propulsive jet - Effect of main parameters on afterbody total drag coefficient

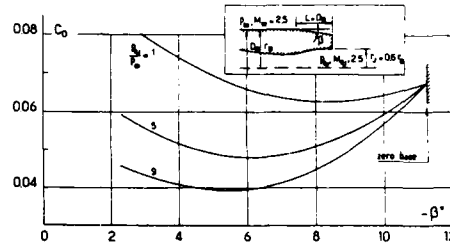


Fig. 66 - Total drag coefficient of a boattailed afterbody with jet - ONERA - AEROSPATIALE model

The last example concerns the total drag of a boattailed afterbody with jet. The curves plotted in Fig. 66 show that the optimum boattail angle tends to decrease when the nozzle expansion ratio increases.

The method of Wagner (1981) is close to the ONERA method. However, in the present application of the Angular Reattachment criterion to the two mixing-layer closure problem, an iterative procedure is included to adjust the reattachment direction φ<sub>R</sub> for achieving **equal reattachment pressure in both shear layers** (this condition is not satisfied in the ONERA application of the Angular Reattachment criterion). The pressure rise up to the reattachment point R is given by assuming an isentropic recompression on the Stagnation Streamline from p<sub>β</sub> to p<sub>R</sub>. Thus in Wagner's method, the attachment direction is no longer that of the confluent inviscid flows downstream of R<sub>T</sub>. Instead, the pressure at the reattachment point R is the same in the two reattaching mixing-layers which seems more satisfactory from a physical point of view. This modification is a first approximation in order to take into account different directions of the slipline at reattachment and downstream of the impingement point.

An interesting extension of the above models has been proposed by Bauer and Fox (1977) which includes effects of boundary-layer, base-bleed, total enthalpy differences and **species differences**. The main features of this analysis are the following :

- the initial boundary-layer is taken into account by considering the complete Korst solution given by Eq. (19) (see Section 3.4.2) ;
- the compressibility and axisymmetry effects on the jet spreading parameter are represented by using relations (16) and (18) (see Section 3.4.2) ;
- a modified reattachment criterion is employed (see Section 3.4.4).

However, the most important feature of this method is the representation of effects resulting from species differences in the base-flow region - including chemistry.

This modeling relies on the following assumptions.

For each mixing-layer let k designate the mass fraction of the contiguous inviscid stream in the local mixture (k is equal to 1 in the external flow and 0 in the dead-air region). It is assumed that the distribution of k can be represented by :

$$k = \frac{1}{2} \left[ 1 + \operatorname{erf} (C_{Mf} \eta) \right]$$

The "shape parameter" C<sub>Mf</sub> is introduced to account for the fact that at separation, the initial species profile is a step function whereas the velocity profile is that of the boundary-layer. Thus with C<sub>Mf</sub> to be determined, the disparity between the profiles can be accommodated. The shape parameter C<sub>Mf</sub> is determined by a mass balance for the external species between the separation section and the section located at the extremity of the mixing region. This gives :

$$\int_0^{Y_E} \rho u dy \Big|_{X=0} = \int_{-\infty}^{Y_E} k \rho u dy \Big|_{X=L}$$

Furthermore, one introduces for convenience the mass fractions  $m_{YE}$  and  $m_{YJ}$  of external streams in the base mixture. Thus, as the mass flow rate of an outer species fed into the dead-air region is given by :

$$q_m = \int_{-\infty}^{Y_s} k \rho u dY$$

we will have for the external stream :

$$(42) \quad m_{YE} = \frac{\left[ \int_{-\infty}^{Y_s} k \rho u dY \right]_E}{\left[ \int_{-\infty}^{Y_s} k \rho u dY \right]_E + \left[ \int_{-\infty}^{Y_s} k \rho u dY \right]_J + m_{JB}}$$

and :

$$m_{YJ} = \frac{\left[ \int_{-\infty}^{Y_s} k \rho u dY \right]_J}{\left[ \int_{-\infty}^{Y_s} k \rho u dY \right]_E + \left[ \int_{-\infty}^{Y_s} k \rho u dY \right]_J + m_{JB}}$$

for the exhaust jet.

In the above expressions,  $m_{JB}$  designates the mass fraction of the injected fluid at the base.

The total enthalpy distribution across each mixing layer is represented by a Crocco relation involving the species distribution :

$$h_t = k h_{tE} \text{ or } J + (1 - k) h_B$$

The problem has basically three unknowns, namely : the base pressure  $p_B$ , the dead-air enthalpy  $h_B$  and, for example, the mass fraction  $m_{YE}$  (since we must have  $m_{YE} + m_{YJ} + m_{JB} = 1$ ,  $q_B$  is given and thus  $m_{YJ}$  results immediately from  $m_{YE}$ ). The solution procedure is a shooting technique on these three quantities which is carried out until the two equations expressing the balance of mass - Eq. (38) - the balance of energy - Eq. (39) completed by Eq. (42) are simultaneously satisfied.

Chemistry is involved in the problem at the level of the computation of the local density  $\rho$  in the mixing layer. This requires determination of the mole fractions of the molecular constituents and the temperature which is made from equilibrium chemistry. The principle of this determination is classical and will not be given here (see Fox, 1979).

An example of base flow calculation with bleed and burning in the dead-air region is presented in Fig. 67 (Fox, 1979). In this configuration, hydrogen was bled into the base region of a blunt-based afterbody immersed in an air stream flowing at a Mach number of 2. Experiments were performed both without and with burning of hydrogen (origin of experiments in Fox, 1979). As shown in Fig. 67, burning entails a large increase of base pressure. The calculation performed by Fox can be considered as being in fair agreement with experiment due to the complexity of phenomena involved in this situation.

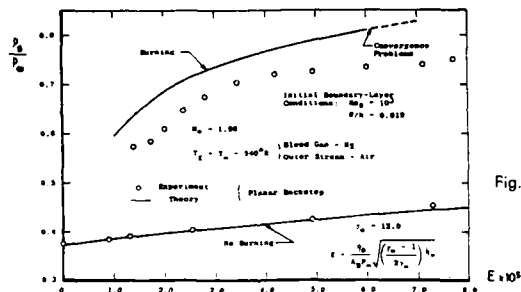


Fig. 67 - Effect on the base pressure of a hydrogen bleed both with and without burning (after Fox, 1979)

**Base-Flows with Plume Induced Separation.** The above base-flow model can also be applied to compute configurations for which the exhaust jet expands strongly at the nozzle exit thus leading to an important increase of the base pressure until separation occurs on the fuselage upstream of the base corner (see Section 2.2 above and Fig. 4). The essential ingredients of the Multi-Component approach remain the same except for one important change : in the case of the supersonic separation of a boundary-layer, the pressure after separation is entirely determined (in a first approximation) by the conditions prevailing at the origin of the separation process. This behavior is the essential result of the so called "Free Interaction Theory" (Chapman et al., 1957). Thus in this case, the base pressure, which is identified with the pressure after separation, is determined by appropriate separation criterion, the unknown now being the location of the separation point  $S$  on the fuselage (plus the dead-air enthalpy for the non-iso-energetic problem).



There exist in the literature several separation criteria for a supersonic turbulent boundary-layer (for a review of these criteria, see Détery and Marvin, 1986). The most popular are those of Reshotko and Tucker (1955), Chapman (see Chapman et al., 1957), Zukoski (1967) and Carrière et al. (1968).

A method for predicting base-flows with plume induced separation along these lines was thus proposed by White and Agrell (1977). This method is a revised and updated version of the one originally published by Addy (see above).

The pressure rise at the separation point on the fuselage is given by a modified form of the Zukoski separation criterion :

$$p_s/p_{0E} = 1 + C M_{0E}$$

In this expression, C is a function of the normalized distance  $s/\delta$  of the separation point from the base corner. This modification takes into account the fact that separation is not an abrupt process but occurs progressively.

A similar criterion has been introduced by Wagner (1983) in order to extend the capability of his method (see above). The function C is then given by the empirical formula :

$$C = C_0 \left[ 1 - \exp(-\alpha s/\delta) \right]$$

with  $C_0 = 0.5$  and  $\alpha = 1$ . It shows that as the distance increases, the pressure of the separated flow tends to the value given by the original Zukoski criterion.

Figure 68 shows an example of results obtained by Wagner (1981) for a cylindrical afterbody with jet tested by Agrell and White (1974). In this case, the base pressure becomes greater than the upstream external pressure so that separation occurs on the afterbody. Agreement with experiment is very good.

The method of Wagner also allows the determination of the separation line location on the afterbody for small angles of attack. However, agreement with experiment is not entirely satisfactory. In fact, extension of Multi-Component Methods (as well as of Inviscid/Viscous Interactive Methods) for treating three-dimensional configurations appears as extremely difficult and hazardous. The complexity of the model could then become such that the global Navier-Stokes approach seems preferable, with the warranty of a more physically realistic model.

A method including enthalpy differences and species difference has been proposed by Fong (1971). It belongs to the general category of classical Multi-Component Methods but incorporates the possibility of having a laminar external flow, a circumstance which can be met at high altitude where the density is extremely small. The treatment of the multi species problem is similar to the one employed by Bauer and Fox. The separation criterion, derived from the Chapman Free Interaction Theory, takes the following form in the laminar case :

$$C_{PB} \equiv (p_B - p_{0E}) / \frac{1}{2} \rho_{0E} u_{0E}^2 = A / (M_{0E}^2 - 1)^{1/4} R_x^{1/4}$$

In the above expression, A is an empirical function of both jet pressure ratio and the nozzle exit Mach number (for more details, see Fong and Ehrlich, 1971).

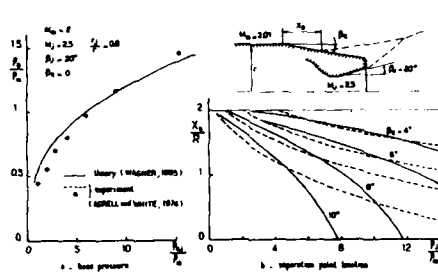


Fig. 68 - Base flow prediction with plume induced separation

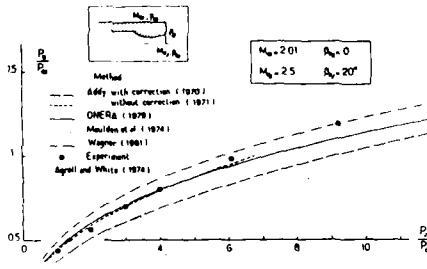


Fig. 69 - Confrontation of multi-component methods - Supersonic base flow with jet (AGARD AR n° 226, 1986)

The method of Moulden et al. (1974) (see also, Wu et al., 1974) is based on a flow model which predicts boundary-layer development over the body and then calculates the confluence of the resulting external shear-layer with the jet exhaust plume (internal shear-layer). The means by which the solution is obtained is as follows : the solution procedure begins by making an initial estimate of the angle through which the external flow is turned at the base. The ensuing pressure change is thus known and the shape of the exhaust plume which expands to the base pressure can be determined by the Method of Characteristics. The solution is classically determined by a mass-flow balance equation. The angle of the external shear-layer is then iteratively adjusted until this balance equation is satisfied.

An external flow separation ahead of the base is deemed to exist if the flow cannot be sufficiently turned by a shock-wave to meet the convergence criterion ; the relation between maximum turning angle and Mach number is determined on an empirical basis. In this case, the flow turning angle is held constant at its maximum value and the shear layer separation point iteratively moved forward from the base until a converged confluence solution is reached.

The present method is applicable to low supersonic speeds up to a maximum of 2. The lower limit is in principle Mach 1 but applications suggest that the lowest speed for useful results is Mach 1.2.

To conclude this Section, Fig. 69 presents a confrontation of four of the above Multi-Component Methods with one of the test cases selected by the AGARD Working Group 08 (see AGARD-AR N° 226, 1986). It appears that none of these methods is entirely satisfactory over the full range of nozzle expansion ratio of the chosen tests (Agrell and White, 1974). Thus there is still room for improvement of the present Multi-Component Methods applied to base flows with exhaust jet, even in the relatively simple case of a cold jet.

### 3.4.7 - Base-Flow Models for Subsonic External Stream

#### 3.4.7.1 - Missile in the Jet-Off Situation

The present flow model, developed within the framework of an ONERA-AEROSPATIALE co-operative project (see Déléry, 1983 and Berrue et al., 1984), is an improved version of the original Vanwageningen (1968) theory which is applied to cylindrical afterbodies in incompressible flows.

The adopted flow model is shown in Fig. 70. Its key components are :

- i - the Dividing Streamsurface ( $\psi_s$ ) issued from the base shoulder S and reaching the axis at the physical reattachment point R. Its trace in a meridian plane is the DSL ( $\delta$ ) which as we know is identical to the Stagnation Streamline ( $s$ ) in the absence of bleed effect ;
- ii - the displacement streamsurface ( $\psi^*$ ) on which flows the supposedly inviscid outer stream ;
- iii - the streamsurface ( $\psi_E$ ) of the inviscid flow passing through the edge E'' of the viscous core (wake) at the reattachment station.

The basic principle of the method is to make an Inviscid/Viscous Interactive calculation with coupling conditions expressed on the displacement surface ( $\psi^*$ ) (see Section 3.3.2 for considerations on the problem of the coupling conditions). In the present method, this surface is constructed in an approximate manner by proceeding as follows :

- i - upstream of the separation point S, ( $\psi^*$ ) is the body surface augmented by the displacement thickness of the incoming boundary-layer ;
- ii - between S and R, the contour of ( $\psi^*$ ) is represented by a polynomial curve which must satisfy the following conditions : a) going through the point S' located at S on the upstream displacement surface with, at S', the same slope and curvature as the DSL, b) passing through an intermediate displacement radius  $r_2^*$  located halfway between the base and R, c) going through the displacement radius  $r_3^*$  at R with continuity of slope and curvature with the downstream displacement surface.
- iii - downstream of R, ( $\psi^*$ ) is represented by an empirical equation (see Vanwageningen, 1968).

It is thus necessary to determine the displacement radii  $r_2^*$  and  $r_3^*$  at stations 2 and 3. This operation necessitates the modeling of the near wake region. For this purpose, it is assumed that the DSL is an arc of ellipse tangent to the afterbody at S and normal to the axis at R. In order to compute  $r_2^*$  and  $r_3^*$ , streamwise velocity profiles must be defined at stations 2 and 3. At 2, the adopted distribution is a composite law consisting of the curve defined by Eq. (14) above the DSL and an arc of ellipse below the DSL. At station 3, the velocity distribution is represented by an empirical law derived from experiments on 2-D incompressible reattachment (Noi, 1971). By a process similar to that presented in Section 3.4.3, the wake radii  $r_2^*$  and  $r_3^*$  are determined by applying conservation theorems for mass and momentum to adequate control volumes. For instance,  $r_3^*$  is computed by considering volume BEE''RB (see Fig. 70). Application of the momentum theorem gives an equation of the form :

$$p_B \frac{r_B^2}{2} + \int_{r_B}^{r_E} (\rho + \rho u^2) r dr = \int_0^{r_3} (\rho + \rho u^2) r dr + \int_{r_3}^{r_E} [\rho] (\psi_E) r dr$$

The last integral has to be evaluated along the streamsurface ( $\psi_E$ ). Thereafter, the displacement radius  $r_3^*$  is computed from the definition equation :

$$\int_0^{r_3} \rho u r dr = \int_{r_3^*}^{r_3} [\rho] [u] r dr$$

where bracketed quantities are relative to the inviscid flowfield. A similar procedure is employed to determine  $r_2$  and  $r_2^*$ .

The calculation procedure is as follows. For a given value of the bubble length  $L = BR$ , an Inviscid/Viscous coupling process is iterated until convergence. Then, the closure relation that determines L is similar to the Chapman-Korst escape criterion : it is postulated that the stagnation pressure on the DSL, at the point where the cavity pressure starts to rise, must be equal to the static pressure at  $p_R$  this pressure being identified with the pressure on the coupling surface at the abscissa of R.

In the present version of the method, the outer inviscid flow is computed by a method of singularities, compressibility effects being taken into account by the Prandtl-Glauert rule.

Figure 71 shows application of the method for three different afterbodies immersed in a stream flowing at a Mach number of 0.85. The first afterbody is cylindrical, the second one has a conical boattail and the third one a conical flare. One notes a fair agreement of the computed base pressure coefficients with the measured values.

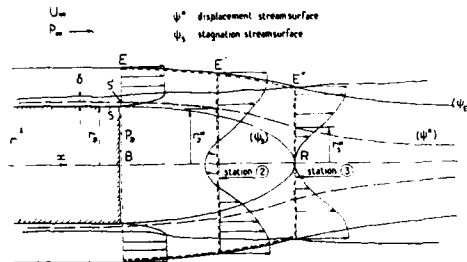


Fig. 70 - Base pressure in axisymmetric subsonic flow - Basic model (after Vanwageningen, 1968)

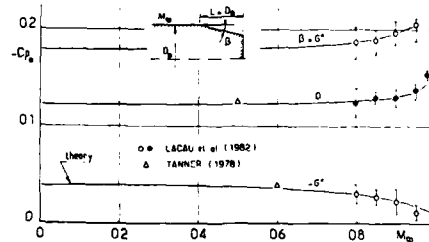


Fig. 71 - Base pressure in subsonic axisymmetric flow - Comparison of calculated and experimental results - ONERA - AEROSPATIALE model

The two other applications show the influence of the boattail/flare angle and of the boattail length (see Fig. 72).

In the theory proposed by Tanner (1973), attention is given to outflow from the dead-air region. This basic concept is explained by referring to Fig. 73. In the region from the separation point to section I, there is assumed to occur a mixing process which corresponds to a constant pressure mixing between a uniform external flow and a dead-air region. Due to this mixing, fluid is withdrawn from the dead-air region. This phenomenon is called "outflow from the dead-air region".

Four important boundaries are defined :

- i - boundary 1, separating the external flow from the mixing region ;
- ii - the mass outflow from the dead-air region takes place through boundary 2 ;
- iii - boundary 3 is the Dividing Streamline ;
- iv - boundary 4 is the streamline in the external flow which cuts the boundary of the mixing region at section I.

At section I, the location of which need not be quantitatively specified, the mass flow between boundaries 2 and 3 has its maximum value, I being such that the backflow into the dead-air region then begins.

Tanner's theory uses two momentum balance equations to express the mass outflow from the dead-air region as a function of the drag coefficient, the latter being expressed in terms of the base pressure coefficient from any potential flow solution.

The first relation is a momentum balance between the entrance section and section I. To write this relation, the velocity distribution across the mixing layer is assumed given by the following approximation of the Görtler solution :

$$\frac{u}{u_e B} = \frac{1}{2} \left\{ 1 + \sin \left[ \frac{\pi \Delta y}{b} - \frac{\pi}{2} \right] \right\}$$

where  $b$  is the width of the mixing-layer,  $\Delta y$  varying from 0 to  $b$ .

The density distribution is then obtained from the Crocco law.

The second relation is obtained by writing a momentum balance equation between section I and a section located in the wake downstream of the reattachment point. There the velocity profile is represented by :

$$\frac{u}{u_e} = \frac{u_m}{u_e} + \frac{1}{2} \left( 1 - \frac{u_m}{u_e} \right) \left[ 1 + \sin \left( \frac{\pi y}{\delta} - \frac{\pi}{2} \right) \right]$$

the value  $u_m = 0.16$  being adopted for the centerline velocity.

The theory is applied with good success to the prediction of the base pressure coefficient of two-dimensional wedge-like obstacles.

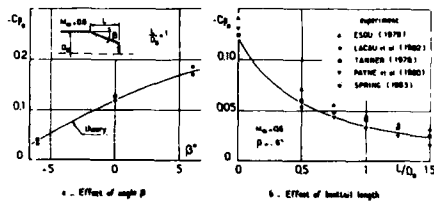


Fig. 72 - Base pressure in subsonic axisymmetric flow - Effect of afterbody geometry - ONERA - AEROSPATIALE model

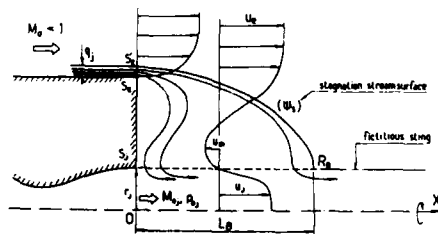


Fig. 74 - Base pressure in axisymmetric subsonic base flow with propulsive jet - Basic flow model (ONERA - AEROSPATIALE)

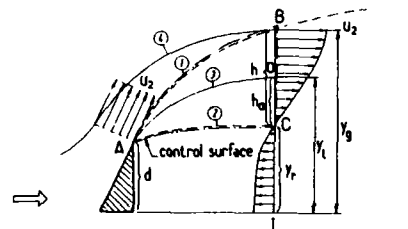


Fig. 73 - The Tanner flow model for subsonic base flows

### 3.4.7.2 - Missile in the Jet-On Situation

The present model, proposed by Berue et al. (1984) is an extension of the previous ONERA-AEROSPATIALE method developed for computing the base-flow in the jet off-condition. In principle, it is only applicable to an afterbody equipped with a nozzle having a small diameter compared to the base diameter and to exhaust jet conditions not too far from adaptation (thus the case of highly underexpanded jet cannot be treated in the present version of the flow model). In these conditions, it is legitimate to consider that the jet acts essentially as a perturbation agency on the dead-air region consisting basically in :

- i - an obstacle effect similar to the action of a sting which would materialize the exhaust jet ;
- ii - a suction effect resulting from the intense entrainment occurring along the boundary of the high speed jet. In fact, this second effect is by far the most important.

The adaptations introduced to represent these effects have been largely inspired by observations deduced from a detailed experimental analysis of the flow past missile afterbodies (Lacau et al., 1982, see Section 2.2). The essential features of the adopted model are the following (see Fig. 74) :

- i - the exhaust jet is replaced by a cylindrical sting whose radius  $r_J$  is equal to the radius of the nozzle exit section. This very simple schematization gives an acceptable representation of the jet in near adaptation conditions. However, this approximation could be easily improved by performing an exact calculation of the inviscid supersonic jet which could allow the treatment of out-of-adaptation configurations (by using the Method of Characteristics or any finite difference solvers of the Euler equations).
- ii - the suction effect is assumed uniformly distributed along the length  $L_J$  of the sting comprised between the base and the point  $R_J$  where the external flow reattaches on the sting. Furthermore, we admit that the suction velocity is normal to the sting surface (or perpendicular to the longitudinal axis OX). Thus the suction effect does not contribute to the balance of the axial component of momentum. The mass flow rate sucked off from the dead-air region by the entrainment effect of the exhaust jet is expressed in the form :

$$\dot{Q}_J = (2\pi r_J L_J) C_{EJ} \rho_{0J} u_{0J}$$

where  $\rho_{0J}$  and  $u_{0J}$  are relative to the inviscid jet of Mach number  $M_{0J}$  in the nozzle exit plane.  $C_{EJ}$  is a coefficient globally representing the entrainment effect. It is assumed that  $C_{EJ}$  is only a function of  $M_{0J}$  and of the ratio  $\lambda = (u_{0J} - u_m)/(u_{0J} + u_m)$  where  $u_m$  is the maximum velocity of the reverse flow in the dead-air region (see Fig. 74) ;

- iii - as in the jet-off case, the Dividing Streamsurface  $\psi_s$  is represented by an elliptical arc with the same definition as in the previous case (see Section 3.4.7.1). However, in order to satisfy mass conservation in the dead-air region at the level of the base, ( $\psi_s$ ) must now pass through a point D' displaced from the surface to allow passage of the mass flowrate  $\dot{Q}_J$  (see Fig. 74).

The solution procedure is the same as in the jet-off case. In particular, since the suction velocity is assumed normal to the longitudinal axis, the balance equations for the axial momentum remain unchanged. However, the extracted mass flow rate must be accounted for in the determination of the displacement surface.

Examples of application are presented in Figs. 75 and 76. They are relative to an afterbody equipped with a small supersonic exhaust nozzle of Mach number  $M_{0J} = 2.9$ .

The first example (see Fig. 75) illustrates the variation of the base pressure coefficient  $C_{pB}$  with upstream external Mach number for different values of the nozzle expansion ratio, the afterbody being cylindrical.

The second example of results (see Fig. 76) shows the evolution of  $C_{pB}$  with the nozzle expansion ratio for three angles of  $\beta$ , the upstream Mach number  $M_{0E}$  being equal to 0.85. Agreement with experiment is generally satisfactory.

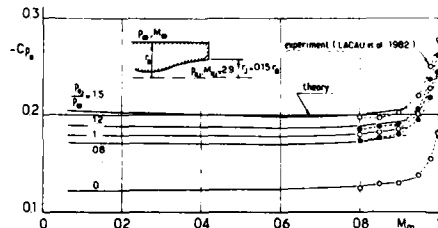


Fig. 75 - Base pressure in subsonic axisymmetric flow with propulsive jet - Comparison of calculated and experimental values - ONERA - AEROSPATIALE model

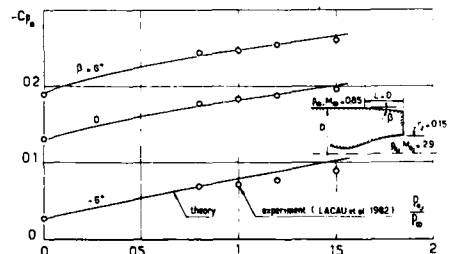


Fig. 76 - Base pressure in subsonic axisymmetric flow with propulsive jet - Effect of angle  $\beta$  - ONERA - AEROSPATIALE model

### 3.4.8 - Application to Multi-Nozzle Configurations

#### 3.4.8.1 - General Description of Phenomena

The phenomena taking place at the base of a multi-nozzle missile are far more complex than those analyzed up till now. In this situation, the structure of the flow in the base region is highly three-dimensional so that pressure is usually no longer uniform on the base surface as in the case of a single nozzle configuration where the differences observed from one point to another are always small.

We shall examine the multi-nozzle situation in the particular case of a four-nozzle configuration which has been the object of many experimental studies (see in particular, Goethert, 1960 ; Musial and Ward, 1961 ; Charczenko and Hayes, 1963 ; Goethert and Matz, 1964).

The sketches deduced from experiments, presented in Fig. 77, define the organization of the base-flow for various expansion ratios of such a propulsion system.

At low altitude, when the nozzle expansion ratio  $p_{0J}/p_{0E}$  is modest (sketch a), the jet entrainment effect ensures the evacuation of the flux issued from the external flow in the central zone close to the axis. This regime, which establishes near

adaptation conditions, is often called the aspiration regime. Then the pressure non-uniformity on the base is hardly marked at all.

When the expansion ratio becomes higher (sketch b), the jet pluming at the nozzle exit provokes their confluence. The resulting important positive pressure gradient entails the development of an intense recirculation flow, first directed towards the base and later evacuated at the jet periphery. The presence in the base center of a stagnation point for this backflow entails high values of the pressure and heat transfer at this point and in its vicinity. This flow regime is called the transitional flow regime.

At high altitude, when  $p_0/p_{0E}$  becomes very large, this effect becomes more important (sketch c) ; the recirculation flow rate increases greatly up to the sonic choking at the passage section (or vent area) available between the nozzles. This situation is called the choked reverse flow regime. In some extreme cases, the backflow directed towards the base becomes supersonic and a normal shock occurs in front of the base surface.

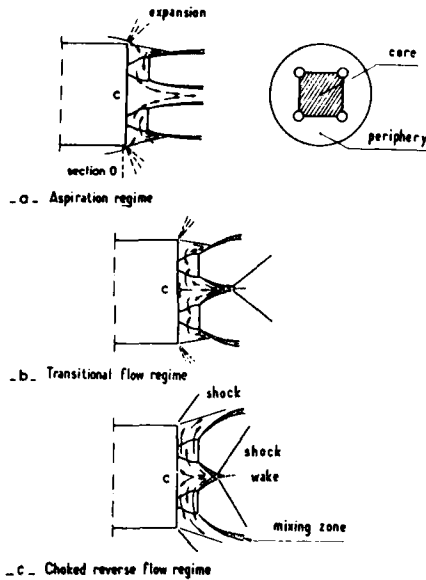


Fig. 77 - Flow structure at the base of a multi-nozzle missile

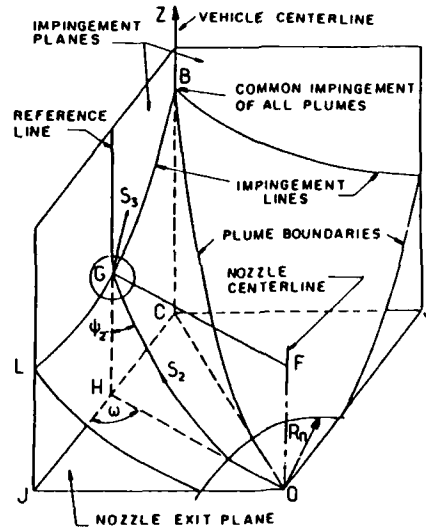


Fig. 78 - Four nozzle arrangement quadrant of inviscid flow field

3.4.8.2 - The Different Flow Models

Several methods following the Multi-Component approach have been developed to predict the essential properties of these flows, essentially the pressure and the heat transfer distributions on the base.

These models generally apply to a particular geometry, the so-called "ring cluster" in which the nozzles are arranged around the periphery of a circle.

The first step in the application of any model is to determine the inviscid boundaries for the exhaust plumes. A quadrant of such a flowfield for a four nozzle cluster is sketched in Fig. 78. One notes that each pair of adjacent plumes impinge in a plane JCBL midway between the nozzles. Inside each plane, there is a line of impingement BL. The impingement lines have a common point B located on the afterbody centerline. The interference point closest to the base is L which is located in the plane containing the axes of two adjacent nozzles ; at this point the impinging flows undergo the largest deflexion. At L, the traces of the plume by a plane perpendicular to the centerline are tangent.

At a point G on the impinging line, the velocity vector  $\vec{V}_1$  tangent to the plume boundary undergoes a deflexion, becoming  $\vec{V}_2$  contained in the impingement plane JCBL. Oblique shock relations allow the determination of  $\vec{V}_2$ . At B, the downstream vector is along the afterbody centerline. The downstream vector at point L is also parallel to the centerline.

Thus at the point where the exhaust jets impinge upon each other, we are confronted with a problem similar to that of the confluence of the external flow and the exhaust jet in the case of a single nozzle afterbody (see Section 3.4.6.2).

By applying Korst's analysis (with representation of the initial boundary-layer by means of the virtual origin concept), Goethert (1960) determines the total flow rate brought into the base region by the four jets. This flow rate  $q_m$  is computed at point L which is considered as a characteristic impingement point. Thus if  $D_m$  designates the sum of the circular arclengths between two contact points L, ( $D_m$  is equal to the diameter of the intersection of each jet by the plane containing the contact points L)  $q_m$  is given by the relation :

$$q_m = \pi D_m \int_{Y_j}^{Y_s} Qu dy$$

in which  $Y_j$  and  $Y_s$  represent respectively the ordinates of the Dividing Streamline and the Stagnation Streamline of each jet turbulent mixing-layer (in this expression, the mixing zone is assumed thin compared to its distance to the nozzle centerline).

In the choked reversed flow regime, the flow rate  $\dot{q}_m$  must be equal to the mass flow rate  $\dot{q}_v$  passing through the base vent area  $A_v$ . If the stagnation pressure of this flow is identified with the base pressure  $p_B$  and if  $T_B$  designates the stagnation temperature in the base flow region, then  $\dot{q}_v$  is given by :

$$\dot{q}_v = C_m \delta(\gamma) p_B A_v / \sqrt{C_D T_B}$$

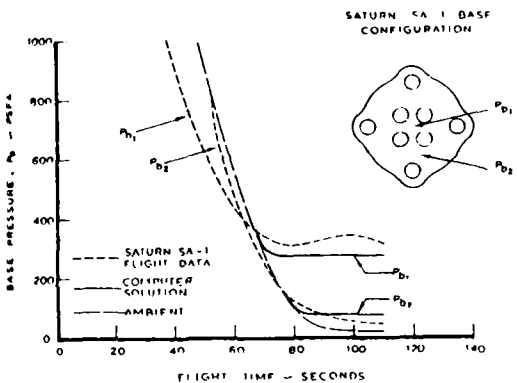
where  $\delta(\gamma)$  is a function of the ratio of specific heats only and  $C_m$  an empirical mass flow coefficient taken equal to 0.5.

Thus by equating  $\dot{q}_m$  and  $\dot{q}_v$ , one obtains an equation allowing the determination of the base pressure.

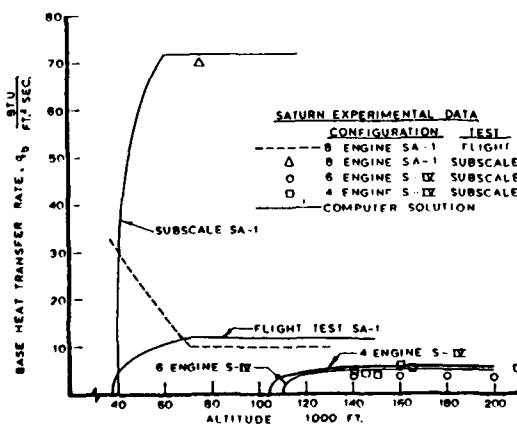
Several other models for multi nozzle configurations have been proposed along essentially the same lines as the Goethert model.

For example, Page and Dixon (1963, 1966) have developed a simple theory using the essential concepts of the initial Korst theory but incorporating the reattachment criterion as modified by Goethert (see Section 3.4.4). The method allows the determination of the base pressure and of the heat transfer on the base surface. Figure 79 shows applications of the flow model of Page and Dixon to the calculation of pressure and heat transfer  $\phi$  in the base region of several Saturn launch vehicles. In these results (which are in relatively fair agreement with experiment), the choking of the reverse flow at high altitude is particularly evident.

Lamb et al. (1969) developed a more refined model in which the jet flowing towards the base along the missile centerline is computed by an integral method using Gaussian distributions for the velocity profiles in this jet. The backflow is assumed to depend essentially on the exhaust jet impingement along the body centerline (point B in Fig. 78). Thus, the analysis is applied in the plane containing this centerline and the nozzle axis. The reattachment zone is computed by using the Lamb and Hood (1968) integral analysis of turbulent reattachment. The computation of the reverse jet impingement allows the determination of the pressure on the base center. As shown in Fig. 80, this model can be used to study the effect of parameters such as nozzle height, lateral spacing of the nozzles, nozzle expansion ratio.



a - BASE PRESSURE COMPARISON FOR SATURN SA-1 FLIGHT VEHICLE



b - BASE HEATING COMPARISON FOR SA-1 & S-IX SATURN CONFIGURATIONS

Fig. 79 - Base flow calculation for multi-nozzle launcher - Page and Dixon's model (1963)

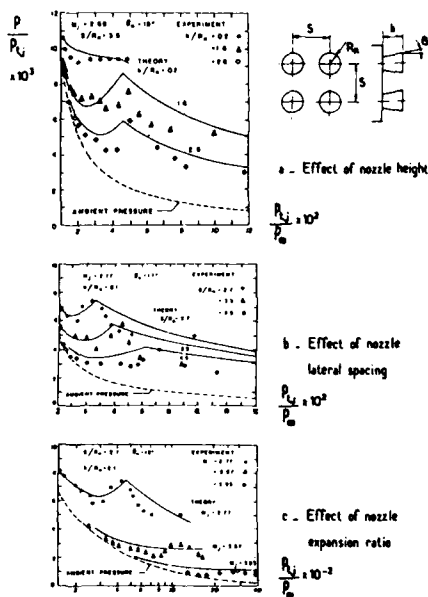


Fig. 80 - Base pressure for a four nozzle cluster - Lamb et al. model (1969)

In the method proposed by Tang et al. (1971), one first considers the impingement of the exhaust jets. In order to simplify the flow structure, the flow region surrounded by the exhaust jets is assumed to depend primarily on the jet intersection in a plane containing the body centerline, like in the Lamb et al. model. Thus one considers only reattachment at point B (see Fig. 78). Then the simplified Korst theory is applied to the mixing layers, initial boundary-layers being accounted for by using the virtual origin concept (see Section 3.4.2). The stagnation pressure  $p_{t2}$  on the Stagnation Streamline is deduced from a simplified control volume analysis applied to the reattachment zone. Hence, knowing  $p_{t2}$ , it is possible to compute the mass flow rate  $q_{mJ}$  and the enthalpy flux  $\Delta h_{mJ}$  transferred into the dead-air region by turbulent mixing (see Section 3.4.5).

The external separated stream is treated by assuming that this stream reattaches on a cylinder whose diameter  $d_R$  is such that  $d_R/d_B = 0.5$ . Application of the reattachment analysis allows the determination of the mass flow-rate  $q_{mE}$  and of the enthalpy flux  $\Delta h_{mE}$ . In this analysis, a Mangler type transformation is introduced to reduce the axisymmetric case to the two-dimensional problem.

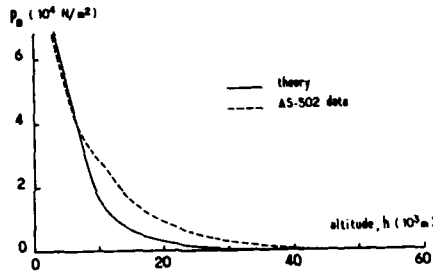


Fig. 81 - Base pressure for the Saturn V launch vehicle - Tang et al. model (1971)

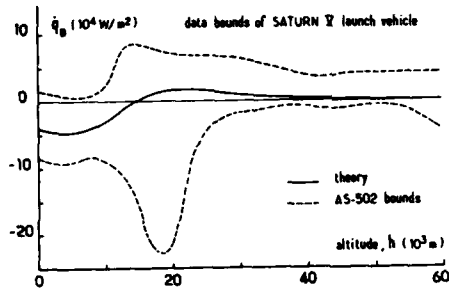
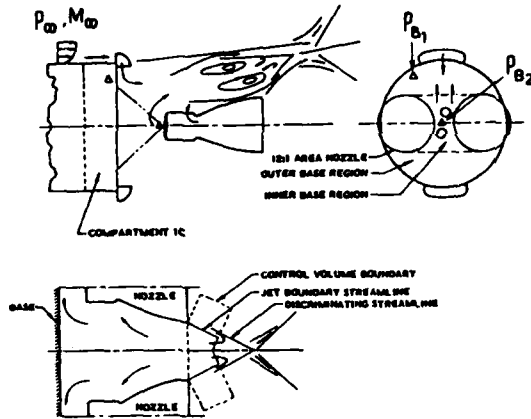
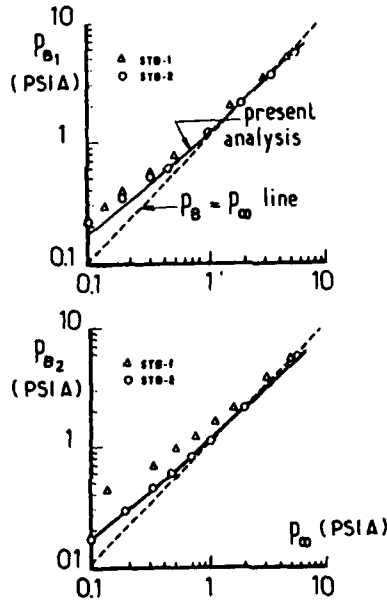


Fig. 82 - Base heat transfer for the Saturn V launch vehicle - Tang et al. model (1971)



a - Titan III base configuration and flowfield

Fig. 83 - Base flow calculation for a dual-engine Booster - Hong's model (1974)



b - Base pressure comparison

The solution, namely the base pressure  $p_B$  and the dead-air temperature  $T_B$ , must be such that the following two balance equations are simultaneously satisfied :

$$(43) \quad q_{mE} + q_{mJ} + q_B = 0$$

$$(44) \quad \Delta h_{mE} + \Delta h_{mJ} + \Delta h_B = 0$$

where  $q_B$  and  $\Delta h_B$  result from an eventual base-bleed.

Thus, the above model takes into account the interference between the jet region and the external flow.

Figure 81 presents predictions for the base pressure compared with the Saturn V launch vehicle data as a function of altitude.

The predicted results are generally below the level of the data. In Fig. 82, a comparison of the prediction with the experimental data bounds of the Saturn V are presented for the base convective heat-transfer rates. The results are well within the data bounds and exhibit the general trends of measured values.

Interference between the jets region and the external stream is also represented in the model proposed by Hong (1973, 1974) for treating the case of a dual-engine configuration. Here the flow is also divided into two regions :

- an inner region comprised between the nozzles and the exhaust jets. Here, the now well-known flow model is applied in the plane containing the nozzles axes, the initial boundary-layers being taken into account by the virtual origin concept. This analysis gives the fluxes  $\dot{q}_{MJ}$  and  $\Delta h_{MJ}$  already defined.
- an outer region representing the influence of the external stream. This part of the flow is determined by reducing the configuration to a single nozzle configuration. The diameter of the equivalent single nozzle is determined by setting its peripheral length equal to the effective peripheral length which would be obtained if the two engines were connected, as shown in Fig. 83. The classical analysis yields  $\dot{q}_{mE}$  and  $\Delta h_{mE}$ .

As in the method of Tang et al., the solution is obtained when the two balance equations (43) and (44) are both satisfied. Figure 83 shows an application of Hong's model to the prediction of the pressure in the base region of the Titan III configuration.

### 3.5 - Solution of the Navier-Stokes Equations

#### 3.5.1 - The Navier-Stokes Equations

In the present Section, the Navier-Stokes equations will be given without justification since the aim of this paper is to provide an overview of applications of these equations for the calculation of the flow past missile afterbodies. More ample information on the mathematical and numerical problems involved in the solution of the Navier-Stokes equations can be found elsewhere (see for example Peyret and Viviand, 1975).

As we know, the Navier-Stokes equations express the conservation of mass, momentum and energy. In their formulation, we will assume that gases are single component and obey the perfect gas equation of state :

$$\rho = \rho RT$$

where R is the universal gas constant divided by the gas molecular weight. Furthermore, gravity and electromagnetic forces are supposed inexistent.

In these conditions, the Navier-Stokes equations take the following form :

- conservation of mass :

$$\frac{\partial \rho}{\partial t} + \nabla \cdot (\rho \vec{V}) = 0$$

- conservation of momentum

$$\frac{\partial (\rho \vec{V})}{\partial t} + \nabla \cdot (\rho \vec{V} \vec{V}) - \nabla \cdot \vec{S} = 0$$

- conservation of energy :

$$\frac{\partial (\rho e)}{\partial t} + \nabla \cdot (\rho e \vec{V}) + (\nabla \cdot \vec{\phi} - \nabla \cdot \vec{V} \cdot \vec{S}) = 0$$

In the above equations,  $\vec{S}$  represents the fluid stress tensor that includes pressure and viscous forces,  $\vec{\phi}$  is the heat flux vector and e the total energy defined by :

$$e = C_v T + \frac{V^2}{2}$$

The other notations are classical.

The equations are written here in conservative form, the dependent variables being - for a two dimensional flow -  $\rho$ ,  $\rho u$ ,  $\rho v$  and  $\rho e$ . Since the Rankine-Hugoniot shock relations are derived by using the conservation form, the shock-jump conditions are automatically satisfied by the above equations so that no special treatment is needed to compute discontinuities.

This kind of formulation allows the calculation of flows containing shock-waves which are automatically determined by the so-called shock capturing technique with the discontinuity being in fact smeared over a limited number of computation grid points. In the more accurate shock fitting technique, shocks are treated as true discontinuities. To our knowledge, use of this relatively complex technique has not been attempted in base-flow calculations.

In most applications, the problem to be solved concerns steady flows and thus only stationary solutions to the Navier-Stokes equations are sought after. However, the flow of interest here being nearly always turbulent, the basically fluctuating nature of the flow is accounted for by introducing some averaging concept. Thus in the classical Reynolds averaging, the field variables are expressed in the form :

$$\begin{aligned} \vec{V} &= \bar{\vec{V}} + \vec{v}' \\ (45) \quad \rho &= \bar{\rho} + \rho' \\ \rho &= \bar{\rho} + \rho' \\ T &= \bar{T} + T' \end{aligned}$$

where, by definition,  $\bar{\vec{v}'} = \bar{\rho}' = \bar{\rho}' = \bar{T}' = 0$



In the above expressions, the barred variables represent time-averaged quantities over a period of time that is long compared to turbulent fluctuations but short compared to low frequency flow unsteadiness (in what follows, it will be tacitly assumed that this kind of unsteadiness does not exist in the base flows under consideration). The primed variables represent fluctuations due to the turbulent nature of the flow.

Presently, the mass-averaged concept introduced by Favre (1966) is frequently used instead of the Reynolds averaging procedure. The Favre procedure leads to a much simpler form of the time-averaged compressible equations. According to this approach, any velocity component - say  $u$  - is expressed in the form :

$$u = \bar{u} + u''$$

where the new mean value  $\bar{u}$  is defined by  $\bar{u} = \bar{\rho}u/\bar{\rho}$ . It follows that  $\bar{\rho}u'' = 0$ , hence the fluctuating part  $u''$  is now such that

$$u'' = -\bar{\rho}'u''/\bar{\rho} \neq 0$$

Without giving any further justification (see Favre for the establishment of the mass-averaged Navier-Stokes equations), in what follows we will consider the time averaged Navier-Stokes equations written with mass averaged quantities.

By using cartesian tensor notation with the usual convention of repeated indices to indicate summation over the entire range of indices and a comma representing partial differentiation, the Navier-Stokes equations for a turbulent flow are the following (see Hasen, 1981, 1982) :

- conservation of mass :

$$(46) \quad \bar{\rho}_{,t} + (\bar{\rho} \bar{u}_j)_{,j} = 0$$

- conservation of momentum :

$$(47) \quad (\bar{\rho} \bar{u}_i)_{,t} + [(\bar{\rho} \bar{u}_i \bar{u}_j) + \bar{p} \delta_{ij} - \bar{\tau}_{ij} - \overline{\bar{\rho} u''_i u''_j}]_{,j} = 0$$

- conservation of energy :

$$(48) \quad (\bar{\rho} \bar{e})_{,t} + [(\bar{\rho} \bar{e} \bar{u}_j + \bar{\phi}_j + \overline{\bar{\rho} u''_j e'} - \bar{u}_i (\bar{\tau}_{ij} - \overline{\bar{\rho} u''_i u''_j})]_{,j} = 0$$

where a higher order mean energy dissipation term in  $u''_i$  has been neglected in the energy equation.

In the above equations,  $\delta_{ij}$  is the Kronecker delta and  $\bar{\rho}$ ,  $\bar{p}$  mean state variables defined by (45).

The turbulent term  $-\overline{\bar{\rho} u''_i u''_j}$  is known as the Reynolds stress tensor. It is most often expressed by means of the Boussinesq eddy viscosity concept which consists in writing by analogy with the viscous stress tensor :

$$-\overline{\bar{\rho} u''_i u''_j} = \bar{\tau}_{ij}/\text{turb.} = \lambda_t \bar{u}_{k,k} \delta_{ij} + \mu_t (\bar{u}_{i,j} + \bar{u}_{j,i})$$

In the above relation,  $\mu_t$  and  $\lambda_t$  are the turbulent viscosity coefficients of the flow which are considered as scalar properties of the fluid. Usually, the second coefficient of turbulent viscosity  $\lambda_t$  is expressed via Stokes Hypothesis, i.e.,

$$\lambda_t = -\frac{2}{3} \mu_t$$

Thus we have :

$$\bar{\tau}_{ij}/\text{total} = (\lambda + \lambda_t) \bar{u}_{k,k} \delta_{ij} + (\mu + \mu_t) (\bar{u}_{i,j} + \bar{u}_{j,i})$$

Similarly, the energy equation contains the turbulent term  $\overline{\bar{\rho} u''_j e'}$  which is interpreted as a turbulent heat transfer term and accordingly represented by the relation :

$$\overline{\bar{\rho} u''_j e'} = \bar{\phi}_j/\text{turb.} = -k_t \bar{T}_{i,j}$$

in which  $k_t$  is a turbulent thermal conductivity. Thus, introducing the turbulent Prandtl number :

$$Pr_t = \frac{\mu_t Cp}{k_t}$$

one has :

$$\bar{\phi}_j/\text{total} = \bar{\phi}_j/\text{lam} + \bar{\phi}_j/\text{turb} = -Cp \left( \frac{\mu}{Pr} + \frac{\mu_t}{Pr_t} \right) \bar{T}_{i,j}$$

where  $Pr$  is the laminar Prandtl number.

Usually, the Prandtl numbers  $Pr$  and  $Pr_t$  are taken as constant (most often :  $Pr = 0.75$  and  $Pr_t = 0.9$  for air flow).

Thus the only quantity still undetermined in the time-averaged form of the Navier-Stokes equations 46 - 47 - 48 is the turbulent viscosity  $\mu_t$ .

Evaluation of  $\mu_t$  constitutes the major problem of turbulent flow calculations. This very complex problem incited a considerable research effort whose consideration would be far beyond the scope of the present review paper. In what follows (see Section 3.5.3), we will only examine the relatively simple turbulence models which have been utilized in base-flow calculations.

Briefly speaking, these models can be classified into two broad categories :

- i - the class of models in which  $\mu_t$  is expressed by an algebraic relation involving the local properties of the mean velocity field and quantities given by algebraic formulae ;
- ii - the class of models in which  $\mu_t$  is computed by a relation involving local properties of the turbulent field. These properties (usually two) obey transport equations which must be solved together with the Navier-Stokes equations.

More sophisticated models exist in which the eddy viscosity concept is given up and the whole Reynolds stress tensor is

computed by transport equations. However, due to their complexity and the difficulty of implementing them in a Navier-Stokes code, up to now these models have not been employed in missile base flow calculations.

Details about the turbulence models used in the Navier-Stokes calculations reviewed in this Paper will be given in Section 3.5.3

The time-averaged Navier-Stokes equations can be written in the following form where the overbars on the terms have been dropped and the values of shear stress and heat fluxes are total values :

$$\begin{aligned} \rho_{,t} + (\rho u)_{,j} &= 0 \\ (\rho u)_{,t} + \left[ (\rho u) u_j + p \delta_{ij} - \tau_{ij} \right]_{,j} &= 0 \\ (\rho e)_{,t} + \left[ (\rho e) u_j + \phi_j - u_i \tau_{ij} \right]_{,j} &= 0 \end{aligned}$$

Now the problem is to solve the above equations for given afterbody geometry and aerodynamics conditions. In most practical situations, a steady solution is looked for. Thus the unsteady equations are in fact integrated by starting from an arbitrarily initial state until a steady state is reached (if it exists). To perform integration in time, the Navier-Stokes equations are discretized, the partial derivatives with respect to time and space variables being replaced by finite difference operators. Where a solution is looked for, the discretization is accomplished by dividing the flow domain into a finite number of grid points constituting a computational mesh. This numerical procedure raises a certain number of problems which will be briefly discussed in the forthcoming Sections.

### 3.5.2 - Method of Numerical Solution

#### 3.5.2.1 - Computational Domain and Co-ordinate System

Computational Domain. In computational fluid dynamics, construction of the grid in the computational domain is perhaps as important as the solution algorithm itself. So great care must be taken in the construction of this grid to be certain that a physically realistic and sufficiently accurate solution of the discretized equations is obtained.

The computational mesh in the physical plane is generally constituted so as to satisfy the double requirements of facilitating expression of boundary conditions - in particular on the afterbody surface - and of resolving with an acceptable accuracy the regions of large gradients. These regions are essentially :

- the shock-waves and the origin of centered expansion waves ;
- the boundary-layers along the fuselage and inside the nozzle ;
- the mixing-layers developing from the separation points at the base shoulder and at the nozzle lip ;
- the wake resulting from the confluence of these mixing layers.

At this stage, a difficulty arises since the location and size of the high gradient regions within the flowfield except for the boundary-layers are not known at the start of the calculation, these regions being part of the solution. Thus the construction of the computation mesh requires some *a priori* information about the solution. This information is generally furnished by experimental results.

An example of a typical grid generated for a base-flow problem in the case of a highly underexpanded jet is shown in Fig. 84a (Deiwert, 1983). Upstream of the base, the grid is body oriented with the axial co-ordinate lines being parallel to the afterbody contour and the radial lines perpendicular to the missile axis. The radial distribution presents a high degree of stretching to resolve the sublayer of the turbulent boundary-layer. Downstream of the base, adequate stretching functions are used to focus resolution near the base corners and to achieve a smooth piecewise continuous distribution of grid points across the exhaust plume and base. In this case, the longitudinal grid lines are aligned so as to closely follow the exhaust plume shape as suggested by experimental observations (schlieren photographs).

For a conical nozzle, the flow issuing from the nozzle is generally assumed a source flow and accordingly, the points are distributed along an arc describing the conical flow at the nozzle exit. In this example, the extremely thin boundary-layer is ignored (as is done by most authors).

Another example of mesh construction is shown in Fig. 84b. This mesh is adapted to the prediction of plume induced separation on bluff-based bodies (Fox, 1984). In this example, the grid has a C-shape. The radial co-ordinate lines - or rays - are concentrated near the nozzle exit in a region practically aligned with the (guessed) plume boundary. In this way, the reattachment region with its associated trailing shock system can be accurately resolved.

In the case of highly underexpanded propulsive jets, the nozzle lip is the origin of an intense centered expansion wave which is most often insufficiently resolved by the grids usually adopted in base flow calculations. This lack of accuracy may lead to large errors in the calculation of the mixing-layer developing along the plume frontier. In particular, the necessity of introducing a certain amount of artificial viscosity (see Section 3.5.2.3) to spread the gradients at the origin of the wave is the source of "numerical entropy" that can exceed the physical entropy production by viscous dissipation.

To overcome this deficiency, Fox (1984) proposed using a boundary line located slightly downstream of the nozzle exit plane. Then, the flow conditions at the grid points placed on this boundary are computed in the vicinity of the nozzle lip by using the Method of Characteristics which allows a fine description of the flow in a corner region.

In order to solve more satisfactorily the problem of grid construction, modern computation methods introduce adaptive gridding schemes. These techniques allow a displacement of the grid lines during the iteration algorithm in such a way that grid refinements remain in regions of high gradients as the solution progresses towards convergence. In the application to base-flow calculations, adaptive mesh was utilized by Hasen (1981) and Deiwert et al. (1984).

To illustrate this technique, we will briefly present the method used by Hasen which is in fact an application of the technique introduced by Hirt et al. (1975) in the solution of free surface flows.

In Hasen's method, the following kinematic equation is applied in the region where the nozzle jet develops :

$$(49) \quad \frac{\partial r}{\partial t} = C_A (v - u \frac{\partial r}{\partial x})$$

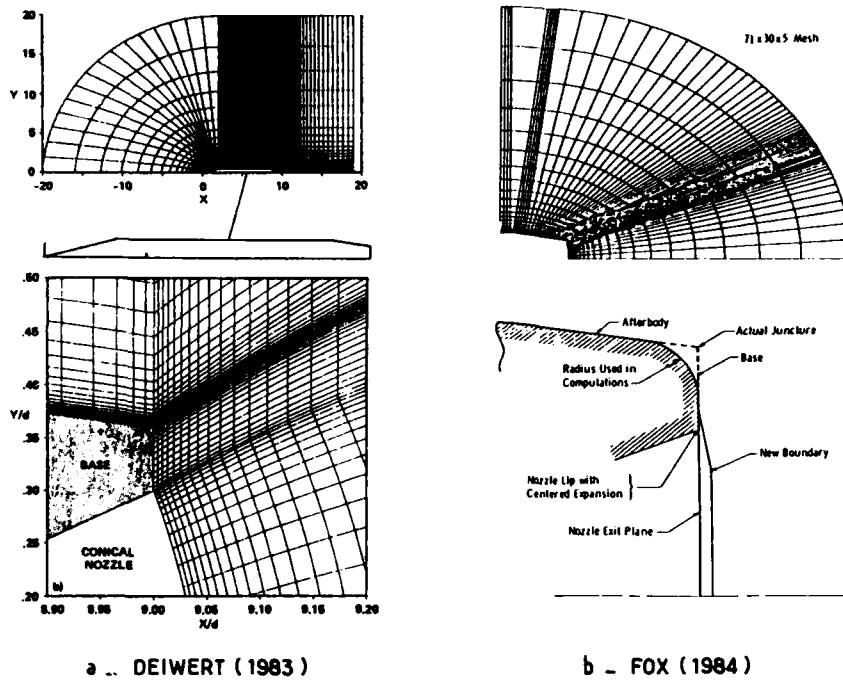


Fig. 84 - Navier-Stokes calculations - Examples of computational grid

In the above equation,  $r$  designates the distance to the axis of a longitudinal grid line and  $C_4$  is a constant specified in the range 0.3 - 0.6 in order to allow the grid to adapt smoothly as the solution converges. Equation 49 ensures the condition that the physical slope of a longitudinal grid line as the solution proceeds towards convergence is the same as that of the velocity vectors near each finite difference cell.

In fact, Eq. 49 is applied to one  $r$ -line only. This line originates from the nozzle lip for overexpanded jets and from the base shoulder for underexpanded jets. Once the location of this grid reference line is established, the fine mesh region is constructed with respect to this line. The adaptive grid scheme is applied once during every iteration of the solution algorithm at the beginning of the calculation. Once the position of the region of high shear ceases changing appreciably between two consecutive iteration numbers, the adaptive grid scheme is turned off in order to save computer time during the remainder of the solution.

Adaptive mesh techniques have now reached a high degree of sophistication; their examination would be beyond the scope of the present paper.

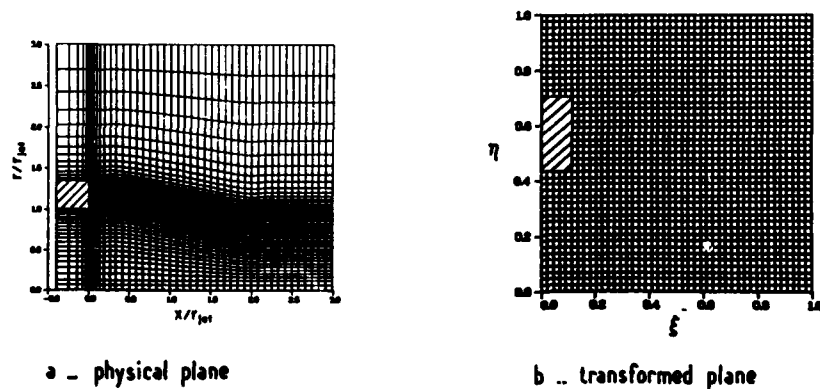


Fig. 85 - Computational co-ordinate system (Hasen, 1981)

**Computational Co-ordinate System.** For the sake of simplicity we will consider axisymmetric flows. Then the Navier-Stokes equations are generally discretized in a transformed plane whose co-ordinate lines  $\xi, \eta$  are such that the constant  $\eta$  lines correspond to the axial co-ordinate lines of the physical plane and the constant  $\xi$  lines to the radial lines (see Fig. 85). Thus a co-ordinate transformation of the following form is carried out :

$$\xi = \xi(X, r, t) ; \quad \eta = \eta(X, r, t) ; \quad \tau = t$$

Hence, if we consider the formulation adopted by Hasen (1981), the Navier-Stokes equations in the transformed  $(\xi, \eta)$  cartesian plane can be written in the matrix form (for an axisymmetric flow) :

$$(50) \quad \frac{\partial \mathbf{U}}{\partial \tau} + \left[ \xi_x \frac{\partial \mathbf{F}}{\partial \xi} + \frac{1}{r} \xi_r \frac{\partial (r, \mathbf{G})}{\partial \xi} \right] + \left[ \eta_x \frac{\partial \mathbf{F}}{\partial \eta} + \frac{1}{r} \eta_r \frac{\partial (r, \mathbf{G})}{\partial \eta} \right] = \frac{\mathbf{H}}{r}$$

in which :

$$\mathbf{U} = \begin{pmatrix} \rho \\ \rho u \\ \rho v \\ \rho e \end{pmatrix} \quad \mathbf{F} = \begin{pmatrix} \rho u \\ \rho u^2 - \sigma_{xx} \\ \rho uv - \tau_{xr} \\ \rho ue + \dot{\phi}_x - u\sigma_{xx} - v\tau_{xr} \end{pmatrix}$$

$$\mathbf{G} = \begin{pmatrix} \rho v \\ \rho uv - \tau_{xr} \\ \rho v^2 - \sigma_{rr} \\ \rho ve - \dot{\phi}_r - u\tau_{xr} - v\sigma_{rr} \end{pmatrix} \quad \mathbf{H} = \begin{pmatrix} 0 \\ 0 \\ -\sigma_H \\ 0 \end{pmatrix}$$

where :

$$\sigma_{xx} = -p + (\lambda + \lambda_t) \operatorname{div} \vec{V} + 2(\mu + \mu_t) \frac{\partial u}{\partial x}$$

$$\sigma_{rr} = -p + (\lambda + \lambda_t) \operatorname{div} \vec{V} + 2(\mu + \mu_t) \frac{\partial v}{\partial r}$$

$$\sigma_H = -p + (\lambda + \lambda_t) \operatorname{div} \vec{V} + 2(\mu + \mu_t) \frac{v}{R}$$

$$\tau_{xr} = (\mu + \mu_t) \left( \frac{\partial u}{\partial r} + \frac{\partial v}{\partial x} \right)$$

$$\dot{\phi}_x = -C_p \left( \frac{\mu}{Pr} + \frac{\mu_t}{Pr_t} \right) \frac{\partial T}{\partial x}$$

$$\dot{\phi}_r = -C_p \left( \frac{\mu}{Pr} + \frac{\mu_t}{Pr_t} \right) \frac{\partial T}{\partial r}$$

$$\operatorname{div} \vec{V} = \frac{\partial u}{\partial x} + \frac{\partial v}{\partial r} + \frac{v}{r}$$

The second coefficients of viscosity are expressed by applying Stokes Hypothesis :

$$(\lambda + \lambda_t) = -\frac{2}{3}(\mu + \mu_t)$$

The above four scalar equations constitute a system enabling the calculation of the four dependent variables  $\rho, \rho u, \rho v$  and  $\rho e$ , the molecular viscosity of air  $\mu$  being computed by Sutherland's formula, the pressure  $p$  by the perfect gas law and the turbulent viscosity given by a suitable model (see Section 3.5.3).

The transformation derivatives  $\xi_x, \xi_r, \eta_x, \eta_r$  figuring in Eq. 50 are obtained numerically from a mapping procedure. Equation 50 is actually in **weak** conservative form because of the varying coefficients in front of derivatives and also because of the source term  $\mathbf{H}$  in the axisymmetric case.

The above equations are the **full** time-averaged Navier-Stokes equations. However, certain authors (Sahu et al., 1982 ; Deiwert, 1983 ; Fox, 1984) have solved a simplified form of these equations known as the **thin layer** approximation. This approximation consists in neglecting the viscous terms containing derivatives along one direction of the transformed co-ordinates  $(\xi, \eta)$ . As seen above, the mesh in the physical plane is usually constructed in such a way that the regions of high shear (namely, the boundary-layers, the plume mixing-layers, the wake), develop, approximately along constant  $\eta$  lines. Thus if these lines have been judiciously chosen, it seems legitimate to consider the  $\xi$ -derivatives as negligible compared to the  $\eta$ -derivatives in the viscous terms.

Hence, adopting the formulation of Deiwert (1983), the thin layer approximation of the Navier-Stokes equations can be written in the following **strong** conservative form :

$$(51) \quad \frac{\partial \mathbf{q}}{\partial \tau} + \frac{\partial \mathbf{E}}{\partial \xi} + \frac{\partial \mathbf{F}}{\partial \eta} + \mathbf{H} = \frac{\partial \mathbf{S}}{\partial \eta}$$

where :

$$q = J^{-1} \begin{vmatrix} Q \\ Q_u \\ Q_v \\ e \end{vmatrix} \quad E = J^{-1} \begin{vmatrix} Q u \\ Q u U + \xi_x p \\ Q v U + \xi_r p \\ (e + p) U - \xi_r p \end{vmatrix}$$

$$F = J^{-1} \begin{vmatrix} Q V \\ Q u V + \eta_x p \\ Q v V + \eta_r p \\ (e + p) V - \eta_r p \end{vmatrix} \quad H = J^{-1} \begin{vmatrix} 0 \\ 0 \\ p/\eta \\ 0 \end{vmatrix}$$

$$S = J^{-1} \begin{vmatrix} 0 \\ (\mu + \mu_t) \left[ (\eta_x^2 + \eta_r^2) \frac{\partial u}{\partial \eta} + \frac{1}{3} (\eta_x \frac{\partial u}{\partial \eta} + \eta_r \frac{\partial v}{\partial \eta}) \eta_x \right] \\ (\mu + \mu_t) \left[ (\eta_x^2 + \eta_r^2) \frac{\partial v}{\partial \eta} + \frac{1}{3} (\eta_x \frac{\partial u}{\partial \eta} + \eta_r \frac{\partial v}{\partial \eta}) \eta_r \right] \\ (\eta_x^2 + \eta_r^2) \left[ 0.5 (\mu + \mu_t) \frac{\partial}{\partial \eta} (u^2 + v^2) + C_p \left( \frac{\mu}{P_r} + \frac{\mu_t}{P_{rt}} \right) \frac{\partial T}{\partial \eta} \right] \\ + \frac{1}{3} (\mu + \mu_t) (\eta_x u + \eta_r v) (\eta_x \frac{\partial u}{\partial \eta} + \eta_r \frac{\partial v}{\partial \eta}) \end{vmatrix}$$

The velocities  $U = \xi_r + \xi_x u + \xi_r v$  and  $V = \eta_r + \eta_x u + \eta_r v$  represent the contravariant velocity components in the  $\xi$  and  $\eta$  directions respectively.

The metric terms of Eq. 51 are defined from :

$$\xi_x = J \eta_{r\eta} \quad \xi_r = -J \eta_{x\eta} \quad \xi_t = J \eta (X_{\eta r r} - X_{r \eta})$$

$$\eta_x = -J \eta_{r\xi} \quad \eta_r = J \eta_{x\xi} \quad \eta_t = -J \eta (X_{r \eta} + r \eta_{r\xi})$$

with:

$$J^{-1} = \eta (X_{\xi r \eta} - X_{\eta r \xi})$$

These expressions are obtained by solving the chain rule expansion of derivatives of the cartesian co-ordinates ( $X, r$ ) with respect to the curvilinear co-ordinates ( $\xi, \eta$ ).

The thin layer approximation to the **three dimensional** time-averaged Navier-Stokes can be found in Deiwert and Rothmund (1983). These will not be given here.

Sahu et al. (1982) considered the intermediate case of an axisymmetric flow with a non-zero circumferential velocity. In this formulation, a third momentum equation for the circumferential motion is retained but the equations contain only spatial derivatives with respect to the co-ordinates  $\xi$  and  $\eta$  in a meridian plane. This formulation allows the calculation of flows past spinning projectiles and also of swirl flows.

As already mentioned, a steady state solution of the Navier-Stokes equations is looked for in most applications. Thus, the conditions imposed on the boundaries of the computational domain must be such that a steady state solution actually exists. This question will now be examined.

### 3.5.2.2 - The Boundary Conditions

In the external flow, an **upstream boundary** AB (see Fig. 86) is chosen at some distance upstream of the base, this distance depending on the existence of a boattail or a flare and also of the possible occurrence of plume induced separation on the fuselage. Most often AB is located at 2 or 3 calibers upstream of the base.

If the incoming flow is supersonic (except in the very thin subsonic part of the turbulent boundary-layer), the four components of the unknown vector  $U$  must be prescribed on AB. These conditions can be supplied either by a preliminary calculation of the flow on the front part of the missile (Deiwert, 1983; Sahu et al., 1982; Thomas et al., 1984; Ravalason, 1985), or obtained from experiment (Hasen, 1981; Fox, 1984; Wagner, 1984).

A similar procedure is adopted for the conditions imposed at the nozzle exit FH. These conditions are given either by a Navier-Stokes calculation of the flow inside the nozzle (Thomas et al., 1984), or more simply, by an inviscid conical solution while ignoring the extremely thin boundary-layer (Deiwert, 1983; Fox, 1984; Wagner, 1984).

For the **lateral boundary** BC, two types of approaches can be adopted :

- i - assuming uniform freestream conditions if this boundary is far enough from the base-flow region (Sahu et al., 1982; Deiwert, 1983; Fox, 1984);
- ii - assuming a simple wave solution which consists in writing that flow properties are constant along left running characteristics crossing this boundary (Hasen, 1981).

The **downstream boundary** CD is unique in that no rigorous assumptions can be made about the variables or their gradients (except if the outgoing flow is entirely supersonic). In practice, this boundary is placed at a sufficient distance downstream that simple extrapolation of the flow variables is used which is expressed by setting the  $\xi$ -derivative of all quantities at zero. When these gradients are not very small, Hasen uses a more refined treatment assuming that a flow gradient accurate to second order can exist.

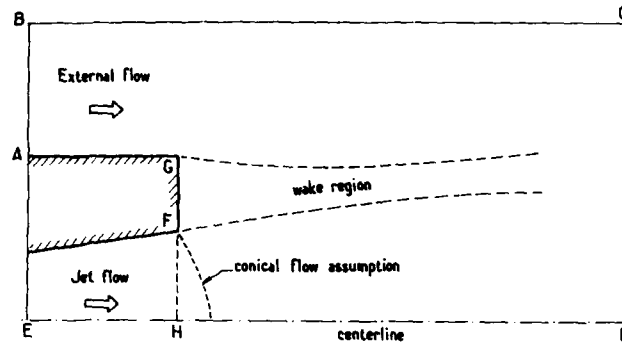


Fig. 86 - Physical domain and boundary conditions

On the afterbody surface AGF, the usual no-slip condition must be prescribed. However, since the meshes used are generally not refined enough to resolve the boundary layer building up on the base, a slip condition is often imposed on GF. The pressure at the wall is usually determined by writing that its derivative normal to the surface is zero.

The thermal condition on the wall can be either a prescribed surface temperature or a zero heat flux condition (adiabatic wall).

On the centerline ED, symmetry conditions are applied.

### 3.5.2.3 - The Technique of Numerical Integration

Since generally a steady state solution is looked for, the consideration of the time dependent Navier-Stokes equations can be viewed as a stratagem used to take advantage of the hyperbolic nature of these equations with respect to time. Thus a final steady flowfield is sought by advancing the solution in time starting from a more or less arbitrary initial flowfield until a converged state is reached, i.e., a state for which all time derivatives are zero (which implies that the prescribed boundary conditions be compatible with the steady solution). In this perspective, time can be viewed as a simple iteration parameter; calculation methods frequently take advantage of this fact to accelerate convergence speed.

Several numerical techniques have been used to solve the time-dependent Navier-Stokes equations applied to base flow problems. This paper does not aim at reviewing these techniques which involve complex mathematical problems. However, as an illustration of the numerical aspects of the Navier-Stokes approach, we will present one of these techniques which has the merit of being conceptually simple. This integration method is the popular Mac Cormack scheme (Mac Cormack 1969, 1970).

The original Mac Cormack scheme is an explicit scheme consisting of predictor and corrector steps which when applied to Eq. (50) yields :

Predictor step

$$\begin{aligned} \bar{U}_{i,j}^{n+1} = & U_{i,j}^n - \frac{\Delta t}{\Delta \xi} \left[ (\xi_x)_{i,j} (F_{i,j}^n - F_{i-1,j}^n) + \frac{1}{r_{i,j}} (\xi_r)_{i,j} (r_{i,j} G_{i,j}^n - r_{i-1,j} G_{i-1,j}^n) \right] \\ & - \frac{\Delta t}{\Delta \eta} \left[ (\eta_x)_{i,j} (F_{i,j}^n - F_{i,j-1}^n) + \frac{1}{r_{i,j}} (\eta_r)_{i,j} (r_{i,j} G_{i,j}^n - r_{i,j-1} G_{i,j-1}^n) \right] + \Delta t H_{i,j} / r_{i,j} \end{aligned}$$

Corrector step

$$\begin{aligned} U_{i,j}^{n+1} = & \frac{1}{2} \left\{ U_{i,j}^{n+1} + U_{i,j}^n - \frac{\Delta t}{\Delta \xi} \left[ (\xi_x)_{i,j} (\bar{F}_{i+1,j}^{n+1} - \bar{F}_{i,j}^{n+1}) + \frac{1}{r_{i,j}} (\xi_r)_{i,j} (r_{i+1,j} \bar{G}_{i+1,j}^{n+1} - r_{i,j} \bar{G}_{i,j}^{n+1}) \right] \right. \\ & \left. + \frac{\Delta t}{\Delta \eta} \left[ (\eta_x)_{i,j+1} (\bar{F}_{i,j+1}^{n+1} - \bar{F}_{i,j}^{n+1}) + \frac{1}{r_{i,j}} (\eta_r)_{i,j} (r_{i,j+1} \bar{G}_{i,j+1}^{n+1} - r_{i,j} \bar{G}_{i,j}^{n+1}) \right] + \Delta t H_{i,j} / r_{i,j} \right\} \end{aligned}$$

In the above expressions, the (i,j) subscripts and the n superscript correspond to the  $\xi$ -,  $\eta$ - and t- positions in the discretized finite difference mesh such that  $\xi = i\Delta\xi$ ,  $\eta = j\Delta\eta$  and  $t = n\Delta t$ . A bar above the n superscript indicates a predicted value. Backward differences are used in the predictor step to approximate the derivatives of F and (rG) while forward differences are used for these derivatives in the corrector step. In the predictor step, forward differences are used to approximate the stress and heat flux derivatives appearing in F and G while in the corrector step, backward differences are used.

The method being explicit, the maximum allowable time step must satisfy conditions known as the Courant-Friedrichs-Lewy (CFL) stability conditions. This criterion fixes a maximum value for  $\Delta t$  which is determined by the minimum grid spacing  $\Delta\xi$  or  $\Delta\eta$ , i.e., the finer the spatial grid, the smaller the allowable time step. The problem of the computation scheme stability will not be discussed here.

As we know, the mesh must be highly refined in turbulent flows to resolve the flow in regions like the boundary-layers and the mixing-layers. Thus the CFL condition imposes extremely small time steps. There results very long computing times to achieve a reasonably converged solution.

Since the unsteady phase of the calculation is generally of no interest, it is possible to save on computing time by adopting a local time step (for example, see Holst, 1977). This technique consists in advancing the solution with different time steps within the mesh, the local  $\Delta t$  being determined by the  $\Delta \xi$  and the  $\Delta \eta$  in the region of the mesh where the solution is advanced. Other procedures not cited here can be employed to reduce the computing time while maintaining good accuracy.

The numerical process advancing the solution from  $t$  to  $t + \Delta t$  can be interpreted as the application of an operator  $L(\Delta t)$  to the solution of the flowfield at time  $t$ . This can be written as :

$$U(\xi, \eta, t + \Delta t) = L(\Delta t) \cdot U(\xi, \eta, t)$$

In order to improve numerical efficiency, the two-dimensional operator  $L(\Delta t)$  is sometimes split into two one-dimensional operators  $L_\xi$  and  $L_\eta$ . This method is commonly known as the method of alternating directions. In this case the solution is advanced in time by the following sequence :

$$(52) \quad U(\xi, \eta, t + \Delta t) = \left[ L_\xi^{M/2} \left( \frac{\Delta t}{M} \right), L_\eta(\Delta t), L_\xi^{M/2} \left( \frac{\Delta t}{M} \right) \right] \cdot U(\xi, \eta, t)$$

$$\text{with: } \Delta t = \Delta t_\xi \quad \text{if } \Delta t_\xi < \Delta t_\eta$$

or

$$(53) \quad U(\xi, \eta, t + \Delta t) = \left[ L_\eta^{N/2} \left( \frac{\Delta t}{N} \right), L_\xi(\Delta t), L_\eta^{N/2} \left( \frac{\Delta t}{N} \right) \right] \cdot U(\xi, \eta, t)$$

$$\text{with: } \Delta t = \Delta t_\eta \quad \text{if } \Delta t_\eta < \Delta t_\xi$$

In these equations,  $M$  and  $N$  are the smallest even integers of the quotients  $(\Delta t_\eta / \Delta t_\xi)$  and  $(\Delta t_\xi / \Delta t_\eta)$  respectively and  $\Delta t_\xi$  and  $\Delta t_\eta$  are the maximum allowable time steps in the  $\xi$  and  $\eta$  directions as determined by the CFL limit. The operators  $L_\xi$  and  $L_\eta$  contain only derivatives of  $F$  and  $G$  with respect to  $\xi$  and  $\eta$  respectively.

The symmetrical form of (52) and (53) is adopted to maintain second order accuracy (for details, see Mac Cormack, 1970 and for application to base flow calculations, Hasen, 1981).

A still greater numerical efficiency can be obtained by using implicit schemes. Such schemes avoid the restrictive stability conditions on the time step of the explicit methods, thus allowing a more rapid convergence of the solution towards the steady state. The most widely used implicit schemes are probably those of Beam and Warming (1976) and Lerat et al. (1984). Also, the Mac Cormack hybrid scheme including both implicit and explicit operators should be mentioned (Mac Cormack, 1979). Implicit schemes lead to relatively complicated mathematical expressions and involve the use of more complex solution algorithms. For these reasons they will not be discussed here.

In order to damp out numerical oscillations which would otherwise occur in regions of rapid flow variations (more particularly shock-waves), damping terms  $FD$  and  $GD$  must be added to  $F$  and  $G$ . These extra terms behave like viscous terms and they are such that their influence on the solution is (in principle) negligible outside regions of infinite gradients (for details on these terms in a base-flow application, see Hasen, 1981).

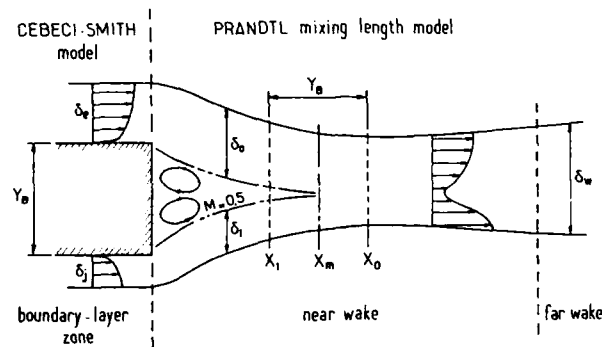


Fig. 87 - Hasen's turbulence modeling in the viscous regions (Hasen, 1981)

### 3.5.3 - The Problem of Turbulence Modeling

#### 3.5.3.1 - Algebraic Turbulence Models

As shown in Fig. 87, the computational domain considered by Hasen contains three distinct regions where different turbulent viscosity models are applied. These regions are : the boundary-layers, the far wake, and the near-wake close to the base.

In the boundary-layer zone, the turbulent viscosity is represented by the Cebeci-Smith two-layer algebraic turbulence model (Cebeci et al., 1970).

In the inner region close to the surface, the expression for  $\mu_t$  is based on Prandtl's mixing length hypothesis, which gives :

$$\mu_{ti} = \rho l^2 \left| \frac{\partial u_i}{\partial y_n} \right|$$

where  $u_r$  is the local velocity component parallel to the wall and  $y_n$  the normal distance from the wall. In this model, the mixing length  $l$  is adapted from Van Driest's sublayer model and is given by :

$$l = 0.4 y_n \left[ 1 - \exp \left( - \frac{y_n}{26\mu} \sqrt{Q \tau_w} \right) \right]$$

$\tau_w$  being the local value of the wall shear stress.

In the outer region,  $\mu_t$  is given by a Clauser-type expression :

$$\mu_{t0} = 0.0168 Q u_{re} \delta_i^* \gamma$$

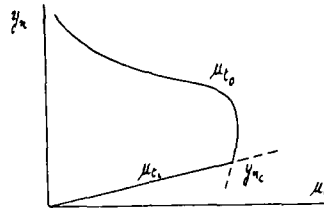
where  $u_{re}$  is the tangential velocity component at the boundary-layer edge and :

$$\delta_i^* = \int_0^{\delta} \left( 1 - \frac{u_r}{u_{re}} \right) dy_n$$

is the "incompressible" displacement thickness.  $\gamma$  designates the Klebanoff intermittency function :

$$\gamma = \left[ 1 + 5.5 \left( \frac{y_n}{\delta} \right)^6 \right]^{-1}$$

As shown in the sketch below, the inner model is applied outward from the wall until  $\mu_{ti} = \mu_{t0}$  at a distance  $y_{nc}$  ; the outer model is then applied from  $y_{nc}$  outward across the remainder of the flow field in the boundary-layer region.



In the far wake zone, the viscosity is computed by a mixing length type expression :

$$(54) \quad \mu_t = Q l^2 |\omega|$$

where  $\omega$  is defined as the vorticity:  $\omega = \frac{\partial u}{\partial r} - \frac{\partial v}{\partial x}$  and  $l$  is given by :

$$l = 0.065 \delta_w$$

where  $\delta_w$  is the wake thickness determined from the distribution of vorticity.

The near-wake region is constituted by the merging of the boundary-layers which separate at the base shoulder and at the nozzle lip. This part of the flowfield contains the dead-air region, the confluence region and the origin of the far wake. Turbulence modeling in such a complex flow is extremely difficult and no really convincing model based on sound physical arguments exists for the base region. Thus, Hasen has adopted a simple algebraic representation ensuring continuity between the boundary-layers and the far wake region.

In the near-wake,  $\mu_t$  is still computed by the mixing length law (54) with length scales that transition from the appropriate boundary-layer thickness upstream to the far wake mixing length downstream.

This transition is accomplished in the following way : referring to Fig. 87 for notations, in the dead-air region the thickness  $\delta$  is defined from the Mach 0.5 contour line, the outer edges of near-wake being detected from the vorticity profiles.

Thus, one adopts :

$$\delta = \delta_E \quad \text{in the external flow,}$$

$$\delta = \delta_J \quad \text{in the jet flow}$$

$$\delta = 0.5 (\delta_E + \delta_J) \quad \text{inside the Mach 0.5 contour line enclosing the dead-air region (the } \delta \text{ distribution is not continuous transversally).}$$

Between the base region and the far wake, a blending zone is introduced in which a continuous evolution of the length scales is accomplished by means of the following interpolation formula :

$$\delta(x) = \delta_w|_{x_0} - (\delta_w|_{x_0} - \delta_E \text{ or } \delta_J|_{x_1}) \exp(-k_I)$$

$$\text{where : } k_I = 2 \left( \frac{x_m}{H_B} + \frac{x}{H_B} - 0.5 \right)$$

$H_B$  represents the width of the base and  $x$  varies within the range :

$$x_m - 0.5 H_B < x < x_m + 0.5 H_B$$

The central abscissa  $x_m$  is such that  $x_m = 2r_B$ .



The algebraic model proposed by Baldwin and Lomax (1978) is frequently used in Navier-Stokes calculations, this model using length scales that do not necessitate the sometimes delicate localization of the edge of the dissipative regions. In base flow calculations, the Baldwin-Lomax model was used in particular by Sahu et al., (1982); Deiwert (1983); Wagner (1984); Ravalason (1985).

This model is moreover a two-layer model. In the inner region the classical Prandtl-Van Driest formulation is adopted :

$$\mu_{ti} = Q I^2 |\omega|$$

$$\text{with : } I = 0.4 y_n \left[ 1 - \exp \left( - \frac{y_n}{26 \mu_w} \sqrt{Q_w \tau_w} \right) \right]$$

$|\omega|$  being the magnitude of the local vorticity.

In the outer region,  $\mu_t$  is determined in the following way :

$$\mu_{to} = 0.0168 C_I F_w F_k (y_n) \quad \text{with } C_I = 1.6$$

$$F_w = \left\{ \begin{array}{l} (y_n)_{max} F_{max} \\ 0.25 (y_n)_{max} \frac{U_d^2}{F_{max}} \end{array} \right\} \quad \text{the smaller}$$

The quantities  $(y_n)_{max}$  and  $F_{max}$  are determined from the function :

$$(55) \quad F(y) = y |\omega| \left[ 1 - \exp \left( - \frac{y_n \sqrt{Q_w \tau_w}}{26 \mu_w} \right) \right]$$

Thus  $F_{max}$  is the maximum value of  $F(y)$  and  $(y_n)_{max}$  is the value of  $y_n$  at which it occurs.

$U_d$  is the difference between the maximum and minimum (total) velocity in the profile (component along a  $\xi$  co-ordinate line), hence :

$$U_d^2 = (u^2 + v^2)_{max} - (u^2 + v^2)_{min}$$

The function  $F_k (y_n)$  is a modified form of the Klebanoff intermittency function :

$$F_k (y_n) = \left\{ 1 + 5.5 \left[ 0.6 \frac{y_n}{(y_n)_{max}} \right]^6 \right\}^{-1}$$

In applications to base-flows, the outer formulation is adopted in the free-shear flow regions (exhaust jet and wake) as well as over regions of separated flows. Then, the Van Driest damping term figuring in (55) is neglected.

In the above formulæ,  $y_n$  represents a distance along the direction of maximum shear (the distance from the wall in the case of a boundary-layer). In Navier-Stokes calculations using the thin-layer approximation,  $y_n$  is identified with the co-ordinate  $\eta$ . Of course, the mesh must be constructed so as to satisfy this condition.

The last algebraic model considered here was used by Sullins et al. (1982) to compute supersonic base-flows with parallel injection. Although these calculations concern the base region of a fuel injection strut of a supersonic combustion ramjet engine, the model could be considered for a missile application.

In the boundary-layer upstream of the base, the Cabeci-Smith two-layer mixing length model is employed. In the far wake, the turbulent viscosity is given by the "equilibrium" formula :

$$(56) \quad \mu_{tEQ} = 0.064 Q u_{ei} \theta_i \gamma$$

In this relation  $\gamma$  is the Klebanoff intermittency function and  $\theta_i$  the "incompressible" momentum thickness defined by :

$$\theta_i = \int_0^{\delta} \frac{u_t}{u_{te}} \left( 1 - \frac{u_t}{u_{te}} \right) dy_n$$

Transition from the base to the far wake is simulated by using an exponential equation inspired from the Waskiewicz et al. (1980) relaxation eddy viscosity model. Thus if  $x$  designates distance from the base,  $\mu_{tEQ}$  the local equilibrium viscosity given by (56) and if  $\mu_{tTE}$  is the viscosity calculated at the base trailing-edge, the local viscosity in the transition region is given by :

$$\frac{\mu_t - \mu_{tTE}}{\mu_{tEQ} - \mu_{tTE}} = \left[ 1 - \exp \left( - \frac{x}{\lambda \delta_{TE}} \right) \right]$$

In this equation,  $\delta_{TE}$  is the boundary-layer thickness at the base shoulder and  $\lambda$  a "relaxation" length scale. The best results were obtained with  $\lambda = 50$ .

### 3.5.3.2 - Transport Equation Models

Thomas et al. (1984) performed base flow calculations with turbulence models using several types of transport equations for turbulent quantities. Among these models, we shall consider here the well known [  $k, \epsilon$  ] model in which the turbulent viscosity is expressed according to the relation :

$$\mu_t = C_\mu Q \frac{k^2}{\epsilon}$$

where  $k$  is the turbulence kinetic energy and  $\epsilon$  its dissipation rate,  $C_\mu$  being a constant taken equal to 0.09.

The two quantities  $k$  and  $\epsilon$  are computed by transport equations of the form (see Jones and Launder, 1972) :

$$\frac{\partial}{\partial t} (\rho k) + \nabla \cdot (\rho \vec{V} k) = P - \rho \epsilon + \nabla \cdot \left( \frac{\mu_t}{\sigma_k} \nabla k \right)$$

$$\frac{\partial}{\partial t} (\rho \epsilon) + \nabla \cdot (\rho \vec{V} \epsilon) = C_{\epsilon 1} \frac{\epsilon}{k} P - C_{\epsilon 2} \rho \frac{\epsilon^2}{k} + \nabla \cdot \left( \frac{\mu_t}{\sigma_\epsilon} \nabla \epsilon \right)$$

where  $P$  represents the production term :

$$P = \bar{S} : \nabla \vec{V}$$

which can also be written with tensor notations :

$$P = \tau_{ij} \frac{1}{2} \left( \frac{\partial u_i}{\partial x_j} + \frac{\partial u_j}{\partial x_i} \right)$$

The following values are adopted for the constants :

$$\sigma_k = 1.0 \quad ; \quad \sigma_\epsilon = 1.3 \quad ; \quad C_{\epsilon 1} = 1.57 \quad ; \quad C_{\epsilon 2} = 1.92$$

The above transport equations are solved in tandem with the Navier-Stokes equations.

In fact, these equations apply only in high Reynolds number flow regions, i.e., far from the wall. In the low speed region of the boundary-layers, some special treatment must be adopted. In the present applications, the near wall region is computed by using an algebraic mixing length model with the Van Driest damping function (see above). The edge of this inner layer is positioned just outside the laminar sublayer.

Boundary conditions for the two transported quantities at this edge are obtained from the dual condition that the eddy viscosity be continuous across the edge and that the turbulent kinetic energy be in local equilibrium (i.e., production of  $k$  = dissipation of  $k$ ).

Calculations of the flow past transonic projectiles with a  $(k, \epsilon)$  model have also been performed by Sahu and Danberg (1984).

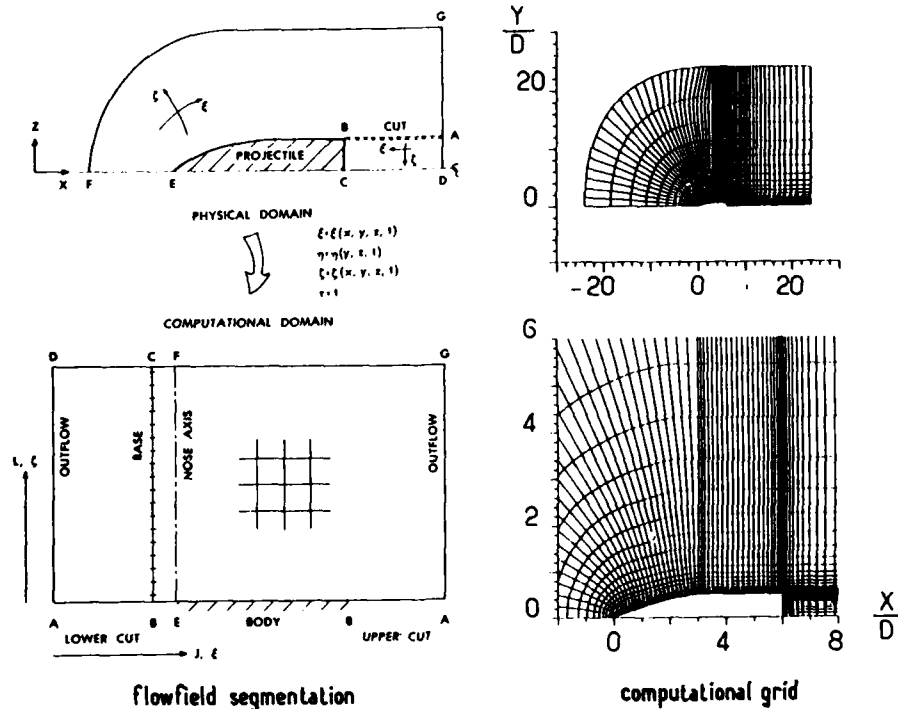


Fig. 88 - Sahu et al. numerical procedure (Sahu et al., 1983)

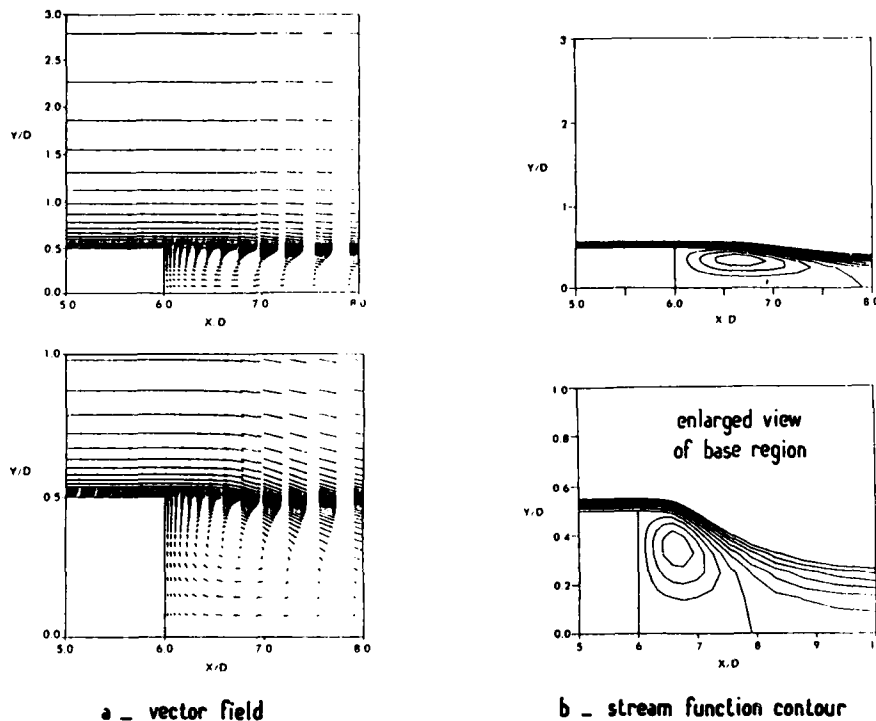


Fig. 89 - Base flow behind a projectile -  $M_\infty = 0.9$   
(Sahu et al., 1982)

### 3.5.4 - Applications to Base-Flow Calculations

In this Section, we shall concentrate on base flow calculations applied to projectile and missile afterbodies. Thus we exclude application of the Navier-Stokes approach to the calculation of wake flows; neither shall we consider plume calculations, although these applications are specially important for detection problems (see Sinha and Dash, 1985).

The first applications considered here deal with turbulent base flows without jet for an axisymmetric geometry. Such flows have been extensively studied by Sahu and co-workers. Although their calculations are relative to artillery shells, the numerical method as well as certain results are of interest for missiles in the jet-off situation.

In the method developed by Sahu et al. (1982, 1983) which uses the Baldwin-Lomax turbulence model, the flowfield is segmented as shown in Fig. 88. This segmentation is employed to compute the entire projectile flowfield including the base-flow. The figure also shows the transformation of the physical domain into the computational domain and the details of the segmentation procedure in both the domains.

The cross hatched region represents the projectile. The line BC is the projectile base and the region ABCD is the base region or the wake. The line AB is a computational cut through the physical wake region which acts as a repetitive boundary in the computational domain. Implicit integration using the Beam-Warming algorithm is carried out in both  $\xi$  and  $\eta$  directions. The presence of the lines BC (the base) and EF (nose axis) in the computational domain should be noted.

According to authors, an important advantage of this procedure lies in the preservation of the sharp corner at the base and allows easy blending of the computational meshes between regions ABCD and AEF. In contrast with methods where the sharp corner must be replaced by a rounded corner to avoid numerical difficulties (see in particular Fox, 1984), no approximation of the actual sharp corner at the base is made.

The method allows the prediction of base-bleed effect which is a very effective means for increasing base pressure, thus reducing base drag. In that case, the velocity and the stagnation temperature of the injected gas are prescribed. The injected mass flow rate  $\dot{q}_B$  depends on the solution since the density of the injected gas depends on the base pressure  $p_B$ . Thus if  $\dot{q}_B$  is prescribed, an iteration loop has to be introduced into the calculation procedure (see Sahu, 1986).

Results for a projectile flying at  $M_\infty = 0.9$  without base-bleed are presented in Fig. 89. As we see, the computation faithfully reproduces the recirculating flow at the base.

As demonstrated by Fig. 90, application of base bleed entails a progressive contraction, as the injection rate  $\dot{I}_B$  is increased, until complete vanishing of the recirculating zone ( $\dot{I}_B$  is defined as the ratio of the injected mass flow rate to the mass flow rate of upstream flow that would pass through an area corresponding to the projectile caliber).

Figures 91a and 91b show the variation of base drag and total drag with Mach number in the transonic range. The reduction of drag due to base-bleed is extremely significant.

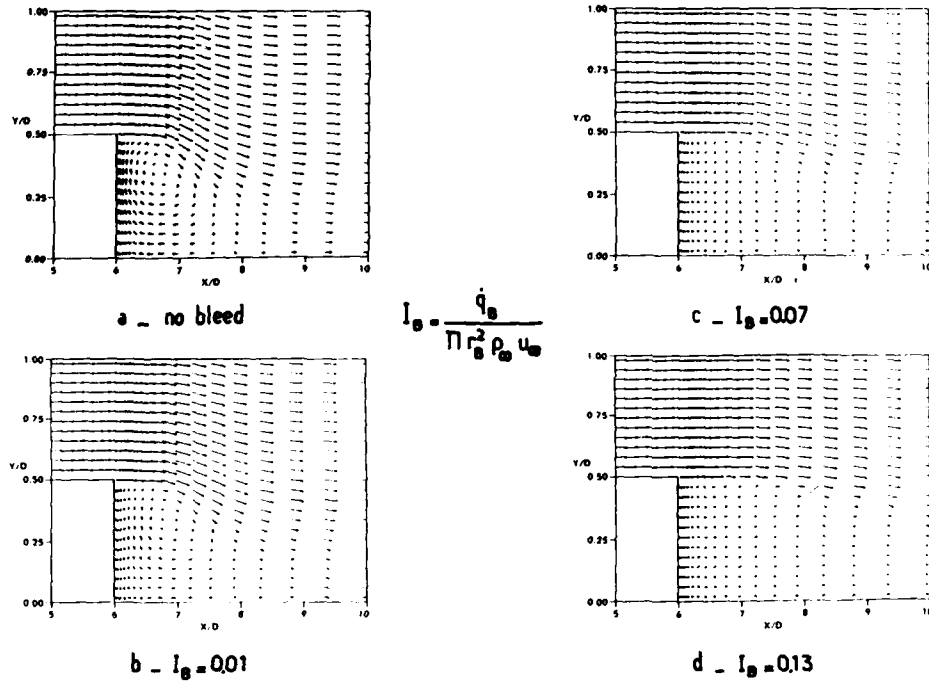


Fig. 90 - Base flow behind a projectile -  $M_\infty = 0.9$  - Base bleed effect (Sahu et al., 1983)

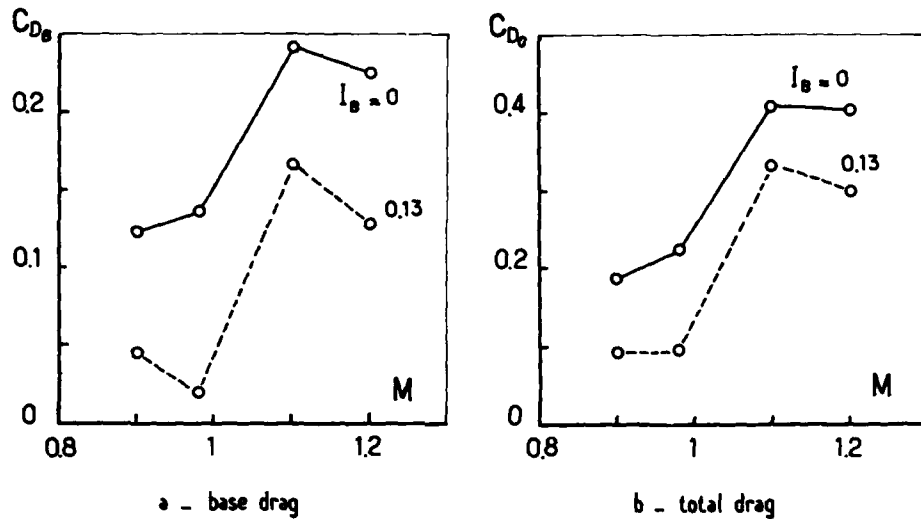


Fig. 91 - Effect of base-bleed on a projectile drag in the transonic range (Sahu et al., 1983)

Further applications to supersonic flows were published by Sahu (1986). Comparison of these calculations with experiment shows generally good agreement.

Base flow calculation in the jet-off condition were also performed by Revalason (1985, see also Hollanders and Revalason, 1986). The numerical method uses a two step procedure : an intermediate solution is computed with an explicit predictor-corrector scheme which is a generalization of the Thommen scheme (Thommen, 1966). This solution is then corrected by an implicit operator (see Lerat et al., 1984). The Baldwin-Lomax turbulence model is also used. Results obtained at high subsonic velocities are in good agreement with experiment.

Applications to base flow with exhaust jet will now be considered.

Ample information on the method developed by Hasen has already been given (see Section 3.5.2). In the present application, the Mach number of the external stream is equal to 1.94 and the jet Mach number in the exit plane is equal to 3. The Mach number contour lines computed for increasing values of the nozzle expansion ratio are represented in Fig. 92. These results are in fair agreement with observed jet structures with the shock pattern being particularly well reproduced.

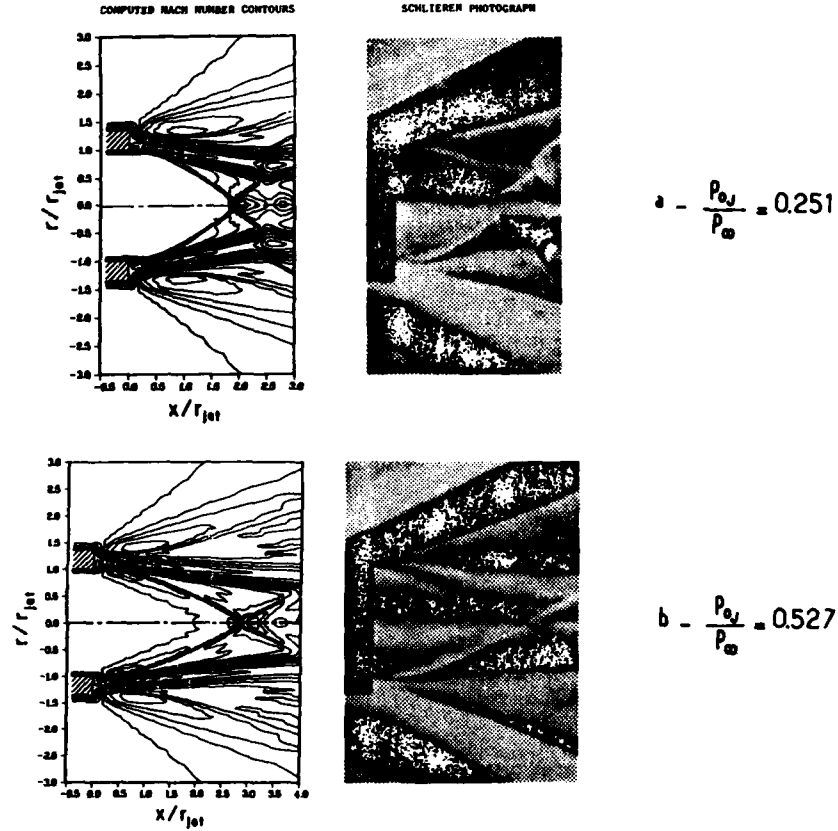


Fig. 92 - Axisymmetric coflowing nozzle solutions  
 $M_\infty = 1.94, M_{0j} = 3$  (Hasen, 1981)

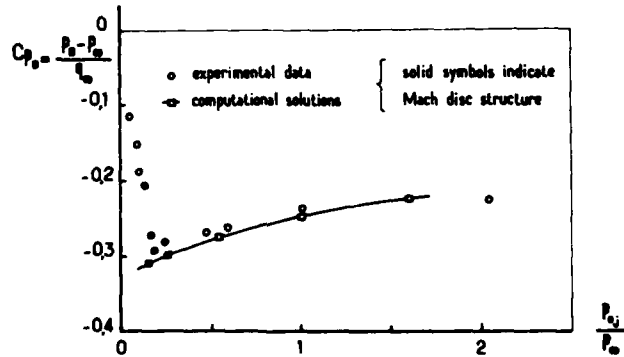
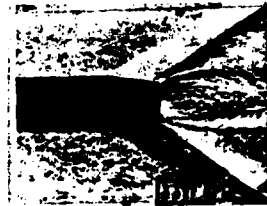
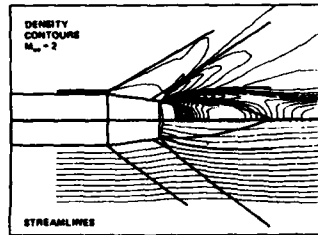


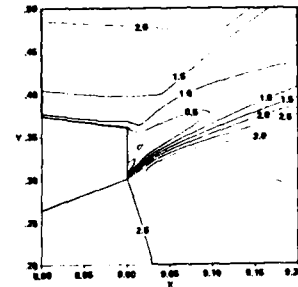
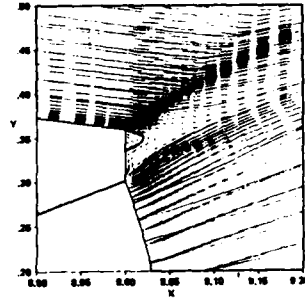
Fig. 93 - Evolution of base pressure coefficient  
 (Hasen, 1981)



a - general flow structure

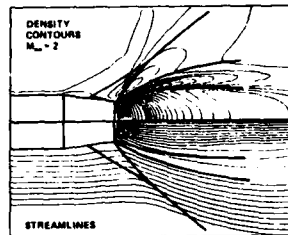
( AGRELL and WHITE 1974 )

$$\frac{p_{e_j}}{p_\infty} = 3$$



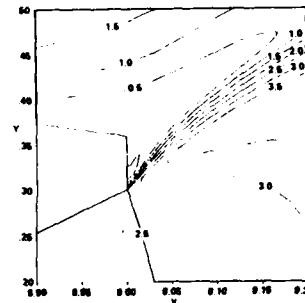
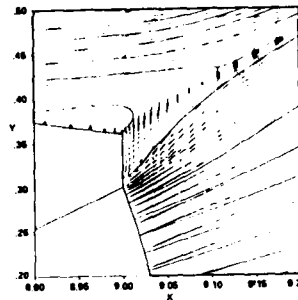
b - base region details

Fig. 94 - Base flow with propulsive jet -  
 $M_\infty = 2, M_{oj} = 2.5$  (Deiwert, 1983)



a - general flow structure

( AGRELL and WHITE, 1974 )



b - base region details

Fig. 95 - Base flow with plume induced separation -  
 $M_\infty = 2, M_{oj} = 2.5$  (Deiwert, 1983)

The evolution of the base pressure coefficient with the nozzle expansion ratio is shown in Fig. 93. Agreement with experiment is very good.

Results published by Deiwert (1983) are presented in Fig. 94 which shows computed density contour lines (top) and streamlines (bottom) for a 8 deg. conical afterbody equipped with a 20 deg. conical nozzle. The other conditions are also given in the figure. The calculation is compared with a schlieren photograph obtained by Agrell and White (1974). The base region detail is shown in Fig. 94b by means of velocity vectors, streamlines and Mach contours. Similar results for a case with plume induced separation on the boattail are presented in Figs. 95a and 95b. Evolution of base pressure and location of the separation point relative to the base are presented in Fig. 96. In the present application, agreement with experiment is poor. According to the author, such large discrepancies are probably due to too coarse calculation of the flow in the expansion region at the nozzle lip. Also attention should be focused on the turbulence model in the vicinity of separation on the afterbody.

In the computer code developed by Wagner (1984), the full time averaged Navier-Stokes equations are solved by using a finite volume method based on Mac Cormack's hybrid integration scheme similar to Jacock's treatment (Jacock et al., 1981). The turbulence is computed by the Baldwin-Lomax model.

The application selected here is relative to a boattailed afterbody. This configuration was carefully probed with a Laser Doppler Velocimeter by Lacau et al. (1982) so that local flowfield measurements including turbulent quantities are available.

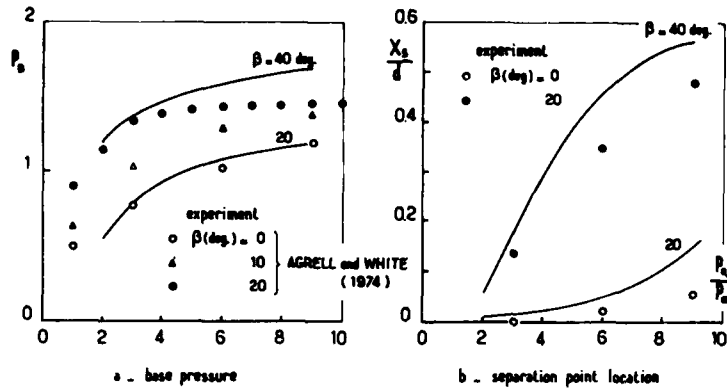
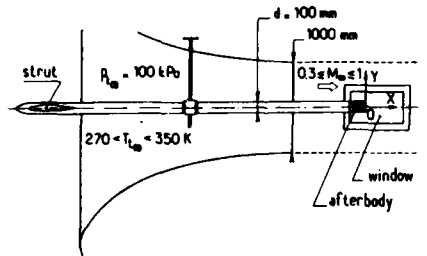
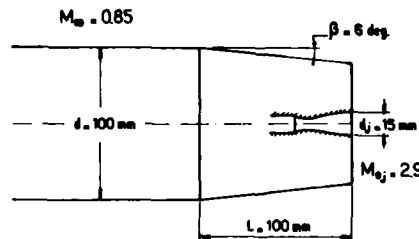


Fig. 96 - Evolutions of base pressure and separation point location with nozzle expansion ratio -  $M_\infty = 2$ ,  $M_{0j} = 2.5$  (Deiwert, 1983)



a - model installation in wind tunnel

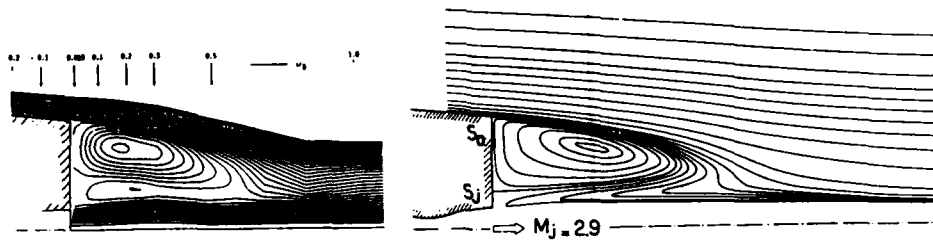


b - afterbody geometry

Fig. 97 - Test case for Navier-Stokes calculation

The model geometry and installation in the wind-tunnel are shown in Fig. 97. The afterbody is placed in an external flow of Mach number 0.85, the exit Mach number of the nozzle being equal to 2.9.

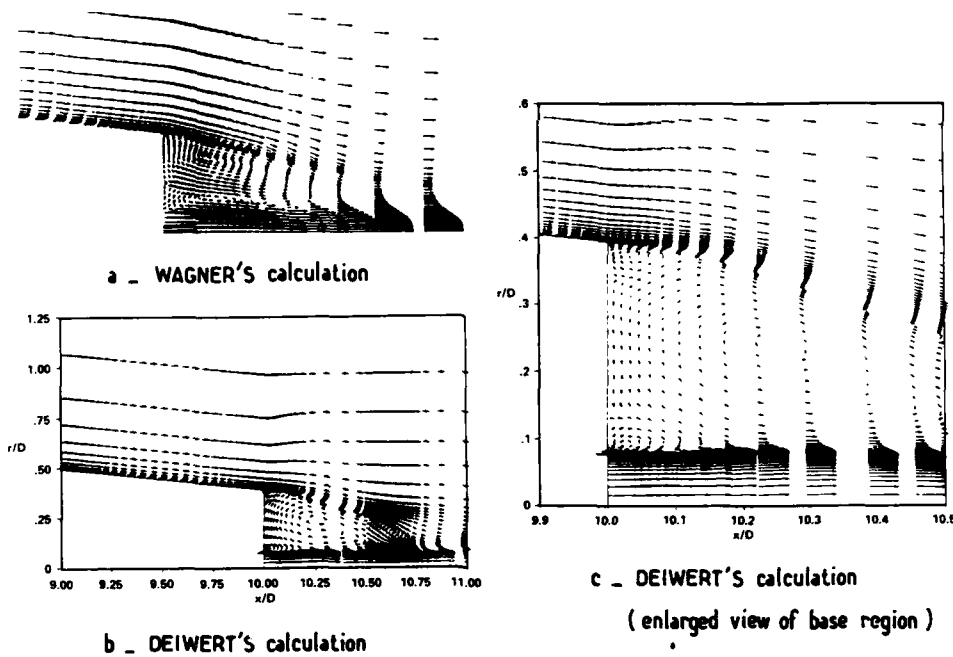
The calculated streamlines in the jet and base-flow region are traced in Fig. 98a. This tracing, which reveals a clockwise rotating main vortex driven by the external stream, agrees fairly well with the experimental flowfield represented in Fig. 98b. The corresponding vector field is plotted in Fig. 99. The figure also shows the vector field obtained by Deiwert for the same configuration. One sees that in the solution given by Deiwert, the main vortex in the separated region rotates in the opposite direction! (These results are more thoroughly commented on in AGARD AR N° 226.)



a - computed streamlines

b - experimental streamlines

Fig. 98 - Base flow with propulsive jet at subsonic speed -  $M_\infty = 0.85$ ,  $M_{0j} = 2.9$ ,  $\rho_{0j} / \rho_\infty = 1.17$  (Wagner, 1984)



a - WAGNER'S calculation

c - DEIWERT'S calculation

(enlarged view of base region)

b - DEIWERT'S calculation

Fig. 99 - Base flow with propulsive jet at subsonic speed - Vector field -  $M_\infty = 0.75$ ,  $M_{0j} = 2.9$ ,  $\rho_{0j} / \rho_\infty = 1.17$

Comparisons between calculated and measured turbulent shear-layer distributions are shown in Fig. 100. The overall agreement is poor, except upstream of the base in the unseparated boundary-layer ( $X/D = -0.1$ ). Downstream of the base, even if some peak values are relatively correct, the spreading of turbulence is poorly predicted. This instructive application illustrates the fact that good agreement between calculation and experiment can be observed with respect to the general flow structure (including surface pressure distributions) while the computed turbulent properties are largely incorrect.



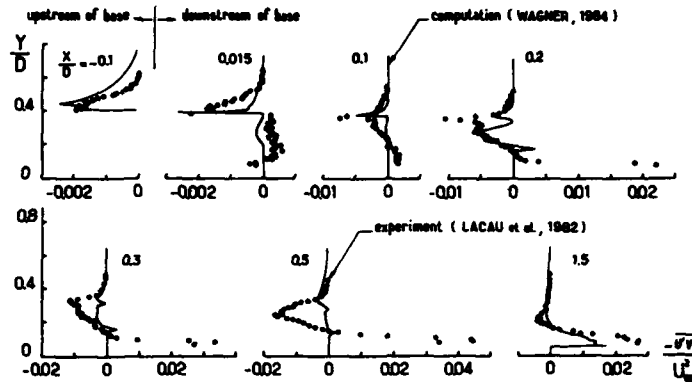


Fig. 100 - Base flow with propulsive jet at subsonic speed - Turbulent shear stress distributions -  $M_\infty = 0.85, M_{oj} = 2.9, p_{oj} / p_\infty = 1.17$

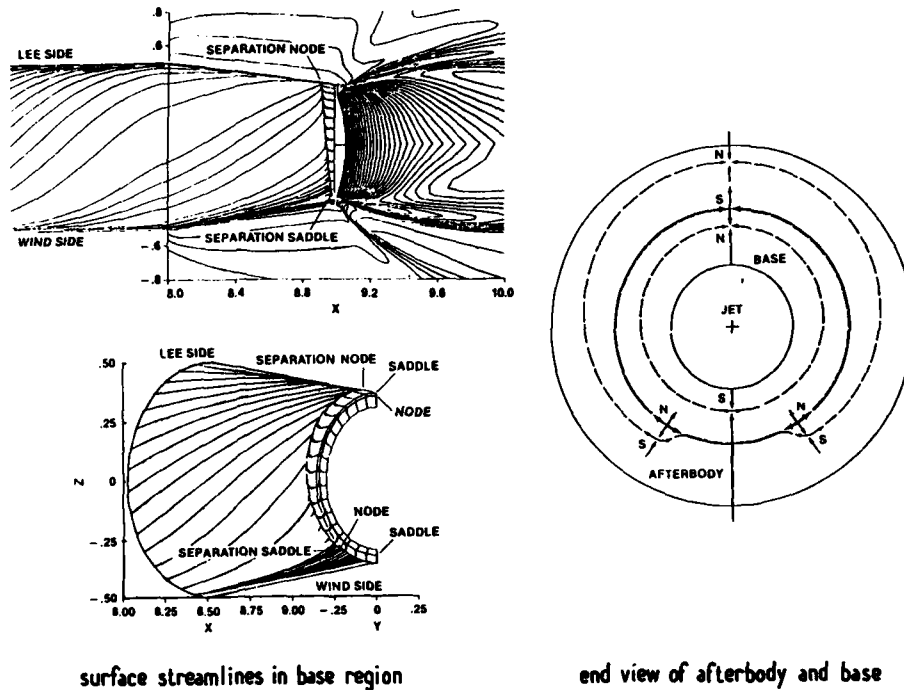


Fig. 101 - Base flow with propulsive jet at angle of incidence  $\alpha = 6$  deg.  $M_\infty = 2, M_{oj} = 2.5$  (Deiwert and Tothmund, 1983)

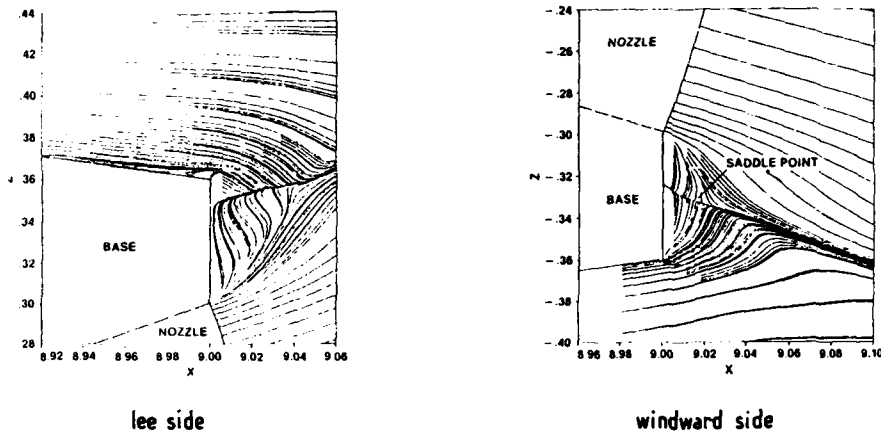
Axisymmetric base-flow calculations in the jet-on condition were also performed by Fox (1984) for the case of plume induced separation on bluff-base bodies, as well as by Thomas et al. (1984) who used transport equation turbulence models. Careful comparisons with experiment of both Navier-Stokes and Multi-Component Methods were made by Petrie and Walker (1985). A more complete evaluation of several Navier-Stokes solvers applied to missile base-flow can be found in AGARD AR N° 226.

The last application considered in this Section is a three-dimensional calculation performed by Deiwert and Rothmund (1983). These authors solved the thin-layer approximation of the Navier-Stokes equations by using an implicit solution procedure. The turbulence model is the Baldwin-Lomax model. The computed case is an axisymmetric body at a 6 degree angle of incidence placed in a free stream at Mach 2. The jet exit Mach number is equal to 2.5 with a static pressure three times that of the free stream.

The afterbody flow detail is represented in Fig. 101 by means of surface streamlines and density contour lines in the vertical plane of symmetry. The surface pattern contains a separation node on the lee generator of the boattail. All surface streamlines

on the lee side of the body flow into this node. A line of separation extends downward from this node on the afterbody surface to a *separation saddle point*, 33 deg. from the wind generator. The flow direction along this line of separation is upward from the saddle to the node.

The trajectories of the fluid particles in the plane of symmetry in the base region are shown in Fig. 102.



### Trajectories of fluid particles in the base region

Fig. 102 - Base flow with propulsive jet at angle of incidence  $\alpha = 6$  deg.  $M_\infty = 2$ ,  $M_{aj} = 2.5$  (Deiwert and Rothmund, 1983)

#### 4 - CONCLUSION

The base region of a missile or a launcher is the seat of complex aerothermal phenomena which can have important repercussions on vehicle performance and may lead to severe heating problems.

The prediction of base-flows is thus particularly important both for accurately determining the missile trajectory (prediction of base drag and eventual loss of stability) and for defining the thermal environment of the base region (heat transfer at the base, risk of exhaust gases after-burning in the dead-air region).

The purpose of this Lecture was to present the state of the art in matters of base-flow calculations. Since a complete review of the methods proposed for computing turbulent separated flows would constitute too great a task, attention has been focused on the basic principles underlying the most currently used theoretical models. Moreover, emphasis has been placed on comparison of results given by these models with experimental data.

In order to facilitate the understanding of the different theoretical approaches, physical descriptions of the flows establishing themselves behind a missile afterbody are first presented. The jet-off and the jet-on situations are successively analyzed by considering carefully made experiments including detailed flowfield measurements.

Next, methods of calculation belonging to three approaches are presented, turbulent methods only being considered.

In the Inviscid/Viscous Interactive (IVI) approach, the inviscid and viscous parts of the flowfield are described by different sets of equations (namely the Euler and the Prandtl equations) and made compatible along a suitably chosen frontier. This approach, which gives extremely good results in the prediction of flows including strong viscous effects (supercritical airfoils, cascade flows, etc...) can be used with success to predict base-flows in the jet-off situation. It could be particularly helpful in the transonic range. However, IVI methods have been scarcely employed to compute base-flows in the presence of an exhaust jet because of the overbearing complexity of the flowfield which renders this approach extremely delicate.

In the Multi-Component approach, introduced by Chapman and Korst in the early 50's, the flowfield is decomposed into a limited number of regions which are first described by simplified models. These regions are then patched together so as to satisfy global compatibility conditions. Because of its versatility and relative conceptual simplicity, the Multi-Component approach has been at the origin of a large number of practical methods which are still routinely used to predict base drag as well as base heating. These acceptably accurate Multi-Component methods which are very economical in computer time are now able by incorporation of a certain dose of empiricism, to compute base-flows in a wide variety of situations (missile without and with propulsive jet, supersonic as well as subsonic external stream, extremely variable afterbody geometry, etc...). Also, thermal effects - including chemistry - can be incorporated into the model and multi-nozzle configurations can be treated.

However, the domain of application of these methods (as well as of IVI methods) is still restricted to two-dimensional or axisymmetric flows and the transonic range is far from having been satisfactorily treated.

The more recently developed third approach consists in solving directly the time averaged Navier-Stokes equations by adequate numerical techniques. Although involving unwieldy numerical problems not yet entirely solved as well as being still extremely costly in computer time, the Navier-Stokes approach constitutes certainly the most satisfactory way to compute complex flows containing large separated regions, strong viscous interactions and complicated shock patterns. The results already obtained in

base-flow calculations are very promising, the flow structure being most often faithfully reproduced with details which are lost in the IVI and Multi-Component methods. However, the quantitative prediction is still imperfect. The deficiencies stem essentially from the difficulty of resolving the zones of intense gradients with sufficient accuracy (the mixing-layer developing along the plume boundary, for example) and also from the rusticity of the turbulence models employed up to now in the near-wake region.

Nevertheless, the Navier-Stokes approach will certainly constitute in the near future the best solution to base-flow problems. It appears also as the most straightforward way to extend prediction capability to three-dimensional configurations (flight at angle of attack, effect of fins, etc...). Indeed, extension of Inviscid/Viscous Interactive and Multi-Component methods to three-dimensional flows leads to such considerable difficulties that recourse to the solution of the Navier-Stokes equations is preferable.

Progress in the development of theoretical models will require execution of carefully made and well documented experiments in order to test the prediction by means of local comparisons of the field quantities-in particular, the turbulent properties. Indeed, assessment of sophisticated theories by comparison with base pressure only is insufficient and sometimes illusory. Experimental information on three-dimensional effects as well as on thermal effects is also urgently needed.

## 5. REFERENCES

- Addy, A.L. (1969) "Analysis of the Axisymmetric Base Pressure and Base Temperature Problem with Supersonic Interacting Freestream Nozzle Flows Based on the Flow Model of KORST et al. - Parts I, II and III". Report N° RD-TR-69-12, US Army Missile Command, Redstone Arsenal, Alabama.
- Addy, A.L. (1970) "Experimental-Theoretical Correlation of Supersonic Jet-on Base Pressure for Cylindrical Afterbodies". Journal of Aircraft, Vol. 7, N°5, pp. 474-478.
- Addy, A.L. ; Korst, H.H. ; White, R.A. and Walker, B.J. (1973) "A Study of Flow Separation in the Base Region and its Effects During Powered Flight". AGARD CP N° 124.
- "Aerodynamics of Base Combustion" (1976) Progress in Astronautics and Aeronautics, Vol. 40, AIAA and MIT Press, New-York.
- AGARD - AR N°226 (1986) Report of the Working Group on Aerodynamics of Aircraft Afterbody (June 1986).
- Agrell, J. and White, R.A. (1974) "An Experimental Investigation of Supersonic Axisymmetric Flow over Boattails Containing a Centered Propulsive Jet". FFA Tech. Nota AU 913.
- Ai, D.K. (1970) "On the Critical Point of the Crocco-Lees Mixing Theory in the Laminar Near Wake". Journal of Engineering Mathematics, Vol. 4, N°2.
- Albert, I.E. (1967) "Integral Theory for Turbulent Flows at Subsonic and Supersonic Speeds". Ph. D. Dissertation, Cal. Inst. of Tech.
- Alber, I.E. and Lees, L. (1968) "Integral Theory for Supersonic Turbulent Base Flows". AIAA Journal, Vol. 16, N°7, pp. 1343-1351.
- Baldwin, B.S. and Lomax J. (1978) "Thin Layer Approximation and Algebraic Model for Separated Turbulent Flows". AIAA Paper N°78-257.
- Bauer, R.C. (1966) "An Analysis of Two-Dimensional Laminar and Turbulent Compressible Mixing". AIAA Journal, Vol. 4, N°9, pp. 2188-2189.
- Bauer, R.C. and Fox, J.H. (1977) "An Application of the Chapman-Korst Theory to Supersonic Nozzle Afterbody Flows". AEDC-TR-76-158.
- Baughman, L.E. and Kochendorfer, F.D. (1957) "Jet Effects on Base Pressures of Conical Afterbodies at Mach Number 1.91 and 3.12". NACA RM-E57E06.
- Beam, R.M. and Warming, R.F. (1978) "An Implicit Factored Scheme for the Compressible Navier-Stokes Equations". AIAA Journal, Vol. 16, N°4, pp. 393-402.
- Benay, R. and Détery, J. (1986) "Modélisation des écoulements au culot des missiles propulsés avec prise en compte des effets thermiques". ONERA RT N°66/7078AY.
- Berner, C. (1986) "Experimental Investigation in Turbulent Flow Separation". ISL Report CO 208/86.
- Barrue, P. ; Lacau, R.G. and Détery, J. (1984) "Modélisation de l'écoulement au culot de missiles". 21ème Colloque d'Aérodynamique Appliqué de l'AAAF, Ecully (France), 7-9 Novembre 1984 ; see also : ONERA TP N°1984-147.
- Bogep, R.C. ; Rosenbaum, H. and Reeves, B.L. (1972) "Flowfield Interactions Induced by Underexpanded Exhaust Plumes". AIAA Journal, Vol 10, N°3, pp. 300-306.
- Bowman, J.E. and Clayden, W.A. (1968) "Boat-Tailed Afterbodies at Mach = 2 with Gas Ejection". AIAA Journal, Vol 6, N°10.
- Bray, K.N.C. ; Gadd, G.E. and Woodger, M. (1955) "Some Calculations by the Crocco-Lees and Other Methods of Interaction Between Shock-Waves and Laminar Boundary-Layers Including Effects of Heat Transfer and Suction". ARC CP 556.
- Cambier, L. ; Ghazzi, W. ; Veuillot, J.-P. and Viviani H. (1981) "A Multi-Domain Approach for the Computation of Viscous Transonic Flows by Unsteady Type Methods". Recent Advances in Numerical Methods in Fluid, Vol. 3 : Viscous Flow Computational Methods, W.G. Habashi, Editor, Pineridge Press ; see also : ONERA TP N° 1985-66.
- Cambier, L. ; Escande, B. and Veuillot, J.-P. (1986) "Calcul d'écoulements internes à grand nombre de Reynolds par résolution numérique des équations de Navier-Stokes". La Recherche Aéropatiale, N° 1986-6.
- Carrière, P. (1960) "Effet d'une injection fluide dans l'esu morte sur les conditions de recollement d'un écoulement plan supersonique". Compte-Rendus de l'Académie des Sciences de Paris, t. 521, pp. 2677-2679.
- Carrière, P. (1961) "Recherches sur l'écoulement autour d'avions ou de fusées". 2nd Otto Lilienthal Conf., Braunschweig.

- Carrière, P. (1965) "Recherches récentes effectuées à l'ONERA sur les problèmes de recollement". 7th International Fluid Mechanics Symposium, Jurata (Poland); see also : ONERA TP N° 275.
- Carrière, P. and Sirieix, M.. (1960) "Facteurs d'influence du recollement d'un écoulement supersonique". 10th International Congress of Applied Mechanics, Stresa (Italy).
- Carrière, P.; Sirieix, M., and Solignac, J.-L. (1968) "Propriétés de similitude des phénomènes de décollement laminaires ou turbulents en écoulement supersonique non uniforme". 12th International Congress of Applied Mech., Stanford Univ. (Aug. 1968) ; see also : ONERA TP N° 659 F.
- Carrière, P.; Sirieix, M., and Détery, J. (1975) "Méthodes de calcul des écoulements turbulents décollés en supersonique". Progress in Aerospace Sciences, Vol. 16, N°4, pp. 385 - 429.
- Cebeci, T.; Smith A. and Mosinskis, G. (1970) "Calculation of Compressible Adiabatic Turbulent Boundary-Layers". AIAA Journal, Vol. 8, N° 11, pp. 1974 - 1982.
- Chang, P.K. (1970) Separation of Flow, Pergamon Press.
- Channapragada, R.S. (1963) "Compressible Jet Spread Parameters For Mixing Zone Analyses". AIAA Journal, Vol. 1, N°9.
- Channapragada, R.S. and Wolley, J.P. (1967) "Turbulent Mixing of Parallel Compressible Non-Isoenergetic Streams". Astronautica Acta, Vol. 13, N°4, pp. 341 - 352.
- Chapman, D.R. (1951) "An Analysis of Base Pressure at Supersonic Velocities and Comparison with Experiment". NACA Report N° 1051.
- Chapman, D.R.; Kuehn, D.M. and Larson, H.K. (1957) "Investigation of Separated Flow in Supersonic and Subsonic Streams with Emphasis on the Effect of Transition". NACA TN-3869.
- Charczenko, N. and Hayes, C. (1963) "Jet Effects at Supersonic Speeds on Base and Afterbody Pressures of a Missile Model Having Single and Multiple Jets". NASA TN D-2046.
- Chow, W.L. (1959) "On the Base Pressure Resulting from the Interaction of a Supersonic External Stream With a Sonic or Subsonic Jet". JAS, pp. 176-180 (March 1959).
- Chow, W.L. (1971) "Recompression of a Two-Dimensional Supersonic Turbulent Free Shear Layer". Developments in Mechanics, Vol. 6, Proc. of the 12th Midwestern Mechanics Conference.
- Chow, W.L. (1984) "Base Pressure of a Projectile Within the Transonic Flight Regime". AIAA Paper N°84-0230 (Jan. 1984).
- Chow, W.L. and Spring, D.J. (1975) "Viscous Interaction of Flow Redevelopment after Flow Reattachment with Supersonic External Streams". AIAA Journal, Vol. 13, N°12, pp. 1576-1584.
- Chow, W.L. and Spring, D.J. (1976) "Viscid-Inviscid Interaction of Incompressible Separated Flows". ASME Paper N° 76-WA/APM-7, Transactions of the ASME, Journal of Applied Sciences.
- Cohen, C.B. and Reshotko, E. (1956) "Similar Solutions for the Compressible Laminar Boundary-Layer with Heat-Transfer and Pressure Gradient". NACA Report 1293.
- Coles, D.E. (1956) "The Law of the Wake in Turbulent Boundary-Layer". J. Fluid Mech., Vol. 1, Part 2, pp. 191-226.
- Crane, L.J. (1957) "The Laminar and Turbulent Mixing of Compressible Fluids". J. Fluid Mech., Vol 3, Part 1, pp. 81-92.
- Crocio, L. and Lees, L. (1952) "A Mixing-Theory for the Interaction Between Dissipative Flows and Nearly Isentropic Streams". JAS, vol. 19, N°10, pp. 649 - 676.
- Deiwert, G.S. (1983) "A Computational Investigation of Supersonic Axisymmetric Flow Over Boattails Containing a Centered Propulsive Jet". AIAA Paper n° 83-0462 (Jan. 1983) ; see also : AIAA Journal, Vol. 22, N°10, pp. 1358-1365 (Oct. 1984).
- Deiwert, G.S. and Rothmund, H. (1983) "Three-Dimensional Flow Over a Conical Afterbody Containing a Centered Propulsive Jet : A Numerical Simulation". AIAA Paper N° 83-1709 (July 1983).
- Deiwert, G.S.; Andrews, A.E. and Nakahashi, K. (1984) "Theoretical Analysis of Aircraft Afterbody Flow". AIAA Paper N° 84-1524.
- Détery, J. (1965) "Recollement d'un jet supersonique de révolution sur une paroi cylindrique coaxiale". La Recherche Aéronautique, n° 104.
- Détery, J. (1983) "ONERA Research on Afterbody Viscid/Inviscid Interaction with Special Emphasis on Base Flows". Proc. of the Symposium on Rocket/Plume Fluid Dynamics Interactions, The University of Texas at Austin, Vol. 3.
- Détery, J. and Masure, B. (1969) "Action d'une variation brusque de pression sur une couche limite turbulente et application aux prises d'air hypersoniques". La Recherche Aéronautique, N° 129, pp. 3 - 12.
- Détery, J. and Marvin, J.G. (1986) "Shock-Wave/Boundary-Layer Interactions". AGARDograph N° 280.
- Détery, J. and Sirieix, M. (1979) "Base Flows Behind Missiles". AGARD LS-98 on Missile Aerodynamics ; see also : ONERA TP N° 1979-14E.
- Dixon, R.J. and Page, R.H. (1966) "Theoretical Analysis of Launch Vehicle Base Flow". AGARD CP N° 4 - Part II
- Dixon, R.J.; Richardson, J.M. and Page, R.H. (1970) "Turbulent Base Flow on an Axisymmetric Body with a Single Exhaust Jet". Journal of Spacecraft, Vol. 7, N° 7, pp. 848-854
- Dorodnitsyn, A.A. (1960) in Advances in Aeronautical Sciences, MacMillan, New-York
- E.S.D.U. (Engineering Sciences Data Unit), N° 79022 Bodies of Revolution (Oct. 1979)

- Favre, A. (1965) "Equations des gaz turbulents compressibles". *Journal de Mécanique*, Vol. 4, N° 3, pp. 361-390 and Vol. 4, N° 4, pp. 391-421
- Fong, M.C. (1971) "An Analysis of Plume-Induced Boundary-Layer Separation". *Journal of Aircraft*, Vol. 8, N° 11, pp. 1107-1113
- Fong, M.C. and Ehrlich, C.F., Jr. (1970) "Propulsion Effects on Aerodynamics Characteristics of Lifting Reentry Vehicles". AFFDL - TR - 70-12 (March 1970)
- Fox, J.H. (1979) "Simple Recompression Model for the Korst Base Pressure Theory". *AIAA Journal*, Vol. 17, N° 3, pp. 311-313
- Fox, J.H. (1979) "A Generalized Base-Flow Analysis with Initial Boundary-Layer and Chemistry Effects". AEDC TR 79 - 46
- Fox, J.H. (1984) "Predicting Plume-Induced Separation on Bluff-Base Bodies". AIAA Paper N° 84-0315 (Jan. 1984)
- Fox, J.H. and Bauer, R.C. (1981) "Analytical Prediction of the Base Pressure Resulting from Hot, Axisymmetric Jet Interaction in Supersonic Flow". AIAA Paper N° 81-1898 (August 1981)
- Gabeaud, A. (1931) "Sur la résistance de l'air aux vitesses balistiques". *Comptes Rendus de l'Académie des Sciences de Paris*, Vol. 192, p. 1630
- Gabeaud, A. (1950) "Base Pressures at Supersonic Velocities". *JAS*, Vol. 17, pp. 525-526 (Aug. 1950)
- Gaviglio, J.; Dussauge, J.-P.; Débiève, J.-P. and Favre, A. (1977) "Behavior of a Turbulent Flow, Strongly out of Equilibrium, at Supersonic Speeds". *The Physics of Fluids*, Vol. 20, N° 10
- Glick, H.S. (1960) "Modified Crocco-Lees Mixing Theory for Supersonic Separated and Reattaching Flow". *Cal. Inst. of Techn., Memo N° 53*
- Goethert, B.H. (1960) "Base Flow Characteristics of Missiles with Cluster-Rocket Exhausts". IAS Paper N° 60-89 (June 1960)
- Goethert, B.H. and Matz, R. (1964) "Experimental Investigation of Base-Flow Characteristics of Four Nozzle Cluster-Rocket Models". AGARDograph N° 87, Vol. 2
- Green, J.E. (1966) "Two-Dimensional Turbulent Reattachment as a Boundary-Layer Problem". AGARD CP N° 4, PART I
- Green, J.E. (1969) "Interaction Between Shock-Waves and Turbulent Boundary-Layers". RAE TR 69 098 ; see also : *Progress in Aerospace Sciences*, Vol. 11, Pergamon Press, Oxford (1970)
- Hama, F.R. (1966) "Experimental Investigation of Wedge Base Pressure and Lip Shock". NASA CR 81031
- Hama, F.R. (1968) "Experimental Studies on the Lip Shock". *AIAA Journal*, Vol. 6, N° 2, pp. 212-219
- Hasen, G.A. (1981) "Navier-Stokes Solution for a Supersonic Coflowing Axisymmetric Nozzle with a Thick Base Annulus". Ph. D. Dissertation, Air Force Institute of Technology, AFIT/DS/AA/81-2
- Hasen, G.A. (1982) "Navier-Stokes Solution for an Axisymmetric Nozzle". *AIAA Journal*, Vol. 20, N° 9, pp. 1219-1227
- Hirt, C.W.; Nichols, B.D. and Romero, N.C. (1975) "A Numerical Solution Algorithm for Transient Fluid Flows". Los Alamos Scientific Laboratory, Report LA-5852
- Hitchcock, H.P. (1951) "On Estimating the Drag Coefficient of Missiles". BRL Memorandum Report N° 545 (May 1951)
- Holden, M.S. (1969) "Theoretical and Experimental Studies of the Shock-Wave/Boundary-Layer Interaction on Curved Compression Surfaces". Proc. of the Symposium on Viscous Interaction Phenomena in Supersonic and Hypersonic Flows, Univ. of Dayton Press
- Hollanders, H. and Ravalason, W. (1986) "Résolution des équations de Navier-Stokes en fluide compressible par une méthode implicite". *La Recherche Aérospatiale*, N° 1986-1, pp. 23-46
- Holst, T.L. (1977) "Numerical Solution of Axisymmetric Boattail Fields with Plume Simulators". AIAA Paper N° 77-224 (Jan. 1977).
- Holt, M. and Meng, J.C.S. (1968) "The Calculation of Base Flow and Near Wake Properties by the Method of Integral Relations". IAF Paper RE 65 (Oct. 1968).
- Hong, Y.S. (1970) "Base Flow Analysis of an Axisymmetric Body with a Central Jet." *Air Force Report N° SAMSO-TR-70-415*.
- Hong, Y.S. (1971) "Base Flow Environment Analysis of a Single Engine Booster". AIAA Paper n° 71-643 (June 1971).
- Hong, Y.S. (1973) "Base Flow Analysis of Multiple-Engine Boosters". The Aerospace Corporation, TR-0074 (4901-01)-1.
- Hong, Y.S. (1974) "Base Flow Analysis for a Dual-Engine Booster". *Journal of Spacecraft*, Vol. 11, n°4, pp. 209-210.
- Hunter, L.G. and Reeves, B.L. (1971) "Results of a strong Interaction Wake-Like Model of Supersonic Separated and Reattaching Turbulent Flows". *AIAA Journal*, Vol. 9, N°4, pp. 703-712.
- Jacocks, J.L.; Peters, W.L. and Guyton, F.C. (1981) "Comparison of Computational and Experimental Jet Effects". AIAA Paper n°81-1492 (June 1981).
- JANNAF Handbook, *Rocket Exhaust Plume Technology*, Chapter 5, Base-Flow, CPIA Publication 263 (July 1981).
- Jones, W.P. and Launder, B.E. (1972) "The Prediction of Laminarization with a Two-Equation Model of Turbulence". *Int. Journal of Heat and Mass Transfer*, Vol. 15, N° 2, pp. 301-314.
- Kirchhoff, G. (1869) "Zur Theorie freier Flüssigkeitsstrahlen". *Crelles Journal für Mathematik*, vol. 70, pp. 289-298.
- Kirk, F.N. (1959) "An Approximate Theory of Base Pressure in Two Dimensional Flow at Supersonic Speeds". RAE TN Aero 2377.
- Klineberg, J.M.; Kubota, T. and Lees, L. (1972) "Theory of Exhaust-Plume/Boundary-Layer Interactions at Supersonic Speeds". *AIAA Journal*, Vol. 10, N°5, pp. 581-588.

- Korst, H.H. (1954) "Auflösung eines ebenen Freistrahlandes bei Berücksichtigung der ursprünglichen Grenzschichtströmung". Österreich. Ing. Arch. VII 2-3.
- Korst, H.H. (1956) "A Theory for Base Pressure in Two Dimensional Flow and Comparison with Experiment". J. Appl. Mech., N°23, pp. 593-600.
- Korst, H.H. and Tripp W. (1957) "The Pressure on a Blunt Trailing Edge Separating Two Supersonic Two-Dimensional Air Streams of Different Mach Numbers and Stagnation Pressures, but Identical Stagnation Temperatures". Proc. of the Fifth Mid-Western Conference on Fluid Mechanics, Univ. of Michigan Press, pp. 187-199.
- Korst, H.H. ; Page, R.H. and Childs, M.E. (1955) "A Theory for Base Pressures in Transonic and Supersonic Flow". Univ. of Illinois, ME TN 392-2.
- Krasinsky (de), J.S. (1966) "A Study of Separated Base Flow Behind Bodies of Revolution in Supersonic Streams" IIAE, Cordoba, Argentina, Informe INF 01-66.
- Kubota, T. ; Reeves, B.L. and Buss, H. (1964) "A Family of Similar Solutions for Axisymmetric Incompressible Wakes". AIAA Journal, Vol. 2, N°8, pp. 1493-1495.
- Kuhn, G.D. and Nielsen, J.N. (1975) "Prediction of Turbulent Separated Flow at Subsonic and Transonic Speeds Including Unsteady Effects". AGARD CP N°168.
- Lacau, R.G. ; Desnoyer, D. and Déléry, J. (1982) "Analyse au vélocimètre laser de l'écoulement en aval d'arrière-corps de missiles". AGARD Symposium on "Missile Aerodynamics", Trondheim, 20-22 Septembre 1982.
- Lamb, J.P. and Hood, C.G. (1968) "An Integral Analysis of Turbulent Reattachment Applied to Plane Supersonic Base Flows". Journal of Engineering for Industry, Trans. of the ASME, pp. 553-560 (Nov. 1968).
- Lamb, J.P. ; Abbud, K.A. and Lenzo, C.S. (1969) "A Theory for Base Pressures in Multi-Nozzle Rocket Configurations". AIAA Paper N°69-570 (June, 1969) ; see also : Journal of Spacecraft, Vol. 7, N° 4, pp. 451-457 (April 1970).
- Le Balleur, J.-C. (1978) "Calculs couplés visqueux-non visqueux incluant décollements et ondes de choc en écoulement bidimensionnel". VKI/AGARD LS-94 on "Three Dimensional and Unsteady Separation at High Reynolds Number".
- Le Balleur, J.-C. (1982) "Viscid-Inviscid Coupling Calculations for Two and Three Dimensional Flows". VKI LS 1982-6 on "Computational Fluid Dynamics".
- Le Balleur, J.-C. (1984) "Numerical Flow Calculations and Viscous-Inviscid Interaction Techniques". Computational Methods in Viscous Flows, Recent Advances in Numerical Methods in Fluids, Vol. 3, Pineridge Press.
- Lees, L. and Reeves, B.L. (1964) "Supersonic Separated and Reattaching Laminar Flows : 1 - General Theory and Application to Adiabatic Boundary-Layer/Shock-Wave Interactions". AIAA Journal, Vol. 2, N°11, pp. 1907-1920.
- Lerat, A., Sidès, J. and Daru, V. (1984) "Efficient Computation of Steady and Unsteady Transonic Flows by an Implicit Solver". Advances in Computational Transonics, W.G. Habashi Editor, Pineridge Press.
- Leuchter, O. (1976) "Effects of Free Stream Turbulence and Initial Boundary-Layer on the Development of Turbulent Mixing Layers". Workshop on Turbulence in Internal Flows (Project SQUID), Airlie House, Virginia (USA), 14 - 15 June 1976 ; see also : ONERA TP N° 1976-155.
- Lighthill, M.J. (1953) "On Boundary-Layer Upstream Influence. II Supersonic Flows without Separation". Proc. Roy. Soc., A 217, pp. 478 - 507.
- Lighthill, M.J. (1958) "On Displacement Thickness". J. Fluid Mech. Vol. 4, Part 2, pp. 383-392.
- Liu, J.K.S. and Chow, W.L. (1979) "Axisymmetric Transonic Turbulent Base Pressures". AIAA Journal, Vol. 17, N°4, pp. 330-331.
- Love, E.S. (1957) "Base Pressure at Supersonic Speeds on Two-Dimensional Airfoils and on Bodies of Revolution with and without Fins having Turbulent Boundary-Layer". NACA TN-3819.
- Mac Cormack, R.W. (1969) "The effect of Viscosity in Hypervelocity Impact Cratering". AIAA Paper N° 69-354.
- Mac Cormack, R.W. (1970) "Numerical Solution of the Interaction of a Shock Wave with a Laminar Boundary-Layer". Lecture Notes in Physics, Vol. 8, Springer-Verlag.
- Mac Cormack, R.W. (1979) "An Efficient Numerical Method for Solving the Time Dependent Compressible Navier-Stokes Equations at High Reynolds Number". NASA TM - 73 129 ; see also : Computing in Applied Mechanics, Applied Mechanics Division, Vol. 18, ASME, New-York
- Mac Donald, H. (1964) "Turbulent Shear-Layer Reattachment with Special Emphasis on the Base Pressure Problem". Aeronautical Quarterly, Vol. 15, pp. 247-280
- Mac Donald, H. (1966) "The Turbulent Supersonic Base Pressure Problem : A Comparison Between a Theory and Some Experimental Evidence". Aeronautical Quarterly, Vol. 17, pp. 105-126
- Maydew, R.C. and Reed, J.F. (1963) "Turbulent Mixing of Axi-Symmetric Compressible Jets (in the Half-Jet Region) with Quiescent Air". SANDIA Corporation, Research Report SC-4764
- Metha, G.K. (1977) "A Theory of the Supersonic Turbulent Axisymmetric Near Wake Behind Bluff-Base Bodies". Ph. D. Dissertation, Georgia Institute of Technology
- Mehta, G.K. and Strahle, W.C. (1977) "A Theory of the Supersonic Turbulent Axisymmetric Near Wake behind Bluff-Base Bodies". AIAA Journal, Vol. 15, N°8, pp. 1059-1060
- Moulden, T.H. ; Wu, J.M. and Spring, D.J. (1974) "On Some Problems Encountered in a Theoretical Study of the External Flow over a Nozzle Configuration in Transonic Flight". AGARD CP N°15

- Mueller, T.J. (1967) "Determination of the Turbulent Base Pressure in Supersonic Axisymmetric Flow". AIAA Paper N°67-446 (July 1967); see also: Journal of Spacecraft, Vol. 5, N°1, pp. 101-107
- Mueller, T.J.; Hall, C.R. Jr and Roache, P.J. (1970) "The Influence of Initial Flow Direction on the Turbulent Base Pressure in Supersonic Axisymmetric Flow". AIAA Paper N°70-555 (May 1970); see also: Journal of Spacecraft, Vol. 7, N°12, pp. 1484-1488
- Murthy, S.N.B. and Osborn, J.R. (1976) "Base Flow Phenomena with and Without Injection: Experimental Results, Theories and Bibliography". Progress in Astronautics and Aeronautics, Vol. 40, AIAA and MIT Press
- Musial, N.T. and Ward, J.J. (1961) "Base-Flow Characteristics for Several Four-Clustered Rocket Configurations at Mach Numbers from 2 to 3.5". NASA TN D-1093
- Narayanan, M. A. B.; Khadgi, Y.N. and Viswanath, P.R. (1974) "Similarities in Pressure Distribution in Separated Flow Behind Backward-Facing Steps". Aeronautical Quarterly (Nov. 1974)
- Nash, J.F. (1962) "An Analysis of Two-Dimensional Turbulent Base Flow Including the Effect of the Approaching Boundary-Layer". ARC R & M N°3344
- Nash, J.F. (1966) Comments on "Review of Recent Developments in Turbulent Supersonic Base-Flow". AIAA Journal, Vol. 4, N°3, pp. 574-575
- Noi, N. V. (1971) "Etude théorique et expérimentale du recollement subsonique incompressible d'un écoulement plan turbulent à sa frontière". Thèse d'Ingénieur Docteur, Faculté des Sciences de l'Université de Paris
- Oswatitsch, K. (1945) "Der Luftwiderstand als Integral des Entropiestromes". Nachr. Akad. Wiss. Göttingen, Math. Phys. Kl. S. 88-90
- Page, R.H. and Dixon, R.J. (1963) "Base Heating on a Multiple Propulsion Nozzle Missile". AIAA Paper N°63-179 (June 1963)
- Page, R.H. and Dixon, R.J. (1964) "Computer Evaluation of an Integral Treatment of Gas Mixing". Proc. of the Third Conference on Performance of High Temperature Systems, Dec. 1964, Pasadena, Calif. and Gordon and Breach, New-York, pp. 345-370 (1969)
- Page, R.H.; Hill Jr, W.G. and Kessler, T.J. (1967) "Reattachment of Two-Dimensional Supersonic Turbulent Flow". ASME Paper N° 67-FE-20
- Payne, P.R.; Hartley, R.M. and Taylor, R.M. (1980) "Afterbody Drag - Volume 1: Drag of Conical and Circular Arc Afterbodies without Jet Flow". DTNSRDC/ASED - N°80/10
- Peters, C.D. and Phares, W.J. (1967) "Analytical Model of Supersonic Turbulent Near-Wake Flows". AEDC - TR N°76-127
- Petrie, H.L. and Walker, B.J. (1985) "Comparison of Experiment and Computations for a Missile Base Region Flowfield with a Centered Propulsive Jet". AIAA Paper N°85-1618 (July 1985)
- Peyret, R. and Viviand, H. (1975) "Computation of Viscous Compressible Flows Based on the Navier-Stokes Equations". AGARDograph N°212
- Ravalason, W. (1985) "Résolution numérique des équations de Navier-Stokes pour les écoulements transsoniques autour d'arrière-corps droits". Thèse, Université des Sciences et Techniques de Lille, France
- Reeves, B.L. and Lees, L. (1965) "Theory of Laminar Near Wake of Blunt Bodies in Hypersonic Flows". AIAA Journal, Vol. 3, N°11, pp. 2061-2074
- Reid, J. and Hastings, R.C. (1961) "The Effect of a Central Jet on the Base Pressure of a Cylindrical Afterbody in a Supersonic Stream". ARC, R & M N°3224
- Reshotko, E. and Tucker, M. (1955) "Effect of a Discontinuity on Turbulent Boundary-Layer Thickness Parameters with Application to Shock Induced Separation". NACA TN 3454
- Roache, P.J. (1973) "Base Drag Calculations in Supersonic Turbulent Axisymmetric Flows". Journal of Spacecraft, Vol. 10, N°4, pp. 285-287
- Roberts, J.B. (1966) "On the Prediction of Base-Pressure in Two-Dimensional Supersonic Turbulent Flow". ARC R & M N°3434
- Rom, J. (1962) "Theory for Supersonic Two-Dimensional Laminar Base Type Flows Using the Crocco-Lees Mixing Concept". TAE Report N°20; see also: JAS, Vol. 29, N°8, pp. 963-968
- Rom, J.; Victor, M.; Reichenberg, M. and Salomon, M. (1972) "Wind Tunnel Measurements of the Base Pressure of an Axially Symmetric Model in Subsonic, Transonic and Supersonic Speeds at High Reynolds Numbers". TAE Report N°134
- Rougier, P. (1970) "Etude expérimentale des phénomènes dynamiques et thermiques liés au recollement d'un jet supersonique. Application à l'étude des éjecteurs supersoniques". Thèse d'Ingénieur-Docteur, Université de Lyon (France)
- Sahu, J. (1986) "Supersonic Flow Over Cylindrical Afterbodies with Base Bleed". AIAA Paper N°86-0487 (Jan. 1986)
- Sahu, J. and Danberg, J.E. (1984) "Navier-Stokes Computations of Transonic Flow over a Projectile with a Two-Equation Model of Turbulence". AFVAL Viscous and Interacting Flow Field Effects, pp. 243-256 (Aug. 1984)
- Sahu, J. and Nietubitz, C.J. (1984) "Numerical Computation of Base Flow for a Missile in the Presence of a Centered Jet". AIAA Paper N°84-0527 (Jan. 1984)
- Sahu, J.; Nietubitz, C.J. and Steger, J.L. (1982) "Numerical Computation of Base Flow for a Projectile at Transonic Speeds". AIAA Paper N°82-1358 (August 1982)
- Sahu, J.; Nietubitz, C.J. and Steger, J.L. (1983) "Navier-Stokes Computations of Projectile Base Flow with and without Base Injection". AIAA Paper N°83-0224 (Jan. 1983)

- Seginer, A. and Rom, J. (1967) "Integral Method for the Calculation of Heat Transfer in Laminar Supersonic Separated Flows". TAE Report N° 78
- Sinha, N. and Dash, S.M. "Overlaid approach for base flow analysis at supersonic velocities. Part I : Basic modeling description - Part II : Applications including base combustion and multi-phase effects". AIAA Paper n° 85-1673 (July 1985).
- Sirieix, S. and Solignac, J.-L. (1966) "Contribution à l'étude expérimentale de la couche de mélange turbulent isobare d'un écoulement supersonique". AGARD CP N° 4, Part I
- Sirieix, M.; Mirande, J. and Détery, J. (1966) "Expériences fondamentales sur le recollement d'un jet supersonique". AGARD CP N° 4, Part I
- Sirieix, M.; Détery, J. and Monnerie, B. (1968) "Etude expérimentale du proche sillage d'un corps de révolution en écoulement supersonique". 19th International Congress of Astronautics, 13-19 Oct. 1968; see also: ONERA TP N° 808
- Solignac, J.-L. and Détery, J. (1972) "Contribution à l'étude aérodynamique des systèmes propulsifs à double-flux". *Israel Journal of Technology*, Vol. 10, N° 1-2, pp. 97-111
- Spring, D.J. (1963) "The Static Stability Characteristics of Several Cone-Cylinder Flare-Cylinder Configurations at Mach Number 0.4. to 4.5". Report N° RF-TR-63-14, US Army Missile Command, Redstone Arsenal, Ala. (USA)
- Stewartson, K. (1954) "Further Solutions of the Falkner-Skan Equation". *Proc. Cambridge Phil. Soc.*, Vol. 50, Part 3, pp. 454-465
- Sullins, G.A.; Anderson Jr, J.D. and Drummond, J.P. (1982) "Numerical Investigation of Supersonic Base Flow with Parallel injection". AIAA Paper N° 82-1001 (June 1982)
- Tang, H.H.; Gardiner, C.P.; Anderson, W.A. and J. Navickas (1971) "Space Shuttle Booster Multi-Engine Base Flow Analysis". *Space Shuttle Aerothermodynamics Technology Conference*, Vol. 2, Heating, NASA TMX 2507
- Tanner, M. (1973) "Theoretical Prediction of Base Pressure for Steady Base Flow". *Progress in Aerospace Sciences*, Vol. 14, pp. 177-225
- Tanner, M. (1978) "Heckwiderstands- und Basisdruckmessungen an einem Flugkörperrumpf bei Anstellwinkeln bis  $\alpha = 25^\circ$  im Unterschall- und Transschallbereich". DFVLR - FB 78-14
- Tanner, M. (1980) "Theoretische Bestimmung des Basisdruckes von Flugkörperrümpfen mit turbulentem Totwasser bei Überschallgeschwindigkeiten". DFVLR-FB 80-29; English Translation ESA-TT-708 (Nov. 1981)
- Tanner, M. (1984) "Empirische Formeln zur Bestimmung des Basisdruckes von Flugkörperrümpfen bei Unterschallgeschwindigkeit". DFVLR-FB 84-23
- Tanner, M. (1986a) "Empirische Formeln für den Basisdruck von Flugkörperrümpfen mit Treibstrahl". DFVLR-FB 86-38
- Tanner, M. (1986b) "Basisdruckmessungen an einem Flugkörperrumpf mit Kreuzleitwerk". DFVLR-FB 86-53
- Thomas, P.D.; Reklis, R.P., Roloff, R.R. and Conti, R.J. (1984) "Numerical Simulation of Axisymmetric Base Flow on Tactical Missiles with Propulsive Jet". AIAA Paper N° 84-1658 (June 1984)
- Thommen, H.U. (1966) "Numerical Integration of the Navier-Stokes Equations". *Z.A.M.P.*, Vol. 17, N° 3, pp. 369-384
- Vanwagenen Jr, R.G. (1968) "A Study of Axially-Symmetric Subsonic Base Flow". Ph. D. Dissertation, University of Washington
- Von Kármán, T. and Moore, N.B. (1932) "Resistance of Slender Bodies Moving with Supersonic Velocities, with Special Reference to Projectiles". *ASME Transactions*, Vol. 54, p. 303
- Wagner, B. (1981) "Jet-Afterbody Interference on Missiles in Supersonic Flow". AGARD CP N° 307
- Wagner, B. (1983) "Estimation of Angle of Attack Effect by Component Analysis and Axisymmetric Navier-Stokes Solutions for Missile Afterbodies with Jet". *Proc. of the Symposium on Rocket/Plume Fluid Dynamic Interactions*, The University of Texas at Austin, Volume 3
- Wagner, B. (1984) "Calculation of Turbulent Flow About Missile Afterbodies Containing an Exhaust Jet". AIAA Paper N° 84-1659 (June 1984)
- Wagner, B. and White, R.A. (1979) "Influence of Fundamental Parameters on the Supersonic Base Flow Problem in Presence of an Exhaust Jet". AIAA Paper, N° 79-0133 (Jan. 1979)
- Waskiewicz, J.D.; Shang, J.S. and Hankey, W.L. (1980) "Numerical Simulation of Near Wake Utilizing a Relaxation Model". *AIAA Journal*, Vol. 18, N° 12, pp. 1440-1445
- Webb, W.H. (1968) "An Approximate Pressure-Angle Relation for the Axisymmetric Supersonic Near-Wake". *AIAA Journal*, Vol. 6, N° 7, pp. 1427-1428
- Weng, C.H. and Chow, W.L. (1978) "Axisymmetric Supersonic Turbulent Base Pressure". *AIAA Journal*, Vol. 16, N° 4, pp. 553-554
- Werlé, H. (1970) Unpublished ONERA document
- White, R. and Agrell, J. (1977) "Boattail and Base Pressure Prediction Including Flow Separation for Afterbodies with a Centered Propulsive Jet and Supersonic External Flow at Small Angles of Attack". AIAA Paper N° 77-958 (July 1977)
- Wu, J.M.; Moulden, T.H. and Spring, D.J. (1974) "On Some Studies of Aft-End Design and its Influence on Plume Induced Separation in Transonic Flight". *Proc. of the 8th JANNAF Plume Technology Meeting*, Colorado Springs, Colo. (USA), July 1974
- Zukoski, E.E. (1967) "Turbulent Boundary-Layer Separation in Front of a Forward-Facing Step". *AIAA Journal*, Vol. 5, N° 10, pp. 1746-1753
- Zumwalt, G.W. (1959) "Analytical and Experimental Study of the Axially Symmetric Base Pressure Problem". Ph. D. Dissertation, Department of Mechanical Engineering, University of Illinois



## NEXT GENERATION MISSILE DESIGN

J. E. Williams  
Unit Chief - Technology  
and  
R. J. Krieger  
Chief - Technology  
McDonnell Douglas Astronautics Company  
P.O. Box 516, St. Louis, MO 63166  
USA

## ABSTRACT

Traditional long range cruise class missiles fly at low altitudes and subsonic speeds. To meet operational requirements, the next generation missiles will fly at relatively high altitudes and supersonic or hypersonic speeds. Because of economic constraints, low cost design and development approaches must be used. To illustrate these approaches, the results of the U.S. Air Force sponsored Aerodynamic Configured Missile (ACM) Program and the subsequent Low Cost Aerodynamic Configured Missile Demonstrator Program are summarized with emphasis on the impact of these studies on future missile concepts. The ACM program objective was to exploit the aerodynamic potential of supersonic cruise and maneuvering missiles to achieve significant improvements in performance. During three phases of effort over a 30 month period, configuration development, wind tunnel testing, and performance analyses were performed. The major uses of the program results to date are described. These uses include points of departure concepts, prediction models, evaluation of prediction models, and evaluation of other missile concepts. For the future, a low cost flight program plan is then described with the goal to demonstrate missile flight at high supersonic Mach numbers with high lift-to-drag ratios. A low cost approach is described which uses existing equipment, standard airframe structural design, the existing ACM data base, trajectory shaping and aggressive program planning. Two flight test options are then identified. These options are a ground and B-52 launch at Vandenberg Air Force Base (VAFB) of a non-recoverable and recoverable blended wing-body concept. The design described is an ACM airframe which provides a test bed for a variety of experiments. Program plans, costs and subset experimental programs are identified including growth versions with higher Mach number capability.

## INTRODUCTION

The Aerodynamic Configured Missile Development Program (ACM) was an Air Force sponsored<sup>1</sup> project which began on 15 April 1977. The technical effort was completed on 15 February 1980. The program objective was to exploit the aerodynamic potential of supersonic missiles to achieve significant improvements in performance. The program was conducted in three phases. Phase I assessed the aerodynamic potential of a variety of concepts which were free of typical design constraints such as subsystems, aircraft carriage, and propulsion. During Phase II, design constraints were integrated into Phase I concepts with minimum compromise of their aerodynamic potential. Two detailed designs were then developed in Phase III.

The original ACM program results<sup>2,3</sup> promised significant improvement in performance through aerodynamic configuration of a missile. The wind tunnel data showed that high lift-to-drag ratios were indeed achievable. But seven years after the beginning of that study, there are no ACM-type missiles in the inventory. Therefore, how have the ACM results been used and how will they be used in the future? Four major uses of the program results have emerged. These all involve use of the experimental data base and are:

1. Points of departure concepts
2. Direct prediction of aerodynamics
3. Evaluation of prediction techniques
4. Evaluation of other missile concepts.

Very little is available in open literature on the use of the ACM data base for point of departure concepts. This is intentional. Most studies by missile contractors are proprietary or classified and the data is unavailable. Often during these same contractor efforts, prediction methods are unavailable or not efficient for their specific configurations. In these cases, the ACM data is modified to reflect the configuration differences and used directly for the aerodynamic predictions. Again, these uses of the data base are typically not reported in open literature.

An extensive use of the ACM data base has been made to evaluate prediction techniques through the Aerodynamic Analysis for Missiles Program<sup>4</sup>. In this study predictions from the Supersonic/Hypersonic Arbitrary Body Program (S/HABP)<sup>5,6,7</sup> and Aerodynamic Preliminary Analysis Systems (APAS)<sup>8</sup> are compared with ACM force and moment data and prediction accuracy assessed. Gregoire used the data base to evaluate S/HABP and the linear theory code PANAIR<sup>9</sup>. More recently, the Air Force has begun an evaluation<sup>10</sup> of the flowfield prediction capability of codes such as S/HABP and the Euler code SWINT<sup>11</sup>. Part of this evaluation will use the ACM surface pressure and oil flow data.

Another application of the data has been made by Jeschke and Rasmussen<sup>12</sup>. Their experimental data bases for wave riders and the ACM concepts are being compared to establish relative merits of these configurations.

These have been the uses of the ACM results to date and will undoubtedly continue into the future. Another view of the future was provided by the recently completed Low Cost ACM Flight Demonstration study<sup>13</sup>. The objective of this program was to study the feasibility of developing a low cost, ACM demonstrator and an associated flight test program which would validate ACM concepts at full scale flight conditions. In addition, the test program would provide a test bed and growth opportunity to higher speed and altitudes.

The program began on 1 June 1982. The technical effort was completed on 15 December 1983. Three tasks were performed. In Task I, a general survey was made of the major options related to formulating a low cost ACM demonstration vehicle and experimental flight program. Task II consisted of the selection of two flight test approaches and a detailed design synthesis study. In Task III an experimental flight test program was formulated along with a total program cost analysis.

This paper expands upon the current uses of the ACM data base by first reviewing the data base, discussing the published results based upon the data base and then describing a possible flight test demonstration program.

#### WIND TUNNEL DATA BASE

During the three phases of ACM, 816 wind tunnel runs were made at the Arnold Engineering Development Center (AEDC) Von Karman Facility (VKF) Tunnel A and Propulsion Wind Tunnel (PWT) 4T. The test conditions are summarized in Fig. 1. Phase I testing<sup>14,15,16,17</sup> emphasized force and moment data on a variety of concepts over a wide range of Mach number and angle of attack. The Phase II testing<sup>18,19</sup> emphasized variations of three primary configurations. A large quantity of foil flow data was obtained to identify shock and vortex interaction regions. Detailed heat transfer and surface pressure data<sup>20,21</sup> were obtained on variations of two primary configurations in Phase III.

The variety of concepts tested during Phase I are sketched in Fig. 2. These were developed from configurations in the literature<sup>22</sup>, aerodynamic design criteria based upon performance<sup>23,24</sup> and shape optimization techniques<sup>25</sup>. Data were obtained and analyses performed<sup>26</sup> for the five classes of shapes: noncircular body, lifting body, favorable interference, wing-body, and blended wing-body.

L/D ratios significantly higher than conventional circular missiles were measured for the Phase I configurations, as shown in Fig. 3. The data also showed the L/D to be only a weak function of vehicle orientation. In addition, blended bodies always had higher L/D than wing-bodies.

This data base is being used in the four categories mentioned previously and has proven the most valuable data of the three phases. The configurations are simple geometries representing a wide range of basic shapes and the data includes subsonic through high supersonic Mach numbers.

The evaluation of prediction techniques by Williams<sup>4</sup> shows the capability of impact methods and linear theory codes to predict these shapes. Although the shapes have relatively simple geometries, prediction capability is only fair. For the blended body, Gregoire<sup>27</sup> shows the linear theory capability of PANAIR up to surprisingly high Mach numbers of 5. The highly swept shape maintains supersonic leading edges at these conditions. These types of comparisons have established the capability of current prediction tools for shaped body aerodynamics.

Based upon the Phase I data and predictions, Phase II configurations were developed<sup>28</sup> by integrating constraints such as propulsion, subsystems, and control. Three configurations were selected for wind tunnel testing<sup>18,19,29</sup>. Figure 4 is a photograph of the noncircular body Phase I and II wind tunnel models. The major changes include the integration of two-dimensional, side-mounted inlets for the ramjet engine, modification of the nose shape to accommodate a specified payload, and the addition of a vertical tail and controls on the wing.

Figure 5 shows the Phase I and II lifting body wind tunnel models. (The Phase II model is painted for oil flow testing). A two-dimensional underslung inlet was integrated into the flat bottom. The nose and boattail shapes changed significantly to accommodate the payload and ramjet combustor, respectively. A vertical tail was added for directional stability and control.

Figure 6 compares the Phase I and II blended wing-body wind tunnel models. The Phase I arrow wing was replaced with a partial M-wing to provide more lift and trailing edge area for controls outboard of the body-wing blending point. Twin vertical tails were also added. The blended body was a boost-glide vehicle and, therefore, required no inlet.

The impact of constraint integration on L/D was found to be configuration dependent as indicated in Figure 7. The noncircular body L/D improved for two reasons. First, portions of the nose side walls were cut away and the nose reshaped to integrate the inlets and payload. This reduced nose wave drag<sup>25</sup>. Second, to meet stability and control requirements a wing was added which improved L/D. Wing area was also added to the lifting body, but the reduction in nose fineness ratio to accommodate the payload offset the benefits of the wing and L/D decreased slightly. The blended body L/D also decreased slightly primarily due to the addition of the vertical tails. Measured lift-to-drag ratios are significantly greater than conventional circular missiles.

Oil flow data were obtained on the Phase II configurations and were used to identify flow interference regions<sup>29</sup>. Figure 8 is an example of the quality and detail of the oil flow data obtained. This is a top view of the M-wing portion of the blended wing body at supersonic Mach numbers and 10 degrees angle of attack. Note the strong interactions which develop at the M-wing notch. Although this interference region did not appreciable change aerodynamic characteristics, it would greatly increase local heating.

This Phase II data base has served primarily for point of departure configurations. For example, the blended wing-body was the point of departure for the flight demonstration configuration<sup>13</sup>.

Phase III testing<sup>20,21</sup> investigated the aerodynamic and aeroheating trades affecting the noncircular and lifting bodies as shown in Fig. 9. The noncircular body low-wing/high-wing trade<sup>30</sup> identified the high wing as having better aerodynamic and similar heating compared to the low wing. The high heating levels in the wing-duct corner were comparable on both wings. The high wing improved lateral-directional stability without loss of L/D. The high wing noncircular body wing tunnel model is shown in Fig. 10.

The lifting body dihedral trade compared flat wing aerodynamic and aeroheating characteristics to those of a dihedral wing. The dihedral wing was selected as the primary wing because it had lower aeroheating levels, improved lateral-directional stability levels, but only slightly reduced L/D.

This data base complemented the Phase II data base and has been used for points of departure. A few of the features of the various ACM concepts have become almost standard concepts to consider at the beginning of advanced design studies. These features include the high fineness ratio bodies, flat bottom, spatular nose and blended body.

An aerodynamic design rationale was developed during ACM and is applied on some research projects. This rationale is summarized in Fig. 11. For example, a low minimum drag coefficient,  $C_{DMIN}$ , was found experimentally to correlate with a high L/D. The body dominates the missile aerodynamics and the body L/D is dominated by  $C_{DMIN}$ . It was also found that a configuration that had a high L/D at a high supersonic Mach number would also show a high L/D at subsonic Mach numbers. Therefore, the initial aerodynamic design of a high L/D configuration can be done at high Mach number and zero-angle-of-attack. At this condition the aerodynamics can be predicted with more confidence than at low Mach number and moderate angle-of-attack.

The location of the longitudinal center of pressure is sensitive to the ramp angle on the flat bottom noses of ACM shapes. Therefore, proper selection of the nose ramp angle can be used to establish the center of pressure location.

The use of right angle, unfaired corners on streamwise surfaces such as nose-inlet and wing-inlet junctions does not have a significant effect on drag and stability. Although local interference heating was measured in the wind tunnel, the increase in heating was small if the corners do not have compression surfaces relative to the freestream.

The flat bottom shapes improve maneuverability independent of the body cross section shape. This was true for every ACM shape wind tunnel tested. This improved maneuver capability coupled with the use of a spatular nose to locate the longitudinal center of pressure, results in very desirable maneuver design characteristics at high angle of attack.

Although corners do not have a strong effect on aerodynamics, local bending reduces drag if it decreases frontal area. Therefore, only blending that reduces volume is desirable.

Although the ACM program included design development and layouts, this information has not been used directly in advanced design. The requirements for each advanced design activity are so different that it is a virtual impossibility that the ACM Phase III concepts would be compatible with all the system constraints. In effect, the Phase III concepts serve as examples of what can be done under a specific set of constraints.

#### FUTURE FLIGHT TEST PLANS

Validation of ACM concepts to date has been limited to the wind tunnel programs described above. The next step, which would involve a flight demonstration, has been investigated in the three task Low Cost ACM Demonstration study<sup>13</sup>.

Task I explored a wide range of low cost approaches to full-scale flight validation of the ACM concepts. Both air launch and ground launch modes were included in the study. For the air launch four aircraft, the B-52, F-15, F-4 and F-100 were selected for study. For each of these, an assessment was made of the ACM placement, compatibility and size, the aircraft performance, the booster required to achieve flight test conditions, pre-flight qualification requirements and costs, and test operations costs.

Candidate solid rocket motor systems were evaluated for both ground launch and air launch platforms to satisfy specified end-of-boost Mach number and altitude requirements for a range of payload weights. Twenty-seven candidate rocket motors were screened for applicability. No airbreathing propulsion options were considered because of their increased cost and risk.

Major Government test ranges were investigated for ACM launch support, boundaries, limiting flight times, instrumentation, safety limitations, and costs.

Equipment was surveyed for applicability to the ACM program using performance, availability, cost, reliability, weight, and volume as major screening parameters. Surplus equipment and equipment available in current programs provided the prime candidates for this effort.

From the results of Task I, two flight test options were recommended for a detailed design synthesis in Task II. These options included a ground and B-52 launch at Vandenberg Air Force Base (VAFB) of a non-recoverable and a recoverable blended wing-body ACM. The flight proven ARIES booster was selected for both the ground and air launch modes. This economically attractive booster, derived from the Minuteman I second stage surplus hardware, provides growth capability in payload and Mach number.

Figure 12 shows a typical ground launch scenario using the ARIES booster. The ACM is mounted in tandem with the booster. Booster thrust vector control is used to control the combination until payload separation after booster burnout. The ACM then climbs to its maximum altitude and begins preprogrammed maneuvers.

Figure 13 depicts the B-52 launch procedure. A strap-on ACM mounting is used to provide aerodynamic stability during the unpowered drop from the X-15 pylon on the B-52. The booster ignites and climbs using thrust vector control. At burnout, separation occurs and the ACM achieves the same trajectory as for the ground launch.

Task II resulted in design layouts, mass properties, aerodynamic characteristics, flight envelope, structural design, and equipment selection and packaging for the ground and air launch versions. Both recoverable and non-recoverable ACM concepts were detailed. Both concepts have identical external dimensions, but differ in internal packaging and structural arrangement. Vehicle geometry was maintained identical to that of the wind tunnel model tested in the ACM development program. Figure 14 summarizes the major design features of the two vehicles and two launch options.

Figure 15 shows the external lines of the blended wing-body configuration. Throughout the design effort a major goal was to maintain the external geometry identical to that of the wind tunnel model tested in the original ACM program. It has an M-wing with twin vertical tails mounted at the span station where the M-wing begins blending into the body. All leading edges are sharp.

The entire structure is stainless steel. The structure consists of both machined parts and thin skin stringer construction. Volume is provided for tungsten ballast. Equipment is either attached to bulkheads, or mounted on frames. Figure 16 shows the general packaging arrangement of the two options.

For Option I, the recovery system is packaged within a smooth container to minimize fouling during deployment. Major subsystems must be packaged in the nose because of the large volume required by this recovery system. The recovery system container could also be used as a large payload bay if recovery were not desired. For the non-recovery option two bays are provided for payloads.

The internal compartments are all lined with Min-K insulation for thermal protection of the equipment. Because existing equipment is being used, the volumetric packaging is not efficient and abundant volume is available for insulation. An independent hydraulic actuator is used for each flap to provide pitch and roll deflections.

The performance boundaries for the stainless steel vehicle design are shown in Figure 17. Because aerodynamic controls are used, a control effectiveness boundary exists at low Mach number or high altitude. At high Mach number a temperature limit exists on the sharp, stainless steel leading edge. At low altitude and high Mach number, the structural g-limit sets the boundary.

The selected ARIES I is a surplus Minuteman second stage (M56A-1) refurbished by Space Vector Corporation, Northridge, California. Its primary use beginning in 1973 has been for launching atmospheric probes for NASA and the Air Force Geophysics Laboratory (AFGL). Most of these launches have been at White Sands Missile Range. The ARIES was also used for the private enterprise Conestoga I launch in Matagorda, Texas.

Figure 18 and 19 show the two booster mounting arrangements. The ground launch version requires an interstage adapter between the ACM and ARIES. The air launch, strap-on concept requires a nose fairing, cradle for the ACM and a cradle for attaching the B-52.

A typical boost-glide trajectory is shown in Fig. 20. The angle of attack for maximum L/D was held to impact so that this trajectory represents a maximum range case.

A factor of safety of 2.0 was applied to all loads used in the ACM structural analysis. This is consistent with no structural ground testing and therefore results in a lower cost, although heavier, design.

The selection of equipment was made with performance and low cost as the two primary criteria. A low total program cost is achieved by selecting equipment already available at the contractor's facility. This not only reduces cost of the equipment, but also reduces engineering manhours because of familiarity with the subsystems and availability of checkout equipment.

The autopilot is configured for pitch damping, roll control and preprogrammed pitch deflections. This is particularly important at high altitudes where dynamic pressure is low and response times large.

Vandenberg Air Force Base (VAFB) was selected because it imposes little restriction on the vehicle design and flight profiles. With respect to most test ranges it has similar subsystem requirements, but has much larger launch corridors and flight distances and can accommodate both ground and air launches. Typical of most ranges, VAFB requires the following subsystems: a transponder for tracking; a pyrotechnic destruct system which is a backup to an aerodynamic destruct system; and a telemetry system compatible with their receivers.

Both ground and air launches are common occurrences. Ground launches due west are typical as shown in Fig. 21 for a typical ground track. However, recovery and the need for aircraft for telemetry under these conditions increases cost because of the distances from shores. Air launches parallel with the coast reduce recovery costs but increase range safety analysis costs.

A launch facility exists at VAFB for the ARIES. As a consequence, no significant cost is incurred in facilities development. The facility is a refurbished Atlas launch complex prepared for the High Performance Target Measurement program. The existing Atlas gantry is used for a missile support building and a new control center and instrumentation room has been added.

A three-flight program of increasing complexity was proposed. The primary purpose is to demonstrate the basic aerodynamic control characteristics of the ACM vehicle. Figure 22 summarizes the flight program for the ground and air launch options.

In Task III, an experimental flight program was formulated and a total program cost analysis was conducted. A three flight program was developed to meet the experimental objectives which include demonstration of: 1) technology required to achieve high L/D, 2) full scale flight aerodynamic coefficients with large viscus forces, 3) high altitude, low dynamic pressure, control characteristics, 4) high maneuver load factor at low angle of attack, and 5) ability to recover demonstration vehicles. These objectives can be accomplished using either ground or air launch options.

An analysis of the program costs was made based on the performance and design definitions developed in this study. Cost estimates were developed for a three flight program with each flight using new hardware of like design, i.e., ground or air launch, recoverable or non-recoverable ACM. As expected, the rough order of magnitude costs show air launch to be more costly than ground launch but the increment between air launch and ground launch is relatively low. Recovery cost estimates are constant for both the air launch and ground launch options. The range of rough order of magnitude costs for these options are between \$9 and \$11 million in 1984 dollars.

Selection of the ARIES booster for the ACM experimental program provides a cost saving ripple effect with several significant features as outlined in Fig. 23. In addition to the ARIES being low cost as the result of originating from the surplus Minuteman I, the booster provides excess performance capability for the ACM flight profiles. This, in turn, permits large design margins for the ACM and allows simplified structural design and structural design analyses. The large design margins eliminates the necessity for structural and structural dynamic testing. The over-designed ACM can be fabricated from standard materials using state-of-the-art fabrication techniques. This allows the structure to be fabricated by small fabrication shops or well equipped model shops. The heavy weight structure permits use of a standard passive thermal protection system and ample volume exists for packaging on-board equipment which facilitates assembly and equipment installation.

Another predominant cost saving feature results from selection of significant equipment from currently active contractor programs. Savings are realized by the use of existing procurement organizations and existing check-out equipment and procedures.

A two-axis control system is proposed for the ACM. As compared to a three-axis system, costs are reduced by simpler mechanism design, less actuators, and reduced software for the pre-programmed flight profiles.

In the category of range and launch support, use of existing range instrumentation support, flying existing flight corridors with short flight durations, and use of the NASA B-52 with the unmodified X-15 pylon, all contribute to low program costs. Recovery cost estimates were minimized for ship recovery through time sharing with naval operations.

#### FUTURE TEST BED PLANS

An important consideration of the flight demonstration vehicle is the ability to serve as a test bed for high speed flight technologies. These may require higher Mach numbers or altitudes, heavier weights, modular changes, more severe maneuver environments or other variations from the current flight envelopes. Because of the excess performance capability of the ARIES booster, these extended flight envelopes can be readily attained. The use of the two stage Minuteman I produces even more growth. These options provide a family of vehicles suitable for various Mach number spectrums from low supersonic to near orbital speeds.

Figure 24 compares the different mounting options of ACM type vehicles on the ARIES, Minuteman I first stage or both stages. Mach numbers from low supersonic to hypersonic are achievable at the end of boost.

New missile designs are required at the higher Mach numbers. Figure 25 shows a hypersonic design which has a blended body but has outboard vertical fins for directional stability and an aft body flare for longitudinal stability. It can, therefore, serve as a test bed at all Mach numbers but will not demonstrate extremely high L/D at lower supersonic speeds.

Any of these concepts can be flown on the variety of trajectories sketched in Fig. 26. Altitude hold flight can be achieved for air-breather simulations. Various maximum range glides simulate boost-glide vehicle flight. Low altitude flights demonstrates various evasive tactics. As a consequence, a wide variety of experiments can be flown at the Mach numbers achievable with the various modular concepts.

#### CONCLUSION

The promise of high lift-to-drag ratio, long range aerodynamic configured missiles has not yet been fulfilled. However, the data base is being used extensively in advanced design studies for points of departure. A flight test plan has been developed to demonstrate ACM technology. Because of the many design trades required to develop a missile design, the full impact of the ACM technologies will probably not be achieved in the next generation missiles. However, shaped missiles will probably appear with L/D's somewhere between conventional and aero-configured concepts in the near future. This will be the first impact of ACM technology on operational vehicles.

#### REFERENCES

1. Aerodynamic Configured Missile Development, Air Force Flight Dynamics Laboratory Contract F33615-77-C-3037 (AFWAL/FIMG), August 1977.
2. Krieger, R. J., et al, "Aerodynamic Configured Missile Development", Final Report, Volume I - Executive Summary, AFWAL-TR-80-3071, September 1980.
3. Krieger, R. J., et al, "Aerodynamic Configured Missile Development", Final Report, Volume II - Configuration Development, AFWAL-TR-80-3071, September 1980.
4. Williams, J. E., Gregoire, J. E., and Hood, R. F., "Aerodynamic Analysis for Missiles - Evaluation of Aerodynamic Prediction Methods", AFWAL-TR-82-3038, June 1982.
5. Gregoire, J. E., and Krieger, R. J., "Aerodynamic Prediction Rationale for Advanced Arbitrarily Shaped Missile Concepts", AIAA Paper 80-0256, January 1980.

6. Gentry, A. E., Smyth, D. N., and Oliver, W. R., "The Mark IV Supersonic-Hypersonic Arbitrary Body Program", AFFDL TR-73-159, November 1973.
7. Krieger, R. J., et al, "Aerodynamic Configured Missile Development", Final Report, Volume III - Missile Aerodynamic Prediction Rationale Using the Hypersonic Arbitrary Body Program, AFWAL-TR-80-3071, July 1980.
8. Bonner, E., Clever, W., and Dunn, K., "Aerodynamic Preliminary Analysis System Part I - Theory", NASA CR-145284, April 1978.
9. Magnus, A. E., and Epton, M. A., "PANAR - A computer Program for Predicting Subsonic or Supersonic Linear Potential Flows About Arbitrary Configurations Using a Higher Order Panel Method", Volume I, Theory Document, NASA CR-3251, 1980.
10. "Missile Aerodynamic Design Method", Air Force Wright Aeronautical Laboratory, Contract F33615-84-C-3002, August 1984.
11. Wardlaw, A. B., et al, "An Inviscid Computational Method for Supersonic Missile Type Bodies - Program Description and User's Guide", NSWC TR 81-459, December 1981.
12. Jeschke, M. C. and Rasmussen, M. L., "Experimental Results for Surface Pressures on Cone Derived Waveriders in the Mach Number Range 3 to 5", AIAA Paper 82-0249, January 1982.
13. Krieger, R. J., et al, "Low Cost ACM Demonstrator", AFWAL-TR-84-3003, February 1984.
14. Lanham, D. L., "Static Force and Pressure Tests of the Aerodynamic Configured Missiles (ACM) at Mach Numbers 3.0 to 5.5", AEDC-TSR-78-V32, September 1978.
15. Crosby, W. A., "Supersonic Static Force and Moment and Oil Flow Tests of the Aerodynamic Configured Missiles", AEDC-TSR-79-V38, July 1979.
16. Stewart, V. W., "Documentation of Static Stability Tests of Aerodynamic Configured Missiles at Subsonic and Transonic Mach numbers", AEDC-TSR-78-P37, September 17, 1978.
17. Krieger, R. J., et al, "Aerodynamic Configured Missile Development", Final Report, Volume IV - Phase I Experimental Program, AFWAL-TR-80-3071, July 1980.
18. Lanham, D. L., "Static Force and Oil Flow Visualization Tests of Aerodynamic Configured Missiles at Mach Numbers 2.5 to 5.0", AEDC-TSR-79-V54, September 1979.
19. Krieger, R. J., et al, "Aerodynamic Configured Missile Development", Final Report, Volume V - Phase II Experimental Program, AFWAL-TR-80-3071, August 1980.
20. Wannewetsch, G., "Static Force, Heat Transfer, and Pressure Tests of Two Aerodynamic Configured Missile (ACM) concepts at Mach Numbers 2.5 to 5.0", AEDC-TSR-80-V20, April 1980.
21. Krieger, R. J., et al, "Aerodynamic Configured Missile Development", Final Report, Volume VI - Phase III Experimental Program, AFWAL-TR-80-3071, September 1980.
22. Krieger, R. J., et al, "Aerodynamic Configured Missile Development", Final Report, Volume II - Appendix A - Aerodynamic Configured Missile Reference Library Summary, AFWAL-TR-80-3071, July 1980.
23. Krieger, R. J., "Aerodynamic Design Criteria for Supersonic Climb-Cruise Missiles", AIAA Paper 79-1671, August 1979.
24. Krieger, R. J., et al, "Aerodynamic Configured Missile Development", Final Report, Volume II - Appendix B - Relations Between Aerodynamic Characteristics and Performance, AFWAL-TR-80-3071, July 1980.
25. Krieger, R. J., "A Technique for Developing Low Drag Nose Shapes for Advanced Supersonic Missile Concepts", AIAA Paper 80-0361, January 1980.
26. Krieger, R. J., Gregoire, J. E., and Hood, R. F., "Unconstrained Supersonic Cruise and Maneuvering Configuration Concepts", AIAA Paper 79-0229, January 1979.
27. Gregoire, J. E., "PANAIR vs. S/HABP: An Evaluation of Two Diverse Approaches to Supersonic Missile Aerodynamics Analysis", AIAA Paper 83-0008, January 1983.
28. Hood, R. F., Krieger, R. J., and Gregoire, J. E., "The Impact of Constraints on Advanced Supersonic Cruise and Maneuvering Missile Concepts", AIAA Paper 80-0257, January 1980.
29. Krieger, R. J., Hood, R. F., and Gillies, D. S., "Correlation of Oil Flow and Aerodynamic Characteristics of Arbitrarily Shaped Advanced Missile Concepts", AIAA Paper 80-1560, August 1980.
30. Gregoire, J. E., and Krieger, R. J., "Aerodynamic Trades Leading to the Development of an Advanced Airbreathing Missile Concept", AIAA Paper 80-1577, August 1980.

11-5404A  
11-9-84

| OCCUPANCY HOURS      | PHASE      |           |           | TOTAL |
|----------------------|------------|-----------|-----------|-------|
|                      | I          | II        | III       |       |
| RUNS                 | 162        | 95        | 85        | 355   |
| FORCE & MOMENT       | 338        | 194       | 29        | 561   |
| PRESSURE             | 34         | 17        | 83        | 104   |
| ON.                  | 14         | 76        | 4         | 94    |
| HEAT TRANSFER        | 0          | 0         | 76        | 76    |
| TOTAL RUNS           | 364        | 287       | 165       | 816   |
| TOTAL CONFIGURATIONS | 27         | 14        | 5         | --    |
| MACH RANGE           | 0.8 - 6.5  | 2.5 - 6.0 | 2.5 - 6.0 | --    |
| ANGLE-OF-ATTACK      | -20 TO +20 | -5 TO +20 | -5 TO +20 | --    |

FIGURE 1 SUMMARY OF ACM DATA BASE

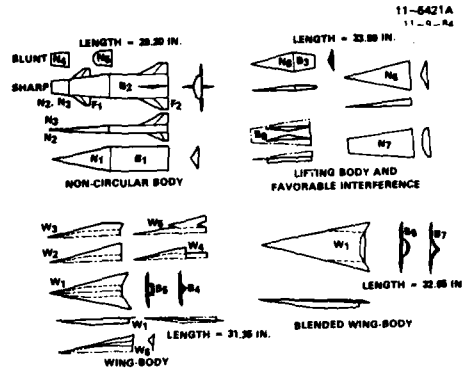


FIGURE 2 PHASE I WIND TUNNEL MODELS

11-5403A  
11-9-84

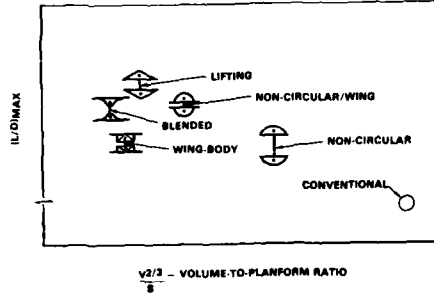


FIGURE 3 PHASE I L/D COMPARISONS

11-1085A  
11-9-84

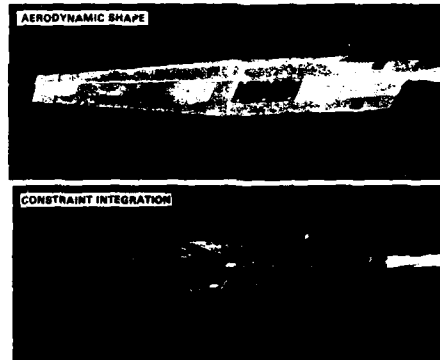


FIGURE 4  
COMPARISON OF PHASE I AND II  
NON-CIRCULAR BODIES

11-1086A  
11-9-84

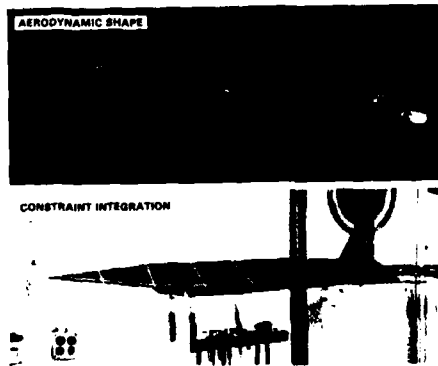


FIGURE 5  
COMPARISON OF PHASE I AND II  
LIFTING BODIES

11-1087A  
11-9-84

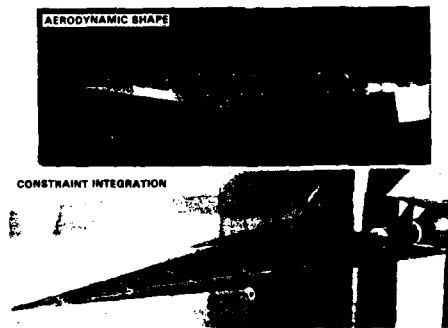


FIGURE 6  
COMPARISON OF PHASE I AND II BLENDED  
WING-BODIES

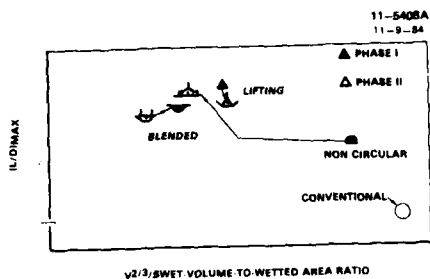


FIGURE 7  
PHASE I AND II MEASURED  
L/D COMPARISONS



FIGURE 8  
M-WING OIL FLOW PATTERNS

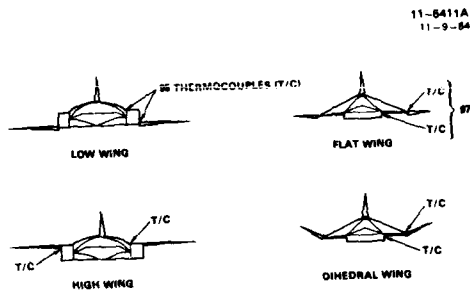


FIGURE 9  
NON-CIRCULAR AND  
LIFTING BODIES AERODYNAMIC  
AND HEATING TRADES



FIGURE 10  
PHASE III NON-CIRCULAR BODY

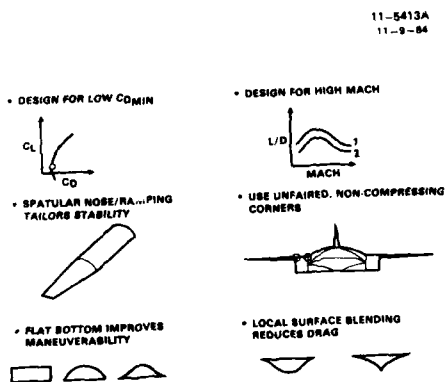


FIGURE 11  
AERODYNAMIC DESIGN  
RATIONALE DEVELOPED FROM ACM

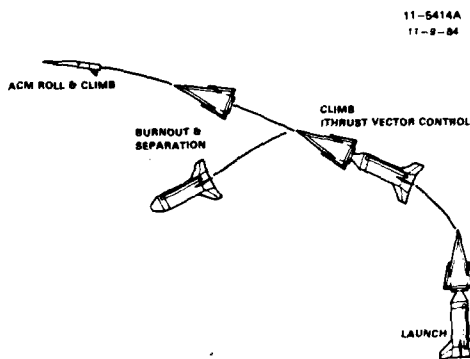
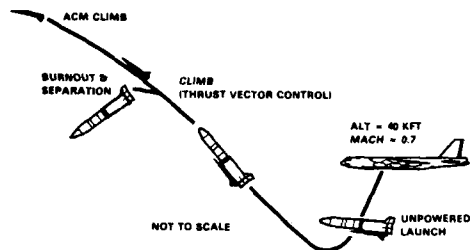


FIGURE 12  
ARIES GROUND LAUNCH SCENARIO



11-5422A  
11-9-84



**FIGURE 13**  
**B-52/ ARIES LAUNCH SCENARIO**

11-5402A  
11-9-84

| DESIGN FEATURE         | SELECTION                  |
|------------------------|----------------------------|
| AIRFRAME MATERIAL      | STEEL                      |
| CONSTRUCTION TECHNIQUE | THIN SKIN/STRINGER         |
| HEAT PROTECTION        | MIN-K INSULATION           |
| GUIDANCE               | ROLL CONTROL/PITCH DAMPING |
| ACTUATORS              | HYDRAULIC                  |
| RUDDER CONTROL         | NONE                       |
| AVIONICS               | HARPOON                    |
| INTERSTAGE ADAPTOR     | EXPLOSIVE BOLTS            |

**FIGURE 14**  
**BLENDED WING-BODY**  
**DESIGN FEATURES**

11-5415A  
11-9-84

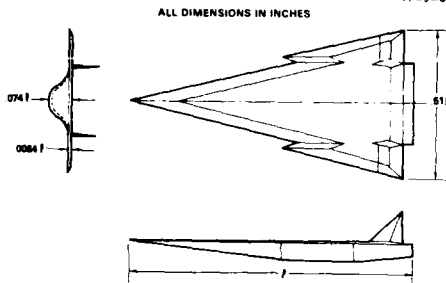


**FIGURE 15**  
**BLENDED WING-BODY CONFIGURATION**

11-5450A  
11-9-84

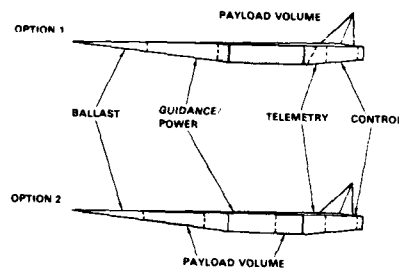


**FIGURE 16**  
**SUBSYSTEM**  
**PACKAGING ARRANGEMENT**

11-5406A  
11-9-84

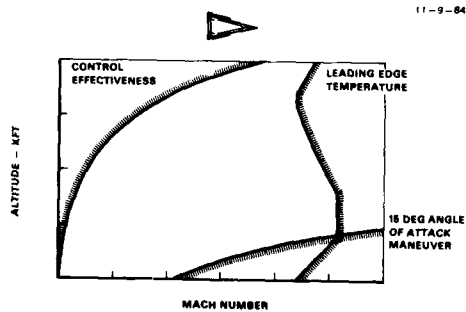


**FIGURE 17**  
**PERFORMANCE BOUNDARIES**

11-5467A  
11-9-84

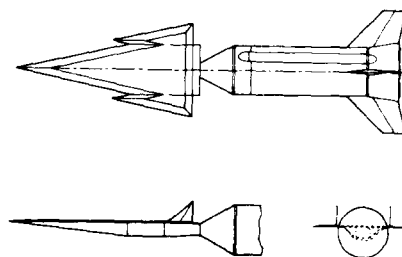


**FIGURE 18**  
**TANDEM ACM/ARIES**  
**GROUND LAUNCH CONCEPT**

11-5468A  
11-9-84

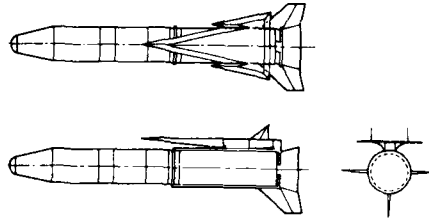


**FIGURE 19  
STRAP-ON ACM/ARIES  
LAUNCH CONCEPT**

11-5416A  
11-9-84

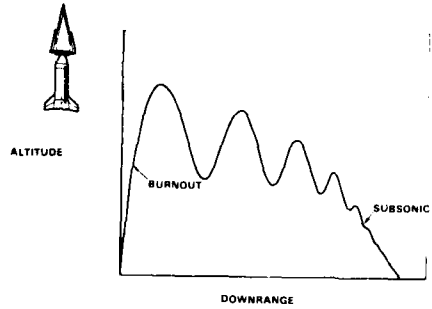


**FIGURE 20  
TYPICAL BOOT-GLIDE TRAJECTORY**

11-5405A  
11-9-84

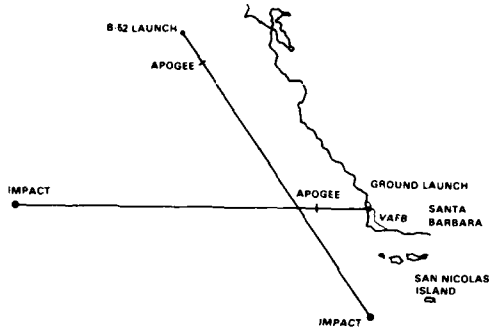


**FIGURE 21  
TYPICAL GROUND TRACKS**

11-5401A  
11-9-84

|                      | PROGRAM 1         | PROGRAM 2         |
|----------------------|-------------------|-------------------|
| • VEHICLE            | BLENDED WING BODY | BLENDED WING BODY |
| • RECOVERY           | NO                | YES               |
| • FLIGHTS            | 3                 | 3                 |
| • LAUNCH MODE        | GROUND            | B 52 X 15 PYLON   |
| • BOOSTER            | ARIES TANDEM      | ARIES STRAP ON    |
| • MAX ALTITUDE (KFT) | 125, 150, 200     | 125, 150, 200     |
| • LAUNCH SITE        | VAFB              | EAFB/VAFB         |



**FIGURE 22  
SUMMARY OF TWO  
FLIGHT TEST PROGRAMS**

11-5425A  
11-9-84

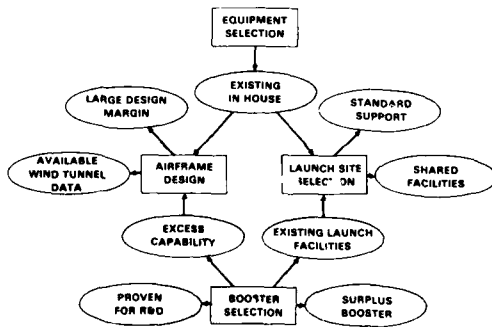


**FIGURE 23  
COST REDUCING FEATURES OF  
THE FLIGHT TEST PROGRAM**

11-5410A  
11-9-84

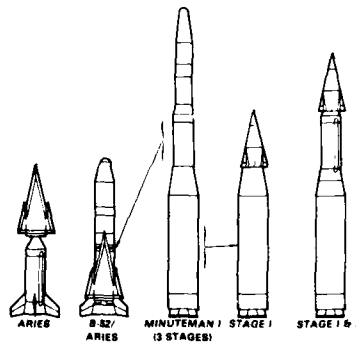


**FIGURE 24  
TYPICAL MINUTEMAN/ACM  
LAUNCH CONCEPTS**

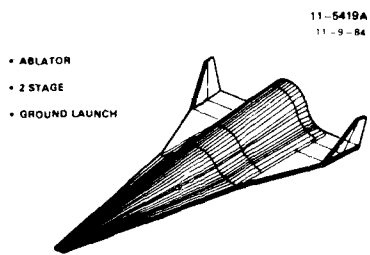


**FIGURE 25**  
**HYPERSONIC BLENDED**  
**WING-BODY CONCEPT**

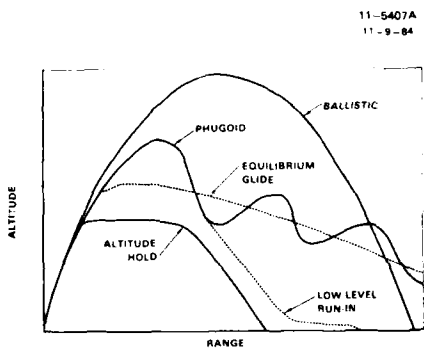


**FIGURE 26**  
**TYPICAL TRAJECTORY SIMULATIONS**

| REPORT DOCUMENTATION PAGE     |   |                      |  |          |        |                             |             |             |  |
|-------------------------------|---|----------------------|--|----------|--------|-----------------------------|-------------|-------------|--|
| 1. Recipient's Reference      | 2. Originator's Reference   | 3. Further Reference | 4. Security Classification of Document |          |        |                             |             |             |  |
|                               | AGARD-R-754   | ISBN 92-835-0452-6   | UNCLASSIFIED                           |          |        |                             |             |             |  |
| 5. Originator                 | Advisory Group for Aerospace Research and Development<br>North Atlantic Treaty Organization<br>7 rue Ancelle, 92200 Neuilly sur Seine, France   |                      |  |          |        |                             |             |             |  |
| 6. Title                      | SPECIAL COURSE ON MISSILE AERODYNAMICS  |                      |  |          |        |                             |             |             |  |
| 7. Presented at               |   |                      |  |          |        |                             |             |             |  |
| 8. Author(s)/Editor(s)        | Various   |                      | 9. Date                                |          |        |                             |             |             |  |
|                               |   |                      | April 1988                             |          |        |                             |             |             |  |
| 10. Author's/Editor's Address | Various   |                      | 11. Pages                              |          |        |                             |             |             |  |
|                               |   |                      | 474                                    |          |        |                             |             |             |  |
| 12. Distribution Statement    | This document is distributed in accordance with AGARD policies and regulations, which are outlined on the Outside Back Covers of all AGARD publications.  |                      |  |          |        |                             |             |             |  |
| 13. Keywords/Descriptors      | <table border="0"> <tr> <td>Missiles</td> <td>Design</td> </tr> <tr> <td>Aerodynamic characteristics</td> <td>Predictions</td> </tr> <tr> <td>Computation</td> <td></td> </tr> </table>   |                      |  | Missiles | Design | Aerodynamic characteristics | Predictions | Computation |  |
| Missiles                      | Design  |                      |  |          |        |                             |             |             |  |
| Aerodynamic characteristics   | Predictions   |                      |  |          |        |                             |             |             |  |
| Computation                   |   |                      |  |          |        |                             |             |             |  |
| 14. Abstract                  | <p>This series of lectures supported by the AGARD Fluid Dynamics Panel and the Von Kármán Institute (VKI) presents the current state of the art in fundamental knowledge and in practical predictive methods in tactical missile aerodynamics. The course is divided into twelve lectures.</p> <p>The first lecture gives a survey of aerodynamic problems encountered on existing and future missiles and of the most important predictive methods. This introduction is followed by a lecture on the criteria that define the required prediction accuracy in terms of allowable errors in missile performance and design parameters. The third lecture covers nonlinear aerodynamic effects including formation of flow separation vortices, vortex wakes and vortical interference, and nonlinear compressibility due to presence of shocks.</p> <p>Several lectures present engineering computation methods used for calculating stability and control for conventional and unconventional missiles. These methods are illustrated by numerous practical examples. They fall into two categories: semi-empirical methods which are based on the equivalent angle-of-attack concept and numerical methods, much more recent, which are based on the resolution of the steady and the unsteady Euler equations with flow separation vortices. The prediction of dynamic derivatives is also presented with a description of the experimental methods.</p> <p>An extensive lecture describes the role of the intake in the propulsion system of turbojet and ramjet powered missiles and addresses both the internal and external aerodynamic aspects of the induction system. A specific paper presents a computer-aided design procedure for use in conceptual design for sizing and shaping supersonic airbreathing missiles. Two other lectures cover respectively the prediction of aerodynamic heating and base flows with and without propulsion. Finally the design of the next generation supersonic and hypersonic missiles is discussed.</p> |                      |  |          |        |                             |             |             |  |

|   |   |   |   |
|---|---|---|---|
| <p>AGARD Report No.754<br/>Advisory Group for Aerospace Research and Development,NATO<br/>SPECIAL COURSE ON MISSILE AERODYNAMICS<br/>Published April 1988<br/>474 pages</p> <p>This series of lectures supported by the AGARD Fluid Dynamics Panel and the Von Kármán Institute (VKI) presents the current state of the art in fundamental knowledge and in practical predictive methods in tactical missile aerodynamics. The course is divided into twelve lectures.</p> <p>The first lecture gives a survey of aerodynamic problems encountered on existing and future missiles and of the most important predictive methods. This introduction is followed by a lecture on the criteria that define the P.T.O</p> | <p>AGARD-R-754</p> <p>Missiles<br/>Aerodynamic characteristics<br/>Computation<br/>Design<br/>Predictions</p> | <p>AGARD Report No.754<br/>Advisory Group for Aerospace Research and Development,NATO<br/>SPECIAL COURSE ON MISSILE AERODYNAMICS<br/>Published April 1988<br/>474 pages</p> <p>This series of lectures supported by the AGARD Fluid Dynamics Panel and the Von Kármán Institute (VKI) presents the current state of the art in fundamental knowledge and in practical predictive methods in tactical missile aerodynamics. The course is divided into twelve lectures.</p> <p>The first lecture gives a survey of aerodynamic problems encountered on existing and future missiles and of the most important predictive methods. This introduction is followed by a lecture on the criteria that define the P.T.O</p> | <p>AGARD-R-754</p> <p>Missiles<br/>Aerodynamic characteristics<br/>Computation<br/>Design<br/>Predictions</p> |
| <p>AGARD Report No.754<br/>Advisory Group for Aerospace Research and Development,NATO<br/>SPECIAL COURSE ON MISSILE AERODYNAMICS<br/>Published April 1988<br/>474 pages</p> <p>This series of lectures supported by the AGARD Fluid Dynamics Panel and the Von Kármán Institute (VKI) presents the current state of the art in fundamental knowledge and in practical predictive methods in tactical missile aerodynamics. The course is divided into twelve lectures.</p> <p>The first lecture gives a survey of aerodynamic problems encountered on existing and future missiles and of the most important predictive methods. This introduction is followed by a lecture on the criteria that define the P.T.O</p> | <p>AGARD-R-754</p> <p>Missiles<br/>Aerodynamic characteristics<br/>Computation<br/>Design<br/>Predictions</p> | <p>AGARD Report No.754<br/>Advisory Group for Aerospace Research and Development,NATO<br/>SPECIAL COURSE ON MISSILE AERODYNAMICS<br/>Published April 1988<br/>474 pages</p> <p>This series of lectures supported by the AGARD Fluid Dynamics Panel and the Von Kármán Institute (VKI) presents the current state of the art in fundamental knowledge and in practical predictive methods in tactical missile aerodynamics. The course is divided into twelve lectures.</p> <p>The first lecture gives a survey of aerodynamic problems encountered on existing and future missiles and of the most important predictive methods. This introduction is followed by a lecture on the criteria that define the P.T.O</p> | <p>AGARD-R-754</p> <p>Missiles<br/>Aerodynamic characteristics<br/>Computation<br/>Design<br/>Predictions</p> |

|   |   |
|---|---|
| <p>required prediction accuracy in terms of allowable errors in missile performance and design parameters. The third lecture covers nonlinear aerodynamic effects including formation of flow separation vortices, vortex wakes and vortical interference, and nonlinear compressibility due to presence of shocks.</p> <p>Several lectures present engineering computational methods used for calculating stability and control for conventional and unconventional missiles. These methods are illustrated by numerous practical examples. They fall into two categories: semi-empirical methods which are based on the equivalent angle-of-attack concept and numerical methods, much more recent, which are based on the resolution of the steady and the unsteady Euler equations with flow separation vortices. The prediction of dynamic derivatives is also presented with a description of the experimental methods.</p> <p>An extensive lecture describes the role of the intake in the propulsion system of turbojet and ramjet powered missiles and addresses both the internal and external aerodynamic aspects of the induction system. A specific paper presents a computer-aided design procedure for use in conceptual design for sizing and shaping supersonic airbreathing missiles. Two other lectures cover respectively the prediction of aerodynamic heating and base flows with and without propulsion.</p> <p>Finally the design of the next generation supersonic and hypersonic missiles is discussed.</p> | <p>required prediction accuracy in terms of allowable errors in missile performance and design parameters. The third lecture covers nonlinear aerodynamic effects including formation of flow separation vortices, vortex wakes and vortical interference, and nonlinear compressibility due to presence of shocks.</p> <p>Several lectures present engineering computational methods used for calculating stability and control for conventional and unconventional missiles. These methods are illustrated by numerous practical examples. They fall into two categories: semi-empirical methods which are based on the equivalent angle-of-attack concept and numerical methods, much more recent, which are based on the resolution of the steady and the unsteady Euler equations with flow separation vortices. The prediction of dynamic derivatives is also presented with a description of the experimental methods.</p> <p>An extensive lecture describes the role of the intake in the propulsion system of turbojet and ramjet powered missiles and addresses both the internal and external aerodynamic aspects of the induction system. A specific paper presents a computer-aided design procedure for use in conceptual design for sizing and shaping supersonic airbreathing missiles. Two other lectures cover respectively the prediction of aerodynamic heating and base flows with and without propulsion.</p> <p>Finally the design of the next generation supersonic and hypersonic missiles is discussed.</p> |
| <p>required prediction accuracy in terms of allowable errors in missile performance and design parameters. The third lecture covers nonlinear aerodynamic effects including formation of flow separation vortices, vortex wakes and vortical interference, and nonlinear compressibility due to presence of shocks.</p> <p>Several lectures present engineering computational methods used for calculating stability and control for conventional and unconventional missiles. These methods are illustrated by numerous practical examples. They fall into two categories: semi-empirical methods which are based on the equivalent angle-of-attack concept and numerical methods, much more recent, which are based on the resolution of the steady and the unsteady Euler equations with flow separation vortices. The prediction of dynamic derivatives is also presented with a description of the experimental methods.</p> <p>An extensive lecture describes the role of the intake in the propulsion system of turbojet and ramjet powered missiles and addresses both the internal and external aerodynamic aspects of the induction system. A specific paper presents a computer-aided design procedure for use in conceptual design for sizing and shaping supersonic airbreathing missiles. Two other lectures cover respectively the prediction of aerodynamic heating and base flows with and without propulsion.</p> <p>Finally the design of the next generation supersonic and hypersonic missiles is discussed.</p> | <p>required prediction accuracy in terms of allowable errors in missile performance and design parameters. The third lecture covers nonlinear aerodynamic effects including formation of flow separation vortices, vortex wakes and vortical interference, and nonlinear compressibility due to presence of shocks.</p> <p>Several lectures present engineering computational methods used for calculating stability and control for conventional and unconventional missiles. These methods are illustrated by numerous practical examples. They fall into two categories: semi-empirical methods which are based on the equivalent angle-of-attack concept and numerical methods, much more recent, which are based on the resolution of the steady and the unsteady Euler equations with flow separation vortices. The prediction of dynamic derivatives is also presented with a description of the experimental methods.</p> <p>An extensive lecture describes the role of the intake in the propulsion system of turbojet and ramjet powered missiles and addresses both the internal and external aerodynamic aspects of the induction system. A specific paper presents a computer-aided design procedure for use in conceptual design for sizing and shaping supersonic airbreathing missiles. Two other lectures cover respectively the prediction of aerodynamic heating and base flows with and without propulsion.</p> <p>Finally the design of the next generation supersonic and hypersonic missiles is discussed.</p> |